

From Terahertz to X-ray: Developing New Graphene-Based Photodetector Technologies

Thesis submitted for the degree of
Doctor of Philosophy
at the University of Leicester

by

Jamie Oscar David Williams MPhys (Manc)
Department of Physics and Astronomy
University of Leicester

2018

From Terahertz to X-ray: Developing New Graphene-Based Photodetector Technologies

Jamie Oscar David Williams

Department of Physics and Astronomy, University of Leicester

Abstract

The latest technological developments have resulted in a push for faster, cheaper and simpler photodetector technologies across a wide range of temperatures, wavelengths and sensitivities for use in industrial and research applications.

Graphene, a 2D allotrope of carbon, is seen as an interesting route for future photodetectors. Recent research into graphene has focussed on fundamental physics, fabrication processes and future commercial applications. Fundamental research has demonstrated many interesting properties, including the potential for high carrier mobility, high conductivity, approximately constant photon absorption and extreme tensile strength. These properties led to promising developments for graphene-based photodetectors, such as the demonstration of ultrafast photodetection on a femtosecond timescale for pulsed lasers.

This document discusses novel graphene-based photodetector technologies from concept to theory, design, fabrication and experimental demonstration. Three detectors, from terahertz to X-ray, were fabricated in essentially the same graphene field effect transistor (GFET) structure, with photons coupling to different components of the detector to provide a measurable photosignal.

A simulated cryogenic, colour sensitive, bilayer graphene single photon counting photodetector exploited the tuneable band gap of bilayer graphene to trade-off resolution against temperature to enable higher temperature operation, requiring less

costly and complex cryogenics, with photons coupling directly to the bilayer graphene. The passive terahertz detector utilised photons from a broadband terahertz source coupling to antennae to generate a photoresponse via the Dyakonov-Shur effect with an $NEP = 0.85 \pm 0.15 \mu\text{WHz}^{-0.5}$, with further work ongoing to demonstrate narrowband terahertz detection. The X-ray GFET was developed to investigate the energy sensitivity to X-ray photons coupling to the absorber based on work in the literature, where charge carrier modulation generates a field that changed the conductivity of the graphene channel. Using pulsed optical lasers to probe the behaviour and sensitivity of the detector gave $\Delta E \sim 480 \text{keV}$ (for $E = 30 \text{MeV}$) with a photoresponse dependent on the gate voltage. No X-ray sensitivity was observed for Fe-55 sources, but it was observed for an X-ray generator; this inconsistency possibly suggests a different mechanism, such as bolometry, to that proposed previously in the literature.

Acknowledgements

There are many people I would like to acknowledge for their input to my work over the last few years. Firstly, I would like to express my enormous gratitude to my supervisors, Jon Lapington, Ian Hutchinson and Mervyn Roy, for their patience, help, support, discussions and ideas over the years, and for their contributions to the papers that have been published in the last few years [1] [2] [3]. I would especially like to thank Jon for the opportunity to explore a wide range of fields including cryogenics, electrical engineering, physics and chemical engineering and the opportunity to lead the EXPRO+ contract with the European Space Agency. Jon and I have had many invaluable discussions about the physics, the results from simulations and experiments from each of the detectors, and ways in which the response could be improved. I would also like to thank Jon for driving me to NPL five times and to Aston University once. My thanks go to Mervyn Roy for the discussions about the fundamental properties of graphene, the theory and mechanisms of the bilayer graphene detector, and the issues that I had when I first started coding the simulations.

I would like to thank the European Space Agency for funding the research into the Terahertz and X-ray detectors. I would especially like to thank Elena Saenz and Alan Owens for the many invaluable discussions about the initial requirements of the Terahertz detector and X-ray detector, respectively, as part of the EXPRO+ contract.

I would like to acknowledge the contribution of those the Hofmann Group at the University of Cambridge who helped me with the fabrication of the devices whilst I was based there in autumn 2015, and their help with the authorship of the Sensors paper in 2016 [2]. I would especially like to thank Jack Alexander-Webber as, without his help and patience, I would not have been able to work on the devices I used for the experimental chapters. I would like to express my gratitude to Stephan Hofmann for giving me the opportunity to work in Cambridge, and for the significant contribution to the Sensors paper [2] that now forms part of section 5.3.1. I would also like to thank Piran Kidambi, Abhay Sagade, Marie-Blandine Martin, Philipp Braueninger-Weimer, Ruizhi Wang, Andrea Cabrero Vilatela in the Hofmann group, and many others at CAPE such as Lorenzo d'Arsie and Andrea de Luca, who taught me the techniques and

advised and helped me through the manufacturing process while I was in Cambridge. I would like to acknowledge the discussions with Jack and Abhay that concluded upon ITO being a potential for the top gate for the bilayer graphene device.

I must also thank several others who have contributed in some way to the work in my thesis. Gauthier Torricelli helped me with the initial theory at the very start of my PhD and wrote some of the code to output the density of states for bilayer graphene, whilst the late George Fraser helped and advised me with the project in the initial few months in his unique way. With regards to the experimental testing of the bilayer graphene detector, I would like to acknowledge the contribution of Rob Limpenny and Luis Mendoza, both of whom provided critical support while I was working on the cryogenic fridge. Without Rob, for instance, I would have been unable to repair the optical fibre feedthrough and hence conduct optical illumination tests at cryogenic temperatures. I would also like to acknowledge the help of the Bioimaging Group in the Department of Physics and Astronomy, and especially Sarah Bugby and Bill McKnight who helped me access the X-ray generator and scintillators.

My significant thanks to Simon Pyatt at the University of Birmingham for wire bonding the devices. I would like to acknowledge the help, support and guidance of Andrei Gorodetsky and Erik Rafailov at Aston University Institute of Physical Technologies, and Mira Naftaly at NPL; without Andrei, Erik and Mira I would not have had the facilities to complete the experimental work with the terahertz sources.

My thanks also go to Andrew Jamieson, formerly at the University of Leicester and now at the University of Glasgow, who raised the potential of graphene acting as a selective protein sensor to build upon his stapled peptide scaffold work and is discussed briefly in this thesis. I would also like to thank the project students who worked with me in 2016 to develop the selective protein sensor concept by identifying a peptide with a potential biomedical application (Rafia Javaid, Shumina Uddin, Kira Rhodes, Arcchana Gajendran, Gabija Petrauskaite and Ridda Mahmood), and to investigate the UV sensitivity of the FUVGFET concept (Alex van den Hof and Amy Mai).

And finally, I want to thank my family and my fiancée, Emma, for being there throughout my PhD, and I would like to apologise to them as I have often been able to

think about little besides this work over the past few years. Whilst all of my family, including my father, Steve, and my mother, Jan, need thanking for everything over the last 26 years, I would also like to acknowledge my late grandfather, Dr Derek Williams, the first research scientist in my family [4] [5] and whom I look to emulate with this thesis.

Table of Contents

| | |
|--|-----------|
| I - PROLOGUE..... | 12 |
| II - LIST OF ACRONYMS..... | 15 |
| III - LIST OF FIGURES AND TABLES..... | 18 |
| CHAPTER 1 - THE ROLE OF GRAPHENE IN THE DEVELOPMENT OF NOVEL PHOTODETECTOR SOLUTIONS | 33 |
| 1.1 <i>Introduction</i> | 33 |
| 1.2 <i>Comparable Photon Counting Photodetector Technologies</i> | 34 |
| 1.2.1 SUPERCONDUCTING TUNNELLING JUNCTION (STJ) | 35 |
| 1.2.2 MICROWAVE KINETIC INDUCTANCE DETECTOR (MKID) | 35 |
| 1.2.3 TRANSITION EDGE SENSOR (TES) | 36 |
| 1.2.4 MICROCHANNEL PLATE PHOTOMULTIPLIER TUBE (MCP-PMT) | 37 |
| 1.2.5 CHARGED COUPLED DEVICE (CCD)..... | 38 |
| 1.2.6 AVALANCHE PHOTODIODES | 38 |
| 1.2.7 SUMMARY OF PHOTODETECTOR TECHNOLOGIES AT DIFFERENT WAVELENGTHS | 39 |
| 1.3 <i>Fundamental Properties of Graphene Relevant to Photodetection</i> | 40 |
| 1.3.1 ELECTRONIC STRUCTURE OF SINGLE LAYER GRAPHENE | 40 |
| 1.3.2 ELECTRONIC STRUCTURE OF BILAYER GRAPHENE..... | 43 |
| 1.3.3 THE FIELD EFFECT AND TRANSPORT PROPERTIES, AND THE EFFECTS OF ADSORBANTS AND SCATTERERS..... | 48 |
| 1.3.4 OPTICAL PROPERTIES..... | 52 |
| 1.3.5 PHONONS IN GRAPHENE | 54 |
| 1.3.5.1 Phonons and Raman Spectroscopy | 54 |
| 1.3.6 HOT ELECTRON CARRIER SCATTERING | 56 |
| 1.3.7 THE EFFECT OF STRAIN ON GRAPHENE | 57 |
| 1.4 <i>Graphene as a Solution for Novel Photodetector Technologies</i> | 58 |
| 1.4.1 USING GRAPHENE FOR VISIBLE PHOTON DETECTION | 60 |
| 1.4.2 USING GRAPHENE FOR TERAHERTZ PHOTODETECTION | 62 |
| 1.4.3 GRAPHENE FOR X-RAY PHOTODETECTION..... | 63 |
| 1.5 <i>Summary</i> | 64 |
| CHAPTER 2 – THEORETICAL STUDIES AND DESIGN OF A BILAYER GRAPHENE SINGLE PHOTON COUNTING PHOTODETECTOR | 66 |
| 2.1 <i>Introduction</i> | 66 |
| 2.2 <i>Developing the Concept</i> | 67 |
| 2.2.1 PHOTOEXCITATION IN BILAYER GRAPHENE | 67 |
| 2.2.2 POSSIBLE RELAXATION PATHS..... | 68 |
| 2.3 <i>Density of States and Optimum Operational Window</i> | 69 |
| 2.4 <i>Developing the Gillespie Algorithm</i> | 71 |
| 2.4.1 PHOTON EXCITATION | 72 |
| 2.4.2 HOLE RELAXATION/VACANCY FILLING | 74 |
| 2.4.3 PHOTOELECTRON RELAXATION..... | 75 |
| 2.5 <i>Simulation Results</i> | 79 |
| 2.5.1 ENERGY CONSERVATION | 79 |

| | | |
|--|---|------------|
| 2.5.2 | CONVERGENCE OF RESULTS | 80 |
| 2.5.3 | NUMBER OF CHARGE CARRIERS PRODUCED AS A FUNCTION OF TIME | 80 |
| 2.5.4 | AVERAGE IONISATION ENERGY, W , AS A FUNCTION OF BAND GAP | 81 |
| 2.5.5 | NUMBER OF CHARGE CARRIERS PRODUCED AS A FUNCTION OF PHOTON ENERGY | 82 |
| 2.5.6 | NUMBER OF CHARGE CARRIERS PRODUCED AS A FUNCTION OF BANDGAP | 85 |
| 2.5.7 | NUMBER OF CHARGE CARRIERS PRODUCED AS A FUNCTION OF THE Π /PHONON RATIO | 86 |
| 2.6 | <i>Detector Design – Finite Differencing Method</i> | 87 |
| 2.6.1 | SIMULATION CONVERGENCE: BOUNDARY CONDITION AND GRID SIZE | 88 |
| 2.6.2 | BAND GAP AS A FUNCTION OF TOP GATE AND DISPLACEMENT FIELD | 93 |
| 2.7 | <i>Detector Design - Proposed Manufacturing Plan</i> | 97 |
| 2.7.1 | SUBSTRATE AND DIELECTRIC | 97 |
| 2.7.2 | BILAYER GRAPHENE | 97 |
| 2.7.3 | CONTACTS | 97 |
| 2.7.4 | TOP GATE DIELECTRIC | 98 |
| 2.7.5 | TOP GATE | 98 |
| 2.7.6 | WIRE BONDING AND MOUNTING | 99 |
| 2.8 | <i>Summary</i> | 100 |
| CHAPTER 3 – THEORETICAL STUDY AND DESIGN OF A PASSIVE TERAHERTZ PHOTON DETECTOR SENSITIVE TO 1.2THZ..... | | 102 |
| 3.1 | <i>Introduction</i> | 102 |
| 3.2 | <i>Exploiting the Dyakonov-Shur Effect</i> | 102 |
| 3.3 | <i>Device Optimisation</i> | 104 |
| 3.3.1 | THEORETICAL STUDY OF DETECTOR PERFORMANCE | 105 |
| 3.3.1.1 | Theoretical Signal Variation with Gate Voltage | 106 |
| 3.3.1.2 | Theoretical Signal Variation with Detector Parameters | 108 |
| 3.3.1.3 | Theoretical Signal Variation with Graphene Sheet Properties | 110 |
| 3.3.1.4 | Summary of Requirements | 113 |
| 3.3.2 | ANTENNA OPTIMISATION FOR 1.2THZ..... | 114 |
| 3.4 | <i>Manufacturing Plan</i> | 120 |
| 3.5 | <i>Summary</i> | 122 |
| CHAPTER 4 – THEORETICAL STUDY AND DESIGN OF A GRAPHENE-BASED X-RAY SINGLE PHOTON COUNTING PHOTODETECTOR | | 123 |
| 4.1 | <i>Introduction</i> | 123 |
| 4.2 | <i>Concept</i> | 123 |
| 4.3 | <i>Device Optimisation</i> | 125 |
| 4.3.1 | OPTIMISING THE ABSORBER: SIMULATION OF ABSORBER DYNAMICS..... | 126 |
| 4.3.1.1 | Photons in the Absorber: GAMOS + CASINO Simulations..... | 126 |
| 4.3.1.2 | Charge Carrier Travel and Relaxation: COMSOL Simulations..... | 127 |
| 4.3.1.2.1 | Basic COMSOL simulations | 127 |
| 4.3.1.2.2 | Setting up the Simulation – Charge Carrier Behaviour..... | 129 |
| 4.3.1.2.3 | Gate Voltage Changing the Detector Behaviour..... | 131 |
| 4.3.1.2.4 | Channel Size Changing the Detector Behaviour | 133 |
| 4.3.1.2.5 | Optimal Behaviour | 136 |
| 4.3.2 | IMPROVING THE BANDWIDTH: CONSIDERING A GDEPFET ARRANGEMENT | 137 |

| | | |
|--|--|------------|
| 4.3.2.1 | GDEPFET Arrangement..... | 137 |
| 4.3.2.2 | A GFET with V_{clear} | 143 |
| 4.3.3 | OPTIMISING THE GATE STRUCTURE: TOP AND DUAL GATED OPTIONS | 147 |
| 4.3.4 | OPTIMISING THE DIELECTRIC: TRANSPORT SIMULATIONS..... | 148 |
| 4.4 | <i>Prototype Device Design</i> | 151 |
| 4.5 | <i>Summary</i> | 152 |
| CHAPTER 5 – DEVICE FABRICATION TECHNIQUES AND MANUFACTURING..... | | 154 |
| 5.1 | <i>Introduction</i> | 154 |
| 5.2 | <i>Fabrication, Phase 0</i> | 154 |
| 5.3 | <i>Device Fabrication Processes</i> | 156 |
| 5.3.1 | GRAPHENE GROWTH..... | 156 |
| 5.3.1.1 | Micromechanical Exfoliation | 156 |
| 5.3.1.2 | Epitaxial Growth | 157 |
| 5.3.1.3 | Chemical Vapour Deposition..... | 158 |
| 5.3.2 | TRANSFERRING GRAPHENE ONTO A SUBSTRATE | 160 |
| 5.3.3 | PATTERNING USING ELECTRON BEAM LITHOGRAPHY AND PHOTOLITHOGRAPHY | 161 |
| 5.3.3.1 | Spin Coating..... | 161 |
| 5.3.3.2 | Electron Beam Lithography | 161 |
| 5.3.3.3 | Photolithography..... | 162 |
| 5.3.3.4 | Post-Baking and Development..... | 163 |
| 5.3.4 | DEPOSITION..... | 164 |
| 5.3.4.1 | Evaporation | 164 |
| 5.3.4.2 | Sputtering..... | 165 |
| 5.3.5 | LIFT-OFF | 166 |
| 5.3.6 | ENCAPSULATION VIA ATOMIC LAYER DEPOSITION (ALD) OF ALUMINA | 167 |
| 5.3.7 | WIRE BONDING..... | 169 |
| 5.4 | <i>Fabrication, Phase I – September 2015</i> | 170 |
| 5.4.1 | TERAHERTZ DETECTOR FABRICATION I: OPTIMISING THE FABRICATION PROCESS..... | 170 |
| 5.4.2 | BILAYER GRAPHENE DETECTOR FABRICATION I: ENSURING UNIFORM ALUMINA COVERAGE | 172 |
| 5.4.2.1 | SEM Analysis of ALD Deposition..... | 172 |
| 5.4.2.2 | AFM Analysis of ALD Deposition | 175 |
| 5.5 | <i>Fabrication, Phase II – October 2015</i> | 177 |
| 5.5.1 | TERAHERTZ AND X-RAY DETECTOR FABRICATION II: ETCHING TO GET A GATED DEVICE | 178 |
| 5.5.2 | BILAYER GRAPHENE DETECTOR FABRICATION II: OPTIMISING THE FABRICATION PROCESS..... | 180 |
| 5.6 | <i>Fabrication, Phase III – November 2015</i> | 184 |
| 5.6.1 | RECTIFYING THE WIRE BONDING PROBLEMS: TRYING A NEW MATERIAL..... | 185 |
| 5.6.2 | TERAHERTZ DETECTOR FABRICATION III: IMPROVING THE DETECTOR FABRICATION | 186 |
| 5.6.3 | X-RAY DETECTOR FABRICATION III: IMPROVING THE DETECTOR FABRICATION | 188 |
| 5.6.4 | BILAYER GRAPHENE DETECTOR FABRICATION II: IMPROVING THE DETECTOR FABRICATION | 192 |
| 5.7 | <i>Summary</i> | 195 |
| CHAPTER 6 – CRYOGENIC TESTING OF THE BILAYER GRAPHENE SINGLE PHOTON COUNTING PHOTODETECTOR..... | | 198 |
| 6.1 | <i>Introduction</i> | 198 |
| 6.2 | <i>Testing at Room Temperature</i> | 198 |

| | | |
|--|--|------------|
| 6.2.1 | APPLYING TOP AND BOTTOM GATE VOLTAGES TO BILAYER GRAPHENE..... | 198 |
| 6.2.2 | DETERMINING THE ENVIRONMENTAL DOPING I | 201 |
| 6.2.3 | DETERMINING THE ENVIRONMENTAL DOPING II: OBSERVING GATE LEAKAGE | 205 |
| 6.2.4 | DYNAMIC CAPACITANCE PROBLEM – OBSERVING PHOTODETECTION..... | 212 |
| 6.3 | <i>Testing the Device at Cryogenic Temperatures</i> | 220 |
| 6.3.1 | PREPARING THE DILUTION REFRIGERATOR, VACUUM SYSTEM AND ELECTRONICS | 220 |
| 6.3.1.1 | Preparation of the Fridge | 221 |
| 6.3.1.2 | Cooling Down and Warming Up the Fridge..... | 222 |
| 6.3.2 | EXPERIMENTAL RESULTS | 224 |
| 6.4 | <i>What is the Mechanism?</i> | 230 |
| 6.5 | <i>Summary</i> | 231 |
| CHAPTER 7 – TESTING THE TERAHERTZ DETECTOR WITH TERAHERTZ SOURCES..... | | 233 |
| 7.1 | <i>Introduction</i> | 233 |
| 7.2 | <i>Device Characterisation</i> | 234 |
| 7.3 | <i>Basic Testing with a Passive Terahertz Source</i> | 234 |
| 7.4 | <i>Testing with Terahertz Laser Sources to show Gate, Frequency and Power Modulation</i> | 239 |
| 7.4.1 | EXPERIMENTAL SETUP AT ASTON UNIVERSITY INSTITUTE OF PHOTONIC TECHNOLOGIES | 239 |
| 7.4.2 | EXPERIMENTAL SETUP AT THE NATIONAL PHYSICAL LABORATORY | 241 |
| 7.4.3 | USING A LOCK-IN AMPLIFIER | 244 |
| 7.4.4 | MODULATING THE SIGNAL VIA THE GATE VOLTAGE | 245 |
| 7.4.5 | MODULATING THE SIGNAL VIA TERAHERTZ POWER | 249 |
| 7.4.6 | SIGNAL VARIATION WITH NARROWBAND ILLUMINATION | 251 |
| 7.4.7 | RECTIFICATION AND THE ASYMMETRY ARGUMENT | 253 |
| 7.4.8 | COMPARING TO THEORY | 255 |
| 7.4.9 | DETECTOR CHARACTERISTICS | 259 |
| 7.5 | <i>Further Device Iteration and Roadmap to Development</i> | 262 |
| 7.6 | <i>Summary</i> | 265 |
| CHAPTER 8 – DETECTOR CHARACTERISATION OF THE SINGLE X-RAY PHOTON COUNTING GFET..... | | 267 |
| 8.1 | <i>Introduction</i> | 267 |
| 8.2 | <i>Characterising the Detector with an Optical Pulsed Laser</i> | 267 |
| 8.2.1 | LASER CHARACTERISATION WITH A SiPM..... | 268 |
| 8.2.2 | TRANSIMPEDANCE AMPLIFIER ARRANGEMENT | 270 |
| 8.2.2.1 | Designing the Transimpedance Amplifier | 271 |
| 8.2.2.2 | Calibrating the Preamplifier | 273 |
| 8.2.2.3 | Initial Illumination | 274 |
| 8.2.2.4 | Signal vs Gate Voltage: What is the Detection Mechanism? | 276 |
| 8.2.2.5 | Attenuating the Laser Pulse – What is the Energy Sensitivity?..... | 279 |
| 8.2.2.6 | Characterisation of Pulse Saturation..... | 281 |
| 8.2.2.7 | Extinguishing the Signal: Co-Located Pulsed and cw Illumination | 282 |
| 8.2.2.7.1 | Continuous Red Laser | 283 |
| 8.2.2.7.2 | Continuous Blue Laser | 285 |
| 8.2.2.7.3 | Improving the Signal Decay Time | 286 |
| 8.2.2.8 | Further Discussion of the Results..... | 287 |
| 8.2.3 | IMPROVING THE SENSITIVITY I: CHARGE SENSITIVE AMPLIFIER..... | 289 |

| | | |
|---|--|------------|
| 8.2.3.1 | Confirming the Initial Results | 290 |
| 8.2.3.2 | Identifying the Graphene Contribution..... | 291 |
| 8.2.3.3 | What is the Mechanism?..... | 292 |
| 8.2.3.4 | Isolating the Signal Contributions | 294 |
| 8.2.3.5 | Characteristics of the Signal Contributions | 296 |
| 8.2.4 | IMPROVING THE SENSITIVITY II: LOCK IN AMPLIFIER | 297 |
| 8.2.5 | IMPROVING THE SENSITIVITY III: VOLTAGE PREAMPLIFIER..... | 301 |
| 8.2.6 | DETECTOR PARAMETERS | 304 |
| 8.3 | <i>Demonstrating X-ray Sensitivity</i> | 305 |
| 8.3.1 | X-RAY SENSITIVITY: USING A LOCK-IN AMPLIFIER | 307 |
| 8.3.2 | X-RAY SENSITIVITY: VOLTAGE PREAMPLIFIERS, COMPTON SCATTERING AND SIPMS | 309 |
| 8.3.3 | X-RAY SENSITIVITY: IS THERE ANY AT ALL? | 312 |
| 8.3.3.1 | Detector Parameters | 319 |
| 8.3.4 | DETECTION MECHANISM AND EXPERIMENTAL VERIFICATION | 320 |
| 8.3.4.1 | Poor Thermalisation | 320 |
| 8.3.4.2 | Photothermoelectric Effect..... | 322 |
| 8.3.4.3 | Bolometry and Calorimetry | 322 |
| 8.3.4.4 | The SiO ₂ Dielectric | 323 |
| 8.3.4.5 | Experimental Verification..... | 324 |
| 8.4 | <i>Further Routes to Improved Device Sensitivity</i> | 325 |
| 8.5 | <i>Summary</i> | 326 |
| CHAPTER 9 – CONCLUSION | | 329 |
| 9.1 | <i>Summary of the Project</i> | 329 |
| 9.2 | <i>Proposed Next Stages of Development</i> | 331 |
| 9.3 | <i>Final Remarks</i> | 332 |
| APPENDIX I – SAMPLE ANALYSIS FOR EUROPEAN SPACE AGENCY | | 335 |
| <i>Appendix I-a – Optical Microscopy</i> | | 335 |
| <i>Appendix I-b – Scanning Electron Microscopy (SEM)</i> | | 338 |
| <i>Appendix I-c – Raman Spectroscopy</i> | | 341 |
| APPENDIX II – CRYOSTAT PUMP DOWN, COOL DOWN AND WARM UP PROCEDURE..... | | 343 |
| APPENDIX III- IMPROVED SENSITIVITY USING AN OSCILLOSCOPE-BASED LOCK IN AMPLIFIER | | 344 |
| APPENDIX IV - ADAPTIVE ELECTRONICS TO OPTIMISE THE X-RAY DETECTOR SENSITIVITY | | 346 |
| APPENDIX V - DEVELOPING A FLEXIBLE UV GFET (FUVGFET) | | 348 |
| APPENDIX VI – GRAPHENE FOR SELECTIVE PROTEIN SENSING | | 351 |
| BIBLIOGRAPHY | | 355 |



Prologue

The requirements for new, faster, cheaper and simpler photodetector technologies that cross a wide range of temperatures, wavelengths, energy and temporal sensitivities, has seen graphene considered as an interesting solution for future photodetectors. Fundamental research into graphene has demonstrated graphene's many unique optoelectronic and mechanical properties [6] including having shown it to be the thinnest and strongest [7] known material, with potential for an extremely high carrier mobility [8] [9] and an approximately constant photon absorption coefficient [10] across a wide range of frequencies. It has been demonstrated to be more conductive than copper [11], and provides a route to probing quantum mechanical effects at room temperature such as the quantum Hall effect [12] and Dirac fermions [13].

My work in this PhD project was to develop the concepts for future graphene-based photodetector technologies, by considering the relevant theory, applying the theory in simulations and analysing the results, designing and fabricating the detectors and then demonstrating photosensitivity. I initially started work to develop a cryogenic bilayer graphene single photon counting photodetector with colour sensitivity at visible wavelengths, with theoretical simulations to understand the behaviour and arrive at an optimal design of this detector. We then successfully bid for an EXPRO+ contract through the European Space Agency that funded us to develop two further detectors, one at terahertz wavelengths and one at x-ray wavelengths. This complements the work to develop the bilayer graphene detector because, in each of the detectors, the photons couple to different elements of what is, essentially, the same device structure, a graphene field effect transistor.

Three months of my PhD was spent at the Centre for Advanced Photonics and Electronics at the University of Cambridge learning and understanding the various techniques involved in the fabrication of a graphene-based detector, and fabricating each of the detectors. Each of these detectors was tested experimentally, including by using cryogenic facilities at the University of Leicester and terahertz laser sources at Aston University and the National Physical Laboratory. These experimental results were compared to theory and to existing photodetectors to highlight benefits and further areas for development.

Throughout my PhD I have contributed to several publications and presentations. When I started my PhD, I contributed to work submitted to the Long Range Office of the Naval Research Laboratory as part of a grant that was awarded in 2013. Parts of the work discussed in this thesis were also submitted to the European Space Agency as part of an EXPRO+ contract between March 2015 and December 2016. To date, I have published my work in these academic papers:

- J. O. D. Williams, J. S. Lapington, M. Roy and I. B. Hutchinson, "Graphene as a Novel Single Photon Counting Optical and IR Photodetector," *IET*, 2015. [1]
- J. O. D. Williams, J. A. Alexander-Webber, J. S. Lapington, M. Roy, I. B. Hutchinson, A. A. Sagade, M.-B. Martin, P. Braeuninger-Weimer, A. Cabrero-Vilatela, R. Wang, S. Hofmann, A. De Luca and F. Udrea, "Towards a Graphene-Based Low Intensity Photon Counting Photodetector," *Sensors*, vol.16, 9, 2016. [2]
- J. O. D. Williams, J. A. Alexander-Webber, J. S. Lapington, M. Roy, I. B. Hutchinson, A. A. Sagade, M.-B. Martin, P. Braeuninger-Weimer, A. Cabrero-Vilatela, R. Wang, A. De Luca, F. Udrea and S. Hofmann, "Towards a Graphene-Based Low Intensity Photon Counting Photodetector," *Conference Proceedings of IEEE IPC, 2016*. [3]

I have also presented this work at many conferences and meetings:

- September 2014 - GDRI-GNT Annual Conference – Strasbourg, France
 - Graphene as a Novel Optical and IR Single Photon Counting Photodetector (Poster)

- February 2015 – IET Graphene-based Technologies Meeting – London, United Kingdom
 - Graphene as a Novel Optical & IR Single Photon Counting Photodetector (Oral Presentation and Poster)
- April 2015 – CEOI-ST Conference – Abingdon, Oxfordshire, United Kingdom
 - Graphene as an Enabler for Earth Observation (Oral Presentation)
- June 2015 – Graphene Week 2015 – Manchester, United Kingdom
 - Bilayer Graphene as a novel single Photon Counting Optical & IR Photodetector (Poster)
- May 2016 – EMN 2D Materials Meeting 2016 – San Sebastian, Spain
 - Towards a Graphene-Based Low Intensity Photon Counting Photodetector (Oral Presentation)
- October 2016 – IEEE International Photonics Conference – Waikoloa, Hawaii, USA
 - Working Towards Graphene-Based Detectors for High Sensitivity Photodetection (Oral Presentation)
- October 2016 – STFC PPRP Meeting – Swindon, Wiltshire, United Kingdom
 - Graphene as a Photosensor (Oral Presentation)
- February 2017 – FPD 17 at the European Space Agency – Noordwijk, Netherlands
 - Development of Graphene-based THz and X-ray Radiation Detectors (Oral Presentation)
- March 2017 – 3rd Annual BIT Congress on Smart Materials – Bangkok, Thailand
 - Development of a Passive Graphene-based Terahertz Detector (Oral Presentation)



List of Acronyms

A number of acronyms are introduced throughout this document.

Chapter 1

- **GFET**: graphene field effect transistor. A typical graphene device that often allows top and/or bottom gating of the graphene.
- **STJ**: superconducting tunnelling junction. A photodetector made up of two superconducting materials with a thin dielectric in between, with charge carriers tunnelling through.
- **eV**: electron volts. A unit of energy. 1eV is the energy provided to one electron by a 1V potential.
- **DROID**: A distributed read-out imaging device used to determine spectral and spatial information from a transition edge sensor.
- **MKID**: microwave kinetic inductance detector. A superconducting photodetector that exploits the change in impedance arising from additional charge carriers generated during a photon absorption.
- **NEP**: noise equivalent power. A figure of merit for the sensitivity of a detector, in $\text{WHz}^{-0.5}$. It is the signal power that gives a signal to noise ratio equal to 1 for a bandwidth of 1Hz.
- **TES**: transition edge sensor. A detector that utilises the change in resistance resulting from the change of the temperature of a superconducting material following the absorption of a photon.
- **MCP-PMT**: microchannel plate photomultiplier tube. Photon converted to an electron in a photocathode that, through a process of charge multiplication, relaxes before it is collected by an anode.
- **CCD**: charged coupled device. A photodetector where each pixel is converted to an electrical charge.
- **SPAD**: single photon avalanche diode. A high sensitivity array structure for single photon detection.
- **SiPM**: silicon photomultiplier. A silicon based avalanche photodiode photodetector able to count single photons, and operates in Geiger mode when biased to a high voltage.
- **FWHM**: full width half maximum. The width of a peak at half of the pulse amplitude.
- **EQE**: external quantum efficiency. A figure of merit for photodetectors. The number of charge carriers collected related to the number of incident photons.

- **DC:** direct current. Current flowing in only one direction.
- **PV:** photovoltage. A gating voltage generates a field to generate an electric field to split electron-hole pairs at a PN junction in differently doped regions of graphene.
- **PTEE:** photothermoelectric effect. Excitation of an electron hole pair causes ultrafast heating and generates a measurable photovoltage.
- **DS:** Dyakonov-Shur effect. The generation of a resonating plasma wave along a channel that generates a measurable photovoltage.
- **GDEPFET:** graphene depleted field effect transistor. Another typical device structure, but requires more fabrication steps.
- **SLG:** single layer graphene. A single layer of sp² carbon atoms arranged in a hexagonal structure.
- **BLG:** bilayer graphene. Two layers of carbon atoms.

Chapter 2

- **EES** – electron electron scattering. Loss of energy from one electron to another via an elastic collision.
- **CB** – conduction band. A level of free electrons above the Fermi level.
- **VB** – valence band. A level of tightly bound electrons below the Fermi level.
- **EPS** – electron phonon scattering. The scattering of an electron by the emission or adsorption of a phonon.
- **II** – impact ionisation. The relaxation of a charge carrier by it causing the excitation of a valence band carrier.
- **AR** – Auger recombination. The excitation of a conduction band charge carrier by the relaxation of another.
- **ITO:** indium tin oxide. A conductive material that is transparent to visible and infrared photons but opaque to UV.

Chapter 3

- **AC** – alternating current. Current flowing in both directions
- **LPCTA** – log periodic circular toothed antenna. An antenna that is self-complimentary with a given ratio between the size of the arms.
- **S11** – a parameter that quantifies the power transfer from the antenna to the graphene channel.

Chapter 4

- **COMSOL** – a finite element analysis software that can simulate physics such as electrodynamics and fluid flow.
- **GAMOS** – medical simulation software used for the adsorption of an X-ray photon by a material.
- **CASINO** – Monte Carlo simulation software for the scattering of charge carriers through a material
- **PZT** – lead zirconium titanate. A material proposed as a dielectric for the GFET.
- **SRH** – Shockley Read Hall recombination. The recombination of an electron and hole in a direct semiconductor such as silicon.

Chapter 5

- **CVD** – chemical vapour deposition. A chemical method for synthesising graphene.
- **hBN** – hexagonal boron nitride.
- **TMD** – transitional metal dichalcogenide, e.g. WS₂.
- **TLG** – trilayer graphene. Three layers of carbon atoms.
- **UVIII** – a photoresist widely used in the fabrication process.
- **PMMA** – a photoresist widely used in the fabrication process.
- **MAN** – a photoresist widely used in the fabrication process.
- **AZ MLOF** – a photoresist widely used in the fabrication process.
- **MFCD26** – a developer chemical used with the UVIII photoresist.
- **MBIK** - a developer chemical used with photoresists in the fabrication process.
- **IPA** – isopropanol.
- **AZ351B** - a developer chemical used with photoresists in the fabrication process.
- **sccm** – standard cubic centimetre per minute.
- **PCB** – printed circuit board.
- **SEM** – scanning electron microscopy.
- **AFM** – atomic force microscopy.
- **TMA** – trimethylaluminium, a precursor gas for the deposition of aluminium oxide in the ALD process.
- **HF** – hydrogen fluoride. A chemical used for etching.

Chapter 6

- cw – continuous wave

Chapter 7

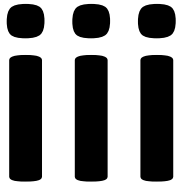
- PC – photocurrent
- SNR – signal to noise ratio
- HDPE – high density polyethylene
- BW – bandwidth, given by Nyquist's theorem
- NEP – noise equivalent power.

Chapter 8

- SiPM – silicon photomultiplier
- FWHM – full width at half maximum
- DEXA - dual-energy X-ray absorptiometry
- GOS – gadolinium oxysulphide
- CZT – cadmium zinc telluride

Chapter 9

- **FUVGFET** – Flexible UV Graphene Field Effect Transistor. Another proposed GFET like structure.



List of Figures and Tables

Figures

FIGURE 1.1. THE PHOTON IS ABSORBED IN THE SUPERCONDUCTING MATERIAL, WHICH BREAKS A COOPER PAIR WITH ONE OF THE ELECTRONS THEN TUNNELLING THROUGH THE INSULATOR AND LEADS TO A TUNNELLING CURRENT. 35

FIGURE 1.2 SHOWING THE KINETIC INDUCTANCE DETECTOR IN AN LC CIRCUIT (BASED ON THE FIGURE FROM REF. [43]). THE PHOTON IS ABSORBED BY THE INDUCTOR MATERIAL WHICH CHANGES THE IMPEDANCE OF THE CIRCUIT AND HENCE THE FREQUENCY OF MICROWAVES PASSED THROUGH THE DETECTOR. 36

FIGURE 1.3 SHOWING A SCHEMATIC OF A TES, AND THE TEMPERATURE DEPENDENT CHANGE IN RESISTANCE OF A TES. TO BOOST THE SIGNAL, THE TES CAN BE LINKED WITH A SQUID [46]. 36

FIGURE 1.4, SHOWING A PHOTOMULTIPLIER TUBE (PMT) (BASED ON A FIGURE FROM REF. [47]). THE PHOTON STRIKES A PHOTOCATHODE WHICH EJECTS AN ELECTRON TOWARDS A DYNODE. CHARGE MULTIPLICATION THROUGH THE DYNODES LIBERATES MORE ELECTRONS UNTIL IT REACHES THE ANODE, AND THE SIGNAL IS OUTPUT. 37

FIGURE 1.5, SHOWING A MICROCHANNEL PLATE DETECTOR. THE PHOTON STRIKES THE PORE WALL AND, THROUGH CHARGE MULTIPLICATION, THE AMPLIFIED SIGNAL IS MEASURED AT THE ANODE. 38

FIGURE 1.6, SHOWING A) THE HONEYCOMB STRUCTURE OF SINGLE LAYER GRAPHENE IN RECIPROCAL SPACE WITH THE K AND K' POINTS IN THE FIRST BRILLOUIN ZONE [2], AND B) THE BAND STRUCTURE OF GRAPHENE (AN ALTERNATIVE VERSION IS AVAILABLE IN REF [56]), SHOWING OTHER AREAS OF HIGH SYMMETRY IN THE BRILLOUIN ZONE, SUCH AS Γ POINT IN THE CENTRE OF THE ZONE. 41

FIGURE 1.7, SHOWING THE LINEAR ENERGY-WAVENUMBER RELATIONSHIP CLOSE TO THE DIRAC POINT, $E = \hbar v_K k$, WITH A FERMI LEVEL THAT IS CHANGED BY APPLYING AN ELECTRIC FIELD [2]. THE LINEAR RELATIONSHIP ALSO SHOWS THAT CHARGE CARRIERS BEHAVE AS MASSLESS FERMIONS CLOSE TO THE DIRAC POINT. 42

FIGURE 1.8, SHOW A) THE DENSITY OF STATES OF GRAPHENE AND B) THE LINEAR RELATIONSHIP NEAR THE DIRAC POINT WHERE IT TENDS TO ZERO. ONE SEES PEAKS AT THE VAN HOVE SINGULARITIES IN THE DENSITY OF STATES AT ENERGIES EQUAL TO THE HOPPING PARAMETER $\pm\gamma_1$ 43

FIGURE 1.9, SHOW LAYER STACKING FOR AA BILAYER GRAPHENE, WITH TWO LAYERS OF GRAPHENE STACKED DIRECTLY ON TOP OF EACH OTHER. THE HOPPING PARAMETER BETWEEN THE LAYERS IS GIVEN BY THE HOPPING PARAMETER γ 43

FIGURE 1.10, SHOWING THE STRUCTURE OF AB (BERNAL) STACKED BILAYER GRAPHENE. IN A) ONE SEES THE ARRANGEMENT OF THE TWO LAYERS, AND B) SHOWS THE HOW THE TWO LAYERS MARKED IN RED AND BLUE RESPECTIVELY AND A HOPPING PARAMETER OF $\sim 0.4\text{eV}$ BETWEEN THE LAYERS [2]. C) SHOWS THE NOMENCLATURE FOR THE DIFFERENT HOPPING PARAMETERS IN BILAYER GRAPHENE, INCLUDING THE NEXT NEAREST HOPPING PARAMETER γ_0 , AND THE NEAREST NEIGHBOUR INTER-PLANE HOPPING PARAMETER, γ_1 44

FIGURE 1.11, SHOWING THE BAND STRUCTURE FOR BILAYER GRAPHENE SHOWING PRISTINE BILAYER GRAPHENE AND THE OPENING OF A BAND GAP FOR GATED BILAYER GRAPHENE WITH AB STACKING (BASED ON A FIGURE FROM REF. [65]). THE PAIR OF BANDS ARE DEGENERATE AT THE DIRAC POINT FOR PRISTINE GRAPHENE. "TRIGONALITY" IS OBSERVED IN GATED BILAYER GRAPHENE AT VERY LOW ENERGIES [6]. 45

FIGURE 1.12, SHOWING THE BAND STRUCTURE FOR BILAYER GRAPHENE AS A FUNCTION OF k_x , k_y AND THE ENERGY E . THE DIRAC POINTS ARE CLEARLY VISIBLE WHERE THE BANDS INTERSECT. 47

| | |
|--|----|
| FIGURE 1.13, SHOWING A) THE PERTURBATION TO THE ENERGY SPECTRUM AT LOW ENERGIES, SHOWING THE FOUR DIRAC POINTS, AND B) THE PERTURBATION TO THE ENERGY SPECTRUM AT LOW ENERGIES, SHOWING THE 120° OPENING ANGLE. | 48 |
| FIGURE 1.14 SHOWING, FOR ONE SPECIFIC SAMPLE, THE DRAIN-SOURCE CURRENT OF GRAPHENE AGAINST GATE VOLTAGE FOR A GIVEN SAMPLE [2] [79]. THE ASYMMETRY IN THIS SAMPLE IS DUE TO THE DIFFERENCE IN ELECTRON AND HOLE MOBILITIES OF THE SAMPLE; THE DIRAC POINT AND ELECTRON AND HOLE MOBILITIES ARE DEPENDENT ON THE SPECIFIC SAMPLE. | 49 |
| FIGURE 1.15, SHOWING THE ALLOWED AND DISALLOWED TRANSITIONS RESULTING FROM PHOTOABSORPTION BY GRAPHENE. DISALLOWED TRANSITIONS ARE PREVENTED DUE TO PAULI EXCLUSION. | 53 |
| FIGURE 1.16, SHOWS THE OPTICAL IMAGE OF CVD SAMPLE GROWN AT THE UNIVERSITY OF CAMBRIDGE. THE IMAGE SHOWS SINGLE LAYER (CENTRE) AND MULTILAYER (CENTRE RIGHT) SAMPLES. | 53 |
| FIGURE 1.17, SHOWING THE PHONON SPECTRA IN GRAPHENE FOR DIFFERENT PHONON MODES [112]. REPRODUCED WITH PERMISSION BY CAMBRIDGE UNIVERSITY PRESS, SUBJECT TO HTTP://WWW.CAMBRIDGE.ORG/ABOUT-US/RIGHTS-PERMISSIONS/PERMISSIONS/PERMISSIONS-REQUESTS | 54 |
| FIGURE 1.18. THE RAMAN SPECTRUM OF A SAMPLE PRODUCED AT THE UNIVERSITY OF CAMBRIDGE. A SMALL D PEAK, AND CLEAR G AND 2D PEAKS ARE OBSERVED AT 1350cm^{-1} , 1580cm^{-1} AND 2700cm^{-1} RESPECTIVELY. | 55 |
| FIGURE 1.19 SHOWING POSSIBLE SCATTERING CHANNELS THROUGH PHONON LOSS IN GRAPHENE FOR THE G, 2D AND D PEAKS [113], ALONG WITH THE CORRESPONDING PHONON EMISSION FEYNMAN DIAGRAM. | 55 |
| FIGURE 1.20 SHOWING IMPACT IONISATION (II) IN DOPED SINGLE LAYER GRAPHENE. AN ELECTRON IS EXCITED INTO THE CONDUCTION BAND, AND THERMALIZES WITH FURTHER ELECTRONS EXCITED FROM THE VALENCE BAND. AR IS THE REVERSE PROCESS. | 56 |
| FIGURE 2.1 SHOWING DIFFERENT CONTRIBUTIONS TO THE OPTICAL CONDUCTIVITY. | 67 |
| FIGURE 2.2. COMPARISON OF SINGLE (LEFT) AND BILAYER (RIGHT) GRAPHENE ELECTRON-PHONON SCATTERING RATES, AND CONTRIBUTIONS TO THE TOTAL RATE [67]. REPRODUCED UNDER COPYRIGHT LICENCE FROM THE AMERICAN PHYSICAL SOCIETY. | 69 |
| FIGURE 2.3 SHOWING THE DENSITY OF STATES FOR BILAYER GRAPHENE WITH A BAND GAP OF 5MEV; RED IS THE π_2 BAND, BLUE IS THE π_1 BAND. | 70 |
| FIGURE 2.4, SHOWING THE OPERATIONAL LIMIT OF A BILAYER GRAPHENE PHOTODETECTOR. IN THIS SIMULATION, $A=1\text{MM}^2$. HELIUM-4 COOLING LIMIT IS 1.4K AND HELIUM-3 LIMIT IS 0.3K. | 71 |
| FIGURE 2.5, SHOWING THE ABSORPTION OF A PHOTON, AND THE EXCITATION OF A SUBSEQUENT RELAXATION OF THE HOT PHOTOELECTRON IN THE CONDUCTION BAND FOR A GIVEN BAND GAP EG | 72 |
| FIGURE 2.6, SHOWING THE OPTICAL CONDUCTIVITY $\sigma(\Omega)\sigma_0$, WHERE Ω IS THE PHOTON ENERGY, FOR BILAYER GRAPHENE A) WITHOUT A BAND GAP, AND B) WITH A BAND GAP, Δ [140]. WITHOUT A BAND GAP, THE OPTICAL CONDUCTIVITY OF BILAYER GRAPHENE DESCRIBES TWO COUPLED LAYERS OF GRAPHENE. FOR BILAYER GRAPHENE WITH A BAND GAP, THE OPTICAL CONDUCTIVITY IN THE CASE OF THE FERMI LEVEL TUNED TO THE CENTRE OF THE BAND GAP ($\mu\gamma = 0$, WHERE IS THE INTERLAYER HOPPING PARAMETER $\gamma=0.4\text{eV}$) SHOWS LOW OPTICAL CONDUCTIVITY FOR PHOTON ENERGIES LESS THAN THE BAND GAP. REPRODUCED UNDER COPYRIGHT LICENCE FROM THE AMERICAN PHYSICAL SOCIETY. | 73 |
| FIGURE 2.7, SHOWING ALLOWED AND DISALLOWED PHOTOELECTRON TRANSITIONS. | 74 |
| FIGURE 2.8, SHOWING A SCHEMATIC OF THE MODEL USED FOR VACANCY FILLING. | 74 |
| FIGURE 2.9, SHOWING THE METHOD USED IN THE ALGORITHM TO ENSURE CONSERVATION OF MOMENTUM/ENERGY. FIGURE 2.9A SHOWS THIS FOR II, WHERE A CIRCLE ABOUT THE INITIAL ELECTRON ENERGY (BLUE IN CONDUCTION BAND, RED IN VALENCE BAND) IS OF RADIUS K_{CHANGE} IN MOMENTUM SPACE, AND EVALUATES THE ENERGY AT EACH POINT AROUND THE CIRCLE UNTIL ENERGY IS CONSERVED. IF NO POINT CONSERVES BOTH, IT PICKS A NEW ENERGY/MOMENTUM AND REPEATS. FOR PHONON LOSS IN FIGURE 2.9B, A RANDOMLY SELECTED PHONON ENERGY RESULTS IN MOMENTUM COMPONENTS THAT ARE SOLVED NUMERICALLY TO ENSURE ENERGY AND MOMENTUM CONSERVATION. | 78 |
| FIGURE 2.10, SHOWING ENERGY CONSERVATION IN THE SIMULATION INCLUDING THE SUM OF THE ENERGY OF THE ELECTRONS IN THE CONDUCTION BAND (PURPLE), THE SUM OF THE ENERGY OF ALL ELECTRONS AND HOLES IN THE SIMULATIONS RELATIVE TO THE FERMI ENERGY (BROWN). THE INITIAL LARGE DROP IN TOTAL ENERGY RESULTS FROM AN EXCITATION OF AN ELECTRON FROM THE π_2 RATHER THAN π_1 VALENCE BAND. | 79 |

| | |
|--|----|
| FIGURE 2.11, SHOWING THE EFFECT OF CHANGING A) $F1$ AND B) $F2$. THE NUMBER OF CHARGE CARRIERS THAT ARE PRODUCED CONVERGES FOR $F1 > 100$ AND $F2 > 1000$ | 80 |
| FIGURE 2.12. THE DISTRIBUTION N_T AT $E_{GAP}=1\text{MEV}$ AND 3.5MEV FOR PHOTONS WITH ENERGY 3.11eV AND 1.55eV , AND WITH $\mu = \Sigma\Pi\Sigma\text{PHONON}=100$ | 81 |
| FIGURE 2.13, SHOWING A) ELECTRON-HOLE PAIR CREATION ENERGY AS A FUNCTION OF BAND GAP WITH $\mu=100$. THE CIRCLES SHOW SIMULATION RESULTS, AND THE RED LINE IS BEST FIT STRAIGHT LINE. B) SHOWS A COMPARISON OF W VS BAND GAP FOR BILAYER GRAPHENE WITH OTHER SEMICONDUCTORS..... | 82 |
| FIGURE 2.14, SHOWING THE NUMBER DISTRIBUTION AS A FUNCTION OF PHOTON ENERGY, FOR $\mu=100$. THE NUMBER OF CHARGE CARRIERS INCREASES WITH PHOTON ENERGY, WHICH SUGGESTS WAVELENGTH SPECIFICITY. | 82 |
| FIGURE 2.15, SHOWING THE ORIGIN OF THE PEAKS FOR THE TRANSITION BETWEEN THE π_1/π_2 AND π_1^*/π_2^* BANDS. THE GREATEST PROBABILITY PEAK OCCURS FOR THE $\pi_1 \rightarrow \pi_1^*$ TRANSITION, WHILE THE $\pi_2 \rightarrow \pi_2^*$ TRANSITION TYPICALLY LEADS TO THE FEWEST NUMBER OF CHARGE CARRIERS. | 83 |
| FIGURE 2.16. COMPARING THE NUMBER OF ELECTRONS PRODUCED AT PHOTON ENERGIES (BLUE DOTS INDICATE A MORE ENERGETIC PHOTON THAN RED) FALLING INTO THE NO TRANSITION REGIME..... | 83 |
| FIGURE 2.17 SHOWING THE DISTRIBUTION OF EVENTS FOR $\lambda=3500\text{NM}$ PHOTON. $\mu=100$. THE MEAN NUMBER OF CHARGE CARRIER IS ~ 33 , WITH $\Sigma=3.05$ | 84 |
| FIGURE 2.18, SHOWING THAT WITH A LARGER BAND GAP, FEWER ELECTRONS ARE PRODUCED, SO THE ELECTRON DISTRIBUTION WILL BE LESS BROAD..... | 85 |
| FIGURE 2.19, SHOWING THE NUMBER DISTRIBUTION AS A FUNCTION OF THE BAND GAP MAGNITUDE. | 85 |
| FIGURE 2.20, SHOWING A) A PLOT INDICATING THE NUMBER OF CHARGE CARRIERS VERSUS TIME SHOWING THE EFFECT OF CHANGING THE Π RATE AND B) THE EFFECT OF CHANGING THE Π RATE FOR $\lambda=3500\text{NM}$ | 86 |
| FIGURE 2.21. THE DETECTOR STRUCTURE USED IN REF. [65]. REPRODUCED UNDER COPYRIGHT LICENCE FROM NATURE PUBLISHING GROUP..... | 87 |
| FIGURE 2.22, SHOWING A) THE OUTPUT FROM THE SIMULATIONS SHOWING THE LAYOUT OF THE DEVICE, WITH A GIVEN HEIGHT OF THE VACUUM ABOVE THE DEVICE, A GIVEN TOP GATE, AN ALUMINA TOP GATE DIELECTRIC AND A SILICON DIOXIDE BOTTOM GATE DIELECTRIC. | 89 |
| FIGURE 2.23 SHOWING A) AND B) THE POTENTIAL THROUGH THE SIMULATION FOR DIFFERENT GRID SIZES DR . B) SHOWS THE SIMULATED POTENTIAL ACROSS THE TOP GATE DIELECTRIC, WHICH SUGGESTS THAT THE SIMULATION RESULTS CONVERGE WITH A FINER GRID SIZE. C) SHOWS HOW THE BAND GAP VARIES ACROSS THE SIMULATION FOR DIFFERENT GRID SIZES DR | 90 |
| FIGURE 2.24 SHOWING A) THE POTENTIAL THROUGH THE SIMULATION FOR DIFFERENT GRID SIZES dz , AND B) THE BAND GAP ACROSS THE SIMULATION FOR DIFFERENT GRID SIZES DZ | 91 |
| FIGURE 2.25 SHOWING A) HOW THE BAND GAP VARIES WITH CHANGING THE VACUUM DISTANCE, AND B) THAT THIS CONVERGES FOR DISTANCES GREATER THAN 250NM | 91 |
| FIGURE 2.26 SHOWING A) THAT THE SOLUTION CONVERGES TO WITHIN 0.0003% WHEN VARYING THE BOTTOM BOUNDARY CONDITION AND VACUUM HEIGHT, AND B) THAT THIS VARIES SIGNIFICANTLY WHEN THE TOP GATE BOUNDARY IS CHANGED TO $dvdz = 0$ INSTEAD..... | 92 |
| FIGURE 2.27 SHOWING THAT THE RESULTS DIVERGE AT THE BOUNDARIES, BUT CONVERGE TO WITHIN $\sim 3\%$ CLOSE TO THE PRESENCE OF THE GRAPHENE. | 92 |
| FIGURE 2.28, SHOWING A) THE CHANGE IN THE BAND GAP WITH INCREASING GATE RADIUS, SHOWING AN INCREASINGLY STEEP TRANSITION BETWEEN THE AREA COVERED BY THE TOP GATE AND THE REST OF THE DETECTOR. B) SHOWS THAT THE SIMULATED SCREENING CHARGE, WHEN MEASURED AT $r' = 0\text{NM}$, SATURATES WITH AN INCREASING GATE RADIUS. | 93 |
| FIGURE 2.29, SHOWING A) THE CHANGE IN SCREENING CHARGE OF THE GRAPHENE WITH INCREASING GATE RADIUS, WITH AN INCREASINGLY STEEP TRANSITION BETWEEN THE AREA COVERED BY THE TOP GATE AND THE REST OF THE DETECTOR. B) SHOWS THAT THE SIMULATED SCREENING CHARGE, WHEN MEASURED AT $r' = 0\text{NM}$, SATURATES WITH AN INCREASING GATE RADIUS. | 94 |
| FIGURE 2.30, SHOWING FIGURE 4 IN REF. [65], WITH THE EXPERIMENTALLY MEASURED BAND GAP, SELF-CONSISTENT TIGHT-BINDING CALCULATED BAND GAP, DFT CALCULATED BAND GAP AND UNSCREENED TIGHT-BINDING MODEL BAND GAP PLOTTED AGAINST THE APPLIED DISPLACEMENT FIELD. REPRODUCED UNDER COPYRIGHT LICENCE FROM NATURE PUBLISHING GROUP..... | 95 |

| | |
|--|-----|
| FIGURE 2.31 SHOWING THE ATTEMPTED FITTING TO DFT AND EXPERIMENTAL LINES FOR THE MEASURED BAND GAP AT $r=0$. THE EXPERIMENTAL RESULTS FROM REF. [65] ARE IN SOME AGREEMENT WITH THE RESULTS SIMULATED IN THIS WORK, AS IT IS OF THE SAME ORDER OF MAGNITUDE. DFT IS SHOWN TO BE IN POOR AGREEMENT AS IT IS APPROXIMATELY A FACTOR 3 SMALLER. | 96 |
| FIGURE 2.32, SHOWING THE BAND GAP AT A GIVEN RADIUS FOR DIFFERENT TOP AND BOTTOM GATE VOLTAGES, WITH DOPING REMAINING ZERO. THE TOP GATE RADIUS IS 500NM. IT INDICATES THAT THE FUNCTIONALITY OF THE BAND GAP AS A FUNCTION OF RADIUS REMAINS CONSTANT, BUT THE MAGNITUDE OF THE BAND GAP SCALES WITH THE APPLIED GATE VOLTAGES. | 96 |
| FIGURE 2.33, SHOWING POTENTIAL SHADOW MASKS FOR A) THE VAN DER PAUW CONFIGURATION, AND B) FOR A SIMPLER TWO-POINT MEASUREMENT. | 98 |
| FIGURE 2.34 SHOWING THE PROPOSED DEVICE LAYOUT ON A SILICON SUBSTRATE WITH A) THE ITO TOP GATE AND B) THE SPRING-LOADED PROBE. THE KEY IS 1) OXYGEN FREE COPPER BLOCK, 2) PCB, 3) SILICON WAFER (1CM X 1CM), 4) SILICON DIOXIDE SUBSTRATE, 5) TWO CONTACT PADS ($\sim 200\mu\text{M} \times 200\mu\text{M}$), 6) GOLD OR ALUMINIUM WIRE BONDS, 7) MOUNTING BOLTS, 8) ALUMINA, 9) ITO AND 10) BILAYER GRAPHENE ($\sim 20\mu\text{M} \times 20\mu\text{M}$). | 99 |
| FIGURE 2.35 SHOWING THE PROPOSED DEVICE LAYOUT ON A SAPPHIRE SUBSTRATE WITH A) THE ITO TOP GATE AND B) THE SPRING-LOADED PROBE. THE KEY IS 1) OXYGEN FREE COPPER BLOCK, 2) SAPPHIRE WAFER, 3) SPUTTERED SILICON, 4) SILICON DIOXIDE SUBSTRATE, 5) TWO CONTACT PADS ($\sim 200\mu\text{M} \times 200\mu\text{M}$), 6) GOLD OR ALUMINIUM WIRE BONDS, 7) MOUNTING BOLTS, 8) ALUMINA, 9) ITO AND 10) BILAYER GRAPHENE ($\sim 20\mu\text{M} \times 20\mu\text{M}$) | 99 |
| FIGURE 2.36 SHOWING A TOP VIEW OF THE BILAYER GRAPHENE SINGLE PHOTON COUNTING PHOTODETECTOR. THE KEY IS 1) OXYGEN FREE COPPER BLOCK, 2) PCB, 3) SILICON WAFER (1CM X 1CM), 4) SILICON DIOXIDE SUBSTRATE, 5) TWO CONTACT PADS ($\sim 200\mu\text{M} \times 200\mu\text{M}$) BASED ON THE DESIGN SHOWN IN FIGURE 2.33B, 6) GOLD OR ALUMINIUM WIRE BONDS, 8) ALUMINA, 9) ITO AND 10) BILAYER GRAPHENE ($\sim 20\mu\text{M} \times 20\mu\text{M}$). | 101 |
| FIGURE 3.1 SHOWING A SCHEMATIC OF THE DEVICE USED TO SHOW THE DYAKONOV-SHUR IN REF. [149], WITH A CHANNEL WITH OF $L=11\mu\text{M}$, $W=28\mu\text{M}$. IN REF [149], THE DEVICE DEMONSTRATED THAT DRAIN CURRENT AND GATE VOLTAGE ARE INVERSELY PROPORTIONAL, WITH A NON-LINEAR DRAIN VOLTAGE-CURRENT RELATIONSHIP. | 103 |
| FIGURE 3.2, SHOWING THE LAYOUT OF A GFET UTILISING THE DYAKONOV-SHUR INSTABILITY [123]. REPRODUCED WITH PERMISSION FROM AIP PUBLISHING. | 104 |
| FIGURE 3.3 SHOWING A) THE PHOTOCURRENT AGAINST THE PHOTON FREQUENCY FOR DIFFERENT MOMENTUM RELAXATION TIME, WHERE s IS THE PLASMA WAVE SPEED; AND B) $\log_{10}(\text{NEP}/\text{NEP}_V)$ AGAINST PHOTON FREQUENCY WITH LOWER NOISE AT HIGHER MOMENTUM RELAXATION TIME. | 106 |
| FIGURE 3.4, SHOWING A) AND B) THE PEAK CURRENT IS OBTAINED CLOSE TO THE DIRAC POINT, AND C) THE PHOTOCURRENT USED IN THE SIMULATIONS, BASED ON THAT IN REF. [154] . THE SIMULATIONS WERE DONE FOR A CHANNEL LENGTH $L=10\mu\text{M}$ AND A CHANNEL WIDTH $W=5\mu\text{M}$ | 107 |
| FIGURE 3.5, SHOWING A) I/I_d AND B) I AGAINST THE CHANNEL LENGTH L . THESE RESULTS SUGGEST THAT THE OPTIMUM CHANNEL LENGTH IS $\sim 10\mu\text{M}$, THE VALUE OF L WHERE THE I REACHES A MAXIMUM. | 108 |
| FIGURE 3.6, SHOWING THE CHANGE IN A) I/I_d AND B) I AS A FUNCTION OF THE DIELECTRIC CONSTANT, SUGGESTING A MAXIMUM AT $\epsilon_r \sim 2$, FOR A $10\text{k}\Omega$ CHANNEL RESISTANCE, 300NM DIELECTRIC THICKNESS AND $U_0=1\text{V}$. C) AND D) SHOW THE CHANGE IN I/I_d AND I , RESPECTIVELY, AS A FUNCTION OF THE DIELECTRIC THICKNESS, $d_{\text{dielectric}}$, FOR A $10\text{k}\Omega$ CHANNEL RESISTANCE AND $U_0 = 1\text{V}$. FOR AN SiO_2 DIELECTRIC THE PEAK CURRENT IS AT $d_{\text{dielectric}} \sim 500\text{NM}$, WHILE FOR Al_2O_3 THE CURRENT INCREASES LIKE $d_{\text{dielectric}}^{0.5}$ | 109 |
| FIGURE 3.7 SHOWING THE SIMULATED VALUES, AS A FUNCTION OF GATE VOLTAGE RELATIVE TO THE DIRAC POINT AND THE SHEET RESISTANCE FOR A) THE SIMULATED VALUE OF I/I_d , B) THE CURRENT, WITH AN AC PHOTOCURRENT OF THE SAME VALUE $\sim 100\text{NA}$ FOR EACH RESISTANCE, AND C) THE RESULTING THEORETICAL PHOTOVOLTAGE THAT WAS EXPECTED. THESE RESULTS SUGGEST THAT THE GREATEST SIGNAL IS OBTAINED OPERATING CLOSE TO THE DIRAC POINT, AND WITH A CHANNEL RESISTANCE $\sim 10\text{k}\Omega$ | 111 |
| FIGURE 3.8, SHOWING THE THEORETICAL A) PHOTOCURRENT AND B) AND C) PHOTOVOLTAGE AS A FUNCTION OF GATE VOLTAGE AND AC PHOTOCURRENT. THIS SHOWS THAT, FOR A GREATER MAGNITUDE PHOTOCURRENT, THE CURRENT INCREASE. THE LARGEST AC PHOTOCURRENT OCCURS CLOSEST TO THE DIRAC POINT. | 113 |
| FIGURE 3.9. DEFINITION OF THE VARIABLES GOVERNING THE DESIGN OF THE LOG-PERIODIC CIRCULAR TOOTHED ANTENNA. THE OPENING ANGLE IS SET TO BE $S_1=S_2$ [156]. | 114 |

| | |
|--|-----|
| FIGURE 3.10 SHOWING THE SIMULATED S11 RESPONSE FOR A LOG PERIODIC CIRCULAR TOOTHED ANTENNA WITH $k=1.5$, USING SONNET LITE SIMULATION SOFTWARE [158]. THE S11 RESPONSE AS A FUNCTION OF ILLUMINATING FREQUENCIES SHOWS SEVERAL RESONANCES, MOST NOTICEABLY AT $\sim 0.9\text{THz}$, 1.2THz , 1.8THz AND 2.5THz | 116 |
| FIGURE 3.11, SHOWING THE SIMULATED S11 RESPONSE FOR A LOG PERIODIC CIRCULAR TOOTHED ANTENNA WITH $k=2$, USING SONNET LITE SIMULATION SOFTWARE [158]. THE S11 RESPONSE AS A FUNCTION OF ILLUMINATING FREQUENCIES SHOWS SEVERAL RESONANCES, MOST NOTICEABLY AT $\sim 0.5\text{THz}$, 0.8THz , 1.2THz AND 1.95THz | 117 |
| FIGURE 3.12 SHOWING THE SIMULATED S11 RESPONSE FOR A BOWTIE ANTENNA, USING SONNET LITE SIMULATION SOFTWARE [158]. THE S11 RESPONSE AS A FUNCTION OF ILLUMINATING FREQUENCIES SHOWS SEVERAL RESONANCES, MOST NOTICEABLY AT $\sim 0.6\text{THz}$, 1.2THz , 1.8THz AND 2.4THz | 118 |
| FIGURE 3.13. SHOWING THE SIMULATED S11 RESPONSE FOR A BEETLE ANTENNA, USING SONNET LITE SIMULATION SOFTWARE [158]. THE S11 RESPONSE AS A FUNCTION OF ILLUMINATING FREQUENCIES SHOWS SEVERAL RESONANCES, MOST NOTICEABLY AT $\sim 0.7\text{THz}$, 1.2THz , 1.8THz AND 2.5THz | 119 |
| FIGURE 3.14 SHOWING HOW THE SIMULATED POWER AT 1.2THz VARIES WITH ANTENNA TERMINATION IMPEDANCE WHICH IS EQUATED TO THE GRAPHENE CHANNEL IMPEDANCE. A TYPICAL GFET CHANNEL RESISTANCE IS $1\text{-}10\text{k}\Omega$ | 120 |
| FIGURE 3.15, SHOWING A) THE “BEETLE” (LEFT) AND BOWTIE (RIGHT) ANTENNAE AND B) THE LOG-PERIODIC, CIRCULAR TOOTHED ANTENNA (NOT TO SCALE). BOTH THESE WERE DESIGNED TO HAVE A RESONATING FREQUENCY AT THE REQUIRED 1.2THz . HERE BLUE IS Si, LIGHT PURPLE IS SiO_2 , YELLOW IS THE Ni-AL CONTACT AND BLACK IS THE GRAPHENE. | 121 |
| FIGURE 4.1 SHOWING THE CONCEPT USED IN REFS. [75] AND [78] FOR THE X-RAY GFET. THE CHARGE CARRIERS ARE EXCITED AFTER INCIDENT RADIATION IS ABSORBED BY THE SEMICONDUCTOR, AND ARE THEN FUNNELLED TOWARDS THE GRAPHENE BY THE APPLICATION OF A GATE VOLTAGE. | 124 |
| FIGURE 4.2 SHOWING CASINO SIMULATIONS FOR THE TRAJECTORY OF ELECTRONS WITH AN INITIAL ENERGY OF A) 10keV , B) 50keV , C) 100keV , AND D) 500keV THROUGH A $500\mu\text{m} \times 500\mu\text{m} \times 500\mu\text{m}$ SILICON WAFER. LOWER ENERGY ELECTRONS, E.G. AT 10keV , ARE MORE QUICKLY STOPPED IN THE WAFER, AND GENERATE FEWER SECONDARY CHARGE CARRIERS THAN ELECTRONS WITH AN INITIAL ENERGY OF 500keV . AT THE HIGHEST ENERGIES, THESE ELECTRONS CAN PASS OUT OF THE WAFER. | 127 |
| FIGURE 4.3 SHOWING A) A SCHEMATIC OF THE INITIAL SIMULATION SETUP, WITH FIVE GRAPHENE SAMPLES OF $10\mu\text{m} \times 10\mu\text{m}$, $20\mu\text{m} \times 20\mu\text{m}$, $30\mu\text{m} \times 30\mu\text{m}$, $40\mu\text{m} \times 40\mu\text{m}$ AND $50\mu\text{m} \times 50\mu\text{m}$. FOR $V_G=1\text{V}$, THE SIMULATED VOLTAGES ACROSS THE SAMPLE OF B) $V(z=500\mu\text{m}, x)$ AND C) $V(z=500\mu\text{m}, y)$ INDICATE HOW THE VOLTAGE VARIES CLOSE TO THE 5 SAMPLES ON THE SUBSTRATE OF INCREASING SIZE. D) SHOWS, FOR $V_G=100\text{V}$, HOW THE VOLTAGE MEASURED DIRECTLY BENEATH EACH SAMPLE VARIES AS A FUNCTION OF SAMPLE POSITION, WITH THE $10\mu\text{m} \times 10\mu\text{m}$ SAMPLE AT $x=50\mu\text{m}$, THE $20\mu\text{m} \times 20\mu\text{m}$ SAMPLE AT $x=110\mu\text{m}$, THE $30\mu\text{m} \times 30\mu\text{m}$ SAMPLE AT $x=190\mu\text{m}$, THE $40\mu\text{m} \times 40\mu\text{m}$ SAMPLE AT $x=250\mu\text{m}$, AND THE $50\mu\text{m} \times 50\mu\text{m}$ SAMPLE AT $x=375\mu\text{m}$. E) SHOWS THE SAME DATA IN TERMS OF THE SAMPLE AREA, WITH THE GREATEST VOLTAGE SIMULATED BENEATH THE SMALLEST GRAPHENE SAMPLE, AND THEREFORE THE GREATEST FIELD ACROSS THE DIELECTRIC. AN ELECTRON-HOLE PAIR GENERATED IN THE ABSORBER WILL CAUSE A MODULATION IN THE FIELD, SO FOR A SMALLER SAMPLE SIZE THIS GIVES THE OPPORTUNITY FOR A GREATER CHANGE IN THE FIELD, AND THEREFORE MORE SENSITIVE DETECTION. | 128 |
| FIGURE 4.4 SHOWING A) THE ARRANGEMENT OF THE PROPOSED GFET, WITH THE SILICON WAFER (SHOWN IN BLUE), THE SiO_2 DIELECTRIC (SHOWN IN GREEN), SINGLE LAYER GRAPHENE (SHOWN IN BLACK) AND CONTACT PADS (SHOWN IN GREY). B) SHOWS THE EQUIPOTENTIALS FOR $V_{\text{GATE}}=-10\text{V}$, $V_{\text{DRAIN}}=0\text{V}$ AND $V_{\text{SOURCE}}=0.01\text{V}$ OUTPUTTED BY THE COMSOL SIMULATIONS. C) SHOWS THE LOG OF THE HOLE CONCENTRATION ACROSS THE SIMULATION; THE ARROWS INDICATE HOW AN INITIAL AREA OF LOW HOLE DENSITY IS FUNNELLED THROUGH THE SILICON WAFER DUE TO THE APPLICATION OF THE GATE VOLTAGE. D) SHOWS HOW THE GATE VOLTAGE CHANGES THE LOG OF THE DENSITY OF ELECTRONS AND HOLES IN THE SILICON. | 131 |
| FIGURE 4.5, SHOWING A) THE SIMULATED HOLE AND ELECTRON CONCENTRATION BENEATH THE GRAPHENE OVER TIME, FOR DIFFERENT VALUES OF THE GATE VOLTAGE V_G . B) SHOWS THE ELECTRON ACCUMULATION TIME AS A FUNCTION OF GATE VOLTAGE, WHICH SHOWS A SIGNIFICANT PEAK FOR $V_G \sim 0\text{V}$. C) SHOWS THAT THE CARRIER RECOMBINATION TIME IS FASTEST FOR $V_G \sim 0\text{V}$ BECAUSE THERE IS NO FIELD TO ACCELERATE THE CHARGE CARRIERS SO THEY RECOMBINE QUICKER BY INTERACTING WITH OTHER CHARGE CARRIERS RATHER THAN BEING FUNNELLED FROM THE DIELECTRIC. | 132 |
| FIGURE 4.6, SHOWING A) THE CHARGE CARRIER CONCENTRATION BENEATH THE GRAPHENE AS A FUNCTION OF TIME AND CHANNEL LENGTH. B) SHOWS THE ABSOLUTE CHANGE IN CARRIER CONCENTRATION BETWEEN THE INITIAL AND | |

ACCUMULATED STATES AS A FUNCTION OF CHANNEL LENGTH, AND C) SHOWS THE FINAL CARRIER CONCENTRATION AS A FUNCTION OF CHANNEL LENGTH, WHICH SHOW A PEAK CONCENTRATION FOR $8\mu\text{m}$ (HOLES) AND $18\mu\text{m}$ (ELECTRONS). D) SHOWS THAT THE ACCUMULATION TIME FOR BOTH ELECTRONS AND HOLES IS REDUCED FOR SMALL CHANNEL LENGTHS, AND E) SHOWS THAT THE RECOMBINATION TIME FOR ELECTRONS OCCURS FOR $L < 16\mu\text{m}$ WITH LITTLE CHANGE FOR THE HOLE RECOMBINATION TIME AS A FUNCTION OF CHANNEL LENGTH. 135

FIGURE 4.7 SHOWING A) THE PROPOSED GDEPFET DEVICE ARCHITECTURE [74], WITH AN N-WELL, SHOWN AS THE RED BOX, GENERATED DIRECTLY BENEATH THE GRAPHENE AND A CLEAR CONTACT TO REMOVE THE CHARGE CARRIERS, AND B) THE ELECTRIC POTENTIAL OF THE DETECTOR DESIGN AS SIMULATED IN COMSOL AND ALSO SHOWN IN REF. [74] 138

FIGURE 4.8 SHOWING A) THE CHANGE IN ELECTRON AND HOLE CONCENTRATION FOR DIFFERENT VALUES OF V_{CLEAR} , AND B) THE FINAL SIMULATED CARRIER CONCENTRATIONS FOR ELECTRONS AND HOLES AS A FUNCTION OF V_{CLEAR} . C) SHOWS THE CHANGE IN HOLE CARRIER CONCENTRATION BETWEEN THE INITIAL AND FINAL CONCENTRATIONS AS A FUNCTION OF V_{CLEAR} WITH THE SMALLEST MAGNITUDE CHANGE FOR $V_{\text{CLEAR}} \sim 0\text{V}$, AN INCREASE IN THE HOLE CONCENTRATION FOR $V_{\text{CLEAR}} > 0\text{V}$ AND A DECREASE FOR $V_{\text{CLEAR}} < 0\text{V}$. D) SHOWS THE EQUIVALENT CHANGE IN ELECTRON CARRIER CONCENTRATION AS A FUNCTION OF V_{CLEAR} WITH A VERY SLOW RELATIONSHIP BETWEEN THE CHANGE IN CARRIER CONCENTRATION AND V_{CLEAR} ESPECIALLY GIVEN THE GREATER THAN FOUR ORDER OF MAGNITUDE CHANGE IN THE CARRIER CONCENTRATION..... 140

FIGURE 4.9, SHOWING A) THE CHANGE IN THE CARRIER CONCENTRATION OVER TIME FOR DIFFERENT INITIAL WELL CONCENTRATIONS, AND B) THE CHARGE CARRIER RELAXATION TIME AS A FUNCTION OF INITIAL WELL CONCENTRATION, WITH A QUICKER RELAXATION TIME FOR LOWER WELL CONCENTRATIONS. 141

FIGURE 4.10, SHOWING A) HOW THE GATE VOLTAGE REDUCES THE CARRIER CONCENTRATION WITHOUT THE NEED FOR V_{CLEAR} , B) THAT THE FINAL CARRIER CONCENTRATION FOR BOTH ELECTRONS AND HOLES IS MINIMISED FOR $V_G < 0\text{V}$, AND C) THAT THE CARRIER CONCENTRATION IS MINIMISED FOR HOLES AND MAXIMISED FOR ELECTRONS FOR $V_G \sim 0\text{V}$. THEREFORE, THE WELL IS CLEARED IN APPROXIMATELY $1\mu\text{s}$ 142

FIGURE 4.11 SHOWING A) THE SCHEMATIC CLOSER TO WHAT WAS EVENTUALLY FABRICATED, WITH THE Si GATE SHOWN IN BLUE, THE SiO_2 ABSORBER SHOWN IN GREEN, THE N-WELL SHOWN IN RED AND Ni-AL CONTACTS SHOWN IN GREY, AND B) THE EQUIPOTENTIALS AS SIMULATED IN COMSOL FOR $V_{\text{CLEAR}} = 10\text{V}$ AND $V_{\text{GATE}} = -15\text{V}$ 144

FIGURE 4.12 SHOWING A) THE CHANGE IN CARRIER CONCENTRATION OVER TIME FOR DIFFERENT VALUES OF V_{CLEAR} , B) THAT THE RECOMBINATION TIME IS MINIMISED FOR $V_{\text{CLEAR}} \sim 2.5\text{V}$, AND C) THAT V_{CLEAR} IS RELATED TO THE CHANGE IN HOLE CONCENTRATION, AND IS MAXIMISED FOR $V_{\text{CLEAR}} < -10\text{V}$ 145

FIGURE 4.13 SHOWING A) THE CHANGE IN CARRIER CONCENTRATION OVER TIME FOR DIFFERENT GATE VOLTAGES, B) THAT THE RECOMBINATION TIME IS LONGEST FOR $V_G \sim 0-5\text{V}$ FOR BOTH ELECTRONS AND HOLES, AND C) THAT THE CHANGE IN HOLE CONCENTRATION IS MAXIMISED FOR $V_G < 0\text{V}$ 146

FIGURE 4.14 SHOWING SCHEMATICS FOR A TOP GATED GFET PROPOSED IN REF. [168] (LEFT) AND A TOP AND BOTTOM GATED DEVICE PROPOSED IN REF. [169]. BOTH STRUCTURES ARE ESSENTIALLY THE SAME AND COULD BE USED IN BOTH ARRANGEMENTS. 147

FIGURE 4.15, SHOWING A) THE RELATIONSHIP BETWEEN CONDUCTIVITY AND d FOR DIFFERENT RATIOS OF n_{ni} , WHERE n_i IS THE IMPURITY DENSITY. THIS SHOWS GOOD AGREEMENT WITH FIGURE 2 FROM REF. [9], WHICH IS SHOWN IN FIGURE 4.15B, ESPECIALLY FOR LOW n_{ni} AND d . C) SHOWS THE RELATIONSHIP BETWEEN CONDUCTIVITY AND n_{ni} FOR DIFFERENT POINT SCATTERING DENSITIES np , WHICH SHOWS THE SAME BEHAVIOUR AND ORDER OF MAGNITUDE OF THE CONDUCTIVITY COMPARED TO FIGURE 3 FROM REF. [9], SHOWN IN FIGURE 4.15D. BOTH FIGURE 4.15B AND FIGURE 4.15D ARE REPRODUCED FROM REF. [9] UNDER COPYRIGHT LICENCE FROM THE AMERICAN PHYSICAL SOCIETY. 149

FIGURE 4.16 SHOWING THE RELATIONSHIP BETWEEN CONDUCTIVITY AND GATE VOLTAGE FOR DIFFERENT A) DIELECTRIC CONSTANTS (FOR A THICKNESS OF 300nm) AND B) THICKNESSES OF THE DIELECTRIC (FOR $\epsilon = 3.8$). FOR THE BEST CONDUCTIVITY, THESE SIMULATIONS SUGGEST A HIGH DIELECTRIC CONSTANT AND/OR A THIN SUBSTRATE IS PREFERABLE. 150

FIGURE 4.17, SHOWING THE TRANSPARENCY OF A 0.5mm THICK SILICON WAFER AS A FUNCTION OF THE INCIDENT X-RAY PHOTON ENERGY, WHICH SHOWS THAT IT IS 100% OPAQUE TO ENERGIES UP TO 10keV , AND 100% TRANSPARENT AT ENERGIES ABOVE 100keV 151

FIGURE 4.18 SHOWING A) AND B) THE DESIGN OF AN X-RAY GFET TEST DEVICE. BLUE IS Si, LIGHT PURPLE IS SiO_2 , YELLOW IS THE Ni-AL CONTACT AND BLACK IS THE GRAPHENE OF DIFFERENT CHANNEL SIZES FOR EACH DEVICE. 152

| | |
|---|-----|
| FIGURE 5.1, SHOWING A) THE LAYOUT OF THE BILAYER GRAPHENE ON THE CHIP MANUFACTURED BY THE UNIVERSITY OF CAMBRIDGE, AND B) AND C) THE RAMAN SPECTRA FOR THE AB-STACKED AND TWISTED STACKED BILAYER GRAPHENE SAMPLES, RESPECTIVELY. ANALYSIS OF THE LOW RAMAN SHIFT MODES ALLOW FOR DIFFERENTIATION BETWEEN THE AB- AND TWISTED MODES, WHILE THE SAMPLES SHOWN IN B) AND C) SHOW THE CHARACTERISTIC G, 2D AND D PEAKS [173]. D) SHOWS THE RESISTANCE-GATE VOLTAGE RELATIONSHIP OF THE AB- AND TWISTED-STACKED BILAYER GRAPHENE SAMPLES, WITH A $V_{\text{DIRAC}} \sim 40\text{V}$ FOR THE AB-STACKED, AND $V_{\text{DIRAC}} \sim 35\text{V}$ FOR THE TWISTED-STACKED. THE RAMAN SPECTRA AND RESISTANCE MEASUREMENTS WERE MADE BY RESEARCHERS AT THE UNIVERSITY OF CAMBRIDGE. | 156 |
| FIGURE 5.2 SHOWING THE OPTICAL MICROGRAPH OF A) AN INDIVIDUAL DOMAIN OF MM SIZED CVD GROWN SINGLE LAYER GRAPHENE ON Cu, PRODUCED BY A RESEARCHER AT THE UNIVERSITY OF CAMBRIDGE, AND B) A SINGLE 155 μm GRAIN OF BILAYER GRAPHENE ON AN SiO_2/Si SUBSTRATE. | 159 |
| FIGURE 5.3. THE DIFFERENCE IN GRAPHENE GROWTH FOR SINGLE LAYER, BILAYER AND TRILAYER GRAPHENE, SHOWING GROWTH UNDERNEATH THE SINGLE LAYER SHEET. | 159 |
| FIGURE 5.4. THE PROCESS FOR THE GRAPHENE TRANSFER. THE PROCESS STAGES ARE: 1) GRAPHENE (BLACK) IS GROWN ON COPPER (ORANGE), 2) PMMA (LIGHT BLUE) IS SPIN COATED ONTO THE SAMPLE (3000REVS FOR 30S AND BAKED FOR 90 SECONDS AT 180 DEGREES), 3) THE BACK SIDE OF THE COPPER IS OXYGEN PLASMA ETCHED, AND THEN IT IS PLACED IN AN IRON CHLORIDE BATH (YELLOW) TO ETCH AWAY, 4) THIS IS TRANSFERRED INTO A WATER (GREY) BATH, 5) THIS IS THEN TRANSFERRED ONTO THE SILICON WAFER BEFORE DRYING AND BAKING FOR 5 MINUTES AT 150 DEGREES, AND 6) THE PMMA IS THEN WASHED AWAY. | 160 |
| FIGURE 5.5 SHOWING A) THE SPIN COATER AND B) THE HOT PLATE. | 161 |
| FIGURE 5.6 SHOWING A) THE CHIP HOLDER RACK, B) THE CHIP HOLDER AND C) THE NANOBEAM EQUIPMENT AT THE UNIVERSITY OF CAMBRIDGE. | 162 |
| FIGURE 5.7, SHOWING THE IMPORTANCE OF DEVELOPMENT TIME TO ENSURE CORRECT DEVELOPMENT OF THE SAMPLE, IN THIS CASE FOR A POSITIVE PHOTORESIST. EACH PHOTORESIST WILL HAVE AN IDEAL DEVELOPMENT TIME, AS OUTLINED IN TABLE 5-2. DEVELOPING THE SAMPLE FOR A TIME LESS THAN THIS WILL UNDERDEVELOP THE SAMPLE, AND FOR A TIME GREATER THAN THIS WILL OVERDEVELOP THE SAMPLE..... | 163 |
| FIGURE 5.8 SHOWING A) THE BESPOKE DIFFUSION PUMP THERMAL EVAPORATOR, LOCALLY KNOWN AS THE BLUE EVAPORATOR, B) THE VESSEL WITH THE CURRENT CAUSING IT TO GLOW, C) THE EDWARDS FTM5 FILM THICKNESS MONITOR, AND D) THE CHIP, COATED IN AN EVAPORATED FOLD FILM, HELD ON BY CAPTON TAPE. | 165 |
| FIGURE 5.9. THE PRECISION ATOMICS METALLIFIER SPUTTER COATER AT THE UNIVERSITY OF CAMBRIDGE. | 166 |
| FIGURE 5.10, SHOWING SAMPLES A) BEFORE AND B) AFTER THE LIFT-OFF PROCESS. | 167 |
| FIGURE 5.11 SHOWING THE TRANSFER CHARACTERISTICS OF A GFET OPERATED IN AIR. THE LARGE HYSTERESIS AT TWO DIRAC POINTS IS DUE TO TRAPPING OF CHARGE CARRIERS. THE ARROWS DENOTE THE SWEEP DIRECTION. | 167 |
| FIGURE 5.12, SHOWING THE ENDURANCE OF ELECTRICAL PROPERTIES OF ENCAPSULATED GFET MEASURED OVER SEVERAL WEEKS IN AMBIENT CONDITIONS [73], REPRODUCED FROM REF. [73] WITH PERMISSION OF THE ROYAL SOCIETY OF CHEMISTRY. THE RESULTS SHOW THE FORWARD AND BACKWARD SWEEP FOR EACH OF THE SAMPLES. THE REPRODUCIBILITY IN THE CHARACTERISTICS IS VERY IMPORTANT IN PHOTON COUNTING APPLICATIONS. | 168 |
| FIGURE 5.13 SHOWING A) THE WIRE BONDER AND B) THE NEEDLE..... | 169 |
| FIGURE 5.14 SHOWING A) THE LENTON AIR OVEN AND B) THE GALLENKAMP VACUUM OVEN USED IN THE ANNEALING PROCESS. | 170 |
| FIGURE 5.15 SHOWING A) THE THICKNESS MONITOR AFTER A DEPOSITION OF 5NM OF Cr FOLLOWED BY 125NM OF Au THROUGH EVAPORATION, RESULTING IN A TOTAL 130NM THICK DEPOSITION, AND B) THE COMPLETED WIRE BONDED SAMPLES..... | 171 |
| FIGURE 5.16, SHOWING SEM IMAGES OF THE SAMPLES FROM PRAGUE BEFORE THE ALUMINA ALD. THEY SHOW A) HOLES AND B) TEARS IN THE TRANSFERRED GRAPHENE, C) REGIONS OF MULTILAYER GRAPHENE, D) LINES ORIGINATING FROM THE ORIGINAL GROWTH, AND E-H) OBVIOUS MARKS LEFT FROM AN IMPERFECT REMOVAL OF PMMA FROM THE ORIGINAL TRANSFER. | 173 |
| FIGURE 5.17. ALUMINA DEPOSITION ANALYSED IN AN SEM. THIS SHOWS A MUCH MORE UNIFORM COVERAGE, ALTHOUGH HOLES IN THE ALUMINA DEPOSITION ARE STILL VISIBLE WHERE THE ALUMINA WAS UNABLE TO NUCLEATE TO THE SURFACE. | 174 |

| | |
|---|-----|
| FIGURE 5.18 SHOWING A) THE OUTPUT FROM THE AFM MEASUREMENTS FOR TWO 20 μ m X 20 μ m SAMPLES. B) SHOWS THE MEASURED HEIGHT OF THE GRAPHENE ON A SILICON/SILICON DIOXIDE WAFER AND A 15NM THICK ALUMINA LAYER, WITH A VARIANCE $\Sigma\sim 331$ PM. D) AND E) SHOW THE SAMPLE, IN 3D, WITH CLEAR DEFECTS AND PMMA RESIDUE FROM THE TRANSFER AND MANUFACTURING PROCESSES. | 177 |
| FIGURE 5.19, SHOWING A) THE ETCHED GRAPHENE CHANNEL AFTER THE DEPOSITION OF THE CHROME-GOLD CONTACTS. B) SHOWS AN EXAMPLE OF ONE OF THE X-RAY DEVICES BEFORE WIRE BONDING, WHILE C) AND D) SHOWS A BEETLE THZ DEVICE AND A LOG-PERIODIC CIRCULAR TOOTHED ANTENNA RESPECTIVELY. E) SHOWS A SUCCESSFUL GATING OF ONE OF THE X-RAY DEVICES ON THE CHIP WITH A VERY NOISY OUTPUT (WITH A DIRAC POINT AT $V_G\sim 50-60$ V), WHILE F), G) AND H) SHOW EXAMPLES OF SUCCESSFULLY GATING THZ DEVICES, WITH A DIRAC POINT FOR EACH OF $V_G>80$ V. | 179 |
| FIGURE 5.20 SHOWING THE DAMAGE TO THE DEVICE RESULTING FROM A BAD LIFT-OFF, AND DUE TO THE FORCE APPLIED TO THE CONTACT PADS BY THE WIRE BONDER. | 180 |
| FIGURE 5.21, SHOWING THE ANALYSIS OF GRAPHENE SAMPLES USING OPTICAL MICROSCOPY TO IDENTIFY THE LOCATION OF A) BILAYER AND MULTILAYER ISLANDS, AND B) LARGER GRAIN BILAYER SAMPLES. USING THE ALIGNMENT MARKERS ALLOWED FOR THE MASK TO BE DRAWN ACCURATELY. | 181 |
| FIGURE 5.22, SHOWING A) THE ETCHING OF THE BILAYER REGIONS OF THE GRAPHENE, B) AFTER THE FIRST CHROME-GOLD EVAPORATION AND C) AND D) AFTER THE SECOND EVAPORATION (50X MAGNIFICATION AND 20X MAGNIFICATION RESPECTIVELY). | 182 |
| FIGURE 5.23, SHOWING THE ITO RESIDUE ON THE EQUIPMENT AFTER DEPOSITION, AND B) THE TRACKS OF ITO COMING FROM THE GRAPHENE BETWEEN THE GOLD SOURCE AND DRAIN TRACKS. | 183 |
| FIGURE 5.24, SHOWING THE MEASURED CURRENT BETWEEN THE SOURCE AND DRAIN OF THE BILAYER GRAPHENE CHANNEL FOR GATE VOLTAGES FROM $V_G=-60$ V TO $V_G=+60$ V APPLIED TO THE BOTTOM GATE (I.E. THE SILICON) OF THE BILAYER GRAPHENE DEVICE. | 184 |
| FIGURE 5.25, SHOWING THE GATE CURRENT MEASURED A) WITHOUT SCRATCHING OFF THE Ni-AL SHORT, B) AFTER SCRATCHING OFF THE SHORT. | 186 |
| FIGURE 5.26, SHOWING SUCCESSFULLY COMPLETED THZ STRUCTURES IN A) "BEETLE" CONFIGURATION", B) BOWTIE CONFIGURATION, C) LOG-PERIODIC CIRCULAR TOOTHED CONFIGURATION AND D) "BEETLE" CONFIGURATION. E) SHOWS THE FORWARD SWEEP AND BACK SWEEP THROUGH VOLTAGES BETWEEN $V_G=0$ V AND 100V SHOWING HOW THE DEVICE GATED, INDICATING A DIRAC POINT AT $V_G>100$ V. | 187 |
| FIGURE 5.27, SHOWING A) THE WORKING X-RAY DEVICE THROUGH ELECTRON BEAM LITHOGRAPHY, AND B) AND C) THE FORWARD SWEEP AND BACK SWEEP OF TWO DIFFERENT X-RAY DEVICES FABRICATED USING THE E-BEAM LITHOGRAPHY ROUTE TO IDENTIFY HOW THE DEVICES GATES, INDICATING A DIRAC POINT AT $V_G\sim 10-20$ V AND $V_G\sim 10-15$ RESPECTIVELY. | 188 |
| FIGURE 5.28, SHOWING THE BAD LIFT-OFF OF THE NICKEL-ALUMINIUM ON THE PHOTOLITHOGRAPHY DEVICES | 189 |
| FIGURE 5.29, SHOWING THE DEVICE WITH AN ALUMINA ENCAPSULATION THAT WAS REMOVED FROM OVER THE CONTACTS BY AN ALUMINA PHOSPHORIC ACID ETCH. | 190 |
| FIGURE 5.30, SHOWING PROBE STATION RESULTS OF DEVICE THAT WERE FABRICATED BY MASKING THE DEVICE BY PHOTOLITHOGRAPHY, WITH A)-E) BEFORE WIRE BONDING, AND F) AND G) AFTER WIRE BONDING. IN ALL CASES GATE HYSTERESIS WAS OBSERVED, WHERE THE CHANGE IN GATE VOLTAGE PROMOTES THE ADSORPTION OF FURTHER ENVIRONMENTAL DOPANTS ONTO THE DEVICE, WHICH CAUSES THE DIRAC POINT TO SHIFT. | 191 |
| FIGURE 5.31 SHOWING FOUR BILAYER GRAPHENE SAMPLES, REFERRED TO BY THE SHAPE OF THE SI WAFER: A) "BENDY LEFT", B) "MOST SQUARE", C) "CENTRAL SCRATCH" AND D) "BENT BOTTOM". | 192 |
| FIGURE 5.32 SHOWING A) THE DEPOSITION OF THE NICKEL AS CONTACTS TO THE ETCHED BILAYER AREAS, AND B) AND C) THE DEVICE AFTER THE DEPOSITION OF THE ITO TOP GATE AND THE INITIAL ETCHING WITH THE HF. | 193 |
| FIGURE 5.33 SHOWING A) THE SAMPLE AFTER THE SECOND ETCHING WITH THE HF AND DEPOSITION OF THE ALUMINIUM CONTACT, AND B) AND C) THE BOTTOM GATE SWEEPS FOR TWO OF THE DEVICES THAT WERE SUCCESSFULLY FABRICATED. | 194 |
| FIGURE 6.1, SHOWING A) HOW THE MAGNITUDE OF THE BAND GAP, EG , VARIES AS A FUNCTION OF THE DISPLACEMENT FIELD; FOR LARGE DISPLACEMENT FIELDS, $EG\sim\gamma 1=0.4$ eV. FOR $V_{T0}=15$ V AND $V_{B0}=45$ V. B) AND C) SHOWS THE THEORETICALLY EXPECTED VALUES AS FUNCTION OF THE TOP AND BOTTOM GATE VOLTAGES FOR THE BAND GAP, AND NET DOPING, RESPECTIVELY. THE LINE WHERE THE SMALLEST BAND GAPS ARE EXPECTED, AND THE LINE OF CHARGE NEUTRALITY | |

| | |
|---|-----|
| – WHERE THERE IS NO NET DOPING, AND THE FERMI LEVEL REMAINS IN THE CENTRE OF THE BAND GAP – ARE NOT PERPENDICULAR AND BOTH PASS THROUGH V_{T0}, V_{B0} | 200 |
| FIGURE 6.2, SHOWING A) THE OSCILLOSCOPE OUTPUT AS A FUNCTION OF TOP AND BOTTOM GATE, WHICH EVENTUALLY SUGGESTED A SHORTED TOP GATE, AND B) THE OSCILLOSCOPE VOLTAGE AS A FUNCTION OF V_B | 201 |
| FIGURE 6.3, SHOWING THE GATE OF THE DEVICE, WITH THE CURRENT MEASURED ON A) THE UP SWEEP AND B) DOWN SWEEP. C) AND D) SHOW THE EQUIVALENT MEASUREMENTS IN TERMS OF THE RESISTANCE. THE BLACK LINE INDICATES THE POSITION OF THE DIRAC POINTS, GIVEN BY THE MAXIMUM RESISTANCE OR MINIMUM CURRENT. | 204 |
| FIGURE 6.4, SHOWING HOW THE DEVICE GATES AS A FUNCTION OF TOP GATE VOLTAGE, FOR DIFFERENT BOTTOM GATE VOLTAGES. THE DIRAC POINT WITH THE MINIMUM RESISTANCE IS AT APPROXIMATELY $V_T=-12V$, WITH A CORRESPONDING $V_B=-30V$ | 204 |
| FIGURE 6.5, SHOWING THE MEASURED CHANGE IN RESISTANCE AS A FUNCTION OF TOP AND BOTTOM GATE VOLTAGES. THE DIRAC POINTS WERE IDENTIFIED AS THE MAXIMUM RESISTANCE AS A FUNCTION OF GATE VOLTAGES. THE MINIMUM RESISTANCE AMONG THESE DIRAC POINTS OCCURRED AT APPROXIMATELY $V_T=11V, V_B=35V$ | 205 |
| FIGURE 6.6, SHOWING TESTS ON THE TOP AND BOTTOM GATES TO ENSURE THE DIELECTRIC WAS INTACT. A) SHOWS GATING OF THE DEVICE BY CHANGING THE TOP AND BOTTOM GATE VOLTAGES, AND IN B) A POSITIVE OR NEGATIVE VOLTAGE PULSE IS OBSERVED WHEN THE GATE VOLTAGE IS INCREASING OR DECREASINGLY RESPECTIVELY..... | 207 |
| FIGURE 6.7, SHOWING THE MEASURED CHANGE IN A) CURRENT AND B) RESISTANCE OF THE GRAPHENE CHANNEL OVER TIME, WHILE C) SHOWS THE RATE OF CHANGE OF THE CURRENT CONVERGES FOR THOSE READINGS CLOSE TO THE DIRAC POINT. D) ILLUSTRATES HOW THE FERMI LEVEL IS CHANGING OVER MINUTES, MOVING TOWARDS HOLE TRANSPORT..... | 209 |
| FIGURE 6.8, SHOWING A STRONG TOP GATE VOLTAGE AND WEAK BOTTOM GATE VOLTAGE-DEPENDENT CAPACITANCE..... | 210 |
| FIGURE 6.9, SHOWING A) THE CHANGE IN MAGNITUDE OF MULTIPLE FAST VOLTAGE PULSES FROM THE CHARGE SENSITIVE PREAMPLIFIER FOR A 10MV INPUT OVER TIME, WITH B) SHOWING THE CORRESPONDING CHANGE IN CAPACITANCE. C) SHOWS THAT, FOR THE TOP GATE, NO EQUIVALENT CHANGE IN CAPACITANCE IS OBSERVED AFTER THE GATE VOLTAGE IS SET. THE DIELECTRIC THAT IS AFFECTED IS CLEARLY THE SiO_2 BOTTOM GATE DIELECTRIC..... | 211 |
| FIGURE 6.10, SHOWING THE EXPERIMENTAL SETUP, WITH THE BLUE SPECKLED REGION INDICATING THE AREA THAT WAS ILLUMINATED BY THE BLUE CW LASER, WITH A 10MV TAIL PULSE APPLYING THE VOLTAGE ACROSS THE CHANNEL, WITH THE RESULTING CURRENT MEASURED BY A PICOAMMETER. | 213 |
| FIGURE 6.11, SHOWING A) ILLUMINATION DEPENDENCE WHICH SHOWS SENSITIVITY TO THE BLUE LASER BUT NOT TO THE RED, B) AND C) TOP GATE VOLTAGE DEPENDENCE FOR $V_B=0V$. D) SHOWS A RATE OF CHANGE OF CURRENT AS A FUNCTION OF GATE VOLTAGE, WHICH VARIES DEPENDING ON WHETHER THE GATING IS BEING CHARGED UP OR DOWN – THIS SUGGESTS SOME LONG TIMESCALE PROCESS OCCURRING IN THE DIELECTRIC..... | 215 |
| FIGURE 6.12, SHOWING A) AND B) THE LASER INTENSITY DEPENDENCE BY ATTENUATING THE LASER SOURCE BY ND FILTERS, RELATED TO THE CHARGING UP OR DOWN OF THE TOP GATE VOLTAGE. C) SHOWS THE RATE OF CHANGE OF CURRENT AS A FUNCTION OF ND VALUE TO INDICATE HOW THE CURRENT IS AFFECTED BY A MORE POWERFUL LASER SOURCE, WHICH IS EXTRAPOLATED IN D) TO INDICATE HOW THE RATE OF CHANGE OF CURRENT IS PROPORTIONAL TO THE TOTAL ILLUMINATING POWER..... | 216 |
| FIGURE 6.13, SHOWING A) NO BLUE LASER SENSITIVITY WHEN THE DEVICE WAS BOTTOM GATED, ATTRIBUTABLE TO THE INDUCED DRIFT IN THE CURRENT MASKING ANY FURTHER CHANGE IN THE CURRENT THAT IS INDUCED BY THE BLUE LASER. B) AND C) SHOWS THAT, AFTER A LONG ILLUMINATION, THE CURRENT STARTS TO RECOVER AT A CONSTANT RATE, SUGGESTING THAT A PROCESS ALLOWING THE PHOTOSENSITIVITY WAS RELAXING OR RECOMBINING. THE DOTTED BLUE LINE SHOWS THE POINT AT WHICH THE LASER WAS REALIGNED TO BETTER ILLUMINATE THE DEVICE, RESULTING IN A FURTHER CHANGE IN THE CHANNEL CURRENT. | 218 |
| FIGURE 6.14 SHOWING THE BOTTOM DIELECTRIC CAPACITANCE OVER TIME, WITH THE YELLOW DATA POINTS THE MEASUREMENTS BEFORE ILLUMINATION, AND THE BLUE DATA POINTS INDICATING THE CAPACITANCE OVER TIME AFTER ILLUMINATION BY THE BLUE LASER. | 219 |
| FIGURE 6.15. PARTS OF THE DILUTION REFRIGERATOR, INCLUDING THE DUMP AND DIFFERENT TEMPERATURE STAGES OF THE FRIDGE, WHICH REACHES AS LOW AS 300MK AT THE BOTTOM..... | 221 |
| FIGURE 6.16. BILAYER GRAPHENE CHIP ATTACHED TO THE FRIDGE UPON A LAYER OF APIAZON THERMAL GREASE. ELECTRICAL CONNECTION TO THE GRAPHENE IS ACHIEVED USING CW2400 SILVER EPOXY..... | 222 |

| | |
|--|-----|
| FIGURE 6.17. LOCATION OF PRESSURE VALVES AND CHANNELS ON THE PUMPING CART. CH3 DISPLAYS THE PRESSURE OF THE TURBO PUMP, WHICH MUST NOT SEE A PRESSURE $>10^{-4}$ MBAR OR IT RISKS BEING DAMAGED. PV3 IS A VALVE THAT CONTROLS THE AIR FLOW THROUGH THE TURBO PUMP, AND PV4 CONTROLS THE FLOW TO THE CRYOSTAT. FULL DETAILS OF THE PUMP DOWN PROCEDURE ARE LISTED IN APPENDIX 2. | 223 |
| FIGURE 6.18, SHOWING THE CHANGE IN FRIDGE TEMPERATURE OVER TIME. IT APPEARS TO GO THROUGH SEVERAL DIFFERENT PHASES, WITH A DIFFERENCE IN THE RATE OF CHANGE OF TEMPERATURE BETWEEN $3K \rightarrow 30K$ AND $30K \rightarrow 290K$ | 224 |
| FIGURE 6.19, SHOWING THE NET CHANGE IN CURRENT OVER TIME FOR THREE TEMPERATURES. WHEN THE DEVICE WAS COOLED, THE RATE OF CHANGE OF CURRENT AT THE DIRAC POINT WAS MUCH LOWER, SUGGESTING THAT THE CHANGE IN CAPACITANCE IS RELATED TO THERMALLY EXCITED STATES OF THE DIELECTRIC LAYER. | 225 |
| FIGURE 6.20, SHOWING THE GATE OF THE DEVICE AS A FUNCTION OF TOP AND BOTTOM GATE VOLTAGE, WITH THE CURRENT MEASURED FOR A) 66K, B) 93K AND C) 148K. THERE IS NO NOTICEABLE CHANGE IN THE ENVIRONMENTAL DOPING VALUES, NOR THE RESISTANCE. | 226 |
| FIGURE 6.21, SHOWING THE ALIGNMENT OF THE OPTICAL FIBRE WITH THE DETECTOR ON THE "COLD FINGER". | 227 |
| FIGURE 6.22 SHOWING, AT 166K, A) THE GATING OF THE DEVICE AS A FUNCTION OF V_T FOR $V_B=30V$, AND B) THE ILLUMINATION OF THE DEVICE FOR DIFFERENT GATE VOLTAGES, WHERE THE DOTTED LINES INDICATE THE CURRENT AS V_T TRANSITIONS BETWEEN ONE GATE VOLTAGE AND ANOTHER. C) SHOWS THE RESPONSE OF THE DEVICE TO BLUE LASER (INDICATED BY THE BLUE BLOCK) ILLUMINATION FOR $V_T=10V, 15V$ AND $20V$. THIS SUGGESTS THAT THIS EFFECT IS ONLY OBSERVABLE AT ELECTRON CARRIER DENSITIES. | 228 |
| FIGURE 6.23 SHOWING, AT 134K, THE CHANGE IN THE CHANNEL CURRENT DUE TO ILLUMINATION OF THE DEVICE BY A) THE BLUE LASER AND B) THE RED LASER, INDICATED BY THE BLUE AND RED BLOCKS RESPECTIVELY. ONE NOTES A WEAK PHOTORESPONSE DUE TO THE ILLUMINATION BY THE BLUE LASER, WITH LITTLE TO NO EFFECT BY THE RED LASER. THE DOTTED LINES INDICATE THE PERIODS OF ILLUMINATION BY EACH LASER. | 229 |
| FIGURE 6.24 SHOWING, AT 66K, THE CHANGE IN CURRENT DUE TO RED AND BLUE LASER ILLUMINATION FOR HOLE AND ELECTRON CARRIER DENSITIES. IN A), FOR HOLE CARRIER DENSITIES ($V_T=20V, V_B=0V$), THERE IS AGAIN NO NOTABLE EFFECT OF EITHER LASER SOURCE. IN B), FOR ELECTRON CARRIER DENSITIES ($V_T=20V, V_B=60V$), THERE IS A NOTICEABLE EFFECT ON THE CHANNEL CURRENT RESULTING FROM ILLUMINATION BY THE BOTH THE RED CW LASER AND THE BLUE CW LASER. | 230 |
| FIGURE 7.1. CURRENT AS A FUNCTION OF GATE VOLTAGE AT AIR PRESSURE AND LOW PRESSURE. AT LOW PRESSURE, THERE IS A SMALL SHIFT IN THE DIRAC POINT TOWARDS $0V$, AND A REDUCTION IN GATE HYSTERESIS. | 234 |
| FIGURE 7.2, SHOWING THE SPECTRAL RADIANCE FOR WAVELENGTHS BETWEEN $0\mu m$ AND $250\mu m$ FOR $T=293K$ | 235 |
| FIGURE 7.3 SHOWING A) THE LAYOUT FOR THE THZ ELECTRONICS, LOCATED IN A HERMETICALLY SEALED BOX, AND B) THE BOX WITH THE 2MM THICK HDPE WINDOW, WHICH IS TRANSPARENT AT TERAHERTZ FREQUENCIES BUT OPAQUE AT UV FREQUENCIES. | 235 |
| FIGURE 7.4 SHOWING A) THE EXPERIMENTAL ARRANGEMENT, WITH A CHOPPER PLACED IN FRONT OF THE BOX, AND B) THE BOX HOLDING A WEAK VACUUM OF ~ 0.1 TORR, WHICH IT HELD FOR APPROXIMATELY ONE HOUR. C) SHOWS THE HDPE WINDOW IS REFLECTIVE OF THE BLACKBODY RADIATION EMITTED FROM THE HUMAN BODY. | 236 |
| FIGURE 7.5 SHOWING A) AND B) EXAMPLE SQUARE WAVES OF VARYING PULSE WIDTH AND MAGNITUDES THAT WERE OBSERVED IN THE PRESENCE OF A BLACKBODY OBJECTS, IN THIS CASE A MUG OF HOT WATER, FOR GATE VOLTAGES OF $V_G = 1V$ AND $V_G = 10V$ RESPECTIVELY. C) IS A SCREENSHOT FROM THE LeCROY OSCILLOSCOPE, WHICH SHOW THE SQUARE WAVES OUTPUT FROM THE DETECTOR. THE SQUARE WAVES ARE OBSERVED IN THE OUTPUT FROM THE DETECTOR, ALTHOUGH THEY ARE NOT SYNCHRONISED WITH THE CHOPPER OUTPUT THAT WAS BEING USED AS THE TRIGGER. D) SHOWS A SCREENSHOT OF THE SIGNAL FROM THE OSCILLOSCOPE WHEN THE DETECTOR WAS REMOVED AND THE COAXIAL CABLE HAD BEEN SHORTED AND ESSENTIALLY ACTING AS AN ANTENNA, WHICH INDICATED THAT THE SQUARE WAVES ORIGINATED FROM ANOTHER SOURCE. | 238 |
| FIGURE 7.6, SHOWING A) AND B) THE ARRANGEMENT OF THE EXPERIMENTAL SETUP AND C) A SCHEMATIC LAYOUT OF THE EXPERIMENTAL SET UP. THE TERAHERTZ EMITTER WAS A TERAVIL LT-GAAs EMITTER. THE CHOPPER ROTATED AT 500HZ, AND WAS USED AS THE REFERENCE FREQUENCY FOR THE LOCK IN AMPLIFIER. D) SHOWS THE NORMALISED POWER OUTPUT OF THE LASER SOURCE AT TERAHERTZ FREQUENCIES, AND E) SHOWS THE KNOWN POWER OUTPUT OF THE TERAVIL EMITTER AS A FUNCTION OF THE TERAHERTZ BIAS VOLTAGE. | 240 |

| | |
|---|-----|
| FIGURE 7.7, SHOWING A) THE GFET MOUNTED IN THE DIECAST METAL BOX AND HOW IT WAS CONNECTED, AND B) THE MEASUREMENTS FROM GATING THE DEVICE, WHICH SHOW A DIRAC POINT AT $V_G \sim -5$ TO $-10V$ | 242 |
| FIGURE 7.8 SHOWING A) A TOPICA CW THz ARRANGEMENT, WITH THE PATH OF THE TERAHERTZ PHOTONS IN PINK, AND THE GRAPHENE DETECTOR IN THE LOCATION OF THE GOLAY CELL AT THE TOP OF THE IMAGE. B) SHOWS THE PULSED TERAHERTZ ARRANGEMENT, WITH A PULSED RED OPTICAL PHOTON (RED LINE) SPLIT OUTSIDE OF THE BOX, ONE BEAM ALLOWING ALIGNMENT OF THE DETECTOR, AND THE OTHER HALF EXCITING A TERAHERTZ PHOTON BEAM (PINK) FROM AN EMITTER HELD AT A BIAS VOLTAGE..... | 243 |
| FIGURE 7.9, SHOWING A) THE SIGNAL OBTAINED FROM THE LOCK-IN AMPLIFIER, V_{LOCKIN} , REPRESENTED ON A HEATMAP AS A FUNCTION OF THE GATE VOLTAGE, V_G , AND THE TERAHERTZ EMITTER BIAS, V_{THz} . B) SHOWS THE SIGNAL FROM THE LOCK-IN AMPLIFIER, FOR A TERAHERTZ EMITTER BIAS $V_{THz}=55V$, AS A FUNCTION OF THE GATE VOLTAGE, V_G ; THIS IS GIVEN BY THE BLACK LINE. THE DRAIN-SOURCE CURRENT IS ALSO PLOT AGAINST GATE VOLTAGE, GIVEN BY THE RED DOTS. THIS SHOWS THAT THE PEAK V_{LOCKIN} OCCURS CLOSE TO THE DIRAC POINT, WITH THE MINIMUM MAGNITUDE SIGNAL FOR $V_G \sim 0V$ | 246 |
| FIGURE 7.10, SHOWING THE MEASURED LOCK IN VOLTAGE AS A FUNCTION OF GATE VOLTAGE FOR DIFFERENT FREQUENCY ILLUMINATION. THE SAME BEHAVIOUR AS A FUNCTION OF GATE VOLTAGE IS OBSERVED, WITH A PEAK CLOSE TO THE DIRAC POINT, AND A MINIMUM AT POSITIVE VOLTAGES, THIS TIME AT APPROXIMATELY $5V$. THESE MEASUREMENTS INCLUDE A SERIES OF SYSTEMATIC ERRORS ARISING FROM THE VOLTAGE AND LASER SOURCES, WHICH MUCH BE REMOVED TO IMPROVE THE CHANCES OF NARROWBAND DETECTION. | 247 |
| FIGURE 7.11, SHOWING A) THE MEASURED SIGNAL AS A FUNCTION OF GATE VOLTAGE FOR THE DEVICE IN A SINGLE ENDED MEASUREMENT, ILLUMINATED BY THE BROADBAND PULSED TERAHERTZ SOURCE, AND B) MEASUREMENTS OF THE SAME DEVICE, BUT USING A DIFFERENTIAL MODE ON THE LOCK IN AMPLIFIER. | 248 |
| FIGURE 7.12, SHOWING A) THE SIGNAL AS A FUNCTION OF APPLIED BIAS AND GATE VOLTAGE ON A HEAT MAP AND B) THE SIGNAL AS A FUNCTION OF APPLIED BIAS TO THE EMITTER, WHICH SCALES QUADRATICALLY AS A FUNCTION OF ANTENNA BIAS VOLTAGE..... | 250 |
| FIGURE 7.13, SHOWING THE MEASURED SIGNAL IN SINGLE ENDED AND DIFFERENTIAL MODE. THE DIFFERENTIAL MODE IS APPROXIMATELY 6 TIMES LARGER. | 251 |
| FIGURE 7.14, SHOWING THE SIGNAL VARIATION FOR DIFFERENT TERAHERTZ FREQUENCY ILLUMINATION, WITH A DYNAMIC RANGE UP TO $100nV$ | 252 |
| FIGURE 7.15, SHOWING A COMPARISON BETWEEN THE THEORETICAL RESPONSE OF THE DETECTOR DUE TO THE LASER ILLUMINATION POWER MULTIPLIED BY THE ANTENNA RESPONSE, AND THE MEASURED RESULTS WITH THE PRESENCE OF THE THREE BAND PASS FILTERS. FURTHER EXPERIMENTAL RESEARCH SHOULD LOOK TO INVESTIGATE THE NARROWBAND TERAHERTZ RESPONSE AS A FUNCTION OF FREQUENCY..... | 253 |
| FIGURE 7.16 SHOWING THE OPTIMISED CONFIGURATION FOR THE MOST STABLE SIGNAL FROM THE DETECTOR. | 255 |
| FIGURE 7.17, SHOWING A HEAT MAP FOR THE THEORETICAL CURRENT AS A FUNCTION OF PHOTON FREQUENCY AND GATE VOLTAGE. RESONANCES OCCUR AS A FUNCTION OF FREQUENCY AT APPROXIMATELY $0.7THz$, $1.2THz$ AND $1.7THz$ DUE TO MODULATION BY THE LASER POWER AND THE ANTENNA RESPONSE, WITH PEAK CURRENT CLOSE TO THE DIRAC POINT OF $V_G \sim -7V$, AND A MINIMUM AT APPROXIMATELY $0V$ | 256 |
| FIGURE 7.18, SHOWING A) THE ANSATZ IPC SELECTED FOR THE SIMULATION, BASED ON THE FUNCTIONALITY SHOWN IN REF. [154]. B) SHOWS THE THEORETICAL RESPONSE OF THE DETECTOR FOR THE INITIAL PHOTOCURRENT SIMULATION SHOWN IN A). C) SHOWS THE NORMALISED PHOTOVOLTAGE RESPONSE OF THE DETECTOR COMPARING THE THEORETICAL RESPONSE AND RESPONSE FROM THE EXPERIMENT IN ASTON, ENABLING A BETTER ESTIMATE OF THE PHOTOCURRENT. D) SHOWS THE THEORETICAL PHOTOVOLTAGE OF THE DETECTOR IN ARBITRARY UNITS AS A FUNCTION OF GATE VOLTAGE. E) SHOWS THE IPC RESULTING FROM FITTING THE THEORETICAL VALUES TO THE EXPERIMENTAL DATA, WHICH IS ALSO OF THE FORM SHOWN IN REF. [154] F) SHOWS THE SAME FORM OF I_{pC} FOR THE SECOND DEVICE, USING MEASUREMENTS TAKEN AT NPL IN DIFFERENTIAL MODE..... | 258 |
| FIGURE 7.19 SHOWING THE MEASURED SIGNAL AS A FUNCTION OF TERAHERTZ POWER, INDICATING A SENSITIVITY OF AT LEAST $5\mu W$ | 259 |
| FIGURE 7.20, SHOWING A) THE MEASURED SIGNAL AS A FUNCTION OF ANTENNA BIAS VOLTAGE WITH THE CALCULATED NOISE FOR $-8V$ GATE VOLTAGE. B) SHOWS THE SIGNAL DIVIDED BY NOISE FOR EVERY DATA POINT, INDICATING AN SNR $\sim 35 \pm 5.6$ FOR AN ANTENNA BIAS OF $55V$ | 260 |

| | |
|--|-----|
| FIGURE 7.21, SHOWING WHERE THE DETECTOR IS NOW – INDICATED BY THE RED CIRCLE - IN COMPARISON TO THE AMBITION OF $NEP \sim 1nWHz^{-0.5}$, GIVEN BY THE BLUE LINE, IN TERMS OF THE NOISE SPECTRAL DENSITY AND THE RESPONSIVITY... | 261 |
| FIGURE 7.22 SHOWING THE JOHNSON NOISE AT ROOM TEMPERATURE AS A FUNCTION OF GATE VOLTAGE, INDICATING A DETECTOR NOISE OF $10-15nVHz^{-0.5}$ | 262 |
| FIGURE 7.23 SHOWING A) AN ITERATED BEETLE ANTENNA STRUCTURE WITH B) ONE MAJOR RESONANCE AT 1.2THZ (50 Ω TERMINATION ON BOTH ENDS) AND C) WITH THE SIMULATED POWER TRANSMISSION FOR A 5K Ω GRAPHENE CHANNEL. | 263 |
| FIGURE 7.24 SHOWING A POTENTIAL DETECTOR DESIGN THAT MAXIMISES THE ASYMMETRY IN THE DETECTOR..... | 265 |
| FIGURE 8.1, SHOWING THE WAVELENGTH DEPENDENCE OF PHOTON ABSORPTION LENGTH FOR SILICON. THE RED AND BLUE LINES SHOW THE ABSORPTION DEPTH AT 650NM AND 405NM LASER WAVELENGTHS RESPECTIVELY. DATA WAS OBTAINED FROM REF. [250] AND REF. [251]..... | 268 |
| FIGURE 8.2, SHOWING THE SIPM PULSE HEIGHT DISTRIBUTION FOR THE A) RED AND B) BLUE LASERS. THE OPE PEDESTAL IS SHOWN FOR THE SMALLEST PULSE HEIGHT, WITH THE INTENSITY OF EACH PE DISTRIBUTED IN A POISSON ENVELOPE FOR DIFFERENT ATTENUATION VALUES. C) AND D) SHOW THE RELATIONSHIP BETWEEN THE PULSE HEIGHT AND PE FOR RED AND BLUE LASERS, RESPECTIVELY, INDICATING THE PULSE HEIGHT PER PE. | 270 |
| FIGURE 8.3, SHOWING THE TRANSIMPEDANCE AMPLIFIER ARRANGEMENT WITH THE GRAPHENE (GREY), SiO ₂ (GREEN) AND Si (BLUE). A 10MV BIAS VOLTAGE WAS APPLIED BETWEEN THE SOURCE AND DRAIN OF THE GRAPHENE, WITH THE PREAMPLIFIER OUTPUT DISPLAYED ON THE OSCILLOSCOPE..... | 270 |
| FIGURE 8.4 SHOWING THE CURRENT AS A FUNCTION OF THE GATE VOLTAGE WITH THE DIRAC POINT AT APPROXIMATELY 10V. As $V_{bias} = 10mV$, THIS INDICATES A CHANNEL RESISTANCE OF 1.2K Ω | 271 |
| FIGURE 8.5. LT SPICE SIMULATION SETUP FOR AMPLIFIER BOARD. R1 REPRESENTS THE LOCATION OF THE GRAPHENE. OTHER COMPONENTS OF THE CIRCUIT WERE DESIGNED FOR HIGH GAIN AND TO FILTER OUT HIGH FREQUENCY AC NOISE. | 272 |
| FIGURE 8.6, SHOWING THE LTSPICE SIMULATION FOR A PULSE IN THE RESISTANCE OF THE GRAPHENE FOR FEEDBACK CAPACITORS OF 1PF, 1NF AND 1 μ F. | 272 |
| FIGURE 8.7, SHOWING THE CALIBRATION OF THE AMPLIFIER FOR A) THE PULSE AMPLITUDE AS A FUNCTION OF CHANNEL RESISTANCE, AND B) THE PULSE AMPLITUDE AS A FUNCTION OF THE NUMBER OF CHARGE CARRIERS RELATED TO THE PRESENCE OF A CAPACITOR. | 273 |
| FIGURE 8.8, SHOWING THE INITIAL RESPONSE TO ILLUMINATION BY DIFFERENT PULSED LASERS. A) SHOWS ILLUMINATION OF THE DETECTOR BY A PULSED RED ($\lambda=650nm$) LASER SOURCE WITH A $\sim 50ps$ (MINIMUM) PULSE WIDTH, WHICH DEMONSTRATES THAT THE PHOTORESPONSE WAS RELATED TO THE TRIGGER FREQUENCY (3 μs OR 12 μs , OR 333kHz OR 83kHz RESPECTIVELY). B) SHOWS THAT THE SIGNAL PULSE HEIGHT IS RELATED TO THE GATE VOLTAGE V_G , SMALLEST FOR $V_G = 0V$ AND LARGER FOR $V_G = -25V$, WHEN ILLUMINATED WITH A PULSED RED LASER SOURCE WITH A 50PS PULSE WIDTH. THERE IS AN OBSERVED PERIODIC NOISE AT $\sim 200kHz$, LIKELY DUE TO NOISE FROM THE LASER. C) SHOWS THAT THE PHOTORESPONSE DIFFERS BETWEEN THE RED AND BLUE PULSED LASER SOURCES AT TWO DIFFERENT V_G , WITH AN INCREASED PULSE HEIGHT WITH THE RED PULSE LASER COMPARED TO THE BLUE, AND A RISE TIME AND A FALL TIME THAT IS FASTER FOR A MORE NEGATIVE V_G | 275 |
| FIGURE 8.9, SHOWING A) THE SIGNAL PULSE HEIGHT INCREASES FOR INCREASINGLY NEGATIVE V_G . IT SATURATES AT $V_G \sim -15V$, LIKELY DUE TO THE LIMITS ON CARRIER TRANSPORT IN THE Si GIVEN BY SRH RECOMBINATION [2]. B) SHOWS THAT THE PULSE HEIGHT FROM THE RED AND BLUE LASER ILLUMINATION BOTH SATURATE AT $V_G \sim -15V$, ALTHOUGH AT SIGNIFICANTLY DIFFERENT AMPLITUDES. THE BASELINE BECOMES NEGATIVE WITH NEGATIVE V_G AS THIS REPRESENTS THE CHANNEL CURRENT WHICH INCREASES AWAY FROM THE V_{Dirac} | 276 |
| FIGURE 8.10 SHOWS A SCHEMATIC FOR THE DETECTION MECHANISM, WITH THE DIPOLE BETWEEN THE ELECTRON AND HOLE PAIR LARGER FOR DEEPER DEPLETION REGIONS UNTIL IT BECOMES LIMITED BY THE SRH RECOMBINATION TIME. THE DIPOLE CREATED CAUSES A FIELD THAT CHANGES THE GRAPHENE CONDUCTIVITY..... | 278 |
| FIGURE 8.11 SHOWING A) HOW THE OBSERVED PULSE HEIGHT DECREASES WITH INCREASING ND ATTENUATION OF THE BLUE PULSED LASER WITH AN 800PS PULSE WIDTH. THE NOTICEABLE DIES OFF AT ABOUT ND1.5. B) SHOWS THAT THE PULSE HEIGHT FROM THE RED PULSED LASER DECREASES WITH ND ATTENUATION. THE OBSERVABLE PEAK DIES OFF AT ABOUT ND2.05. C) SHOWS THE RELATIONSHIP BETWEEN THE PULSED HEIGHT AND THE ESTIMATED TOTAL ENERGY DEPOSITED ON THE DETECTOR FROM A SINGLE LASER PULSE, EQUIVALENT TO THE ENERGY DEPOSITED FROM A SINGLE X-RAY PHOTON. THIS SUGGESTS THAT THE ENERGY SENSITIVITY IS $\sim 300keV$. D) SHOWS THE PULSE HEIGHT IN TERMS OF THE TOTAL NUMBER OF PHOTONS INCIDENT ON THE ABSORBER PER PULSE FROM THE RED PULSED LASER. | 280 |

| | |
|---|-----|
| FIGURE 8.12, SHOWING A) THE BASELINE VOLTAGE VERSUS GATE VOLTAGE WITH THE RED LASER FOR A RANGE OF ND VALUES, SHOWING NO CHANGE WITH PULSE AMPLITUDE, B) OSCILLOSCOPE VOLTAGE AGAINST GATE VOLTAGE AT DIFFERENT ATTENUATIONS, SHOWING THE DIFFERENCE IN THE SIGNAL AMPLITUDE WITH DIFFERENT ATTENUATORS (RED LASER, ~50PS PULSE WIDTH), C) THE NORMALISED OSCILLOSCOPE VOLTAGE AGAINST GATE VOLTAGE AT DIFFERENT ATTENUATIONS, SHOWING NO CHANGE WITH DIFFERENT ATTENUATORS (RED LASER, ~50PS PULSE WIDTH), AND D) THE OSCILLOSCOPE VOLTAGE AGAINST GATE VOLTAGE AT DIFFERENT ND VALUES, SHOWING NO CHANGE WITH DIFFERENT ATTENUATORS (BLUE LASER, 800PS PULSE WIDTH). | 282 |
| FIGURE 8.13, SHOWING A) CONTINUOUS ILLUMINATION WITH DIFFERENT SOURCES – NO ILLUMINATION, FULL LASER ILLUMINATION, PARTIAL RED LASER ILLUMINATION AND RED LASER ILLUMINATION THROUGH A HIGH GRIT ND DIFFUSER [259]. B) SHOWS THE PHOTORESPONSE FOR $V_G = -5V, -10V, -15V$ AND $-25V$ WHICH SUGGESTS THAT THE SIGNAL CAN BE RETRIEVED, ALBEIT SMALLER, BY MAKING V_G MORE NEGATIVE. THE AMPLITUDE OF THE SIGNAL FOR DIFFERENT V_G AND ILLUMINATION USING C) THE RED PULSED LASER (PULSE WIDTH=800PS) AND D) THE BLUE PULSED LASER (PULSE WIDTH=800PS) SHOWS HOW THE SIGNAL STILL SATURATES AT SIMILAR V_G , BUT THE SIGNAL MAGNITUDE DECREASES WITH INCREASING ILLUMINATING INTENSITY. | 283 |
| FIGURE 8.14 SHOWING THE OSCILLOSCOPE VOLTAGE AS A FUNCTION OF CONTINUOUS LASER FLUX. WITH A GREATER FLUX, THE PULSE HEIGHT DECREASES. AT MORE NEGATIVE GATE VOLTAGES, THE PULSE HEIGHT IS GREATER..... | 284 |
| FIGURE 8.15. A COMPARISON OF THE $I - VG$ CURVE BEFORE AND AFTER BLUE CW LASER ILLUMINATION, SHOWING THE PREDICTED SHIFT IN THE CURRENT..... | 285 |
| FIGURE 8.16. RED PULSED – BLUE CW ILLUMINATION SHOWING A) THE CHANGE IN SIGNAL WITH V_G AND B) THE PULSE AMPLITUDE AS A FUNCTION OF FLUX. THE PULSE HEIGHT FROM THE DETECTOR IS REDUCED WITH INCREASING CW LASER FLUX, BUT IT MAINTAINS THE SAME SATURATION BEHAVIOUR AS PREVIOUSLY OBSERVED. | 286 |
| FIGURE 8.17. BLUE PULSED – BLUE CW ILLUMINATION SHOWING A) THE CHANGE IN SIGNAL WITH V_G AND B) THE PULSE AMPLITUDE AS A FUNCTION OF FLUX. THE PULSE HEIGHT FROM THE DETECTOR IS REDUCED WITH INCREASING CW LASER FLUX, BUT IT MAINTAINS THE SAME SATURATION BEHAVIOUR AS PREVIOUSLY OBSERVED. | 286 |
| FIGURE 8.18, SHOWING THE POSITION OF THE CHARGE SENSITIVE PREAMPLIFIER AFTER THE GRAPHENE (LEFT) AND CONNECTED TO THE GATE (RIGHT). | 289 |
| FIGURE 8.19 SHOWING A) THE DEPENDENCE ON THE GATE VOLTAGE IN THE CHARGE SENSITIVE PREAMPLIFIER ARRANGEMENT, WITH SATURATION IN THE PULSE AMPLITUDE ATTRIBUTED TO LIMITS ON CARRIER TRANSPORT IN THE SILICON DUE TO SRH RECOMBINATION. B) SHOWS AN EXPONENTIAL-LIKE DECAY IN THE PULSE HEIGHT WITH INCREASING ATTENUATION. C) SHOWS AN INCREASE IN THE PULSE HEIGHT WITH INCREASING NUMBERS OF INCIDENT LASER PHOTONS, WHILE D) SHOWS THE ENERGY DEPOSITED IN THE ABSORBER, SUGGESTING ENERGY SENSITIVITY TO $\sim 175keV$ | 291 |
| FIGURE 8.20, SHOWING THE DIFFERENCE IN THE PULSE BETWEEN $V_{BIAS}=10mV$ AND $0mV$ TO SHOW A SMALL PULSE CONTRIBUTION ATTRIBUTED TO THE CHANGE IN GRAPHENE RESISTANCE FOR A GATE VOLTAGE OF A) $0V$ AND B) $-30V$. THIS CONTRIBUTION, BY APPLYING $V_{BIAS}>0V$, HAS A RISE TIME AND FALL TIME OF ORDER $100ns$ | 292 |
| FIGURE 8.21, SHOWING THE ORIGIN OF THE TWO COMPONENTS OF THE PHOTOSIGNAL. A) COMPARES THE ARRANGEMENT FOR $V_{BIAS}=0mV$ AND $V_{BIAS}=10mV$, INDICATING WHY A SIGNAL IS SEEN EVEN WHEN $V_{BIAS}=0mV$. THE RED ARROW INDICATES THE FIELD ACROSS THE DIELECTRIC LAYER, AND THE YELLOW ARROW INDICATES THE DC CURRENT THROUGH THE GRAPHENE. B) SHOWS THE MECHANISM FOR THE ABSORPTION OF THE PHOTON IN THE SILICON WAFER, AND ILLUSTRATES HOW THE SILICON WAFER AND THE CONTACTS ARE CAPACITIVELY COUPLED, WHILE THE DC CURRENT THROUGH THE GRAPHENE IS VARIED BY CHANGING THE FIELD WHEN $V_{BIAS}=10mV$ | 293 |
| FIGURE 8.22, SHOWING THE WIRING OF THE CHARGE SENSITIVE PREAMPLIFIER ARRANGEMENT WITH A RESISTOR EACH SIDE OF THE GRAPHENE TO GIVE A VOLTAGE CHANGE THAT GIVES A MEASURABLE CHANGE IN CHARGE DUE TO THE PRESENCE OF THE CAPACITOR. THE GRAPHENE IS REPRESENTED AS A VARIABLE RESISTOR, WHICH IS CONTROLLED BY THE GATE VOLTAGE. | 294 |
| FIGURE 8.23. THE DIFFERENT MAGNITUDE SIGNAL FROM THE SOURCE SIDE AND DRAIN SIDE OF THE GRAPHENE (WHICH REMAINS THE SAME WHEN THE CHARGE SENSITIVE PREAMPLIFIERS ARE SWAPPED OVER – I.E. THE BLUE SIGNAL REMAINS LARGER THAN THE RED SIGNAL) | 295 |
| FIGURE 8.24, SHOWING THE CHANGE IN THE PULSE AMPLITUDE WITH INCREASING V_G , AND THE PROPORTION OF THE SIGNAL THAT ARISES FROM THE CHANGE IN GRAPHENE CURRENT AND CAPACITIVE COUPLING BETWEEN THE SILICON AND THE CONTACTS. THE MAGNITUDE OF V_{PULSE} FOR THE PULSES WITH $V_{BIAS}=10mV$ AND $V_{BIAS}=0mV$, AND THE SIGNAL ATTRIBUTED TO THE GRAPHENE, SHOW SATURATION WITH INCREASINGLY NEGATIVE V_G | 296 |

FIGURE 8.25, SHOWING THE MAGNITUDE OF V_{PULSE} BY ATTENUATING THE INCIDENT LASER SIGNAL. A) SHOWS THE NUMBER OF RED PULSED LASER PHOTONS INCIDENT ON THE GRAPHENE. B) SHOWS THE EQUIVALENT SENSITIVITY OF THE DETECTOR FOR $V_{BIAS}=10\text{mV}$ AND 0mV AND HENCE ALLOWING THE SIGNAL ATTRIBUTABLE TO THE GRAPHENE TO BE IDENTIFIED..... 297

FIGURE 8.26 SHOWING THE CHANNEL CURRENT-GATE VOLTAGE RELATIONSHIP FOR DEVICES BUILT ON A) AND B) UNDOPED SILICON SAMPLES, AND C) AND D) DOPED SILICON SAMPLES. A CLEAR DIRAC POINT IS SEEN IN IN A), WHICH HAS GOOD ELECTRON AND HOLE MOBILITY AND $V_{DIRAC}\sim 20\text{V}$, WHEREAS THE OTHER SAMPLES HAVE GOOD HOLE MOBILITY AND POOR ELECTRON MOBILITY SO THE DIRAC POINT IS LESS OBSERVABLE..... 298

FIGURE 8.27, SHOWING A) THE MEASURED V_{RMS} FROM THE LOCK IN AMPLIFIER AS A FUNCTION OF THE GATE VOLTAGE WHEN THE SAMPLE IS ILLUMINATED BY THE RED PULSED LASER ATTENUATED BY ND1.7. THE ORANGE LINE, INDICATING MEASUREMENTS FROM $V_G=1\text{V}$ TO 16V , SHOWS A GREATER V_{RMS} THAN OTHER READINGS AT THE SAME V_G . THIS IS POTENTIALLY DUE TO MISALIGNMENT OF THE LASER OR ATTENUATOR BETWEEN THESE SAMPLES WHICH WOULD RESULT IN AN INCREASED PHOTO RESPONSE DUE TO INCREASED ILLUMINATION, WHICH WAS CORRECTED FOR THE DATASETS $V_G=20\text{V}\rightarrow 1\text{V}$ AND $V_G=1\text{V}\rightarrow 40\text{V}$. ALTERNATIVELY, THIS MAY BE DUE TO GATE HYSTERESIS AFFECTING THE ELECTRICAL PROPERTIES OF THE CHANNEL. HOWEVER, IN B) THE FITTED LINE TO THE AVERAGE OF ALL THE MEASURED V_{RMS} VALUES STILL SHOWS THE SAME SATURATING BEHAVIOUR AT GREATER V_G , ALBEIT WITH GREATER ERROR ON THE MEASUREMENTS BETWEEN $V_G=1\text{V}$ AND $V_G=16\text{V}$ 299

FIGURE 8.28, SHOWING A) THE SETUP USED FOR OPTIMISED DETECTION. B) SHOWS THE PHOTO RESPONSE, $V_{LOCK-IN}$, WHEN THE DEVICE IS ILLUMINATED BY A RED PULSED LASER AS A FUNCTION OF THE ND ATTENUATION FOR DIFFERENT R_{LOAD} AND CAPACITOR VALUES. IMPEDANCE MATCHING THE LOAD RESISTOR TO THE GRAPHENE RESISTANCE, $R_{LOAD}=R_{GRAPHENE}$, INCREASED $V_{LOCK-IN}$ BY A FACTOR ~ 10 . WHEN THE CAPACITOR WAS CHANGED FROM 2.2pF TO 22pF , THE MEASURED $V_{LOCK-IN}$ AGAIN INCREASED BY A FACTOR ~ 10 . THE NOISE IN THE MEASUREMENTS, V_{NOISE} , WAS MEASURED BY CALCULATING BY ATTENUATING THE SIGNAL BY ND7, SUCH THAT THE INCIDENT $PE\ll 1$ AND THEREFORE VERY LITTLE ILLUMINATION OF THE DETECTOR. A PHOTO RESPONSE $V_{LOCK-IN}>V_{NOISE}$ SUGGESTED SENSITIVITY AT THIS ATTENUATION. FOR ND4, THIS IS THE EQUIVALENT OF 10^3 PHOTONS, OR $\sim 3\text{-}5\text{keV}$. THE BLACK AND PINK ASTERISKS INDICATE THE SIGNAL FOR $V_{BIAS}=10\text{mV}$ AND $V_{BIAS}=0\text{mV}$, REPLICATING THE MEASUREMENTS FROM THE PREVIOUS SECTION, WITH A SMALL INCREASE WITH V_{BIAS} APPLIED..... 300

FIGURE 8.29 SHOWING THE DETECTOR ELECTRONICS USED WITH THE VOLTAGE PREAMPLIFIER. 302

FIGURE 8.30, SHOWING A) THE PREVIOUSLY OBSERVED GATE DEPENDENT PHOTOPEAK MAGNITUDE, WHICH SATURATES AT $\pm 5\text{-}10\text{V}$. IN B), THE SIGNAL CHANGES WHEN $V_{BIAS}=10\text{mV}$ IS APPLIED ACROSS THE GRAPHENE AND THE DEVICE IS ILLUMINATED BY AN UNATTENUATED LASER PULSE FOR $V_G=20\text{V}$ AND IN C) THE DIFFERENCE OF THE AVERAGE OF THOSE READINGS SUGGESTS THAT THE SIGNAL IS FORMED OF A COMPONENT FROM AC COUPLING BETWEEN THE ABSORBER CONTACTS, AND A COMPONENT FROM THE GRAPHENE $V_{GRAPHENE}$. IN D), THE MAGNITUDE OF $V_{GRAPHENE}$ INCREASES FOR INCREASING V_{BIAS} ACROSS THE GRAPHENE. 304

FIGURE 8.31, SHOWING A HISTOGRAM OF THE ENERGY DETECTED BY THE GFET, EXTRAPOLATED FROM FIGURE 8.30B. FITTING TO THIS GIVES $\text{FWHM}=1130\text{keV}$. THERE IS ALSO A SMALL SATELLITE PEAK AT $E\sim 22.5\text{MeV}$ 305

FIGURE 8.32 SHOWING A) THE ABSORPTION COEFFICIENT FOR SILICON AT DIFFERENT ENERGIES, AND B) THE CALCULATED TRANSPARENCY OF A 0.5mm THICK SI WAFER. 306

FIGURE 8.33 SHOWING AN r^{-2} -LIKE DECREASE IN THE SIGNAL AS THE RADIOACTIVE SOURCE IS BEING MOVED AWAY FROM THE DETECTOR, ALTHOUGH THIS SIGNAL IS WELL WITHIN THE NOISE. THESE RESULTS SUGGEST THAT THERE IS LITTLE TO NO DETECTOR SENSITIVITY TO THIS SOURCE. FURTHER WORK IS REQUIRED TO IMPROVE THE SNR IN THIS ARRANGEMENT. 308

FIGURE 8.34 SHOWING THE RESPONSE FOR DIFFERENT V_G AND X-RAY SOURCES USING A GOS SCINTILLATOR 20mm ABOVE THE GRAPHENE SAMPLE. 309

FIGURE 8.35, SHOWING A) THE THEORETICAL TRANSPARENCY OF THE EXPERIMENTAL SETUP AS A FUNCTION OF DISTANCE AND PHOTON ENERGIES – THE SILICON IS OPAQUE AT LOW PHOTON ENERGIES AND TRANSPARENT AT HIGHER PHOTON ENERGIES. B) SHOWS THAT THE THEORETICAL PROPORTION OF COMPTON SCATTERING EVENTS IS GREATEST FOR THE MOST ENERGETIC PHOTON ENERGIES, ALTHOUGH WITH ONLY 1% OF THE INCIDENT PHOTONS GENERATING COMPTON SCATTERING EVENTS IN THE SILICON WAFER. C) SHOWS THE SIGNAL FROM THE SIPM WITH A CSI SCINTILLATOR FOR A $\text{Cd-}109$ SOURCE, WITH D) COMPARING THE RESPONSE FROM THE SIPM (TOP) AND GRAPHENE (BOTTOM). THERE IS NO OBSERVABLE PEAK THAT SUGGESTS X-RAY SENSITIVITY. 311

FIGURE 8.36, SHOWING A) THE EXPERIMENTAL SETUP, WITH THE GFET DIRECTLY ILLUMINATED BY THE AMPTEK X-RAY GENERATOR. B) SHOWS THE OUTPUT X-RAY ENERGY SPECTRUM OF THE AMPTEK GENERATOR, PREVIOUSLY SHOWN IN REF. [271]. C) SHOWS THE MEASURED CURRENT THROUGH THE GRAPHENE AS A FUNCTION OF V_G 313

FIGURE 8.37, SHOWING A) THE EFFECT OF CHANGING THE V_G , WITH A RATE OF INCREASE OF THE CURRENT FROM ILLUMINATION TO PEAK REFLECTING THE $\Delta I \Delta V_G$ OF THE DEVICE, GIVEN BY FIGURE 8.36C, AT THAT V_G , WITH THE CURRENT DECREASING FOR ELECTRON CARRIER DENSITIES AS THE MODULATED GATE VOLTAGE APPROACHES V_{Dirac} . THE X-RAY SOURCE WAS TURNED ON AT 0 SECONDS, AND THE DASHED LINES INDICATE WHEN THE X-RAY SIGNAL WAS TURNED OFF. B) SHOWS THE RATE OF CHANGE OF CURRENT AGAINST $\Delta I \Delta V_G$ OBTAINED FROM FIGURE 8.36C, WHICH SHOWS THAT A GRAPHENE SAMPLE WITH A GREATER MOBILITY WILL RESULT IN A GREATER CHANGE IN THE CURRENT. NOTE THAT THE $\Delta I \Delta V_G$ VALUE FOR $\Delta I \Delta t = -200 \mu A s^{-1}$, OBTAINED FOR $V_G = 100V$ FOR ELECTRON CARRIER DENSITIES, WAS UNAVAILABLE SO IS REPRESENTED BY THE HORIZONTAL LINE GIVEN FOR $\Delta I \Delta V_G > 0$ 315

FIGURE 8.38, SHOWING THE SIGNAL FOR DIFFERENT FOR V_{XR} FOR A) $I_F = 5 \mu A$, B) $I_F = 10 \mu A$ AND C) $I_F = 100 \mu A$. D) SHOWS THE RESULTS FOR C) WITH A MOVING WINDOW FUNCTION 10S WIDE APPLIED TO THE RESULTS. THESE RESULTS SHOW THAT AN INCREASING V_{XR} , AND HENCE INCREASING MAXIMUM POWER, CAUSES THE PEAK ΔI TO INCREASES, WITH THE CHANGE OCCURRING AT A FASTER RATE. THE X-RAY SOURCE WAS TURNED ON AT $t = 0$ SECONDS, AND THE DASHED LINES INDICATE WHEN THE X-RAY SIGNAL WAS TURNED OFF. IN FIGURE 8.38C, THE SIGNAL IS DECREASED EVENT WHEN THE X-RAY SOURCE WAS STILL IRRADIATING THE DETECTOR – THIS WAS ATTRIBUTED TO THE EXTINGUISHING OF THE SIGNAL VIA THE SATURATION OF THE DEPLETION REGION. 317

FIGURE 8.39, SHOWING THE SIGNAL FOR A) $V_{XR} = 10kV$ AND $I_F = 10-100 \mu A$, AND B) $V_{XR} = 25kV$ AND $I_F = 25$ AND $100 \mu A$. THESE SHOW THAT, WITH AN INCREASING BEAM CURRENT, AND HENCE TOTAL ILLUMINATION POWER, THE PEAK SIGNAL CURRENT INCREASES WITH THE CHANGE OCCURRING AT A FASTER RATE. IN A) THE X-RAY SOURCE WAS TURNED ON AT 0 SECONDS AND IN B) IT WAS TURNED ON AT THE FIRST DASHED LINE, AND FOR BOTH DATASETS THE FINAL DASHED LINE INDICATES WHEN THE X-RAY SIGNAL WAS TURNED OFF. THIS CLEARLY SHOWS THAT THE SIGNAL TURNS ON AND OFF WITH THE X-RAY SOURCE. 318

Tables

TABLE 1-1. BRIEF SUMMARY OF COMPETITIVE PHOTODETECTOR TECHNOLOGIES, INCLUDING OPERATING PARAMETERS AND FIGURES OF MERIT. 34

TABLE 1-2. SUMMARY OF A SELECTION OF PHOTODETECTOR TECHNOLOGIES, WITH UP AND COMING GRAPHENE-BASED TECHNOLOGIES HIGHLIGHTED IN GREY FOLLOWED BY OTHER POTENTIAL SOLUTIONS. 59

TABLE 3-1. LIST OF OPTIONS FOR GFET MANUFACTURING. 113

TABLE 4-1, SUMMARISING HOW THE GATE VOLTAGE AND CHANNEL LENGTH CAN BE USED TO OPTIMISE THE TEMPORAL BANDWIDTH AND THE DYNAMIC RANGE. 136

TABLE 5-1. PREBAKING TEMPERATURES AND TIMES FOR THE MOST COMMON PHOTORESISTS. 161

TABLE 5-2. LIST OF THE POSTBAKE TEMPERATURES AND TIMES FOR SOME COMMON PHOTORESISTS, AND THE DETAILERS OF WHICH DEVELOPER TO USE. 163

TABLE 5-3. SPUTTER PARAMETERS FOR DIFFERENT METALS. 166

TABLE 5-4. STATUS OF DEVICES THAT WERE FABRICATED BETWEEN SEPTEMBER AND NOVEMBER 2015 AT THE UNIVERSITY OF CAMBRIDGE. 197

TABLE 8-1, SHOWING THE CALCULATED BUILT-IN VOLTAGE AND DEPLETION REGION SIZE IN A FORWARD-BIASED SILICON WAFER FOR $N_a = 1 \times 10^{14} \text{cm}^{-3}$ (EQUIVALENT TO P-TYPE SILICON OF $\rho \sim 100 \Omega \text{cm}$), $N_d = 1 \times 10^{14} \text{cm}^{-3}$, AND $T = 300K$. FOR A GREATER GATE VOLTAGE, THE WIDTH OF THE DEPLETION REGION GETS WIDER. 277

TABLE 8-2, SUMMARISING THE DETECTOR SNR AND NEP FOR DIFFERENT VALUES OF V_{XR} FOR $I_F = 100 \mu A$, CALCULATED AROUND THE SIGNAL PEAK IN FIGURE 8.38C. 319

1

The Role of Graphene in the Development of Novel Photodetector Solutions

1.1 Introduction

Single photon counting photodetectors require an incident single photon to be absorbed and give rise to a measurable signal. Many different technologies have been developed for photodetection and photon counting across a wide range of operating wavelengths, temperatures, and time and energy resolutions. For instance, photomultipliers, avalanche diodes [14] and transition edge sensors [15] can operate with single photon resolution but without wavelength specificity in the optical range. Other detector technologies do exist that allow for single photon counting with optical wavelength specificity [16], but most operate at extreme cryogenic temperatures [17].

These detectors have many different applications, in areas as diverse as medical and space sciences or security applications. For instance, a photon counting photodetector has applications on a satellite for the detection of faint, distant stars and exoplanets, or in fluorescence spectroscopy for use in characterizing biological samples. Single photon counting photodetectors also have quantum information applications, ranging from quantum key distribution (QKD) [18] [19] to time-correlated fluorescence spectroscopy of quantum wells [20]. These new quantum applications are making significant demands on existing technologies due to the required signal to noise ratio, detection efficiency, spectral range and photon number resolution [21] [22].

Graphene is an allotrope of carbon, specifically arranged in a 2D hexagonal lattice structure with sp^2 bonded carbon atoms. It has captured the world's attention since it was first isolated in 2004 [11][23] due to a unique combination of mechanical and optoelectronic properties [6][8] [9] [10] [11] [24]. Graphene has many properties with

great potential to develop new photodetector technologies that could outperform other existing materials.

In this first chapter, existing photodetection technologies across a wide range of energies are discussed, and then the fundamental properties of graphene relevant to photodetector technologies are presented. Consideration of ongoing research into graphene-based photodetectors then motivates the work to develop a bilayer graphene single photon counting photodetector for visible photons, a single X-ray photon counting graphene field effect transistor (GFET) and a GFET designed to utilise the Dyakonov-Shur effect for photons with a frequency of 1.2THz.

1.2 Comparable Photon Counting Photodetector Technologies

Many different techniques are currently capable of, and utilised for, single photon counting and low photon intensity photodetection over a wide range of photon energies and operating temperatures, with the figure of merit for some of these listed in table 1-1. For instance, for single photon counting of visible photons, STJs and MKIDs offer wavelength specificity and good temporal and energy resolution but operate at cryogenic temperatures, while avalanche photodiodes operate at room temperature, have good temporal resolution but lack wavelength specificity and energy resolution.

| Detector Type [25] | Operating Temperature | Operational Wavelength | Timing Resolution | Energy Resolution $\frac{E}{\delta E}$ | Responsivity | Size of Active Area | Photon Intensity |
|---|------------------------------|-------------------------------|--------------------------|---|---|----------------------------|-------------------------|
| Superconducting Tunnelling Junction [26] [27] | <1K | 1nm-100 μ m | 1 μ s | <20 (for E=1.8eV) <6 (for E=3.1eV) ~200 (E=0.4keV) ~500 (E=5.9keV) | >~100AW ⁻¹ | ~1mm ² | Single photon |
| MKID Detector [28] [26] [29] [30] [31] | 0.1K-1K | X-ray to IR | ~1 μ s | >20 | 10 ⁻⁷ rad per quasi-particle | > 1000 pixel array. | Single photon |
| Avalanche Photodiodes [32] [33] [34] | -20 °C -90 °C | ~ <1 μ m | 40ps+ | ~16 (for E=5.9keV) ~45 (for E=5.9keV) | ~50AW ⁻¹ | <~25mm ² | Single photon |
| Transition Edge Sensors [35] [36] [37] | 0.1K | ~1nm | 0.5ms | ~70 (for E=0.1keV) ~7000 (for E=10keV) | ~100000 AW ⁻¹ on transition region | ~5cm ² | Single photon |
| Microchannel plate photomultiplier tube [38] [39] | 300K | X-ray to IR | 25+ps | Most of spectrum - none Soft X-ray – V.poor | 5-1000mAW ⁻¹ | >1000mm ² | Single photon |

Table 1-1. Brief summary of competitive photodetector technologies, including operating parameters and figures of merit.

1.2.1 Superconducting Tunnelling Junction (STJ)

A superconducting tunnelling junction (STJ), figure 1.1, can be used for single photon counting at cryogenic temperatures with a wide wavelength detection range. An STJ works by utilising the absorbed photon energy to break Cooper Pairs of electrons in a superconducting film, typically tantalum [26][28]. STJs have an effective band gap of order 1meV, and operate at a low temperature $\sim 300\text{mK}$ to ensure low dark noise.

STJs have a time-tagging capability, a temporal resolution of order microseconds and a typical energy resolution of order 1eV for soft X-ray photons, and 0.1-0.2eV for near-infrared and visible photons, with the Fano limit as the inherent energy resolution [26] [28]. STJs have a typical responsivity of $>100\text{AW}^{-1}$, and an active area of $\sim 1\text{mm}^2$. STJs have a limitation to the maximum array size; DROIDS, distributed readout imaging detectors, are a route to large arrays of STJs with applications in imaging [40].

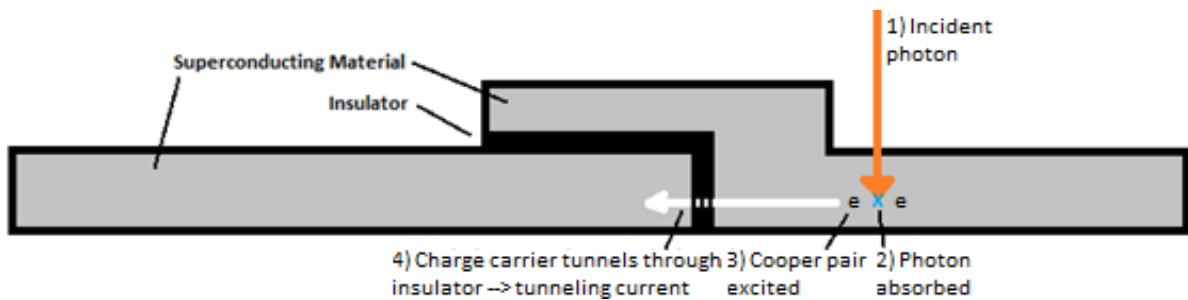


Figure 1.1. The photon is absorbed in the superconducting material, which breaks a Cooper pair with one of the electrons then tunnelling through the insulator and leads to a tunnelling current.

1.2.2 Microwave Kinetic Inductance Detector (MKID)

A microwave kinetic inductance detector (MKID) is sensitive to a wide range of photon energies. A circuit comprising a capacitor and an inductor forms a microwave resonator, figure 1.2; an absorbed photon splits Cooper pairs in the superconducting film (typically TiN) which alters the dynamic inductance of the inductor, changing the resonator frequency within the range 1-10GHz [41]. To observe the change in phase and amplitude, very sensitive measurements are made before charge carriers recombine in time periods of order 10^{-3} - 10^{-6} s.

This technique has been used to build a 1000 pixel detector array [42], which typically operates at temperatures of order 100mK [43] and has demonstrated position sensitivity with a noise equivalent power (NEP) of $\sim 10^{-17}\text{WHz}^{-1/2}$ [26] [28] [29] [30].

Ongoing research activities are being performed to investigate the use of graphene as an MKID [44] [45].

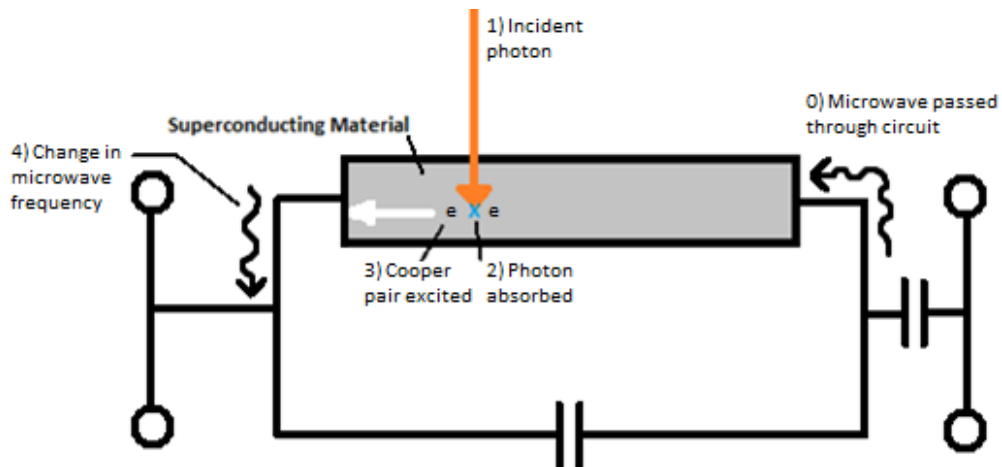


Figure 1.2 showing the Kinetic Inductance Detector in an LC circuit (based on the figure from ref. [43]). The photon is absorbed by the inductor material which changes the impedance of the circuit and hence the frequency of microwaves passed through the detector.

1.2.3 Transition Edge Sensor (TES)

A transition edge sensor (TES), a type of microcalorimeter, operates at the critical temperature of a superconducting material, T_c , which can vary between 10mK to 1-4K depending on the material used. A TES utilises the temperature dependent resistance of the sample operating at T_c which, in the case of a tungsten film, is at $T_c = 178\text{mK}$ [46]. The absorption of a photon causes a change in temperature and leads to a sharp change in the resistance [36], making it possible to determine the energy of an incident photon, figure 1.3.

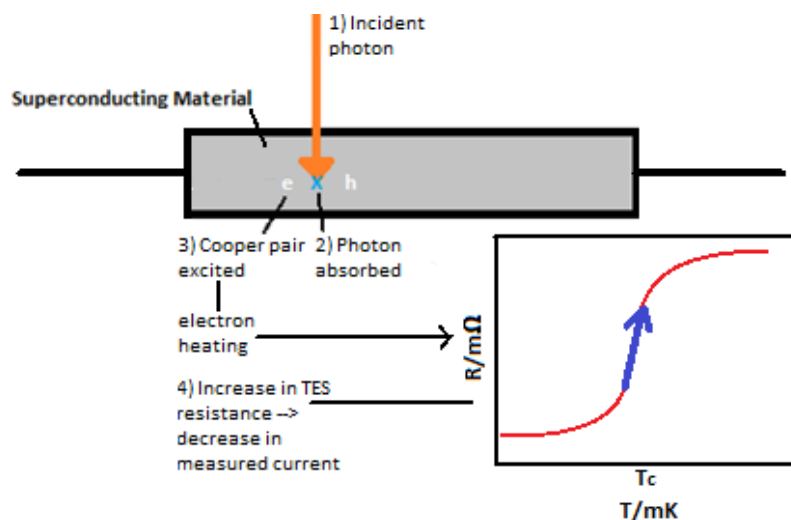


Figure 1.3 showing a schematic of a TES, and the temperature dependent change in resistance of a TES. To boost the signal, the TES can be linked with a SQUID [46].

The figure of merit for a microcalorimeter resistive thermometer is defined as $\alpha = \frac{T}{R} \frac{dR}{dT}$, equivalent to the rate of change of the resistance against temperature at the transition temperature. In this transition region a TES has a very high responsivity, of order 100000 AW^{-1} [35] [36] [37]. Furthermore, the energy resolution of a TES is approximated by $\Delta E \sim 2.35 \sqrt{4kT^2 \frac{C}{\alpha}}$, where C is the microcalorimeter heat constant and α is the figure of merit [36]. This gives an energy resolution of approximately $\frac{E}{\delta E} = 70$ and 7000 for $E = 0.1\text{keV}$ and 10keV respectively.

1.2.4 Microchannel Plate Photomultiplier Tube (MCP-PMT)

Microchannel plate photomultiplier tubes (MCP-PMT) are another option for single x-ray photodetection that, unlike STJs and calorimeters, are able to operate at room temperature. MCP-PMTs have many applications in medical physics and space sciences. MCP-PMTs can operate across a wide wavelength range, and demonstrate a very high time resolution of order 10s of picoseconds. However, they only have moderate energy resolution at soft X-ray wavelengths.

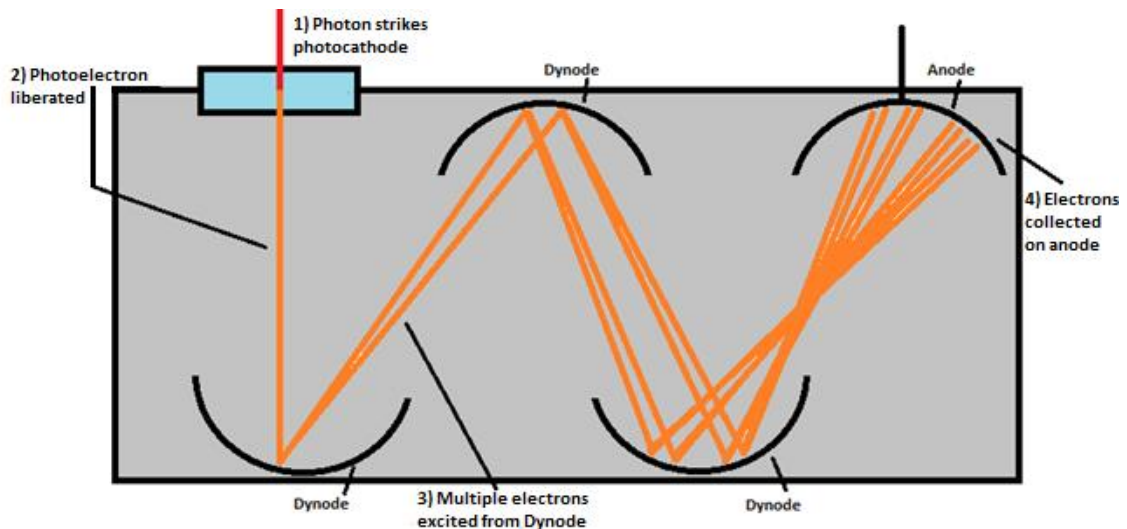


Figure 1.4, showing a photomultiplier tube (PMT) (based on a figure from ref. [47]). The photon strikes a photocathode which ejects an electron towards a dynode. Charge multiplication through the dynodes liberates more electrons until it reaches the anode, and the signal is output.

In an MCP-PMT, when an incident photon strikes a photocathode it liberates a photoelectron via the photoelectric effect. The photoelectron is accelerated to adjacent dynodes, held at different potentials, with secondary charge carriers being

produced as the charge carrier relaxes. This continues until the electrons reach the anode, and the signal is measured, figure 1.4.

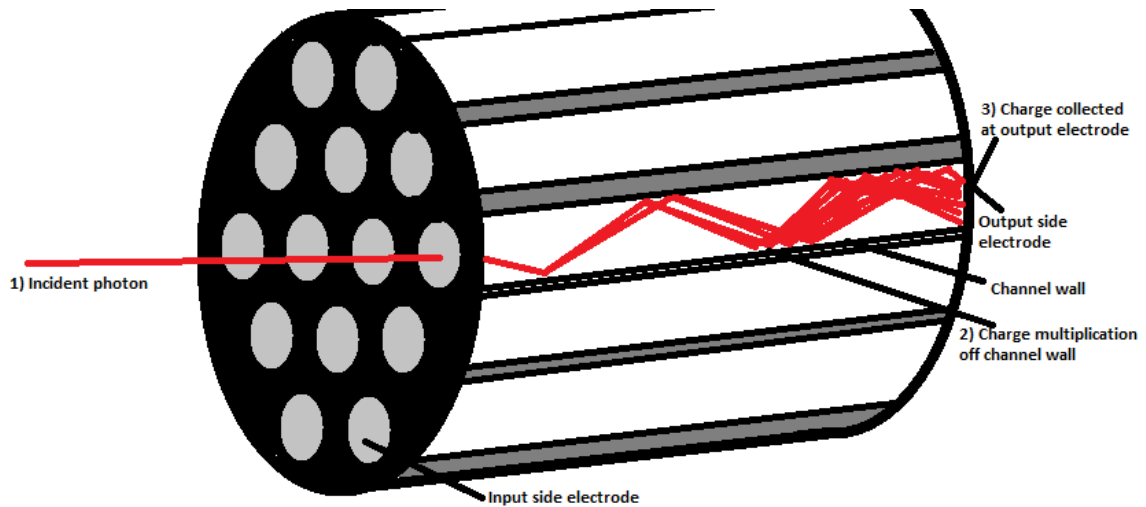


Figure 1.5, showing a microchannel plate detector. The photon strikes the pore wall and, through charge multiplication, the amplified signal is measured at the anode.

1.2.5 Charged Coupled Device (CCD)

A charged coupled device (CCD) is another type of detector used for photodetection of visible, UV and X-ray photons, in an array that comes in a variety of different sizes. A CCD works by absorbing photons in doped silicon, which generates charge carriers in the absorber. The charge carriers are separated by an applied electric field, accelerated toward the interface layer, and collected in potential wells. The charge is then readout through a readout node, generating an image related to the charge accumulated in each cell [48].

CCDs typically have an energy resolution of below 140eV, with $\frac{E}{\delta E} > 37$, for Fe-55 [48], with a readout rate from 0.1MHz-20MHz and Quantum Efficiency close to 100% for $\lambda \sim 550\text{nm}$.

1.2.6 Avalanche Photodiodes

Photoavalanche diodes, such as SPAD and SiPMs, work by a photoabsorption causing an avalanche current due to impact ionisation. For a SiPM for PET, energy sensitivity has shown to be 20% FWHM at 511keV, with timing resolution of 1.4ns FWHM [49]. This timing resolution has been as low as approximately $\sim 40\text{ps}$ [32] [33] [34], with an energy resolution $\frac{E}{\delta E} = 16-45$ depending on the operation temperature, at 250K and

180K respectively for $E = 5.9\text{keV}$. They have also been shown to have a responsivity of $\sim 50\text{AW}^{-1}$.

1.2.7 Summary of Photodetector Technologies at Different Wavelengths

For detection at visible frequencies, current technologies include Avalanche Photodiodes, MCP-PMT, MKIDs and STJs. Detectors such as MKIDs and STJs operate at cryogenic temperatures with good temporal and energy resolutions [26] [27] [28] [29] [30] [31]. However, operating at cryogenic temperatures $\sim 100\text{mK}$, which is required to prevent dark noise, requires the use of Helium-3 and expensive cryogenic techniques, so these types of photodetector are expensive to manufacture and operate. Avalanche Photodiodes operate at room temperature, with temporal resolution comparable to STJs but with no energy resolution unless for x-rays and gamma rays with a scintillator, while MCP-PMTs provide picosecond timing resolution, but have no energy resolution at visible wavelengths and have a diminished responsivity. A detector with a combination of wavelength specificity, low dark noise and fast temporal resolution operating without the need for complex and costly cryogenic techniques is therefore unfulfilled.

Several techniques can be used for X-ray photodetection; for instance, at cryogenic temperatures, STJs offer microsecond temporal resolution and an energy resolution of $\frac{E}{\delta E} \sim 500$, while TESs provide less time resolution but improved energy resolution and very good responsivity. At room temperature, MCPs operate at higher temperatures and provide a timing resolution up to $\sim 25\text{ps}$, but only energy resolution at soft X-ray wavelengths. A combination of temporal bandwidth, energy resolution and operation at room temperature is therefore unfulfilled by current technologies.

Many different detectors can sense terahertz radiation, such as bolometers and calorimeters. MCPs show sensitivity from infrared to x-rays in combination with a suitable photocathode; in the infrared, MCPs have $\sim 25\text{ps}$ time resolution and no energy sensitivity. Photon Counting Terahertz Interferometry (PCTI) has been proposed to enable wide bandwidth terahertz photodetection [50] [51] [52] [53]; this technique utilises the pulsed nature of terahertz frequency photons, whereby detection by two or more telescopes can be used to measure the intensity correlation.

PCTI requires detectors with a high count rate of 1-100MHz and a time resolution better than 1ps [52]. A high count rate and time resolution would therefore have a wide range of applications.

1.3 Fundamental Properties of Graphene Relevant to Photodetection

Graphene has many properties that means it could provide an interesting solution for single photon counting photodetection [54], with applications in many areas. Graphene has already been used for ultrafast photodetection of order femtoseconds [55] for pulsed lasers, its high carrier mobility enabling greater operational bandwidth. In addition, the tuneable band gap in bilayer graphene may enable sensitive photon counting photodetectors to operate with a trade-off between resolution and operational temperatures, with possible benefits. In this section, the most important properties of graphene, relevant to photodetection, are presented.

1.3.1 Electronic Structure of Single Layer Graphene

Graphene is a 2d lattice of sp^2 carbon atoms arranged in a hexagonal structure. The structure is made up of two triangular sub lattices [6] with one atom from each sublattice in the elementary cell. The low energy band structure of graphene is dictated by π states which form symmetrical cones touching at the so-called Dirac point, figure 1.6a; graphene is therefore described as a zero-band gap semiconductor. Other areas of symmetry exist, such as a Γ point in the centre of the Brillouin Zone, the point with the greatest difference in energy between the conduction band and valence band, figure 1.6b.

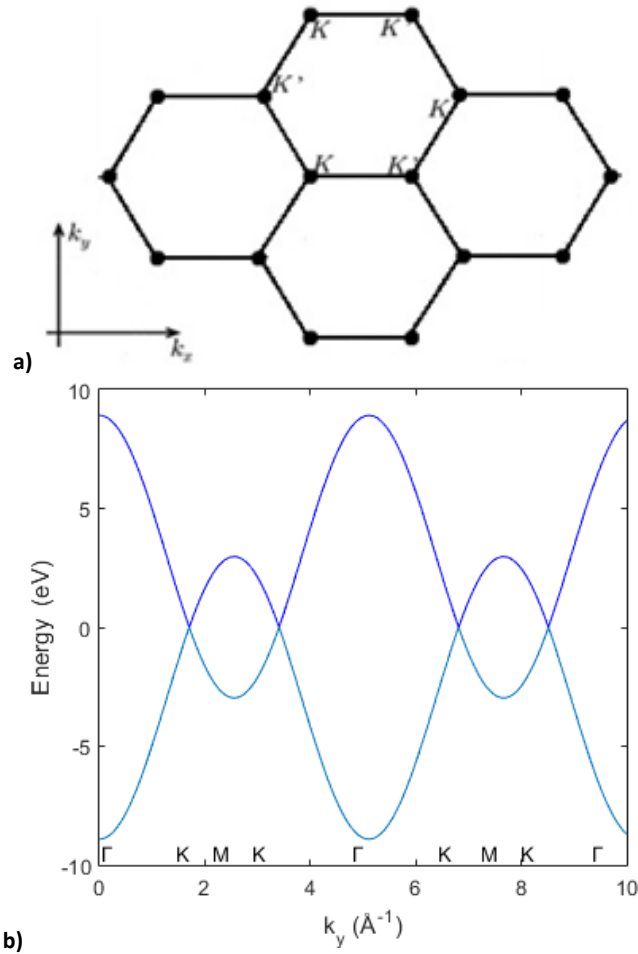


Figure 1.6, showing a) the honeycomb structure of single layer graphene in reciprocal space with the K and K' points in the first Brillouin Zone [2], and b) the band structure of graphene (an alternative version is available in ref [56]), showing other areas of high symmetry in the Brillouin Zone, such as Γ point in the centre of the Zone.

The energy spectrum for single layer graphene can be calculated by considering a tight-binding model. Using the same approach as Wallace, the Hamiltonian in the nearest-neighbour approximation is [6] [24]

$$H(k) = \begin{pmatrix} 0 & \gamma_0 S(k) \\ \gamma_0 S^*(k) & 0 \end{pmatrix}, \quad \text{Equation 1.1}$$

where γ_0 is the nearest neighbour hopping parameter, and

$$S(\vec{k}) = 2 \exp\left(\frac{ik_x a}{2}\right) \cos\left(\frac{k_y a \sqrt{3}}{2}\right) + \exp(-ik_x a). \quad \text{Equation 1.2}$$

At the Dirac point $S(K) = S(K') = 0$.

In the next-nearest-neighbour approximation with the near-neighbour hopping parameter γ_1 , the energy spectrum is given by [6]

$$E(k) = \pm\gamma_0|S(k)| + \gamma_1 \left[2 \cos(k_y a \sqrt{3}) + 4 \cos\left(\frac{k_y a \sqrt{3}}{2}\right) \cos\left(\frac{3k_x a}{2}\right) \right]. \quad \text{Equation 1.3}$$

The band structure close to the Dirac point is symmetric about the Dirac point (i.e. electrons and holes should have the same properties) and linear in energy as a function of wavenumber, $E = \hbar v k$ [57], figure 1.7. The relationship between energy and wavenumber is therefore comparable to that of light, and unlike conventional parabolic dispersions in semiconductors, which indicates that the charge carriers close to the Dirac point behave like massless Dirac fermions [58] [59]. This can also be shown by expanding the Hamiltonian about the Dirac points and showing that this is a solution to the 2D Dirac equation [60]. Furthermore, charge carriers in graphene display chirality, which is expected for massless Dirac fermions [61] and is crucial for relativistic effects [6].

The Fermi velocity, v_F , for charge carriers is given by $v_F = \frac{3a|\gamma_0|}{2} \sim \frac{c}{300} = 1 \times 10^6 \text{ms}^{-1}$, [6] [24] [62] where $\gamma_0 \sim -2.97 \text{eV}$ is the nearest neighbour hopping parameter. Other techniques can also be used to deduce the Fermi velocity, such as using Shubnikov-de Haas oscillations [13]; previous work has obtained $v_F \sim 1.9\text{-}2.2 \times 10^6 \text{ms}^{-1}$ [63].

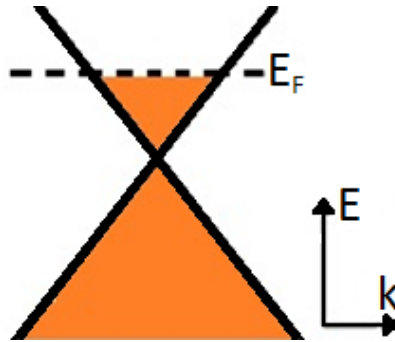


Figure 1.7, showing the linear energy-wavenumber relationship close to the Dirac point, $E = \hbar v k$, with a Fermi level that is changed by applying an electric field [2]. The linear relationship also shows that charge carriers behave as massless fermions close to the Dirac point.

The density of states, $N(E)$, can be calculated from

$$N(E) = 2 \int \frac{d^2 k}{(2\pi)^2} \delta(E - E(k)) \quad \text{Equation 1.4}$$

which, for single layer graphene, leads to the density of states shown in figure 1.8a. The peaks are at $\pm\gamma_0$, corresponding to the Van Hove singularities [64]. At lower energy states in single layer graphene, closer to the Dirac point, one finds [6]

$$N(E) = \frac{2|E|}{\pi(\hbar v)^2}, \quad \text{Equation 1.5}$$

as shown in figure 1.8b.

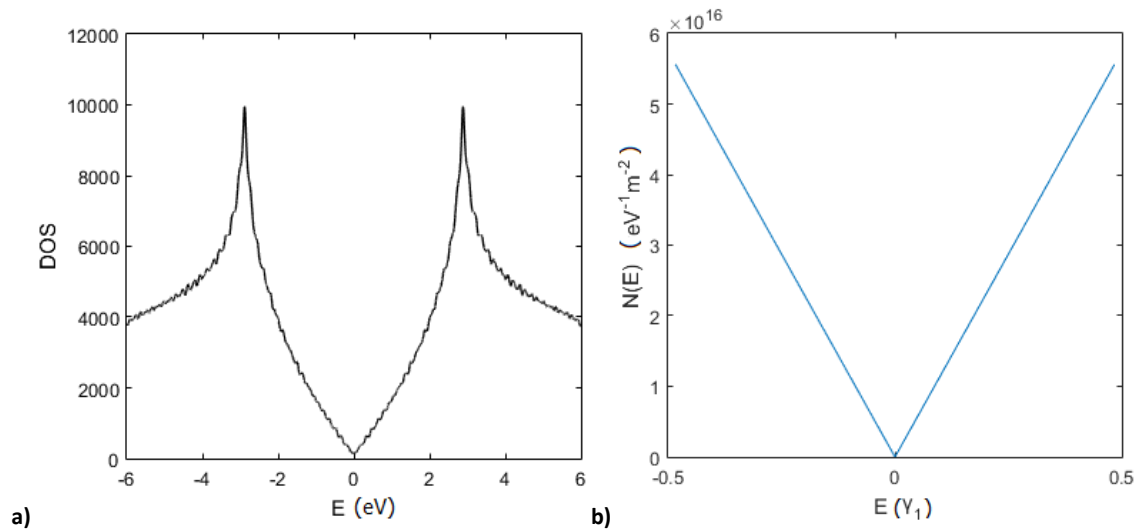


Figure 1.8, show a) the density of states of graphene and b) the linear relationship near the Dirac point where it tends to zero. One sees peaks at the Van Hove singularities in the density of states at energies equal to the hopping parameter $\pm\gamma_1$.

1.3.2 Electronic Structure of Bilayer Graphene

Bilayer graphene is also of interest in the development of photodetector technologies. The two layers in bilayer graphene can be stacked at any angle to each other, called the “twisting” angle [65]; two special cases are AA-stacked and AB-stacked graphene, where the two layers lie directly above (twisting angle = 0° degrees) or are offset (twisting angle = 90°) respectively. AA-stacked graphene is shown in figure 1.9, with a hopping parameter γ between the layers.

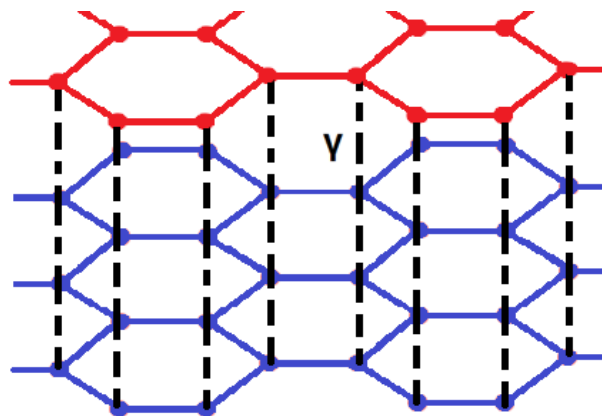


Figure 1.9, show layer stacking for AA bilayer graphene, with two layers of graphene stacked directly on top of each other. The hopping parameter between the layers is given by the hopping parameter γ .

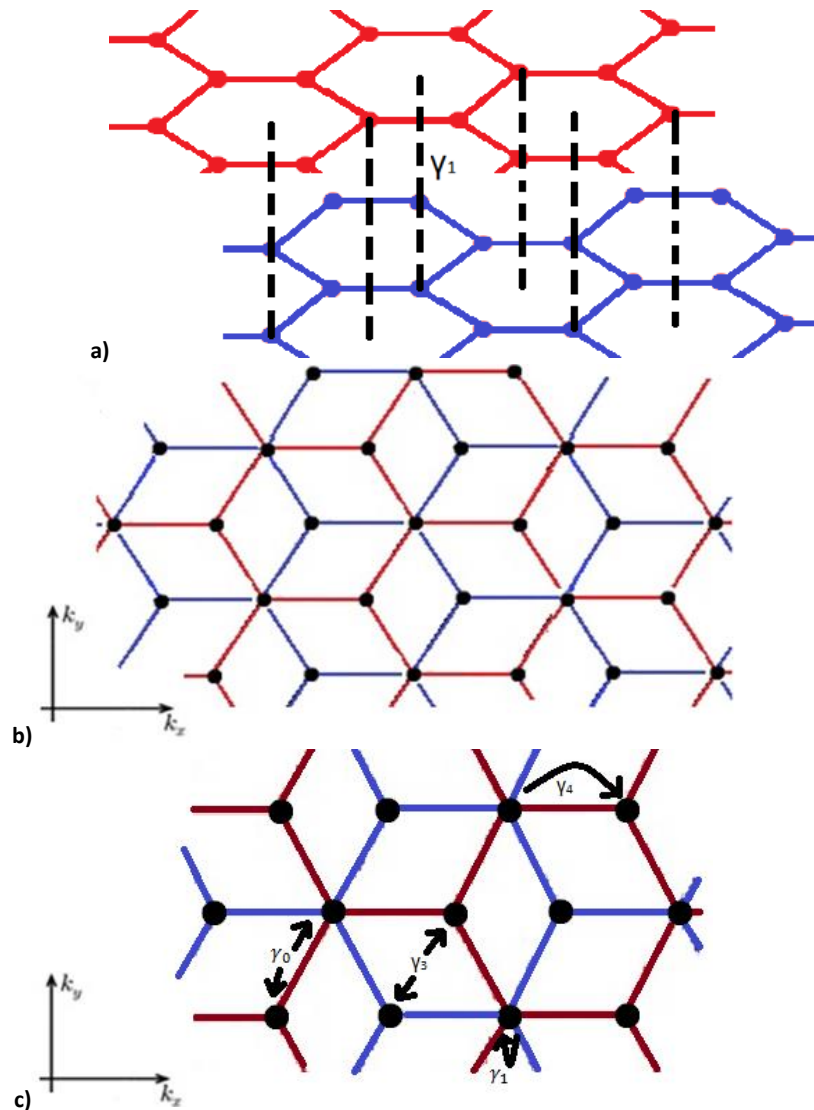


Figure 1.10, showing the structure of AB (Bernal) stacked bilayer graphene. In a) one sees the arrangement of the two layers, and b) shows how the two layers marked in red and blue respectively and a hopping parameter of $\sim 0.4\text{eV}$ between the layers [2]. C) shows the nomenclature for the different hopping parameters in bilayer graphene, including the next nearest hopping parameter γ_0 , and the nearest neighbour inter-plane hopping parameter, γ_1 .

AB (Bernal) stacked bilayer graphene has an offset in the arrangement, figure 1.10a [66] and figure 1.10b, as the Γ point in the centre of the Brillouin Zone lies directly above the K point of the other layer (and vice versa). This leads to different hopping parameters, outlined in figure 1.10c [6], where γ_0 is the nearest neighbour in-plane hopping parameter and γ_1 is the nearest neighbour inter-plane hopping parameter. The energy spectrum for Bernal stacked bilayer graphene can be derived given these hopping parameters. In this case, one assumes any further hopping parameters, γ_2 , γ_3 and γ_4 are negligible in this approximation as the effect of these are small, and the cross-terms arising from it set to zero. Therefore, using a similar approach to the previous section, the Hamiltonian becomes [6]

$$H(k) = \begin{pmatrix} 0 & \gamma_0 S(k) & \gamma_1 & 0 \\ \gamma_0 S^*(k) & 0 & 0 & 0 \\ \gamma_1 & 0 & 0 & \gamma_0 S^*(k) \\ 0 & 0 & \gamma_0 S(k) & 0 \end{pmatrix}, \quad \text{Equation 1.6}$$

where $S(k)$ has the same definition as before. This gives a different band structure compared to that of single layer graphene, with the presence of the second graphene layer causing a pair of degenerate bands, often called the π_1 band in the valence band and the π_1^* band in the conduction band [67], which intersect at the Dirac point. A further pair of bands, the π_2 band and π_2^* band, are split by γ_1 from the π_1 bands as shown in figure 1.11 [67].

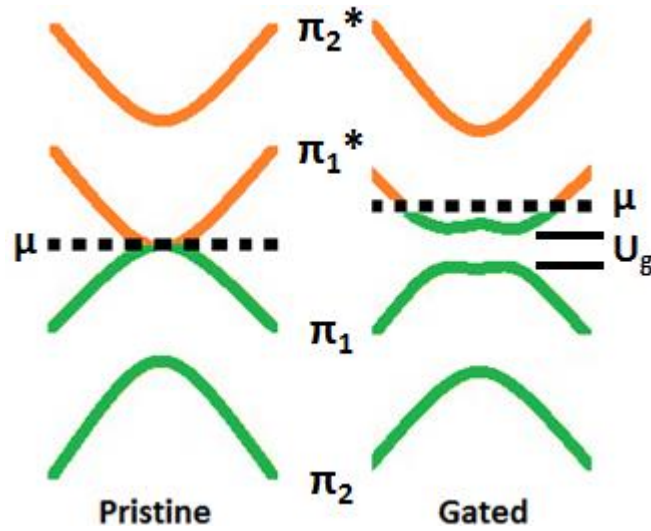


Figure 1.11, showing the band structure for bilayer graphene showing pristine bilayer graphene and the opening of a band gap for gated bilayer graphene with AB stacking (based on a figure from ref. [65]). The pair of bands are degenerate at the Dirac point for pristine graphene. “Trigonality” is observed in gated bilayer graphene at very low energies [6].

A tuneable bandgap can be opened in bilayer graphene using many different techniques including top and bottom gating, the controlled adsorption of water [68] or hydrogen [69], applying strain [70], and molecular doping [71]. This applies a (pseudo)potential, resulting in a perturbation in the Hamiltonian that breaks the interlayer symmetry and opens a band gap. The band gap magnitude is given by

$$U_g = \frac{|U|\gamma_1}{\sqrt{\gamma_1^2 + U^2}}, \quad \text{Equation 1.7}$$

where U_g is the band gap, U is the interlayer asymmetry and γ_1 is the interlayer hopping parameter; the magnitude of the band gap saturates $U_g \rightarrow \gamma_1$ for large U [12].

An approach for opening a tuneable band gap for AB-stacked bilayer graphene is to apply an electric field perpendicular to the layers [65], figure 1.11, a technique that shows no hysteresis and allows tuning of the Fermi level and magnitude of the band gap. This can be done by using a dual gated graphene field effect transistor (GFET) [65] [72]. The band gap opens due to the application of a displacement field, which is a function of the potential applied through each of the gates, the environmental doping applied due to the substrates, and the thickness and relative permittivity of those substrates.

Applying a potential V to the Hamiltonian in equation 1.6 leads to [6]

$$H(k) = \begin{pmatrix} \frac{V}{2} & \gamma_0 S(k) & \gamma_1 & 0 \\ \gamma_0 S^*(k) & \frac{V}{2} & 0 & 0 \\ \gamma_1 & 0 & -\frac{V}{2} & \gamma_0 S^*(k) \\ 0 & 0 & \gamma_0 S(k) & -\frac{V}{2} \end{pmatrix}, \quad \text{Equation 1.8}$$

and hence energy eigenvalues given by

$$E^2 = \gamma_0^2 |S(k)|^2 + \frac{\gamma_1^2}{2} + \left(\frac{V}{2}\right)^2 \pm \sqrt{\left(\frac{\gamma_1^2}{2}\right)^2 + (\gamma_1^2 + V^2)\gamma_0^2 |S(k)|^2}, \quad \text{Equation 1.9}$$

where $\gamma_0=2.97\text{eV}$ and $\gamma_1=0.4\text{eV}$ [6] are the intralayer and interlayer hopping parameters, respectively, and $S(k)$ as defined previously.

Plotting equation 1.9 leads to the energy distribution in momentum space shown in figure 1.12a, with a band gap in the spectrum proportional to V ; the dispersion is not linear around the Dirac point, but parabolic in the Next-Nearest-Neighbour approximation. Furthermore, by considering $\frac{d^2E}{dk^2}$ one finds the charge carriers are not massless, but have an effective mass of $m^* = \frac{\gamma_1}{2v^2} = 0.054m_e$ [6].

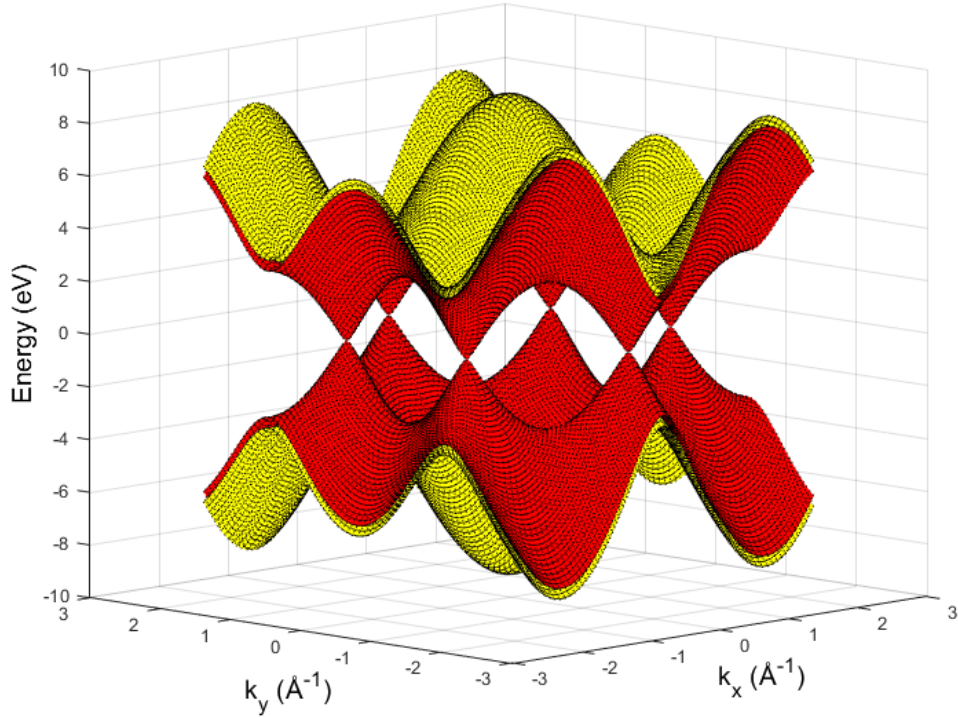


Figure 1.12, showing the band structure for bilayer graphene as a function of k_x , k_y and the energy E . The Dirac points are clearly visible where the bands intersect.

Gated bilayer graphene has a “Mexican hat” shaped band structure in the π_1 and π_1^* states close to the Dirac point at very low energies, figure 1.13a. This is called trigonality, which essentially perturbs the energy spectrum in figure 1.12 by adding an additional term to the (approximated) energy spectrum that is related to the hopping parameter γ_3 ,

$$E_{trigonality} = (3\gamma_3 a)^2 k^2 + \frac{3\gamma_3 \hbar^2 k^3}{m^*} \cos(3\varphi_k), \quad \text{Equation 1.10}$$

where γ_3 is the hopping parameter from one atom on one layer to the other atom in the Brillouin zone in the other graphene layer [12], k is the momentum, m^* is the effective mass of the charge carriers, and $\varphi_k = \arctan\left(\frac{k_y}{k_x}\right)$ is the opening angle between the \vec{k} vector and the k_x axis [6]. This leads to four Dirac points, the “usual” one plus three at an opening angle of 120° each as shown in figures 1.13a and 1.13b.

The Lifschitz energy is defined as $E_L = \frac{\gamma_1}{4} \left(\frac{v_3}{v}\right)^2$, the energy where the three additional peaks disappear and transition to one distinct point. Above this energy the effects of trigonality do not need to be considered, whereas one must consider trigonality below the Lifschitz energy.

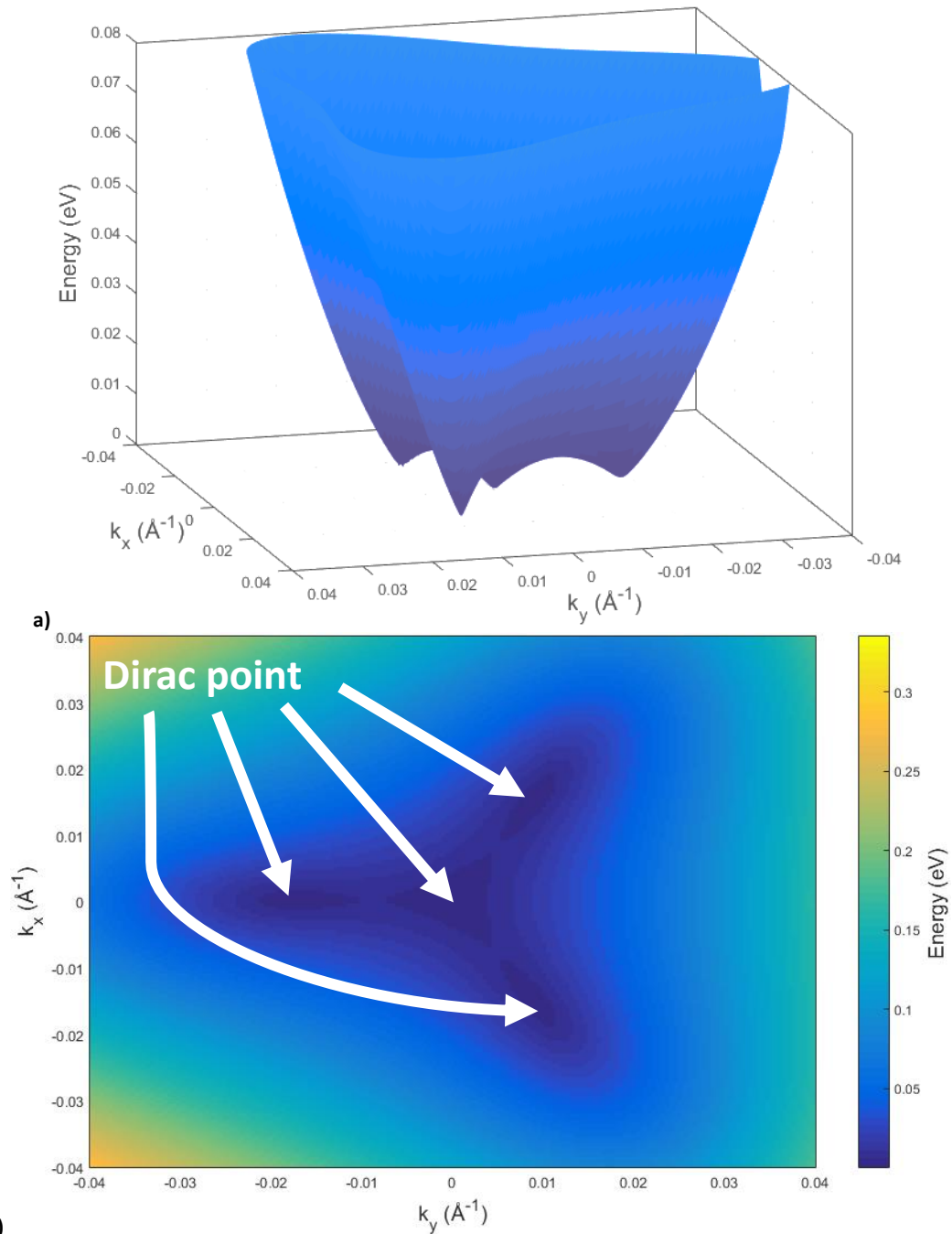


Figure 1.13, showing a) the perturbation to the energy spectrum at low energies, showing the four Dirac points, and b) the perturbation to the energy spectrum at low energies, showing the 120° opening angle.

1.3.3 The Field Effect and Transport Properties, and the Effects of Adsorbants and Scatterers

As the charge carriers in single layer graphene behave as massless Dirac fermions, graphene is able to support carrier mobilities as high as $10^6 \text{cm}^2 \text{V}^{-1} \text{s}^{-1}$ for suspended graphene [63] from $\sim 5\text{K}$ [8] to higher temperatures [9]. As with most properties, this is strongly dependent on the environment and support, so varies depending on the

support for the graphene and whether it is encapsulated. The carrier density (or doping level) of graphene is continuously tuneable from p-type to n-type through charge transfer, often unintentionally due to external factors such as air exposure and substrate effects. Fully encapsulated graphene devices on silicon/silicon dioxide support mobilities in the order of $10^3 \text{cm}^2 \text{V}^{-1} \text{s}^{-1}$ at room temperature [73].

The doping and Fermi level of graphene can be varied through the field effect [13], whereby changing an electric field applied to the graphene can change the carrier type from electron to hole, and vice versa, resulting in a change in conductivity [13] [74] [75] [76] [77] [78] shown, for example, in figure 1.14 [2] [79]. The changing electric field can be done, for example, by applying a gate voltage from a gate (e.g. Si) across a dielectric or through the absorption of a photon in an absorber, which results in the generation of more charge carriers in the absorber that then generates a field across the dielectric. Utilising the field effect has enabled detection of X-rays with a relatively simple device fabrication and detector measurements [74] [75] [80] [81] [82] [83].

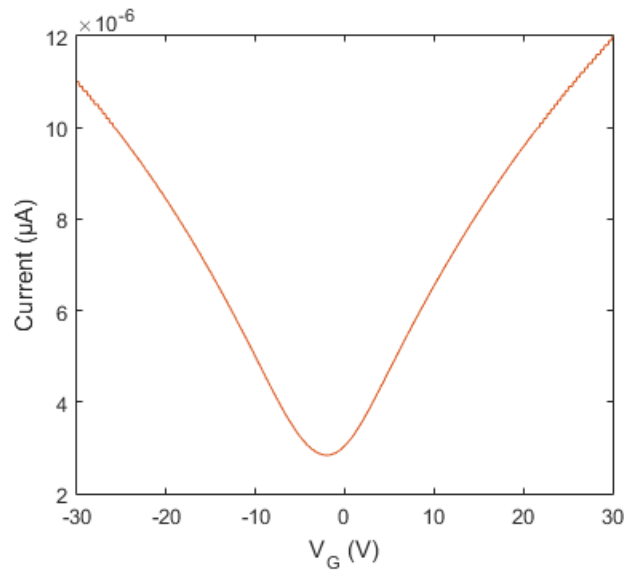


Figure 1.14 showing, for one specific sample, the drain-source current of graphene against gate voltage for a given sample [2] [79]. The asymmetry in this sample is due to the difference in electron and hole mobilities of the sample; the Dirac point and electron and hole mobilities are dependent on the specific sample.

The minimum current occurs at the Dirac point, V_{Dirac} ; in figure 1.14 this is at $V_G \sim -2\text{V}$ which shows that the graphene is slightly n-type. At the Dirac point the conductivity of graphene is proportional to $(V_G - V_{Dirac})^2$. This minimum conductivity has been derived and shown to be of order e^2/h [84], although no analytical result has

concluded upon a definitive constant in the literature. A number of groups have considered an approach with respect to Mott's considerations [6] [85] [86], while others have discussed it in terms of Zitterbewegung [87], and a Landauer–formula approach [88]. The minimal conductivity in graphene has been measured experimentally to within 10% of an average of $\frac{h}{4e^2}$, indicating that this is a constant and is not sample dependent [13]. However, other results suggest that the minimum conductivity is dependent on the size, temperature, Fermi energy, intervalley scattering strength and impurity scattering strength [64].

A linear conductivity-gate voltage relationship is obtained far away from the Dirac point, where the gradients to the left and right of the Dirac point indicates the sample dependent hole and electron mobilities respectively [13] [89]. Annealing can remove some defects from the surface of the sample, resulting in a $V_G^{1/2}$ dependence for the conductivity due to scattering by point defects [90]. However, operation of this device in air after annealing can lead to increased p-type doping from the air, and potentially lead to a degradation of operational behaviour.

The effect of the support on the mobility arises from the effect of surface scattering on charge carriers. Matthiessen's Rule [91],

$$\frac{1}{\mu} = \frac{1}{\mu_{ext}} + \frac{1}{\mu_{int}(T)}, \quad \text{Equation 1.11}$$

can be used to determine the extrinsic defect and intrinsic electron-phonon interaction contributions to the mobility [92].

Coulomb scattering [64] and carrier scattering in a constant potential both provide contributions to the resistivity, equivalent to [93]

$$\rho = \frac{h}{e^2} \frac{n_{imp}}{n} \quad \text{Equation 1.12}$$

and [6]

$$\rho = \frac{h}{e^2} n_{imp} R^2 \quad \text{Equation 1.13}$$

respectively, where n_{imp} is the density of impurities, n is the charge carrier density, and R is the size of the impurity cluster [94]. The contribution from constant potential is much smaller or negligible compared to the former. The mobility is therefore inversely proportional to the number of Coulomb scatterers in the substrate. The effect of adding dopants to the graphene to increase coulomb scattering has been examined in many different experiments such as refs. [95] and [96].

To reduce scattering due to the substrate, one option is to use hexagonal Boron Nitride (hBN). Like graphene, hBN is a 2d hexagonal lattice structure with boron in one sub lattice and nitrogen in another sub lattice. hBN is relatively inert, free of loose bonds or surface charge traps, and the hBN surface should suppress rippling in graphene [97]. Encapsulation with hBN can, therefore, improve the sample mobility, with a mobility value of $390,000\text{cm}^2\text{V}^{-1}\text{s}^{-1}$ realised in recent experiments [45].

To further reduce scattering due to the substrate and hence improve the mobility, graphene can be designed in a suspended structure so it is not in contact with the substrate. In this arrangement, mobilities up to $10^6\text{cm}^2\text{V}^{-1}\text{s}^{-1}$ can be realised [8] [9] [63], with a resistivity also related to the tension and temperature [90] [98] [99].

The resistance of the graphene channel as a function of gate voltage is dependent on both temperature T as well as scatterers [100], The resistance at the Dirac point increases in magnitude with decreasing temperature, with the minimum conductivity $\sigma_{CNP} \propto T^\theta$, where θ is a fitting term. This is attributed to temperature dependent conduction through electron and hole puddles due to a non-uniform Fermi level. For a suspended graphene structure, in the absence of tension, resistivity has a $T^{5/2} \log T$ dependence [98], attributed to flexural phonons dominating over in-plane modes. In the suspended graphene construction with tension, at low temperatures the resistivity is proportional to $T^{5/2}$, and is proportional to T^2 at high temperatures [98]

The effect of adsorbates has been studied for many different molecules, such as water [68] and hydrogen (in the form of graphane) [69], and more complex molecules such as SnO_2 [101]. These adsorbants perturb the density of states [102] and provide additional defects that decrease the electron scattering time and hence increase the sample resistivity. Graphene in ambient conditions causes issues such as gate

hysteresis; this is mitigated by encapsulating the device with an alumina layer which will be discussed in chapter 5.

1.3.4 Optical Properties

For a photon to excite an electron-hole pair it must have an energy greater than twice the Fermi level, $E = \hbar\omega > 2|\mu|$, due to the Pauli Exclusion Principle [103] [104], with the resulting vertical transition due to conservation of energy and momentum, figure 1.15.

The optical conductivity of graphene has contributions from both intra-band electron-phonon scattering processes and inter-band electron transitions [105], which can be deduced from experiment [106]. At visible frequencies graphene has a wideband absorption of 2.3% [10] per layer. This can be derived from Fermi's golden rule for the absorption of a photon which excites an electron from $-\frac{E_{photon}}{2}$ to $\frac{E_{photon}}{2}$ [6]. For

$$P = \frac{2\pi}{\hbar} |M|^2 N(\varepsilon), \quad \text{Equation 1.14}$$

where $\varepsilon = \frac{E_{photon}}{2} = \frac{\hbar\omega}{2}$, P is the absorption probability per unit time, $|M|^2 = \frac{e^2 v^2}{8\omega^2} |\vec{E}|^2$, \vec{E} is the electric field vector, and N is the density of states, one finds

$$P = \frac{e^2}{4\hbar^2\omega} |\vec{E}|^2. \quad \text{Equation 1.15}$$

Therefore, the absorption energy per unit time is $W_a = \frac{e^2}{4\hbar} |\vec{E}|^2$. With an incident energy flux equivalent to $W_i = \frac{c}{4\pi} |\vec{E}|^2$, then the proportion of photons absorbed by the graphene, η , is given by

$$\eta = \frac{W_a}{W_i} = \frac{\pi e^2}{\hbar c} = \pi\alpha \approx 2.3\% \quad \text{Equation 1.16}$$

where the coefficient is critically dependent on α , the fine structure constant [10]. A slow wavelength dependence has been observed in the absorption coefficient whilst investigating inter- and intra-band optical transitions using IR reflection spectroscopy, which was attributed to dispersion due to substrate reflection and from p-doping of the exfoliated graphene [106].

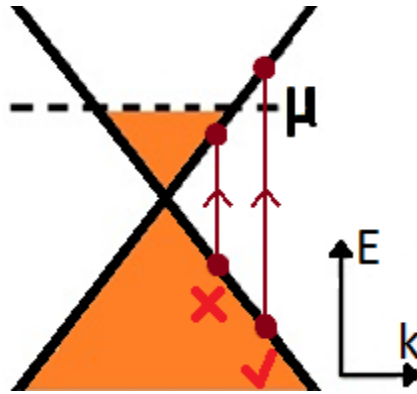


Figure 1.15, showing the allowed and disallowed transitions resulting from photoabsorption by graphene. Disallowed transitions are prevented due to Pauli exclusion.

The optical properties of graphene can be used to characterise the quality and indicate the number of layers of different samples through optical microscopy; in figure 1.16 clear islands of single, bilayer and multilayer graphene are visible due to the optical contrast. In Appendix I, graphene samples synthesised at five institutions were studied. The optical contrast of the sample can be optimised by varying the thickness of the dielectric; with a green filter, for instance, the optical contrast would be maximised for a dielectric thickness of $\sim 90\text{nm}$ or $>280\text{nm}$ [107].

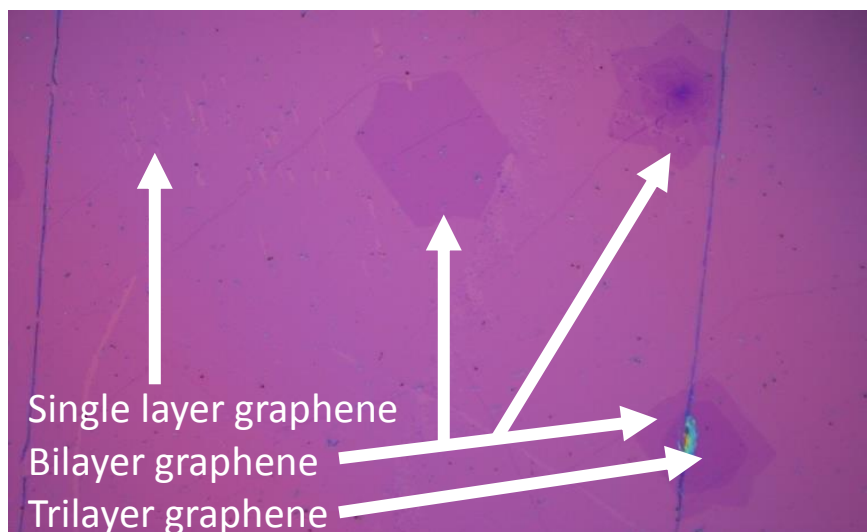


Figure 1.16, shows the optical image of CVD sample grown at the University of Cambridge. The image shows single layer (centre) and multilayer (centre right) samples.

The constant 2.3% absorption coefficient per layer of graphene leads to low photoresponsivity and low external quantum efficiency (EQE) [108] [109] [110]. Plasmonic nanostructures can be exploited to improve the EQE, and can enhance the photocurrent by up to 1500% [108] through a process of plasmon gain c.f. optical gain of semiconductor interband lasers at optical and infrared frequencies [111]. Plasmons

are high-frequency collective electron density oscillations [104] [111] and have a wide range of applications in graphene-based photodetection.

1.3.5 Phonons in Graphene

Graphene has thermal properties that can be attributed to the behaviour of phonons. Phonons are vibrations in the lattice, which can either be classified as acoustic – if the vibrations cause the atoms in the crystal to move from their equilibrium positions – or optical if the bond stretches and causes the atoms to move in opposite directions. In graphene, at low temperature, optical phonons become less active.

There are six different phonon modes for graphene. These are the out of plane (Z), longitudinal (L) and transverse (T), which can all either be acoustic (A) or optical (O) phonons. At most frequencies, the modes are linear as a function of wave vector q , although the ZA mode is quadratic in q , figure 1.17 [12] [112]. These ZA modes are attributed as the cause of many of the unique thermal properties of graphene [112].

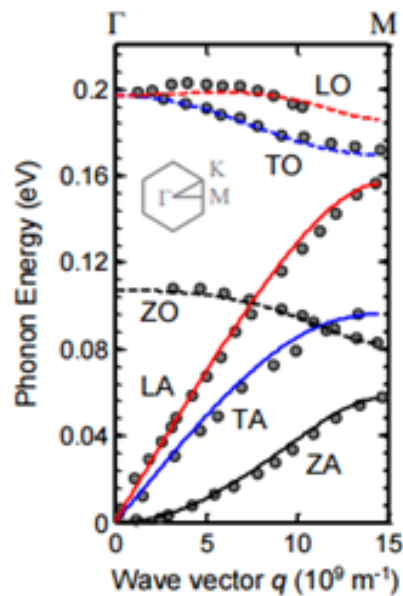


Figure 1.17, showing the phonon spectra in graphene for different phonon modes [112]. Reproduced with permission by Cambridge University Press, subject to <http://www.cambridge.org/about-us/rights-permissions/permissions/permissions-requests>

1.3.5.1 Phonons and Raman Spectroscopy

Phonons in graphene give rise to a unique and distinctive Raman spectrum, figure 1.18. Pristine graphene shows a large G peak at 1580cm^{-1} , and a 2D (or G') peak at 2700cm^{-1} . For samples with defects a further (D) peak is observed at 1350cm^{-1} . The Raman

spectrum for graphene can be used to characterise, for example, the number of layers and the defect and dopant densities [113] of a sample. The Raman spectrometer measures the change in energy of a photon due to inelastic scattering by phonons within a sample. With the Fermi level at the Dirac point, an incident photon excites an electron to the conduction band. This relaxes through the emission of phonons, before emitting a photon. The change in energy through phonon loss is then calculated.

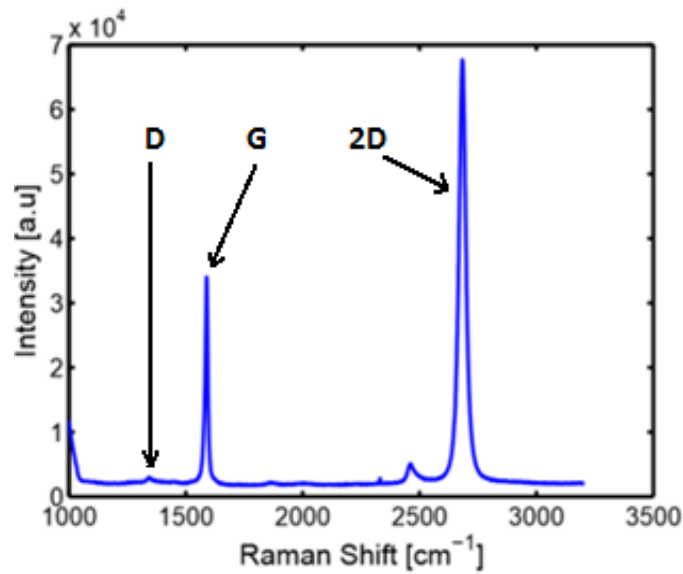


Figure 1.18. The Raman spectrum of a sample produced at the University of Cambridge. A small D peak, and clear G and 2D peaks are observed at 1350cm^{-1} , 1580cm^{-1} and 2700cm^{-1} respectively.

The key electron-phonon scattering channels in graphene are given in figure 1.19, [113], both schematically and as a Feynman diagram. For the G and 2D peaks, one and two phonons are emitted respectively. For the D peak, a scattering event from a dopant/defect results in the emission of a phonon leading to a D peak.

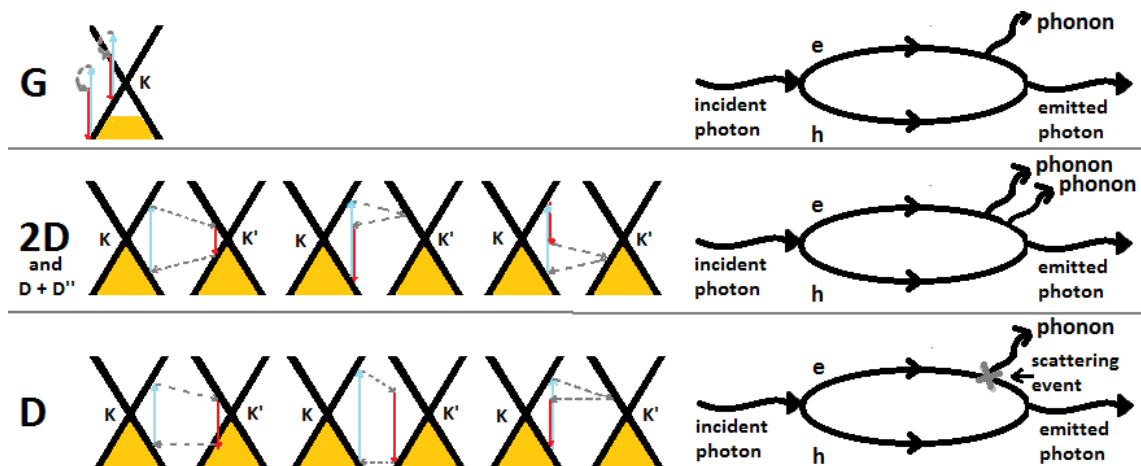


Figure 1.19 showing possible scattering channels through phonon loss in graphene for the G, 2D and D peaks [113], along with the corresponding phonon emission Feynman diagram.

The 2D peak can be used to determine the number of layers for the sample, whilst the number of defects in the sample is proportional to the ratio of the G and D peak intensities [113]. Other peaks, such as the D'+ZO' peak (1725cm^{-1}) can also be used to characterise the layer number. Other properties can be calculated using Raman spectroscopy, such as electron-phonon coupling utilising the phonon dispersion at a given point [113], and the shear modulus of multilayer graphene [114] [115].

Raman characterisation of graphene samples from five different institutions across Europe for the European Space Agency can be found in Appendix I.

1.3.6 Hot Electron Carrier Scattering

The excitation of an electron into the conduction band following the absorption of a photon results in a hot electron. The photothermoelectric effect, for instance, works by the excitation of an electron-hole pair causing ultrafast heating of charge carriers on a picosecond timescale, and has been successfully used for photodetection [55] [116].

Hot electrons thermalise via several different processes, such as impact ionisation and Auger recombination. Impact ionisation is the loss of energy by a hot electron in the conduction band causing the excitation of a valence band electron, and hence resulting in charge multiplication, figure 1.20. Auger recombination is the reverse process, with one conduction band electron relaxing back to the valence band, with another electron being further excited in the conduction band.

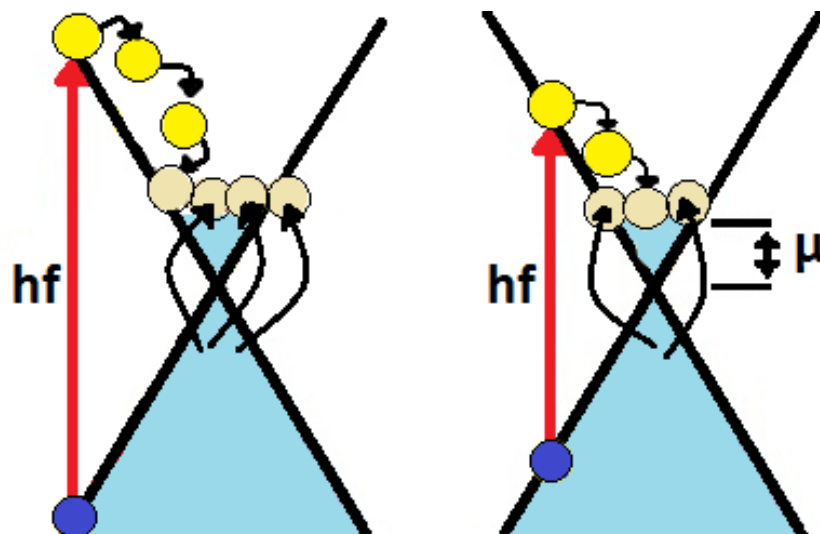


Figure 1.20 showing impact ionisation (II) in doped single layer Graphene. An electron is excited into the conduction band, and thermalizes with further electrons excited from the valence band. AR is the reverse process.

Hot carrier scattering has been observed experimentally, often by exciting charge carriers using an ultrafast laser pulse [117] [118] [119]. The efficiency of energy transfer from primary electron-hole pairs to secondary hot carriers has been shown to be closely related to the initial charge carrier energy. The conversion is close to 100% at low energies, whilst at $E = 1.7\text{eV}$ the conversion is approximately 80% with the remaining energy lost due to phonons [117].

For a pulsed laser photon energy of 1.5eV, where intervalley scattering is negligible due to the momentum change required [118] [119], coulomb-induced carrier scattering on a very short timescale is observed - occurring even when the pulse is turned off - and leads to charge multiplication of ~ 4.3 . Thermalisation of these hot electrons has shown to be incredibly fast, with thermalisation occurring within the first 100fs. The impact ionisation and Auger recombination timescales have then been calculated, given $\tau = \frac{n}{\gamma}$, where γ differs between processes. At equilibrium, $\tau_{II} = 22\text{fs}$ and $\tau_{II} = 425\text{fs}$ for strong and weak exciting pulses respectively [118] [119].

1.3.7 The Effect of Strain on Graphene

In addition to optical and electrical properties, graphene also demonstrates unique mechanical properties. By applying strain to the graphene, a pseudo-vector potential is introduced into the Hamiltonian for graphene, resulting in the pseudo-Aharonov-Bohm effect [6], and a perturbation that breaks the band symmetry and can open a band gap.

Graphene, whilst being bent and strained, has been used to develop different photodetectors and sensors. For instance, flexible photodetectors using centimetre-scale grown graphene samples have been developed with an external and internal responsivity of 45.5AW^{-1} and 570AW^{-1} respectively to a laser intensity of $0.1\text{nW}\mu\text{m}^{-2}$ [120]. This is maintained down to a bending radius of 6cm.

Strain sensors have been developed by research groups including the Coleman group at the Trinity College Dublin. They have developed elastic bands coated in graphene that have shown strain sensitivity to 900%, making this sensitive enough to measure heart beats and breathing [17]. Scope for strain sensing through flexible graphene field

effect transistors can also be realized by the same techniques, utilising the measurable change in current through the graphene resulting from the application of strain.

1.4 Graphene as a Solution for Novel Photodetector Technologies

This chapter has, so far, considered the current state of the art of the most common photon counting photodetectors, with the figure of merits stated in table 1-1. This suggests that no detector exists with the required combination of features for the current demands of the applications of single photon counting photodetectors, such as high detection efficiency with wavelength specificity, high temporal resolution and low dark count [38]. For single photon counting of visible photons, currently one must trade-off between wavelength specificity, low dark noise, fast temporal resolution, and operating without the need for scarce or costly resources such as expensive cryogenics, whilst for single X-ray detection, there is no detector with a combination of count rate, energy resolution and operation at room temperature. For THz detection, a high signal bandwidth and time resolution would have a wide range of applications.

Many of the most fundamental properties of graphene relevant to photodetection were considered in section 1.3. These fundamental properties of graphene include the potential to have a very high carrier mobility (up to $10^6 \text{cm}^2 \text{V}^{-1} \text{s}^{-1}$), hot carrier scattering on a femtosecond timescale which has enabled ultrafast photodetection, and for plasmons to be excited by incident terahertz radiation. It also has, in AB-stacked bilayer graphene, a tuneable band structure that enables the opening and closing of a band gap. Graphene, therefore, has several properties that may provide interesting and viable solutions to future technology issues and limitations.

Graphene-based photodetector techniques have been an exciting topic of research in recent years, with studies covering the detection of photons over a wide range of wavelengths, including terahertz, visible and X-ray wavelengths. There are four main mechanisms are utilised for photodetection using graphene [116]:

- the photovoltaic (PV) effect, whereby a gating voltage generates an electric field to split electron-hole pairs at a PN junction between differently doped regions of graphene. Charge multiplication is achieved through relaxation via carrier-carrier scattering, leading to improved photodetection efficiency [55].

- the photothermoelectric effect (PTEE), where an electron-hole pair is excited and causes ultrafast heating of charge carriers on a femtosecond timescale. As this relaxes across a temperature gradient, a measurable photovoltage is induced via the Seebeck effect [121]. The temperature change is measured, and the thermal resistance is related to the incident radiation power.
- the bolometric effect, where the absorption of a photon leads to heating of the graphene and resulting changes in the carrier mobility or the conductance and hence the channel current [116] [122].
- the Dyakonov-Shur (DS) effect, where a terahertz wave impinges on and couples to an antenna and excites a plasmon resonance. This induces an AC voltage between source and drain that, through rectification of the graphene channel, creates a DC photovoltage that can be readout [123] [124].

| Detector Type [25] | Operating Temperature | Operational Wavelength | Timing Resolution | Energy Resolution $\frac{E}{\delta E}$ | Responsivity | Size of Active Area | Photon Intensity |
|--|-----------------------|------------------------|--------------------|--|-----------------------|-------------------------|-----------------------|
| Ultrafast Graphene-based Photodetector. PTEE. [55] | 40-300K | 500-1500nm | ~50fs | Photovoltage greater for lower temperatures. | ~100 μ A W^{-1} | ~10 μ m | 50 μ W |
| X-ray GFET on SiC substrate. Field effect. [74] [75] [80] [81] [82] [83] [125] | 300K | ~0.01-0.03nm | - | Estimated up to 333 (for E=1MeV) | 0.1A W^{-1} | 20 μ m x 4 μ m | 15kV, 15 μ A → |
| X-ray GFET on Si substrate. Field effect. [80] [81] [82] [83] [74] [75] | 4.3K | ~0.01-0.03nm | - | - | - | ~10 μ m | 40kV, 80 μ A |
| Ultrafast GFET [126]. PV. | 300K | 1.55 μ m | ~25ps (2ps theory) | - | 0.5mA W^{-1} | 1 μ m x 2.5 μ m | 3mW |
| THz GFET. DS effect [123] [124] | 300K | 100 μ m | ~1s | - | 100mV W^{-1} | 10 μ m | - |
| Quantum Dot. FET [21] [127] | 4K | 805nm | 1 μ s-1ms | - | 650A W^{-1} | 15 μ m | ~3.5mW |
| Black Phosphorus FET [128] [129] | 323-383K | <940nm | ~1ms | - | 4.8mA W^{-1} | ~10 μ m | ~500 μ W |

Table 1-2. Summary of a selection of photodetector technologies, with up and coming graphene-based technologies highlighted in grey followed by other potential solutions.

The current state of the art of graphene-based and 2d material-based photodetector technologies is outlined in table 1-2, which outlines impressive characteristics using several of these detection mechanisms. In the rest of this section, the potential

benefits of graphene photodetection for visible, terahertz and X-ray wavelengths are discussed, and the ideas that were developed further are motivated and outlined.

1.4.1 Using Graphene for Visible Photon Detection

Detection of visible photons is currently accomplished by detector technologies including Avalanche Photodiodes, MCP-PMTs, MKIDs and STJs, and require a trade-off between single photon counting, operating temperature, temporal resolution and wavelength specificity. MKIDs and STJs operate at cryogenic temperatures with wavelength specificity and good temporal and energy resolutions. Avalanche Photodiodes operate at room temperature, although with poor energy resolution because of the lack of an appropriate gain mechanism, while MCP-PMTs also provide picosecond timing resolution, but have no energy resolution at all.

Many groups have investigated the potential for graphene as a photodetector for visible photon laser pulses. Research has shown that the high carrier mobility and unique transport properties of graphene enable a theoretically very high bandwidth and a timing resolution on the femtosecond scale. Using the photovoltaic effect, Xia et al [126] have shown sensitivity to 1.55 μm laser illumination with a 3mW energy deposition, leading to a bandwidth of 40GHz, although theoretically up to 500GHz. Furthermore, work by the Koppens group [55] [116] exploited the photothermoelectric effect to obtain a time resolution sub-50fs. This is 1000 times faster compared to a time resolution of approximately 25ps for an MCP-PMT [38] and 10^5 times faster than the approximately 1 μs time resolution for an STJ [26] [27]. Current GFETs have also shown a good photoresponsivity (8.61 AW^{-1} in ref. [130], versus 5-1000 mAW^{-1} for an MCP-PMT [38] and $>100\text{AW}^{-1}$ for an STJ [26] [27]), and a good internal quantum efficiency [109]. Work is also ongoing to develop a graphene-based MKID device that utilises plasmons, and requires the graphene to be encapsulated by hBN and cooled to 30K to achieve mobility $\sim 400000\text{cm}^2\text{V}^{-1}\text{s}^{-1}$ [44] [45].

Little research is ongoing to utilise the properties of graphene for single photon counting, without the need for wavelength dispersive elements. For a good single photon counting photodetector, the detector needs to be fast and to have good charge multiplication mechanisms, and for wavelength specificity a band gap is

required otherwise charge carriers would relax out of the conduction band. This research focussed on the application of AB-stacked bilayer graphene as it has the potential for a high carrier mobility as high as $40000\text{cm}^2\text{V}^{-1}\text{s}^{-1}$ [12], which could enable a very fast detector, while the hot carrier relaxation mechanisms described in section 1.3.6 conceptually gives charge carrier multiplication.

The tuneable band gap of AB-stacked bilayer graphene was conceptualised as enabling colour sensitivity. A more energetic photon will generate more charge carriers, and the number of charge carriers is also inversely proportional to the magnitude of the band gap. Conceptually when more charge carriers are generated, for a higher energy photon and a small band gap, a better detector resolution is obtained. However a smaller band gap means more dark noise unless the device was cooled to a lower temperature, while a higher temperature means higher dark noise or a larger band gap. The tuneable band gap of AB-stacked bilayer graphene allows for this trade-off between temperature, band gap and resolution, as opposed to the fixed effective band gap of Cooper pairs in an STJ $\sim 100\text{meV}$ which means an STJ has to operate at cryogenic temperatures $\sim 300\text{mK}$. Eventually this could lead to a detector where the resolution could be compromised to operate at temperatures higher than current single photon counters, which could allow reduced costs through the use of cheaper cryogenics, and lighter payloads if incorporated onto a satellite.

The theoretical feasibility study for this detector concept is discussed further in chapter 2, with results presented that lead to an initial prototype design of the detector. This device was fabricated, as discussed in chapter 5, and then tested the ability for the detector to detect single photons and resolve colour. The novelty of this concept arises by exploiting the tuneable band gap to control the parameters of the detector, the detection method proposed in this technique, and the ability to operate at higher temperatures than other similar detectors, enabling cheaper operation. This detector could have applications in a number of areas, such as in fluorescence spectroscopy for medical applications, and spectroscopy for exoplanet detection.

1.4.2 Using Graphene for Terahertz Photodetection

Many different detectors, such as bolometers and calorimeters, can sense infrared radiation. MCPs [39] and Avalanche Photodiodes [131] are also able to detect in the near infrared, with recent work in the literature discussing an Avalanche Photodiode operating at 200MHz [132]. There are few widely-available detector technologies that are capable of detection at terahertz frequencies. These detectors could potentially have applications in areas of science and industry, including space science, medicine, communications and non-invasive security. For example, Photon Counting Terahertz Interferometry (PCTI) is a technique that has been proposed [50] [51] [52] [53] for terahertz imaging of distant objects in space, which requires detectors with a high-count rate of 1-100MHz and a time resolution better than 1ps [52].

Terahertz photodetection using graphene has been achieved by using several different techniques. The photothermoelectric effect, for example, was used to achieve a noise equivalent power (NEP) less than $1100\text{pWHz}^{-1/2}$ whilst operating at room temperature [133]. Other groups have used the Dyakonov-Shur effect [123] [124] [134] for terahertz photodetection, which have demonstrated excellent NEP less than $30\text{nWHz}^{-0.5}$ at room temperature [124] and as low as $1\text{nWHz}^{-0.5}$ [116]. Bolometers operating at sub-THz frequencies have also been developed [54] [135], which have shown good sensitivity and the ability to count single terahertz photons with a good energy resolution [54].

Each group investigating graphene-based photodetection in the terahertz regime has considered different combinations of frequency range, photodetection mechanism, bias voltage applied to the graphene and antenna structure. In this research, the behaviour of a passive terahertz detector sensitive to frequencies around 1.2THz that utilised the Dyakanov-Shur effect was explored, a combination of parameters which is unexplored in the literature. The Dyakanov-Shur effect was chosen as the literature [123] suggested that this mechanism could enable both broadband and narrowband terahertz detection. As this effect also uses a simple field effect transistor structure, it has some flexibility in the device design such as channel length, substrate dielectric constant and substrate thickness.

The work to design the detector is outlined in chapter 3, which considered the optimisation of the detector response for frequencies around 1.2THz, including the design of an antenna with an optimise S11 parameter at 1.2THz. The fabrication of the detector is presented in chapter 5. The experimental testing of the detector, as a function of gate voltage and terahertz power, for example, is discussed in chapter 7.

A new detector in this regime would enable a new area of physics to be investigated and for applications in areas such as astronomy, non-penetrative security and medical sciences. This could potentially lead to a graphene-based terahertz detector that enables photon counting terahertz interferometry [50] [51] [52] [53], and a smaller pixel size could allow for a greater resolution resulting from a greater pixel density.

1.4.3 Graphene for X-Ray Photodetection

Field effect transistor detectors have been developed to exploit photodetection mechanisms for X-ray photons. Much of the research into graphene field effect transistors (GFETs) for X-ray detection has been developed by the Jovanovic group [74] [75] [80] [81] [82] [83] [125]. They demonstrated detection of X-ray photons from an X-ray generator (15kV, 15 μ A & 40kV, 80 μ A) using a GFET structure with a SiC substrate at room temperature, and another X-ray GFET on an undoped silicon substrate, but operating at 4.3K [75]. X-ray photons are absorbed in the absorber and generate charge carriers that modulate the field applied to the graphene resulting in a measurable change in the resistance. This suggested an energy resolution as $\frac{E}{\delta E} \sim 330$ for 1MeV, with a responsivity of 0.1AW⁻¹ for the SiC-based device [74] [75] [80] [81] [82] [83] [125]. These detectors have a signal decay time of ~ 1000 s for the Si absorber and ~ 40 s for the SiC absorber, which makes the current state of the art detectors [78] inappropriate for high speed, low intensity single photon counting photodetection.

The research by the Jovanovic group prompts consideration of the potential energy sensitivity that a simple X-ray GFET detector with a silicon wafer is capable of, and how fast it could operate. The single X-ray photodetector was designed and fabricated, as discussed in chapters 4 and 5 respectively. The detector parameters were probed with a pulsed laser to simulate the deposition of energy from an absorbed X-ray photon, to understand the potential operation of the detector and estimate the sensitivity, as

discussed in chapter 7. A graphene-based single X-ray photodetector has not yet been achieved, let alone at room temperature, so would be novel. Applications would include medical applications for greater resolution radiometry, along with space-based applications for X-ray astronomy.

There are potential routes to iteration of the device structure, including the addition of a second gate to the GFET or to encapsulate the GFET channel to reduce the effect of environmental dopants on the GFET and improve the consistency of measurements. A GDEPFET structure may also provide routes to improve detector bandwidths.

1.5 Summary

This section has considered the current state of the art of single photon counting photodetectors, and discussed the compromises that must be made for each detector. For instance, STJs operate with colour sensitivity across a wide range of frequencies, but must be operated at cryogenic temperatures. MCP-PMTs, on the other hand, can be operated at room temperature but have little to no energy resolution.

Graphene has been presented in this chapter as a possible solution for future single photon counting photodetectors. Many of the most important properties have been discussed, such as the transport properties, tuneable band gap and field effect. The current state of the art graphene-based photodetectors at different photon frequencies were then compared to other existing detectors, which demonstrated the potential for sensitive, fast graphene-based photodetector solutions. As a result, several areas of potential research were highlight for detectors of photon frequencies from terahertz to X-ray that have not yet been considered in the literature, and could potentially have applications in several different areas:

- A bilayer graphene single photon counting photodetector with wavelength specificity, without the need for dispersive elements. This would exploit the tuneable band gap of bilayer graphene and the potential sample mobility, and could theoretically be operated at higher temperatures than existing cryogenic detector. The theoretical investigation into this work is discussed in chapter 2.
- A terahertz photodetector that utilises the Dyakonov-Shur effect with antennae that are designed to respond to 1.2THz. A successful detector could enable new

applications in areas such as security and space. The theoretical investigation into this work is discussed in chapter 3.

- A single X-ray photodetector to investigate the potential energy sensitivity of a simple GFET structure, and how fast the detector could operate. Previous research has developed detectors that are too slow for single x-ray detection, so successful development of this detector would have potential applications in space science, medical physics etc. The theoretical investigation into this work is discussed in chapter 4.

2

Theoretical Studies and Design of a Bilayer Graphene Single Photon Counting Photodetector

2.1 Introduction

As discussed in the previous chapter, many techniques are available for single photon counting at visible wavelengths, although these often require complex and costly cryogenic cooling to $\sim 100\text{mK}$ to overcome dark noise. Furthermore, many of these detectors do not offer a route to colour sensitivity without the need for wavelength dispersive elements.

In this chapter, a bilayer graphene-based single photon counting photodetector is conceptualised and the relevant physics are discussed. Theoretical simulations for the detector were developed to indicate the likely operational properties and parameters of the detector, including colour sensitivity and a trade-off between temperature and band gap/resolution, the latter of which could allow for the use of cheaper and less complex cryogenic techniques.

Firstly, the density of states was calculated to investigate the optimum operational window [1] [2]. A Monte Carlo simulation using a Gillespie algorithm [136] was then developed to simulate the absorption of an incident photon on the graphene lattice, the excitation of a photoelectron and its subsequent relaxation in the conduction band. The design of the detector was then considered, based on that shown in ref. [65], using a finite element method to evaluate the potential applied to the graphene from the top and bottom gates in preparation for fabrication.

The work in this chapter was largely published in reference [1].

2.2 Developing the Concept

A cryogenic bilayer graphene single photon counting photodetector was conceptualised that could utilise the tuneable Fermi level and band gap of AB stacked bilayer graphene through top and bottom gating [65], along with the impressive carrier mobility of graphene that has enabled high operational bandwidth in other graphene photodetectors [126]. Conceptually, a photon absorbed by the bilayer graphene excites an electron-hole pair, with the electron excited into the conduction band. This relaxes to lower energies through several possible channels, including the excitation of further charge carriers into the conduction band. At the end, the number of electrons that are produced are counted, and the energy of the original photon is resolved.

To develop the concept and theoretical simulations for this detector, one needs to consider the physics associated with photoexcitation in bilayer graphene and the possible relaxation paths that an excited charge carrier could follow.

2.2.1 Photoexcitation in Bilayer Graphene

In a previous section the vertical excitation of a photoelectron from the valence band to the conduction band was discussed. Bilayer graphene has four bands, two in the valence band and two in the conduction band. Transitions between bands is possible subject to Pauli blocking, and provides a contribution to the optical conductivity [12], figure 2.1. An intraband transition rate equal to $\sigma_{\pi_1\pi_1} \propto \gamma_1 \log \left[\frac{\gamma_1 + 2|E_F|}{\gamma_1} \right] \delta(\hbar\omega - \gamma_1)$ in the valence band is negligible in this case due to the lack of available states.

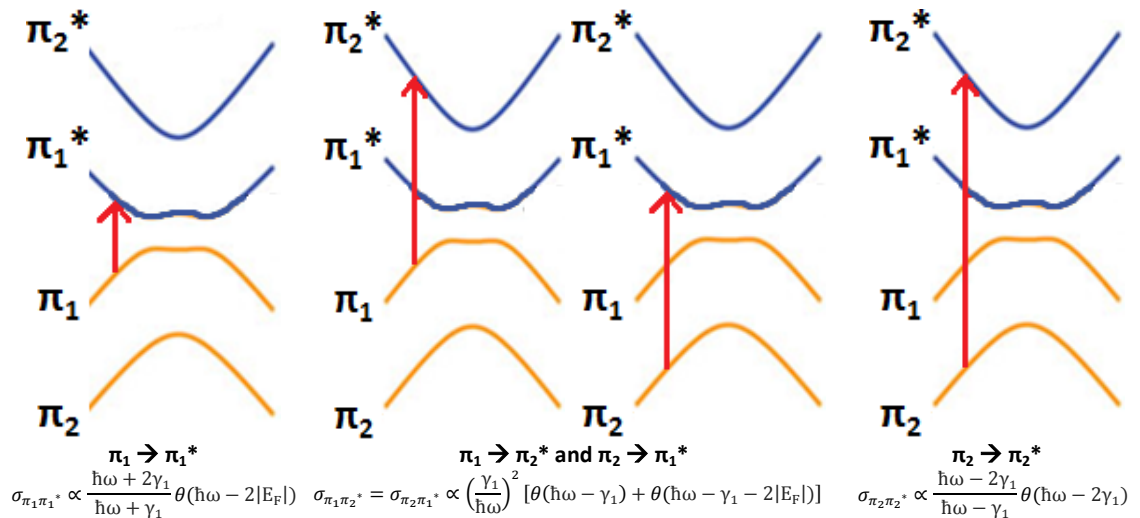


Figure 2.1 showing different contributions to the optical conductivity.

2.2.2 Possible Relaxation Paths

An excited photoelectron will thermalise to lower energies. This can occur through many different paths, depending on variables such as temperature, band gap and conduction band density. Four of the main contributions are electron-electron scattering, electron-phonon scattering, impact ionisation and Auger recombination.

Electron-electron scattering (EES) is the inelastic scattering between two electrons in the conduction band (CB) and does not affect the total energy or the number of electrons in the CB. The rate of collisions is inversely proportional to the mean free time and proportional to the density of electrons. For bilayer graphene, the rate of electron-electron scattering, σ_{E-E} , is approximated by

$$\sigma_{E-E} = \frac{1}{\tau_{MFT}} = \frac{v_F}{\lambda} = 2k_f \frac{\hbar k_f}{m_e} = \pi n \frac{2\hbar}{m_e}, \quad \text{Equation 2.1}$$

where τ_{MFT} is the mean free time, v_F is the Fermi velocity, k_f is the Fermi wavenumber, λ is the wavelength, n is the density of charge carriers and m_e is the mass of an electron.

Another possibility is electron-phonon scattering (EPS) which is the scattering of an electron due to the emission (absorption) of a phonon to (from) the lattice [112], resulting in energy lost (gained) from the electrons. The electron-phonon scattering rate is defined as [137]

$$\sigma_{\text{Phonon}} = \sigma_{\text{Acoustic}} + \sigma_{\text{Optical}} \approx \frac{D_0^2}{\rho_m \omega_0 (\hbar v_F)^2} \left[(E_k - \hbar \omega_0) \left[\frac{1}{e^{k_B T} - 1} + 1 \right] \theta(E_k - \hbar \omega_0) + (E_k + \hbar \omega_0) \left(\frac{1}{e^{k_B T} - 1} \right) \right], \quad \text{Equation 2.2}$$

where ω_0 is the phonon frequency, E_k is the electron energy, T is the temperature, ρ_m is the mass density, D_0 is the deformation potential constant, λ is the wavelength, v_F is the Fermi velocity, k_f is the Fermi wavenumber and n is the density of charge carriers. The bilayer graphene rate can be approximated to that previous stated for single layer graphene as the scattering rate differs by less than an order of magnitude, especially at low electron energies, figure 2.2 [67].

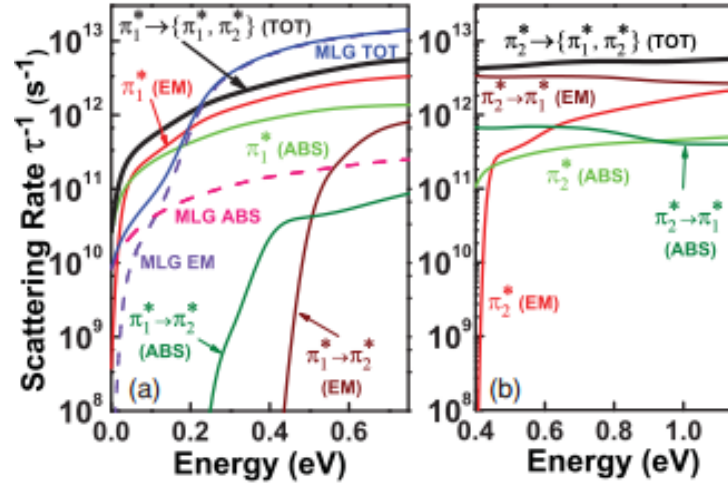


Figure 2.2. Comparison of single (left) and bilayer (right) graphene electron-phonon scattering rates, and contributions to the total rate [67]. Reproduced under copyright licence from the American Physical Society.

In the previous chapter, hot electron scattering, impact ionisation (II) and Auger recombination (AR) were considered for single layer graphene with weak exciting pulses [117] [119]. Little work has been done for single photon excitation, with work such as ref. [138] not especially easy to implement in these simulations. Therefore, arbitrary II and AR rates are introduced in this chapter, which relate both rates to the electron phonon scattering rate in equation 2.2. Given the temperature, band gap and carrier density used in the simulations, it was assumed that the II rate would dominate over the electron phonon scattering rate, as discussed in section 2.4.3, although introducing these II and AR rates does not rely on this assumption. The II and AR rates could be identified qualitatively from experimental results.

2.3 Density of States and Optimum Operational Window

Initially, the expected dark noise for the detector needed to be estimated. Further simulations were also developed to understand how the tuneable band gap could be utilised to reduce the number of charge carriers that are thermally excited. To calculate the density of states, $n(E)$, numerically one applies [6]

$$n(E) = 2.2 \int_0^\infty \frac{k dk}{2\pi} \delta(E - E(k)) = \frac{2}{\pi} \frac{k(E)}{|dE/dk|}, \quad \text{Equation 2.3}$$

where k is the wavenumber and E is the electron energy. In bilayer graphene, with no band gap and at lower energies, this becomes

$$n(E) = \frac{2 m^*}{\pi \hbar^2}, \quad \text{Equation 2.4}$$

where m^* is the effective mass. Beyond the small energy approximation, and with an induced band gap, one must apply the full integral over the first Brillouin zone. This leads to the density of states, figure 2.3, that shows Van Hove singularities at $E = \pm\gamma_1$, with a zero density up to $E_G/2$ in the π_1^* band and to $E_G/2 + \gamma_1$ in the π_2^* band, where E_G is the magnitude of the band gap and γ_1 is the interlayer hopping parameter.

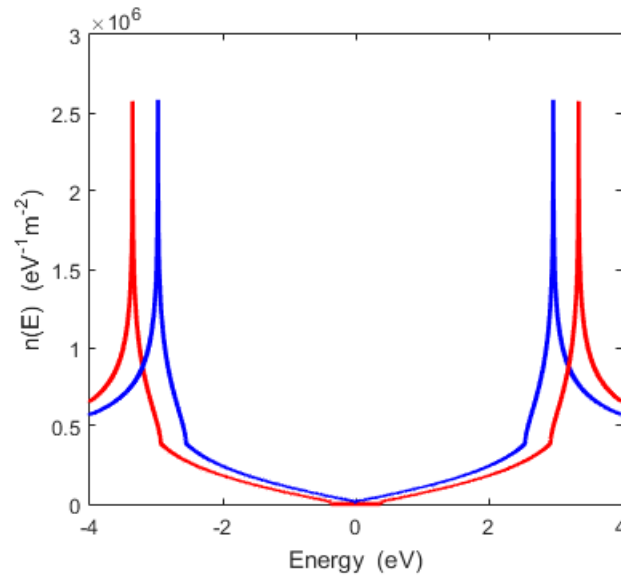


Figure 2.3 showing the density of states for bilayer graphene with a band gap of 5meV; red is the π_2 band, blue is the π_1 band.

By integrating the Fermi-Dirac distribution,

$$N = \int_0^{E_{\text{photon}}/2} dE \frac{1}{\exp\left(\frac{E}{k_b T}\right) + 1} n(E), \quad \text{Equation 2.5}$$

over the first Brillouin zone, where E is the electron energy and T is the temperature, the number of thermally produced charge carriers in the conduction band per unit area, N , is calculated. The integration limit given by $\frac{E_{\text{photon}}}{2}$ arises from the possible photon excitations from the valence band to the conduction band for visible photon energies that are relevant for this detector. The number of charge carriers is then given by NA , where A is the sample area.

A single photon counting photodetector requires low dark noise, and hence $NA < 1$ where there is theoretically no dark current. The temperature and band gap were

varied to look for solutions where $NA = 1$, with the intention to operate in the ideal regime where $NA < 1$, figure 2.4. For instance, a 1mm^2 graphene sample at $T=1\text{K}$, with a band gap of 5meV , was found to have a value of $NA = 0.85$ charge carriers.

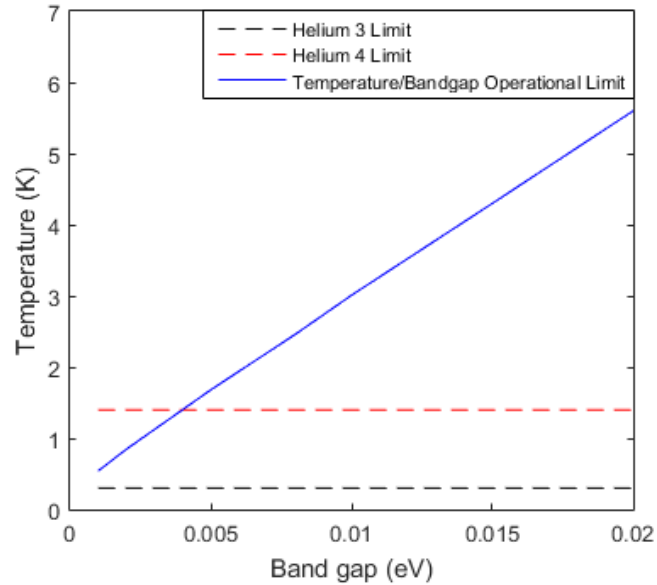


Figure 2.4, showing the operational limit of a bilayer graphene photodetector. In this simulation, $A=1\text{mm}^2$. Helium-4 cooling limit is 1.4K and Helium-3 limit is 0.3K .

The operational limit is critically dependent on the bilayer graphene density of states, and the tuneable band gap in AB-stacked bilayer graphene enables this operational limit to be exploited by trading off resolution by running with a larger band gap to enable operation at higher temperatures. For instance, according to these simulations, a detector could easily be run with no thermal noise at 0.01eV band gap at 2K , but not at 4K . This would allow operation above temperature limits for helium 3 and helium 4 cryogenic systems, as shown in figure 2.4. This suggests that the photodetector could be operated at temperatures not requiring the use of He-3, which would reduce the cost of operating the detector by reducing the cost of cryogenic systems.

2.4 Developing the Gillespie Algorithm

A Monte Carlo simulation was developed using the Gillespie Algorithm [136] to determine the likely properties of the photodetector [1]. The approach taken uses a similar method to that applied to silicon [139]. The model assumed that the detector operated within the limit described in figure 2.4, i.e. electrons in the conduction band result solely from the initial photoexcitation (or subsequent relaxations), shown schematically in figure 2.5. In addition, the Fermi level was tuned to the centre of the

band gap, and excitation only occurred when the photon energy is greater than or equal to the energy difference between the valence and conduction bands. The code was initiated as three separate programs, “photon excitation”, “vacancy filling” and “photoelectron relaxation”.

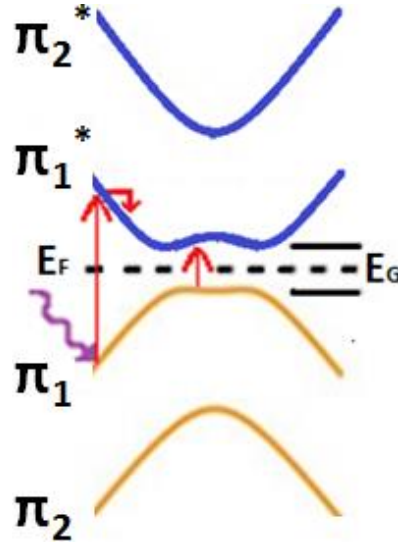


Figure 2.5, showing the absorption of a photon, and the excitation of a subsequent relaxation of the hot photoelectron in the conduction band for a given band gap E_G .

2.4.1 Photon Excitation

The given rate of incident photons on the graphene is

$$\sigma_{Photon} = \frac{IA}{E_{Photon}}, \quad \text{Equation 2.6}$$

where I is the irradiance, A is the area of the sample, $E_{Photon} = \hbar\omega$, and ω is the photon frequency. Of these incident photons, 2.3n% will be absorbed [10], where n is the number of layers.

In section 2.2.1 the optical conductivity rates for the four different interband transitions for photoexcitation when $T=0K$ were given by

$$\sigma_{\pi_1\pi_1^*} \propto \frac{\hbar\omega + 2\gamma_1}{\hbar\omega + \gamma_1} \theta(\hbar\omega - 2|E_F|), \quad \text{Equation 2.7}$$

$$\sigma_{\pi_1\pi_2^*} = \sigma_{\pi_2\pi_1^*} \propto \left(\frac{\gamma_1}{\hbar\omega}\right)^2 [\theta(\hbar\omega - \gamma_1) + \theta(\hbar\omega - \gamma_1 - 2|E_F|)], \quad \text{Equation 2.8}$$

and

$$\sigma_{\pi_2\pi_2^*} \propto \frac{\hbar\omega - 2\gamma_1}{\hbar\omega - \gamma_1} \theta(\hbar\omega - 2\gamma_1), \quad \text{Equation 2.9}$$

where ω is the photon frequency, γ_1 is the interlayer hopping parameter equal to 0.4eV, E_F is the fermi energy, and $\theta(x)$ is the Heaviside function [12]. These rates can also be used as a good approximation for cases where $T>0$ and $\Delta>0$, where Δ is the band gap. For the case where $\Delta=0$ and $T=0$, the optical conductivity is shown in figure 2.6a [140]. With the opening of a band gap, Δ , no photons will be absorbed at energies less than Δ , as shown in figure 2.6b [140]. Therefore, for greater values of Δ , this causes a translation in the conductivity spectrum to slightly higher energies. For cases where $T >0$, electron excitations from the valence band to the conduction will produce dark noise. Therefore, a large conduction peak will form with increasing temperature, and hence it will shift again in the optical conductivity (although this time to lower energies). However, as the detector operates where Δ is small and with no dark noise, it can be safely approximated that the rates given in ref. [12] and illustrated in figure 2.1, are appropriate for the conditions used for these simulations.

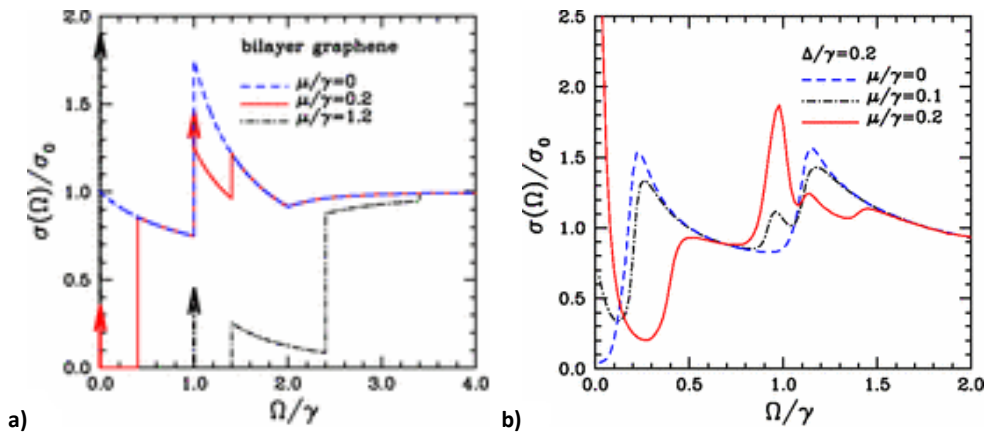


Figure 2.6, showing the optical conductivity $\sigma(\Omega)/\sigma_0$, where Ω is the photon energy, for bilayer graphene a) without a band gap, and b) with a band gap, Δ [140]. Without a band gap, the optical conductivity of bilayer graphene describes two coupled layers of graphene. For bilayer graphene with a band gap, the optical conductivity in the case of the Fermi level tuned to the centre of the band gap ($\mu/\gamma=0$, where is the interlayer hopping parameter $\gamma=0.4\text{eV}$) shows low optical conductivity for photon energies less than the band gap. Reproduced under copyright licence from the American Physical Society.

The simulation was initiated for the absorption of photons: when the photon is absorbed, a location in reciprocal space is chosen where the difference between the valence band and conduction band is equal to the energy of the photon. Allowed transitions are shown on the left of figure 2.7, and disallowed transitions on the right, with the disallowed transitions due to the Pauli blocking. To conserve energy and momentum, no horizontal photon transitions are allowed for the excitation. An array

filled with momentum space coordinates and the time the electron is excited to the conduction band is outputted from the code. An equivalent array is outputted for the creation of the corresponding hole in the valence band.

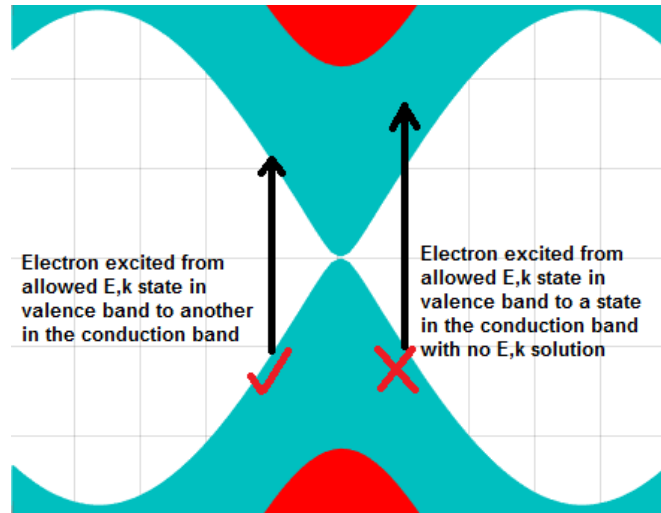


Figure 2.7, showing allowed and disallowed photoelectron transitions.

2.4.2 Hole Relaxation/Vacancy Filling

Secondly, the effect of hole relaxation in the valence band was considered, as shown in figure 2.8. For each hole, the valence band electron was assumed to relax to fill the hole, with a new hole being formed. The energy difference between the initial and final location of the electron is emitted as a photon, and there is a 2.3% probability per layer of the photon being absorbed. The effect of this is an additional, inefficient, means of exciting electrons, and is the equivalent of Auger recombination for holes.

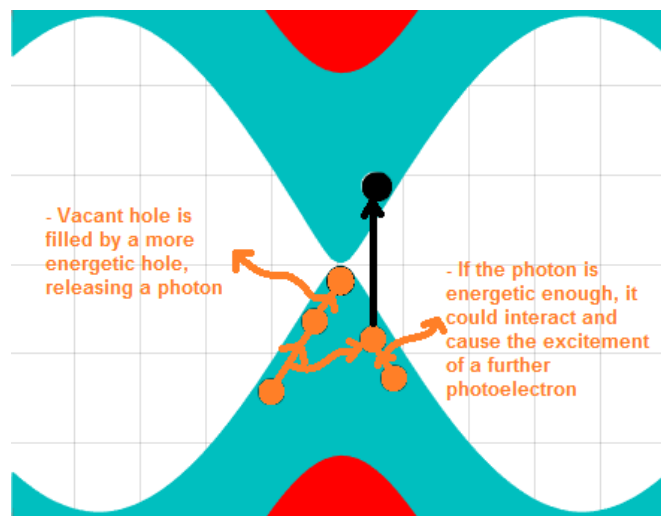


Figure 2.8, showing a schematic of the model used for Vacancy Filling.

2.4.3 Photoelectron Relaxation

The relaxation of the photoelectron was then simulated; the hot carrier could relax through several different relaxation paths, and the Gillespie algorithm included the rates for electron-phonon scattering (EPS), impact ionisation (II), Auger recombination (AR) and electron-electron scattering (EES). As a cryogenic detector, the simulations are run at $T \rightarrow 0\text{K}$ and the conduction band density $n \rightarrow 0$ which leads to $\sigma_{Optical} \approx 0$ and $\sigma_{E-E} \approx 0$ respectively. It was assumed that plasmon excitation [141] is negligible in these conditions because of the low Fermi level.

Following the photoexcitation, only one electron resided in the conduction band. Each of the EES, EPS and AR relaxation rates were assumed to be significantly lower than II, as the former are dependent on the conduction band density, whereas II is valence band density dependent [119]. With no II or AR rate defined for bilayer graphene at low temperatures and low conduction band density in the literature, to run the simulations the parameter $\mu = \sigma_{II}/\sigma_{Phonon}$ was defined.

In figure 2.2, the EPS rate increases with increasing energy towards an asymptote of order 10^{12}s^{-1} , whereas in ref. [55] and ref. [142] the impact ionisation rate leads to photodetection on the tens of femtosecond scale, with a rate of order 10^{14}s^{-1} . This is despite the fact that the work in ref. [142] uses pump terahertz probing with an absorbed photon density of 10^{11}cm^{-2} which leads to more electrons excited to the conduction band. This would lead to more “competition” between the various scattering rates compared to the case of a single hot photoelectron in the conduction band (the latter case being the focus of this work), due to the greater conduction band density leading to greater EES, EPS and AR rates, and a lower valence band density leading to a decreased II rate.

Initially, σ_{II} and σ_{AR} were arbitrarily defined as $\sigma_{II} = \sigma_{AR} = 100\sigma_{Phonon}$ to allow the simulation to run, with the intention of deducing the qualitative rate during the experimental phase. Running the simulation with this condition and that the simulation loops and restarts an individual relaxation after 1000 attempts to try to find a solution where one of the relaxation channels occurred, while conserving energy and momentum, provided no solutions where Auger recombination is allowed. This was

due to the few vacancies in the valence band that exist along with the necessity to conserve energy and momentum when these are filled. As the rate of Auger recombination is so slow compared to the timescales for other processes, the contribution from Auger recombination was ignored, $\sigma_{AR} \sim 0$, to improve the speed of the simulations. Both impact ionisation and electron phonon scattering occurred during the simulations, but no solutions were found where phonon emission caused a transition from the conduction band to the valence band. Therefore, Auger recombination and phonon emission processes were said to be ineffective in causing relaxation out of the conduction band.

If impact ionisation relaxation processes had been found not to satisfy energy and momentum, this relaxation would not have been able to occur in the simulation, and electron phonon scattering would have been the only relaxation channel possible. This was not found to be the case, with significantly more solutions occurring due to II than EPS, which was therefore said to dominate over a relaxation process via acoustic phonon excitation (i.e. $\sigma_{II} > \sigma_{EPS}$), primarily due to the valence band and conduction band densities respectively.

EXAMPLE

As an example, an electron is excited to the conduction band with energy $\frac{E_Y}{2}$ at the first iteration. On the second iteration, following the first relaxation, it loses a random amount of energy and, in this case, excites an additional electron to the conduction band which has energy in the conduction band of half the amount lost (because of the energy required to promote it from the valence band). This continues over more iterations until convergence in the number of electrons in the conduction or a specified cut-off time.

| | Iteration 1 | Iteration 2 | Iteration 3 | Iteration 4 | Iteration 5 | Iteration 6 |
|----------------------|-------------|--------------------|-----------------------------|--------------------------------------|--------------------------------------|--------------------------------------|
| Energy of electron 1 | $E_Y/2$ | $(E_Y/2) - E_{1a}$ | $(E_Y/2) - E_{1a} - E_{2a}$ | $(E_Y/2) - E_{1a} - E_{2a} - E_{3a}$ | $(E_Y/2) - E_{1a} - E_{2a} - E_{3a}$ | $(E_Y/2) - E_{1a} - E_{2a} - E_{3a}$ |
| Energy of electron 2 | 0 | $E_{1a}/2$ | $E_{1a}/2 - E_{2b}$ | $E_{1a}/2 - E_{2b} - E_{3b}$ | $E_{1a}/2 - E_{2b} - E_{3b}$ | $E_{1a}/2 - E_{2b} - E_{3b}$ |
| Energy of electron 3 | 0 | 0 | $E_{2a}/2$ | $E_{2a}/2 - E_{3c}$ | $E_{2a}/2 - E_{3c}$ | $E_{2a}/2 - E_{3c}$ |
| Energy of electron 4 | 0 | 0 | $E_{2b}/2$ | $E_{2b}/2$ | $E_{2b}/2$ | $E_{2b}/2$ |
| Energy of electron 5 | 0 | 0 | 0 | $E_{3a}/2$ | $E_{3a}/2$ | $E_{3a}/2$ |
| Energy of electron 6 | 0 | 0 | 0 | $E_{3b}/2$ | $E_{3b}/2$ | $E_{3b}/2$ |
| Energy of electron 7 | 0 | 0 | 0 | $E_{3c}/2$ | $E_{3c}/2$ | $E_{3c}/2$ |
| Energy of electron 8 | 0 | 0 | 0 | 0 | 0 | 0 |
| Energy of electron 9 | 0 | 0 | 0 | 0 | 0 | 0 |

The Gillespie algorithm [136] was used for the simulation, with each of the relaxation events chosen randomly, weighted based on the relevant rates, and solved numerically to find solutions where energy and momentum are conserved. The time step between events was based on the event rate. Additionally, the code stated that nothing can happen if each of the rates was equal to zero, so the electron remains at the same location in momentum space. The simulation ran from the initial photoexcitation to a given time, by which point the number of electrons in the conduction band had reached a maximum. The number of charge carriers that was produced was extracted and stored in an array.

In the simulation, relaxation primarily occurred via phonon excitation and impact ionisation. Both processes require a change in energy and momentum. For phonon loss, a random energy phonon is produced based on the phonon energy spectrum. As the “Mexican Hat” shaped perturbation at the Dirac point is small and below the Lifschitz energy it does not affect the parabolic energy-momentum relationship of the band structure at higher energies. Therefore, a parabolic approximation relating the energy transferred and the corresponding change in momentum during a relaxation step was used, given by

$$E_t = E_{phonon} = \frac{\hbar^2 k_{change}^2}{2m} . \quad \text{Equation 2.10}$$

The change in the momentum components were then calculated whilst cycling through possible angles φ until both energy and momentum are conserved, given by equations 2.11 and 2.12,

$$k'_x = k_x + k_{change} \cos(\varphi) = k_x + \delta k_x \quad \text{Equation 2.11}$$

and

$$k'_y = k_y + k_{change} \sin(\varphi) = k_y + \delta k_y \quad \text{Equation 2.12}$$

For impact ionisation (II), a random proportion of the electron energy was chosen to be transferred during an inelastic collision. The energy transferred, E_t , was approximated by applying a limiting value α between 0 and 1, with a random number r chosen between 0 and 1. The parabolic relationship between the energy and momentum in bilayer graphene was again approximated to relate the energy

transferred and the corresponding change in momentum during a relaxation step, given by

$$E_t = \frac{\hbar^2 k_{change}^2}{2m} = r\alpha E . \quad \text{Equation 2.13}$$

A random point in momentum space was selected in the valence band close to the Dirac point, and the momentum components were again calculated whilst cycling through possible angles φ , equations 2.11 and 2.12, to ensure energy and momentum conservation in both bands. The randomly chosen point could be from the π_1 or π_2 band. This is illustrated in figures 2.9a and 2.9b, for phonon loss and impact ionisation.

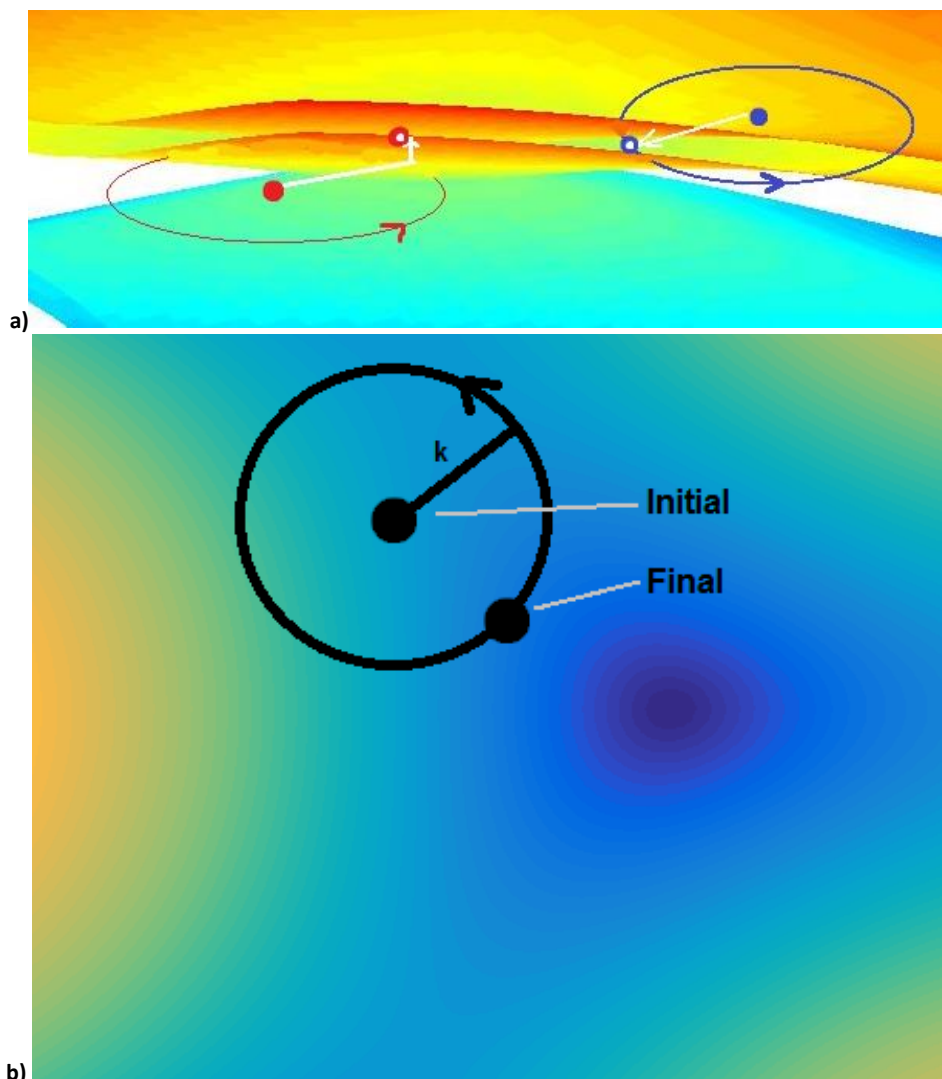


Figure 2.9, showing the method used in the algorithm to ensure conservation of momentum/energy. Figure 2.9a shows this for II, where a circle about the initial electron energy (blue in conduction band, red in valence band) is of radius k_{change} in momentum space, and evaluates the energy at each point around the circle until energy is conserved. If no point conserves both, it picks a new energy/momentum and repeats. For phonon loss in figure 2.9b, a randomly selected phonon energy results in momentum components that are solved numerically to ensure energy and momentum conservation.

In both cases, the energy of the conduction band electron after the relaxation event was given by

$$E' = \frac{\hbar^2(k+\delta k)^2}{2m} = \frac{\hbar^2(k^2+2k.\delta k+\delta k^2)}{2m} = E + E_t + E_{ct} \quad \text{Equation 2.14}$$

where E_t is defined as negative (a loss of energy), and $E_{ct} = \frac{\hbar^2}{m}(k_x\delta k_x + k_y\delta k_y)$.

2.5 Simulation Results

In this section, the results of the simulations are presented, and any further approximations and comparable results are discussed.

2.5.1 Energy Conservation

Initially the energy conservation of the simulation was demonstrated, subject to a tolerance of 5%. The variation above and below this initial energy is stochastic, so over many runs this averages to a constant value. The purple line in figure 2.10 shows the sum of the energy of the electrons in the conduction band. The brown line shows the sum of the energy of conduction band electrons (i.e. the Fermi energy to the electron location) and the energy of the holes (i.e. the energy required to promote an electron from an initial location in the valence band to the Fermi energy). In this case, such a large initial drop is seen in the total conduction band energy (purple line) due to the excitation of an electron from the π_2 rather than π_1 valence band.

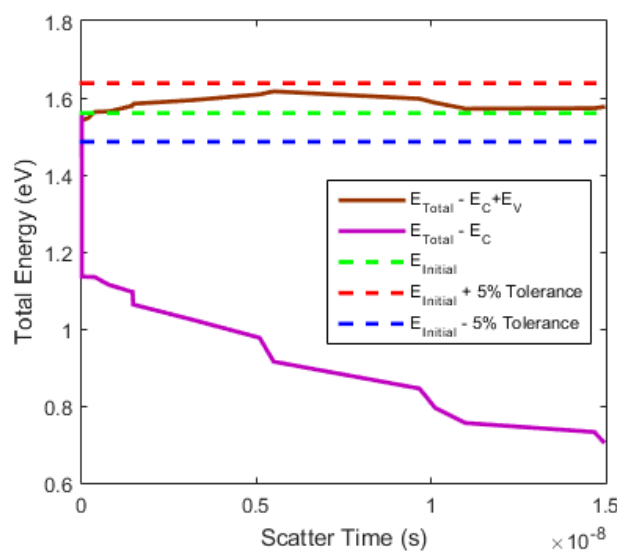


Figure 2.10, showing energy conservation in the simulation including the sum of the energy of the electrons in the conduction band (purple), the sum of the energy of all electrons and holes in the simulations relative to the Fermi energy (brown). The initial large drop in total energy results from an excitation of an electron from the π_2 rather than π_1 valence band.

2.5.2 Convergence of Results

As discussed in the previous section, to allow for a relaxation that conserves energy and momentum, the simulation cycles about a point with a given radius in momentum space searching for a valid solution. An initial angle is chosen at random, and the simulation iterated this angle with $\delta\theta$ not a factor of 360° . The simulation kept iterating F_1 times to attempt to find a solution – if this failed, the solution could reset F_2 times with a new starting point to iterate about. If this still failed to find a solution conserving energy and momentum, the code resets entirely.

The simulation was intended to run with values of F_1 and F_2 where the number of charge carriers that are produced converges to ensure an efficient yet complete simulation. In figure 2.11a, for an increasing value of F_1 , the number of charge carriers produced converges for $F_1 > 100$; for further simulations, F_1 was defined as $F_1 = 198$. In figure 2.11b the number of charge carriers produced converges for $F_2 \sim 1000$, and therefore F_2 was defined as $F_2 = 1000$.

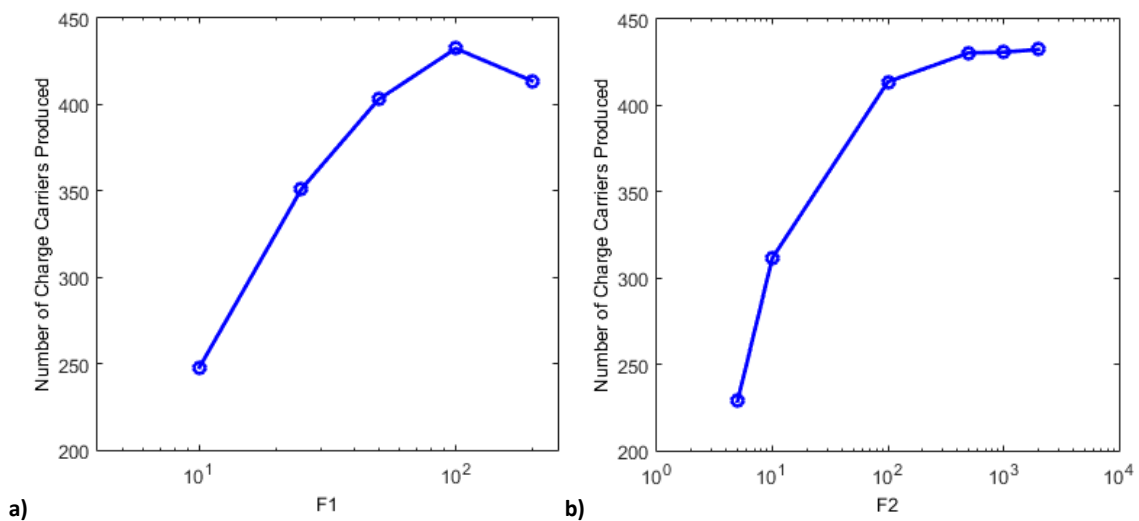


Figure 2.11, showing the effect of changing a) F_1 and b) F_2 . The number of charge carriers that are produced converges for $F_1 > 100$ and $F_2 > 1000$.

2.5.3 Number of Charge Carriers Produced as a function of time

The first simulations were run over a given time, for different initial energies and band gaps. The results show that the number of electrons that are produced increases with the initial photon energy, figure 2.12. Additionally, as the band gap is increased the number of electrons produced is significantly reduced and at a slower rate.

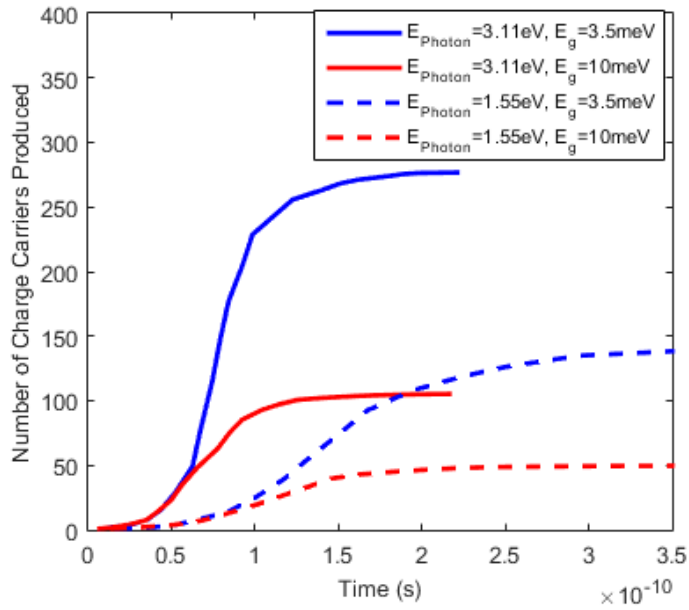
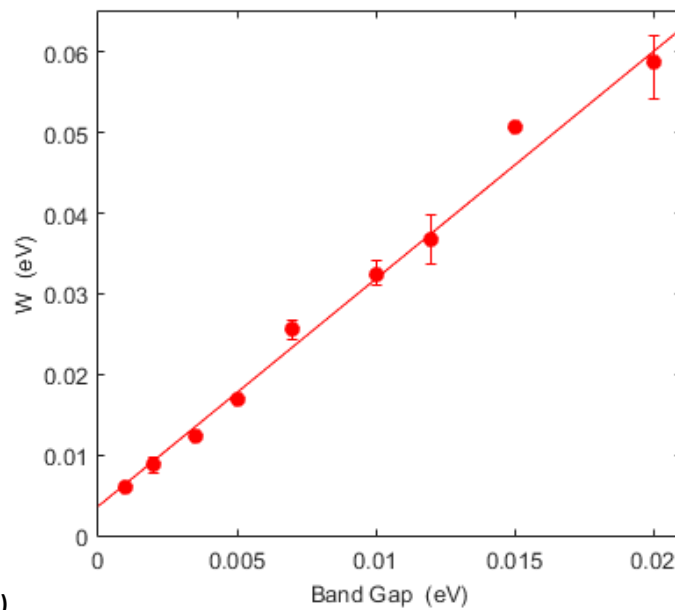


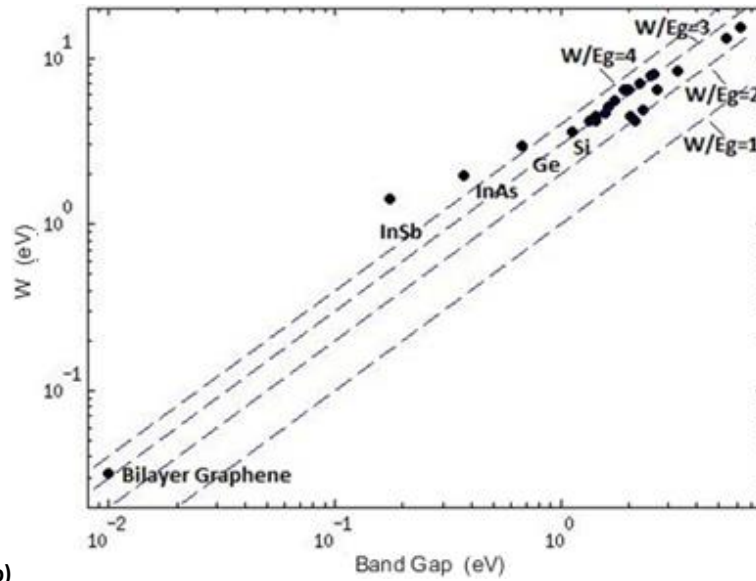
Figure 2.12. The distribution $N(t)$ at $E_{\text{gap}}=1\text{meV}$ and 3.5meV for photons with energy 3.11eV and 1.55eV , and with $\mu = \frac{\sigma_{\text{II}}}{\sigma_{\text{Phonon}}} = 100$.

2.5.4 Average Ionisation energy, W , as a function of band gap

By simulating with different size band gaps and photon energies the average electron-hole pair creation energy, $W = \frac{E_{\text{photon}}}{N}$, was calculated, figure 2.13a. This gave a W to band gap ratio of 3-4, comparable to semiconductors such as silicon and germanium, figure 2.13b [143].



a)



b) Figure 2.13, showing a) Electron-hole pair creation energy as a function of band gap with $\mu=100$. The circles show simulation results, and the red line is best fit straight line. B) shows a comparison of W vs band gap for bilayer graphene with other semiconductors.

2.5.5 Number of Charge Carriers Produced as a function of Photon Energy

From the average ionisation energy, W , it was possible to deduce that a more energetic initial photon produced more charge carriers. Figure 2.14 shows a histogram of the number of charge carriers that are produced for a red ($\lambda=800\text{nm}$) and blue ($\lambda=400\text{nm}$) photon; clearly, for a more energetic photon, more electrons are produced. Wavelength specificity is observed as the noticeable difference in the distributions at each wavelength with respect to the number of produced charge carriers.

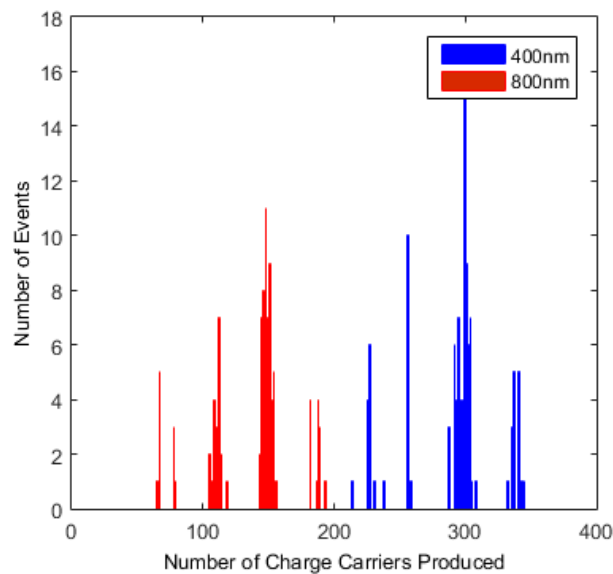


Figure 2.14, showing the number distribution as a function of photon energy, for $\mu=100$. The number of charge carriers increases with photon energy, which suggests wavelength specificity.

The four noticeable peaks in the simulation arise from the four possible excitations from the π_1 and π_2 bands to the π_1^* and π_2^* bands respectively. The gap between the centre of the peaks is equal to $\Delta N \sim \frac{\gamma_1}{W}$, where γ_1 is the hopping parameter between layers, and W is the average ionisation energy.

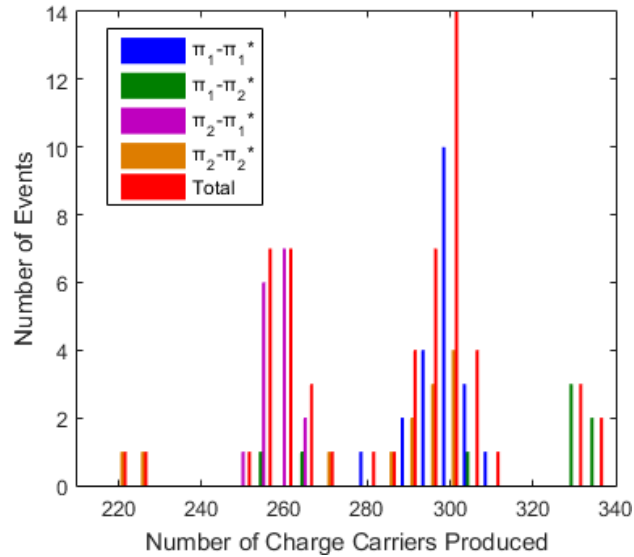


Figure 2.15, showing the origin of the peaks for the transition between the π_1/π_2 and π_1^*/π_2^* bands. The greatest probability peak occurs for the $\pi_1 \rightarrow \pi_1^*$ transition, while the $\pi_2 \rightarrow \pi_2^*$ transition typically leads to the fewest number of charge carriers.

The characteristic peak of an event is highly dependent on the initial transition between the bands (i.e. $\pi_1 \rightarrow \pi_1^*$, $\pi_1 \rightarrow \pi_2^*$, $\pi_2 \rightarrow \pi_1^*$ or $\pi_2 \rightarrow \pi_2^*$), figure 2.15. This arises because a transition from the π_2 band requires more energy to excite to the conduction band than an excitation from π_1 , and hence less energy to allow for further electron excitations, figure 2.16. Furthermore, no II transition can occur for an electron with energy between $0.5E_G$ (i.e. the bottom of the degenerate π_1^* band at the Dirac point) and $1.5E_G$. With a more energetic photon (i.e. 400nm) and a more energetic initial energy in the conduction band ($\pi_1 \rightarrow \pi_2^*$ transition), more electrons will be produced before they fall into this “no transition” region.

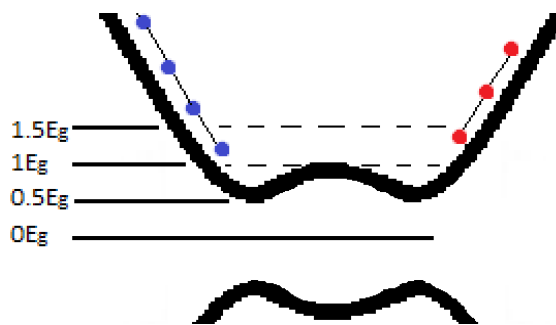


Figure 2.16. Comparing the number of electrons produced at photon energies (blue dots indicate a more energetic photon than red) falling into the no transition regime.

The presence of the four peaks in figures 2.14 and 2.15 makes energy resolution of the incident photon problematic. The energy resolution of a photoelectron is given by [144]

$$\frac{\sigma_E}{E} \propto \frac{\sigma_{N_{PE}}}{N_{PE}} = \frac{\sqrt{FN_{PE}}}{N_{PE}} \propto \frac{1}{\sqrt{N_{PE}}}, \quad \text{Equation 2.15}$$

where F is the Fano factor and N_{PE} is the number of photoelectrons generated. In ref. [59] the Fano factor was shown to have the form $F \approx 1 - \frac{2}{\pi}$ by calculating the transmission coefficients of wavefunctions for normally incident onto a sample of thickness L_x and circumference L_y , and then taking the limit where $L_y \gg L_x$.

The energy resolution is estimated as $\sigma \sim 30$ and $\sigma \sim 36$ for the blue and red photon respectively; thus, for a more energetic photon, more photoelectrons are produced, with a reduced uncertainty of the measurement and a greater energy resolution. For the main peak in each distribution, the energy resolution is estimated to be $\sigma = 2.17$ and $\sigma = 2.88$ for the blue and red photon distribution (at 300 and 150) respectively.

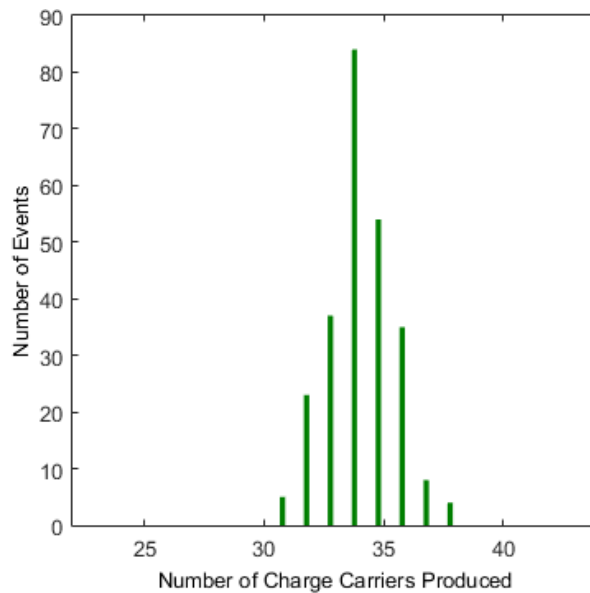


Figure 2.17 showing the distribution of events for $\lambda=3500\text{nm}$ photon. $\mu=100$. The mean number of charge carrier is ~ 33 , with $\sigma=3.05$.

For a photon energy less than $\gamma_1=0.4\text{eV}$ (i.e. in the IR spectrum), only one peak was observed because there is only enough energy for the $\pi_1 \rightarrow \pi_1^*$ transition. This is shown as a single large peak in the distribution for a photon with $\lambda=3500\text{nm}$ and $E_G=3.5\text{meV}$ in figure 2.17. This has a $W:E_G$ value in the range 3-4, as seen at visible wavelengths, and $\sigma=3.05$.

2.5.6 Number of Charge Carriers Produced as a function of Bandgap

The magnitude of the band gap affects the region where II transitions are unable to occur, as well as the energy required to excite a valence band electron. A larger band gap reduces the total number of charge carriers produced as the photoelectron relaxes more quickly into the region between $0.5E_g$ and $1.5E_g$, where no further II transitions and excitations can occur, figure 2.18. This means fewer electrons are excited and hence the distribution is less broad. An increasing band gap also means an increasing dominance of the $\pi_1-\pi_1^*$ transition because, as the band gap size increases, it becomes increasingly likely that a photon will not have enough energy to cause the other photoexcitation. Simulations for $E_g=3.5\text{meV}$ and 10meV give a distribution range of 120 and 70 respectively for blue photons, figure 2.19. The results also show agreement with $W/E_g \sim 3 - 4$.

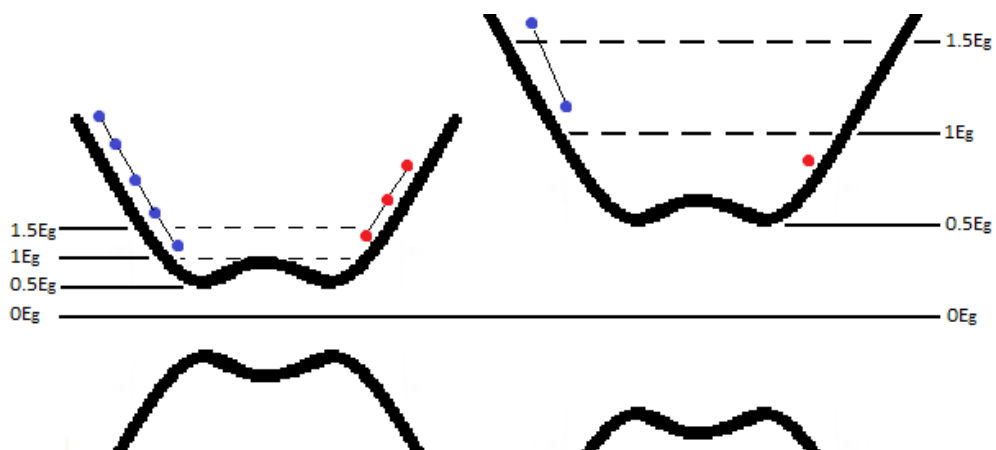


Figure 2.18, showing that with a larger band gap, fewer electrons are produced, so the electron distribution will be less broad.

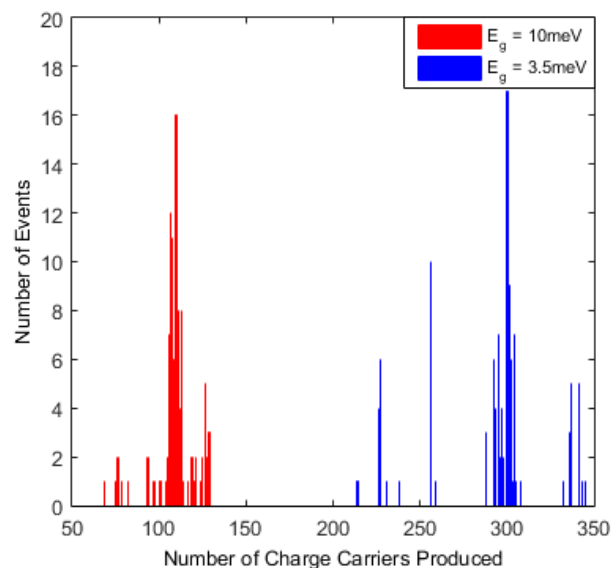


Figure 2.19, showing the number distribution as a function of the band gap magnitude.

The energy resolution varies as a function of the band gap; with a larger band gap, fewer electrons are produced, but σ is smaller. For a 10meV band gap, $\sigma \sim 12$, whereas for a 3.5meV band gap $\sigma \sim 32$. With a smaller band gap, the potential energy resolution would improve due to the increased number of charge carriers that are produced, equation 2.15. However, the potential energy resolution would be diminished also affected by the increased standard deviation, σ , in the number of charge carriers that are produced, and the distinct fringes that are again seen.

2.5.7 Number of Charge Carriers Produced as a function of the II/Phonon Ratio

Initially, an arbitrarily defined II rate was selected by using a ratio to the photon rate, μ . While the II rate is dominating over other charge carrier thermalizing channels, the II rate only affects the rate of further charge carrier generation and not the final number of charge carriers, which is reached at an increasing time inversely proportional to μ . This is shown in figure 2.20a for a photon of $\lambda=400\text{nm}$, and $E_G = 3.5\text{meV}$.

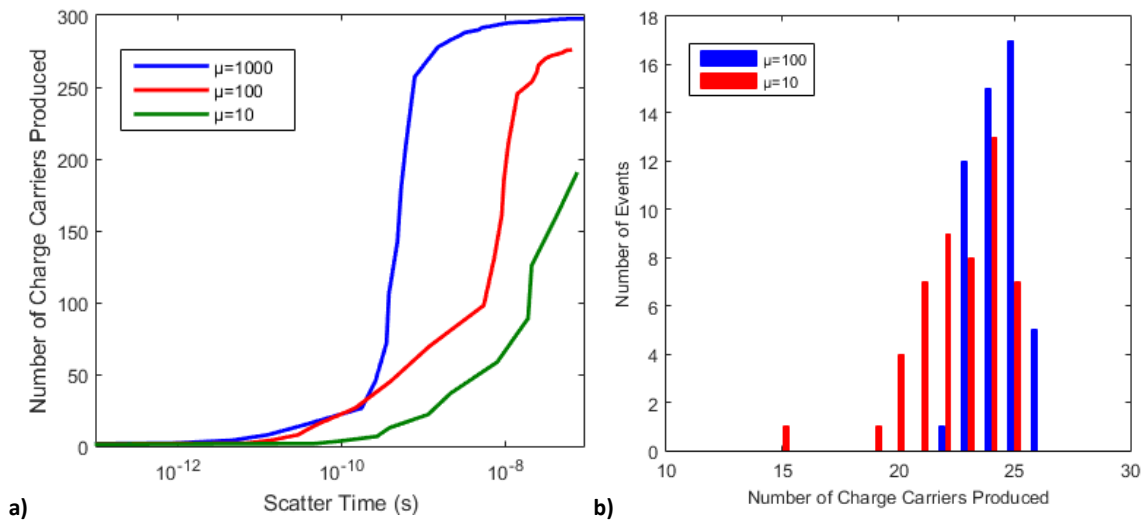


Figure 2.20, showing a) a plot indicating the number of charge carriers versus time showing the effect of changing the II rate and b) The effect of changing the II rate for $\lambda=3500\text{nm}$

Integrating over the entire active scattering time (i.e. the time during which electrons continue to relax and collect at the bottom of the conduction band) gives an estimate of the total number of charge carriers produced. The II rate is then indicative of the active scattering time, with an active scattering time of order 10^{-8}s illustrated in figure

2.20a. Furthermore, when varying the ratio, there is no change in the number distribution, as shown in figure 2.20b.

2.6 Detector Design – Finite Differencing Method

The design for this work was based on the device structure in ref. [65], figure 2.21, that was used to show opening of a tuneable band gap in dual gated bilayer graphene. It is critical to optimise the dimensions of the materials and geometries to allow for small band gaps and zero doping.

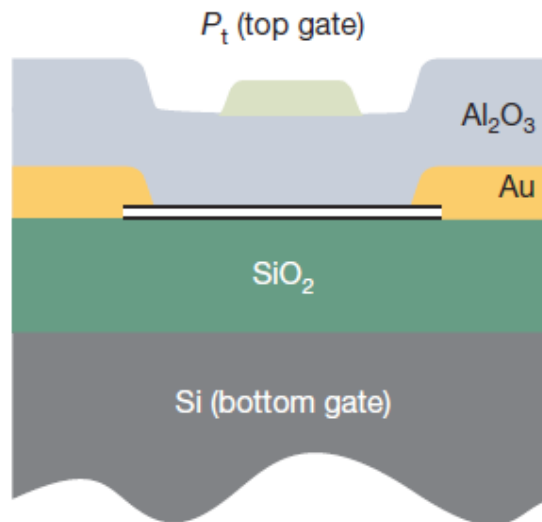


Figure 2.21. The detector structure used in ref. [65]. Reproduced under copyright licence from Nature Publishing Group.

In figure 2.21, Si is the bottom gate, with a thin SiO₂ insulating layer between the Si and the bilayer graphene. Electrodes (in figure 2.21 these are Au) are attached the graphene allowing for transport measurements and could be used for counting charge carriers in the conduction band. The graphene is entirely coated in a thin insulating layer, typically Al₂O₃, before a top gate (in this case Pt) is deposited.

By applying a voltage to the top gate (Pt) and bottom gate (Si), the band gap is opened by a displacement field breaking the interlayer symmetry of magnitude

$$\bar{D} = \frac{1}{2}(D_b + D_t). \quad \text{Equation 2.16}$$

In this case,

$$D_b = \varepsilon_b(V_b - V_b^0)/d_b, \quad \text{Equation 2.17}$$

$$D_t = -\varepsilon_t(V_t - V_t^0)/d_t, \quad \text{Equation 2.18}$$

ϵ and d are the dielectric constant and the thickness of the dielectric respectively, and V_b^0 and V_t^0 are the voltage-equivalent offset due to environmental doping from the bottom and top gate respectively, as discussed in ref. [65]. The difference,

$$\delta D = D_b - D_t, \quad \text{Equation 2.19}$$

is the quantity of doping. As this needs to be minimised, $D_b = D_t$.

2.6.1 Simulation Convergence: Boundary Condition and Grid Size

To optimise the design of the detector a finite differencing method is used; this code was previously used in ref. [145]. The code solves Laplace's equation discretised on a grid of variable grid size in cylindrical polar coordinates. This enables the geometries of the gates and the potential applied to them to be optimised, and for any edge effects near the gate or graphene to be investigated.

The geometry of the simulation was defined based on the number of layers, the location of the graphene in the setup, the dielectrics chosen and the potential applied at the gates. In the simulation geometry, figure 2.22, the dielectric constant and thickness for the dielectric layers were defined as $\epsilon_b=3.9$ and $d_b=285\text{nm}$ for the bottom gate SiO_2 layer, $\epsilon_t=7.5$ and $d_t=100\text{nm}$ for the top gate Al_2O_3 layer respectively, replicating those values given in ref. [65]. A top gate was located above the alumina layer, and the entire device was on a silicon wafer. Above the top gate, a vacuum layer was defined between the gate and the boundary of the simulation space. The graphene was a boundary condition between dielectrics which acts as a screening charge, where

$$\epsilon_1 E_1 - \epsilon_2 E_2 = \sigma = \alpha V(z_g), \quad \text{Equation 2.20}$$

ϵ_i is the dielectric constant, E_i is the electric field, σ is the surface density, α is a constant and $V(z_g)$ is the voltage at a given height z_g .

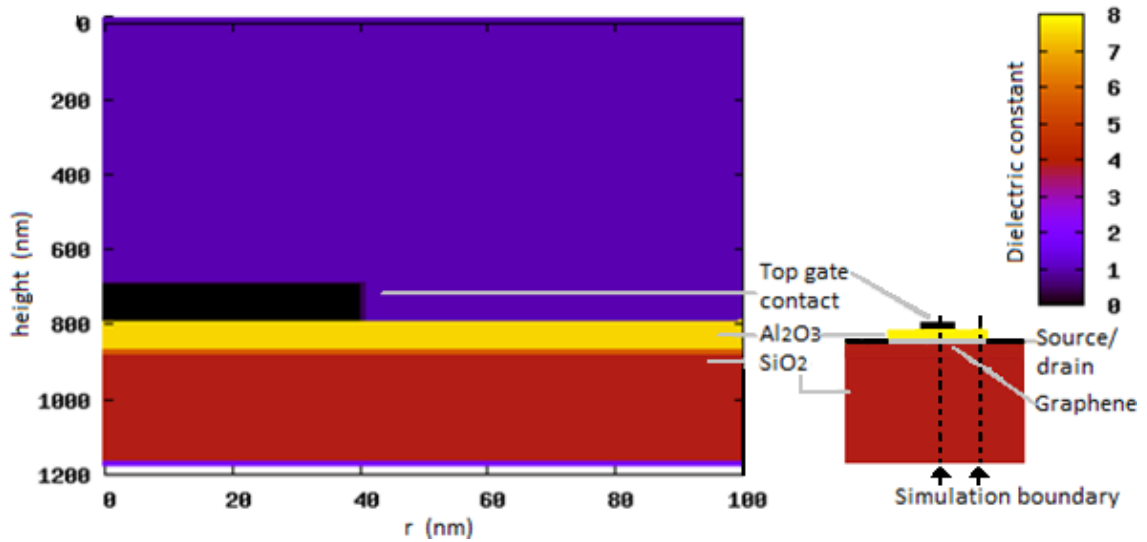


Figure 2.22, showing a) the output from the simulations showing the layout of the device, with a given height of the vacuum above the device, a given top gate, an alumina top gate dielectric and a silicon dioxide bottom gate dielectric.

The potentials simulated for the top and bottom gates are selected such that it is a charge neutrality point, and hence the Fermi level was set to the centre of the band gap. Assuming that $\tilde{V}_b = V_b - V_b^0$ and $\tilde{V}_t = V_t - V_t^0$, and then equating D_b and D_t from equations 2.17 and 2.18 respectively, the relationship between the top and bottom gate voltages required for the Fermi level to be in centre of the band gap was found to be $\tilde{V}_t = -\frac{d_t \epsilon_b}{d_b \epsilon_t} \tilde{V}_b$. For a bottom gate voltage $\tilde{V}_b=10V$, and the previously stated figures for the dielectric constants and dielectric thicknesses, this leads to $\tilde{V}_t=-1.82V$.

The boundary conditions of the simulation can be defined as $dv/dr = 0$ or $V(r) = 0$, where r is the radius of the simulation, and $dv/dz = 0$ or $V(z) = 0$, where z is the height of the simulation. The radius of the top gate, R , and the height of the vacuum above the simulation, z' , can also be specified.

Initially, the convergence of the potential and the calculated band gap, with respect to grid size and boundary conditions, was considered. The r boundary condition was set to $dv/dr = 0$ for a solution space $r = 1000nm$, the top gate radius was defined as $R = 1000nm$, and the height of the vacuum above the device $z = 500nm$. The

convergence was calculated using a difference of squares convergence, $\sqrt{(x_i - x_j)^2/n}$,

where X_i and X_j are elements of the data, and n is the number of data points in the

series. Figure 2.23a shows how the simulated potential across the detector varies with grid size, which varies most noticeably across the top gate dielectric, figure 2.23b. The entire simulation converges to within 0.6% with finer grid size dr , and within 5% across the alumina dielectric shown in figure 2.23b. Equally, the band gap across the radius of the detector was simulated with different grid size dr , figure 2.23c, which converge with smaller dr to within $\sim 1\%$.

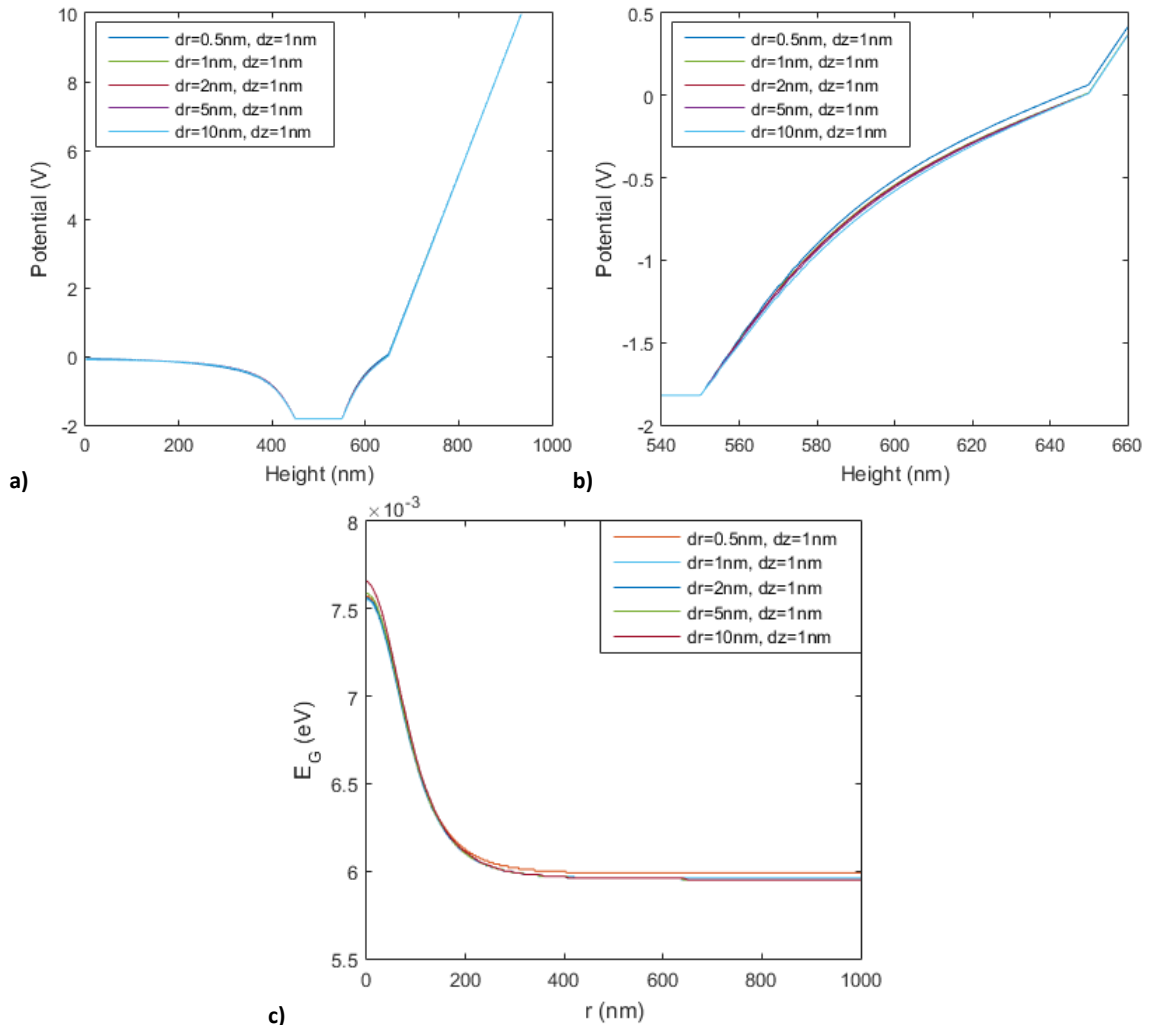
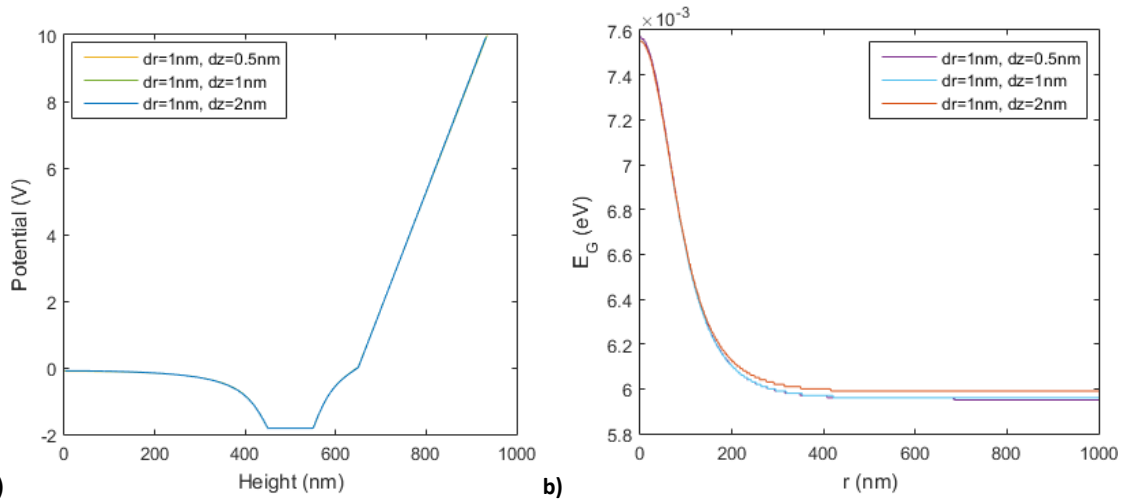


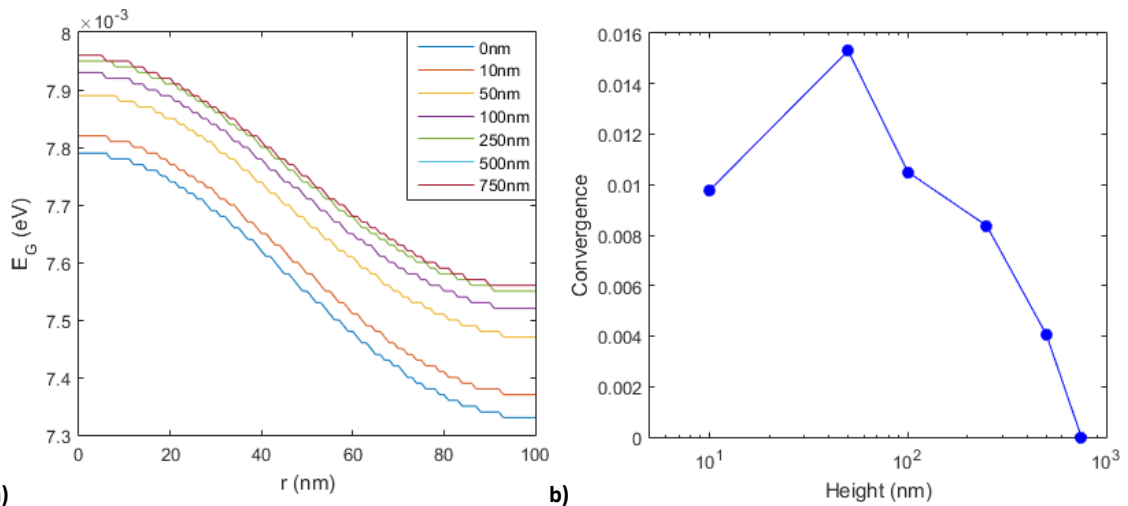
Figure 2.23 showing a) and b) the potential through the simulation for different grid sizes dr . B) shows the simulated potential across the top gate dielectric, which suggests that the simulation results converge with a finer grid size. C) shows how the band gap varies across the simulation for different grid sizes dr .

Similarly, figures 2.24a and 2.24b show the convergence with respect to dz for the voltage and the band gap. This converges to within 0.9% and 1% respectively.



a) **Figure 2.24 showing a) the potential through the simulation for different grid sizes dz , and b) the band gap across the simulation for different grid sizes dz .**

The magnitude of the band gap as a function of the vacuum thickness between the top gate and the edge of the simulation, figure 2.25a, was investigated to ensure that the simulation converges. The results suggest that the simulated values for the band gap increase with the vacuum thickness, but converge towards the same values within a tolerance of less than $3 \times 10^{-5}\text{eV}$ ($<1\%$ of the simulated band gap side of $\sim 8 \times 10^{-3}\text{eV}$) for a vacuum thickness above of 500nm , figure 2.25b.



a) **Figure 2.25 showing a) how the band gap varies with changing the vacuum distance, and b) that this converges for distances greater than 250nm.**

The potential across the simulation was then considered by changing the boundary conditions, with the ability to set the bottom gate voltage and the top edge of the simulation to a given voltage, or to set this to $dv/dz = 0$. For a combination of boundary conditions with $\tilde{V}_b = 10\text{V}$, $\tilde{V}_t = 0\text{V}$ or $dv/dz = 0$, and a solutions space $r \geq 1000\text{nm}$ and $z \geq 100\text{nm}$, the simulation converges to within 0.3% , figure 2.26a.

On the other hand, for a boundary condition on the bottom gate where $dv/dz = 0$, there is approximately a 4-fold decrease in the simulated magnitude of the band gap, figure 2.26b. This is not an arrangement that represents the bilayer graphene device, however, as there is no gate voltage applied to the bottom gate and represents a device structure that replicates about the bottom of the device structure.

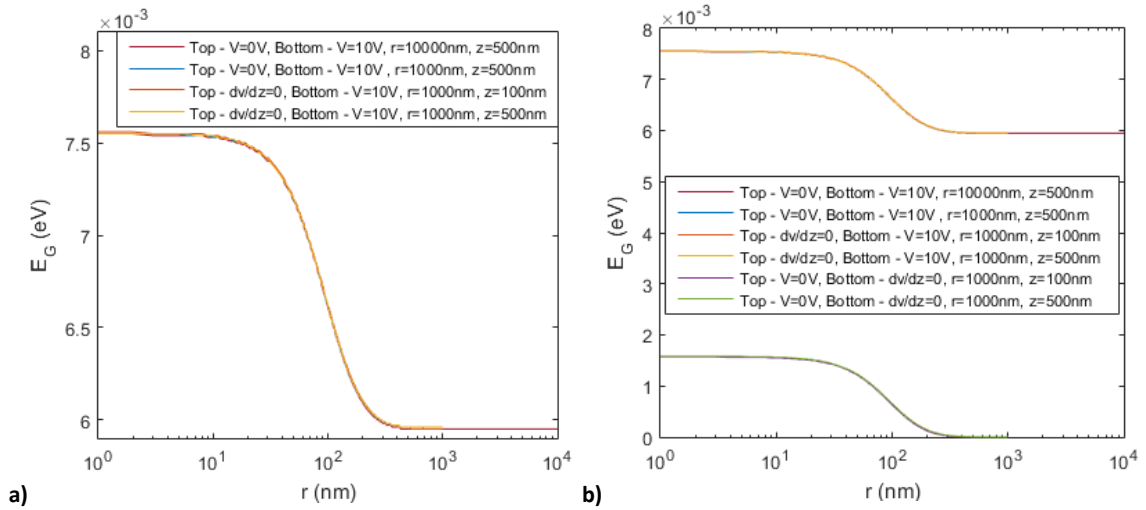


Figure 2.26 showing a) that the solution converges to within 0.0003% when varying the bottom boundary condition and vacuum height, and b) that this varies significantly when the top gate boundary is changed to $dv/dz = 0$ instead.

Figure 2.27 demonstrates that the solutions diverged for some of the boundary conditions; however, at the discontinuity between the dielectrics at approximately 600nm where the graphene is located, the results converge to within $\sim 3\%$.

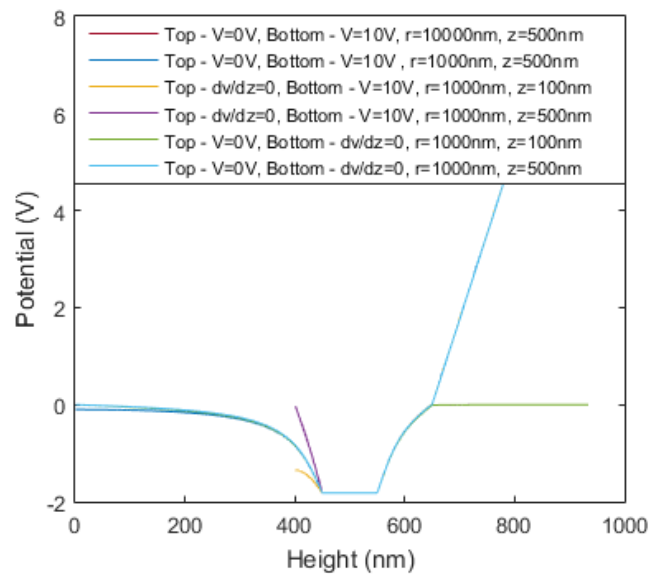


Figure 2.27 showing that the results diverge at the boundaries, but converge to within $\sim 3\%$ close to the presence of the graphene.

Therefore, for an appropriate boundary condition $dv/dr = 0$, the solutions converged for vacuum distances above 500nm, for a bottom boundary condition of $dv/dz = 0$, and for solution spaces above 1000nm. For the following simulations, $dr = dz = 1\text{nm}$, and the distance between the gate and the boundary filled with vacuum was 500nm.

2.6.2 Band Gap as a Function of Top Gate and Displacement Field

For the single photon counting photodetector, a uniform band gap is required across the graphene channel, and not one that varies slowly between the gated region and the remaining graphene. A constant band gap magnitude is necessary for improved operation of the proposed detector, as the energy required to generate photoelectrons will be easily controllable. In this section, the band gap and screening charge is investigated as a function of the size of the gate.

The band gap was investigated to demonstrate how it varied as a function of simulation radius r for different gate radius R , figure 2.28a. For larger gate radii, the discontinuity in the transition region between the area covered by the gate to that not covered by the gate became increasingly steep.

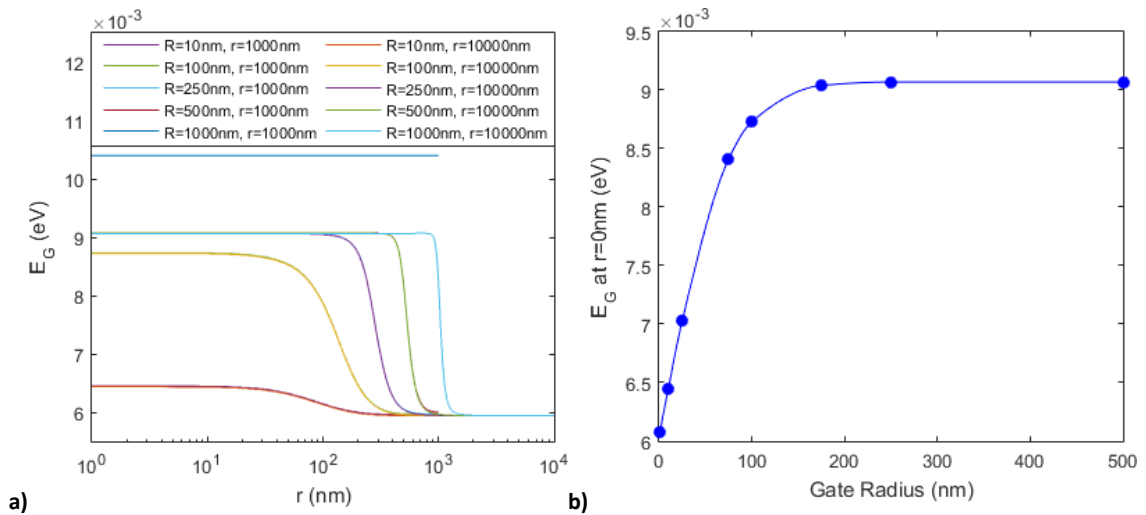


Figure 2.28, showing a) the change in the band gap with increasing gate radius, showing an increasingly steep transition between the area covered by the top gate and the rest of the detector. B) shows that the simulated screening charge, when measured at $r = 0\text{nm}$, saturates with an increasing gate radius.

Simulations of the scenario where $R = r = 1000\text{nm}$ did not agree with the result for $R = 1000\text{nm}$ and $r = 10000\text{nm}$, with the former resulting in a band gap approximately 1.5meV greater than the latter. This was attributed to the boundary conditions chosen

for this simulation $dv/dr = 0$, equivalent to an infinitely repeating simulation that would affect the total displacement field that opens the band gap. When measured at the centre of the device, i.e. for $r = 0\text{nm}$, the measured band gap saturates for an increasingly large top gate radius, figure 2.28b.

The simulated screening charge shows similar behaviour regarding the transition region at the edge of the top gate, figure 2.29a. When measured at $r = 0\text{nm}$, this screening charge also saturates with increasing gate radius, figure 2.29b.

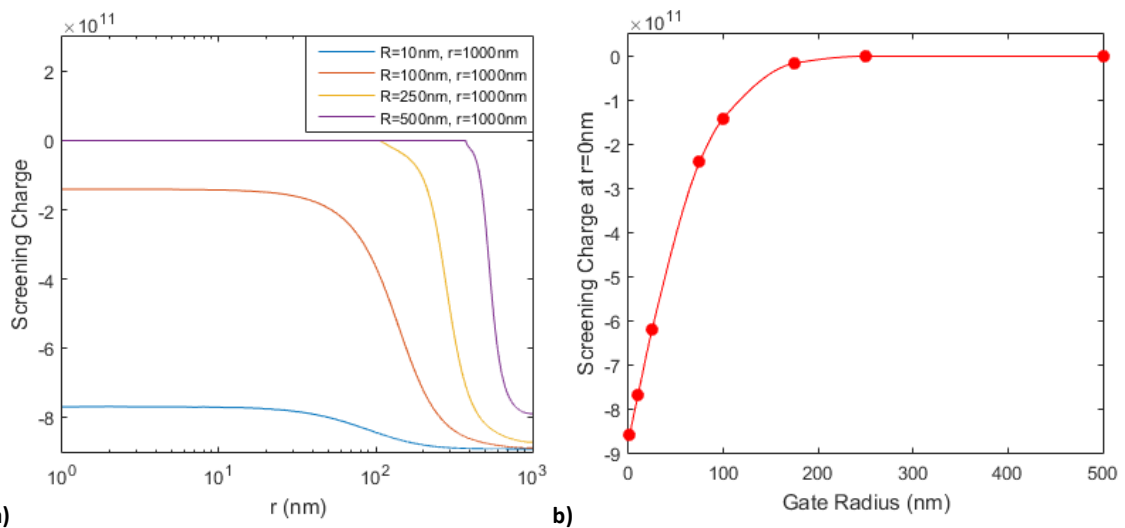


Figure 2.29, showing a) the change in screening charge of the graphene with increasing gate radius, with an increasingly steep transition between the area covered by the top gate and the rest of the detector. B) shows that the simulated screening charge, when measured at $r = 0\text{nm}$, saturates with an increasing gate radius.

Further simulations were undertaken to compare these results to those presented in ref. [65], reproduced in figure 2.30. Figure 2.30 shows how the magnitude of the band gap at a given displacement field varies depending on how it is simulated – using either a self-consistent tight-binding model, DFT, or an unscreened tight-binding model. A self-consistent tight-binding model was found to give the best agreement with the experimental results, as discussed further in ref. [65].

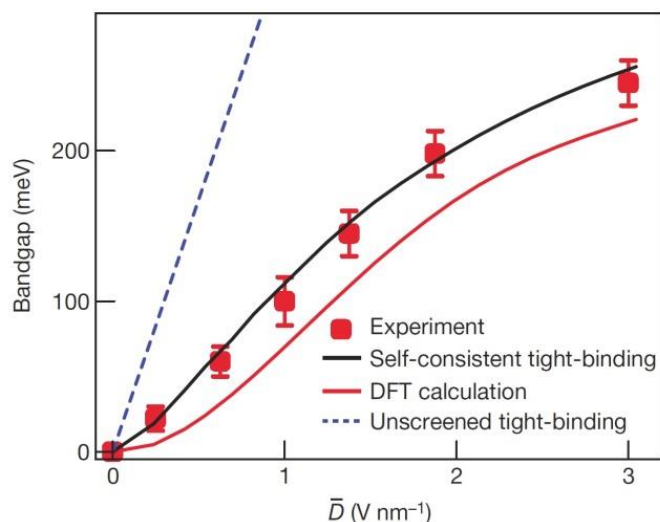


Figure 2.30, showing figure 4 in ref. [65], with the experimentally measured band gap, self-consistent tight-binding calculated band gap, DFT calculated band gap and unscreened tight-binding model band gap plotted against the applied displacement field. Reproduced under copyright licence from Nature Publishing Group.

Using the values of \tilde{V}_b and \tilde{V}_t applied to the top and bottom gates, the displacement field was calculated by using equation 2.16 and plotted against the band gap measured at the centre of the simulation, $r = 0\text{nm}$. For small displacement fields, and therefore small band gaps, the simulated band gap increases linearly with displacement field, figure 2.31. It is also the same order of magnitude as the experimental results (and therefore the self-consistent tight-binding model) discussed in ref. [65], but diverges with increasing displacement field. This could arise because the simulation software, originally used in ref. [145], might not simulate accurately enough the non-linearity between the band gap and displacement field for the greater displacement fields shown in figure 2.30. Also, in agreement with the results from ref. [65], DFT shows poor agreement with these simulated results, as it is a factor of 3 less than the simulated results shown in figure 2.31.

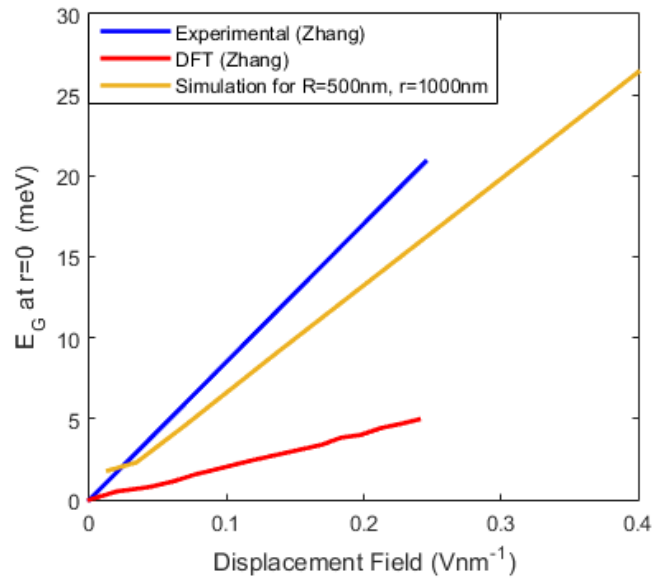


Figure 2.31 showing the attempted fitting to DFT and Experimental lines for the measured band gap at $r=0$. The experimental results from ref. [65] are in some agreement with the results simulated in this work, as it is of the same order of magnitude. DFT is shown to be in poor agreement as it is approximately a factor 3 smaller.

Furthermore, changing the displacement field only affected the magnitude of the band gap, and does not indicate any change in the functionality of the transition region between the area covered by a 500nm radius top gate and the rest of the simulation space, as shown in figure 2.32.

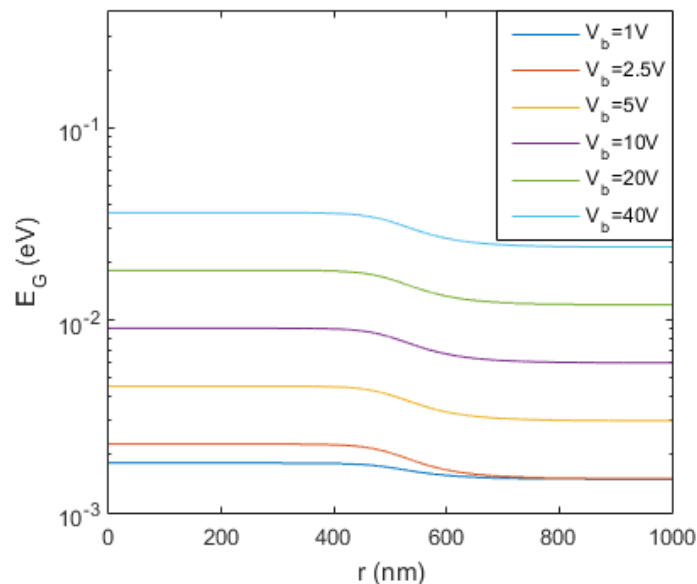


Figure 2.32, showing the band gap at a given radius for different top and bottom gate voltages, with doping remaining zero. The top gate radius is 500nm. It indicates that the functionality of the band gap as a function of radius remains constant, but the magnitude of the band gap scales with the applied gate voltages.

In conclusion, these simulations suggested that, for maximum uniformity of the band gap opening, the top gate needed to cover the entire graphene layer, or to have a very

small contact point with the rest of the device. The options to realising these possibilities are discussed in the next section.

2.7 Detector Design - Proposed Manufacturing Plan

Using the results from the previous section, a route to manufacturing a prototype detector based on the structure shown in figure 2.21 [65] was proposed. In this section, several different options are considered and the advantages and disadvantages of each are stated.

2.7.1 Substrate and Dielectric

Two options were available to manufacture as the substrate. The first, more “conventional”, option was a silicon wafer acting as the bottom gate, of order 10mm width, 10mm length and ~ 0.5 mm thickness, with a 285nm thick layer of SiO_2 sputtered onto the surface of the silicon wafer.

An alternative that was considered was to build the device on a sapphire wafer, which would electrically isolate the device but maintain good thermal conductivity with the cryogenic fridge where it would be tested. This design would reduce capacitive coupling, to reduce the risk of AC coupled regions transmitting a signal when the route via the insulating substrate transmitting the DC signal is blocked. On top of this, a gold deposit would be made to act as the bottom gate, and then a 285nm thick SiO_2 dielectric would be sputtered onto it.

2.7.2 Bilayer graphene

AB (Bernal) stacked bilayer graphene was required to allow for band gap opening; many different techniques are available to manufacture the graphene, with chemical vapour deposition (CVD) arguably proving one of the most realistic routes for future homogeneous, scalable graphene growth. The bilayer graphene would be transferred onto the substrate and etched to a channel size of ~ 10 - $100\mu\text{m}$.

2.7.3 Contacts

A standard material used for contacts is Cr-Au, although others are available. They are fabricated by masking the surface, for instance through electron-beam lithography,

photolithography or shadow masking, and then evaporating or sputtering a material onto the sample.

Several potential designs for the contacts were possible, including a van der Pauw configuration [146] and a simple two-point measurement, figures 2.33a and 2.33b respectively. A simple two-point arrangement is sufficient to enable measurements of the conductivity of the graphene channel, although a van der Pauw configuration is also capable of measuring sheet resistance. The contacts were designed to extend out to pads approximately $250\mu\text{m} \times 250\mu\text{m}$ to allow for easier wire bonding.

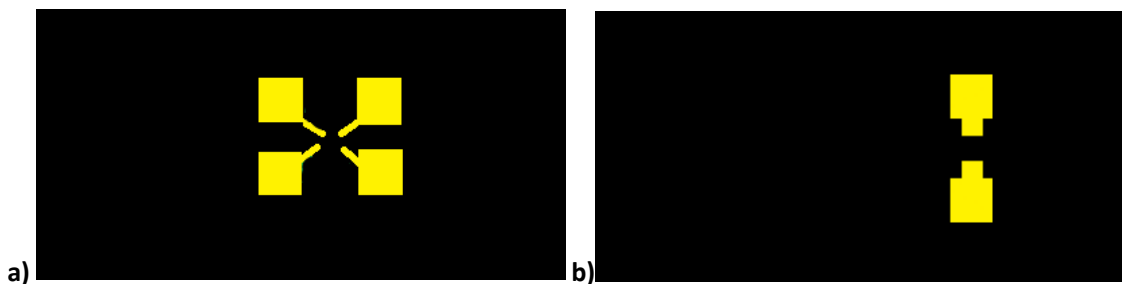


Figure 2.33, showing potential shadow masks for a) the van der Pauw configuration, and b) for a simpler two-point measurement.

2.7.4 Top Gate Dielectric

An insulating alumina coating was designed to be deposited via atomic layer deposition (ALD) onto the sample. This coating is electrically insulating, thermally conductive and optically transparent, and enabled later testing with an optical fibre.

2.7.5 Top Gate

In the previous section, simulations suggested either a top gate with a small footprint, or covering the entire channel, would ensure a uniform band gap across the sample. For the former option, a spring-loaded probe would be brought in contact with the graphene – however this was felt to be very tricky to manufacture.

The second option required an electrically conductive, transparent material to be identified that could be deposited to act as the gate; in previous work this has been platinum [65]. Indium tin oxide (ITO) was proposed as it is easy to sputter, and is transparent to visible light and opaque to UV, figure 2.34 [147]. Alternatively, aluminium zinc oxide (AZO) has similar properties to ITO, but AZO is cheaper and can

easily be etched [148] – when combined with ITO this could be a viable and cheaper top gate material for industrial fabrication.

Both options, based on both the silicon and sapphire bases, are presented in figures 2.34 and 2.35 respectively.

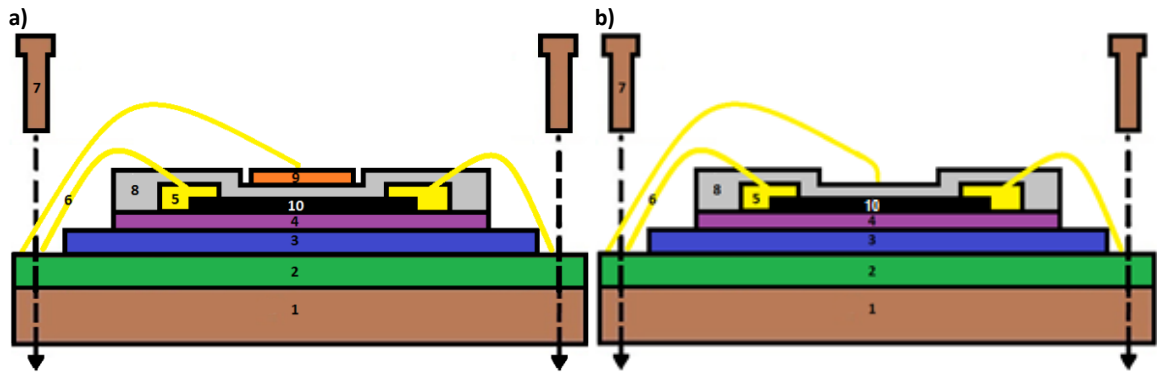


Figure 2.34 showing the proposed device layout on a silicon substrate with a) the ITO top gate and b) the spring-loaded probe. The key is 1) oxygen free copper block, 2) PCB, 3) silicon wafer (1cm x 1cm), 4) silicon dioxide substrate, 5) two contact pads (~200µm x 200µm), 6) gold or aluminium wire bonds, 7) mounting bolts, 8) alumina, 9) ITO and 10) bilayer graphene (~20µm x 20µm).

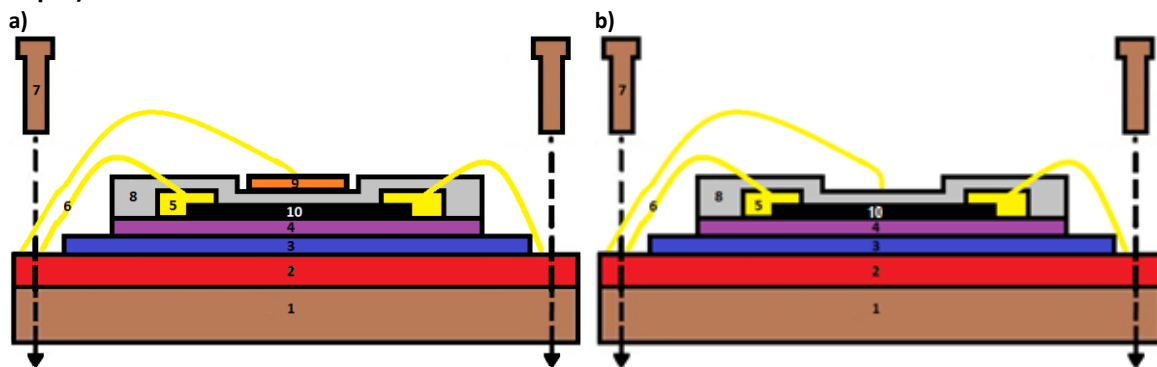


Figure 2.35 showing the proposed device layout on a sapphire substrate with a) the ITO top gate and b) the spring-loaded probe. The key is 1) oxygen free copper block, 2) sapphire wafer, 3) sputtered silicon, 4) silicon dioxide substrate, 5) two contact pads (~200µm x 200µm), 6) gold or aluminium wire bonds, 7) mounting bolts, 8) alumina, 9) ITO and 10) bilayer graphene (~20µm x 20µm)

2.7.6 Wire Bonding and Mounting

The device was designed to be tested in the cryogenic fridge, so it was designed to be in thermal contact with, but electrically isolated from, the fridge. The design for the device showed it mounted on a PCB, with gold or aluminium wire bonds running from the PCB contacts to those on the chip to allow for transport measurements and to gate the graphene. The PCB could then be directly bolted to an oxygen free copper block that acts as an adapter to allow it to be bolted directly onto the cryogenic fridge.

2.8 Summary

In summary, a theoretical model to investigate the likely behaviour of the proposed bilayer graphene-based single photon counting photodetector has been developed. The detector was then developed through finite element analysis of the gates.

The simulation results demonstrate the feasibility of a new type of ultrafast photon counter operating at optical and IR wavelengths. Such a device could be operated at approximately 100MHz, although higher frequencies may be possible with improved calculations of the impact ionisation rate to give the detector comparable or superior results to other detectors. A value for the electron-hole pair creation energy, W , was obtained as a function of the band gap. The ratio between W and the band gap is found to be comparable to that of other detectors such as Si and Ge [143]. Colour sensitivity was observed due to the differentiable peaks for 400nm and 800nm photons, although energy resolution is degraded by the multiple observed peaks. Additionally, positive results were shown in the mid-infrared due to the lack of peaks in the number distribution for photon energies less than $\gamma_1=0.4\text{eV}$, suggesting the ability to detect near infrared photons too. The detector has scope to enable a trade-off between operating temperature and energy resolution, allowing for a cryogenic single photon counting photodetector to operate at temperatures that do not require helium-3 cooling albeit with reduced energy resolution. This approach could enable a lower cost detector to be developed for space science where extreme levels of cooling are complex and expensive.

The simulated results enabled the prototype detector to be designed, based on the schematic from ref. [65]. The prototype single pixel detector design has a silicon substrate with a 300nm thick silicon dioxide insulating layer; this option was selected as the materials are more readily available, and the techniques required to process these materials are much more refined. Two contacts are deposited on top of the graphene to provide electrical connections to the graphene. A top gate dielectric of alumina is then deposited through atomic layer deposition (ALD), approximately 50nm thick so that a smaller top gate voltage is required to produce the same displacement field, as defined by equations 2.17 and 2.18, while ensuring the alumina layer is of a

uniform thickness and that it reliably acts as a dielectric. For the top gate, ITO contacts are deposited; ITO is typically used in transparent electronics and is opaque at UV photon energies but is transparent at visible photon energies. The proposed design is shown in figure 2.36.

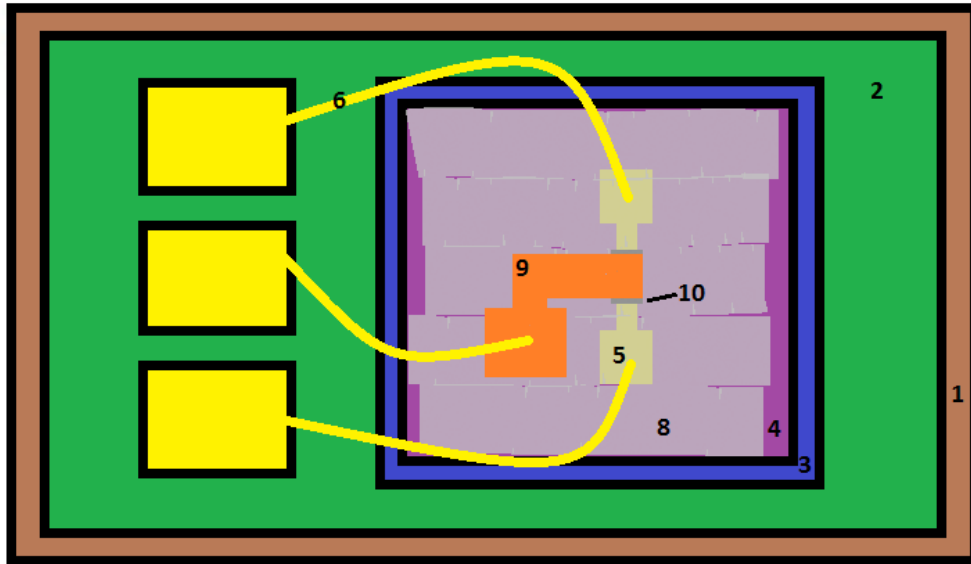


Figure 2.36 showing a top view of the bilayer graphene single photon counting photodetector. The key is 1) oxygen free copper block, 2) PCB, 3) silicon wafer (1cm x 1cm), 4) silicon dioxide substrate, 5) two contact pads (~200 μ m x 200 μ m) based on the design shown in figure 2.33b, 6) gold or aluminium wire bonds, 8) alumina, 9) ITO and 10) bilayer graphene (~20 μ m x 20 μ m).

In conclusion, the theoretical results given in this chapter suggest that bilayer graphene could be feasible as a single photon counting, colour sensitive photodetector. The results presented earlier in this chapter indicated behaviour of the detector that could be verified in the experimental phase. Finite element analysis of the detector structure led to the design of the detector, and the manufacture of this device is discussed in chapter 5.

3

Theoretical Study and Design of a Passive Terahertz Photon Detector Sensitive to 1.2THz

3.1 Introduction

As part of this project, a successful bid for an EXPRO+ contract from the European Space Agency was made to undertake two projects, one looking at terahertz photodetection, discussed in this chapter, and the other looking at X-ray photodetection, covered in chapter 4. The European Space Agency provided a specification for the THz detector to be sensitive to photon frequencies at 1.2THz and for it to operate at room temperature.

Several different techniques can be used for photodetection at terahertz frequencies, such as the photothermoelectric effect and bolometry [116]. This chapter considers the use of the Dyakonov-Shur effect to develop a passive THz photodetector, and consider the relevant physics to develop potential designs to be manufactured and tested in later chapters.

3.2 Exploiting the Dyakonov-Shur Effect

Introduced in section 1.4, the Dyakonov-Shur effect is an effect that has been widely used for terahertz photodetection [116] where a terahertz photon impinges on an antenna, and generates a plasma wave in the channel that leads to the generation of a DC voltage [55].

A terahertz photon incident on the detector couples to the antenna, and generates a plasma wave between the source and drain in a channel of size L [149]. Eigenfrequencies of the plasma wave are given by $\omega_N = \omega_0(1 + 2N)$, where N is a positive integer, and the fundamental frequency $\omega_0 = \frac{\pi s}{2L}$, where s is the wave velocity. The AC voltage generated between the source and drain leads to a DC photovoltage

from a rectification process, typically a local change in the Fermi level, that can be read out by a lock-in amplifier. A device used to show the Dyakonov-Shur effect is shown in figure 3.1.

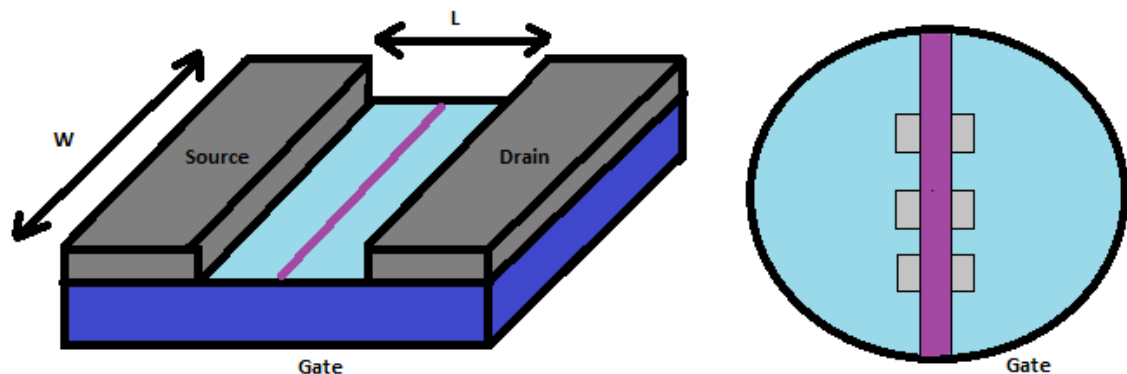


Figure 3.1 showing a schematic of the device used to show the Dyakonov-Shur in ref. [149], with a channel with of $L=11\mu\text{m}$, $W=28\mu\text{m}$. In ref [149], the device demonstrated that drain current and gate voltage are inversely proportional, with a non-linear drain voltage-current relationship.

As the charge carriers in the channel act as a 2D electron gas, the behaviour of the plasma can be described by the hydrodynamic theory, where charge carriers are described by the inherently non-linear continuity equation and the Euler equation [150]. Depending on the dimensions of the channel, the plasma wave can lead to different behaviours of the detector. Broadband detection occurs when the generated plasma waves are said to be overdamped, and the plasma wave travels between the source and the drain in a time greater than the momentum relaxation time, τ . On the other hand, when the plasma wave reaches the drain in a time less than τ , the plasma wave is said to be weakly damped and in a so-called resonant regime. Utilising the resonant regime for terahertz photodetection can lead to a signal response that is 5-20 times stronger than the broadband non-resonant signal, and is characterized by peaks at odd multiples of the lowest plasma-wave frequency [151]. Being able to achieve this requires the correct dimensions for the channel, and a channel mobility that can sustain the plasma wave speed.

Exploiting the Dyakonov-Shur effect for room temperature terahertz detection requires a rectification of the signal. One way of doing this is to exploit a rectification in the carrier density via oscillations of the gate potential that then modulate the channel current. This was demonstrated in ref. [124], for instance, where the terahertz photons impinge on antennae that are connected to the source and the gate, and lead to modulation of the carrier density that results in a change in the channel conductivity.

On the other hand, in ref. [123], a FET structure is proposed as a means of exciting plasmons across the channel, figure 3.2, that arise from terahertz radiation impinging on GFET contacts designed as antennae. The gate is kept at a voltage U_0 relative to the source to fix the average carrier density, across a substrate of thickness d . An AC potential U_a is generated between the source and drain along the graphene channel of length L between the gates and width W . A DC voltage is then measured at the drain, due to a non-linear photoresponse occurring due to a local change in the carrier density and the non-linearity of the continuity equation, and provides a rectification of the signal [123] [150] [152].

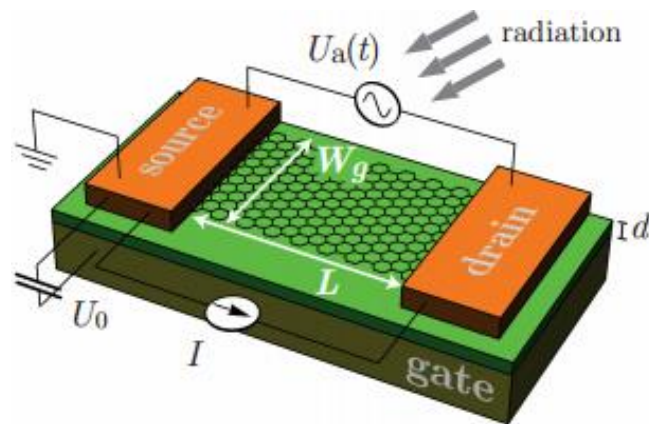


Figure 3.2, showing the layout of a GFET utilising the Dyakonov-Shur Instability [123]. Reproduced with permission from AIP Publishing.

While the Dyakonov-Shur effect has been successfully exploited for THz detection at room temperature using the structure discussed in ref. [124], the detector structure chosen for ongoing research was based on that shown in figure 3.2 [123] due to the ease of fabrication and the ability to operate passively if desired. Ref. [123] makes no recommendation of gate or antennae structure, and nor does it propose any future route to manufacture. Therefore, to operate with sensitivity to photon frequencies around 1.2THz, the detector parameters had to be optimised and new antennae structures had to be designed.

3.3 Device Optimisation

To develop the detector for sensitivity to photons of a frequency of 1.2THz, the detector performance needed to be understood with regards to parameters such as channel size and channel resistivity, and optimised. This theoretical study was undertaken by extending the numerical simulations completed in ref. [123].

3.3.1 Theoretical Study of Detector Performance

The potential performance of the detector was investigated by calculating the photocurrent, I , resulting from an incident terahertz photon of frequency ω impinging on the antennae of a detector that are connected to the source and drain. As discussed in ref. [123], the photocurrent is given by

$$\frac{I}{I_d} = 1 + 2\beta(\omega\tau)F(\omega, \tau), \quad \text{Equation 3.1}$$

where I_d is the diffusive current given by

$$I_d = \sigma_0 \frac{U_0 W_G}{2L} \left(\frac{U_a}{2U_0} \right)^2 = \frac{U_a^2}{8RU_0}, \quad \text{Equation 3.2}$$

$$F(\omega, \tau) = \frac{\cosh((2K_2L)) + \cos(2K_1L) - 2}{\cosh(2K_2L) - \cos(2K_1L)}, \quad \text{Equation 3.3}$$

U_0 is the gate voltage relative to V_{Dirac} , U_a is the AC photovoltage generated between the contacts, $\beta(x) = \frac{2x}{\sqrt{1+x^2}}$, ω is the frequency of the incident photon, L is the channel length, R is the channel resistance, and K_1 and K_2 are the real and imaginary parts of the wave number K respectively. The channel conductivity, $\sigma_0 \propto \frac{E_F\tau}{h}$, arises from the Drude model [123] [153], and can be used to obtain the momentum relaxation time, τ , which is the average time between two collisions of a particle.

In figure 3.3a and 3.3b, $\frac{I}{I_d}$ and $\log\left(\frac{NEP_I}{NEP_V}\right)$ are plotted against $\frac{\Omega}{\omega_p} = \frac{2L\Omega}{\pi s}$ respectively to replicate the figures in ref. [123]. In this case, Ω is the frequency of the incident THz radiation, $\omega_p = \frac{\pi s}{2L}$ is the resonant plasma angular frequency, s is the plasma wave velocity, L is the length of the graphene channel, NEP is the noise equivalent power and $\frac{NEP_I}{NEP_V}$ is the ratio between the current noise and voltage noise [123]. With increasing τ , and hence greater conductivity, the peaks in $\frac{I}{I_d}$ at regular values of $\frac{\Omega}{\omega_p}$ become increasing sharp as the response enters the resonant regime behaviour. For larger τ , i.e. for low resistance graphene channels, there is also a lower simulated $\log\left(\frac{NEP_I}{NEP_V}\right)$, as shown in figure 3.3b, with a larger signal leading to an improved signal to noise and hence NEP.

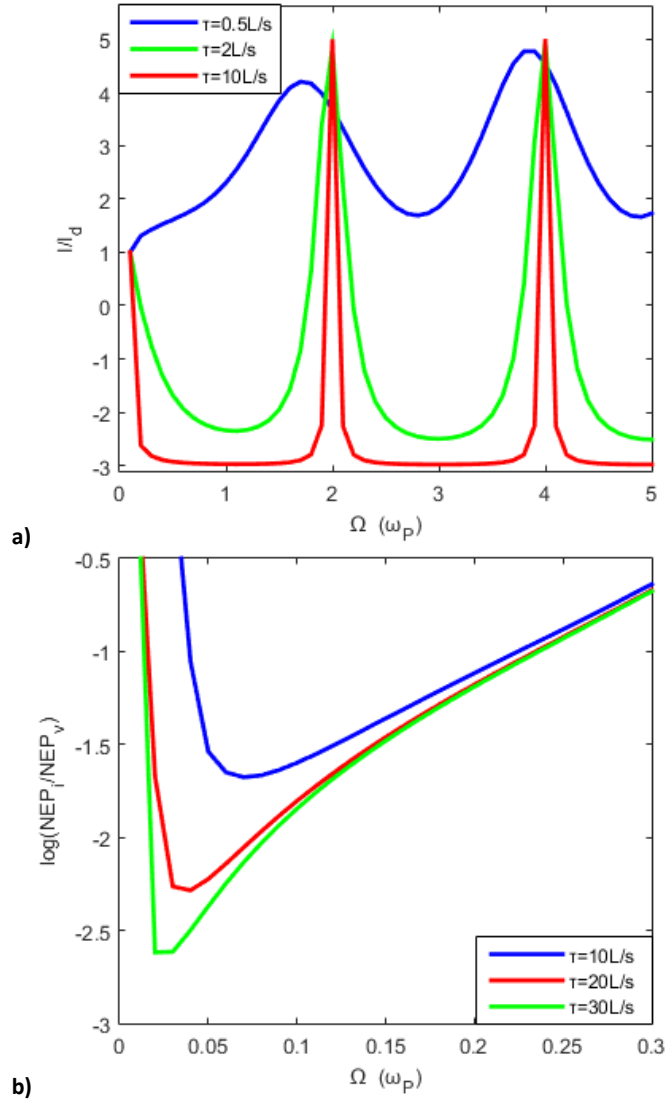


Figure 3.3 showing a) the photocurrent against the photon frequency for different momentum relaxation time, where s is the plasma wave speed; and b) $\log\left(\frac{\text{NEP}_I}{\text{NEP}_V}\right)$ against photon frequency with lower noise at higher momentum relaxation time.

3.3.1.1 Theoretical Signal Variation with Gate Voltage

As $\frac{\Omega}{\omega_p} = \frac{2L\Omega}{\pi s}$, by varying U_0 it is possible to control the Fermi level, plasma wave speed, fundamental plasma angular frequency and diffusive photocurrent. Therefore, by changing U_0 , the photocurrent can be maximised for a given photon frequency whilst trading off the noise for optimised device response. This enables a degree of tuneability in the operation of the detector to maximize the response of the detector over the wide frequency range of interest.

I/I_d was calculated for different gate voltages, figure 3.4a, by using typical GFET current-gate voltage measurements, in this case using n-type graphene with a Dirac

point at approximately -6V (with a corresponding resistance of approximately 15k Ω), to a measured resistance of approximately 5k Ω at approximately 10V.

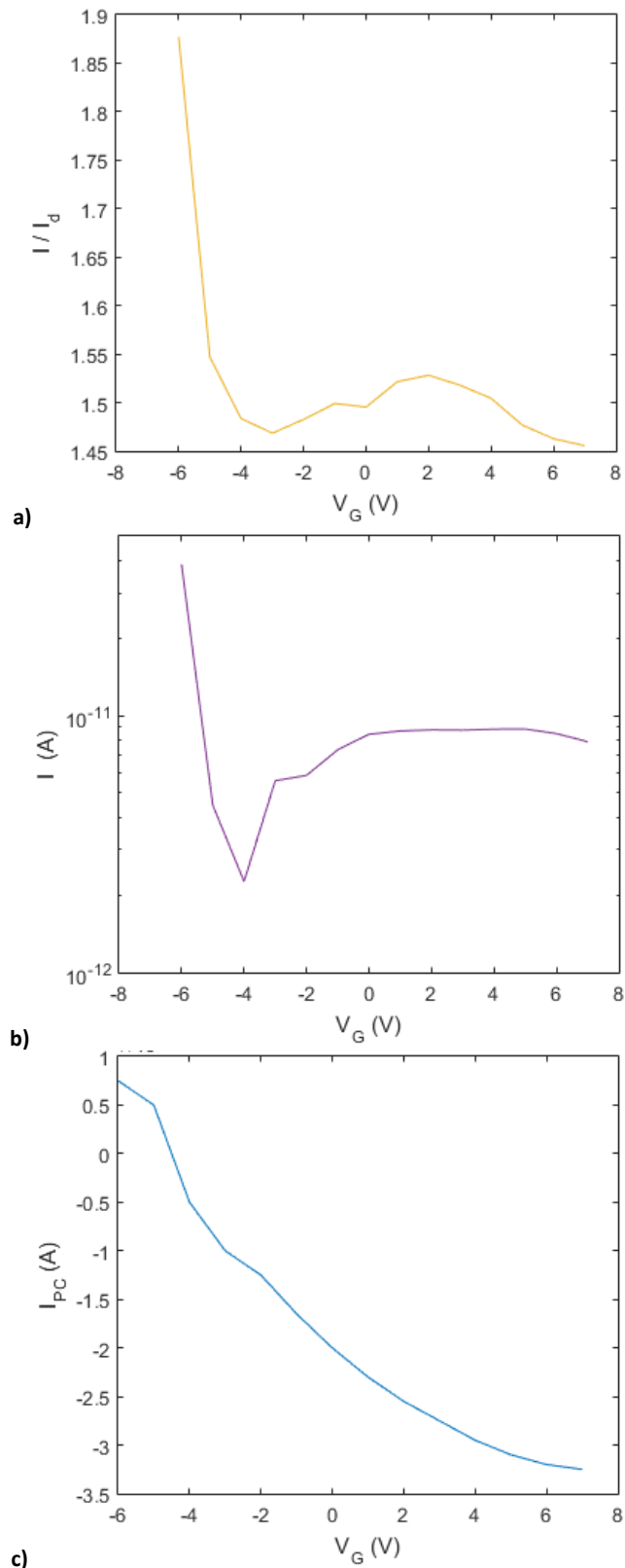


Figure 3.4, showing a) and b) the peak current is obtained close to the Dirac point, and c) the photocurrent used in the simulations, based on that in ref. [154]. The simulations were done for a channel length $L=10\mu\text{m}$ and a channel width $W=5\mu\text{m}$.

The theoretically expected current was then calculated, figure 3.4b, which shows the complementary results to figure 3.4a for I/I_d . Varying the gate voltage gives a $V_g^{0.5}$ like increase in the theoretically expected current before tending towards a maximum, figure 3.4b. The current was estimated by using a photocurrent based on the results in ref. [154], figure 3.4c, to provide an estimate for the diffusive current I_d , which was then multiplied by I/I_d to give the theoretical I value. These currents would be measurable with considered, low noise, electronics.

3.3.1.2 Theoretical Signal Variation with Detector Parameters

Besides U_0 , there is a wide parameter space that had to be considered for the device design, including the channel length, dielectric thickness and dielectric constant. This enabled a variety of solutions to be selected for the parameters of the detector that provided maximal photocurrent results at the intended frequencies around 1.2THz – the choice would then be limited by fabrication processes.

The results shown in figure 3.4 were simulated for the channel length $L=10\mu\text{m}$. As a function of channel length, the theoretical photocurrent was calculated in the same manner as in section 3.3.1.1, figure 3.5. These simulations suggest that the current due to illumination by 1.2THz photons increases for longer channel lengths until it reaches a maximum for channel length $L \geq 10\mu\text{m}$. To improve the prospect for more reliable manufacturing, a greater device yield and reduce the instances of grain boundaries in the channel, a smaller channel length was selected, and hence $L \sim 10\mu\text{m}$.

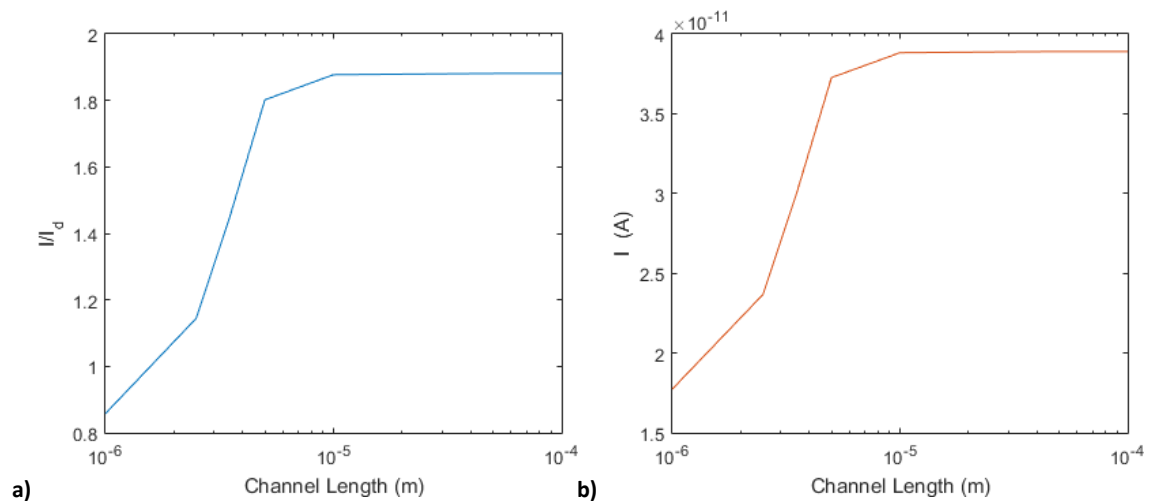


Figure 3.5, showing a) I/I_d and b) I against the channel length L . These results suggest that the optimum channel length is $\sim 10\mu\text{m}$, the value of L where the I reaches a maximum.

Other parameters of the GFET design were also iterated. All results thus far had been done assuming an SiO₂ dielectric with a thickness of ~300nm. This was chosen for ease of manufacture since it is a common process parameter. However, simulations also considered changes in the dielectric thickness and material to motivate alternatives for the future design of the detector.

As a function of the dielectric constant used, simulations suggested that the current reaches a maximum for a relative dielectric constant $\epsilon_r \sim 2$, figures 3.6a and 3.6b. The most commonly used dielectric materials are SiO₂, Al₂O₃ and HfO₂; SiO₂ has the lowest relative dielectric constant, $\epsilon_r \sim 3.8$, and therefore the greatest simulated current. However, for higher permittivity materials (e.g. for alumina, $\epsilon_r \sim 9$) in comparison to SiO₂, there is only a ~10% decrease in the simulated current, so it is possible that alumina could also play a role in the future.

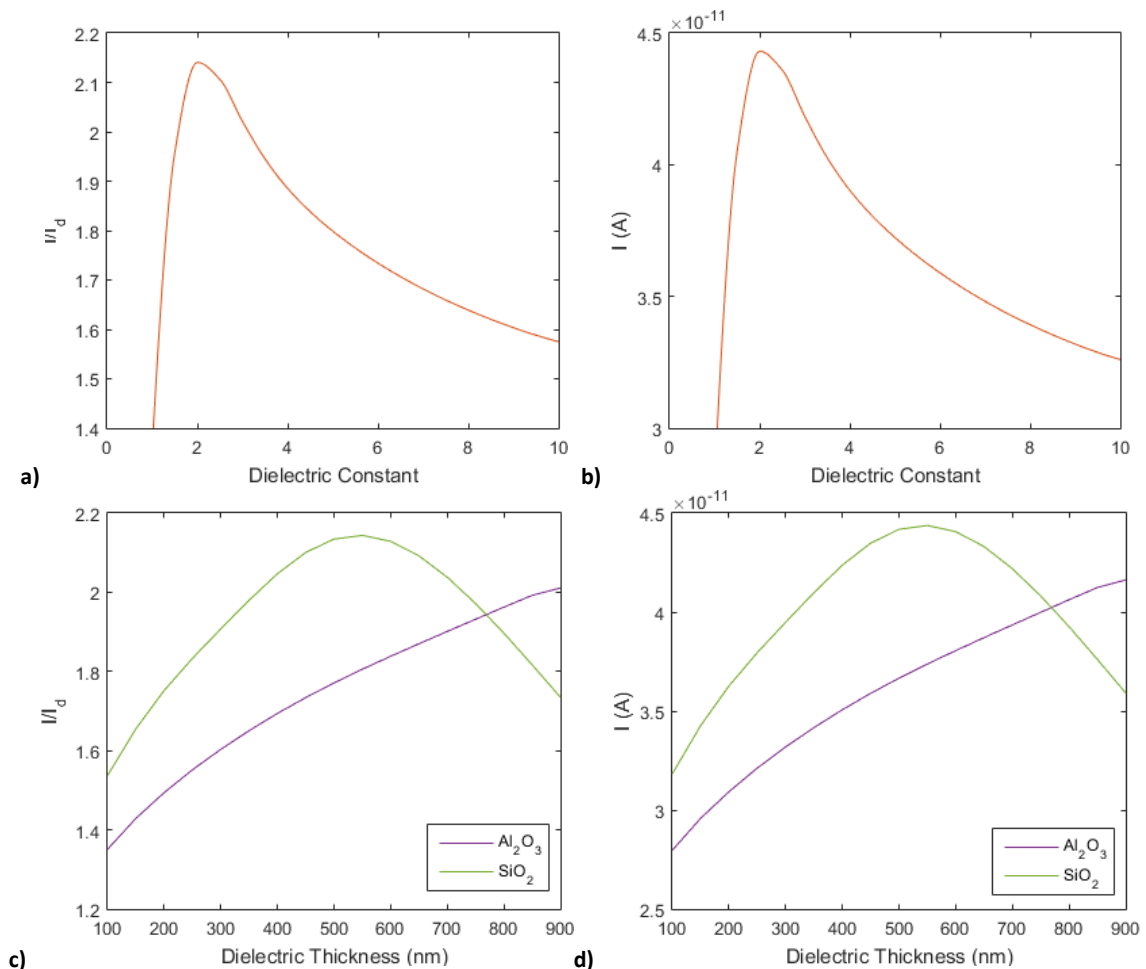
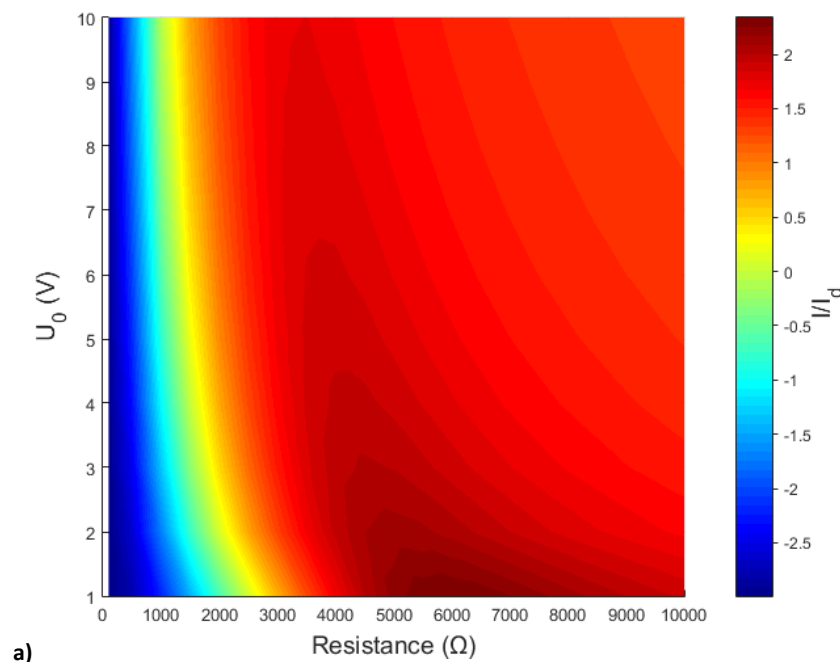


Figure 3.6, showing the change in a) I/I_d and b) I as a function of the dielectric constant, suggesting a maximum at $\epsilon_r \sim 2$, for a 10k Ω channel resistance, 300nm dielectric thickness and $U_0=1V$. C) and d) show the change in I/I_d and I , respectively, as a function of the dielectric thickness, $d_{dielectric}$, for a 10k Ω channel resistance and $U_0 = 1V$. For an SiO₂ dielectric the peak current is at $d_{dielectric} \sim 500nm$, while for Al₂O₃ the current increases like $d_{dielectric}^{0.5}$.

Equally so, the thickness of the dielectric, $d_{dielectric}$, was also iterated. The theoretical photocurrent, shown in figure 3.6d, reaches a maximum at $\sim 500\text{nm}$ for an SiO_2 dielectric. For dielectric thicknesses between 100nm and 900nm , the theoretical photocurrent with an Al_2O_3 dielectric increases like $d_{dielectric}^{0.5}$. However, as the theoretical current only varied weakly with the dielectric thickness, $d_{dielectric} \sim 300\text{nm}$ was selected as it is a common process parameter and is easy to obtain commercially.

3.3.1.3 Theoretical Signal Variation with Graphene Sheet Properties

Further simulations were undertaken to see how varying the channel resistance leads to changes in the simulated current and photovoltage after illumination by photons with a frequency of 1.2THz . Values of I/I_d were simulated as a function of both the gate voltage relative to the Dirac point and the channel resistance, figure 3.7a, and from this the current and photovoltage were deduced for a constant $I_{PC} \sim 100\text{nA}$ in the same manner as previous sections, figures 3.7b and 3.7c respectively. The greatest value for I/I_d was obtained for a value of $U_0 \sim 1\text{V}$ and with a channel resistance $\sim 6\text{k}\Omega$. The greatest current and photovoltage was obtained for $U_0 = 1\text{V}$, with a channel resistance close to $10\text{k}\Omega$ for a simulated I_{PC} for all resistances of 100nA . This suggests that the detector should produce the largest signal operating close to the Dirac point, and with a channel resistance $\sim 10\text{k}\Omega$ that is readily achievable today.



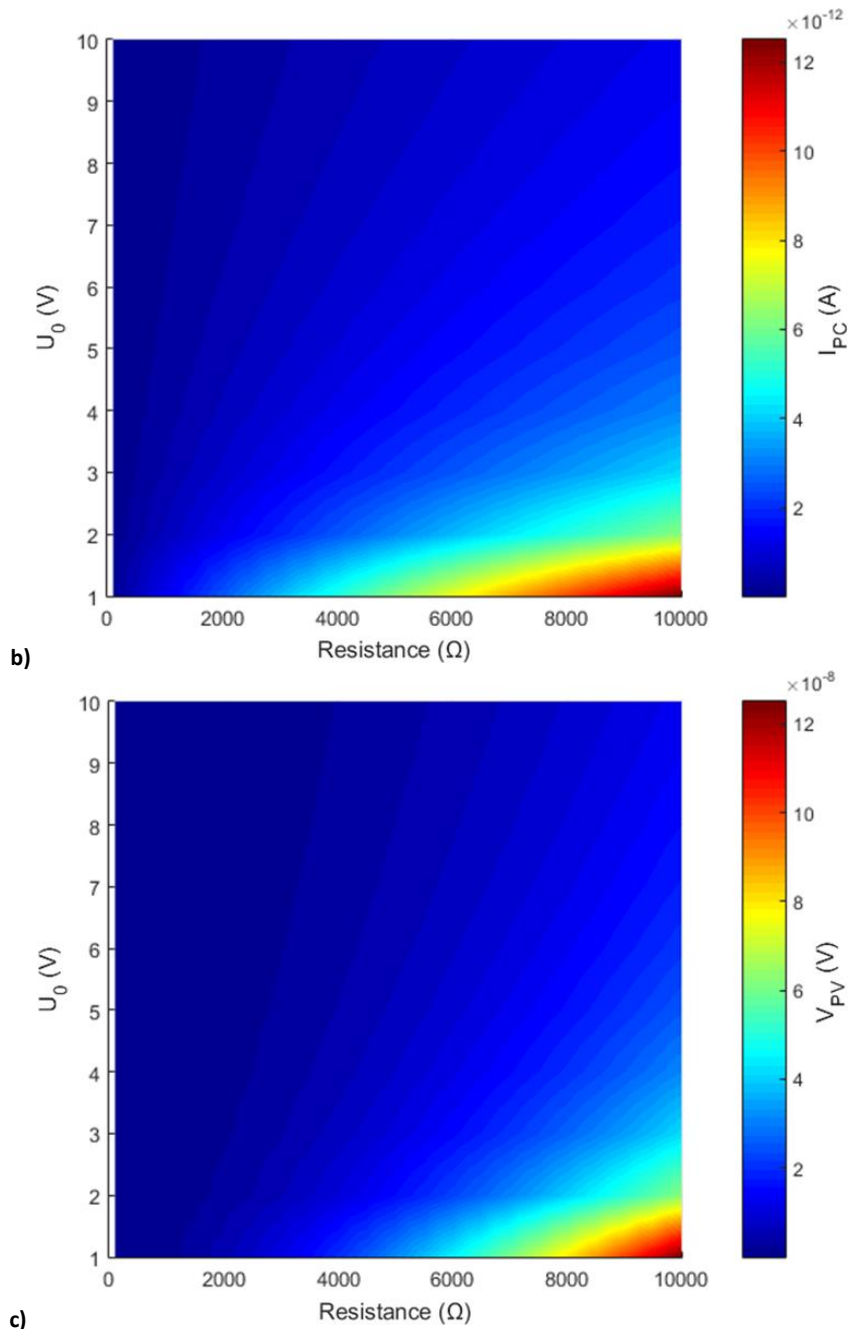
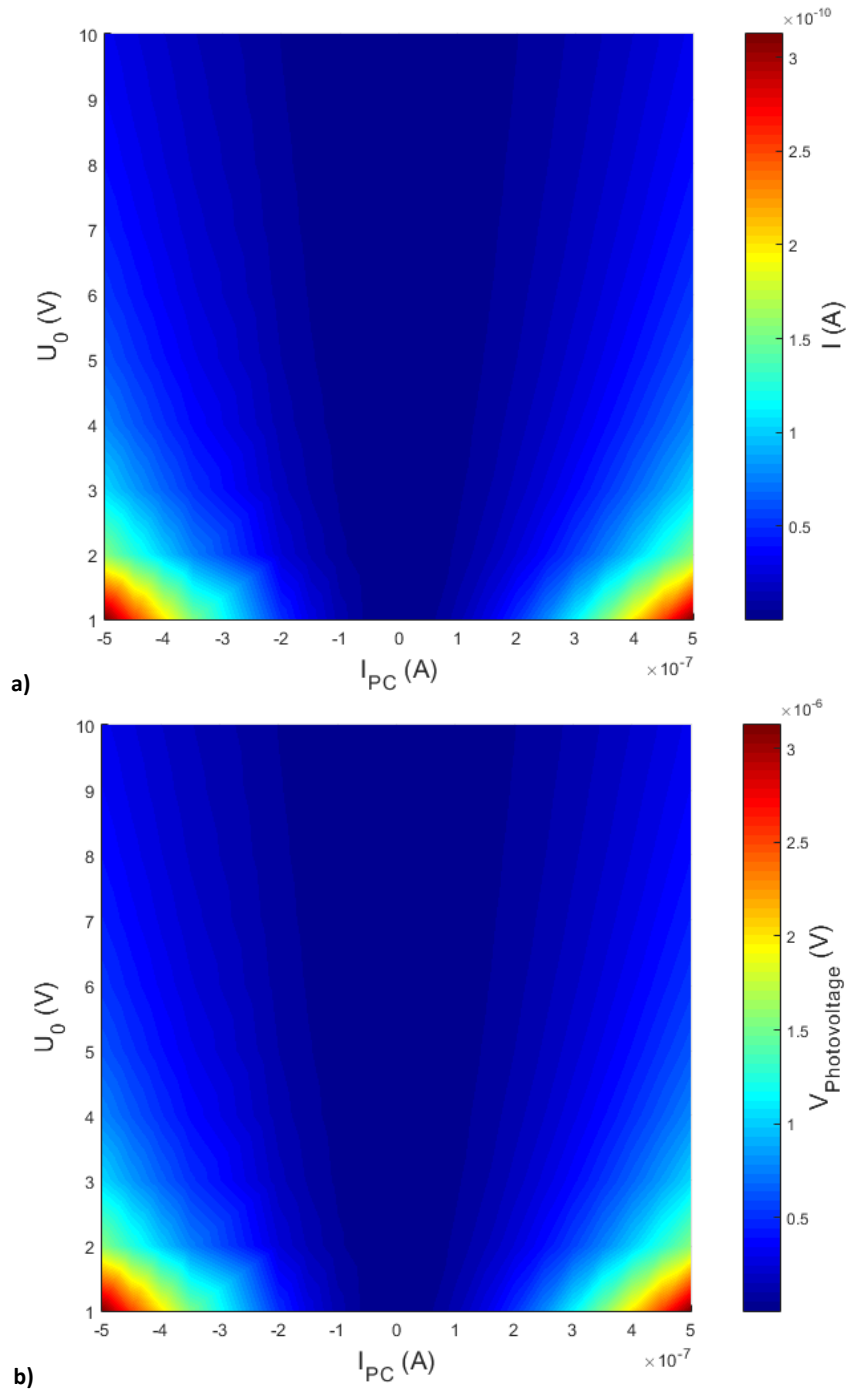


Figure 3.7 showing the simulated values, as a function of gate voltage relative to the Dirac point and the sheet resistance for a) the simulated value of I/I_d , b) the current, with an AC photocurrent of the same value $\sim 100\text{nA}$ for each resistance, and c) the resulting theoretical photovoltage that was expected. These results suggest that the greatest signal is obtained operating close to the Dirac point, and with a channel resistance $\sim 10\text{k}\Omega$.

The magnitude of I_{PC} was also varied to see the relationship between I_{PC} simulated values for the current and photovoltage, figure 3.8a and figure 3.8b respectively. These results show that the greatest photovoltage is obtained for the greatest magnitude I_{PC} ; as discussed in ref. [154], a positive I_{PC} is measured adjacent to the Dirac point. This is also shown in figure 3.8c where, as a function of I_{PC} for different values of U_0 and a

channel resistance of $10\text{k}\Omega$, the magnitude of the simulated photovoltage varies like I_{PC}^2 , and decreases for greater values U_0 away from the Dirac point.



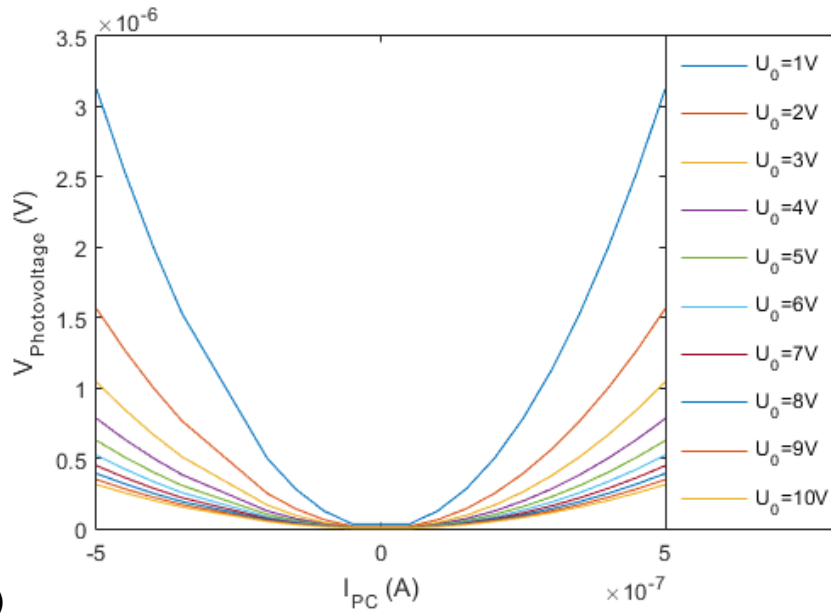


Figure 3.8, showing the theoretical a) photocurrent and b) and c) photovoltage as a function of gate voltage and AC photocurrent. This shows that, for a greater magnitude photocurrent, the current increase. The largest AC photocurrent occurs closest to the Dirac point.

3.3.1.4 Summary of Requirements

These simulations have shown that the performance of the detector can be optimised by selecting an appropriate dielectric material and thickness, designing the detector with appropriate channel dimensions for an idealised graphene sample, and applying an appropriate gate voltage. Optimising the detector provided for several solutions in parameter space, summarised in table 3-1; some of these are not necessarily realistic at the moment given the current state of the art of detector fabrication, but it provides further opportunities in the future.

| | L | W | Substrate Thickness | Substrate Material | Gate Voltage U_0 (V) | Graphene Resistance (k Ω) |
|-----------------|------------------|-----------------|---------------------|--------------------------------|------------------------|-----------------------------------|
| Option 1 | 10 μm | 5 μm | 1000nm | Al ₂ O ₃ | ~1 | - |
| Option 2 | 10 μm | 5 μm | 200nm | SiO ₂ | 0-1 | - |
| Option 3 | 10 μm | 5 μm | 300nm | SiO ₂ | 0-3 | ~10 |

Table 3-1. List of options for GFET manufacturing.

For a channel width of 5 μm , which was selected to improve the prospects of more reliable manufacturing, the graphene channel length should be at least 10 μm , and with a resistance of order 10k Ω . The photovoltage produced by this detector would be greatest at a low U_0 for a detector designed on an Si/SiO₂ wafer with an SiO₂ thickness of 300nm.

3.3.2 Antenna Optimisation for 1.2THz

The other critical design and optimisation requirement was the design of the antenna. Ideally, the antenna impedance would be matched to that of the graphene channel to ensure the maximum power transfer, and it must resonate at the frequency that the detector is optimised for. Many different antennae designs are available; the most common ones are the bowtie antenna and the log periodic circular toothed antenna.

The log periodic circular toothed antenna is a self-complementary antenna (as the void between the antenna nodes are the same shape as the antennae nodes themselves), and means that this antenna has a wide bandwidth and constant impedance given by the Mushiake relationship, equal to $60\pi\Omega$ [155]. The size of the arms of the antenna can be varied, with the width of the arms increasing by a factor k for each arm, figure 3.9, and given by $\frac{R_n}{r_n} = k$.

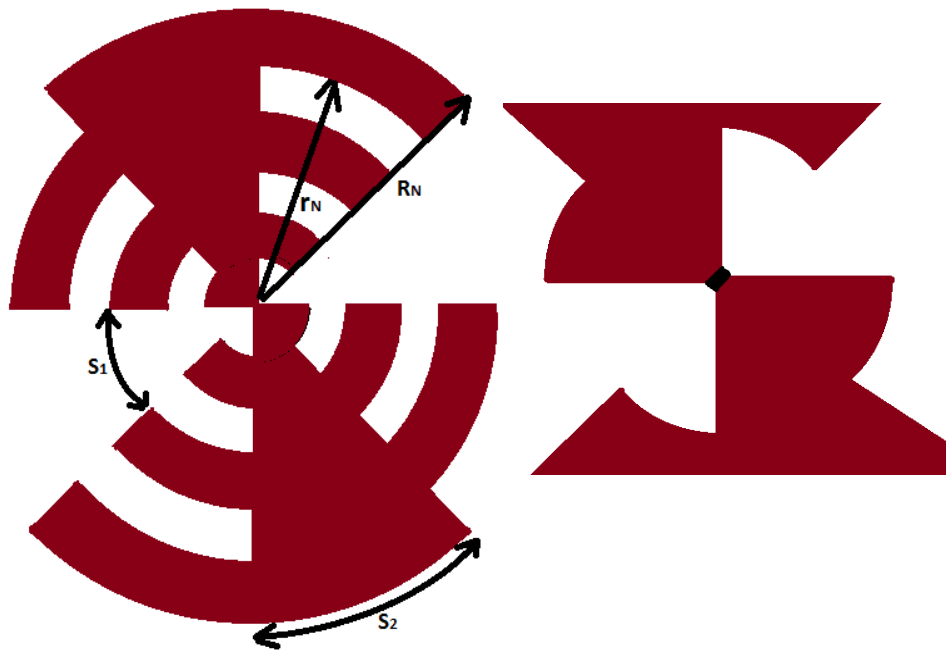


Figure 3.9. Definition of the variables governing the design of the log-periodic circular toothed antenna. The opening angle is set to be $S_1=S_2$ [156].

The S_{11} parameter characterises the power reflected by an antenna termination (in this case the coupling between the antenna and the graphene channel) back on itself (i.e. back into the antenna) [156] [157]. The antenna designs were iterated to obtain the most negative S_{11} magnitude response at 1.2THz (in dB), so that the power reflected at the gate – given by $P = 10^{dB/10}$ – is least and therefore the power transferred across the gate is greatest. Sonnet Lite simulation software [158], which

used finite element analysis, was used to simulate the S11 parameter of an antenna across a range of frequencies, which allowed for the antenna design to be iterated and the S11 parameter measured at 1.2THz to be optimised. The impedance of the terminations was varied, with a 50Ω and 50Ω impedance across the two ports, and then a more realistic 5kΩ (on the graphene end) and 50Ω impedance.

An ideal antenna would also be impedance matched between the GFET channel and the antenna, to ensure the maximum transfer of power [159]. Of the power impinged on the antenna, a proportion is transferred to the graphene channel, given by [160]

$$P_{transferred} = \frac{V^2 Z_{Antenna}}{(Z_{Antenna} + Z_{graphene})^2}, \quad \text{Equation 3.4}$$

where V is the voltage applied to the antenna and $Z_{Antenna}$ and $Z_{graphene} = R_{graphene}$ are the impedance of the antenna and graphene respectively. By taking the derivative with respect to $Z_{Antenna}$,

$$\frac{\delta P_{transferred}}{\delta Z_{Antenna}} \propto \frac{1}{(Z_{Antenna} + Z_{graphene})^2} - \frac{2Z_{Antenna}}{(Z_{Antenna} + Z_{graphene})^3}, \quad \text{Equation 3.5}$$

it can then be demonstrated that impedance matching yields the greatest power transferred by setting $\frac{\delta P_{transferred}}{\delta Z_{Antenna}} = 0$, which yields $Z_{Antenna} = Z_{graphene}$.

The log-periodic circular toothed antenna, for instance, is not impedance matched as the antenna has an impedance of approximately 200Ω as opposed to a graphene channel impedance of order 1-10kΩ. For an antenna with $Z_{Antenna} \sim 200\Omega$ and $Z_{graphene} = R_{graphene} = 1\text{k}\Omega$, $\frac{P_{transferred}}{V^2} \sim 1.3 \times 10^{-4} \Omega^{-1}$, while for a greater channel resistance, $Z_{graphene} = R_{graphene} = 20\text{k}\Omega$, $\frac{P_{transferred}}{V^2} \sim 5 \times 10^{-7} \Omega^{-1}$. Therefore, with better impedance matching between the antenna and the graphene channel, there is a greater proportion of the power transferred. Although the impedance matching and hence power transmission was not ideal, the antenna response was optimised for frequencies around 1.2THz but provides room for further iteration of the antennae design to improve the power transmission of the detector.

Several different antenna structures were investigated; outlined in figures 3.10-3.13 are four of the most promising structures – two log-periodic circular toothed antennae

(one for $k=1.5$, one for $k=2$), a bowtie antenna, and a beetle antenna. The beetle adapted the bowtie antenna as a route to improving the magnitude of the S11 resonance at 1.2THz.

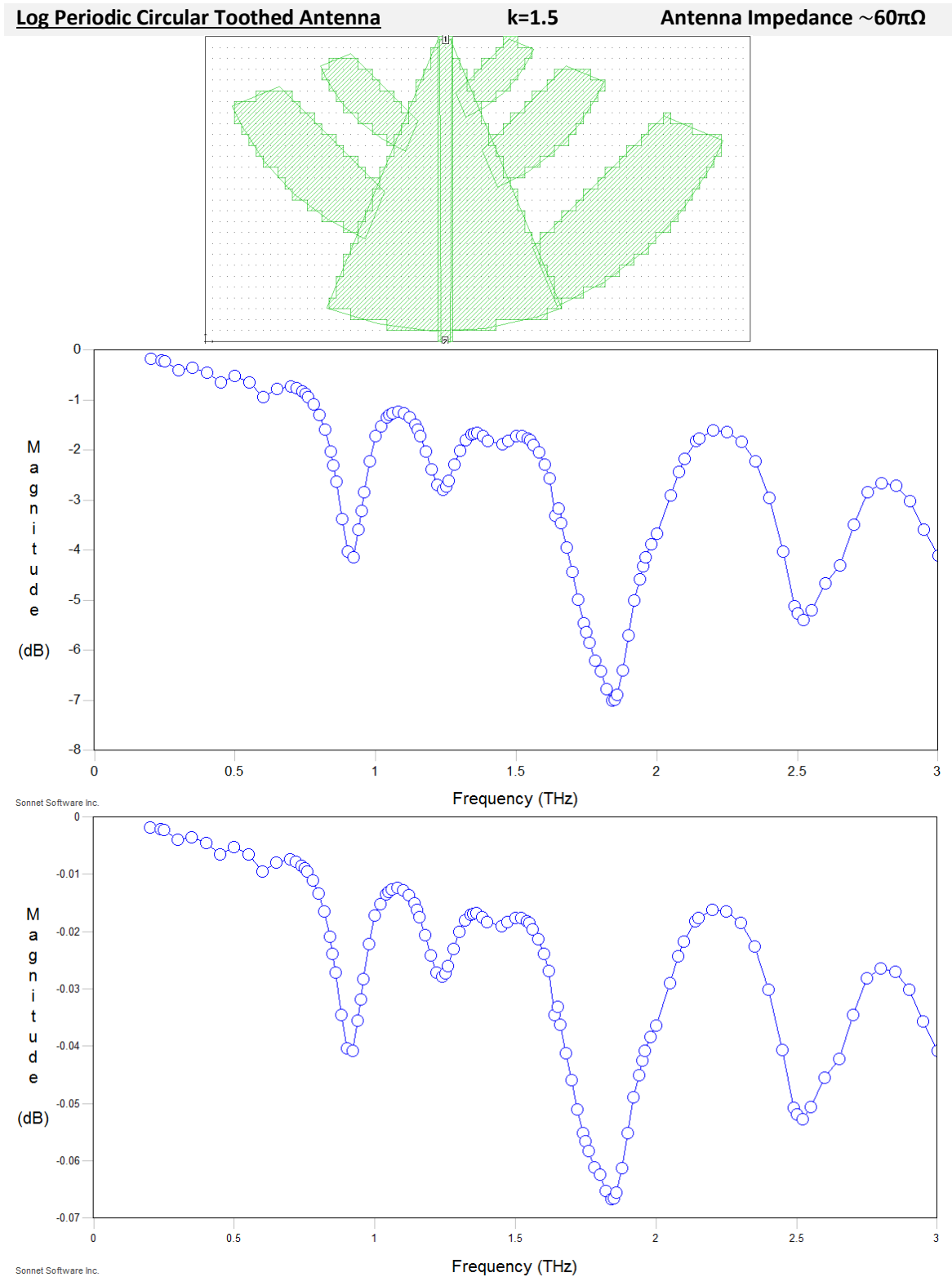


Figure 3.10 showing the simulated S11 response for a log periodic circular toothed antenna with $k=1.5$, using Sonnet Lite simulation software [158]. The S11 response as a function of illuminating frequencies shows several resonances, most noticeably at $\sim 0.9\text{THz}$, 1.2THz , 1.8THz and 2.5THz .

Log Periodic Circular Toothed Antenna

k=2

Antenna Impedance $\sim 60\pi\Omega$

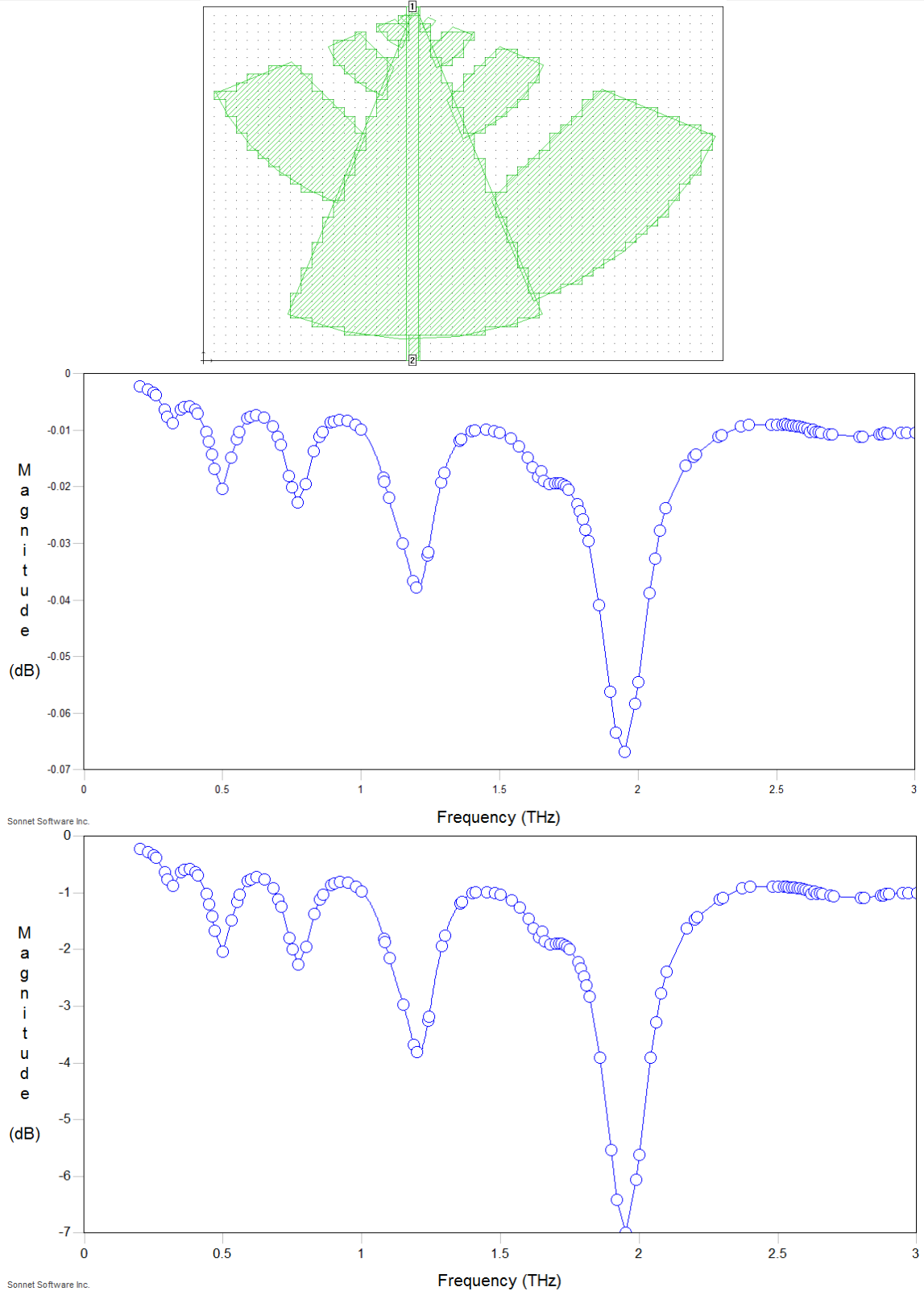


Figure 3.11, showing the simulated S11 response for a log periodic circular toothed antenna with $k=2$, using Sonnet Lite simulation software [158]. The S11 response as a function of illuminating frequencies shows several resonances, most noticeably at $\sim 0.5\text{THz}$, 0.8THz , 1.2THz and 1.95THz .

Bowtie Antenna

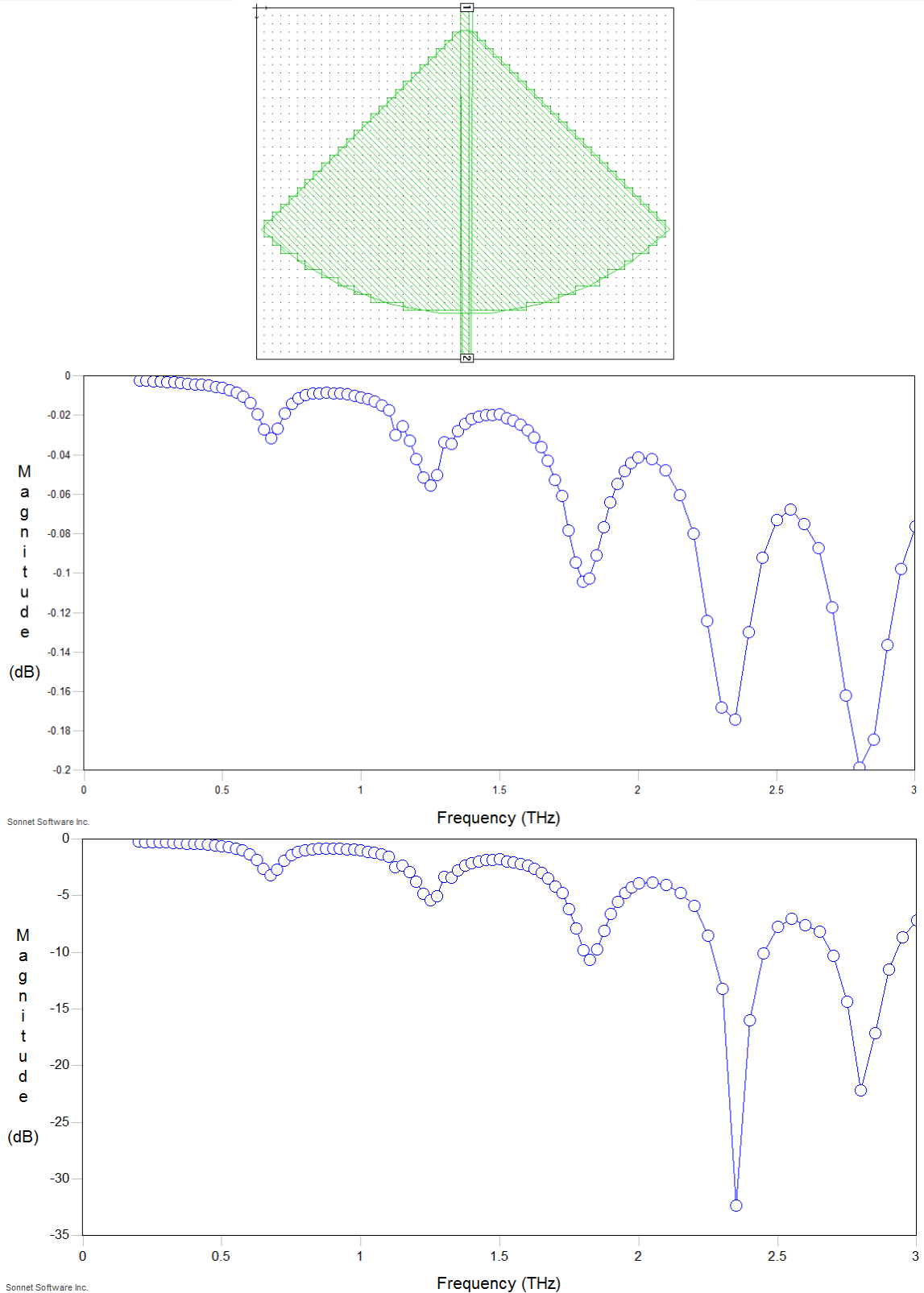


Figure 3.12 showing the simulated S11 response for a bowtie antenna, using Sonnet Lite simulation software [158]. The S11 response as a function of illuminating frequencies shows several resonances, most noticeably at ~ 0.6 THz, 1.2 THz, 1.8 THz and 2.4 THz.

Beetle Antenna

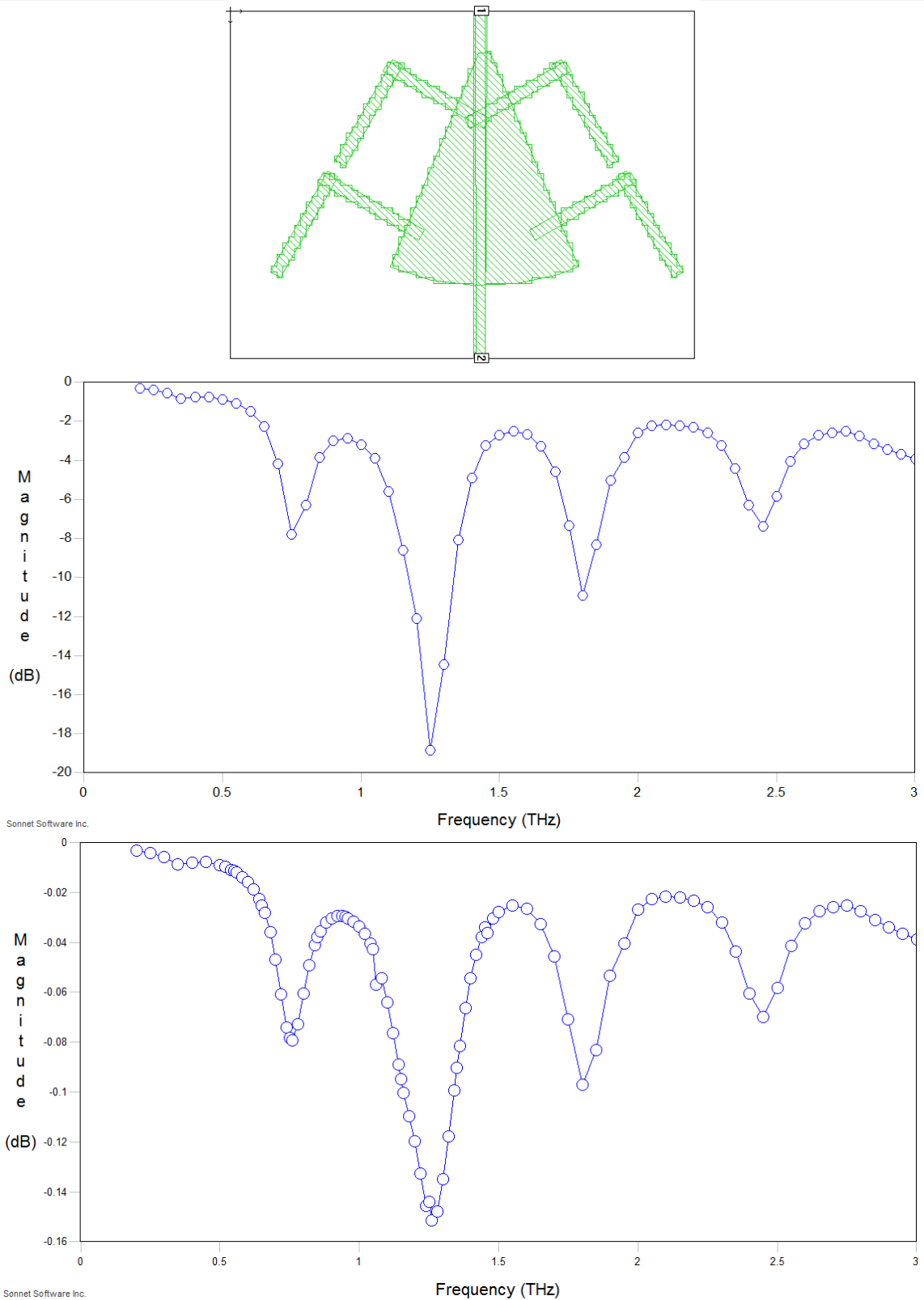


Figure 3.13. showing the simulated S11 response for a beetle antenna, using Sonnet Lite simulation software [158]. The S11 response as a function of illuminating frequencies shows several resonances, most noticeably at $\sim 0.7\text{THz}$, 1.2THz , 1.8THz and 2.5THz .

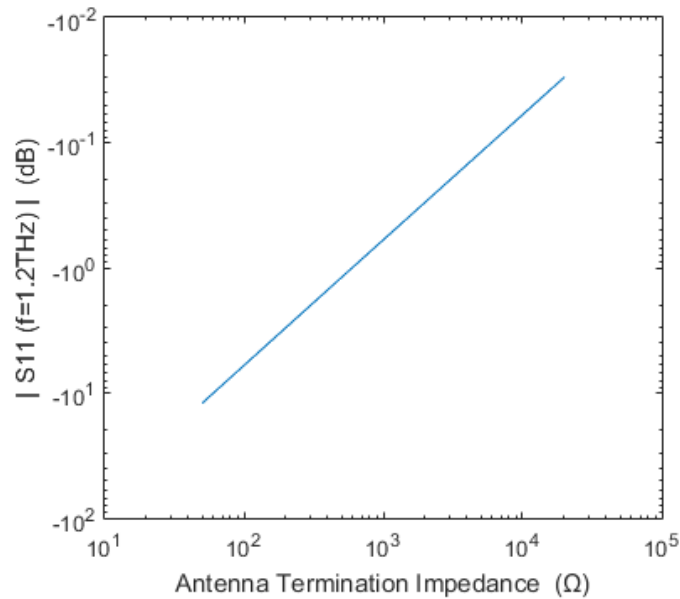


Figure 3.14 showing how the simulated power at 1.2THz varies with antenna termination impedance which is equated to the graphene channel impedance. A typical GFET channel resistance is 1-10kΩ.

In each of the simulations there is a noticeable difference in the S11 parameter depending on the termination impedance used, with simulations using a termination on one end with a 50Ω impedance, and the other (graphene) end with initially a 50Ω impedance, and then a much more realistic 5kΩ impedance. As a function of the graphene impedance, for the beetle antenna, the observed S11 magnitude at 1.2THz goes like $|S11| = 10^{\varphi} R^{\gamma}$, figure 3.14, where $\varphi \sim -1$ and $\gamma \sim 2.75$ are fitting terms that are related to the voltage generated across the antenna and the quantity of that power reflected [157]. Therefore, for the largest power transfer, simulations suggested that the detector required a low resistance graphene channel.

3.4 Manufacturing Plan

Using the simulations that have been presented so far in this chapter, the detector was designed on a silicon wafer with a 300nm thick silicon dioxide insulator between the silicon and a graphene channel of 10μm x 5μm, with the graphene channel etched to the required dimensions and metallisation deposited for the contacts and antennae.

The size of the channel means that the device is optimised for frequencies around 1.2THz whilst operating in the overdamped, “long gate”, broadband regime, where plasma waves have been shown to be excited, although not in a resonant regime; this is discussed further in ref. [151]. While this means that the signal response is

potentially smaller than it otherwise would have been for resonant regime, the larger graphene channel means that the prospects for greater device yield and more reliable manufacturing is potentially improved.

The simulations for the response of the antennae lobes led to three detector designs, each of order 100-150 μm from the graphene to the edge of the antennae, which were considered for the manufacturing process:

- Log-periodic circular toothed antenna (LPCTA), with the ratio between the arms of the electrode set to 1.5.
- Bowtie antenna with approximately 100 μm radius and an arc length of approximately 100 μm .
- “Beetle” antenna, which adapts a bowtie antenna. Each leg is approximately 25 μm +50 μm long, with approximately 50 μm between the legs on each side. The bowtie is approximately 100 μm radius and an arc length of approximately 100 μm .

The beetle antenna was eventually selected, as this offered the most novelty and the greatest response at 1.2THz.

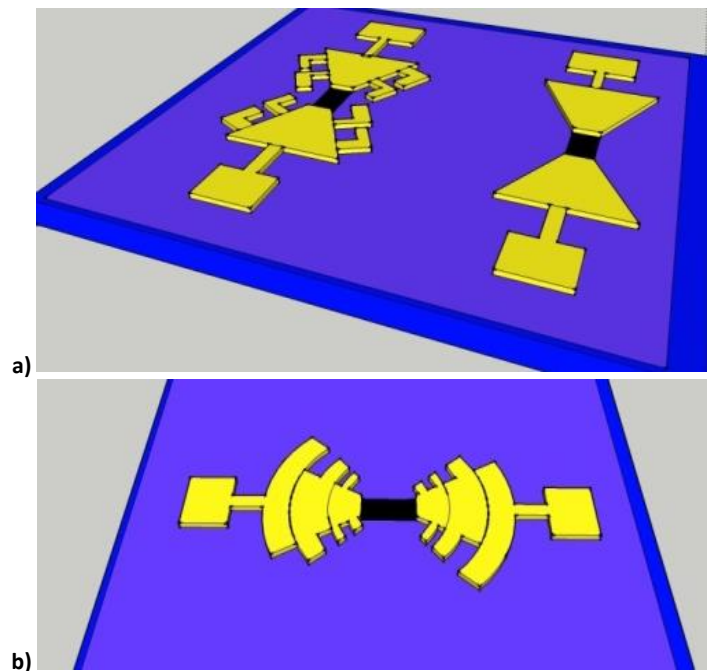


Figure 3.15, showing a) The “beetle” (left) and bowtie (right) antennae and b) the log-periodic, circular toothed antenna (not to scale). Both these were designed to have a resonating frequency at the required 1.2THz. Here blue is Si, light purple is SiO₂, yellow is the Ni-Al contact and black is the graphene.

3.5 Summary

In this chapter, the concept initially outlined in ref. [123] for a terahertz detector that operates using the Dyakonov-Shur effect has been discussed. Given the specification outlined by the European Space Agency, simulations were undertaken to understand the predicted voltage and current as a function of different detector parameters, and improve the theoretical response to illumination by photons with a frequency of 1.2THz by simulating different designs for the antenna. Several different solutions to the antennae design are available, including the log-periodic circular toothed antenna and the bowtie and variant “beetle” type antennae. These results show that the expected response should be gate voltage dependent, whilst conceptually it should be able to operate passively.

These simulations have been used to design the detector in a field effect transistor structure using standard fabrication processes and incorporating the beetle antenna. The fabrication of the detector will be outlined in chapter 5.

4

Theoretical Study and Design of a Graphene-based X-ray Single Photon Counting Photodetector

4.1 Introduction

As discussed in the previous chapter, as part of this project a successful bid was made to the European Space Agency for funding research into two detectors. In this chapter, research into the graphene-based X-ray detector in a GFET-structure is presented.

In this section, work to optimise the design of the X-ray GFET with regards to potential energy sensitivity and speed of the detector is discussed, with the intention of working towards the detection of single X-ray photons. Each element of the detector structure is considered, with simulations used to optimise the absorber dynamics and transport properties of the detector. The results influenced the design of the device ready for manufacturing.

4.2 Concept

GFETs, and theoretically studied GDEPFETs, utilise the field effect to measurably change the channel conductivity of the graphene. As outlined in chapter 1, graphene field effect transistors have used different techniques to demonstrate sensitivity to optical photons and X-ray photons. For instance, using the photovoltaic effect, GFET structures have demonstrated sensitivity to optical photons with a photocurrent response up to 40GHz, although theoretically this may exceed 500GHz [126].

GFET sensitivity to X-ray photons has previously been reported [74] [75] [80] [81] [82] [83] [125], that shows modulation of the channel current due to irradiation by an X-ray generator (15kV, 15 μ A and 40kV, 80 μ A). This has a responsivity of 0.1AW⁻¹, a reported energy resolution of $\frac{E}{\delta E} \sim 10000$ at 1MeV, and a signal decay time of 10s of seconds.

Conceptually, for X-ray detection, the X-ray photon is absorbed in the absorber, figure 4.1, and generates an electron-hole pair which is funnelled towards the substrate dielectric through the application of a gate voltage. The generated charges carriers modulate the charge carrier density in the absorber, with a resulting change in the conductivity of the graphene [78] [81] [83] [161].

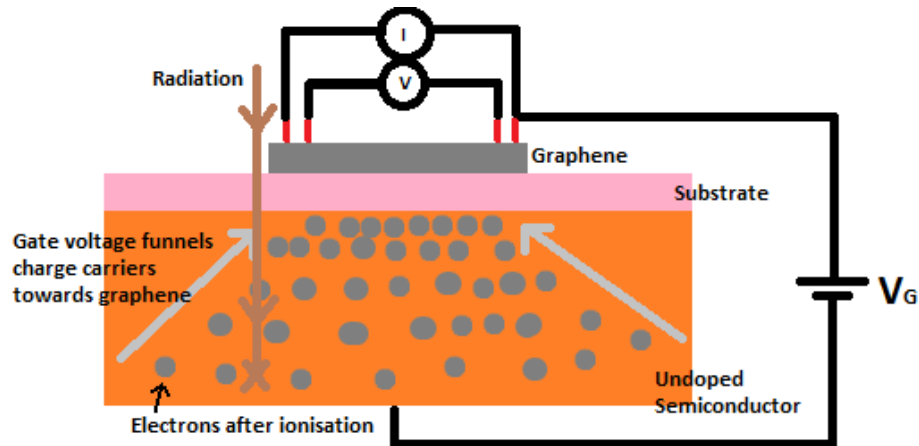


Figure 4.1 showing the concept used in refs. [75] and [78] for the X-ray GFET. The charge carriers are excited after incident radiation is absorbed by the semiconductor, and are then funnelled towards the graphene by the application of a gate voltage.

This concept differs from other Si-based X-ray detectors, such as a silicon drift detector (SDD) [162], which have a typical energy resolution $\frac{E}{\delta E} \sim 47$ [163], where charge carriers are generated in a silicon absorber, accelerated towards the electrodes and then collected by a junction gate field effect transistor (JFET). Other types of X-ray detectors include MCP-PMTs, which have ~ 25 ps time resolution and energy resolution at soft X-ray energies, and STJs that have X-ray energy sensitivity $E/\delta E \sim 500$ but require cryogenic cooling, as described in chapter 1.

Using the silicon as the absorber, exploiting the gain mechanisms in the silicon, and using the graphene as the readout mechanism via the change in the conductivity has potential benefits for cost and simplicity of manufacture and use, and the speed and sensitivity of the detector. Manufacturing the detector on a silicon wafer can use well refined manufacturing processes that are limited by the state of the art of graphene fabrication techniques. The detector would be simpler and cheaper to use, as it would be achieved by a simple measurement of the channel conductivity, and could operate at room temperature rather than at cryogenic temperatures required by MCP-PMTs and STJs. It could conceivably operate at faster detection times because of the

potential mobility of the graphene sample and the figures of merit indicated previously in section 1.4. It could also provide improved sensitivity, as graphene detectors that utilise the change in conductivity of the graphene channel have been demonstrated for single gas molecules detection, as discussed in ref. [164], so this potentially provides a good basis for an X-ray single photon counting photodetector.

Therefore, this GFET concept provides potential benefits as it could enable a simple measurable change in current or resistance to indicate irradiation by an X-ray, and with the detector potentially able to run with faster detection times at room temperature.

4.3 Device Optimisation

Applying a gate voltage to the absorber controls the graphene channel conductivity, opens a depletion region in the absorber, and funnels the charge carriers towards the dielectric. The accumulation of charge carriers in the absorber generates a further field across the dielectric layer, akin to a change in the gate voltage, that changes the carrier density of the graphene, resulting in a photosignal via the measurable change in conductivity of the graphene.

To maximise the measured signal, the change in conductivity with respect to the change in gate voltage, $\delta\sigma/\delta V_G$, where σ is the conductivity and V_G is the gate voltage applied to the device, is not the only parameter that needs to be optimised. The charge carriers generated in the absorber must also be funnelled as efficiently as possible through the absorber towards the dielectric, and the depletion region opened in the absorber must be as large as possible. Although this detector was intended for room temperature operation, further sensitivity could be gained by operating at lower temperatures as this would increase $\delta\sigma/\delta V_G$, as outlined in ref. [100].

To optimise the detector for X-ray photodetection, each element of the detector was considered. In this section, results from simulations that vary the absorber material and doping, the size of the graphene channel, the geometry of the detector and the thickness and material of the dielectric are presented to motivate the design with regards to the speed of the signal and the conductivity of the detector.

4.3.1 Optimising the Absorber: Simulation of Absorber Dynamics

The absorber is typically a semiconductor, which may be undoped [75] or doped [78]. Many different absorber materials can be used depending on the intended photon energy and operational temperature. Silicon is a routine selection because of its relatively low cost, whilst one using SiC can be used at higher temperatures due to the large band gap of approximately 3.1eV and the ability to grow graphene in situ. Other materials such as CdTe can be selected depending on the photon energy to be detected, due to the higher stopping power of the material; CdTe has a band gap of 1.52eV [74], and hence could be used as an absorber at room temperature.

The dynamics of charge carriers in the absorber can be used to optimise the device geometry and material. In ref. [78], the standard software package *CASINO* was used to track 400keV electrons through a 500 μ m thick silicon wafer. Their results show that, without funnelling, a significant number of electrons leave the absorber during scattering when they reached energies \sim 400keV [78].

In this section, results are presented from simulations using *COMSOL*, *GAMOS* and *CASINO* simulation software to investigate the geometry of the absorber, and the effect of the graphene channel dimensions and the magnitude of the potential and field applied. In these simulations, only silicon wafers and silicon dioxide dielectrics are considered as the device fabrication process using these materials is most refined, making the process cheaper and easier [74]. A great deal of ongoing research is investigating graphene on other substrates, which could motivate future work.

4.3.1.1 Photons in the Absorber: GAMOS + CASINO Simulations

Simulation software can be used to simulate the interaction of photons with a substrate, and the subsequent charge carrier behaviour. *GAMOS* [165] uses a Monte Carlo algorithm to simulate the absorption of an X-ray photon by a target material. *CASINO* [166] uses another Monte Carlo algorithm to simulate the movement of excited charge carriers through the target material. Previous work used *CASINO* to simulate the movement of 400keV electrons through a silicon block of 500 μ m thickness, width and depth [80]. These simulations were replicated for initial electron

energies of 10keV, 50keV, 100keV and 500keV, as shown in figure 4.2. Higher energy electrons travel further and penetrate deeper into the silicon wafer before stopping, and the greatest energy charge carriers can pass out of the wafer entirely [80]. Higher energy electrons scatter and cause secondary electrons to be excited in the wafer.

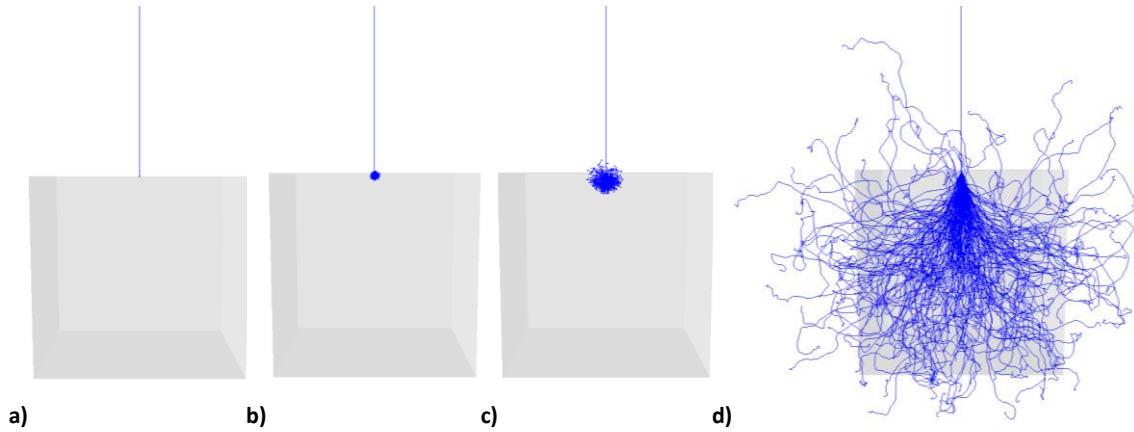


Figure 4.2 showing CASINO simulations for the trajectory of electrons with an initial energy of a) 10keV, b) 50keV, c) 100keV, and d) 500keV through a 500µm x 500µm x 500µm silicon wafer. Lower energy electrons, e.g. at 10keV, are more quickly stopped in the wafer, and generate fewer secondary charge carriers than electrons with an initial energy of 500keV. At the highest energies, these electrons can pass out of the wafer.

4.3.1.2 Charge Carrier Travel and Relaxation: COMSOL Simulations

COMSOL [167] was used to simulate the behaviour of charge carriers in the silicon absorber, such as the charge carrier recombination time and how charge carriers are funnelled towards the dielectric layer due to the gate voltage. As the gate voltage controls the funnelling of the charge carriers, the opening of the depletion region and the Fermi level of the graphene, the optimal position may not be where $\delta\sigma/\delta V_G$ is greatest but where all three factors result in the greatest signal. Maximising the field applied to the graphene across the dielectric helps to improve the detector sensitivity.

4.3.1.2.1 Basic COMSOL simulations

A basic simulation was developed to consider how the gate voltage applied from the bottom of the silicon varies across a simulated 500µm x 500µm x 500µm block. For this simulation, five graphene samples (10µm x 10µm, 20µm x 20µm, 30µm x 30µm, 40µm x 40µm and 50µm x 50µm) were assumed to be grounded on an infinitesimally thin SiO₂ dielectric layer, figure 4.3a. The voltage across the block was then studied for different gate voltages applied to the bottom of the silicon block.

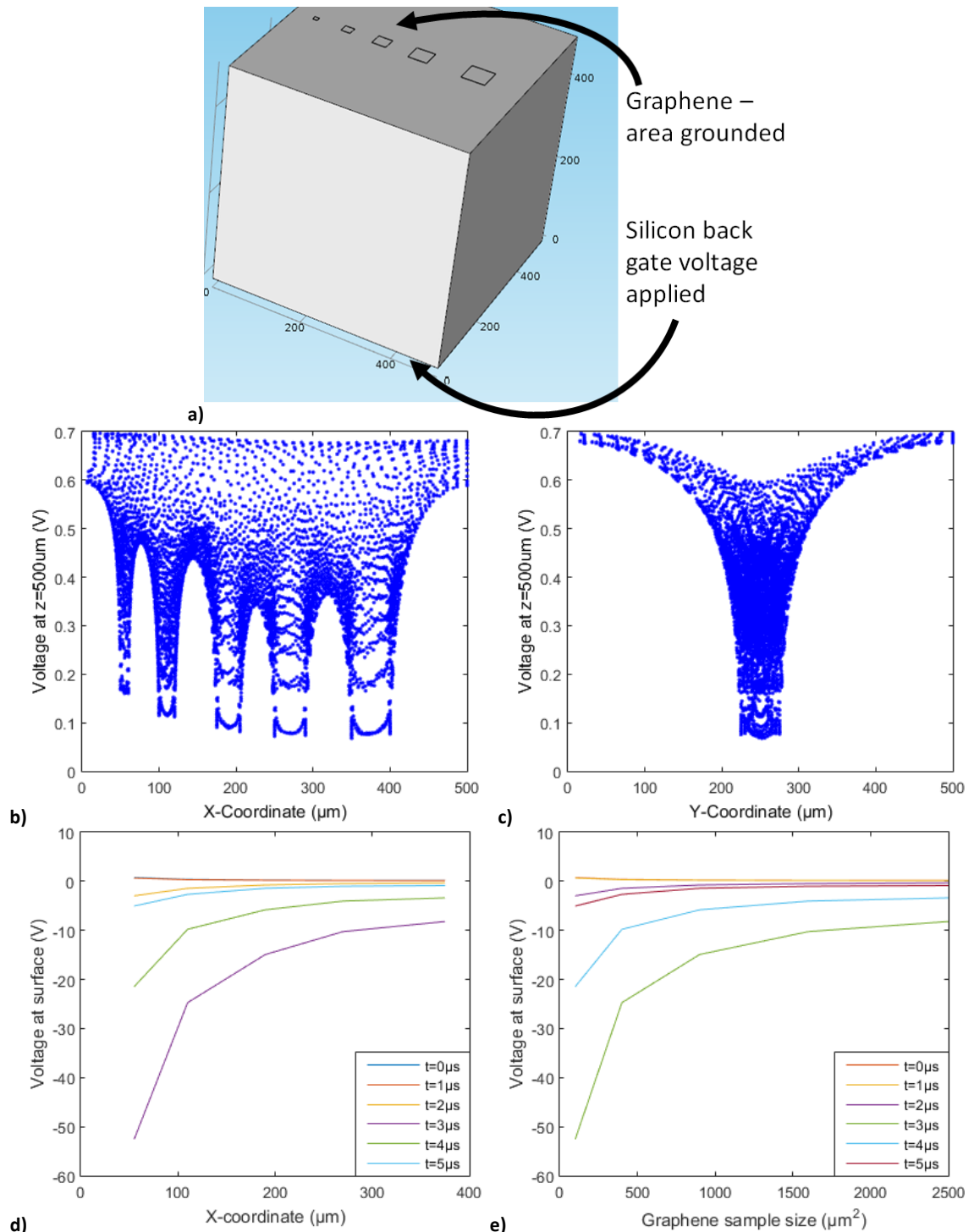


Figure 4.3 showing a) a schematic of the initial simulation setup, with five graphene samples of $10\mu\text{m} \times 10\mu\text{m}$, $20\mu\text{m} \times 20\mu\text{m}$, $30\mu\text{m} \times 30\mu\text{m}$, $40\mu\text{m} \times 40\mu\text{m}$ and $50\mu\text{m} \times 50\mu\text{m}$. For $V_G=1\text{V}$, the simulated voltages across the sample of b) $V(z=500\mu\text{m},x)$ and c) $V(z=500\mu\text{m},y)$ indicate how the voltage varies close to the 5 samples on the substrate of increasing size. D) shows, for $V_G=100\text{V}$, how the voltage measured directly beneath each sample varies as a function of sample position, with the $10\mu\text{m} \times 10\mu\text{m}$ sample at $x=50\mu\text{m}$, the $20\mu\text{m} \times 20\mu\text{m}$ sample at $x=110\mu\text{m}$, the $30\mu\text{m} \times 30\mu\text{m}$ sample at $x=190\mu\text{m}$, the $40\mu\text{m} \times 40\mu\text{m}$ sample at $x=250\mu\text{m}$, and the $50\mu\text{m} \times 50\mu\text{m}$ sample at $x=375\mu\text{m}$. E) shows the same data in terms of the sample area, with the greatest voltage simulated beneath the smallest graphene sample, and therefore the greatest field across the dielectric. An electron-hole pair generated in the absorber will cause a modulation in the field, so for a smaller sample size this gives the opportunity for a greater change in the field, and therefore more sensitive detection.

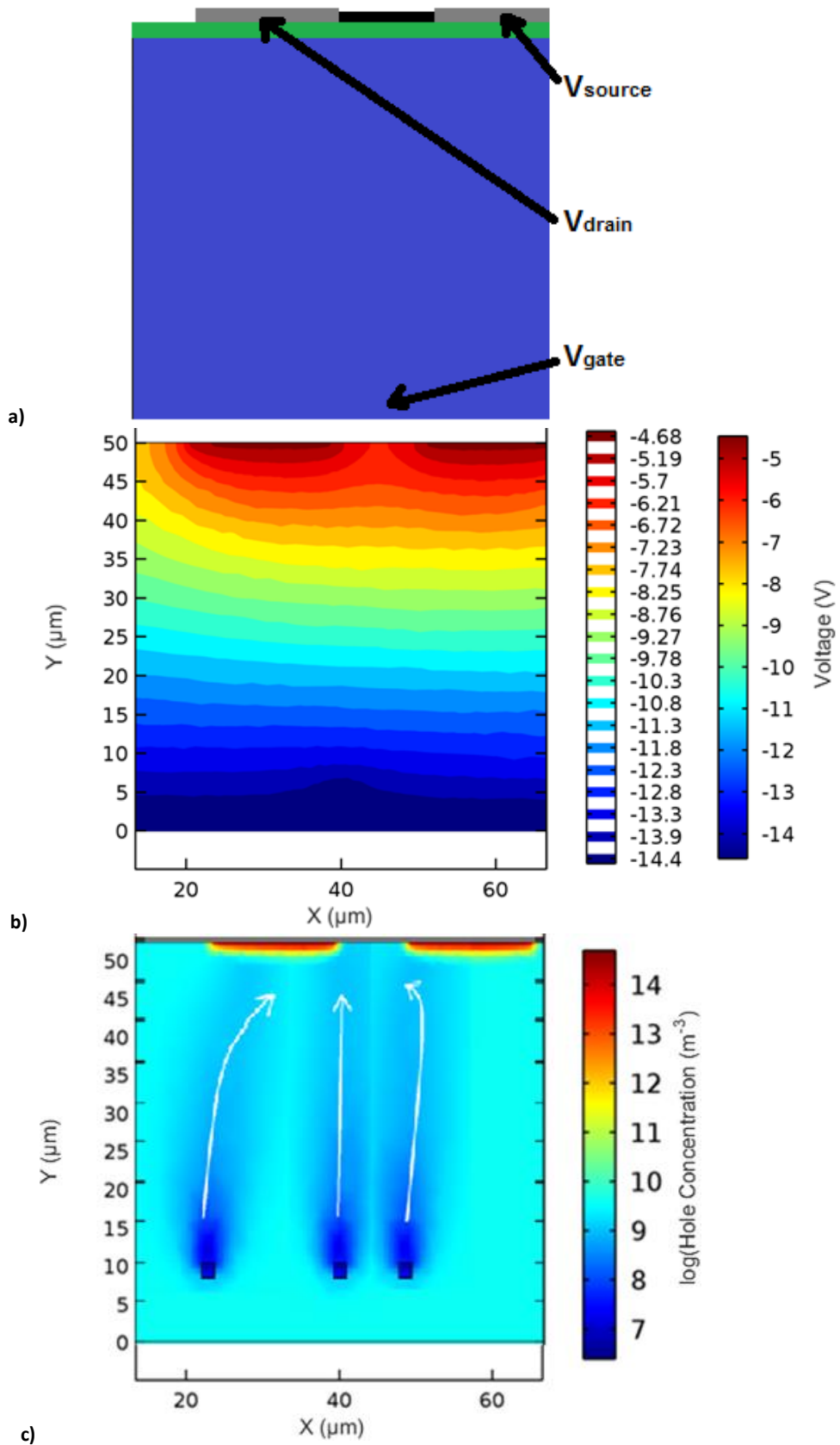
The simulated voltages $V(z=500\mu\text{m},x)$ and $V(z=500\mu\text{m},y)$, measured at the top of the silicon wafer, are shown in figures 4.3b and 4.3c respectively, with the voltage varying significantly close to the graphene samples. The higher potential close to the gate and the lower potential, shown in figures 4.3b and 4.3c, close to the graphene would establish a field that would funnel electron-hole pairs, generated in the absorber due to the absorption of an incident photon, towards the graphene sample, independent of initial position.

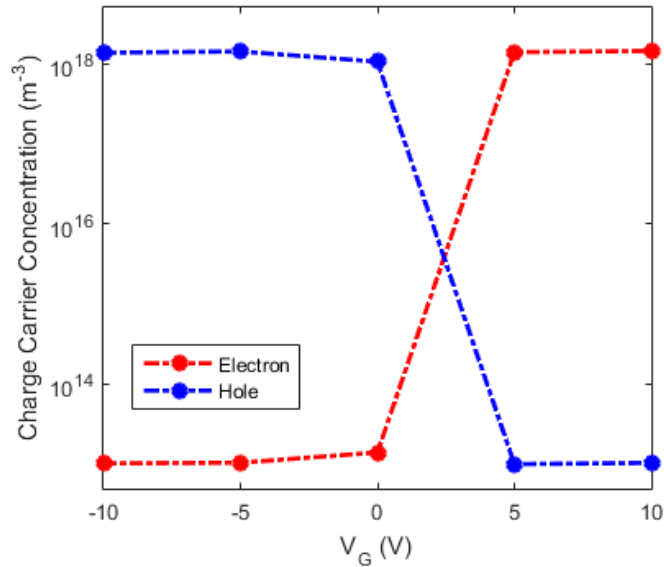
The simulated voltage directly beneath the centre of the sample on the top of the silicon wafer are shown in figure 4.3d, with the $10\mu\text{m} \times 10\mu\text{m}$ sample at $x=50\mu\text{m}$, the $20\mu\text{m} \times 20\mu\text{m}$ sample at $x=110\mu\text{m}$, the $30\mu\text{m} \times 30\mu\text{m}$ sample at $x=190\mu\text{m}$, the $40\mu\text{m} \times 40\mu\text{m}$ sample at $x=250\mu\text{m}$, and the $50\mu\text{m} \times 50\mu\text{m}$ sample at $x=375\mu\text{m}$. These results suggest that the greatest magnitude voltage was simulated beneath the $10\mu\text{m} \times 10\mu\text{m}$ sample.

These results were recast in terms of the sample area, as shown in figure 4.3e. These results suggest that, beneath a small graphene sample of order $10\mu\text{m} \times 10\mu\text{m}$, the voltage is approximately twice that of a sample double the lateral size. An electron-hole pair generated in the absorber will cause a modulation in the field across the dielectric, so a larger potential beneath a sample and larger field across the dielectric could enable a greater modulation in the field and offer the possibility of more sensitive detection.

4.3.1.2.2 Setting up the Simulation – Charge Carrier Behaviour

The simulation was then amended to an arrangement more closely related to the one that was to be developed into the X-ray detector, figure 4.4a, with equipotentials shown in figure 4.4b for a silicon wafer of resistivity $\rho=1000\Omega\text{cm}$. In the simulations, an excess of electrons and holes related to the energy of the incident photon are generated in a region deep within the silicon wafer. The charge carriers are funnelled towards the graphene, independent of the initial ionisation position, figure 4.4c, and related to the gate voltage that is applied, figure 4.4d.





d)

Figure 4.4 showing a) the arrangement of the proposed GFET, with the silicon wafer (shown in blue), the SiO₂ dielectric (shown in green), single layer graphene (shown in black) and contact pads (shown in grey). B) shows the equipotentials for $V_{gate}=-10V$, $V_{drain}=0V$ and $V_{source}=0.01V$ outputted by the COMSOL simulations. C) shows the log of the hole concentration across the simulation; the arrows indicate how an initial area of low hole density is funnelled through the silicon wafer due to the application of the gate voltage. D) shows how the gate voltage changes the log of the density of electrons and holes in the silicon.

Using COMSOL, the charge carrier concentration directly beneath the graphene was simulated over time for different gate voltages and well densities and channel lengths. The charge carrier accumulation time and relaxation time were measured, where the accumulation time is the time required to gather charges at a point directly beneath the graphene, and the relaxation time is the time taken for these charges to decay. This gave an indication of the possible bandwidth.

The difference in carrier concentration beneath the graphene between the accumulated state (where the charge carrier concentration reached equilibrium) and the initial state was used to give an indication of the dynamic range.

4.3.1.2.3 Gate Voltage Changing the Detector Behaviour

Changing the gate voltage varies the size of the depletion region, and the rate at which charge carriers are funnelled through the absorber. This enabled the behaviour of the detector to be optimised for improved dynamic range and temporal bandwidth by seeking the operating parameters with the greatest change and fastest change in carrier concentration, respectively.

The charge carrier concentration directly beneath the graphene was simulated over time for different gate voltages, figure 4.5a. This shows the holes and electrons concentration going from the initial state to an “accumulated” state, and then recombining. There is a noticeable change of approximately two orders of magnitude in the hole concentration between the start and end of the simulation, which is most likely because the charge density returns to the equilibrium with the p-doping density across the silicon wafer.

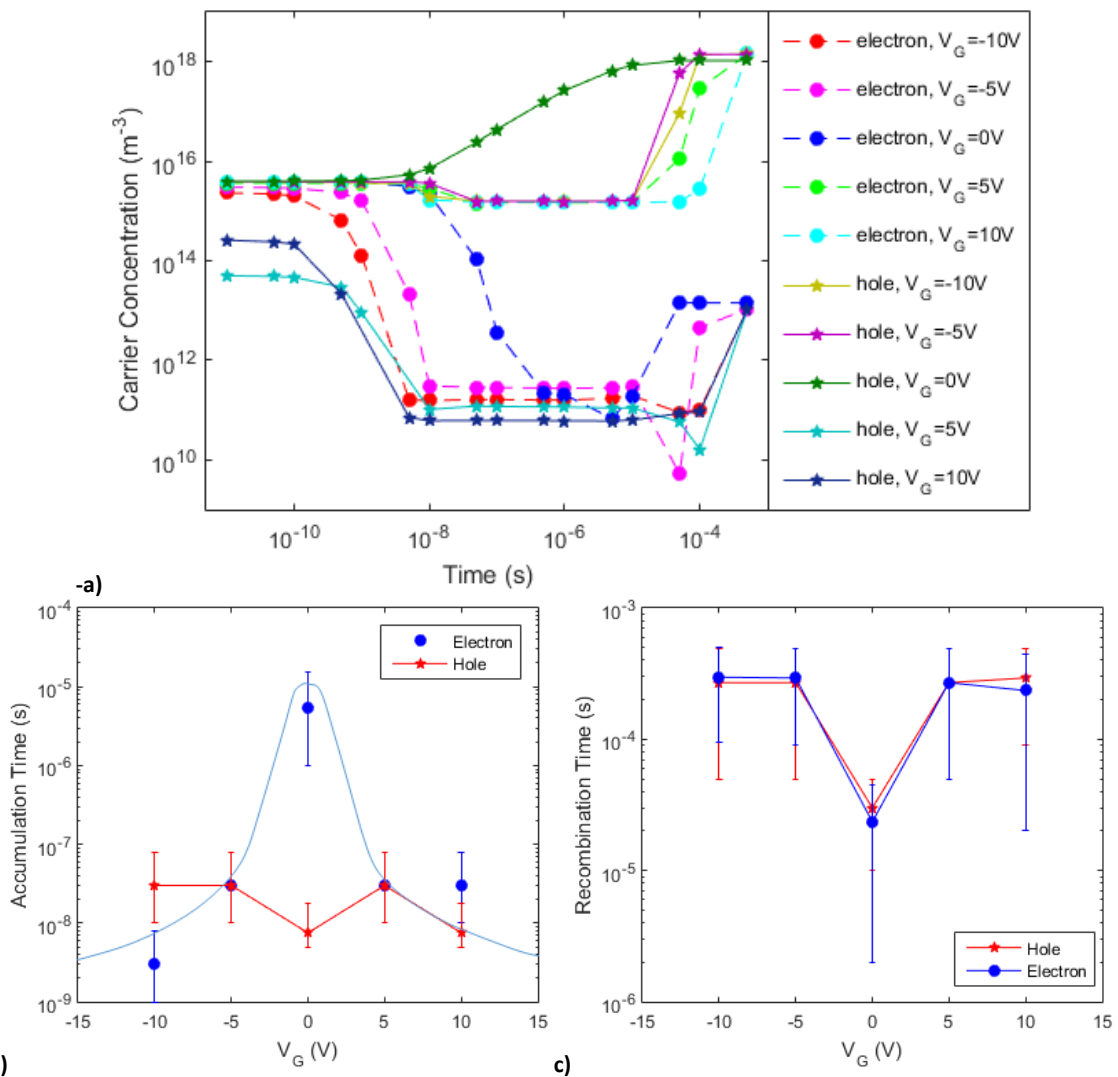


Figure 4.5, showing a) the simulated hole and electron concentration beneath the graphene over time, for different values of the gate voltage V_G . B) shows the electron accumulation time as a function of gate voltage, which shows a significant peak for $V_G \sim 0V$. C) shows that the carrier recombination time is fastest for $V_G \sim 0V$ because there is no field to accelerate the charge carriers so they recombine quicker by interacting with other charge carriers rather than being funnelled from the dielectric.

The time from the initial state to the accumulated state was calculated as a function of gate voltage, figure 4.5b, which shows a peak in the electron response for $V_G \sim 0V$. This

peak occurs because there is no field established in the silicon to accelerate charge carriers towards/away from the dielectric, and therefore the charge carriers move more slowly towards the surface. The accumulation time for holes is approximately constant, most likely because the simulated silicon wafer was p-doped.

The recombination time was also calculated as a function of gate voltage, and shows a local minimum for both electrons and holes at $V_G \sim 0V$, figure 4.5c. Again, there is no field applied across the silicon when $V_G \sim 0V$ so, in this case, charge carriers move more slowly away from the dielectric than when $V_G \neq 0V$. Therefore, for $V_G \sim 0V$, the charge carriers interact randomly with other charge carriers and recombine, rather than being funnelled out of the substrate by the gate voltage, maintaining a higher charge density, and thus taking longer to recombine.

The gate voltage, therefore, shows control of the charge carrier accumulation and recombination times. Some of the charge carriers is likely to recombine while being funnelled by the field established by the gate voltage, so a greater magnitude gate voltage $V_G \neq 0V$ is likely to lead to a greater dynamic range too.

4.3.1.2.4 Channel Size Changing the Detector Behaviour

The size of the graphene channel was also investigated to maximise the charge carriers that gather beneath the graphene, building upon results in chapter 4.3.1.2.1. The charge carriers are subjected to a field between the gate voltage and the source and drain voltages, with $V_S = 0.01V$ and $V_d = 0V$ applied to these contacts respectively such that they are essentially grounds. $V_S = 0.01V$ was chosen to ensure that the current through the graphene channel would be of order $1\mu A$ and not at risk of any damage. The further apart these contacts are (i.e. with a larger channel size L), the greater the area covered by the accelerated charge carriers, and therefore the charge carrier density is reduced.

The hole and electron charge carrier densities were simulated over time for different channel lengths L , figure 4.6a, with a weak relationship between channel length and accumulation and recombination times.

The dynamic range is calculated as the absolute change of carrier concentration between the initial and accumulated states, as shown in figure 4.6b, for $V_G = 10V$. This shows a slow decrease in the hole density beneath the substrate with increasing L because the holes are spread over a greater area. There is a very slow increase in the electron density, as the electrons accelerated towards the gate voltage are spread over a greater area, so the change directly beneath the graphene is reduced. Similarly, this is shown in figure 4.6c for the final carrier density directly beneath the graphene, with a peak carrier concentration at $L \sim 8\mu m$ for holes and $L \sim 18\mu m$ for electrons.

For both electrons and holes there is a small peak in the absolute change of charge carrier concentration at $L \sim 14\mu m$, as shown in figure 4.6b. This is perhaps because the wider channel length would mean a lower charge carrier density in the accumulated state, and therefore a greater change in carrier concentration. Despite the same initial conditions, at greater channel lengths the initial carrier concentration is lower, as can be observed in figure 4.6a – possibly because of charge carrier being funnelled towards the two contacts or the gate, and therefore the overall change in carrier concentration is lower for $L > 14\mu m$.

The simulated accumulation and recombination times is shortest for a small channel length, and increases slowly with increasing L , as shown in figure 4.6d and 4.6e respectively. This is because the field directly beneath the graphene is weaker with increasing L as the contacts, which are essentially ground, are further apart, and therefore the charge carriers are accelerated less towards/away from the graphene. One notes a difference of a factor 10^3 in the timescale of the accumulation time and relaxation time respectively; if the simulated relaxation time could be improved, then the potential count rate could be improved from ~ 10 kHz to ~ 10 MHz.

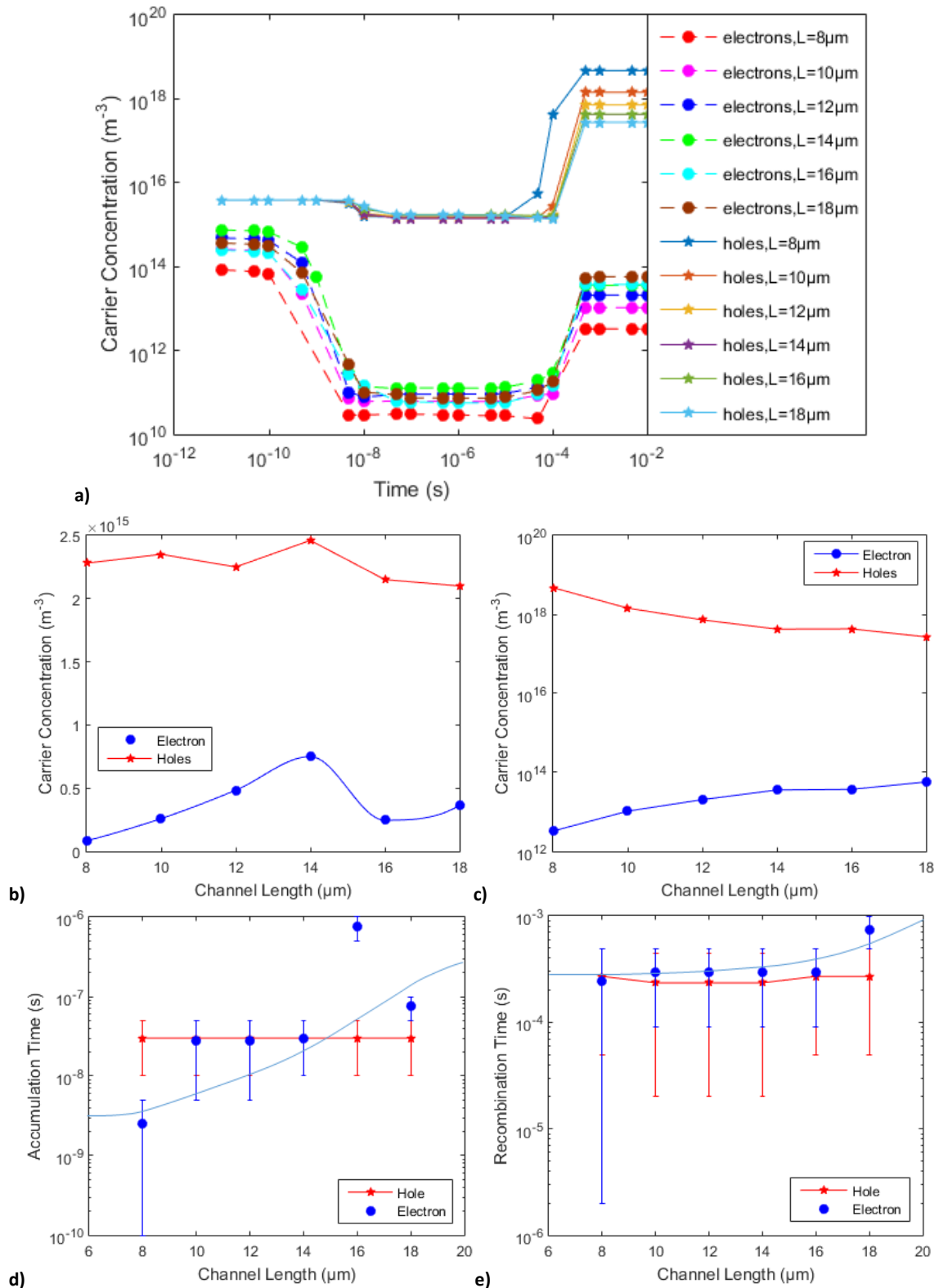


Figure 4.6, showing a) the charge carrier concentration beneath the graphene as a function of time and channel length. B) shows the absolute change in carrier concentration between the initial and accumulated states as a function of channel length, and c) shows the final carrier concentration as a function of channel length, which show a peak concentration for $8\mu m$ (holes) and $18\mu m$ (electrons). D) shows that the accumulation time for both electrons and holes is reduced for small channel lengths, and e) shows that the recombination time for electrons occurs for $L < 16\mu m$ with little change for the hole recombination time as a function of channel length.

4.3.1.2.5 Optimal Behaviour

The most sensitive detector would be one where the fewest number of charge carriers induces the largest magnitude field on the graphene. Simulations earlier in this chapter, such as figure 4.4c, show that the charge carriers under a gate voltage funnel towards the graphene and are position independent. The simulations in chapters 4.3.1.2.3 and 4.3.1.2.4 show how the dynamic range and temporal bandwidth can be optimised by considering the gate voltage and channel length, as stated in table 4-1.

| Parameter | Wanting to Optimise | E/H? | Where is it optimised? |
|--|---------------------|-----------|---|
| Gate Voltage (for $L = 10\mu\text{m}$) | Temporal Bandwidth | Electrons | Accumulation time shortest for $V_G \neq 0V$ Recombination time shortest for $V_G \sim 0V$ |
| | | Holes | Accumulation time shortest for $V_G > 0V$ Recombination time shortest for $V_G \sim 0V$ |
| | Dynamic Range | Electrons | $V_G \neq 0V$ |
| | | Holes | $V_G \neq 0V$ |
| Channel Length (for $V_G = 10V$) | Temporal Bandwidth | Electrons | Accumulation + recombination times shortest for $L \sim 8\mu\text{m}$ |
| | | Holes | Accumulation time constant $\sim 30\text{ns}$ Recombination time constant $\sim 300\mu\text{s}$ |
| | Dynamic Range | Electrons | Greatest change in carrier concentration between initial and accumulated state for $L = 14\mu\text{m}$ |
| | | Holes | Greatest change in carrier concentration between initial and accumulated state for $L = 8\mu\text{m}$ and $L = 14\mu\text{m}$ |

Table 4-1, summarising how the gate voltage and channel length can be used to optimise the temporal bandwidth and the dynamic range.

The temporal bandwidth is optimised by finding the quickest accumulation and recombination times for both holes and electrons as a function of V_G and channel length L . The shortest accumulation times occurred at $V_G > 0V$ for both carrier types, and the shortest recombination time occurred at $V_G \sim 0V$, as previously discussed. The optimal length to minimise the accumulation and recombination times was $L \sim 8\mu\text{m}$ for electrons, and was approximately constant as a function of length for holes.

To obtain the best dynamic range, a field needs to be established to funnel charge carriers, and therefore $V_G \neq 0V$. The greatest change in carrier concentration between the initial and accumulated states, and therefore the best dynamic range, occurred in the range $8 \leq L \leq 14\mu\text{m}$ for both electrons and holes.

These simulations suggest that the channel length optimises the dynamic range and temporal bandwidth for $L \sim 8-14\mu\text{m}$, with benefits to operating the detector for

$V_G \neq 0V$. With a greater magnitude gate voltage, the accumulation time of charge carriers beneath the graphene decreases. As the gate voltage is also controlling the channel conductivity, a dual gated arrangement may be worthwhile as it would enable independent control of the channel conductivity and the absorber dynamics.

4.3.2 Improving the Bandwidth: Considering a GDEPFET Arrangement

One of the restrictions arising from the research by the Jovanovic group with regards to X-ray photodetector applications is the very slow decay time of the initial signal arising from the large energy transfer from the X-ray photon, which can lead to charge build up/saturation and a loss of resolution. They propose a graphene depleted field effect transistor (GDEPFET) arrangement to speed up the signal and hence improve the operating bandwidth [74].

Their proposed structure uses an n-type Si substrate, with graphene acting as the channel that would usually be in the silicon for a standard FET. Ion implantation is used to form a well beneath the graphene channel to more effectively gather charge carriers together, which maximises the field applied to the graphene and hence the change in conductivity via the field effect. The charge carriers are then swept out by applying a clear voltage, V_{clear} , of order 150V, which in their simulations gives a ~ 5 order of magnitude change in the decay time of the electron concentration in the well, allowing a route to improved temporal bandwidth of the detector. A clear voltage $\sim 150V$, however, raises concerns about the stability of the device, with the potential that this may damage the gate dielectric.

In this section, the viability of a GDEPFET-like structure is discussed. The effect of applying $V_{clear} \sim 10-20V$ to the absorber is presented with regards to the accumulation and recombination time, initially in a structure based on that discussed in ref. [74], and then in a simpler GFET structure more like that discussed in section 4.3.1.2.2.

4.3.2.1 GDEPFET Arrangement

Using COMSOL simulation software, the arrangement based on that proposed in ref. [74] was built, with a schematic shown in figure 4.7a. To clear the charges, ref. [74] provided values for the voltages applied to each contact: $V_{drain} = -2.5V$, $V_{source} = -0V$,

$V_{back} = -0V$ and $V_{graphene} = -1V$. This is simulated and gives the expected equipotentials, as shown in figure 4.7b.

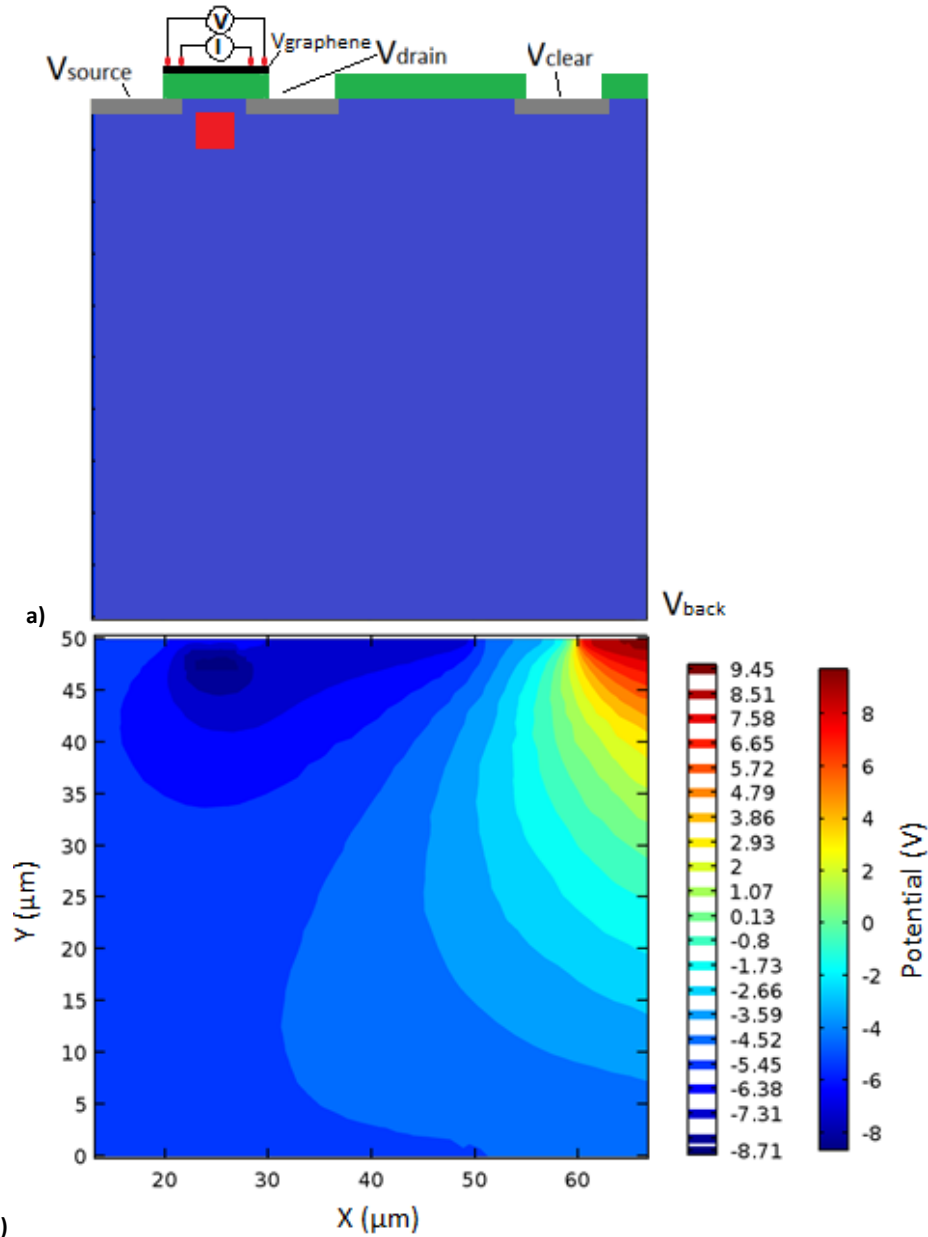
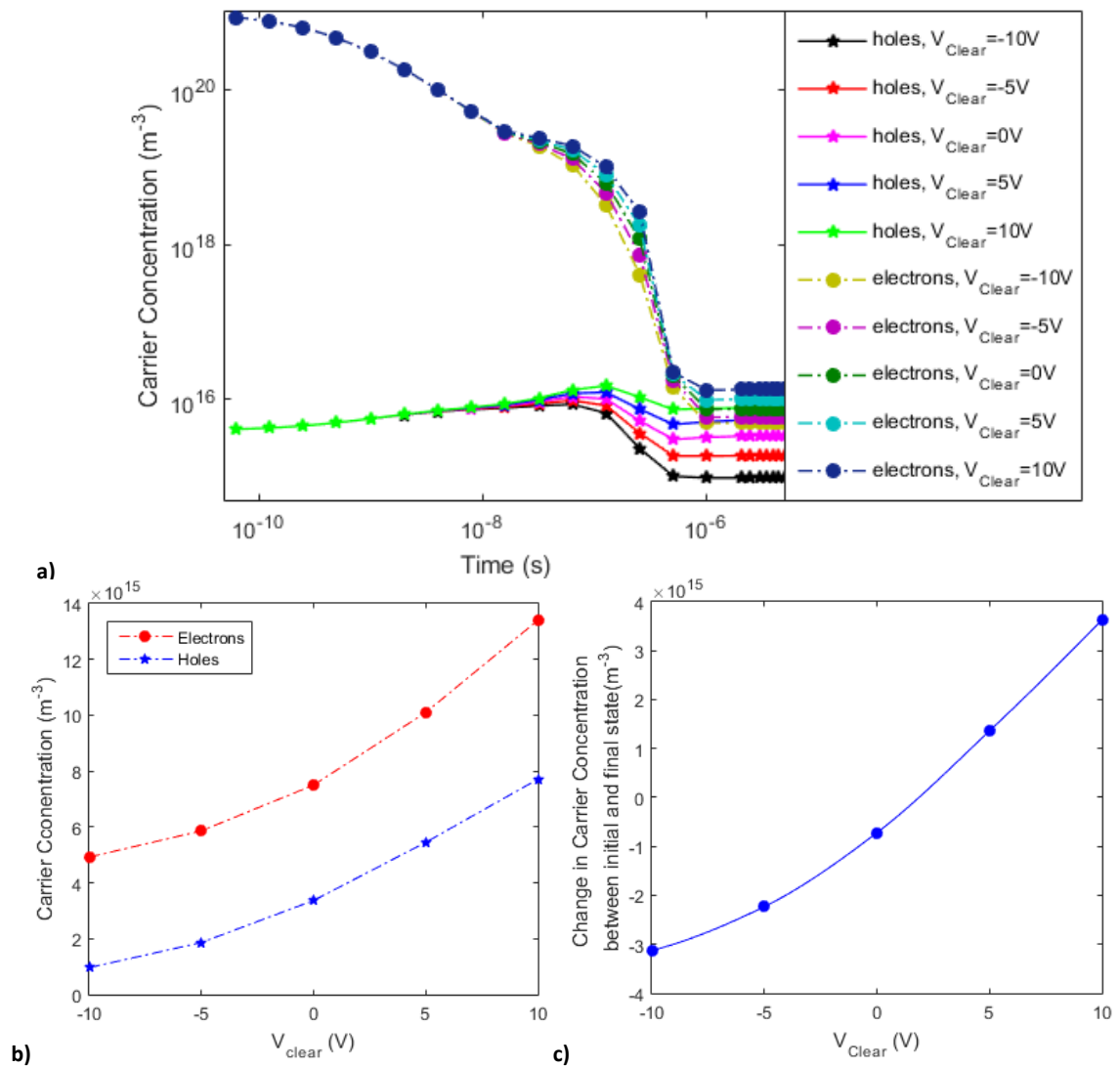
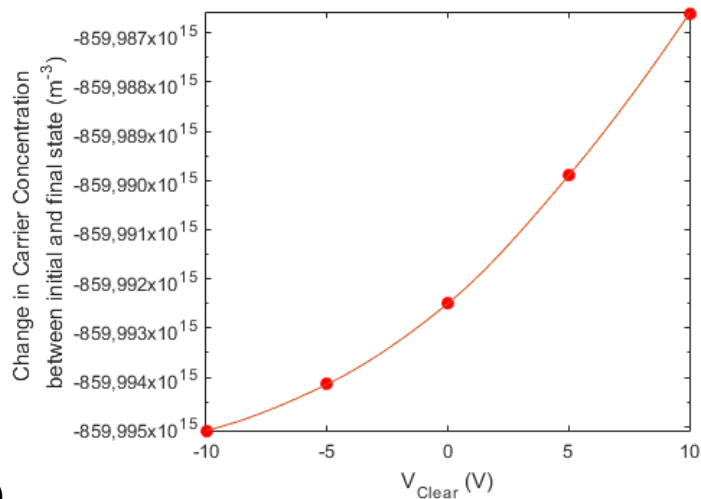


Figure 4.7 showing a) the proposed GDEPFET device architecture [74], with an n-well, shown as the red box, generated directly beneath the graphene and a clear contact to remove the charge carriers, and b) the electric potential of the detector design as simulated in COMSOL and also shown in ref. [74].

Firstly, the parameters specified in ref. [74] were used to investigate the change in the electron concentration in the centre of the well, with a donor trap density of $10^{21}m^{-3}$ and an initial electron concentration of $10^{21}m^{-3}$ to ensure the well is heavily n-type, as discussed in ref. [74]. V_{clear} took values of $0V$, $\pm 5V$ and $\pm 10V$. Figure 4.8a shows that V_{clear} reduces the charge carriers in the well, with little change in the time taken to reach the equilibrium concentration. However, the addition of V_{clear} does change the

final equilibrium concentration, with a lower final electron concentration for $V_G < 0V$, figure 4.8b, which suggests a better dynamic range due to a greater change in concentration. The overall change in hole concentration between the initial and final states is greatest for $V_{clear} \neq 0V$, figure 4.8c, because of the field that V_{clear} establishes to funnel charge carriers out of the well. In figure 4.8d there is a near uniform change in the electron carrier concentration, which might be expected given the four order of magnitude change in the electron concentration seen in figure 4.8a, and the final simulated value of the carrier concentration shown in figure 4.8b.





d)

Figure 4.8 showing a) the change in electron and hole concentration for different values of V_{clear} , and b) the final simulated carrier concentrations for electrons and holes as a function of V_{clear} . C) shows the change in hole carrier concentration between the initial and final concentrations as a function of V_{clear} , with the smallest magnitude change for $V_{clear} \sim 0V$, an increase in the hole concentration for $V_{clear} > 0V$ and a decrease for $V_{clear} < 0V$. D) shows the equivalent change in electron carrier concentration as a function of V_{clear} , with a very slow relationship between the change in carrier concentration and V_{clear} , especially given the greater than four order of magnitude change in the carrier concentration.

The carrier concentration also changes with respect to the initial carrier concentration in the centre of the well, which was analysed for $V_g = V_{clear} = 10V$, figure 4.9a. Irrespective of the initial charge carrier density, electrons and holes tend towards the same final concentration, but with different relaxation times, figure 4.9a. A well carrier density of $10^{21}m^{-3}$ relaxes in up to $5\mu s$, which leads to a theoretical upper temporal bandwidth of 200kHz. A lower density of $10^{16}m^{-3}$ relaxes within $\sim 10ns$, figure 4.9b, which corresponds to a temporal bandwidth of $\sim 100MHz$.

However, an initial well density of $10^{16}m^{-3}$ corresponds to a decrease in the well density by a factor of ~ 2 , as opposed to a factor 10^4 decrease for an initial well density of order $10^{20}m^{-3}$, figure 4.9a. A smaller change in the well density results in a smaller change in the field applied to the graphene channel, resulting in a smaller change in the channel conductivity and a smaller dynamic range.

The relaxation time of the detector is, therefore, strongly related to the number of charge carriers in the well; with a smaller initial well density, the detector relaxes quicker but with a compromised dynamic range. A greater charge carrier density in the well can be achieved with a more energetic incident photon, as a higher energy is required to generate more charge carriers. Assuming 100% of the generated charge

carriers are funnelled into the well and an average ionisation energy, W , for silicon equal to 3.6eV, a photon energy of 81keV is required to give a 10^{20}m^{-3} carrier density in a $5\mu\text{m} \times 5\mu\text{m} \times 5\mu\text{m}$ well.

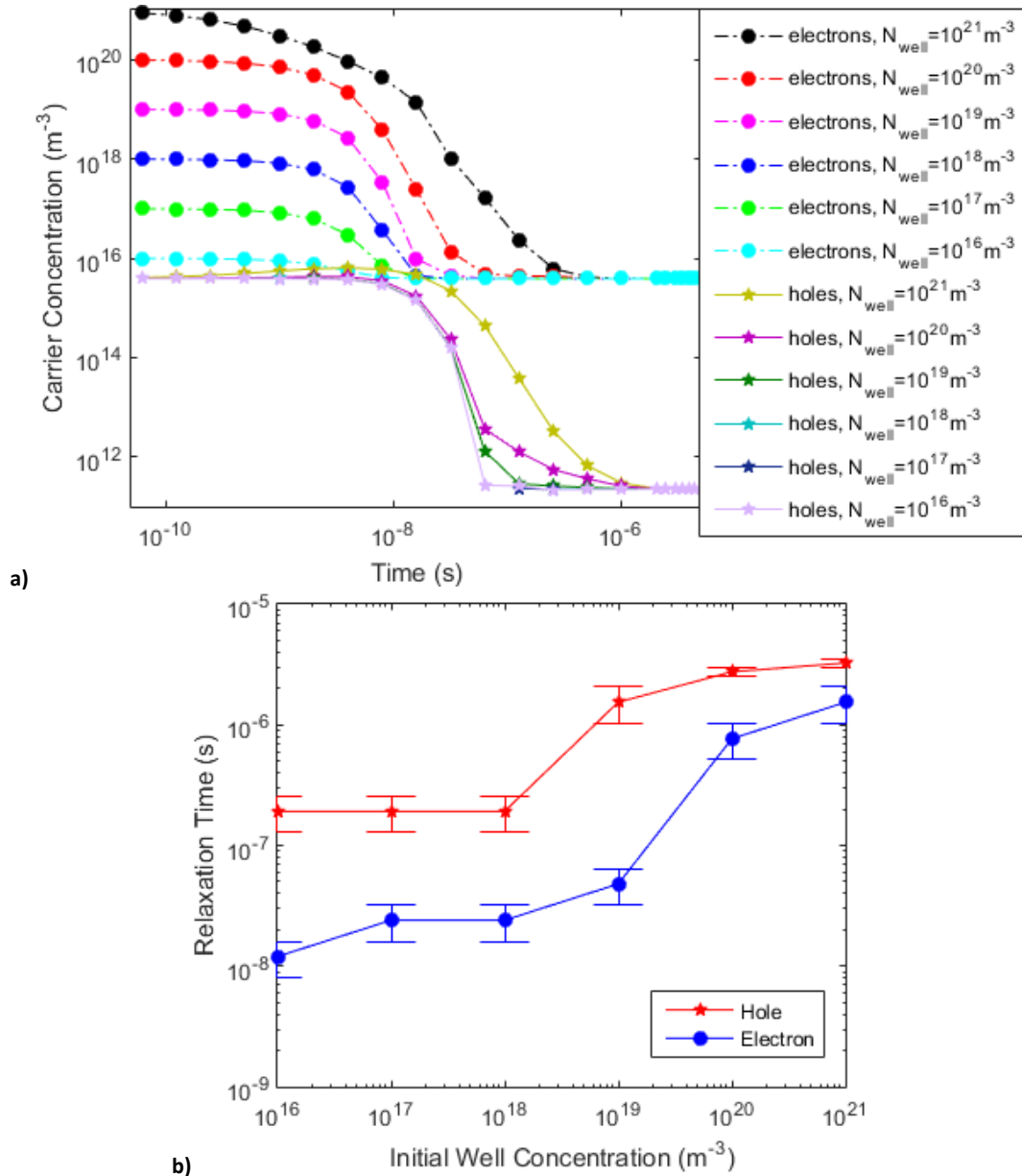


Figure 4.9, showing a) the change in the carrier concentration over time for different initial well concentrations, and b) the charge carrier relaxation time as a function of initial well concentration, with a quicker relaxation time for lower well concentrations.

The gate voltage applied to the silicon wafer can also be varied; in the previous section the gate voltage was seen to drive the relaxation time, so there is scope for the clear voltage to be omitted and just the gate voltage used to clear the well.

The clearing of the well was simulated over time for several different gate voltages, figure 4.10a. The simulations suggest that the gate voltage drives both the final

concentration in the well and the relaxation time. The final concentration is lowest for $V_G < 0V$ for both electrons and holes, figure 4.10b, and therefore the dynamic range is greatest.

The electron and hole relaxation times were also calculated to be of order a few μs , figure 4.10c. The hole relaxation time was shortest for $V_G \sim 0V$, in agreement with figure 4.5c, because there is no field to funnel the charge carriers. For $V_G \neq 0V$, holes were accelerated towards/away from the well, the carrier density is greater and therefore it takes longer to recombine. For the electrons, the shortest relaxation times arise for $V_G > 5V$, such that electrons are accelerated towards the gate voltage and away from the well.

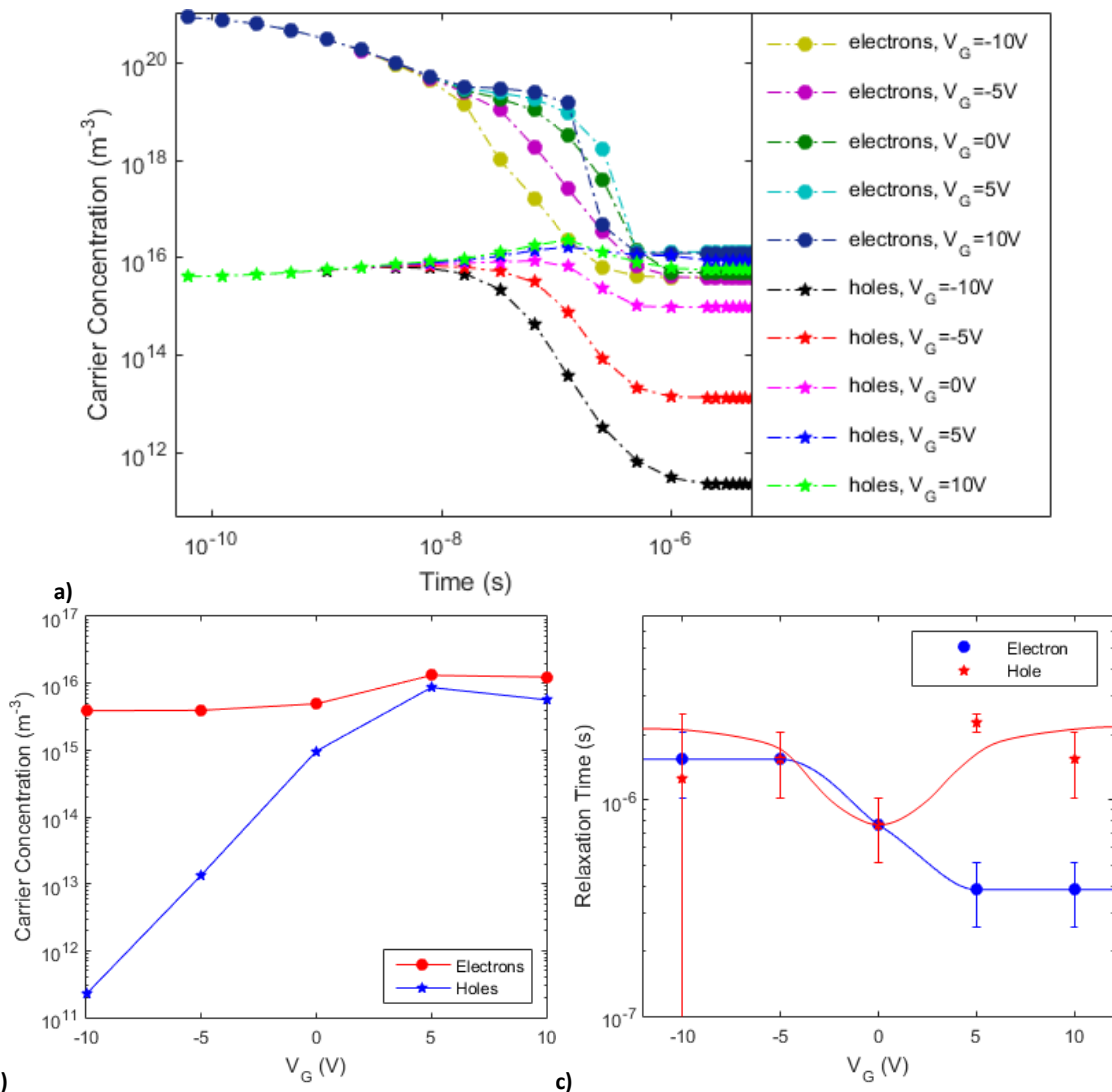


Figure 4.10, showing a) how the gate voltage reduces the carrier concentration without the need for V_{clear} , b) that the final carrier concentration for both electrons and holes is minimised for $V_G < 0V$, and c) that the carrier concentration is minimised for holes and maximised for electrons for $V_G \sim 0V$. Therefore, the well is cleared in approximately $1\mu s$.

For the fastest detector, a low concentration of charge carriers in the well would give the fastest relaxation time, but this sacrifices the dynamic range because it corresponds to a smaller change in the well density, as shown previously in figure 4.9a. To obtain a greater dynamic range, a more energetic incident single photon is required. However, assuming the well can be filled to the necessary carrier density, simulations suggest that a good compromise between the dynamic range and the shortest time to clear the well is obtained when the detector is operated with $V_G \sim -5V$.

4.3.2.2 A GFET with V_{clear}

The same simulations were repeated for a slightly different schematic, figure 4.11a, which more closely resembled the GFET detector, and again included a well generated by ion implantation. In “clear” mode, this was simulated for V_{clear} and V_{source} from 0V to $\pm 10V$, $V_{source} = 0.01V$, and $V_{drain} = 0V$, with equipotentials shown in figure 4.11b.

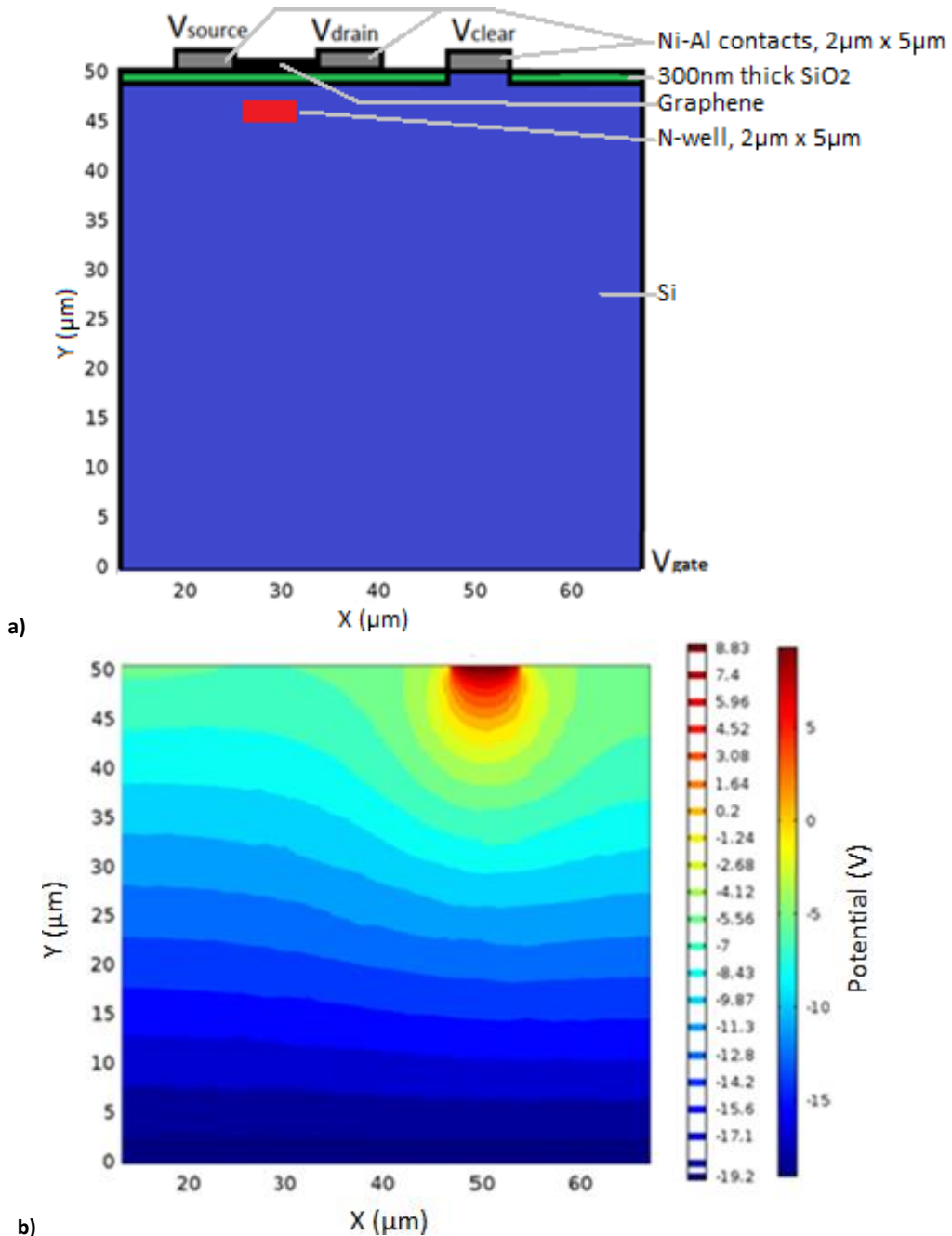


Figure 4.11 showing a) the schematic closer to what was eventually fabricated, with the Si gate shown in blue, the SiO₂ absorber shown in green, the n-well shown in red and Ni-Al contacts shown in grey, and b) the equipotentials as simulated in COMSOL for $V_{clear}=10V$ and $V_{gate}=-15V$.

By changing the value of V_{clear} , for $V_{gate} = 10V$, the intention is again to clear the well as efficiently as possible. V_{clear} was varied to investigate the change in carrier concentration over time, figure 4.12a, with the simulated hole concentration peaking and then returning to approximately the initial value. For both electrons and holes, the recombination time is shortest for $V_{clear} > 2.5V$, figure 4.12b, while the greatest change in hole concentration occurs for $V_{clear} < -10V$, as shown in figure 4.12c.

The recombination time shown in figure 4.12b is ~ 100 times faster than observed in figure 4.6e. As discussed in the previous section, in the well the donor trap density was defined as 10^{21}m^{-3} , with an initial electron concentration of 10^{21}m^{-3} such that the well was heavily n-type [74]. Unlike previous sections, in these simulations charge carriers are confined within this well. Therefore, when $V_{clear} > 0\text{V}$ is applied, holes will be swept towards the well and electrons towards the V_{clear} gate. This will cause the electrons and holes to recombine much quicker, causing the recombination time to be shorter than simulated without the well.

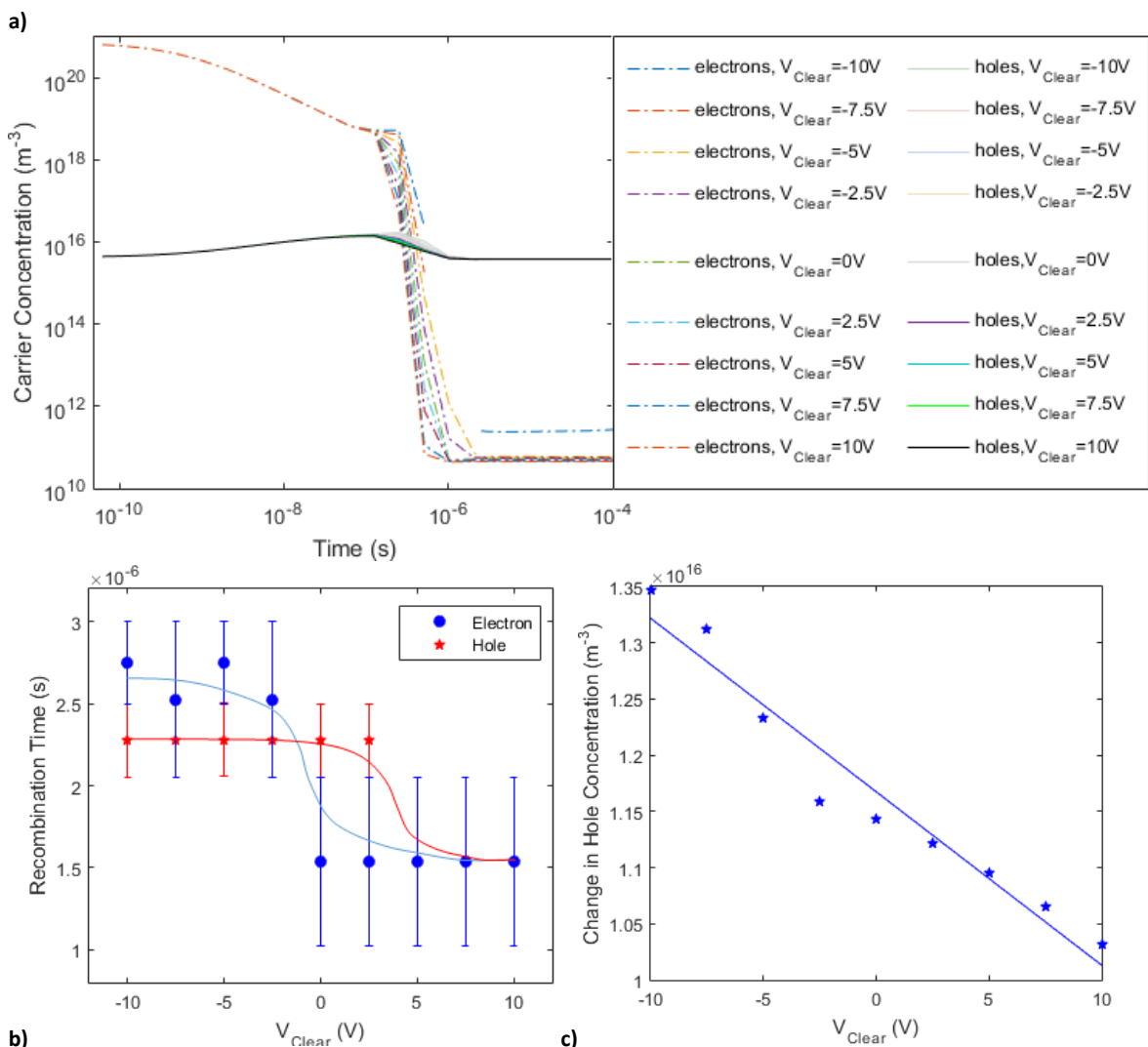


Figure 4.12 showing a) the change in carrier concentration over time for different values of V_{clear} , b) that the recombination time is minimised for $V_{clear} \sim 2.5\text{V}$, and c) that V_{clear} is related to the change in hole concentration, and is maximised for $V_{clear} < -10\text{V}$.

The gate voltage can be used to replicate the effect of the clear voltage; for these simulations, $V_{clear} = 0\text{V}$, and the gate voltage alone drives the charge carrier concentration as a function of time, figure 4.13a. The recombination time is estimated

from figure 4.13b of order $1\mu\text{s}$ and longest for $V_G \sim 0\text{V}$, which is expected as this means there is no field to funnel the charge carriers away from the well. This is a factor 10 faster than was observed without the presence of a well, e.g. figure 4.6e. Furthermore, the dynamic range of the relaxation was estimated, and figure 4.13c shows that the greatest dynamic range was seen for $V_G < 0\text{V}$.

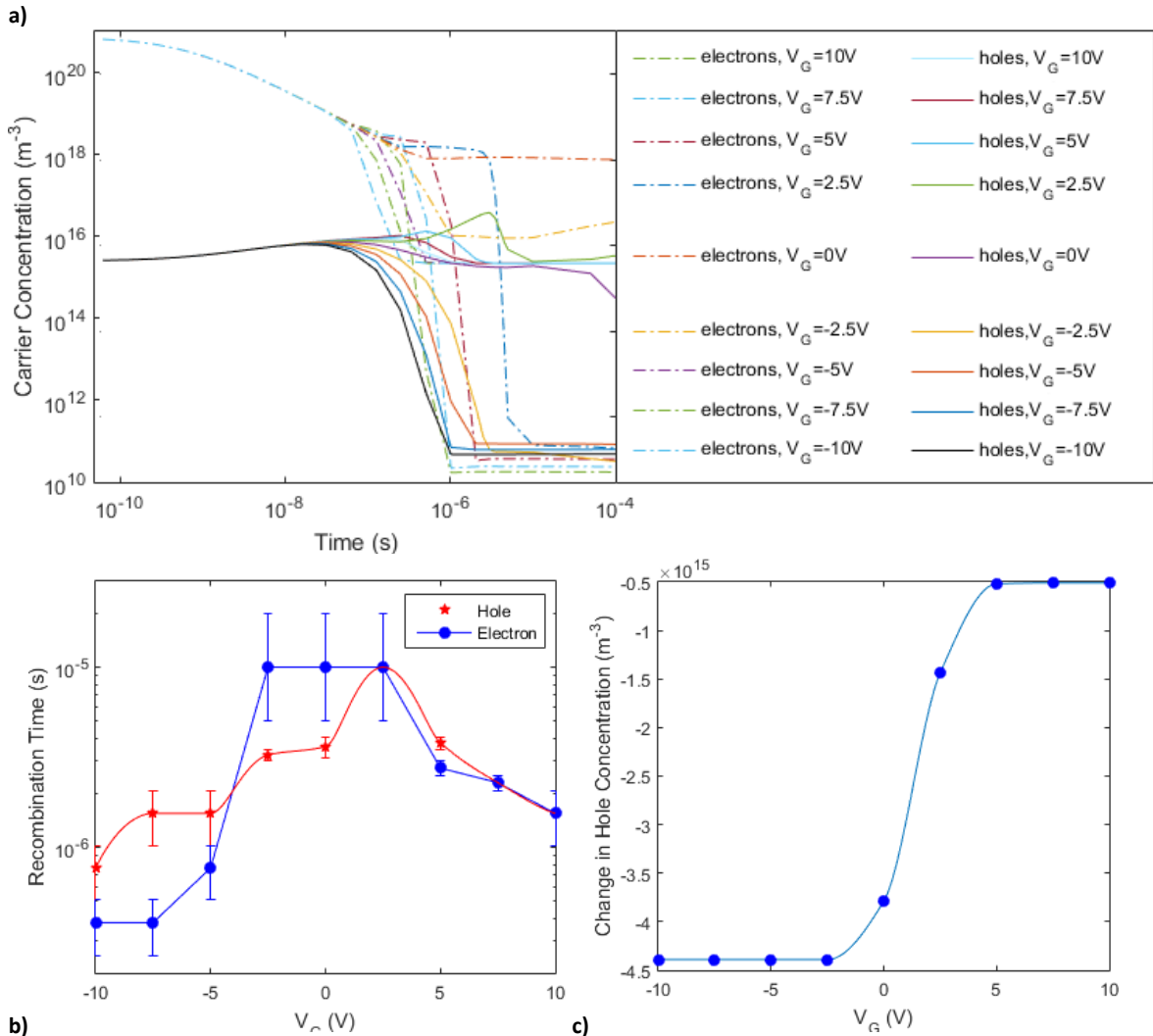


Figure 4.13 showing a) the change in carrier concentration over time for different gate voltages, b) that the recombination time is longest for $V_G \sim 0\text{V}$ for both electrons and holes, and c) that the change in hole concentration is maximised for $V_G < 0\text{V}$.

To improve the detector sensitivity, one was required to maximise the number of charge carriers beneath the graphene, and to improve the bandwidth the charge carriers need to be extracted as quickly as possible. These simulations show that, by constraining charges beneath the graphene within a well and clearing these by applying a voltage, the temporal bandwidth could be improved by a factor ~ 100 . Furthermore, simulations show that any voltage can affect the charge carrier

recombination time, which need not necessarily be a secondary voltage source applied to the absorber in addition to V_G .

However, the addition of a well through ion implantation as well as direct metallisation onto the silicon through the dielectric vastly increases the cost and complexity of the device. Through device optimisation, including geometry and materials, it may be possible to improve the simulated bandwidth without the need for some form of V_{clear} or ion well. For instance, simulations have demonstrated some dependence on V_G , so a dual-gated system could enable variation in both the graphene channel conductivity and bandwidth without the added complexity of a further metallisation onto the graphene and/or an ion implantation-generated well.

4.3.3 Optimising the Gate Structure: Top and Dual Gated Options

To improve the sensitivity of the GFET, charge carriers are “funnelled” towards the graphene by applying a gate voltage, with the field across the dielectric independent of the initial absorption location. The gating also controls the conductivity of the graphene channel. The device could be arranged with either a back gate, as proposed by the Jovanovic group, a top gate [168], or as a back- and top-dual-gated structure [169], figure 4.14.

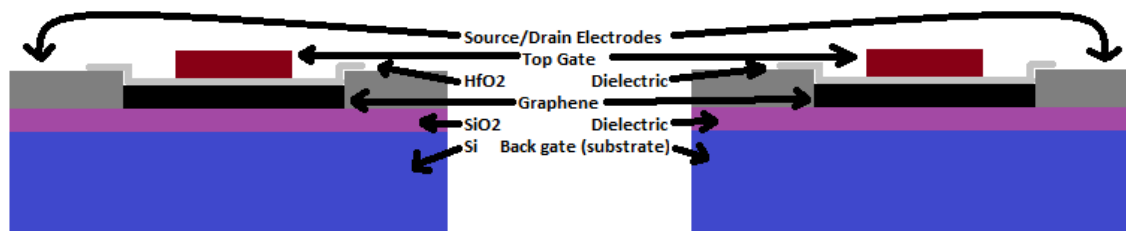


Figure 4.14 showing schematics for a top gated GFET proposed in ref. [168] (left) and a top and bottom gated device proposed in ref. [169]. Both structures are essentially the same and could be used in both arrangements.

A top-gated GFET structure was proposed in ref. [168]. This detector demonstrated high transconductances, current saturation, $I_{on}/I_{off} \sim 7$ and top gate and bottom gate capacitances of 552nFcm^{-2} and 12nFcm^{-2} respectively whilst operating at 1.7K [168].

Another possible structure is the dual, top and bottom, gated GFET proposed in ref. [169], where the back gate develops a two-dimensional electron gas in the graphene

layer, whilst the top gate controls the Fermi level by changing the magnitude and polarity of the applied potential. This allows for greater control over the depletion region in the silicon and the conductivity of the graphene independently. This top and bottom gated structure is also used to open a band gap in bilayer graphene [65], as discussed in chapter 2.

4.3.4 Optimising the Dielectric: Transport Simulations

A dielectric is required to prevent leakage of charge carriers from the gate to the drain; this dielectric material is typically silicon dioxide, with a thickness of order 300nm. Other materials have been used as the dielectric in graphene field effect transistors such as aluminium oxide, which has a high gate capacitance and “self-healing” ability through oxidation in air or annealing [76] [170], and PZT which has enabled higher carrier mobility up to $7 \times 10^4 \text{cm}^2 \text{Vs}^{-1}$ for few layer graphene [171]. Other exotic dielectrics have been proposed, such as an ion gel for use on a plastic substrate to enable a flexible detector [172].

Some of the components of the detector can be iterated to improve the likely carrier transport properties, such as the dielectric constant and substrate thickness. Initial simulations to determine the conductivity,

$$\sigma = \frac{e^2}{\hbar} \frac{2E_F \langle \tau \rangle}{h}, \quad \text{Equation 4.1}$$

replicating those from ref. [9] are shown in figures 4.15a and 4.15c. In this case, E_F is the Fermi energy,

$$\langle \tau \rangle = \int d\epsilon_k \epsilon_k \tau(\epsilon_k) \left(-\frac{df}{d\epsilon_k}\right) / \int d\epsilon_k \epsilon_k \left(-\frac{df}{d\epsilon_k}\right), \quad \text{Equation 4.2}$$

$f(\epsilon_k)$ is the Fermi distribution function, ϵ_k is the energy,

$$\frac{1}{\tau(\epsilon_k)} = \frac{\pi}{\hbar} \sum_{a, \vec{k}'} n_i^{(a)} \left| \frac{v^{(a)}(q)}{\epsilon(q)} \right|^2 (1 - \cos^2 \theta) \delta(\epsilon_k - \epsilon_{k'}), \quad \text{Equation 4.3}$$

\vec{k} is the momentum, $q = |\vec{k} - \vec{k}'|$, $n_i^{(a)}$ are the densities of the different scatterers, θ is the scattering angle between the wave vectors \vec{k} and \vec{k}' , and

$$v(q, d) = 2\pi e^2 \exp(-qd) / \kappa q \quad \text{Equation 4.4}$$

where κ is the dielectric constant, $\epsilon(q)$ is the RPA dielectric screening function and d is the scattering distance from the graphene in Angstrom. A greater conductivity is realised for a scattering distance deeper in the absorber because of a reduction in the number of coulomb scatterers, figure 4.15a, and hence a greater n/n_i ratio, figure 4.15c, where n is the number of charge carriers and n_i is the impurity density.

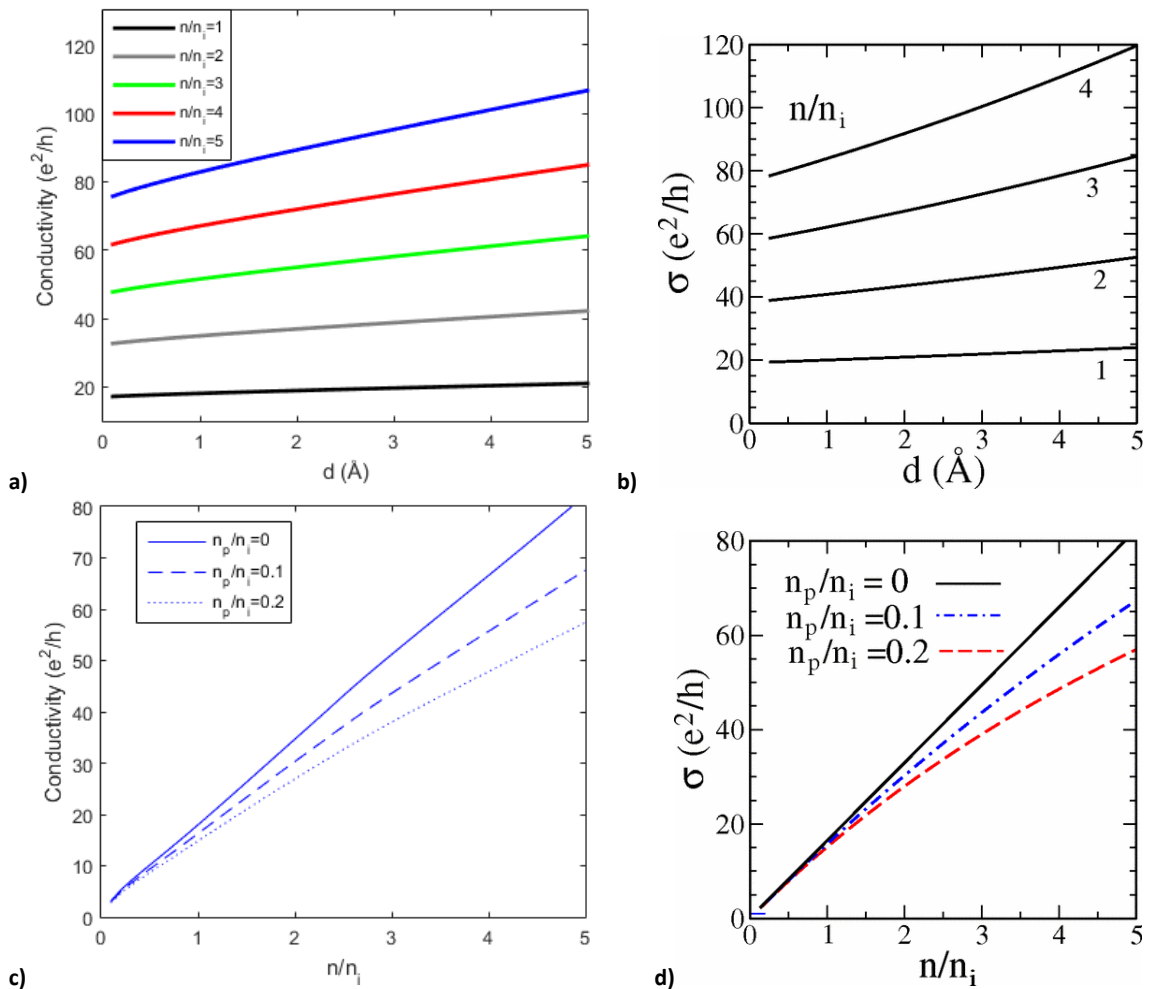


Figure 4.15, showing a) the relationship between conductivity and d for different ratios of n/n_i , where n_i is the impurity density. This shows good agreement with figure 2 from ref. [9], which is shown in figure 4.15b, especially for low n/n_i and d . C) shows the relationship between conductivity and n/n_i for different point scattering densities n_p , which shows the same behaviour and order of magnitude of the conductivity compared to figure 3 from ref. [9], shown in figure 4.15d. Both figure 4.15b and figure 4.15d are reproduced from ref. [9] under copyright licence from the American Physical Society.

The simulations were extended from those in ref. [9] to consider how the conductivity varies as a function of other parameters including gate voltage, dielectric constant and

dielectric thickness. The Fermi level in equation 4.2 was varied by applying a gate voltage. For a given thickness, in this simulation equal to 300nm, the highest conductivities are obtained for the highest dielectric constants, as shown in figure 4.16a. Meanwhile, for a given dielectric constant – in this case the dielectric was assumed to be SiO₂ – the highest conductivities were realised for the thinnest dielectric, with a weak non-linearity as a function of gate voltage, figure 4.16b.

The theoretical mobility of the graphene was crudely estimated via the gradient of the data in figure 4.16a. This is not a 100% reliable estimate as other factors limit the mobility of the graphene, including surface scattering due to the substrate and the grain size of the synthesised graphene. These simulations, for a dielectric thickness of 300nm and a dielectric constant of 3.8, gives a mobility of order $4 - 5 \times 10^4 \text{cm}^2 \text{V}^{-1} \text{s}^{-1}$.

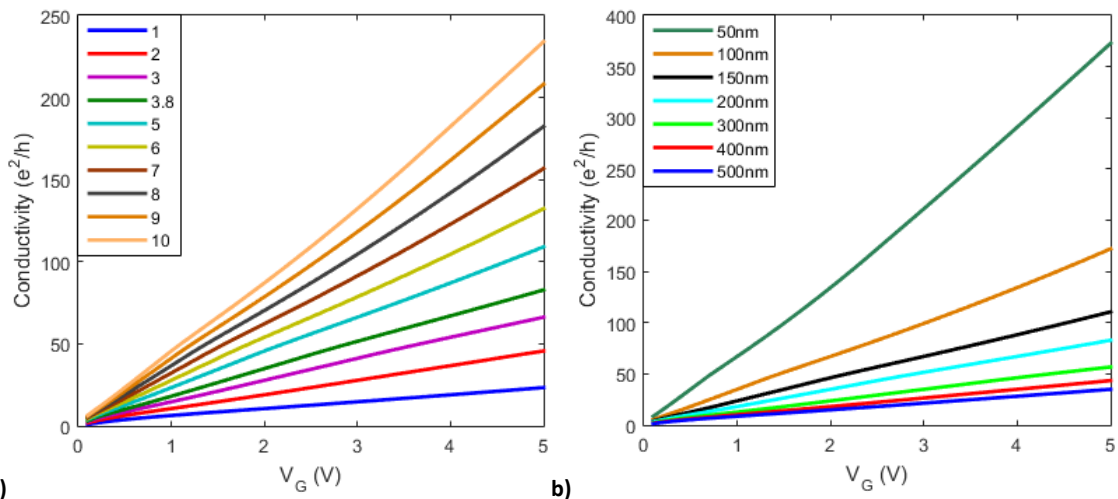


Figure 4.16 showing the relationship between conductivity and gate voltage for different a) dielectric constants (for a thickness of 300nm) and b) thicknesses of the dielectric (for $\epsilon=3.8$). For the best conductivity, these simulations suggest a high dielectric constant and/or a thin substrate is preferable.

The results from these simulations show how the design of the detector influences the transport properties of the graphene. It shows how the expected conductivity increases for greater dielectric constants and for thinner dielectric thicknesses; it also shows a linear relationship with gate voltage. In the following section and chapter, the design and manufacture of the detector on a Si wafer with a 300nm thick SiO₂ dielectric due to the ease and cost of fabrication and manufacture is presented. However, assuming forthcoming improvements in the fabrication process, results in this section enable further consideration of future design opportunities that improve the transport characteristics of the graphene FET.

4.4 Prototype Device Design

As previously discussed, the design of the detector was optimised for improved behaviour of the detector by considering elements such as the absorber material, the dielectric material and thickness, and the size of the graphene channel.

The choice of absorber is related to the energy of the incident photon and the intended operational environment. For this detector, an appropriate geometry was required such that the absorption of photons is efficient and effective, and the charge build up in the absorber decays as quickly as possible to enable good temporal bandwidth. A 0.5mm thick p-type silicon absorber with a resistivity of $\sim 100\Omega\text{cm}$ (dopant density of order $\sim 10^{14}\text{cm}^{-3}$) was selected as it is readily available and allows for a good compromise between absorption of low energy X-ray photons and dark noise, is opaque to X-ray energies up to 10keV as shown in figure 4.17, and provides well-refined routes to device manufacture.

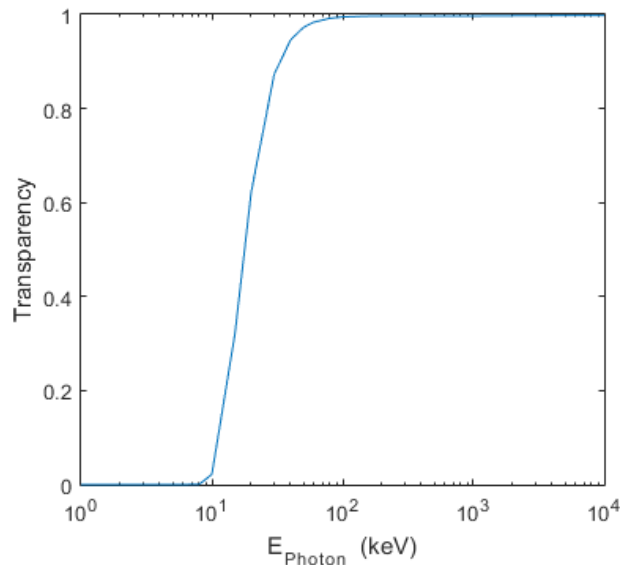


Figure 4.17, showing the transparency of a 0.5mm thick silicon wafer as a function of the incident X-ray photon energy, which shows that it is 100% opaque to energies up to 10keV, and 100% transparent at energies above 100keV.

The choice of dielectric thickness and material affects the transport properties; for this detector a very high mobility was desirable to realise an ultrafast detector. The thickness and material of the insulating dielectric layer, which prevent charge carriers from leaking from the absorber into the graphene channel but affects the mobility of

the charge carriers in the graphene, was selected as 300nm thick SiO₂, as this is the most commonly available dielectric for a Si wafer.

Simulations have shown the effect of the size of the graphene on the temporal bandwidth and dynamic range of the detector. Initial simulations showed that the largest voltage occurred beneath the smallest graphene sample – a larger voltage applies a larger field and therefore potentially resulting in a greater change in the channel conductivity, enabling a more sensitive detector. Further simulations showed that a channel length of approximately 8-14μm leads to optimal carrier concentration beneath the channel with improved detection times.

In summary, the detector was designed on a Si substrate with $\rho \sim 100\Omega\text{cm}$, with a 300nm thick SiO₂ insulating layer. The graphene channel, using CVD grown graphene transferred onto the Si wafer, was of different sizes from 5μm x 10μm up to ~50μm x 100μm. These were connected to nickel-aluminium source and drain pads, as shown in figures 4.18; nickel providing low contact resistance with the graphene and aluminium for better wire bonding. Simulations have, however, motivated other options such as different absorbers and different dielectric parameters.

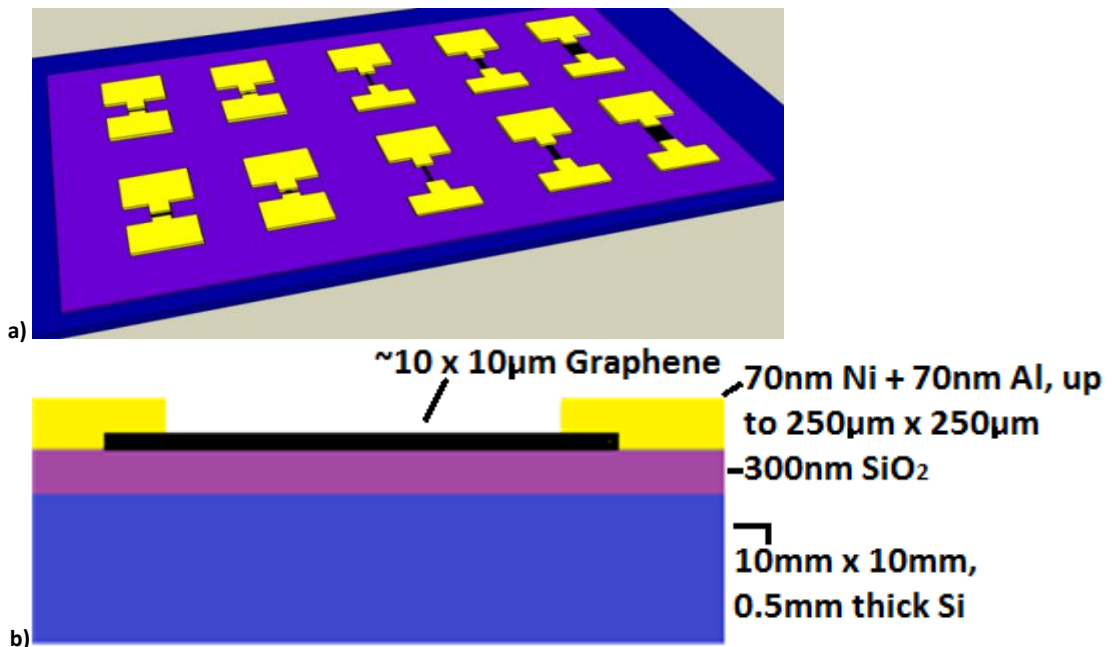


Figure 4.18 showing a) and b) the design of an X-ray GFET test device. Blue is Si, light purple is SiO₂, yellow is the Ni-Al contact and black is the graphene of different channel sizes for each device.

4.5 Summary

In this section, the concept of a graphene field effect transistor for X-ray photon detection was introduced, and compared this to the current state of the art from research by the Jovanovic group which are not suitable for single X-ray photon detection.

Several components of the detector have been simulated, including the absorber material and the thickness and material of the dielectric. While the detector was designed on a Si substrate with a 300nm SiO₂ dielectric, simulations suggested that thinner dielectrics and greater dielectric constants provide routes for improved transport properties, which may enable a thin alumina dielectric to give improved performance in the future. These simulations indicate future routes to manufacture may include CZT or thicker Si wafers that may improve X-ray photon absorption and reduce dark noise. Simulations have also shown how a smaller graphene channel size gives benefits with regards to dynamic range and temporal bandwidth.

To improve the temporal bandwidth, a GDEPFET-like structure was simulated to investigate the benefit of a charge carrier well generated through ion implantation and an additional voltage source to clear charges from the absorber. While benefits were observed from simulations, other options are available to iterate the device design that are less complex and costly.

The design of the detector, arising from the simulations in this chapter, was then manufactured. This will be discussed in the next chapter.

5 Device Fabrication Techniques and Manufacturing

5.1 Introduction

In chapters 2, 3 and 4, simulations for the bilayer graphene single photon counting photodetector, the passive terahertz photodetector and the single X-ray GFET photodetector were developed to understand the likely behaviour, and optimise the design, of each detector.

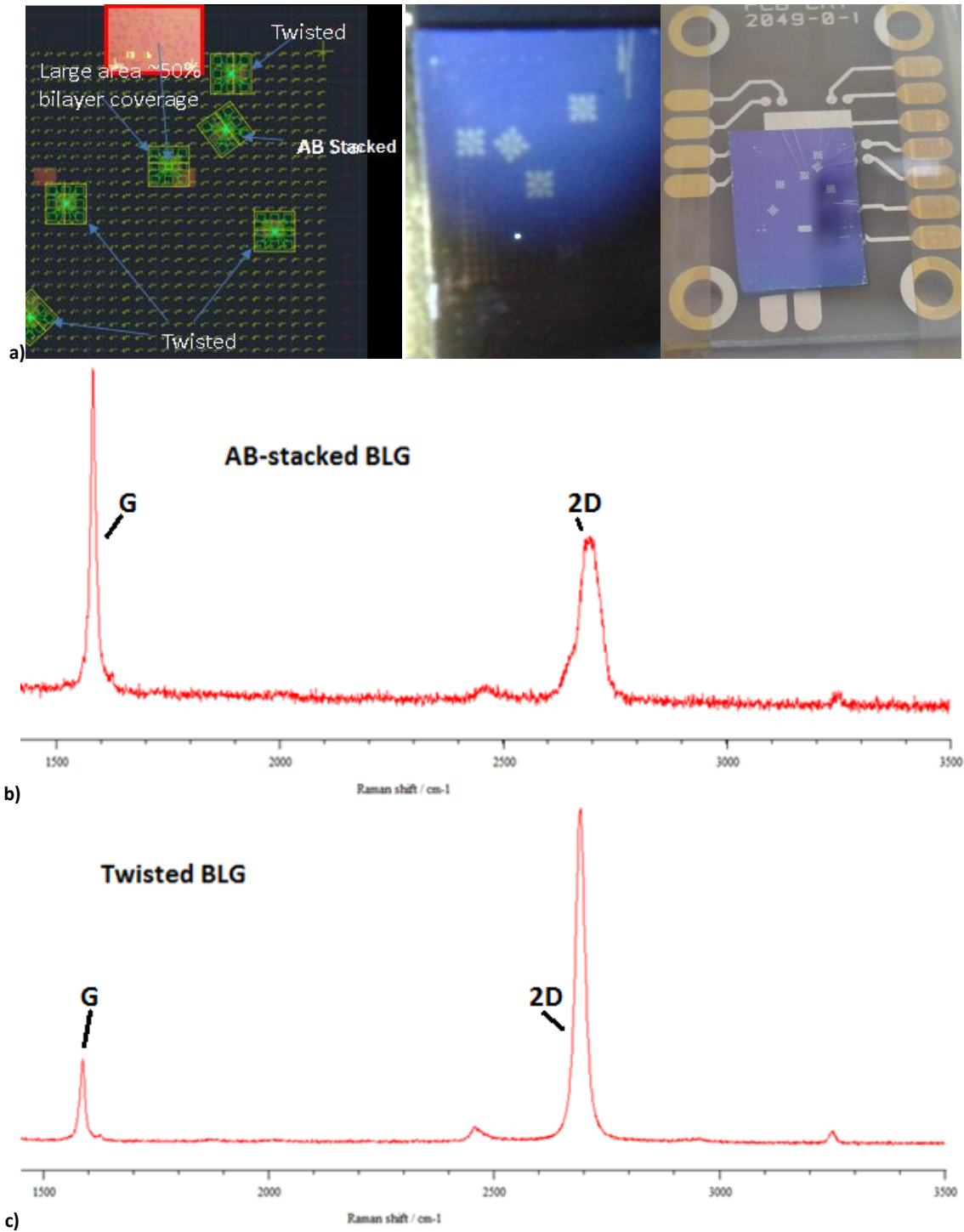
This chapter discusses the fabrication of each of these devices at the Centre for Advanced Photonics and Electronics (CAPE) at the University of Cambridge using state of the art equipment and techniques, as well as the critical procedures for all stages of fabrication, including graphene synthesis and transfer, lithography and encapsulation. The manufacturing process was completed in three phases, each of approximately 3-4 weeks, in the autumn of 2015. Most of Phase I was spent being trained on the different techniques, while Phases II and III were spent fabricating and iterating the devices.

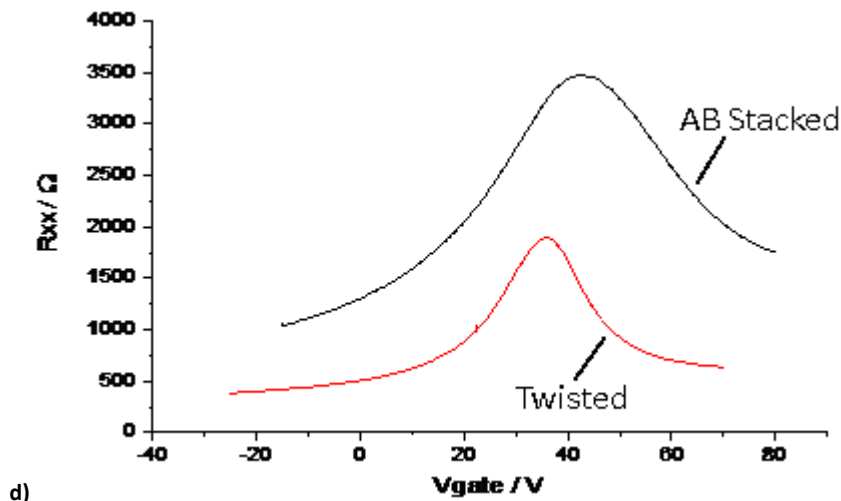
Some of the work outlined in this section was published in ref. [2].

5.2 Fabrication, Phase 0

Prior to the start of the manufacturing process a GFET device was manufactured at the University of Cambridge and delivered to the University of Leicester to allow for an initial test of the experimental setup. The device had samples of AB- and twisted-stacked, CVD-grown, bilayer graphene on a Si/SiO₂ substrate, figure 5.1a; the final device required an alumina substrate and an ITO top gate to also be deposited on the device. The AB- and twisted-stacked bilayers were identified through Raman spectroscopy, figures 5.1b and 5.1c respectively. The channel resistance as a function

of gate voltage was characterised for both the AB- and twisted-stacked bilayer graphene samples, figure 5.1d, by applying $V_{sd}=0.01V$ between the source and drain and measuring the current for different gate voltages.





d) Figure 5.1, showing a) the layout of the bilayer graphene on the chip manufactured by the University of Cambridge, and b) and c) the Raman spectra for the AB-stacked and twisted stacked bilayer graphene samples, respectively. Analysis of the low Raman shift modes allow for differentiation between the AB- and twisted modes, while the samples shown in b) and c) show the characteristic G, 2D and D peaks [173]. D) shows the resistance-gate voltage relationship of the AB- and twisted-stacked bilayer graphene samples, with a $V_{Dirac} \sim 40V$ for the AB-stacked, and $V_{Dirac} \sim 35V$ for the twisted-stacked. The Raman spectra and resistance measurements were made by researchers at the University of Cambridge.

5.3 Device Fabrication Processes

The fabrication of a graphene-based device requires many different processes and techniques. Most of the techniques are well refined, but a significant amount of ongoing research aims to better understand these processes with a view to potential industrial application. In this section, some of the key processes for graphene device fabrication are outlined, and the key areas of research are identified.

5.3.1 Graphene Growth

There are many ways to synthesise a graphene sample, including micromechanical exfoliation, chemical vapour deposition (CVD) and epitaxial growth. Each one of these has advantages and disadvantages, especially with regards to graphene coverage, stacking, homogeneity and future commercial application. The requirements for a device present constraints and challenges on the route to synthesising graphene, so the most appropriate way of obtaining the graphene must be considered.

5.3.1.1 Micromechanical Exfoliation

Micromechanical exfoliation is the original technique used to isolate graphene by Geim and Novoselov in 2004. This technique uses tape to “peel apart” the layers of graphite

to form graphene [174]. Repeated peeling allows control of the number of layers of the sample. The sample is pressed against the required substrate and binds via van der Waals interactions [175]; it can then be used in electronic applications.

This technique provides easy, cheap and reliable access to graphene flakes and has been widely used experimentally to explore the properties of single-crystalline graphene and related device structures on the nano- to micrometre scale [176]. Whilst these samples are relatively easy to obtain, the samples commonly have poor homogeneity [176], and other techniques fulfil the industrial demands for quality. It is also difficult to scale these beyond dimensions of order centimetres [177]. This technique is therefore an unlikely candidate for future commercialisation and industrial use.

5.3.1.2 Epitaxial Growth

Epitaxial growth of graphene involves the thermal decomposition of high-quality silicon carbide wafers [177] [178] [179] [180] [181] at high temperatures, often over 1000°C [178] [179] [180], and in an atmosphere, such as a vacuum or argon, to control the Si sublimation process [182]. Research is ongoing to reduce the temperature required for epitaxial growth by exploiting the catalytic conversion of sp^3 carbon to sp^2 carbon in sp^2 carbon rich substrates such as SiC and Fe-mediated diamond [183] [184].

The synthesis of epitaxial graphene is well refined and has generated high quality samples that are suitable for electronic applications [177]. The growth creates an intercalated buffer layer between the SiC and graphene, which is large enough to be used as an insulator at room temperature allowing for the manufacture of SiC-graphene gate electronics directly [181]. For Si-face SiC, the hydrogenation of the buffer layer can yield an additional graphene layer [185] [186] [187].

Epitaxial growth is therefore a promising candidate for future reproducible, industrial-scale, graphene synthesis. However, the necessity for high temperature and low pressure in the growth may limit the commercial outlook for epitaxial growth graphene on cost grounds, and because it allows no flexibility in the substrate which is limited to 4" high quality SiC.

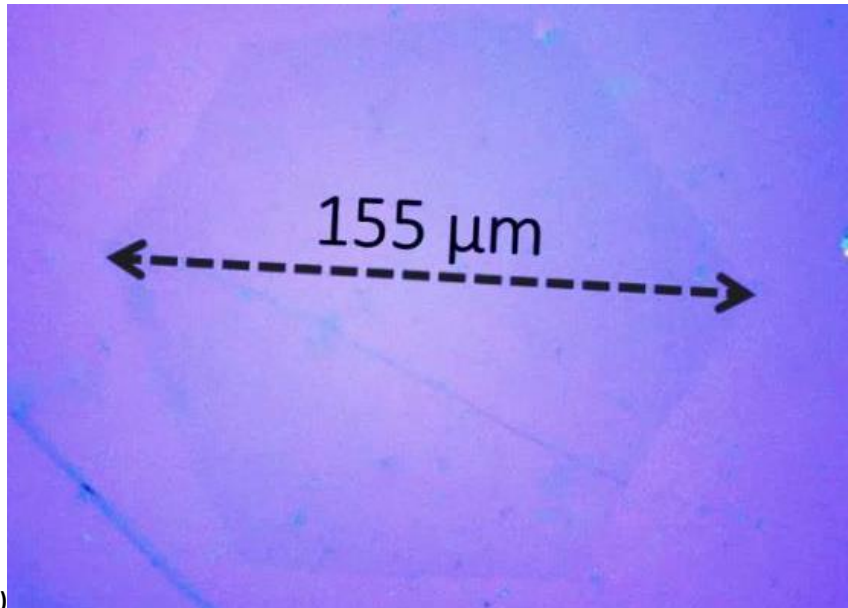
5.3.1.3 Chemical Vapour Deposition

CVD has emerged as an excellent technique to scalably and economically synthesise high quality graphene [176] [188] [189], hexagonal boron nitride (hBN) and transition metal dichalcogenide (TMD) films such as MoS_2 and WS_2 [176] [190] [191] [192] [193] [194] [195], as well as offering routes to the direct growth of 2D heterostructures [196] [197] [198].

In the CVD process, a planar catalyst with high carbon solubility [176] is exposed to a hydrocarbon in an inert atmosphere at a constant temperature, typically 650-1100°C [177] [199], so the carbon nucleates on the surface of the catalyst. The catalyst is typically a transition metal such as Cu, Ni, Co and Pt, or semiconductor surfaces such as Ge [200] [189] [201]; these substrates may enable improved homogeneity, growth cost reductions [201], substrate reuse [189], and quicker growth [202]. An improved understanding of CVD growth mechanisms [176] [200] [203] [204] has already enabled single-crystal domains of order centimetres to be grown, figure 5.2a.

CVD-grown AB-stacked graphene bilayer films with a grain size of order 100s of microns grown on Cu via oxygen activation has recently been reported [205] [206]. A grain of bilayer graphene $>100\mu\text{m}$ that is readily achievable by CVD, figure 5.2b. However, further understanding of the growth mechanism for bilayer graphene is required to obtain larger grain sizes [207] [208].





b) Figure 5.2 showing the optical micrograph of a) an individual domain of mm sized CVD grown single layer graphene on Cu, produced by a researcher at the University of Cambridge, and b) a single 155 μm grain of bilayer graphene on an SiO_2/Si substrate.

Variation in the parameters involved in the CVD process, such as growth time, catalyst pretreatments and precursor pressures, enables control in the number of layers and the grain size of bilayer islands [176], and can introduce twisting angles between the graphene layers. Multilayer islands are thought to grow from the substrate, with an initial layer growing and then additional layers penetrating through the sheet and growing underneath the single layer around a nucleation point, figure 5.3 [209].



Figure 5.3. The difference in graphene growth for single layer, bilayer and trilayer graphene, showing growth underneath the single layer sheet.

For high quality bilayer graphene samples, it is possible to obtain mobility of $60000\text{cm}^2\text{V}^{-1}\text{s}^{-1}$ at 1.7K when encapsulated between boron nitride flakes [205]; this competes with results for exfoliated bilayer graphene with grain sizes of $\sim 10\text{s}$ of μm [122]. However, the growth of bilayer graphene using techniques other than CVD may provide benefits with regards to device reproducibility and scalability.

For these devices, single layer and AB-stacked bilayer graphene samples are required. The graphene samples were grown via CVD on untreated copper foils at the University of Cambridge using a reactor where the temperature and pressure of the vessel can be controlled.

5.3.2 Transferring Graphene onto a Substrate

Several techniques allow for the transfer of graphene films from the growth substrate (e.g. Cu) onto the required substrate (e.g. Si) [210] [211] [212]. A common technique used for CVD graphene grown on a copper foil (figure 5.4, stage 1) begins by spin coating the graphene/copper with poly(methyl methacrylate) (PMMA) (figure 5.4, stage 2). Graphene grows on both sides of the copper, but preferentially on the top side as this side is exposed to the hydrocarbon source; the graphene grown on the back side of the copper is removed by oxygen plasma for ~10 seconds.

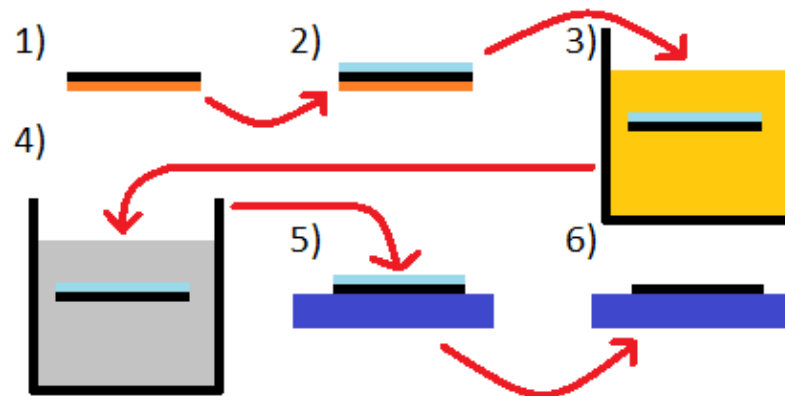


Figure 5.4. The process for the graphene transfer. The process stages are: 1) Graphene (black) is grown on copper (orange), 2) PMMA (light blue) is spin coated onto the sample (3000revs for 30s and baked for 90 seconds at 180 degrees), 3) The back side of the copper is oxygen plasma etched, and then it is placed in an iron chloride bath (yellow) to etch away, 4) This is transferred into a water (grey) bath, 5) This is then transferred onto the silicon wafer before drying and baking for 5 minutes at 150 degrees, and 6) The PMMA is then washed away.

The PMMA+graphene+Cu is then placed in an FeCl_3 bath for approximately 30 minutes (stage 3) to etch away the copper from the PMMA+graphene – it can take longer if the graphene was not fully etched from the reverse side of the copper, and may be sonicated to remove any non-uniformity in the etching. After the etching step, the PMMA+graphene is a floating film which is transferred to a deionised (DI) bath on a glass slide (stage 4). The PMMA+graphene is then transferred to a second DI bath, and

from there is picked up on a silicon wafer (stage 5). The sample is left to dry in ambient conditions, briefly baked, and washed in acetone and IPA (stage 6).

5.3.3 Patterning using Electron Beam Lithography and Photolithography

At different stages in the fabrication process the device needs to be masked, for instance to etch the graphene or to deposit contacts. This requires a photoresist to be spin coated onto the sample, the mask to be etched through e-beam lithography or photolithography, and then for the photoresist to be developed.

5.3.3.1 Spin Coating

To spin coat, one of the photoresists is placed onto the sample and is spun for approximately 40 seconds at 3000revs before being baked at a specific temperature for a given time, table 5-1. This prebaking is to activate a catalyst in the photoresist. The spin coater and hot plate are shown in figure 5.5.

| Photoresist | Prebake temperature/degrees Celsius | Prebake time/seconds |
|-------------|-------------------------------------|----------------------|
| UVIII | 120 | 120 |
| PMMA | 180 | 90 |
| MAN | 90 | 60 |
| AZ MLOF | 110 | 60 |

Table 5-1. Prebaking temperatures and times for the most common photoresists.

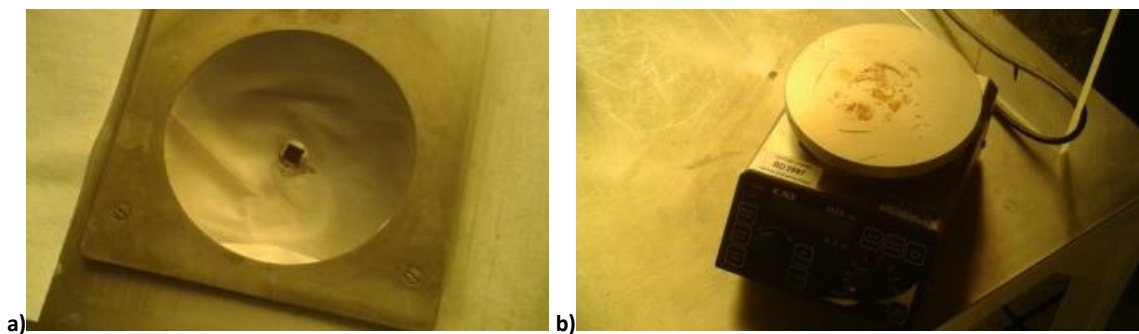


Figure 5.5 showing a) the spin coater and b) the hot plate.

5.3.3.2 Electron Beam Lithography

E-beam lithography uses an electron beam to expose photoresist to a design, with a typical nanometre scale resolution, which is then developed. To begin the electron beam lithography process, the chip is placed in the chip holder, figure 5.6b, which is placed inside the Nanobeam e-beam lithography equipment, figure 5.6c, and the air

lock pumped down to a pressure $\sim 10^{-7}$ mbar when the chip can then be loaded. Before the process starts, the chip is aligned using the in-built SEM; the alignment must be done quickly to prevent accidental development of the photoresist. The patterning process takes approximately 5 minutes for a typical simple device with a beam current of 11nA with UVIII photoresist, and of order hours for the same design for a device with a PMMA photoresist, as PMMA requires a lower beam current.

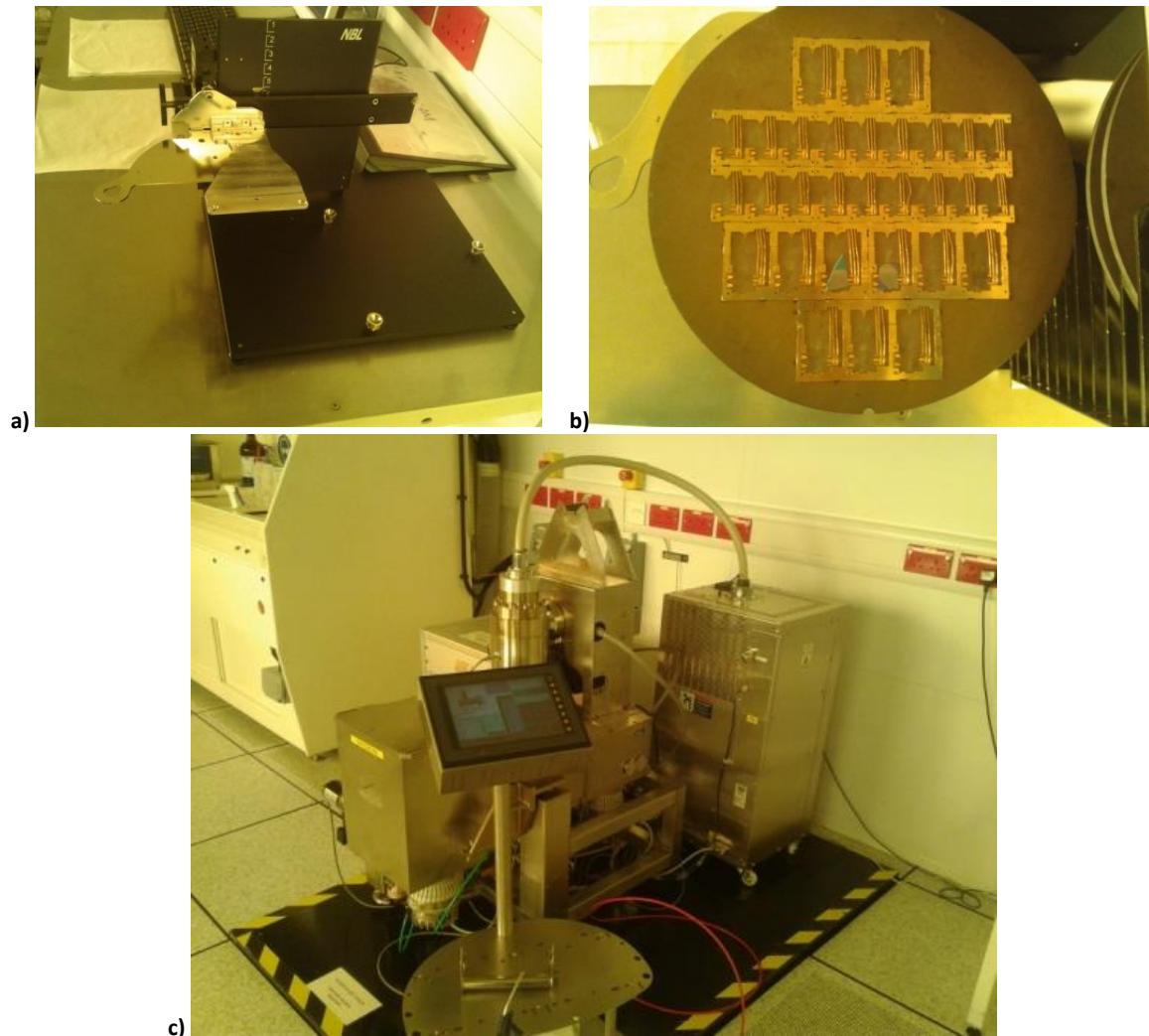


Figure 5.6 showing a) the chip holder rack, b) the chip holder and c) the Nanobeam equipment at the University of Cambridge.

5.3.3.3 Photolithography

An alternative to electron beam lithography is photolithography. Photolithography is a much quicker process, but allows considerably less flexibility in the design as it requires a physical mask to be manufactured. It works by using a physical mask that is developed by exposing the sample to an intense light source for ~ 7 s.

5.3.3.4 Post-Baking and Development

After the lithography step, the sample may need to be postbaked and/or developed depending on the photoresist used, table 5-2. The postbaking step activates the catalyst in the photoresist. To develop the sample, it is placed in a specific developer for a given time, and then into water before being dried in nitrogen. When the photoresist is successfully developed, it often turns purple when viewed under a microscope with no holes or non-uniformity in the colour.

| Photoresist | Postbake Time (s) | Postbake Temperature (°C) | Developer | Development Time (s) |
|-------------|-------------------|---------------------------|-----------------------|----------------------|
| UVIII | 45 | 120 | MFCD26 | 45 |
| PMMA | N/A | N/A | 1:3 MBIK:IPA then IPA | 10 |
| MAN | N/A | N/A | 1:4 AZ351B:water | 60 |
| AZ MLOF | N/A | N/A | AZ351B | 30-60 |

Table 5-2. List of the postbake temperatures and times for some common photoresists, and the detailers of which developer to use.

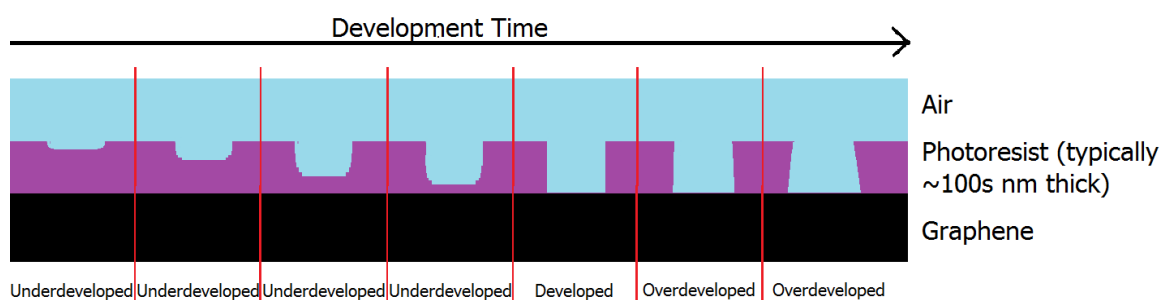


Figure 5.7, showing the importance of development time to ensure correct development of the sample, in this case for a positive photoresist. Each photoresist will have an ideal development time, as outlined in table 5-2. Developing the sample for a time less than this will underdevelop the sample, and for a time greater than this will overdevelop the sample.

Positive photoresists work by becoming soluble to a specific developer when it is exposed during the lithography step [213] [214]. During the development process, the developer is then used to remove areas that have been exposed. As shown in figure 5.7, the time of the development is crucial to correct masking: too short time and it will be underdeveloped and any future process (e.g. masking) will be lifted off when placed in acetone/IPA, or if it is developed for too long then too much of the photoresist will be removed, called “undercut”, which may cause more of the sample to be exposed. Overdevelopment is especially problematic where metallisation is densely packed, where undercuts could join up and could result in issues such as electrical shorts.

Equivalently, negative photoresists become less soluble when they are exposed during the lithography step, so essentially harden to protect the sample [214]. The development process then removes areas that have not been developed, ready for the next process such as etching.

5.3.4 Deposition

Two methods for deposition were used in this project, evaporation and sputtering.

5.3.4.1 Evaporation

Deposition through evaporation relies upon a high current passing through a filament and pot with a metal that vaporises and coats everything, including the sample that is to be covered.

The thermal evaporator used for this process, commonly referred to as the “Blue Evaporator”, figure 5.8a, was bespoke and built at the University of Cambridge. A sample is placed inside the chamber shown in figure 5.8a, and then a diffusion pump cooled with liquid nitrogen is used to reduce the chamber pressure to 10^{-6} mbar. This promotes cleaner deposition of the material onto the wafer, and improved binding to the wafer because of the greater mean free path of the vaporised atoms. A current, of order several amps, is passed through a ceramic vessel containing the material to be evaporated. The ceramic pot glows, as shown in figure 5.8b, before the metal melts and then vaporises.

The shutter initially covers the chip to prevent any contaminants coating the device, and then the shutter is removed and the deposition begins to slowly coat the sample. Deposition directly onto the Edwards FTM5 film thickness monitor, figure 5.8c, allows direct control of the thickness of the deposited material. After deposition, the chamber is vented with nitrogen, and the samples are removed, figure 5.8d.



Figure 5.8 showing a) the bespoke diffusion pump thermal evaporator, locally known as the Blue Evaporator, b) the vessel with the current causing it to glow, c) the Edwards FTM5 film thickness monitor, and d) the chip, coated in an evaporated fold film, held on by Capton tape.

5.3.4.2 Sputtering

An alternative method to deposit a metal is sputtering, which works by generating a plasma, with the resulting ion accelerated into a metal target to liberate atoms that coats the sample. Sputter coating is a route to better binding between the metal and the surface because the coating atoms have higher energy than for evaporation.

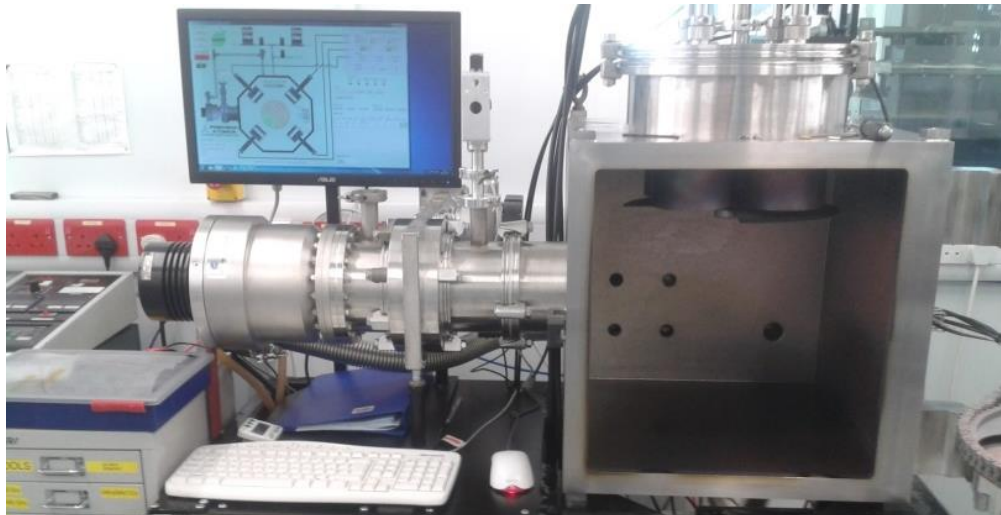


Figure 5.9. The Precision Atomics Metallifier Sputter Coater at the University of Cambridge.

The required targets are mounted in a metal sputter coater, such as the Precision Atomics Metallifier [215], figure 5.9, and then the vessel is pumped down to a pressure $\sim 10^{-6}$ mbar. Depending on the required target, the chamber pressure, argon flow rate, beam energy, presputter time and sputtering time must all be selected, table 5-3. The beam energy indicates the energy to generate the plasma and excite the argon ion into the target. The presputter time and sputter times are related to the time to clear contaminants off the target with the shutter in place and to deposit to the correct thickness respectively. After the deposition is complete, the device is cooled before the vessel is vented.

| Metal | Chamber Pressure (mbar) | Argon Flow Rate (sccm) | Beam Energy (W) | Presputter Time (s) | Sputter Time |
|--------------|--------------------------------|-------------------------------|------------------------|----------------------------|--------------------------------|
| W | 3.5×10^{-3} | 32 | 100 | 600 | 400s for 50+nm |
| Ni | 2.5×10^{-3} | 20 | 100 | 600 | 423s for 50nm 494s for 70nm |
| Al | 3.5×10^{-3} | 32 | 100 | 300 | 300s for 39nm |
| ITO | 3.2×10^{-3} | 40 | 50 | 500 | 1500s for 157nm |

Table 5-3. Sputter parameters for different metals.

5.3.5 Lift-Off

A lift-off step removes the metal deposition from areas of undeveloped photoresist, figure 5.10a, by placing the sample in acetone. The acetone loosens the bond between the soft, undeveloped photoresist coated with the metal and the layer beneath. Air is bubbled through a pipette onto the sample to lift the metal off; a “good lift-off” is one where no residue is left on the chip and the metal is removed in large chunks, figure

5.10b. After all metal chunks are removed, the chip is transferred into IPA and then dried.

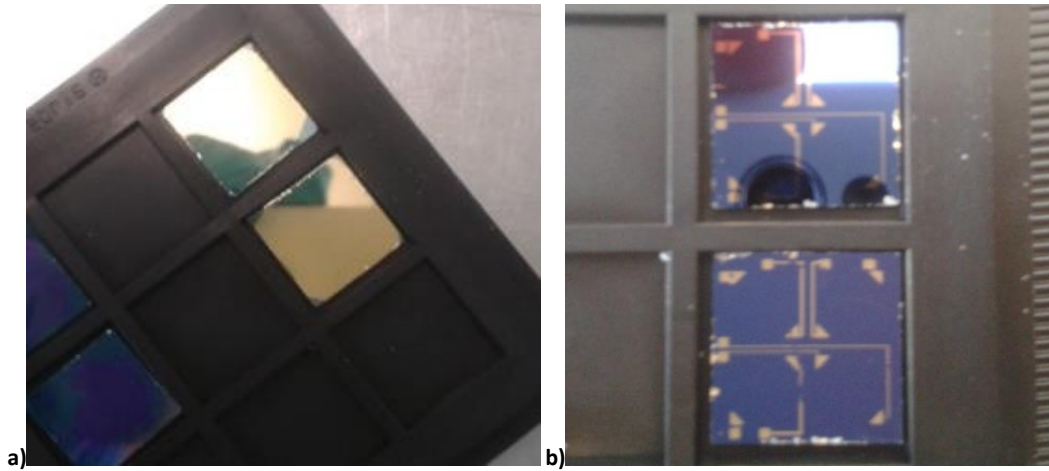


Figure 5.10, showing samples a) before and b) after the lift-off process.

5.3.6 Encapsulation via Atomic Layer Deposition (ALD) of Alumina

The charge carrier mobility and reproducibility of electrical measurements of the graphene can be affected by contaminants in the environment adsorbing onto the sample. Graphene operating in ambient conditions causes adsorption onto the graphene and Si/SiO₂ interface creating traps that affect charge carriers transport [68]. When the device is gated, there is a noticeable difference in the current on the “upsweep”, going to greater gate voltages, and the “downsweep”, returning to the initial gate voltage, with two observable Dirac points; this is known as gate hysteresis [73], shown in figure 5.11.

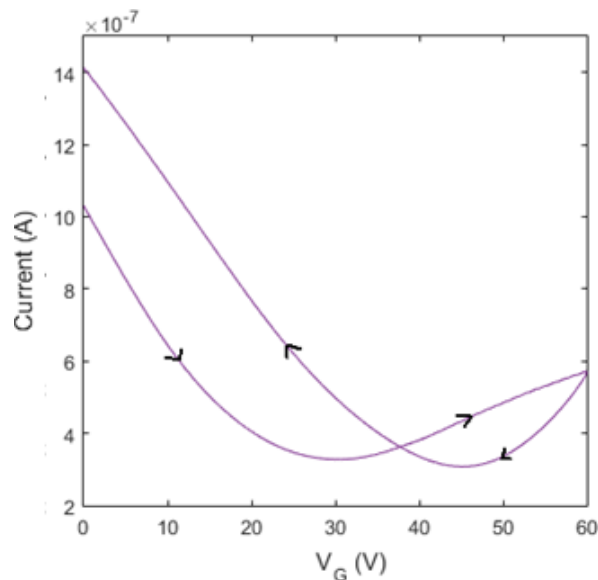


Figure 5.11 showing the transfer characteristics of a GFET operated in air. The large hysteresis at two Dirac points is due to trapping of charge carriers. The arrows denote the sweep direction.

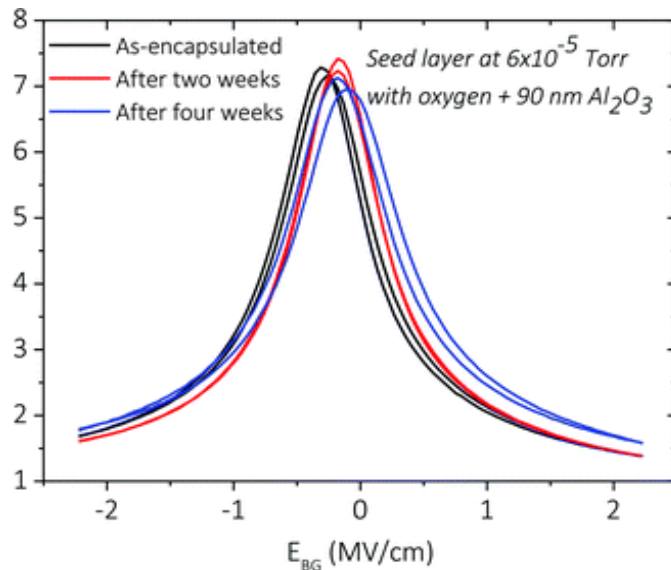


Figure 5.12, showing the endurance of electrical properties of encapsulated GFET measured over several weeks in ambient conditions [73], reproduced from ref. [73] with permission of the Royal Society of Chemistry. The results show the forward and backward sweep for each of the samples. The reproducibility in the characteristics is very important in photon counting applications.

Due to this high sensitivity, reproducible electrical characteristics are a key challenge that can be addressed by considering techniques such as encapsulation [73] [216] [217] to reduce atmospheric effects or controlled doping [218] [219]. Encapsulation using an alumina deposition has been shown to protect the sample against environmental doping for at least one month [73], and hence protects against gate hysteresis [73], figure 5.12. A seed layer is required for successful encapsulation; the amount of leakage is dependent on the seed layer, and without this the device is not protected [73]. Encapsulation also improves the charge carrier mobility; in a recent experiment, the sample initially had a measured mobility of $1505\text{cm}^2\text{V}^{-1}\text{s}^{-1}$ with a Dirac point voltage of 76.3V, and after encapsulation with an alumina deposition a mobility of $2970\text{cm}^2\text{V}^{-1}\text{s}^{-1}$ was measured, with a Dirac point voltage of 0.4V. Encapsulation also protects against process contaminations, with the alumina layer removed before deposition of contacts [220].

Alumina deposition used a Savannah ALD reactor at the University of Cambridge. Samples are placed inside the chamber that is then pumped down. The surface is wetted with water or ozone, and then water and TMA precursor are pulsed into the chamber. Each layer is 1\AA thick, so a 15nm deposition requires 150 layers of alumina which takes approximately 2 hours.

5.3.7 Wire Bonding

To bond directly to the chip, it must be mounted on a PCB using Die attach heated to 200°C. The chip is then cooled to 120°C and a wire bonder, figure 5.13a, is used to connect gold wires $\sim 25\mu\text{m}$ diameter between the PCB and contact pads on the chip using a wedge bond process. The wire bonds can be positioned on the chip by moving the mouse on the wire bonder to align the needle. The needle was approximately 5cm long and 1.5mm in diameter [221], figure 5.13b, which make threading the wire difficult give the $\sim 25\mu\text{m}$ diameter of the Au wire.



Figure 5.13 showing a) the wire bonder and b) the needle

5.4 Fabrication, Phase I – September 2015

Phase I of fabrication occurred in September 2015. This phase included training on the different manufacturing techniques, the fabrication of the initial terahertz and X-ray detectors, and an investigation into the required thickness of the alumina dielectric for the bilayer graphene-based detector.

5.4.1 Terahertz Detector Fabrication I: Optimising the Fabrication Process

In this section, the initial terahertz detectors were fabricated to allow for optimisation of the manufacturing process. These terahertz detectors were fabricated with log periodic circular toothed ($k=1.5$ and $k=2$), bowtie and “beetle” antennae as designed in chapter 3. Each of these was designed to have a resonant frequency between 1 and 1.4THz, and was of size of order $200\mu\text{m}$.

After initially failing to develop, the silicon wafer was cleaned and reused, and the e-beam mask successfully developed on the second attempt. Contacts were deposited by evaporating 2nm Cr and 100nm Au onto the sample. Devices were then mounted onto a PCB and wire bonded, although it was found to be very difficult to successfully get the wire bond to stick to the Cr-Au electrode with parts of the electrode peeling away during the wire bonding process.



a) b)
Figure 5.14 showing a) the Lenton air oven and b) the Gallenkamp vacuum oven used in the annealing process.

The samples were annealed to improve the adhesion of the wire bond to the electrode. One device was placed in a Lenton high-temperature air oven, figure 5.14a, for 75 minutes at 150°C, while a second device was placed in a Gallenkamp OVL570 010J vacuum oven, figure 5.14b. It was found to be slightly easier to wire bond to the one processed using the vacuum oven, so the chips were removed from the PCB and placed in a vacuum oven at 150°C for 165 minutes. This improved the annealing, with two devices successfully wire bonded. The remaining devices were then placed in the vacuum oven at 170 degrees for 210 minutes. This annealing may, however, cause increased p-doping of the graphene resulting in a shift of the Dirac point to higher positive gate voltages [222].

Further devices were manufactured with variations to the fabrication stages, including a range of resist development parameters. To improve the wire bonding to the devices, these chips had a 5nm Cr deposition, followed by a 125nm thick deposition of Au, to form a 130nm thick contact, figure 5.15a. The Cr deposition was partially contaminated by Au as the two pots were shorted together in the vessel, so the Au heated up at the same time as the Cr. These devices did not need to be annealed to be successfully wire bonded, figure 5.15b, although it was still not particularly easy.

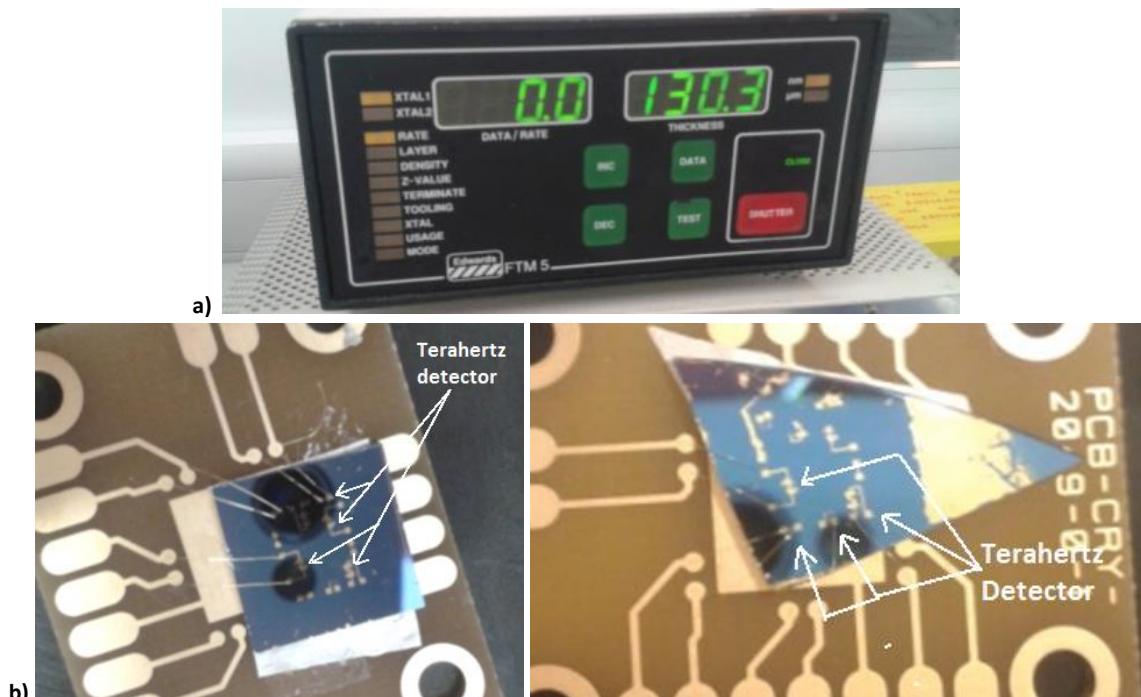


Figure 5.15 showing a) the thickness monitor after a deposition of 5nm of Cr followed by 125nm of Au through evaporation, resulting in a total 130nm thick deposition, and b) the completed wire bonded samples.

5.4.2 Bilayer Graphene Detector Fabrication I: Ensuring Uniform Alumina Coverage

The bilayer graphene device required an alumina dielectric deposition of a uniform thickness and global coverage to ensure that a uniform band gap is opened across the sample. In this section, a thin alumina deposition is analysed using Scanning Electron Microscopy (SEM) and Atomic Force Microscopy (AFM) to determine the necessary thickness for the dielectric.

5.4.2.1 SEM Analysis of ALD Deposition

Scanning electron microscopy (SEM) utilises a 100eV-30keV electron beam, thermionically excited from a filament (typically tungsten), to interact with the sample and cause inelastic and elastic scattering, resulting in high energy backscattered electrons and lower energy secondary electrons to be excited within the sample. These electrons are detected and can be used to recreate images with a resolution down to 1nm. The technique is typically done at very low vacuum to prevent scattering from any atmospheric defects in the environment [223] [224]. SEM has many applications in addition to high resolution imaging, such as for chemical analysis [223] and layer characterisation [225]; layer characterisation of samples for the European Space Agency is discussed in Appendix Ib.

Samples of CVD-graphene grown at the Institute for Physical Chemistry in Prague, and transferred on to a Si wafer were characterised before and after the deposition of a 15nm ALD alumina layer. SEM analysis of the sample before the ALD deposition, figure 5.16, show holes and tears in the graphene (figure 5.16b), obvious marks left from an imperfect removal of PMMA from the original transfer (e.g. figure 5.16e and figure 5.16h), and lines originating from the original growth (figure 5.16d).

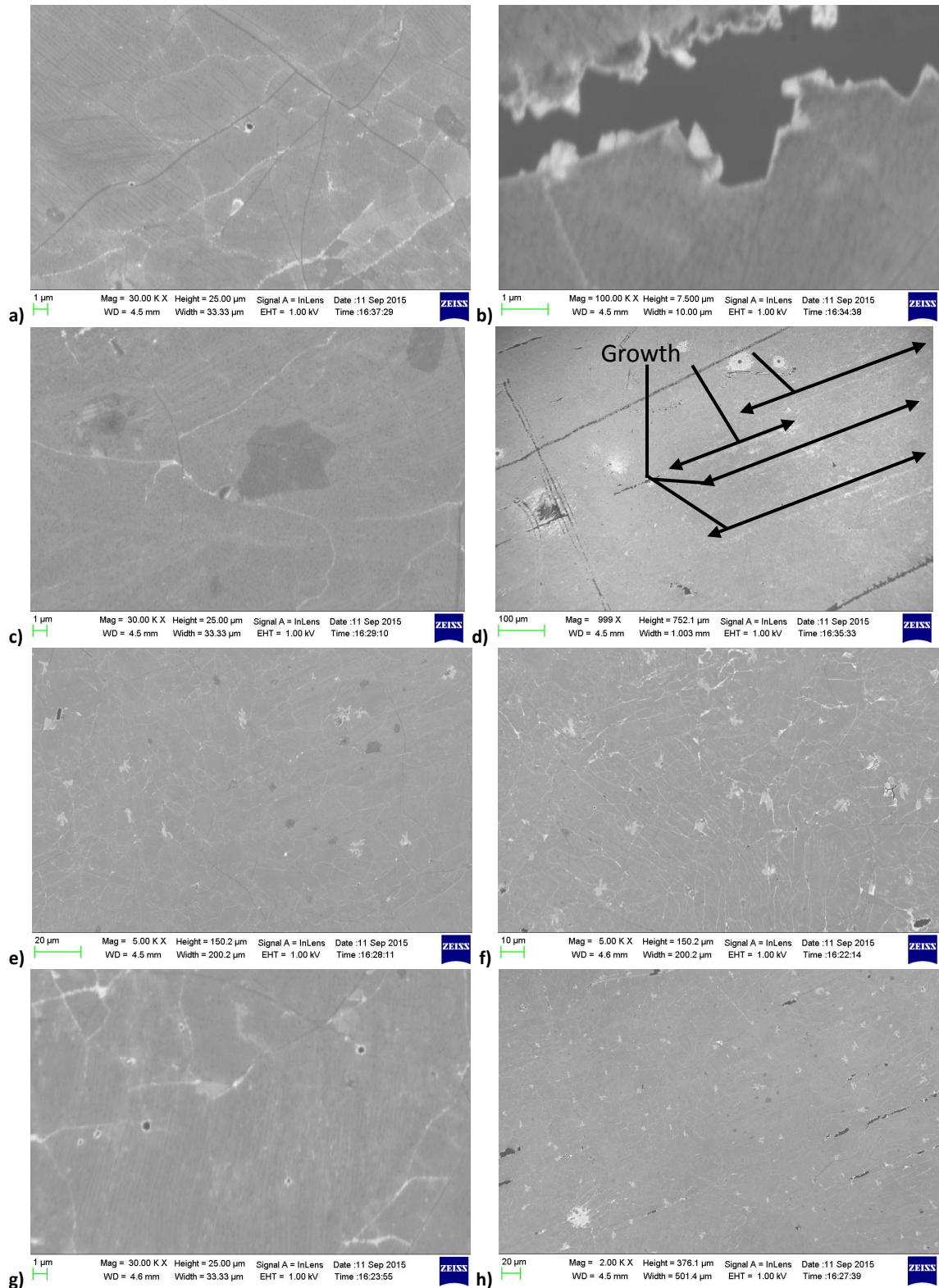


Figure 5.16, showing SEM images of the samples from Prague before the alumina ALD. They show a) holes and b) tears in the transferred graphene, c) regions of multilayer graphene, d) lines originating from the original growth, and e-h) obvious marks left from an imperfect removal of PMMA from the original transfer.

The ALD deposition was an initial 5nm of trimethylaluminium(TMA) precursor and ozone wetting, and then a further 10nm of TMA and water. The ozone allows for

better adhesion to the graphene. The SEM images, figure 5.17, show a relatively uniform coverage, although there are visible holes in the alumina layer that originate from the original holes/tears in the graphene or from unclean graphene. Regardless of the thickness of the deposition, the alumina would not nucleate to the silicon in these areas. To mitigate this, the graphene needs to be cleaned thoroughly with acetone/IPA before ALD deposition, whilst AB-stacked areas need to be selected away from defects in the graphene. If any holes in the alumina layer appear at this stage then, in further processing, these areas can be avoided.

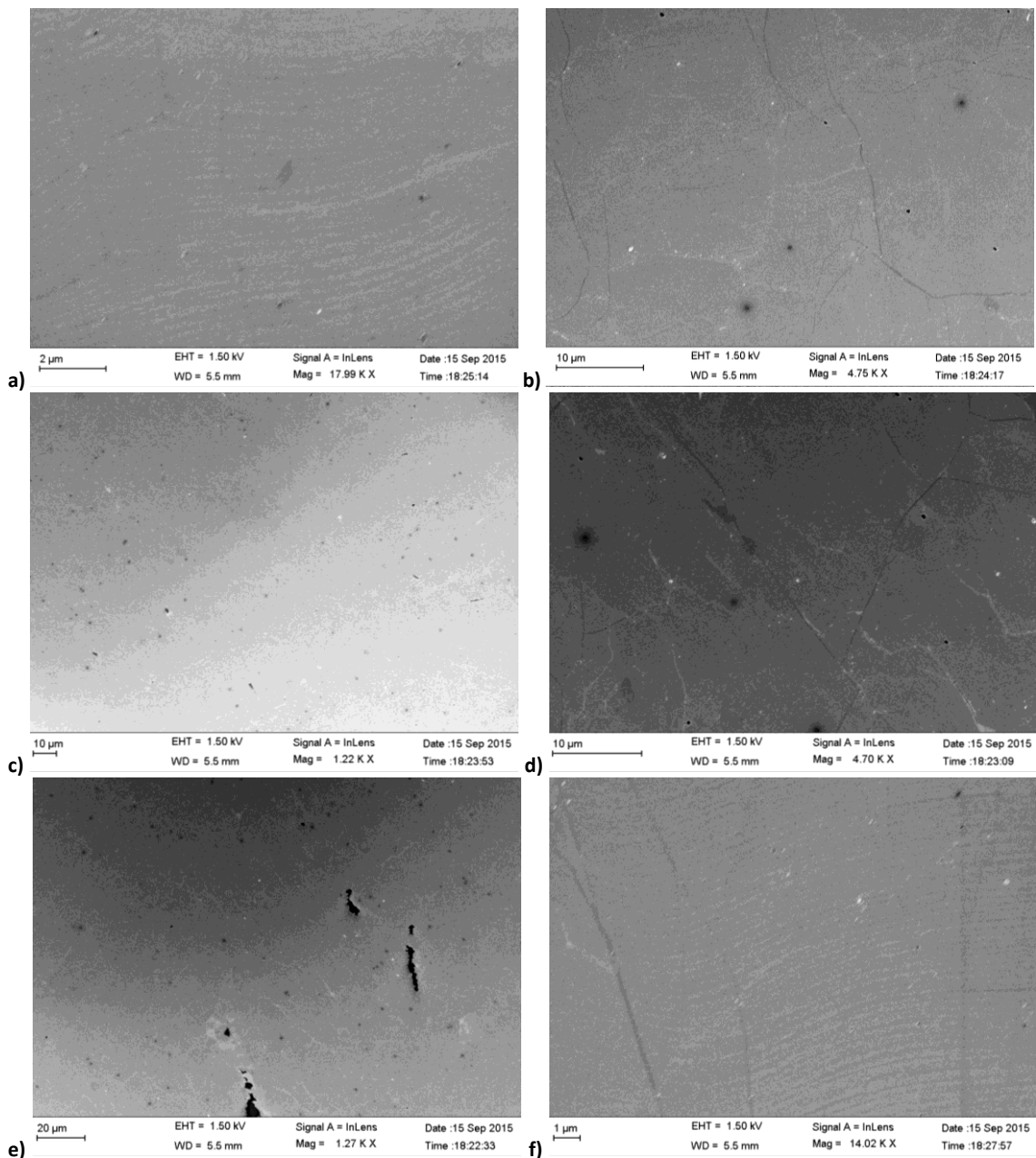


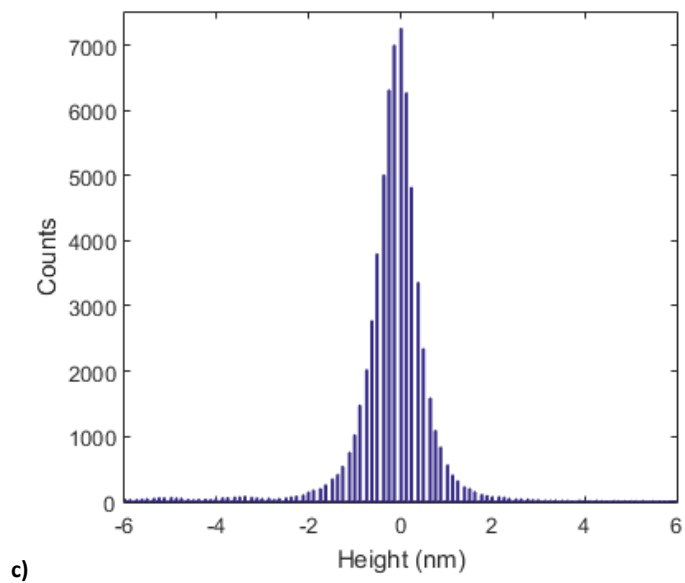
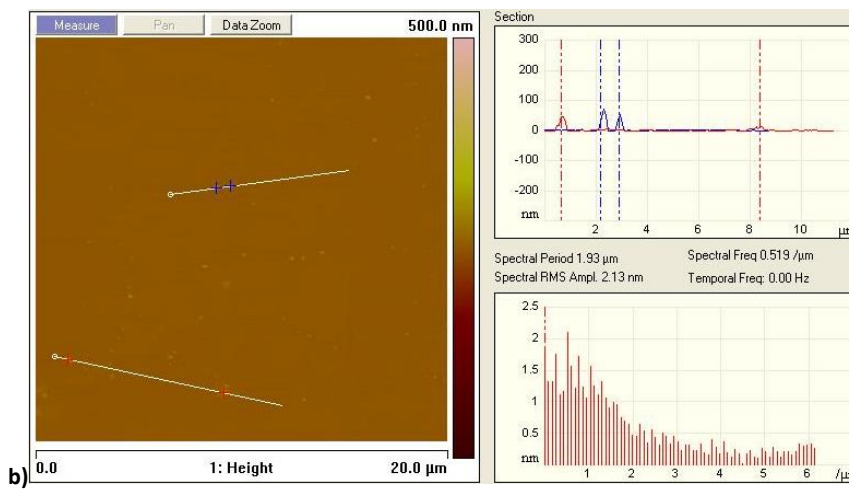
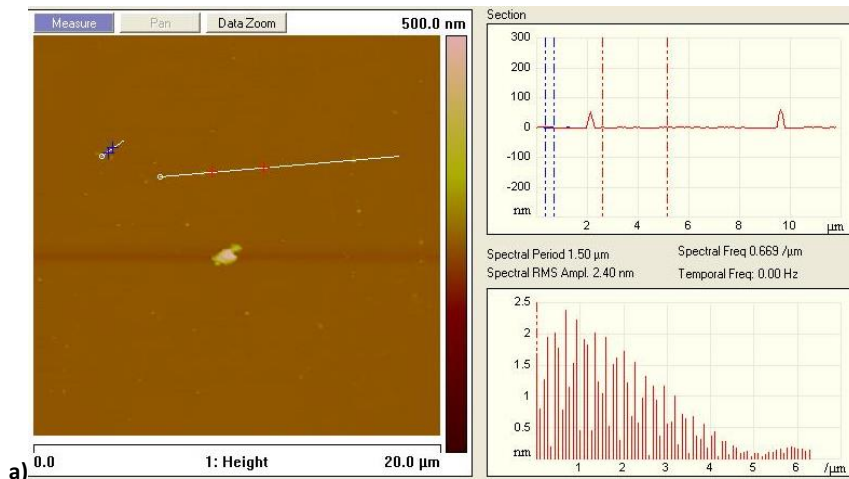
Figure 5.17. Alumina deposition analysed in an SEM. This shows a much more uniform coverage, although holes in the alumina deposition are still visible where the alumina was unable to nucleate to the surface.

5.4.2.2 AFM Analysis of ALD Deposition

Atomic Force Microscopy (AFM) scans across a sample and looks for deflections in the position of the AFM tip from the surface. It can work in many different modes; a common one is “non-contact mode” where the cantilever is oscillated at its resonant frequency. The force between the tip and the sample changes the frequency of the cantilever, and this can be converted to a measurable deflection, allowing characterisation of the sample [226]. AFM, and analogous techniques such as electrostatic force microscopy and scanning gate microscopy [227] [145], can characterise many properties of a sample such as the layer thickness with a height resolution below 10pm [228], adhesion strength of adsorbants to the graphene surface (of order nanonewtons, which could affect the sample mobility), surface potential and stiffness [229].

AFM was used to analyse the alumina coverage across different regions of the bilayer graphene sample within a 20 μ m x 20 μ m active area. The output from the AFM for two areas of one graphene sample is shown in figures 5.18a and 5.18b. Both figures show a largely flat surface for the graphene on a silicon/silicon dioxide wafer and a 15nm thick alumina layer; by histogramming the measured height from the AFM, figure 5.18c, the variance in the height was estimated as $\sigma \sim 331$ pm. This variance is equivalent to $\sim 3 \times 1\text{\AA}$ thick ALD alumina layers, and could be due to the ALD deposition and/or the surface roughness of the silicon, and defects and dirt from the transfer and manufacturing processes.

In figures 5.18a and 5.18b there are readings across the surface that indicate a deflection of ~ 50 nm. These large deflections are attributable to PMMA residue, previously observed in figure 5.16e-h, that remains on the sample after transfer, and other defects due to the transfer and manufacturing processes. These large defects are clearly seen in 3d in figures 5.18d and 5.18e; it is critical to work in a clean environment, with a clean sample, to ensure that the detector is not affected by these residues and defects.



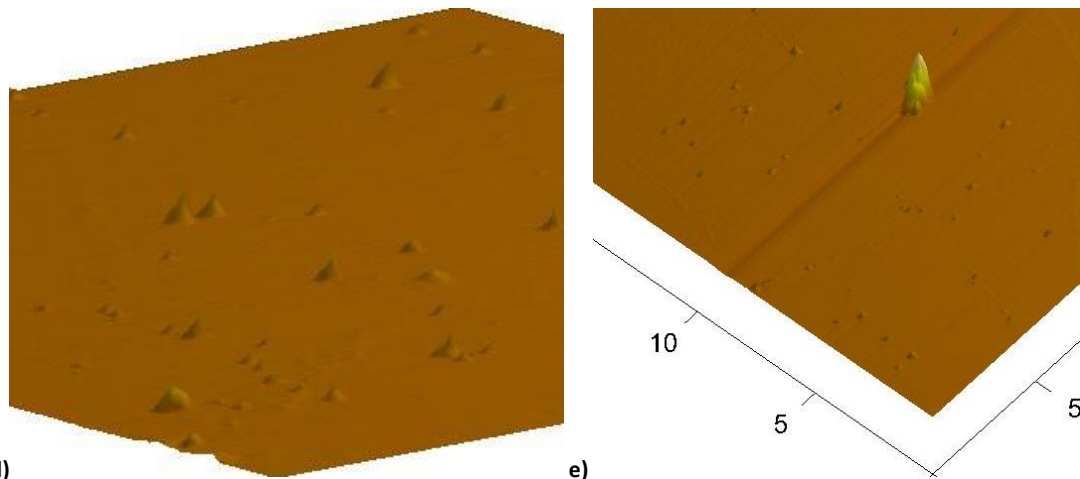


Figure 5.18 showing a) the output from the AFM measurements for two $20\mu\text{m} \times 20\mu\text{m}$ samples. B) shows the measured height of the graphene on a silicon/silicon dioxide wafer and a 15nm thick alumina layer, with a variance $\sigma \sim 331\text{pm}$. D) and e) show the sample, in 3d, with clear defects and PMMA residue from the transfer and manufacturing processes.

5.5 Fabrication, Phase II – October 2015

Phase II of fabrication occurred in October 2015. Following the work in Phase I, it was possible to draw several conclusions that drove the approach in Phase II:

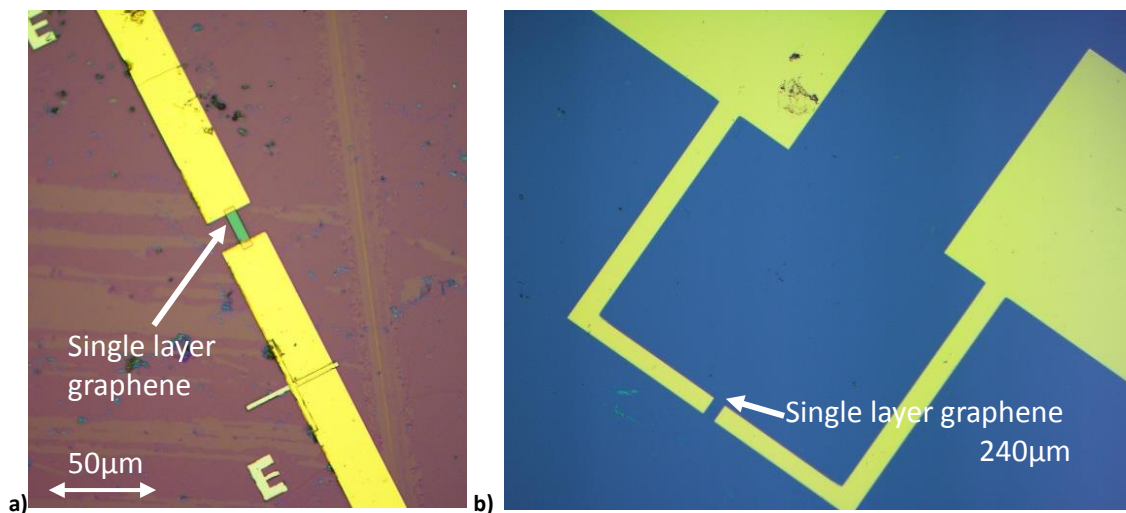
- SEM and AFM analysis of a 15nm thick deposition of alumina layer coating graphene on a silicon dioxide/silicon wafer allowed for characterisation of the sample.
 - SEM analysis indicated several areas of PMMA residue, some greater than 100nm. This indicated how crucial cleanliness is to the fabrication process, which was aided by fabricating the devices in 10k, 1k and 100 class cleanrooms.
 - AFM analysis showed that the mean change in height of the sample was $\sim 0\text{nm}$, with a variance $\sigma \sim 331\text{pm}$. σ is equivalent to $\sim 3 \times 1\text{\AA}$ thick ALD alumina layers, but could also be attributable to surface roughness of the silicon. This suggests that a 15nm thick alumina dielectric layer is locally flat within at least 2%, so a 15nm thick layer was used in Phase II.
- The ability to wire bond to a device is improved by vacuum annealing, although it can result in significant p-doping. As discussed in ref. [222], when the sample is in the vacuum, dopants such as H_2O and O_2 will adsorb from the surface to reach equilibrium, so the dopant concentration is significantly lower. When the

sample is then exposed to the air, water and oxygen molecules are then more readily able to fill the vacancies on the sample, leading to greater p-doping of the graphene.

In this phase, further progress was made in fabricating the THz and X-ray GFETs, as well as the bilayer graphene devices. An etch step to define the graphene channel was missed from the fabrication stages in the previous section, so this was added to the process in Phase II.

5.5.1 Terahertz and X-Ray Detector Fabrication II: Etching to get a Gated Device

The terahertz and X-ray detectors were fabricated on the same silicon substrates with a resistivity $\rho=1-100\Omega\text{cm}$. The masks were patterned using e-beam lithography, and the graphene was etched, figure 5.19a. Contacts were formed by evaporating a 7.5nm thick film of Cr and then 150nm of Au, figure 5.19b-d, with no encapsulation layer. The devices were probed, with initial resulting showing a gate voltage dependence and a Dirac point $>80\text{V}$, figures 5.19e-h.



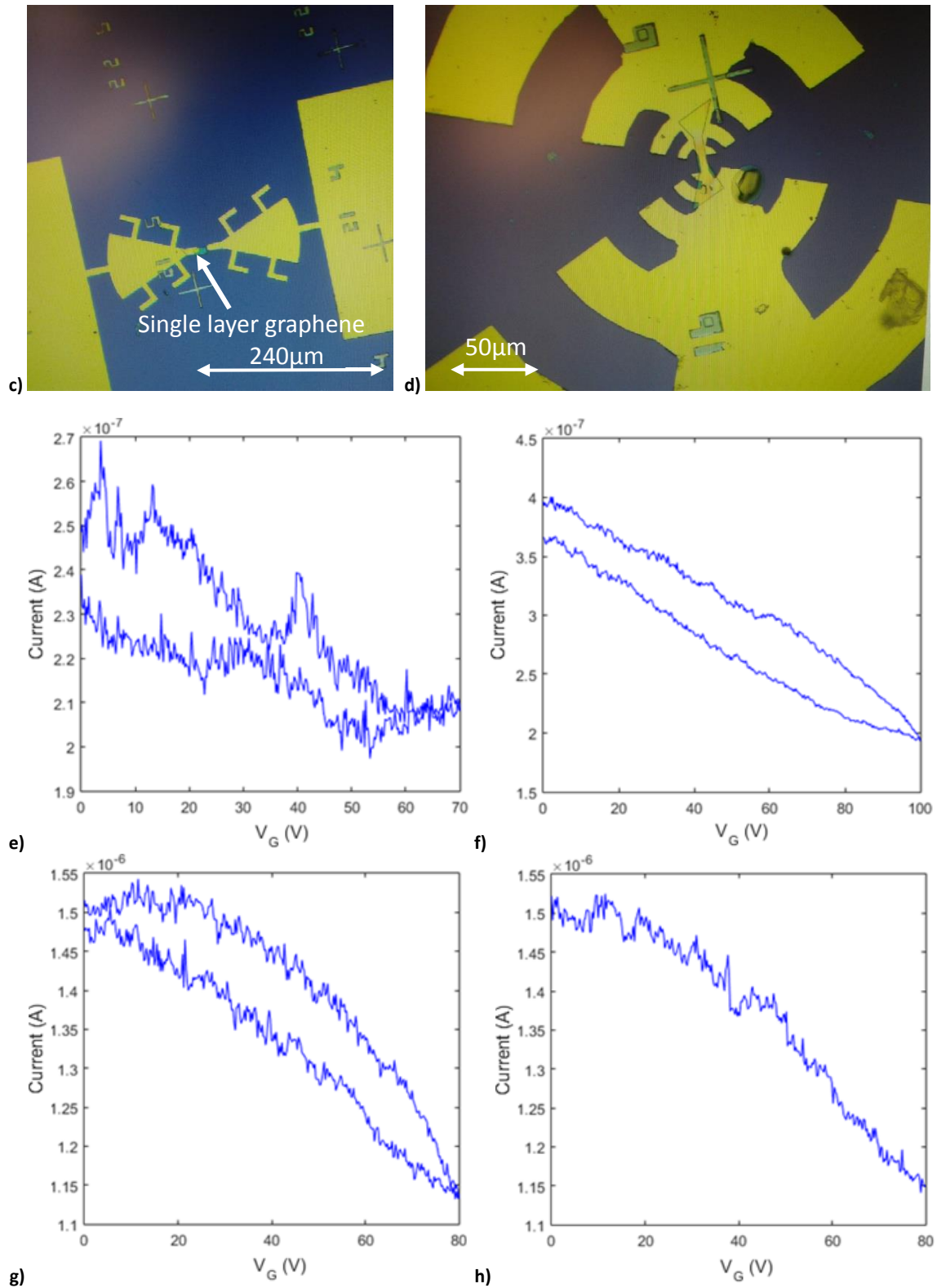


Figure 5.19, showing a) the etched graphene channel after the deposition of the chrome-gold contacts. B) shows an example of one of the X-ray devices before wire bonding, while c) and d) shows a beetle THz device and a log-periodic circular toothed antenna respectively. e) shows a successful gating of one of the X-Ray devices on the chip with a very noisy output (with a Dirac point at $V_G \sim 50-60\text{V}$), while f), g) and h) show examples of successfully gating THz devices, with a Dirac point for each of $V_G > 80\text{V}$.

It was again noted how difficult it was to wire bond to some of these devices, as per the observations in Phase I. For instance, the contact pads were peeling off the substrate due to the force applied by the wire bonder needle, figure 5.20. One gated connection was made, figure 5.19e, but in later testing the tracks fractured and the device failed. The wire bonding problems and the fracturing of the tracks may occur from poor adhesion of the Cr-Au contact to the graphene and substrate, so an improved contact material would make adhesion better.

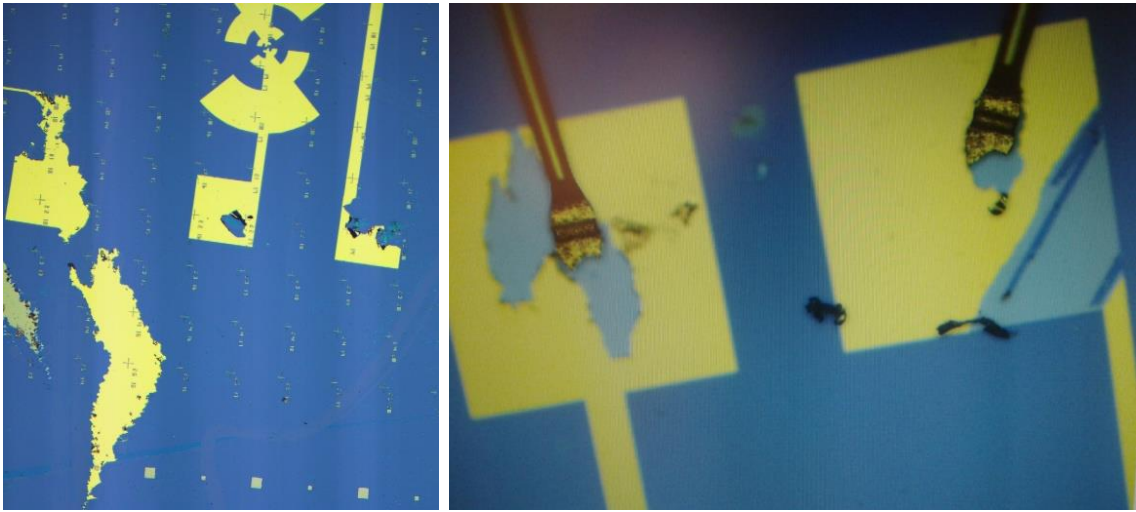


Figure 5.20 showing the damage to the device resulting from a bad lift-off, and due to the force applied to the contact pads by the wire bonder.

5.5.2 Bilayer Graphene Detector Fabrication II: Optimising the Fabrication

Process

Samples of graphene with bilayer and multilayer regions were grown on copper and transferred onto silicon wafers to provide many small bilayer and multilayer islands, figure 5.21a, and much larger bilayer graphene samples with a grain size up to approximately 70 μm , figure 5.21b.

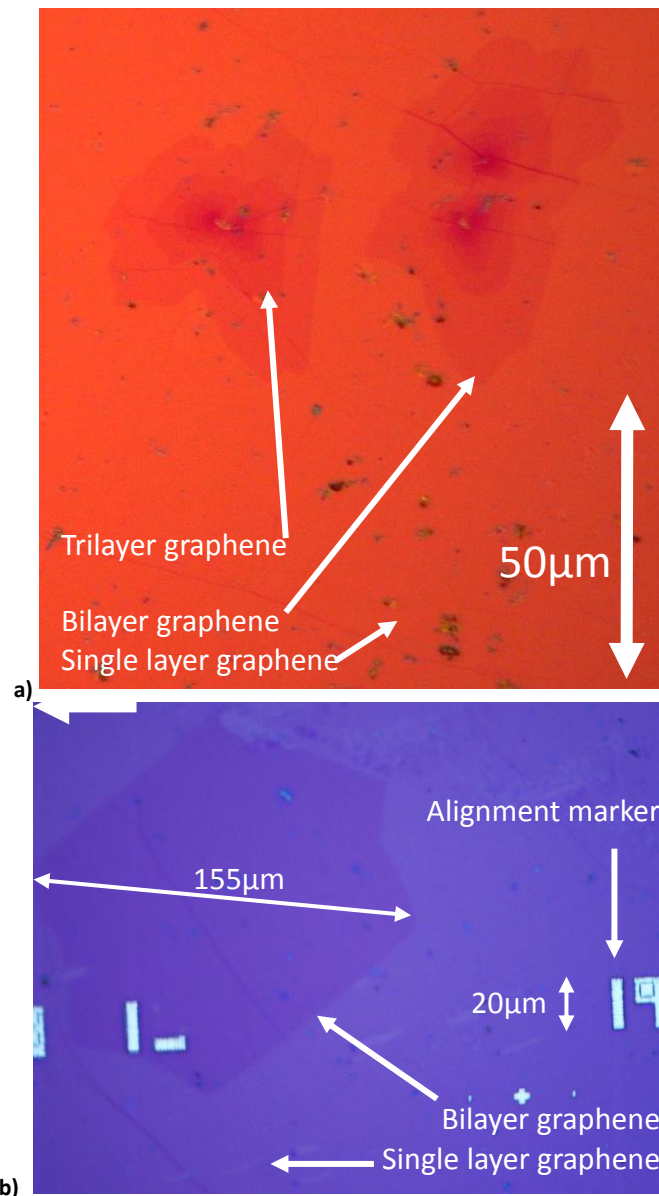


Figure 5.21, showing the analysis of graphene samples using optical microscopy to identify the location of a) bilayer and multilayer islands, and b) larger grain bilayer samples. Using the alignment markers allowed for the mask to be drawn accurately.

The samples were analysed to identify bilayer and multilayer areas to design masks that were then patterned using e-beam lithography. Contacts of 7.5nm Cr and 150nm Au were evaporated onto the sample; it became apparent that the Cr-Au had not adhered to the surface as only some of the gold remained after the evaporation and lift-off, figure 5.22b. The contacts were masked again and a further 8.5nm Cr and 150nm Au evaporated onto the sample, which this time survived the lift-off step, figure 5.22c-d. The cause of the lack of adhesion of the Cr-Au to the substrate, and the previously discussed difficult wire bonding, could both be attributed to bad adhesion

between the silicon substrate and the evaporated chrome and gold films, or perhaps due to overdevelopment of the mask.

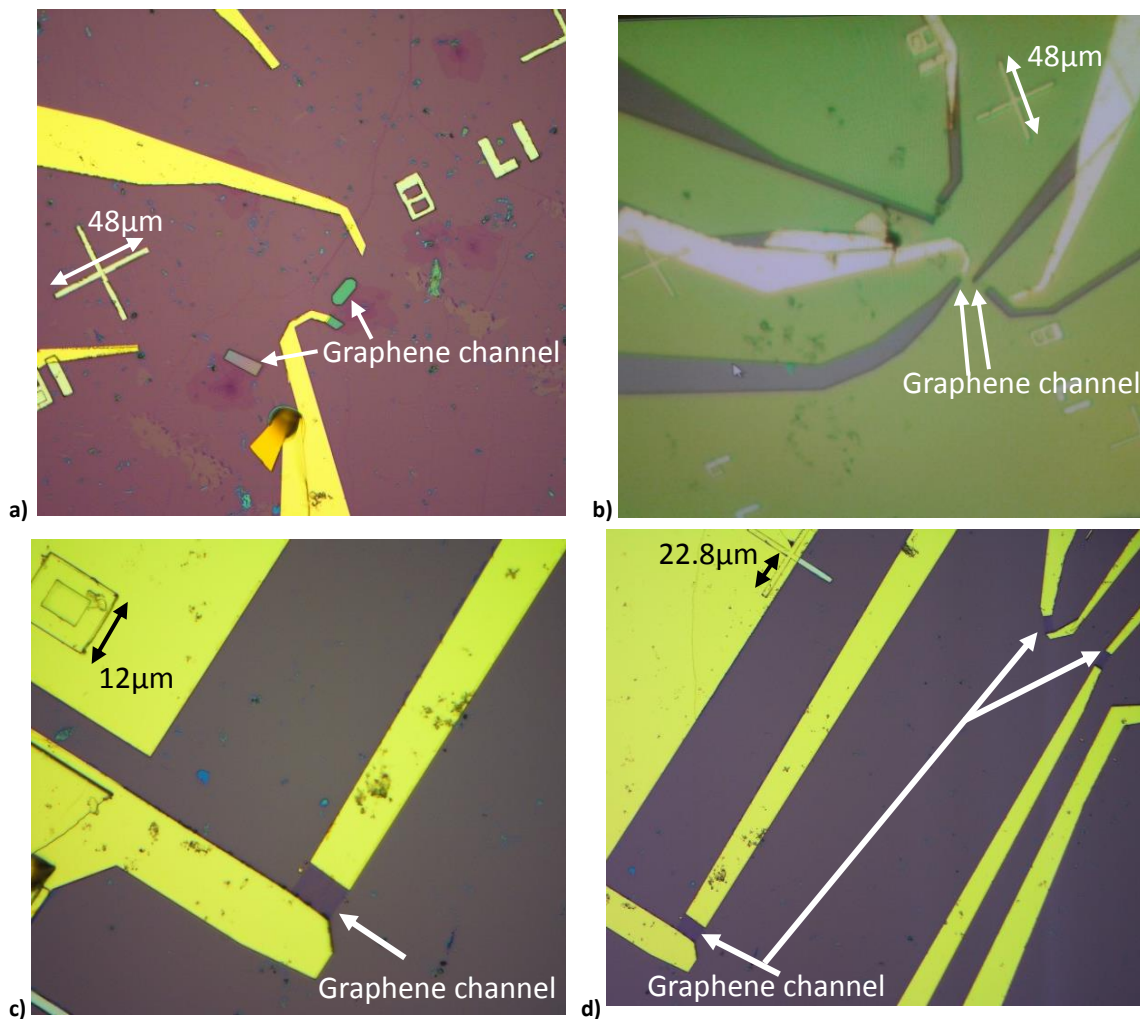


Figure 5.22, showing a) the etching of the bilayer regions of the graphene, b) after the first chrome-gold evaporation and c) and d) after the second evaporation (50x magnification and 20x magnification respectively).

The top gate substrate was deposited through ALD; this was the 15nm thickness that was identified in the previous phase. The ALD process used a water pulse rather than ozone pulse as ongoing research into the process suggested that this provided better and more uniform nucleation [230].

The top gate was masked via e-beam lithography; a PMMA photoresist was selected over UVIII as the developer for the latter, MFCD26, contains phosphoric acid which would etch away the alumina in locations intended for the top gate deposition. ITO was sputtered onto the surface for 500s to give a ~50nm thick top gate; which left a

purple residue on the equipment, figure 5.23a, and a visible colour contrast on the chip, figure 5.23b.

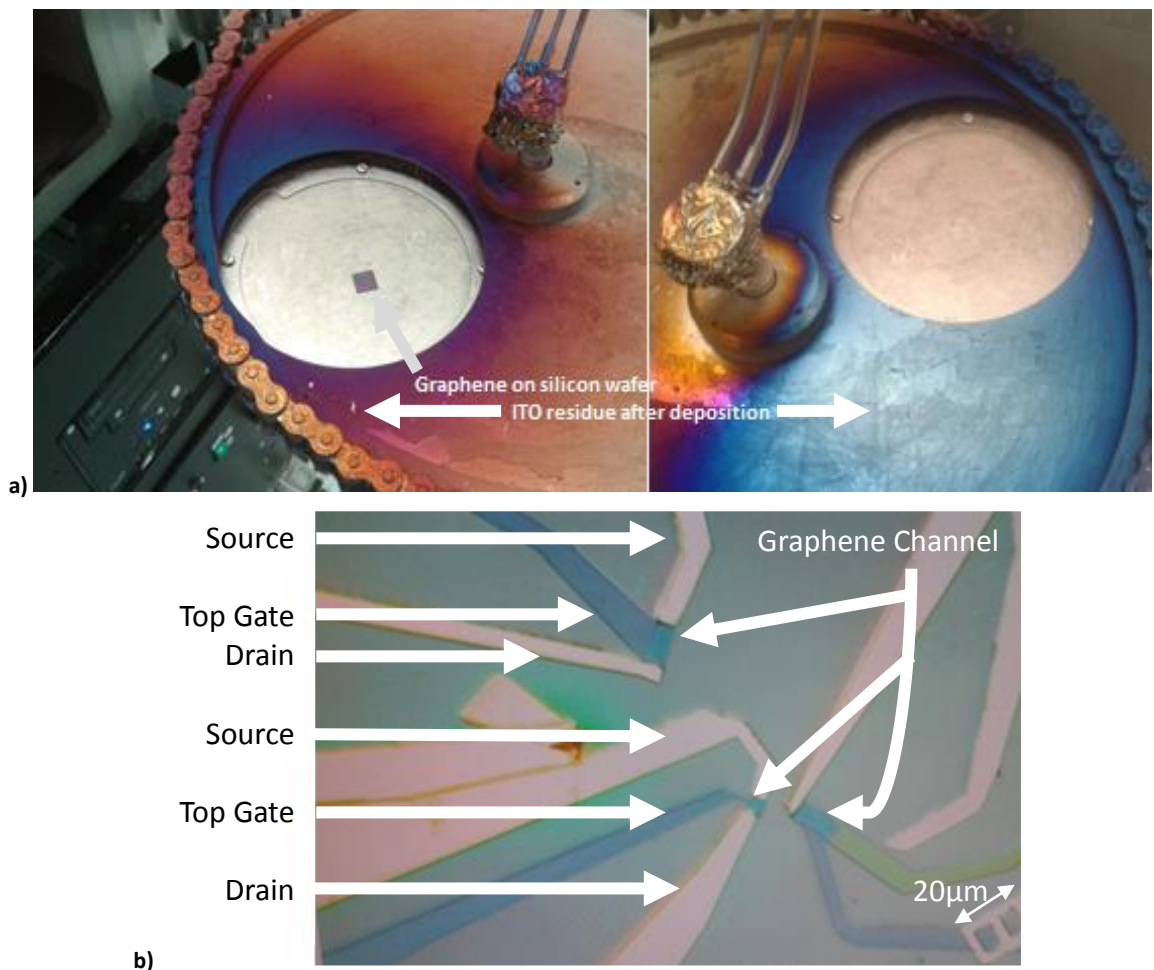


Figure 5.23, showing the ITO residue on the equipment after deposition, and b) the tracks of ITO coming from the graphene between the gold source and drain tracks.

To access the contacts to enable wire bonding, UVIII photoresist was masked over the contacts and developed with MFCD26 developer so the phosphoric acid content would etch away the alumina to enable the device to be successfully wire bonded. However, wire bonding was again found to be problematic as the gold was still readily peeling off, in some cases worse than in Phase I. Most wire bonds that were successfully connected required such a force to bind that they shorted to the bottom and/or top gate. One device was successfully wire bonded; gating the device shows a much higher electron mobility than hole mobility, figure 5.24, and a Dirac point at about 20V.

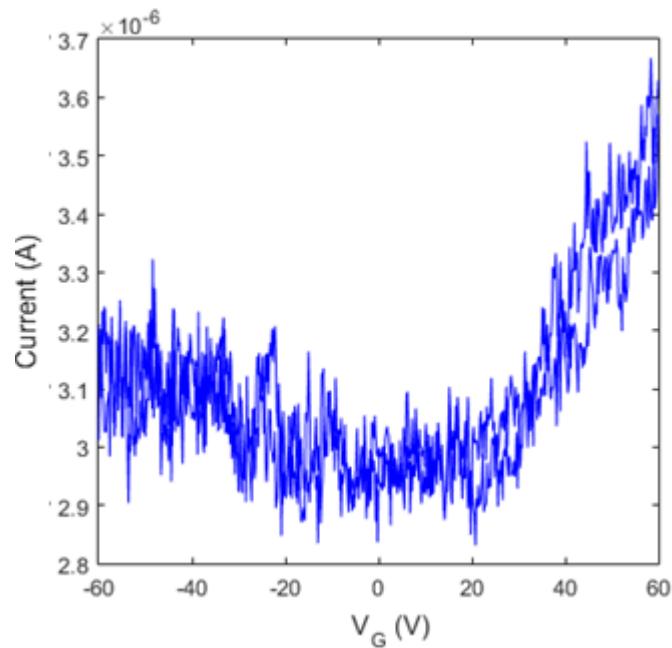


Figure 5.24, showing the measured current between the source and drain of the bilayer graphene channel for gate voltages from $V_G = -60\text{V}$ to $V_G = +60\text{V}$ applied to the bottom gate (i.e. the silicon) of the bilayer graphene device.

5.6 Fabrication, Phase III – November 2015

Phase III of fabrication occurred in November 2015. Based on the work in Phases I and II, this phase of work looked to further develop the fabrication of the devices. Several issues were raised in Phases I and II that needed to be considered, overcome or mitigated in Phase III. For instance:

- Wire bonding remained a significant challenge, which was attributed to the bonding between the Si and Cr-Au with the issue arising in the evaporator due to a dirty atmosphere. A different contact material such as Ni-Al needed to be considered, which could perhaps be sputtered rather than evaporated. Alternative means of wire bonding, such as ball bonding, also require a thicker contact deposition, of order $0.25\mu\text{m}+$. Furthermore, if fewer devices with larger bonding pads were on a chip, it could enable connections to be made to the devices using silver epoxy, removing the need for wire bonding entirely.
- For ease of manufacture the devices were manufactured in bulk, with a bilayer graphene device on one chip, X-ray on another and THz on another.
- A thicker layer of alumina, deposited via ALD, was required – 15nm was too thin as it was shorted through, while 80/90nm was used in fabrication of other devices, such as those in ref. [65]. A layer 50nm thick was intended.

- Photolithography provided a quicker route to masking for simple GFET structures, so this was also considered.

For each device, CVD graphene samples had been grown and transferred onto large Si wafers, which were then cut up with a diamond scribe, before tungsten alignment marks were deposited.

5.6.1 Rectifying the Wire Bonding Problems: Trying a New Material

As most devices had problems that arose due to wire bonding, a critical task in Phase III was to identify a recipe for a material that would be easy to wire bond to and would not damage the silicon dioxide dielectric. A sputtered Ni-Al film was proposed: ~50+nm Ni to give good adhesion to the silicon substrate, and ~70+nm Al to give good adhesion for wire bonding.

To test this material it was sputtered, without a mask, onto a silicon wafer. This was attached to a PCB, and it was found to be very easy to wire bond together; it required only one attempt with the wire bonder whereas previously it required several. A sheet resistance of the material was measured as approximately 450 Ω .

The gate current was measured to check that the wire bonding process had not damaged the silicon dioxide dielectric; if the gate current had breached a current limit of 10nA then the material would have failed. Initial tests showed that the gate current did breach 10nA, figure 5.25a, although this was because the sputter coater deposition had shorted directly between the Ni-Al and silicon. By crudely scratching off the excess Ni-Al with a sharp blade, the short was removed, and the device was successfully retested with a gate current on 100pA scale, figure 5.25b.

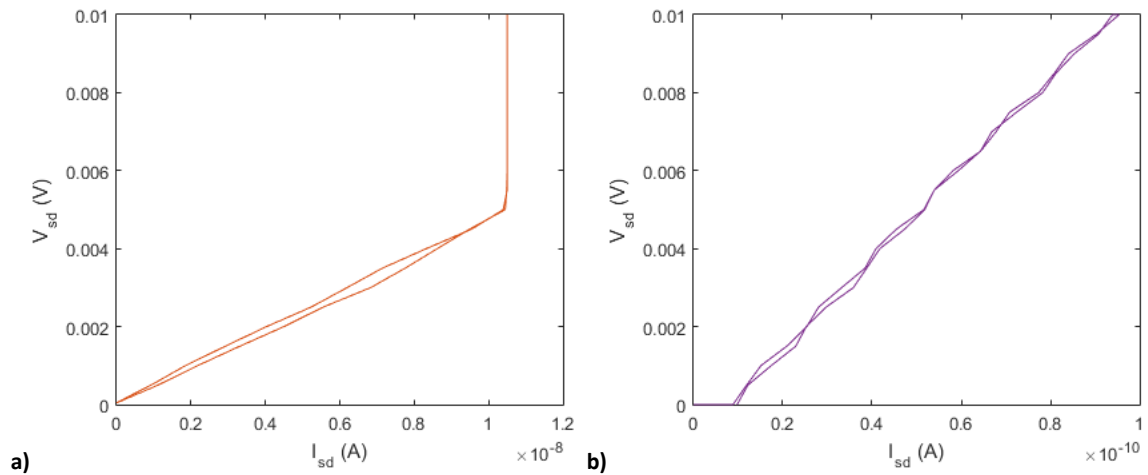


Figure 5.25, showing the gate current measured a) without scratching off the Ni-Al short, b) after scratching off the short.

5.6.2 Terahertz Detector Fabrication III: Improving the Detector Fabrication

The terahertz devices were fabricated, using a procedure that built upon the findings in Phases I and II. Graphene channels were masked using e-beam lithography before being etched, and then contacts were masked with e-beam lithography although accidentally overdeveloped. The contacts were formed by sputtering 70nm of nickel followed by a further 70nm nickel deposition, and then sputtering aluminium for 600s; the nickel was deposited in two stages to enable good binding to the graphene and to give the required thickness of nickel, whilst the aluminium made wire bonding easier. At this point, some of the alignment between the contacts and graphene channels was observed to be imperfect and thus some of the devices were not functioning.

A second set of chips was fabricated with better developed contacts, which were then sputtered with nickel for 500s followed by a 700s deposition of aluminium, figures 5.26a-d. These were wire bonded and checked on the probe station with some successful results, e.g. figure 5.27e with a Dirac point $\sim 100V$.

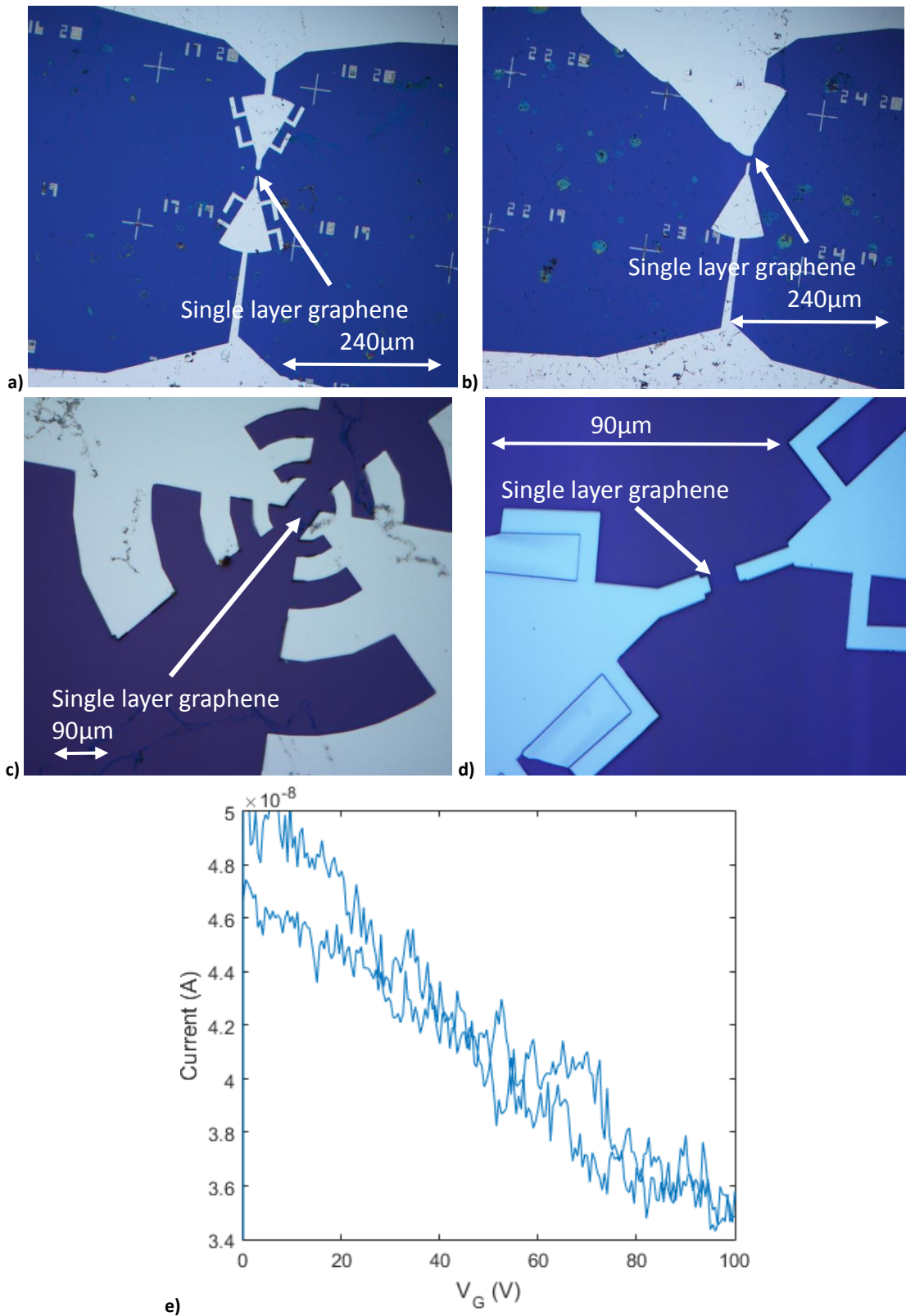


Figure 5.26, showing successfully completed THz structures in a) "beetle" configuration, b) bowtie configuration, c) log-periodic circular toothed configuration and d) "beetle" configuration. E) shows the forward sweep and back sweep through voltages between $V_G=0V$ and $100V$ showing how the device gated, indicating a Dirac point at $V_G > 100V$.

5.6.3 X-Ray Detector Fabrication III: Improving the Detector Fabrication

In this phase, X-ray GFETs were fabricated using two different methods, one with further use of e-beam lithography to mask the chips, whilst the other used photolithography to mask the contacts.

For the process using electron beam lithography, the contacts were patterned and the graphene channels were etched in the usual way. The contacts were sputtered with 75nm Ni and ~75nm Al, figure 5.27a. These were wire bonded and gated, with the V_{Dirac} at $V_G \sim 17V$ and $V_G \sim 12.5V$, figures 5.27b and 5.27c, respectively.

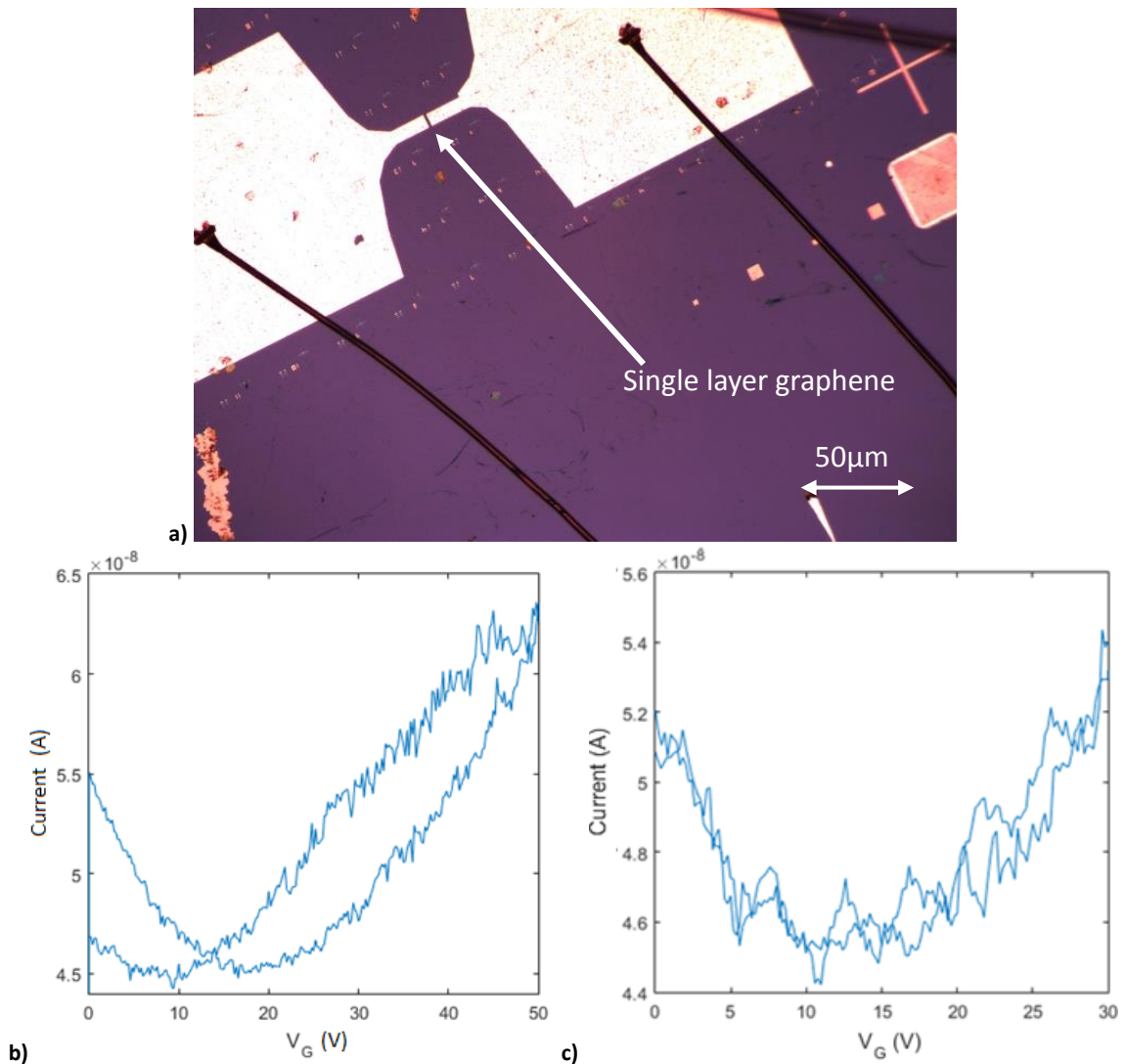


Figure 5.27, showing a) the working x-ray device through electron beam lithography, and b) and c) the forward sweep and back sweep of two different X-ray devices fabricated using the e-beam lithography route to identify how the devices gates, indicating a Dirac point at $V_G \sim 10-20V$ and $V_G \sim 10-15$ respectively.

The devices masked via photolithography were spin coated and then exposed to the photolithography equipment for 7s. After being developed, these devices were sputtered with a different combination of thicknesses of Ni and Al (two nickel depositions each 50nm thick, with the intention of ALD alumina coating; two nickel depositions, each 70nm thick, followed by sputtering aluminium for 600s; and 50nm nickel followed by two depositions of aluminium, each for 500s), to see if there is any difference in wire bonding ability.

The devices are shown after sputter coating and lift-off, which shows some difficulty in the lift-off stage as shown in figure 5.28a-b. The graphene samples were then etched using an AZ MLOF negative mask.

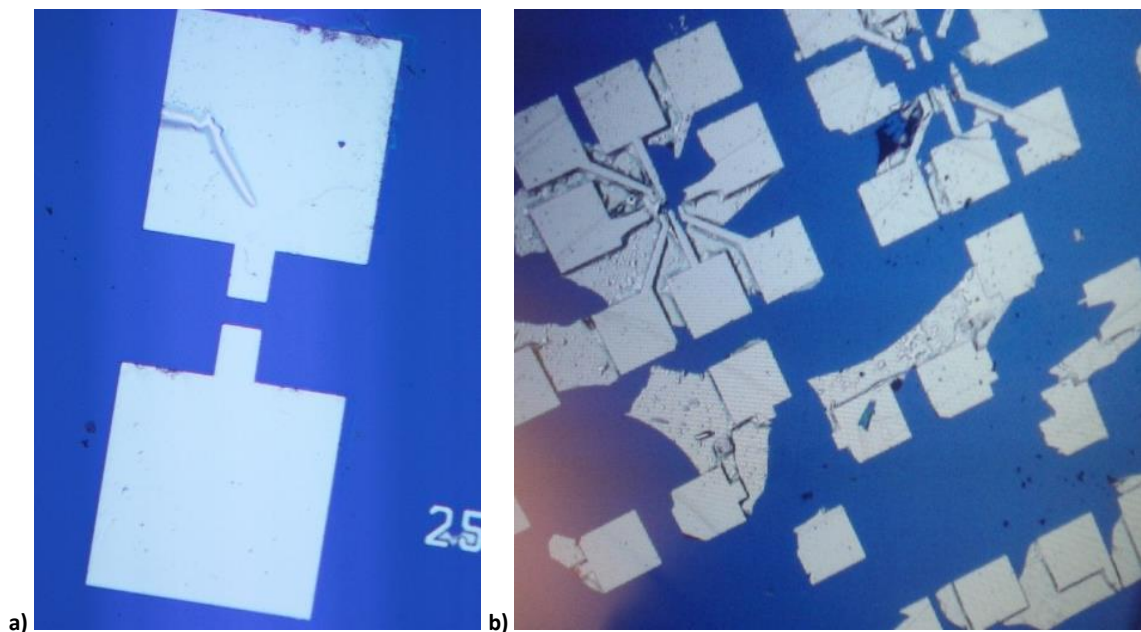


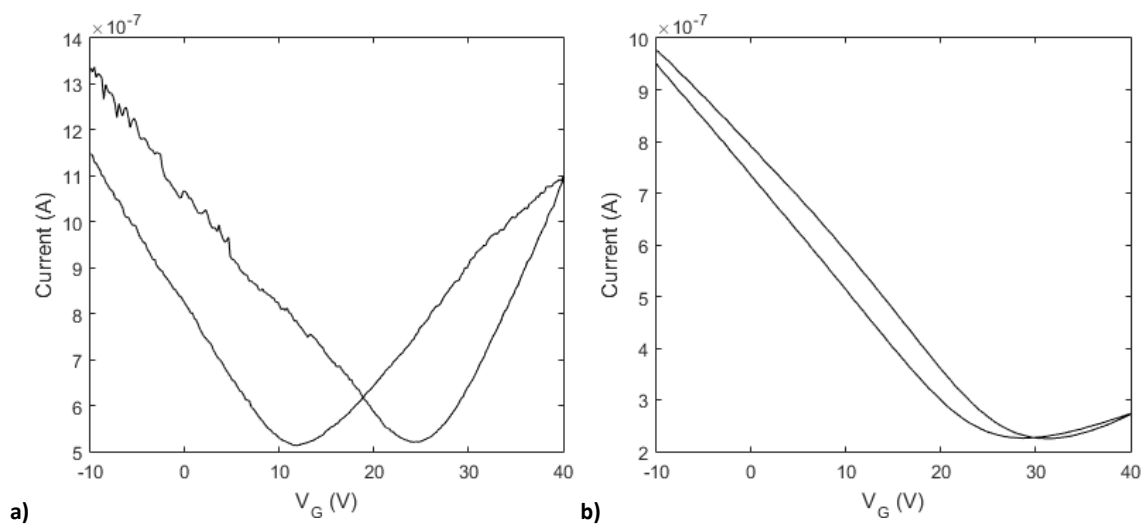
Figure 5.28, showing the bad lift-off of the nickel-aluminium on the photolithography devices

One of the samples was encapsulated with 50nm alumina. To enable the contacts to be wire bonded, the alumina coating over the contacts was etched in phosphoric acid – this only partially removed the alumina, and weakened the bond between the substrate and the nickel, figure 5.29. As a result, when the device was tested on the probe station and wire bonded it was very difficult to obtain a successful result.



Figure 5.29, showing the device with an alumina encapsulation that was removed from over the contacts by an alumina phosphoric acid etch.

The other samples were wire bonded and probed, figure 5.30. It was found to be very easy to wire bond to each device, with the Ni-Al contact proving very resilient regardless of the Ni and Al thickness. All of the measurements shown in figure 5.30 demonstrate gate hysteresis, which occurs because the application of a gate voltage promotes charge transfer in the graphene and trapping of carriers that results in a field that promotes adsorption of further environmental dopants onto the device, such as H₂O and O₂, resulting in a shift in position of the Dirac point [231] [232]. Therefore, gate hysteresis and the presence of environmental dopants prevent more reproducible electrical measurements. Improved reproducibility of electrical measurements can be achieved through encapsulation, as discussed in chapter 5.3.6.



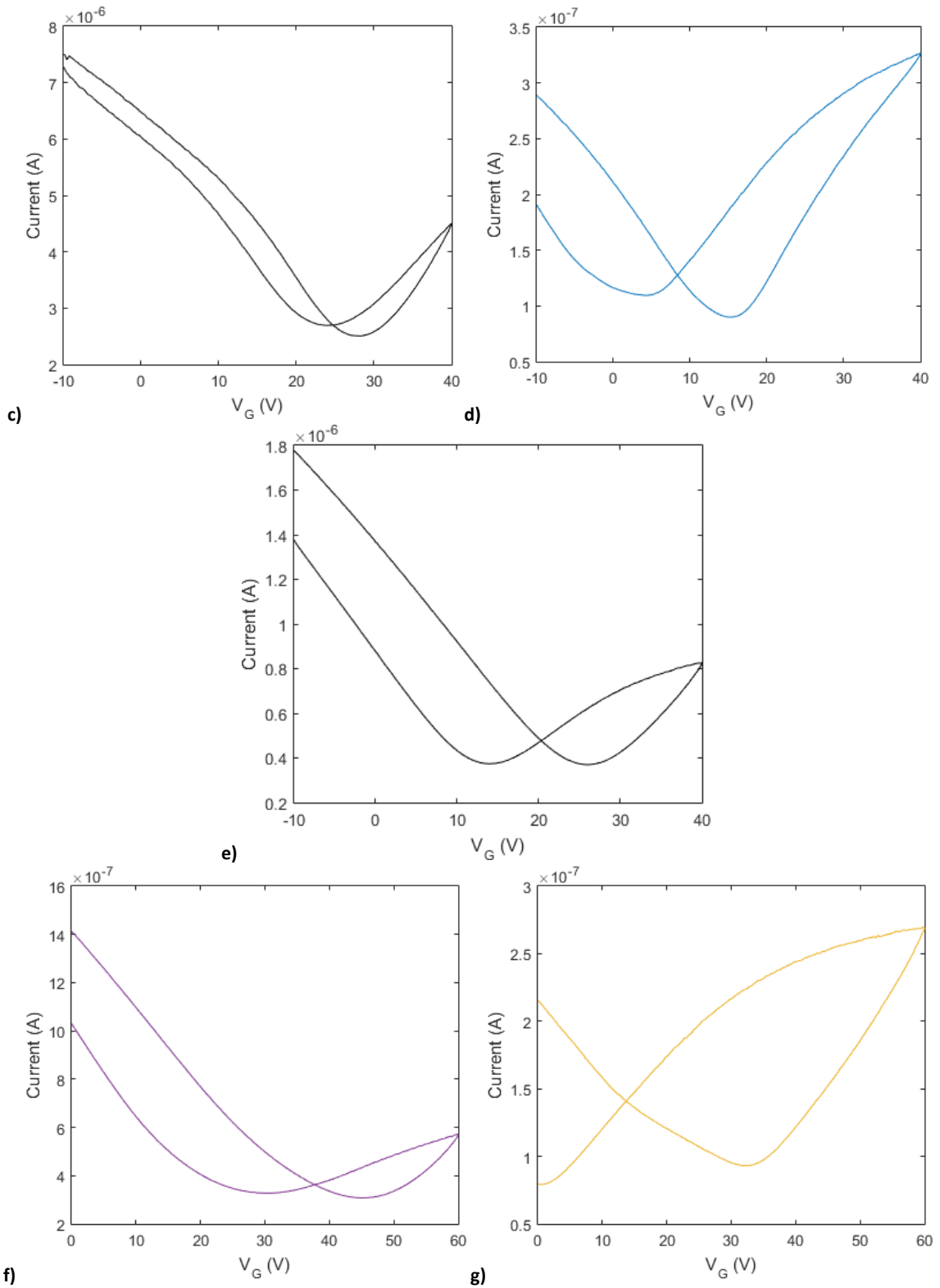


Figure 5.30, showing probe station results of device that were fabricated by masking the device by photolithography, with a)-e) before wire bonding, and f) and g) after wire bonding. In all cases gate hysteresis was observed, where the change in gate voltage promotes the adsorption of further environmental dopants onto the device, which causes the Dirac point to shift.

5.6.4 Bilayer Graphene Detector Fabrication II: Improving the Detector

Fabrication

In this section of work, new bilayer graphene-based detectors were fabricated using Ni-Al for the contact pads. The graphene samples, figure 5.31, were analysed and masks were drawn up that were masked and etched in the standard way using electron beam lithography.

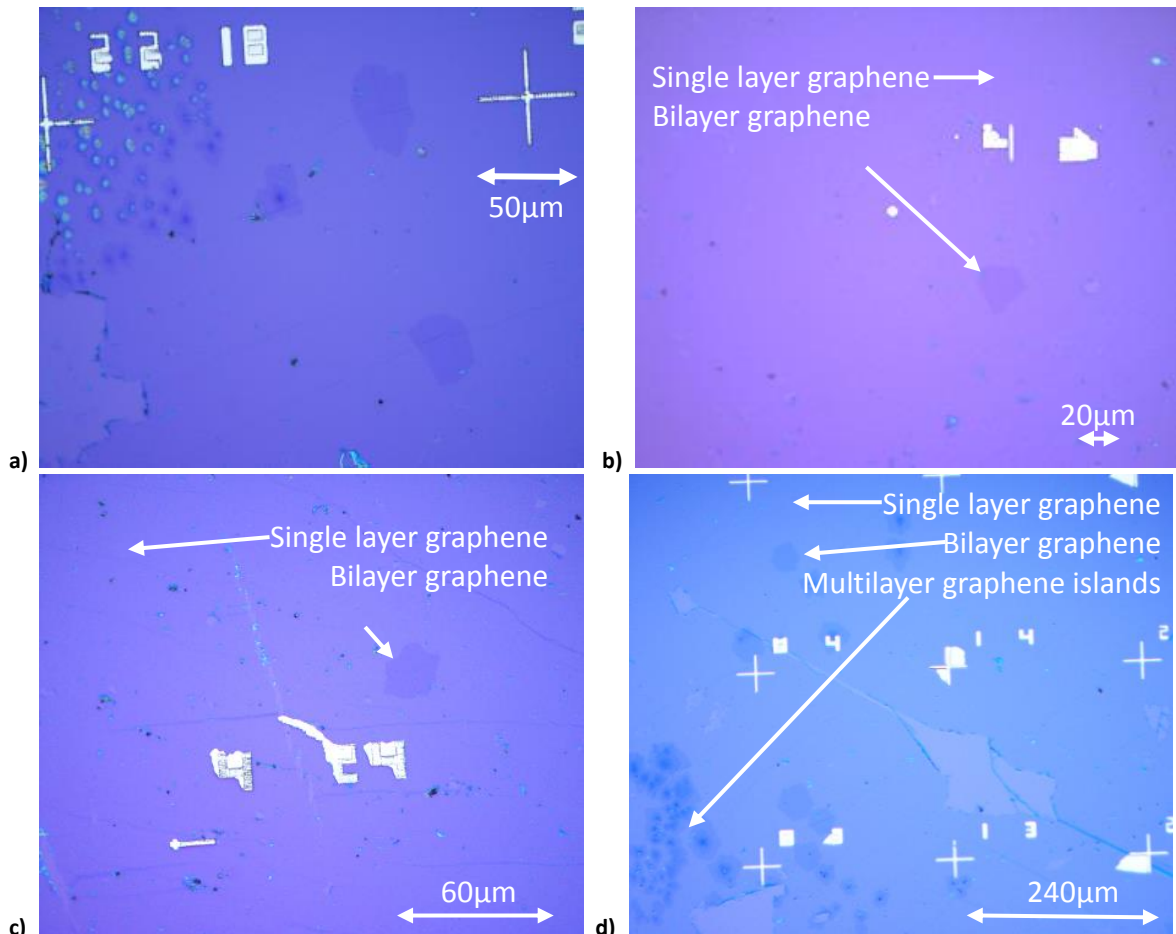


Figure 5.31 showing four bilayer graphene samples, referred to by the shape of the Si wafer: a) "bendy left", b) "most square", c) "central scratch" and d) "bent bottom".

Contacts were deposited by sputtering nickel of 50nm+50nm, figure 5.32a. No aluminium was deposited at this staged due to the alumina etch step later in the fabrication process. An ALD layer was deposited ~40-50nm thickness. A PMMA photoresist was spin coated onto the device before masking the top gate and depositing sputtered ITO for 500s, figure 5.32b-c.

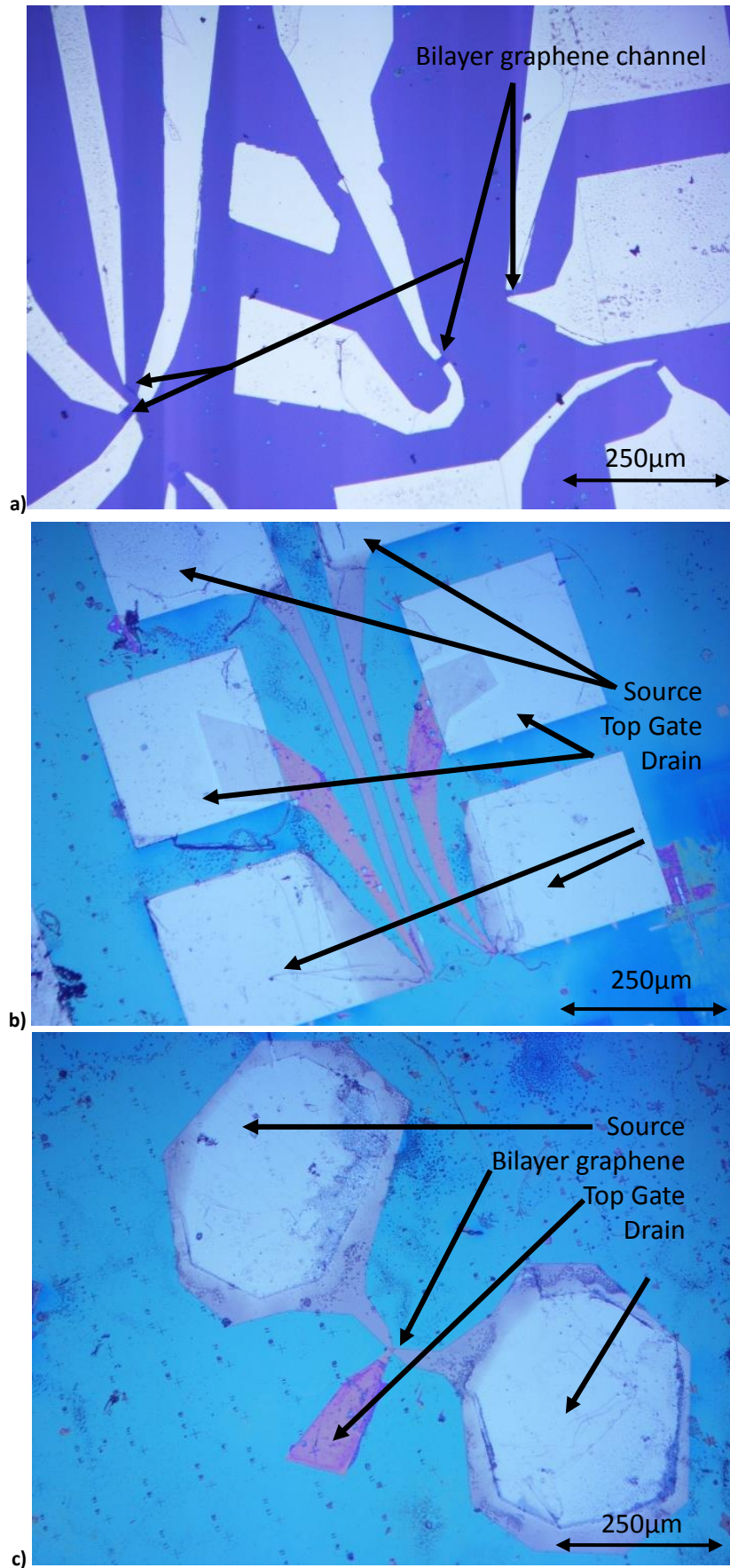


Figure 5.32 showing a) the deposition of the nickel as contacts to the etched bilayer areas, and b) and c) the device after the deposition of the ITO top gate and the initial etching with the HF.

The alumina layer had to be etched back from the contacts; the chip was spin coated with UV88 and masked by electron beam lithography, before an etch step in HF. The first HF step scarred the samples and looked like it was removing the photoresist. The UV88 photoresist was washed off with IPA and repeated with PMMA, although the PMMA was incorrectly developed – ending the development with water and not IPA.

One sample was etched in a phosphoric acid bath, which preferentially etched away the alumina and photoresist over the pads, but also created a “spiders web” like coating over the rest of the device. Another sample was then etched in a HF etchant, which this time worked well. This was immediately sputtered with aluminium for 700s, figure 5.33a. The lift-off was not 100% perfect, which required debris to be scratched off to prevent two of the devices shorting. The chip was successfully wire bonded, with two devices gated with a Dirac point of $V_G \sim 35V$ and $V_G \sim 30V$, figures 5.33b and 5.33a respectively.

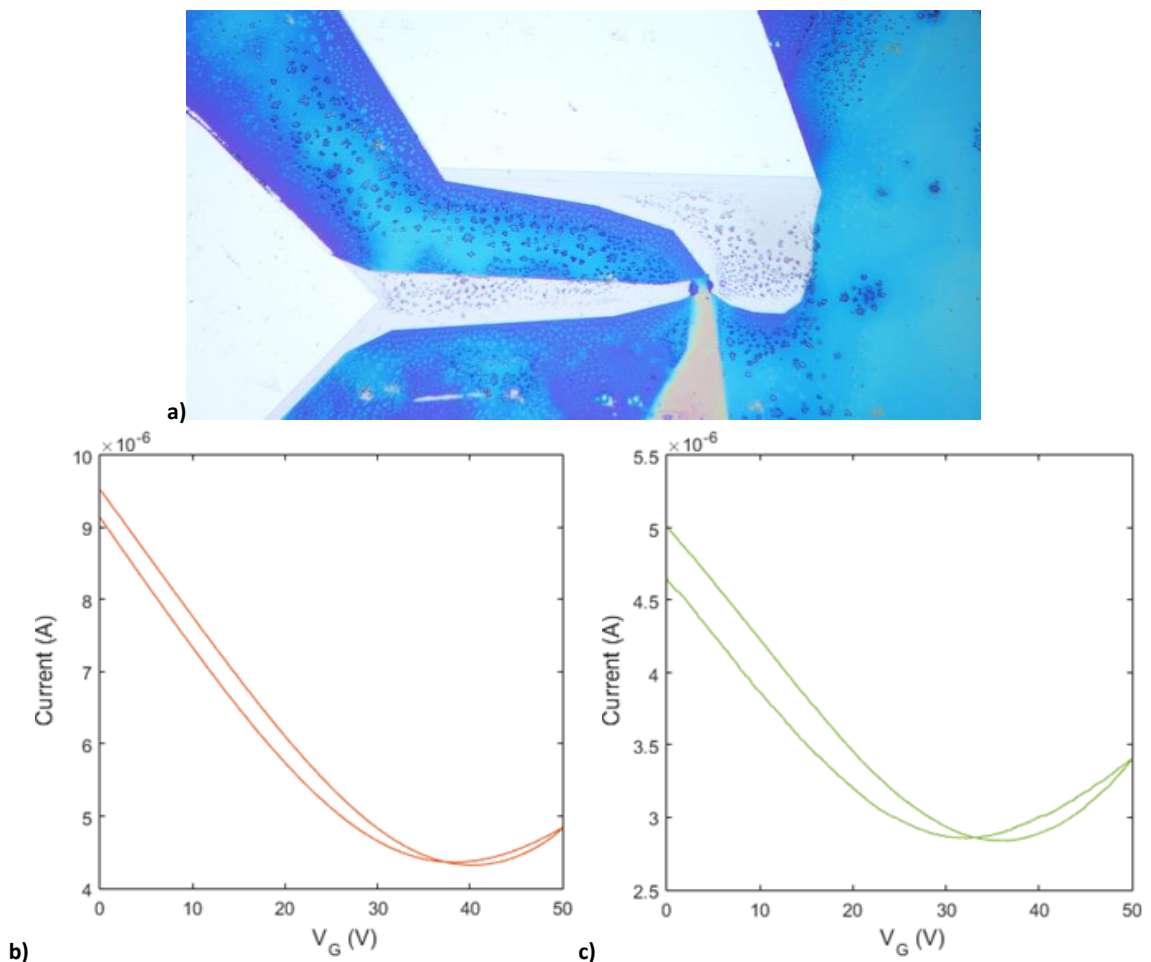


Figure 5.33 showing a) the sample after the second etching with the HF and deposition of the aluminium contact, and b) and c) the bottom gate sweeps for two of the devices that were successfully fabricated.

5.7 Summary

This chapter has outlined the critical steps required to fabricate graphene-based devices, and how these were applied to fabricate each of the devices during the three months of work at the University of Cambridge. The state of the art of each technique has been outlined, with this moving very quickly given the ongoing research and development in this area. Several routes to synthesise large domain graphene have been considered, and of these chemical vapour deposition arguably provides the most promising route to industrial scale, commercially viable synthesis of graphene.

Many issues were highlighted during the design and fabrication of the device that had to be overcome by iterating the processes that were used. For instance, improvements were made to the adhesion of the contact pads to the silicon substrate by sputtering nickel-aluminium rather than evaporating chrome-gold. Improvements were also made in areas relating to the etching of the alumina by using a PMMA photoresist and HF rather than other options including phosphoric acid and UVIII.

The work presented in this chapter highlighted the stages required to successfully process a graphene sample on a silicon/silicon dioxide wafer into the required device. This process took several stages, which included multiple lithography steps, thin film deposition and etching:

1. Sputter tungsten alignment markers onto the sample.
 - Chamber pressure: 3.5×10^{-3} mbar
 - Argon flow rate: 32sccm
 - Beam energy: 100W
 - Presputter time: 600s
 - Sputter time: 400s for ~50nm
2. If required: use optical microscopy to determine the areas that contain desired multilayer graphene samples
3. Design the required mask using a CAD package such as AutoCAD
4. Mask and etch the channel.
 - a. Spin coat a negative photoresist
 - Spin speed 3000rpm for 30s
 - b. Prebake
 - Prebake temperature: 90°C (for MAN)
 - Prebake time: 60s (for MAN)
 - c. Mask using lithography (e-beam or photolithography).
 - Beam current: ~2nA (for MAN)
 - d. Develop the sample.

- *Developer:* 1:4 AZ351B: water (for MAN)
- *Developer time:* 60s
- e. Etch the contact using an O₂ plasma.
 - *O₂ plasma time:* ~10s
- f. Clean with acetone/IPA.
- 5. Mask the contact and deposit the contact.
 - a. Spin coat a negative photoresist
 - *Spin speed* 3000rpm for 40s
 - b. Prebake
 - *Prebake temperature:* 180°C (for PMMA)
 - *Prebake time:* 90s (for PMMA)
 - c. Mask using lithography (e-beam or photolithography).
 - *Beam current:* ~2nA (for PMMA)
 - d. Develop the sample.
 - *Developer:* 1 MBIK : 3 IPA, then in IPA (for PMMA)
 - *Developer time:* 10s (for PMMA)
 - e. Thin film deposition of nickel using a metal sputter coater.
 - *Chamber pressure:* 2.5×10^{-3} mbar
 - *Argon flow rate:* 20sccm
 - *Beam energy:* 100W
 - *Presputter time:* 600s
 - *Sputter time:* 423s for ~50nm, wait for ~1 min, then sputter for a further 423s for ~50nm
 - f. Thin film deposition of aluminium using a metal sputter coater.
 - *Chamber pressure:* 3.5×10^{-3} mbar
 - *Argon flow rate:* 32sccm
 - *Beam energy:* 100W
 - *Presputter time:* 300s
 - *Sputter time:* 700s for ~91nm
 - g. Lift off process in acetone/IPA.
- 6. If required: atomic layer deposition of a layer of alumina as the dielectric.
 - *Precursor* Trimethylaluminium (TMA)
 - *Wetting* Water
- 7. If required: etch the ALD alumina away from the contacts.
 - a. Follow steps 5a-d
 - b. Etch with HF for ~30s
- 8. If required: deposit the top gate contact.
 - a. Follow steps 5a-d
 - b. Thin film deposition of indium tin oxide (ITO) using a sputter coater.
 - *Chamber pressure:* 3.2×10^{-3} mbar
 - *Argon flow rate:* 40sccm
 - *Beam energy:* 50W
 - *Presputter time:* 500s
 - *Sputter time:* 1500s for 157nm
- 9. Wire bond the sample
 - *Diattach temperature* 200°C
 - *Bonding temperature* 120°C
 - *Wire material* Gold
 - *Wire thickness* 25µm
 - *Bonding technique* Wedge bonding

After the three months of work at the University of Cambridge, many different devices had been fabricated of different qualities and designs. These were all fabricated in essentially the same GFET structure. As listed in table 5-4, some of these had faults related to the inability to wire bond because of the poor adhesion between the substrate and contacts, whilst others were only partly fabricated ready for further processing. Some of these devices in table 5-4 were used for the next stage of research, while further devices continued to be produced at the University of Cambridge for this project, using the same manufacturing processes and parameters outlined above.

| Phase | Device Description | Status |
|-------|--------------------|--|
| 1 | THz | Struggled to wire bond to. |
| 2 | THz | One wire bonded to, but not good quality tracks. Damaged in tests. |
| | X-Ray | Unable to wire bond to. |
| | Bilayer Graphene | Unable to wire bond to. |
| 3 | THz | Two successfully wire bonded. Others required etching and contacts/graphene transfer ready. |
| | X-Ray | Many successfully wire bonded. |
| | Bilayer Graphene | 1 x completed 1 x required HF etch and aluminium deposition 1 x required e-beam over the contact pads, HF etch and aluminium deposition 1 x required top gate e-beam and sputter, e-beam over the contact pads, HF etch and aluminium deposition 1 x required contact e-beam and deposition, alumina coating, top gate e-beam and sputter, e-beam over the contact pads, HF etch and aluminium deposition. |

Table 5-4. Status of devices that were fabricated between September and November 2015 at the University of Cambridge.

6

Cryogenic Testing of the Bilayer Graphene Single Photon Counting Photodetector

6.1 Introduction

In chapter 2, the bilayer graphene single photon counting photodetector concept was introduced, and the detector was designed using the results of several different simulations. The processes used to fabricate the detector were discussed in chapter 5, and devices were also produced by collaborators at the University of Cambridge.

In this chapter, the experimental work to identify photodetection by the bilayer graphene detector is discussed. Initially, the voltage-equivalent offset due to environmental doping of the graphene was identified at room temperature, following the technique used in ref. [65]. This was needed to determine the size of the band gap, before the device was illuminated with a cw laser. The detector was then mounted in a dilution refrigerator, cooled to cryogenic temperatures and then tested again.

6.2 Testing at Room Temperature

6.2.1 Applying Top and Bottom Gate Voltages to Bilayer Graphene

In chapter 2.6, the doping of bilayer graphene and opening of the band gap, originally introduced in ref. [65], was presented. By applying top and bottom gate voltages to the bilayer graphene, a displacement field is generated across the top and bottom dielectric layers as a function of the dielectric material and thickness, equations 2.17 and 2.18. The average of these breaks the interlayer symmetry and opens a band gap, equation 2.16, with the magnitude of the band gap given by [12]

$$E_G = \frac{|\bar{D}|\gamma_1}{\sqrt{\bar{D}^2 + \gamma_1^2}}, \quad \text{Equation 6.1}$$

where γ_1 is the hopping parameter and \bar{D} is the total displacement field given by equation 2.16. At large displacement fields calculated using equation 2.16, the band gap tends towards $\gamma_1=0.4\text{eV}$ as shown in figure 6.1a.

The magnitude of the displacement fields generated by the top and bottom gates given by equations 2.17 and 2.18 is also related to voltage-equivalent offsets V_{t0} and V_{b0} , originally introduced in ref. [65], which occur due to environmental doping by the top and bottom gate dielectrics respectively. These need to be characterised to more reliably determine the band gap. For instance, for $V_{t0}=15\text{V}$ and $V_{b0}=45\text{V}$, the band gap that would be expected given equation 2.16 and equation 6.1 is shown in figure 6.1b. This shows a line where a small or zero band gap would be expected, which passes through $V_{t0}=15\text{V}$ and $V_{b0}=45\text{V}$, while the magnitude of the band gap tends towards $E_G \sim \gamma_1 = 0.4\text{eV}$ for top and bottom gate voltages far away from V_{t0} and V_{b0} .

Similarly, the net carrier doping can be estimated by the difference in the displacement fields given by the equations 2.17 and 2.18. Again, with voltage-equivalent offsets that occur due to environmental doping from the top and bottom gates of $V_{t0}=15\text{V}$ and $V_{b0}=45\text{V}$, the net carrier doping as a function of top and bottom gate voltage was calculated using equation 2.19. This shows a line of charge neutrality, i.e. where the net carrier doping equals zero, and therefore the Fermi level sits in the middle of the band gap, which passes through $V_{t0}=15\text{V}$ and $V_{b0}=45\text{V}$.

Therefore, it is critical to accurately characterise V_{t0} and V_{b0} because gate voltages around this point provide solutions that open a small band and cause the Fermi level to sit in the middle of the band gap.

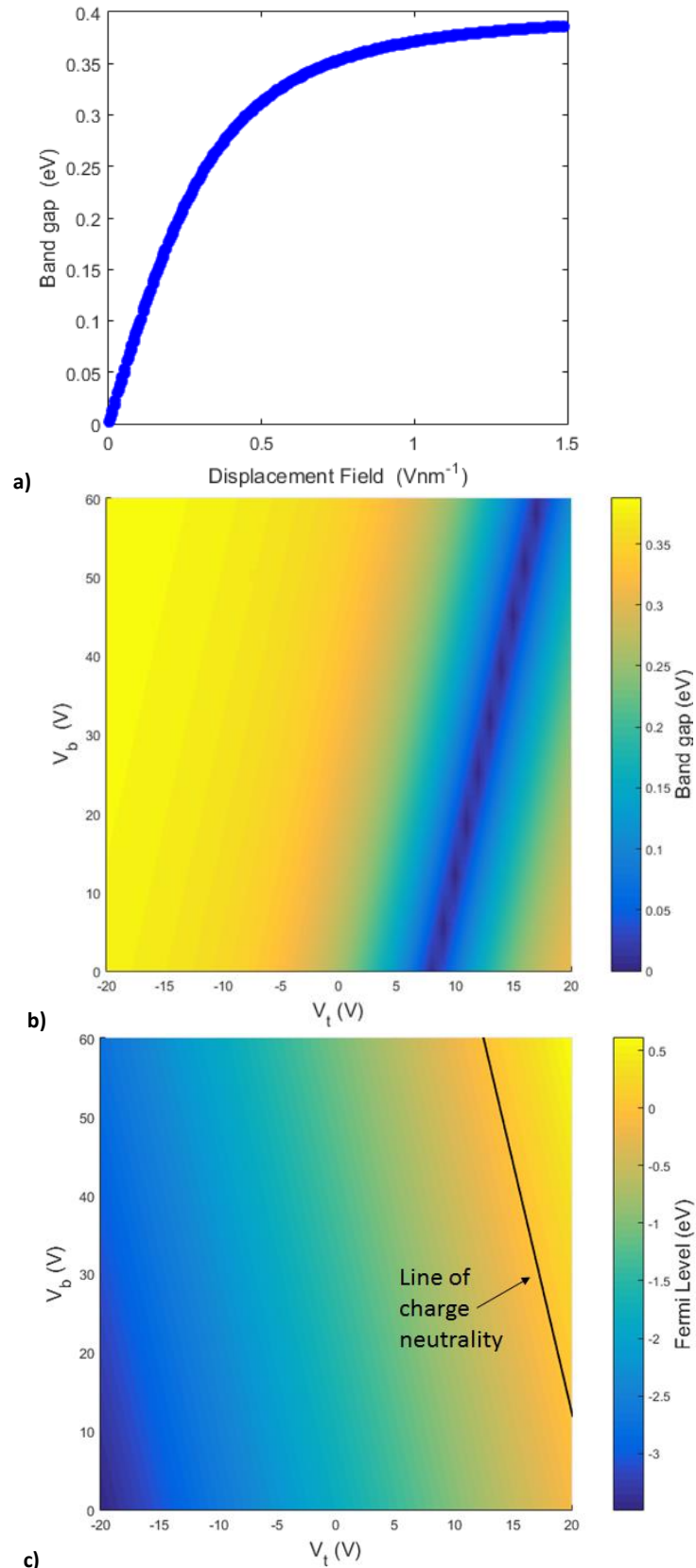


Figure 6.1, showing a) how the magnitude of the band gap, E_G , varies as a function of the displacement field; for large displacement fields, $E_G \sim \gamma_1 = 0.4 \text{ eV}$. For $V_{t0} = 15 \text{ V}$ and $V_{b0} = 45 \text{ V}$. B) and c) shows the theoretically expected values as function of the top and bottom gate voltages for the band gap, and net doping, respectively. The line where the smallest band gaps are expected, and the line of charge neutrality – where there is no net doping, and the Fermi level remains in the centre of the band gap – are not perpendicular and both pass through V_{t0}, V_{b0} .

6.2.2 Determining the Environmental Doping I

To determine the environmental doping parameters V_{t0} and V_{b0} , the graphene channel current was measured as a function of the top and bottom gate voltages.

The first devices to be characterised were those manufactured during the three months in Cambridge. $V_{bias} = 10\text{mV}$ was applied between the source and drain by a Keithley 6517b electrometer, and the current was measured as a function of the top and bottom gate voltages. However, when the Keithley output was turned on, the output uncontrollably spiked to $V_{bias} \sim 100\text{mV}$, which risked damaging the device; this was a surprise as the Keithley is an expensive, reliable and precise piece of equipment. As a result, a 1.5V battery in a potential divider arrangement was used instead.

The bilayer graphene was then connected to an ADA4817 current feedback op-amp in a transimpedance arrangement, so the current through the channel was read out on an oscilloscope as a voltage and varied with the top and bottom gate voltage. The output voltage on the oscilloscope was measured and plotted against gate voltage, figure 6.2, with the intention of calibrating the op-amp for current against oscilloscope voltage. Figures 6.2a and 6.2b show a minimum magnitude oscilloscope voltage as a function of bottom gate voltage at $V_b \sim 20\text{V}$. This corresponds to a minimum current, and therefore a Dirac point at approximately 20V, which means that the device was p-doped. The device failed to gate via the top gate due to a bad connection or an electrical short circuit during manufacture. When attempting to rectify this issue, the gate voltage shorted through the graphene, and the channel was destroyed.

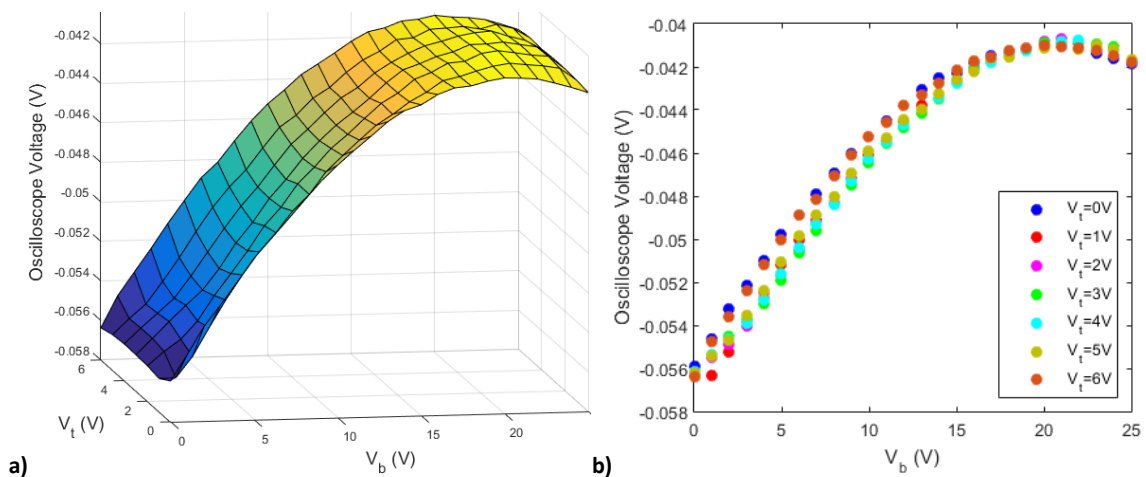
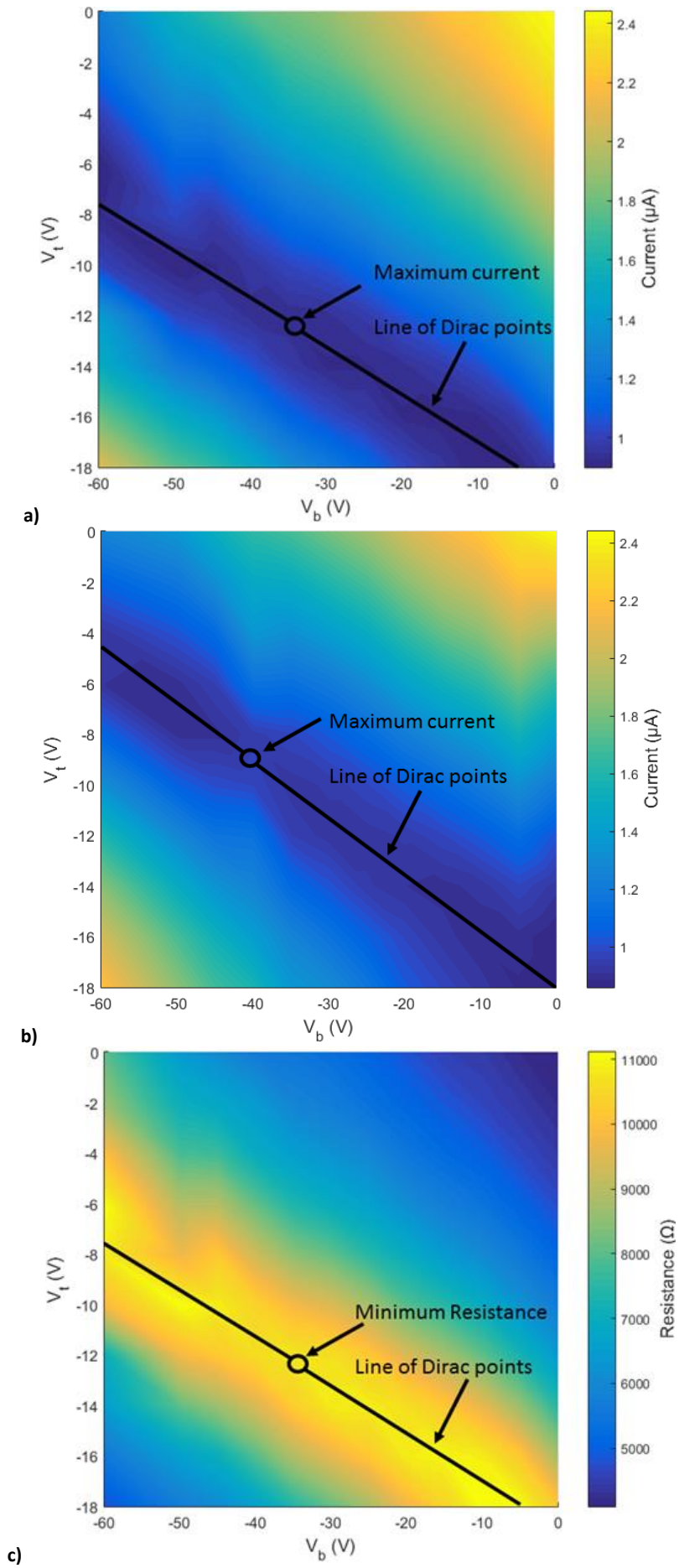


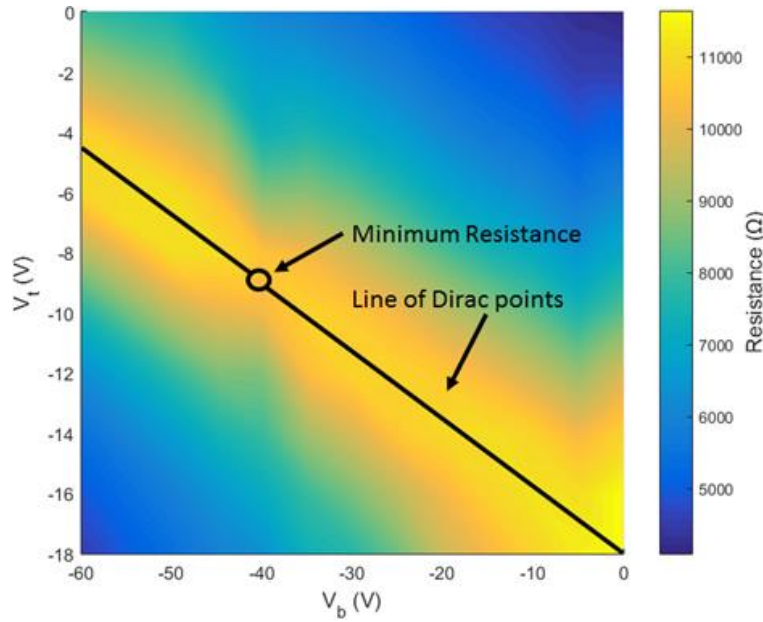
Figure 6.2, showing a) the oscilloscope output as a function of top and bottom gate, which eventually suggested a shorted top gate, and b) the oscilloscope voltage as a function of V_b .

New devices using AB-stacked bilayer graphene were fabricated by the University of Cambridge. As before, $V_{bias} = 10\text{mV}$ was applied between the source and drain of the device, and the resulting channel current was measured as a function of the top and bottom gate voltage. Figures 6.3a and 6.3b show the current for the down sweep (i.e. $V_b = 0\text{V} \rightarrow -60\text{V}$, $V_t = 0\text{V} \rightarrow -18\text{V}$) and the up sweep (i.e. $V_b = -60\text{V} \rightarrow 0\text{V}$, $V_t = -18\text{V} \rightarrow 0\text{V}$), and equivalently in figures 6.3c and 6.3d, respectively, for the channel resistance.

The environmental doping parameters V_{t0} and V_{b0} were identified by following the technique presented in ref. [65]. Given equations 2.16-2.19, in the case of $V_t = V_{t0}$ and $V_b = V_{b0}$, the displacement field to open a break the interlayer asymmetry and open a band gap $\bar{D} = \frac{1}{2}(D_b + D_t) = 0$, and the net carrier doping $\delta D = D_b - D_t = 0$ as well. As $\delta D = 0$, this occurs at the Dirac point as there is no net carrier doping. Also, because $\bar{D} = 0$, there is no band gap, so the channel resistance at the Dirac point is lower than if a band gap had been opened. Therefore, the results presented in figure 6.3 can be used to identify V_{t0} and V_{b0} by seeking the Dirac point (i.e. the minimum channel current (or maximum channel resistance) for a given V_t or V_b) with the greatest current (or, equivalently, the lowest channel resistance).

In both figure 6.3a and figure 6.3b, there is a line indicating the position of the Dirac point as a function of V_t and V_b . Along this line, the maximum Dirac point current is observed, on the up sweep, at approximately $V_b = -40\text{V}$, $V_t = -9\text{V}$, figure 6.3a, and at approximately $V_b = -35\text{V}$, $V_t = -13\text{V}$ on the down sweep, figure 6.3b. At these points, the displacement field, the net carrier doping and the band gap all tend to 0. Therefore, $V_{b0} \sim -35\text{V} - -40\text{V}$, and $V_{t0} \sim -9\text{V} - -13\text{V}$.





d)

Figure 6.3, showing the gate of the device, with the current measured on a) the up sweep and b) down sweep. C) and d) show the equivalent measurements in terms of the resistance. The black line indicates the position of the Dirac points, given by the maximum resistance or minimum current.

This can also be represented by plotting the channel resistance against V_t for different values of V_b , figure 6.4. This shows that the position of the peak resistance as a function of V_t is inversely proportional to that of V_b . In the case of the upsweep, this shows a curve fitted to the maximum resistance measured for each V_b , which shows a minimum resistance at $V_t \sim -12V$ corresponding to $V_b \sim -30V$. Therefore $V_{t0} \sim -12V$ and $V_{b0} \sim -30V$.

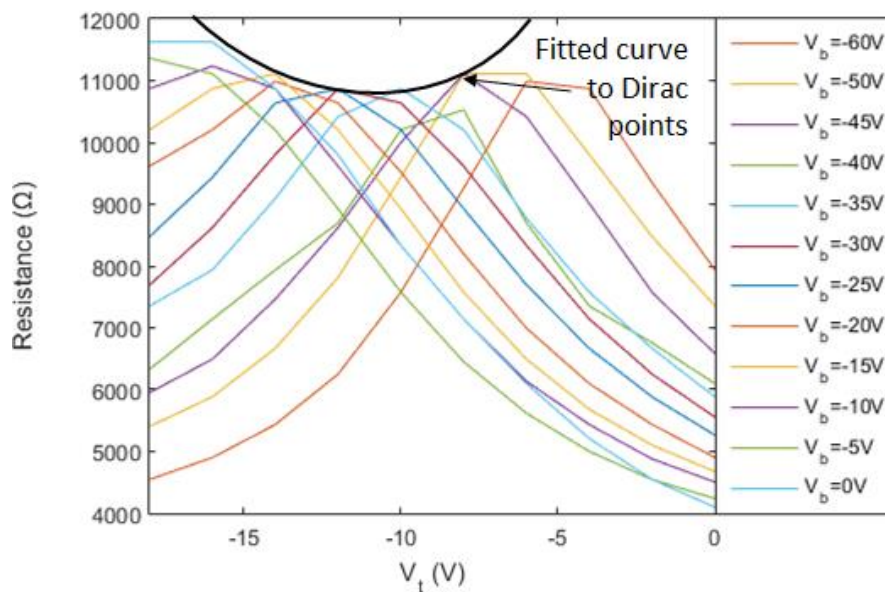


Figure 6.4, showing how the device gates as a function of top gate voltage, for different bottom gate voltages. The Dirac point with the minimum resistance is at approximately $V_t = -12V$, with a corresponding $V_b = -30V$.

These results allowed for the expected band gap and net carrier doping to be calculated for any combination of V_t and V_b . It also identifies a regime, along the line of charge neutrality and around $V_t = V_{t0}$ and $V_b = V_{b0}$, which leads to a small band gap with a Fermi level that remains in the centre of the band gap. Further device iteration could reduce the measured V_{t0} and V_{b0} by optimising the dielectric thicknesses, materials or dimensions of gates, etc.

6.2.3 Determining the Environmental Doping II: Observing Gate Leakage

It was noted after testing the device again using the previously measured parameters that they did not tally with those outlined in the previous section. In the previous section the environmental doping parameters V_{t0} and V_{b0} were estimated as $V_{t0} \sim -12V$ and $V_{b0} \sim -40V$. However, when it was measured again a few weeks later, it was measured as $V_{t0} \sim 11V$, $V_{b0} \sim 38V$, where the minimum resistance of all the Dirac points is indicated in figure 6.5. These values were obtained by using the same technique as described in the previous section, where the minimum resistance among a series of Dirac points (which is given by the maximum resistance as a function of V_b for a given V_t) indicated the value of V_{t0} and V_{b0} .

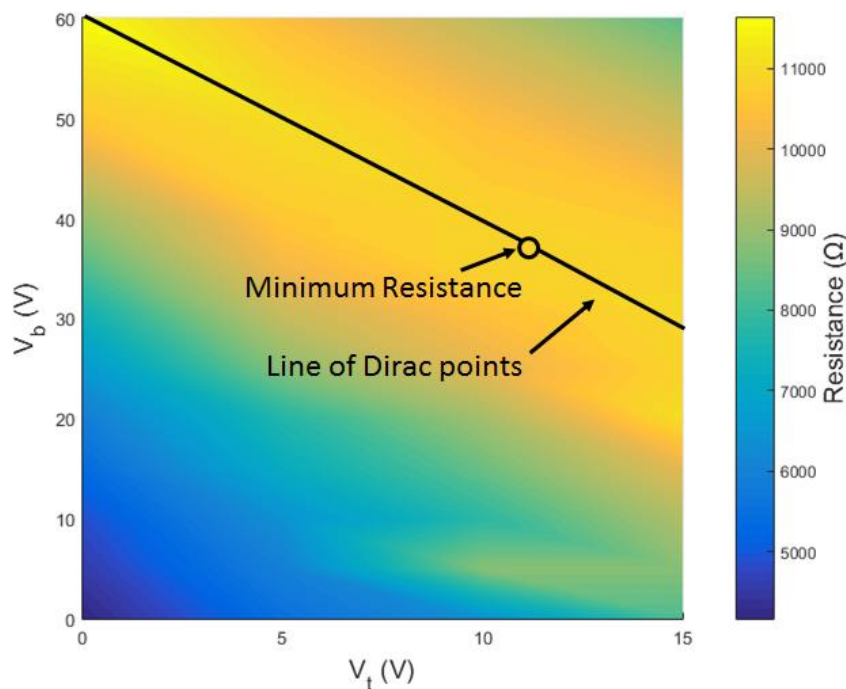


Figure 6.5, showing the measured change in resistance as a function of top and bottom gate voltages. The Dirac points were identified as the maximum resistance as a function of gate voltages. The minimum resistance among these Dirac points occurred at approximately $V_t=11V$, $V_b=35V$.

This shift could be due to a few different factors; 1) human error, i.e. that the terminals had initially been connected the wrong way around, or 2) that the alumina dielectric was failing by leaking charge carriers, and as a result the graphene was beginning to be p-doped, as outlined in ref. [73].

Furthermore, many instances of the graphene channel current shifting dynamically were noted, which meant it was very hard to obtain reliable current measurements for given top and bottom gate voltages. There were three possible reasons identified for this: that the gate dielectric had failed and had started to leak charge carriers from either 1) the top gate, in which case the sample would not be able to be gated properly, or 2) from the environment and hence it was p-doping, for instance in the way that an encapsulation layer can start to leak if the alumina seed layer is insufficient as discussed in ref. [73]; alternatively, 3) that it was a dynamic change in the silicon itself. Each of these was considered in turn.

If one of the dielectrics had failed, then it would not be easy to show that the device gated. Device gating, by taking the initial value once the gate voltages had been set, is observed in figure 6.6a with the variation in top and bottom gate voltages both leading to a change in the channel conductivity; for the yellow line, with $V_b=60V$ and V_t between 0-20V, a Dirac point is observed at approximately $V_t=15V$. Additionally, when the graphene detector was placed in series with a load resistor, and voltage preamplifier placed between the two, a quick change in the gate voltage resulted in a voltage pulse, figure 6.6b. This again indicates that the gate is not leaking, and having the desired effect of changing the channel current through the field effect.

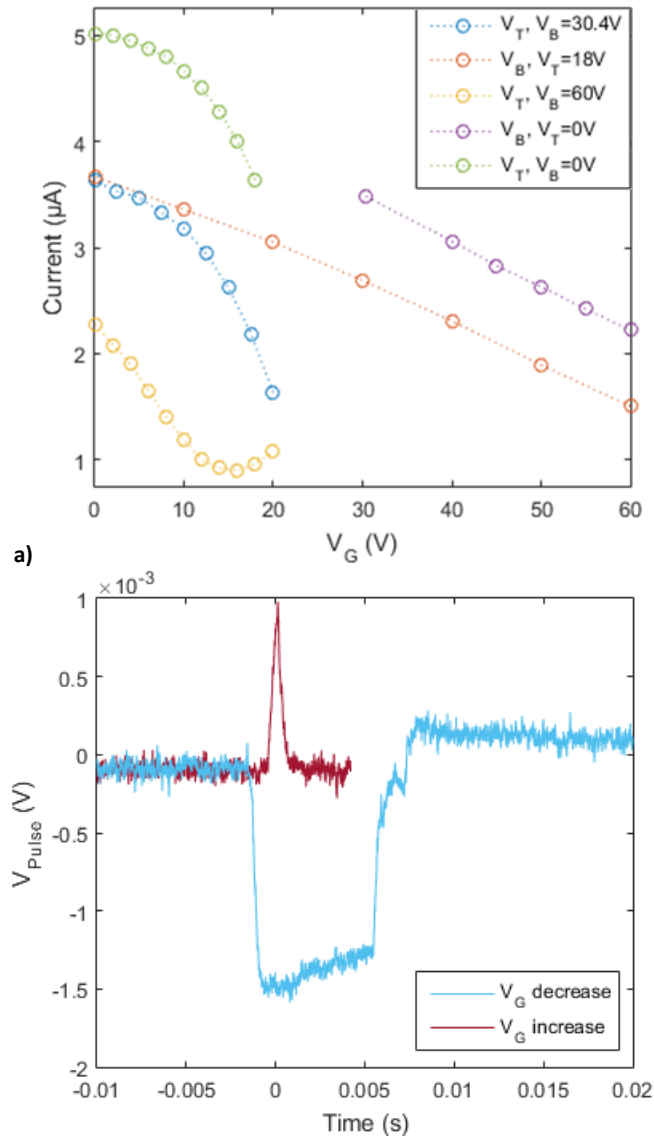
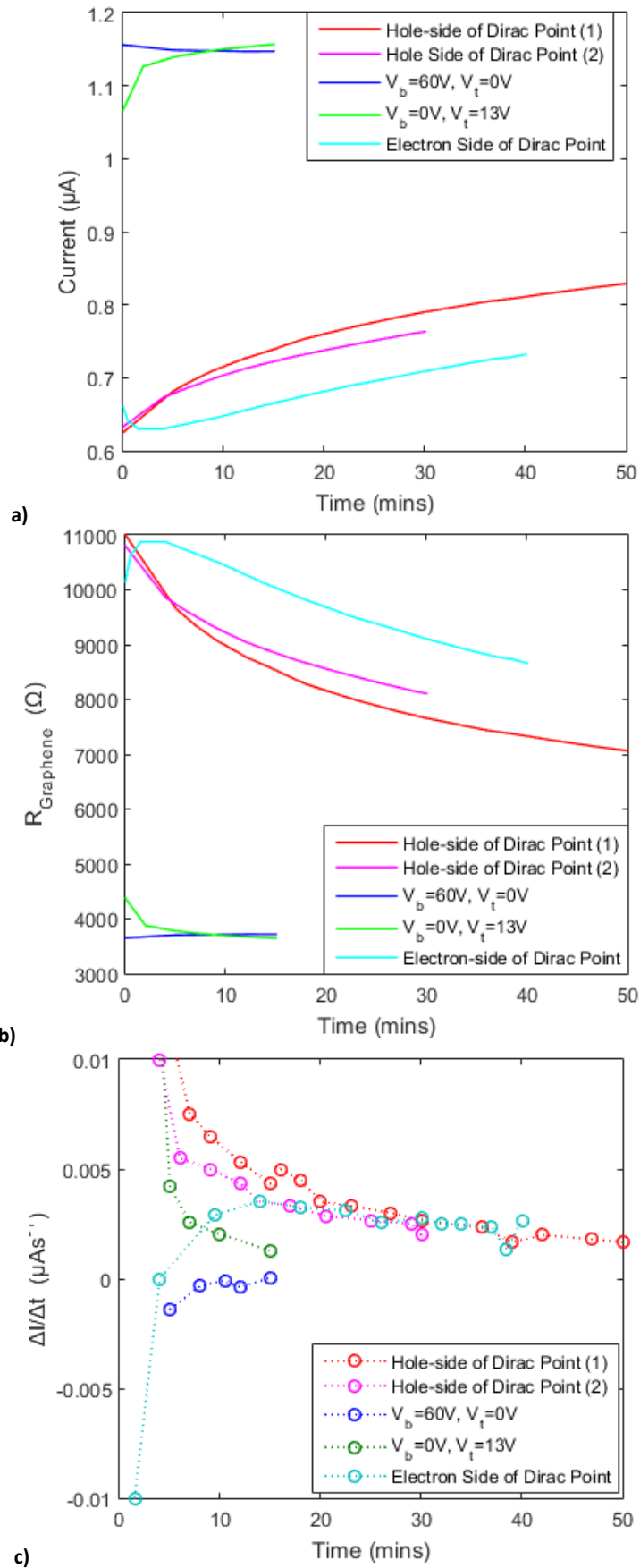
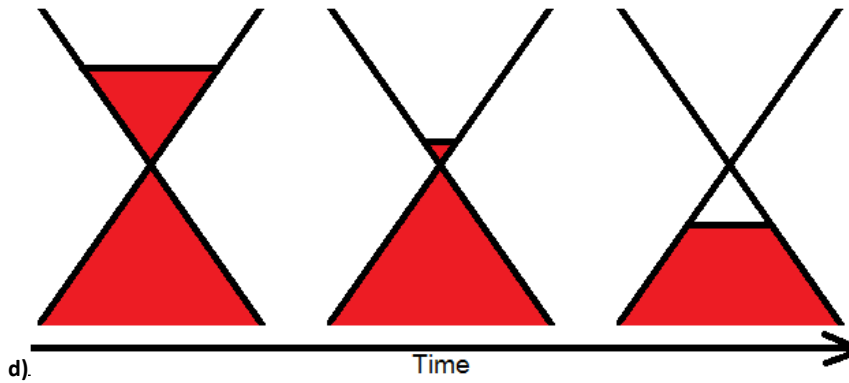


Figure 6.6, showing tests on the top and bottom gates to ensure the dielectric was intact. a) shows gating of the device by changing the top and bottom gate voltages, and in b) a positive or negative voltage pulse is observed when the gate voltage is increasing or decreasing respectively.

To consider hypothesis 2, if the top gate dielectric was not an effective insulator but allowing a gate current to leak charge carriers into the graphene, then one may expect to see p-doping or gate hysteresis, but not necessarily a dynamic change in current on a timescale of minutes as these results demonstrate. The high voltage needed to tune the graphene channel close to the Dirac point causes a noticeably faster change in the current than when the carrier density is tuned further from the Dirac point, figure 6.7a. The rate of change of current is shown in figure 6.7c, with the readings taken close to the Dirac point converging to the same rate. For the light blue line in figure 6.7a, the carrier density was initially tuned to electron transport, but over time the current transitions through the Dirac point to hole transport, illustrated in figure 6.7d.





d). Figure 6.7, showing the measured change in a) current and b) resistance of the graphene channel over time, while c) shows the rate of change of the current converges for those readings close to the Dirac point. d) illustrates how the Fermi level is changing over minutes, moving towards hole transport.

To consider hypothesis 3, regarding a dynamic change in the silicon, silicon dioxide, graphene, alumina or ITO, a charge sensitive preamplifier was connected to the drain and a 50-100mV step was applied across the SiO₂ and then Al₂O₃ dielectric to estimate the capacitance. The resulting voltage pulse across the dielectric was measured by the charge sensitive preamplifier, and by using a known calibration the top gate capacitance was estimated at approximately 0.5pF, which is of the order of magnitude that was expected theoretically. The bottom gate dielectric capacitance was much larger, of order 10s of pF and two orders of magnitude greater than one would expect theoretically from the graphene channel alone, which was attributed to the silicon coupling not only to the graphene, but the source and drain contacts as well.

The setup was then reversed, and a 10mV tail pulse was applied through the drain – a charge sensitive preamplifier was connected to the bottom gate, with a power supply for the gate voltage DC coupled through a 2MΩ resistor. The bottom gate capacitance was measured as a function of top and bottom gate voltage by measuring the magnitude of the first triggered pulse from the charge sensitive preamplifier and using a calibration to equate this to the capacitance; figure 6.8 shows the change in capacitance for both top and bottom gate voltage. Interestingly, the equi-capacitance lines given by $V_t \propto -V_b$ are also the form that would be expected for the line of charge neutrality, which demonstrates the relationship between gate capacitance and the displacement field due to the applied gate voltages.

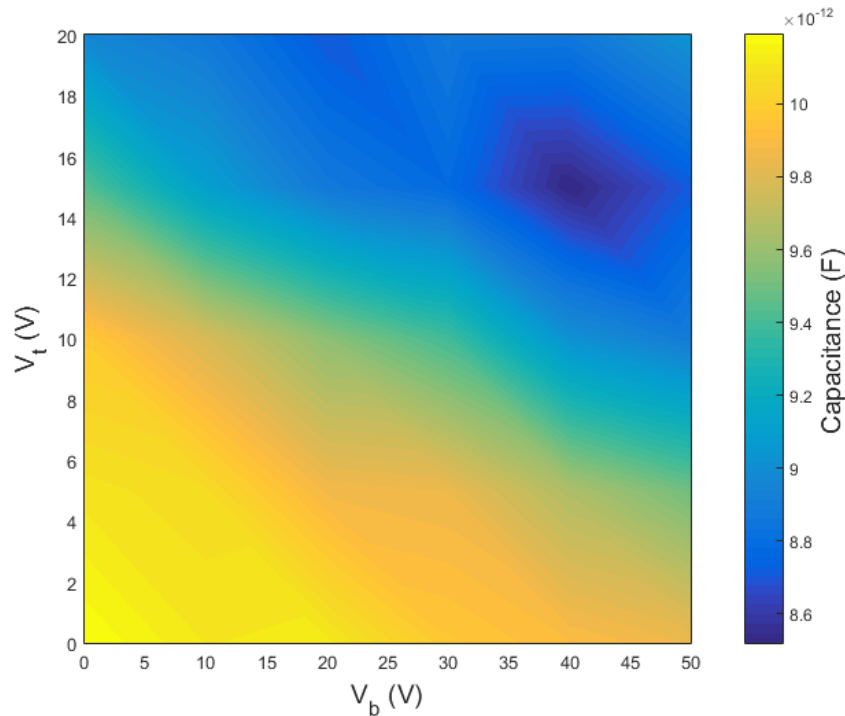


Figure 6.8, showing a strong top gate voltage and weak bottom gate voltage-dependent capacitance.

To observe how the capacitance varies over time, from an initial gate voltage of $V_t = V_b = 0V$, the gate voltages were tuned to $V_t=20V$ and $V_b=60V$, which many readings suggested was close to the Dirac point. The resulting change in the magnitude of voltage pulses from the charge sensitive preamplifier, arising due to the field effect, was seen in the first 10s in figure 6.9a, before it starts to recover and reach equilibrium. Figure 6.9b shows the corresponding change in capacitance, with a change in order 2pF, much closer to the theoretical values that are expected for capacitive coupling to the graphene alone. This is only seen for the SiO_2 dielectric, with no equivalent behaviour observed in the voltage pulse magnitude for the alumina when the charge sensitive preamplifier is coupled to the top gate, figure 6.9c. This dynamic change in capacitance of the silicon dioxide dielectric could be attributed to a change of thickness of the dielectric layer due to Si/ SiO_2 interface states becoming thinner over time, and/or by an increase in the relative permittivity of the dielectric due to changes in the Si/ SiO_2 interface states.

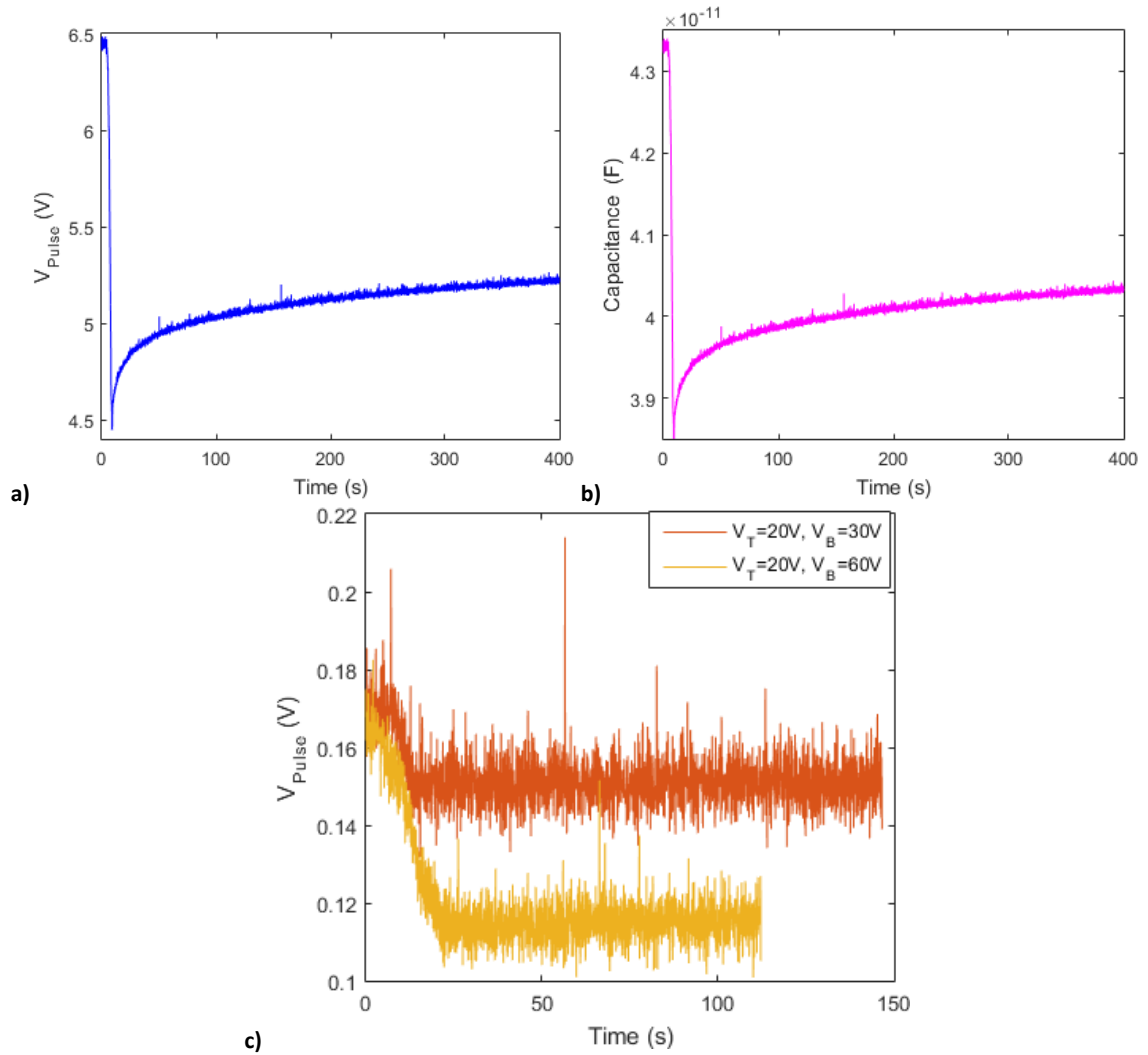


Figure 6.9, showing a) the change in magnitude of multiple fast voltage pulses from the charge sensitive preamplifier for a 10mV input over time, with b) showing the corresponding change in capacitance. c) shows that, for the top gate, no equivalent change in capacitance is observed after the gate voltage is set. The dielectric that is affected is clearly the SiO₂ bottom gate dielectric.

The dynamic change in capacitance causes problems for gating the bilayer graphene to open a band gap. From equations 2.16-2.19 it is expected that the displacement field is expected to be constant. Here, however, one notes a time dependent bottom gate capacitance, $C_b(t)$, where

$$C_b(t) = \varepsilon(t)_b \varepsilon_0 \frac{A}{d(t)_b}, \quad \text{Equation 6.2}$$

$\varepsilon(t)_b$ is the dielectric constant of the bottom dielectric and $d(t)_b$ is the thickness of the dielectric layer, and both could be time-dependent. Also, ε_0 is the vacuum permittivity and A is the area of the sample. This leads to a time dependent displacement field from the bottom gate, $D_b(t)$, where

$$D_b(t) = \varepsilon(t)_b \frac{(V_b - V_{b0})}{d(t)_b} = \frac{C_b(t)}{\varepsilon_0 A} (V_b - V_{b0}), \quad \text{Equation 6.3}$$

V_b is the voltage applied by the bottom gate and V_{b0} is the environmental induced doping due to the substrate. This led to a time dependent band gap, $E_G(t)$, that can be deduced using equation 6.1, where

$$E_G(t) = \frac{|\bar{D}(t)|\gamma_1}{\sqrt{\gamma_1^2 + \bar{D}(t)^2}} = \frac{0.5|D_b(t) + D_t|\gamma_1}{\sqrt{\gamma_1^2 + (0.5|D_b(t) + D_t|)^2}}, \quad \text{Equation 6.4}$$

$\gamma_1=0.4\text{eV}$ is the interlayer hopping parameter, $D_b(t)$ and D_t are the displacement fields applied via the bottom and top gates respectively given by equations 2.17 and 2.18, and $\bar{D}(t)$ is the corresponding total displacement field applied by using equation 2.16. Similarly, by applying equation 2.19, a time dependent displacement field also leads to a time dependent net carrier doping.

Therefore, the measured change in channel current is a result of the change in doping and band gap of the bilayer graphene due to the change in the displacement field. For stable detection, as has always been maintained, the doping must remain in the centre of a constant small band gap. One way to overcome the time dependent capacitance at room temperature may be to vary the top gate over time too to maintain the necessary values for the doping and band gap.

6.2.4 Dynamic Capacitance Problem – Observing Photodetection

In the previous section, the observed dynamic change in channel current was presented and attributed to a time dependent change in the capacitance of the bottom gate, which caused the doping and band gap to change as a function of time. Other options were considered to explain these results, such as gate leakage and the effect of environmental doping, and were ruled out.

Continuous wave (cw) lasers, a red (650nm) and a blue (405nm) laser, were applied to the graphene to investigate any response to the injection of charge carriers. A cw laser source was chosen as a pulsed laser may also lead to the excitation of an electron hole pair in the silicon, resulting in a signal that would likely swamp that from the bilayer graphene. The laser source was intended to excite charge carriers in the bilayer graphene from the valence band to the conduction band, which would be manifested

as a change in the current, with the current also dependent on the band gap and doping controlled by the V_b and V_t .

The experimental setup was non-ideal, figure 6.10, as $V_t = V_b = 0V$, with a 10mV tail pulse at a frequency of 1MHz applied across the graphene whilst looking for a response on a picoammeter. This experimental arrangement was used as, immediately preceding this test, the tail pulse was applied across the dielectric to estimate the capacitance, as discussed in the previous section. However, as has been previously discussed, for $V_b > 0V$ there is a strong drift in the current and so any change in current because of the laser would be masked by the current drifting.

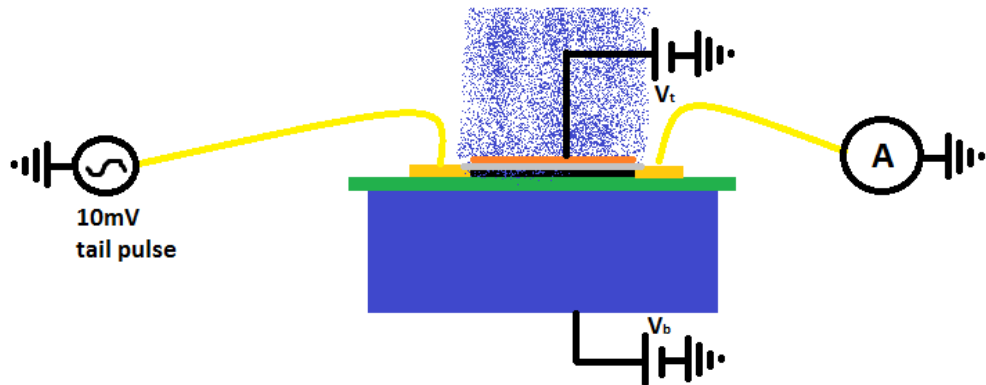
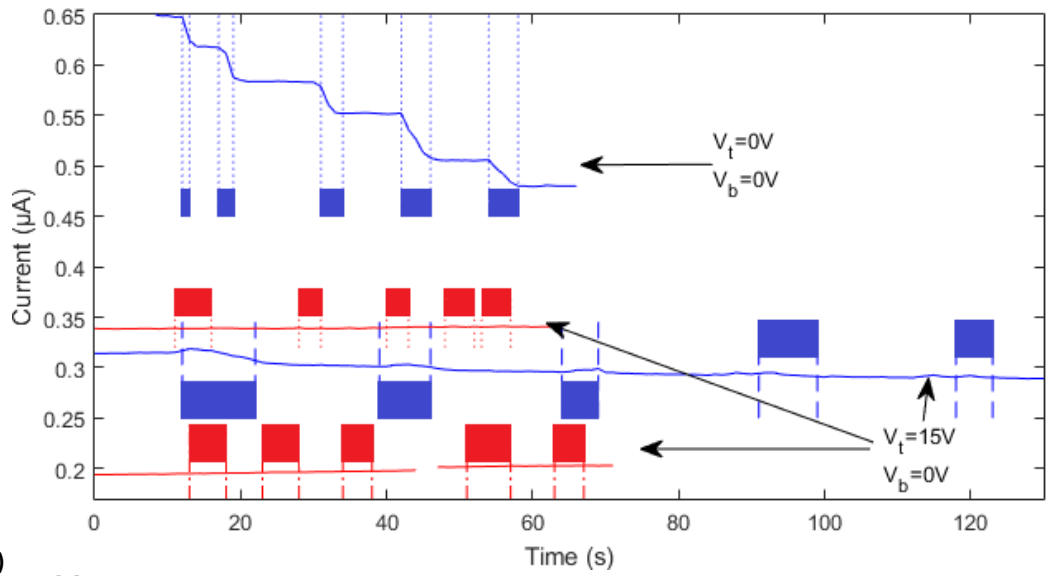


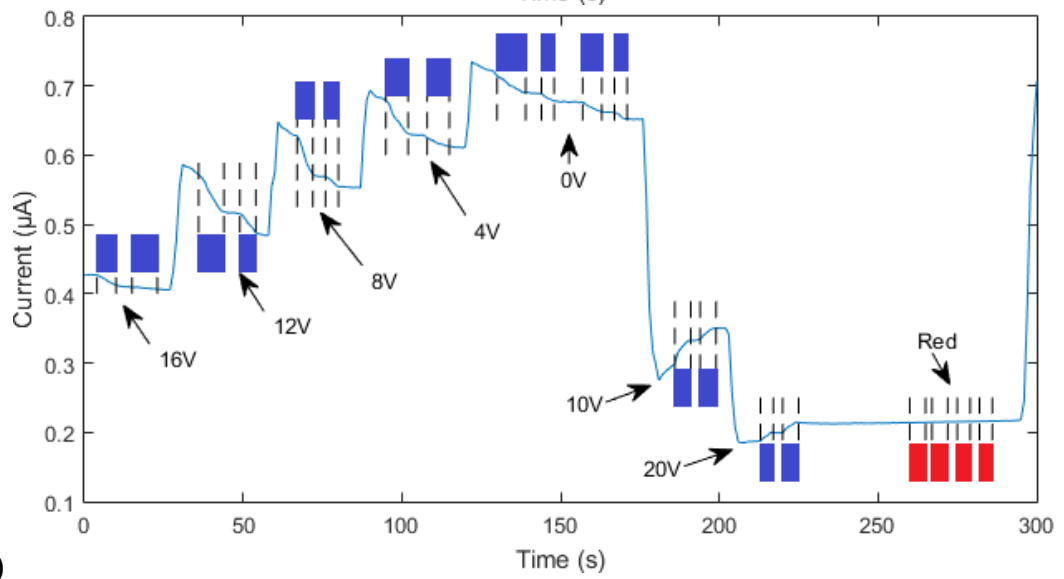
Figure 6.10, showing the experimental setup, with the blue speckled region indicating the area that was illuminated by the blue cw laser, with a 10mV tail pulse applying the voltage across the channel, with the resulting current measured by a picoammeter.

Step changes in the current were observed after illumination by the blue laser but not the red laser, figure 6.11a. The response was seen to be gate dependent, figure 6.11b-c, with the rate of change of channel current when the device was being illuminated by the blue laser related to V_t . It was critical to isolate the origin of this photosensitivity to determine whether this was due to absorption by the bilayer graphene, dielectric states or the silicon substrate.

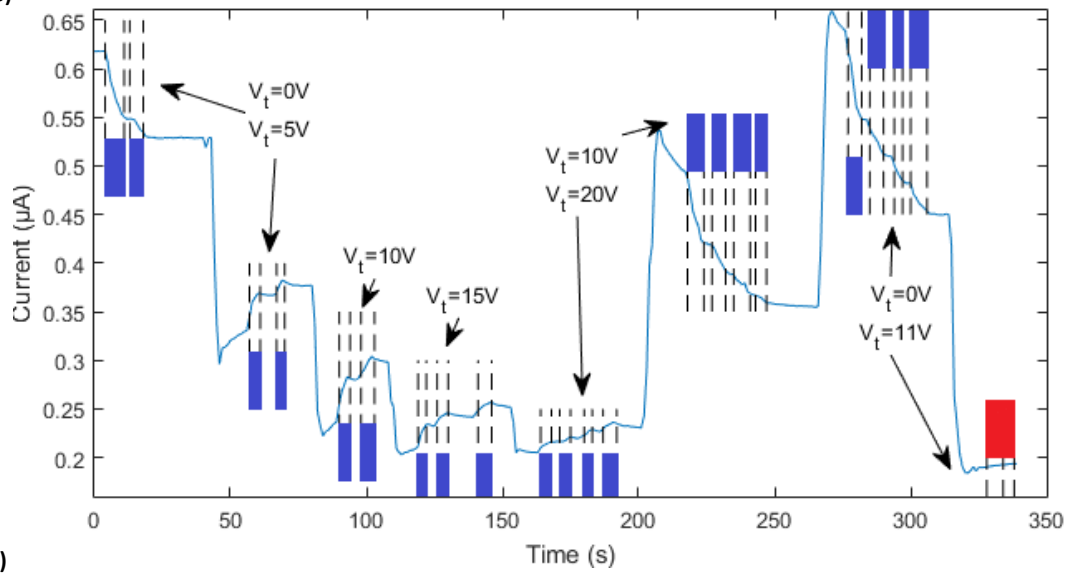
The rate of change of current also appeared to be related to whether the gate voltage was being increased or decreased, as shown in figure 6.11d, with a peak change observed at $V_t = 8-12V$ for $V_b = 0V$, perhaps due to a slowly increasing/decreasing capacitance of the dielectric under the influence of the gate voltages. There was also a noticeable difference between the rate of change of current with the laser illumination on and off, indicating that the current change is not due to the drift in the current.



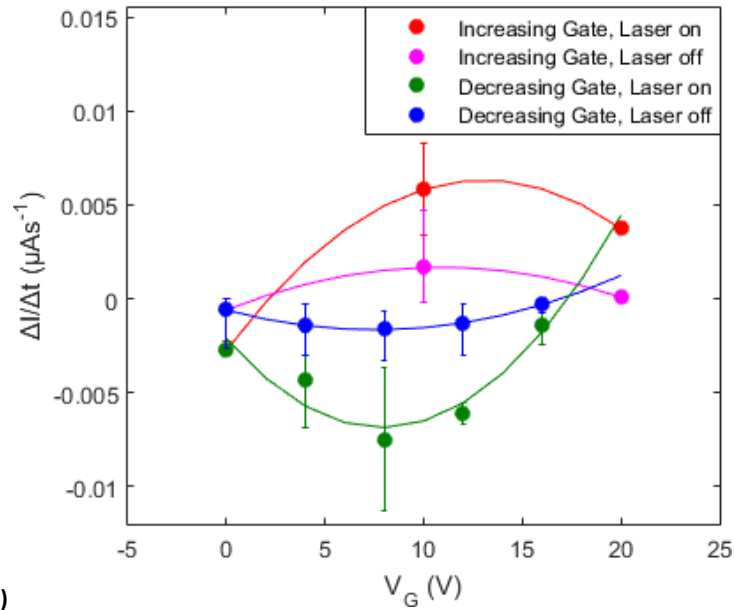
a)



b)



c)



d) Figure 6.11, showing a) illumination dependence which shows sensitivity to the blue laser but not to the red, b) and c) top gate voltage dependence for $V_b=0\text{V}$. d) shows a rate of change of current as a function of gate voltage, which varies depending on whether the gating is being charged up or down – this suggests some long timescale process occurring in the dielectric.

The response was also shown to be intensity dependent by using ND filters to attenuate the laser source, figure 6.12a-b. Using these results, the rate of change of the measured channel current over time during illumination by the laser, $\Delta I/\Delta t$, was calculated and plotted as a function of the ND attenuation for $V_t=0\text{V}$ and $V_t=15\text{V}$, figure 6.12c-d. $\Delta I/\Delta t$ is the same order of magnitude in both cases, but the readings for $V_t=0\text{V}$ were taken when V_t was being decreased, while the readings for $V_t=15\text{V}$ were taken when V_t was being increased, which again suggests a charge up/charge down process arising from the gate voltage which is effecting the capacitance.

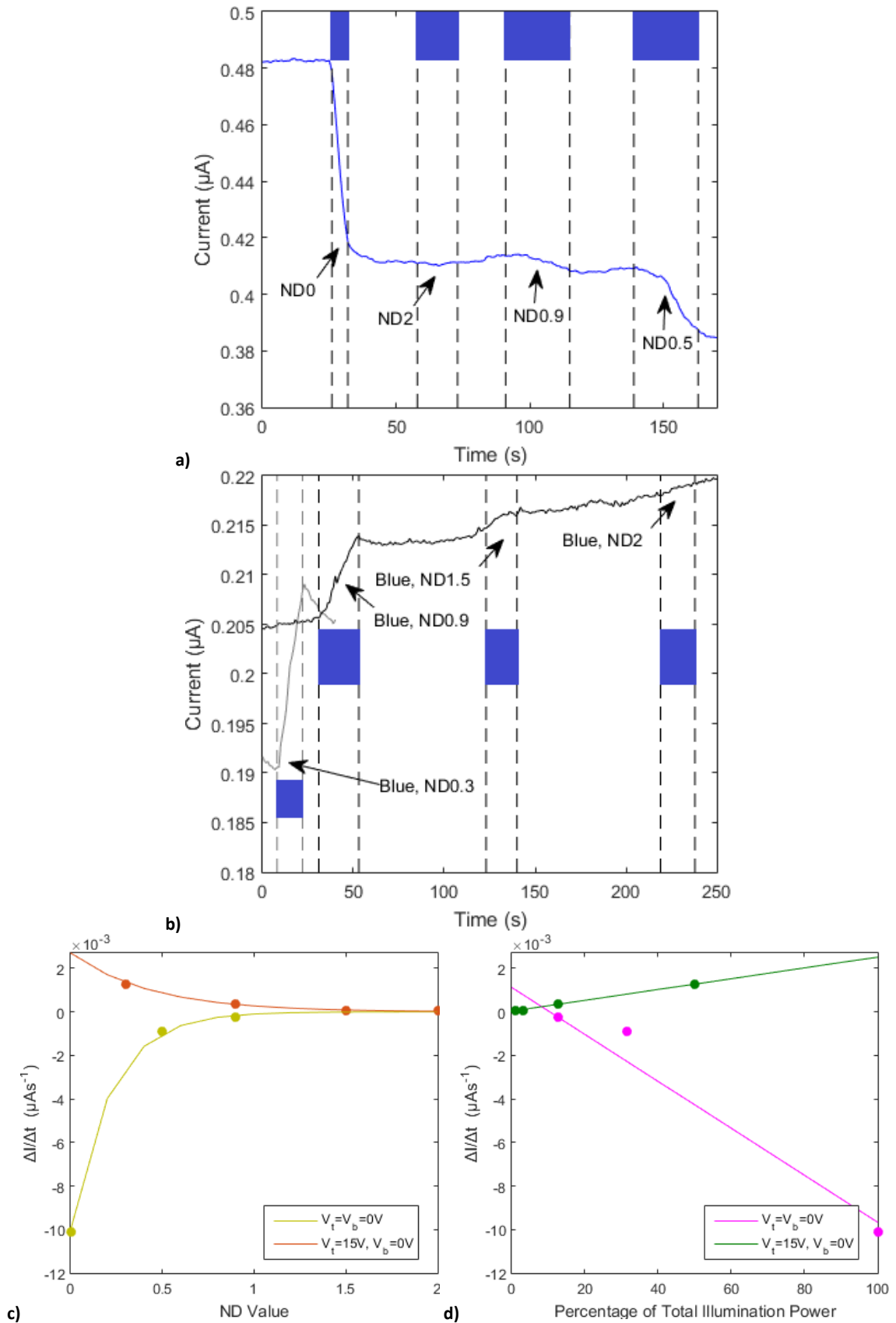
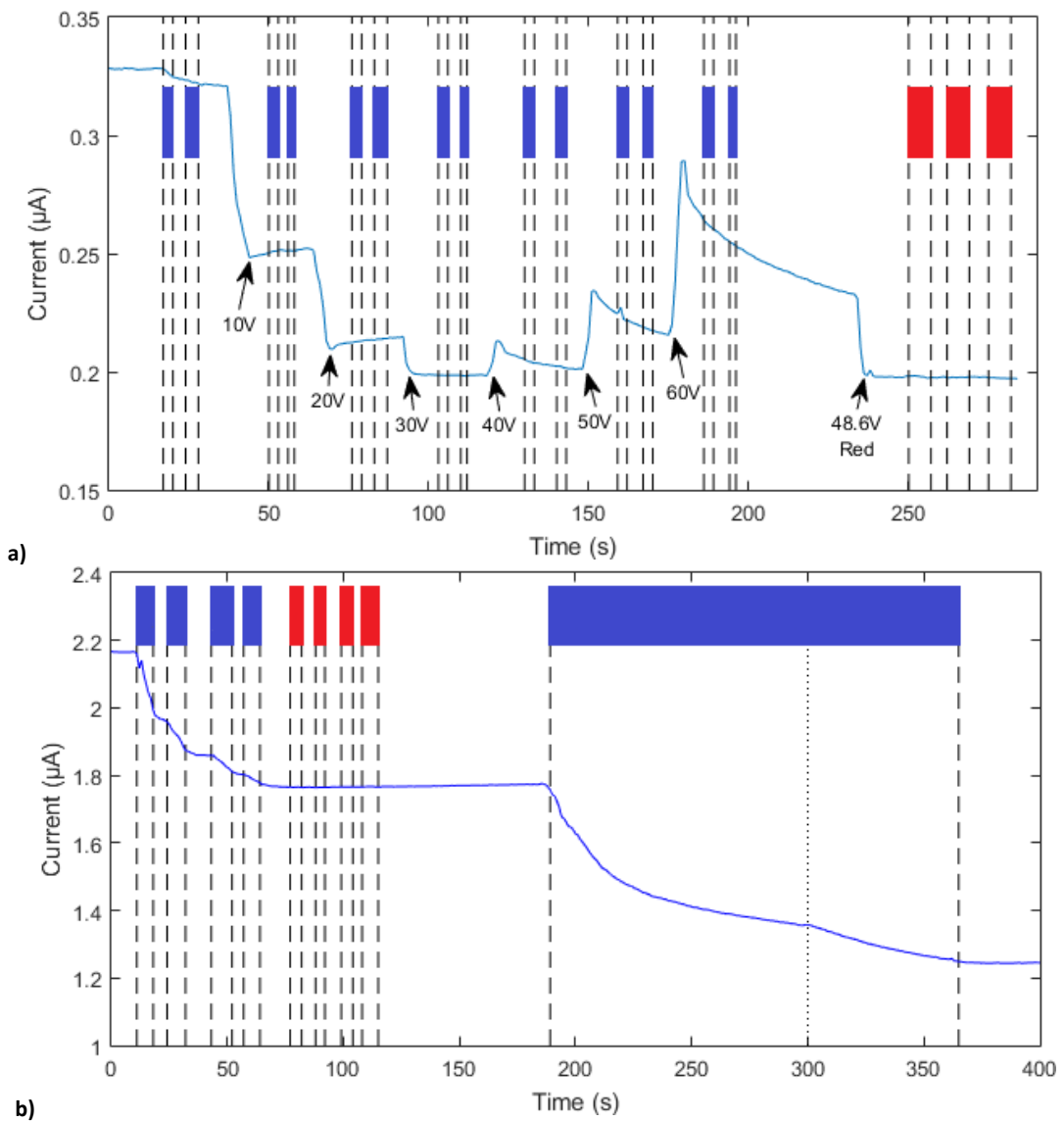
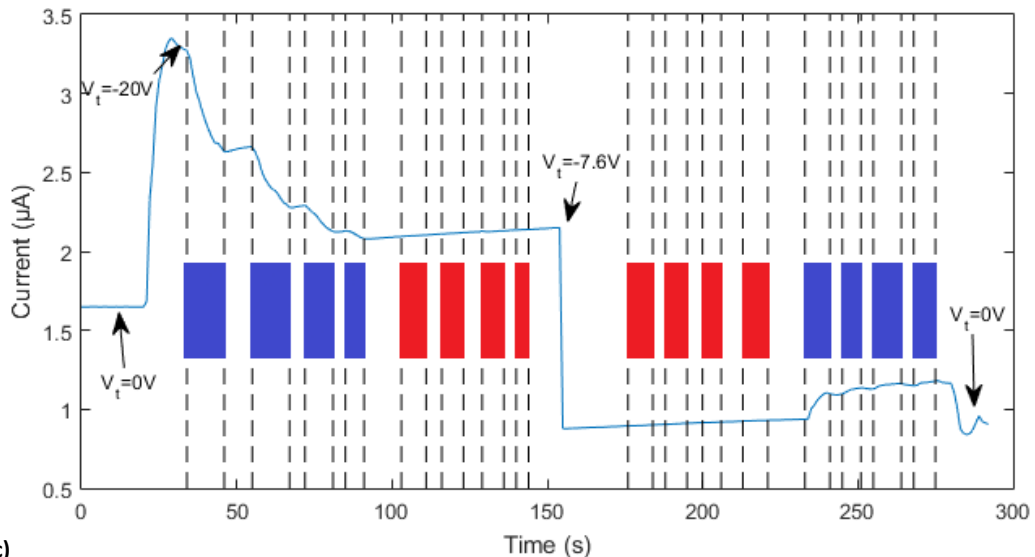


Figure 6.12, showing a) and b) the laser intensity dependence by attenuating the laser source by ND filters, related to the charging up or down of the top gate voltage. C) shows the rate of change of current as a function of ND value to indicate how the current is affected by a more powerful laser source, which is extrapolated in d) to indicate how the rate of change of current is proportional to the total illuminating power.

The signal was only noticed when the bottom gate was floating or held at 0V; there was no current response when the device was bottom gated and illuminated by the blue laser, figure 6.13a, because of the drifting of the channel current. Furthermore, in figure 6.13b-c, one notes that the change in channel current started to slowly increase after the illumination with the blue laser at a constant rate, as though the process enabling the photoabsorption was recombining or relaxing. In addition, long illumination by the blue laser also caused the current to decay exponentially, suggesting that the mechanism enabling the photoabsorption was saturating.





c) Figure 6.13, showing a) no blue laser sensitivity when the device was bottom gated, attributable to the induced drift in the current masking any further change in the current that is induced by the blue laser. b) and c) shows that, after a long illumination, the current starts to recover at a constant rate, suggesting that a process allowing the photosensitivity was relaxing or recombining. The dotted blue line shows the point at which the laser was realigned to better illuminate the device, resulting in a further change in the channel current.

The photosensitivity that was observed could only be explained by an absorption mechanism within the silicon, silicon dioxide or graphene. Considering each of these in turn, if the absorption was in:

- the bilayer graphene: one would expect to tune the Fermi level via the gate voltage so that the photoresponse would vary. While there is gate voltage dependence, figure 6.11, when the Fermi level is tuned to negative gate voltages for a band gap $E_G \sim 0.4\text{eV}$ and a Fermi level $E_F \sim -3\text{eV}$, there should not be sensitivity to blue photons as they do not have sufficient energy to excite an electron from the valence band to the conduction band. However, there is still observed blue laser sensitivity, which suggests another mechanism is providing the photosensitivity. For a small band gap, the signal is dominated by thermal noise at room temperature, so investigating the cryogenic cooling was vital. Additionally, the bilayer graphene absorption coefficient is much lower than that for silicon, so any response from the silicon may dominate that from the bilayer graphene.
- the silicon dioxide: one would expect to see the blue laser have an effect as it has a shorter absorption coefficient and therefore it is absorbed in the silicon closer to the silicon dioxide dielectric. Any e-h pairs that are generated would

recombine quickly in any hole traps in the insulating layer, changing the doping from p-dopants in the dielectric, which shifts the Dirac point as shown in figure 6.7d and is discussed further in chapter 8. The e-h pairs need to be generated somewhere in the detector, typically in a depletion region, although blue photon sensitivity was demonstrated even for $V_G = 0V$. This couldn't be a Schottky diode effect (with a thin insulating layer) as there is an insulating gate. Does the depletion region exist without the gate voltage being applied, or where else could the e-h pairs be generated?

- the silicon: one would expect to require a depletion region to exist. As is discussed further in chapter 8, cw laser sources extinguish a photoresponse by saturating the depletion region – this suggests another mechanism is operating here.

In a further test, a 10mV step was applied to the drain and a charge sensitive preamplifier was used to measure the resulting voltage pulse in the bottom gate during illumination by the blue laser. This shows that the blue laser causes a change in the dielectric capacitance when it illuminates the device, as shown in figure 6.14.

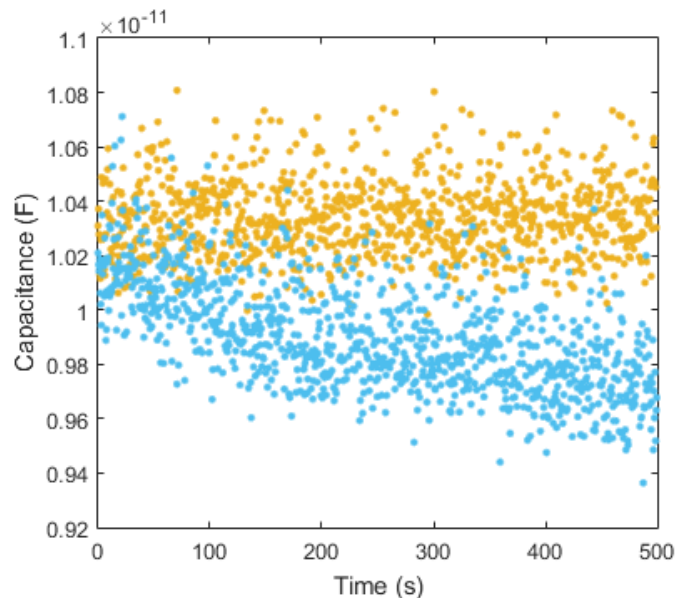


Figure 6.14 showing the bottom dielectric capacitance over time, with the yellow data points the measurements before illumination, and the blue data points indicating the capacitance over time after illumination by the blue laser.

Whilst not certain, it is likely that the mechanism for the photodetection is linked to the dielectric and hole traps there, especially given the illumination-dependent capacitance of the dielectric and the blue-red colour sensitivity. Further tests at

cryogenic temperatures were then used to help explain these observations further, and try to identify any component of the signal arising from the graphene.

6.3 Testing the Device at Cryogenic Temperatures

As discussed in section 2.3, this device can theoretically be operated with a temperature-band gap trade off, such that it can operate at a higher temperature but a large band gap such that $NA < 1$, where N is the number of thermally produced charge carriers in the conduction band per unit area, and A is the area of the sample. Operating with a small band gap, at room temperature, leads to the thermal excitation of a charge carrier concentration $\sim 2 \times 10^{14} \text{m}^{-2}$ in the conduction band of the graphene sample. Cooling to cryogenic temperatures would reduce this thermal excitation, and have other effects e.g. in the silicon wafer, such as ion trapping and a reduction in the charge carrier concentration of the silicon wafer [233].

Therefore, a dilution refrigerator was used to cool down the device, with the intention of reducing some of these thermal effects to identify if these were the cause of the issues observed in previous sections. The earlier tests were repeated to observe the behaviour at cryogenic temperatures. This section begins by discussing the arrangement of the fridge and vacuum systems, before going on to test the device.

6.3.1 Preparing the Dilution Refrigerator, Vacuum System and Electronics

The dilution refrigerator is a Heliox He_3 He_4 refrigerator capable of reaching temperatures as low as 0.3K, designed by Oxford Instruments [234]. The fridge is pumped down to ultra-high vacuum (UHV) by using a roughing pump and then a turbo pump. To cool down to 0.3K [235], firstly He_4 is used to cool and condense the He_3 in the pot which drops the temperature to approximately 2K.

As He_3 gas is lighter than He_4 , He_3 has a lower binding energy which results in a low latent heat energy, and therefore a higher vapour pressure [234]. This allows for the vapour pressure to be decreased to further reduce the temperature of the system. This is achieved by pumping the He_3 using the Sorption pump (the Sorb). The Sorb works by utilising gases that adsorb onto a large surface at cold temperatures, which

can be used to lower the He₃ vapour pressure and thus the temperature. The He₃ is pumped by the Sorb into the “dump”, which cools the temperature to 0.3K.

The fridge, with the location of components such as the Sorption pump and dump, are shown in figure 6.15. Three different stages of the fridge cool to different temperatures because of the temperature gradient across the fridge, with one stage cooled to 77K, another stage cooled to 4K, and stage 3 cooled to 300mK.

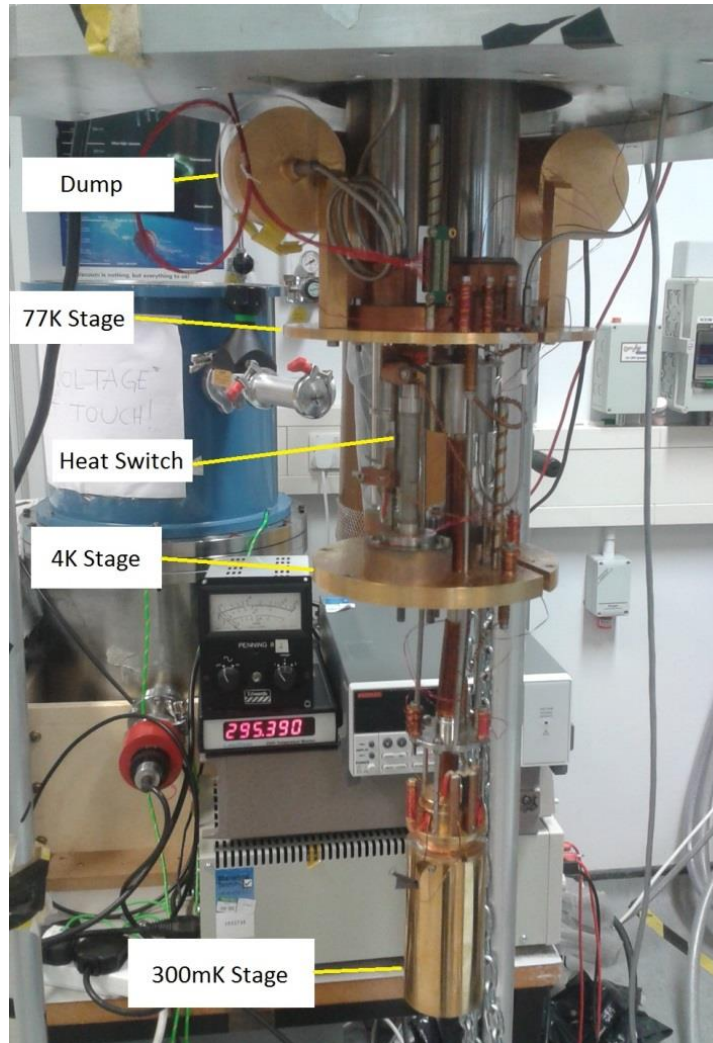


Figure 6.15. Parts of the dilution refrigerator, including the Dump and different temperature stages of the fridge, which reaches as low as 300mK at the bottom.

6.3.1.1 Preparation of the Fridge

To prepare the fridge for the experimental work, various changes had to be made to the cryogenic fridge. For instance, pairs of twisted copper cables were cut and stuck to bobbins with a thermally conductive, low-temperature resilient varnish to enable gate and bias voltages to be applied to the bilayer graphene. After 24 hours curing, the

bobbins were mounted in the fridge to ensure a good thermal gradient between room temperature and cryogenic temperatures.

The chip was bolted into the fridge upon a layer of Apiazon thermal grease, and then the copper wires were carefully mounted to the source, drain and gate connections, figure 6.16. The connection was made using electrically conductive, two-part, Circuitworks CW2400 silver epoxy, which sets in approximately 24 hours. CW2400 silver epoxy is rated to down to -90°C [236], although many epoxies work well below their rating temperature [237] and CW2400 silver epoxy has previously been used at cryogenic temperatures [238].

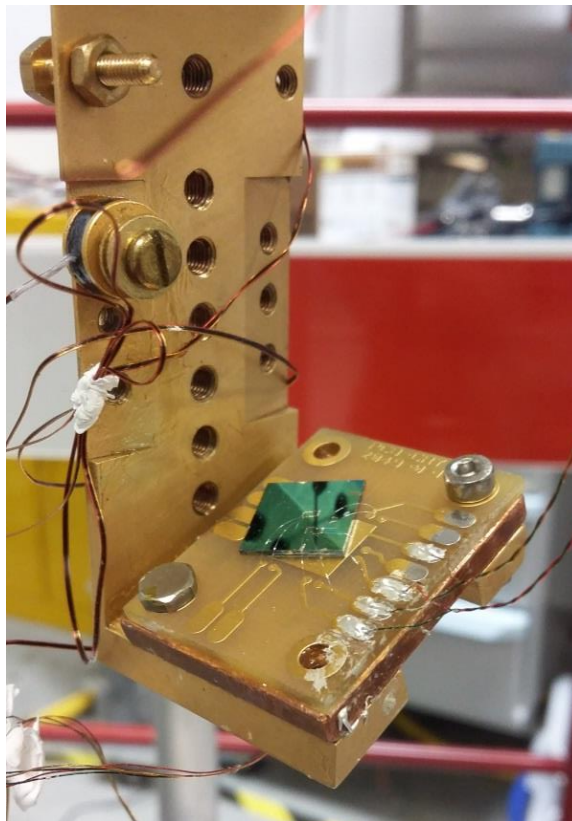


Figure 6.16. Bilayer Graphene chip attached to the fridge upon a layer of Apiazon thermal grease. Electrical connection to the graphene is achieved using CW2400 silver epoxy.

6.3.1.2 Cooling Down and Warming Up the Fridge

A step-by-step procedure, outlined in detail in Appendix II, is followed to pump down the pumping cart and the fridge, and to achieve cryogenic cooling, to cool the sample to 0.3K.

Pumping down the fridge begins by using a roughing pump on a pumping cart, figure 6.17, that can work from atmospheric pressures to pressures of order 10^{-5} mbar. The roughing pump backs the turbo, which is activated when the input pressure is $\leq 10^{-4}$ mbar. It is crucial to ensure that the turbo pump is not subjected to an input pressure $>10^{-4}$ mbar or a backing pressure $>10^{-2}$ mbar, as it risks overheating and damaging the turbo pump.

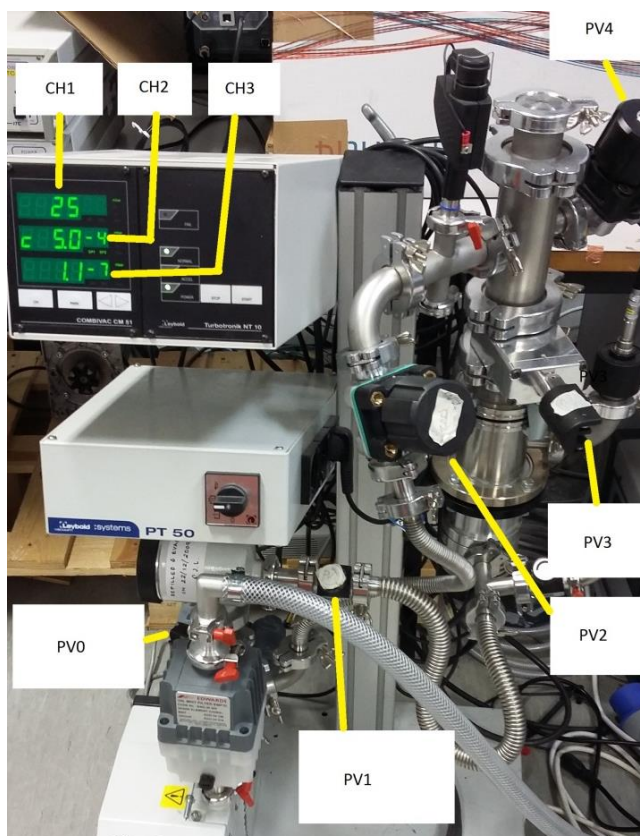


Figure 6.17. Location of pressure valves and channels on the pumping cart. CH3 displays the pressure of the turbo pump, which must not see a pressure $>10^{-4}$ mbar or it risks being damaged. PV3 is a valve that controls the air flow through the turbo pump, and PV4 controls the flow to the cryostat. Full details of the pump down procedure are listed in Appendix 2.

After cooling commences, the turbo pump is used to reduce the pressure in the chamber, resulting in a decrease in the temperature. The cooling power of the fridge eventually becomes greater than that of the pumping cart so, at that point, the fridge is isolated to prevent outgassing/debris accumulation in the fridge. Furthermore, He_3 is used as an exchange gas to accelerate the cooling down process. Heaters in the fridge, in the form of a resistor, can be activated to heat individual components of the fridge to facilitate the condensation of He_3 , reduce the thermal energy in the fridge, and cool the fridge 3-4K to ~ 0.3 K. The fridge is warmed up by turning off the heaters and

stopping the pumping, and then the temperature of the fridge rises to room temperature over a period of 24 hours.

While the fridge was being cooled from 240K to 3K and then warmed back to room temperature, the temperature was noted every 5 minutes. The measurements show an asymmetry, figure 6.18, as it is much slower to cool down than to warm up. There are several observed phase changes during cooling down and warming up, such as 240K \rightarrow 50K, 50K \rightarrow 3K, 3K \rightarrow 30K and 30K \rightarrow 290K.

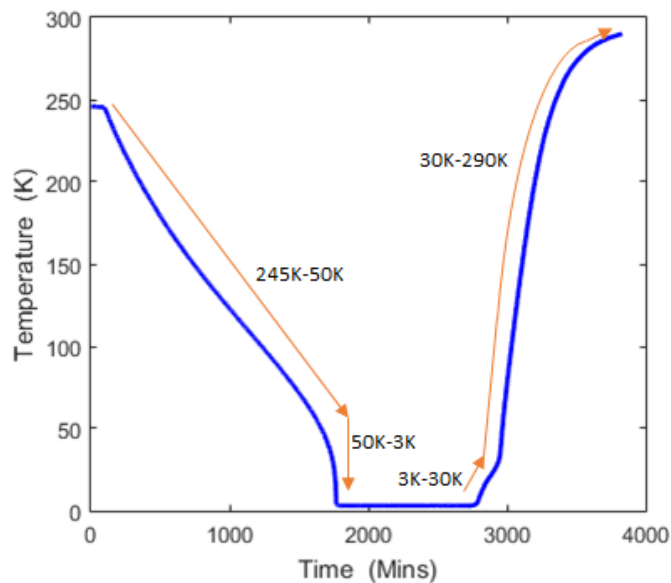


Figure 6.18, showing the change in fridge temperature over time. It appears to go through several different phases, with a difference in the rate of change of temperature between 3K \rightarrow 30K and 30K \rightarrow 290K.

6.3.2 Experimental Results

The detector was cooled down in the cryostat to investigate how the dynamic change in capacitance, as noted in section 6.2.2, varies with temperature, to further explore the mechanism that causes the capacitance issues. The device was gated to close to the Dirac point, with $V_b \sim 34.5V$ and $V_t \sim 14-16.7V$; at this point at room temperature, one noted a strong change in current over time, as shown in figure 6.7a. The change in current was measured for the detector at three temperatures, 293K, 157.6K and 93K, figure 6.19, which suggests that the net drift in current decreased when the device was cooled. Therefore, the dynamic change in capacitance could have occurred due to thermal noise or thermal excitation of the Si/SiO₂ states.

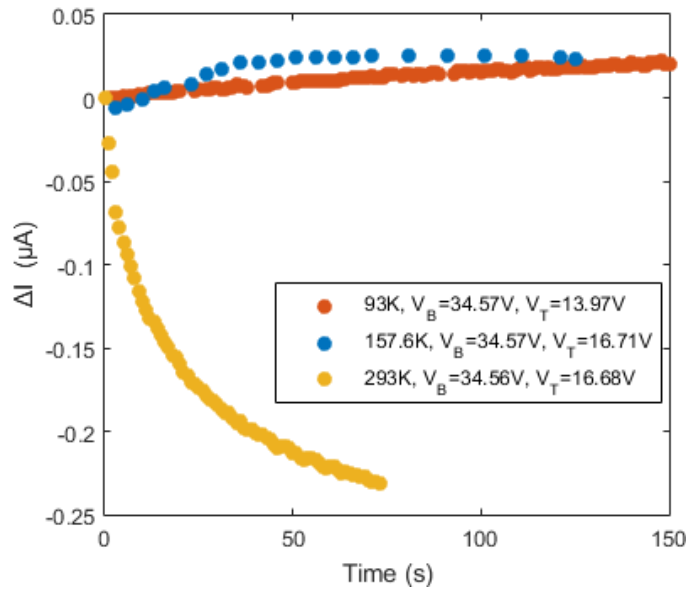
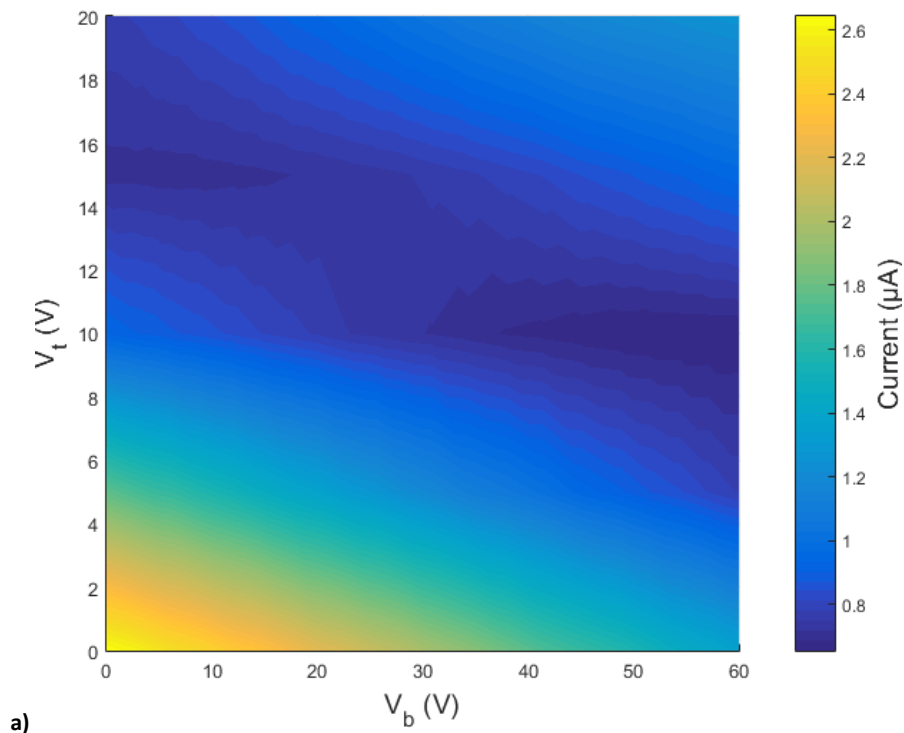


Figure 6.19, showing the net change in current over time for three temperatures. When the device was cooled, the rate of change of current at the Dirac point was much lower, suggesting that the change in capacitance is related to thermally excited states of the dielectric layer.

At low temperatures, the device was gated as a function of top and bottom gate voltages to investigate how the environmental doping was affected at low temperatures. Besides the current measurement itself being easier to reliably take due to reduced drifting of the current, the gating of the device at 66K, 93K and 148K, figures 6.20a-c respectively, showed little change in V_{t0} and V_{b0} compared to room temperature; readings indicated $V_{t0} \sim 12V$ and $V_{b0} \sim 25-35V$.



a)

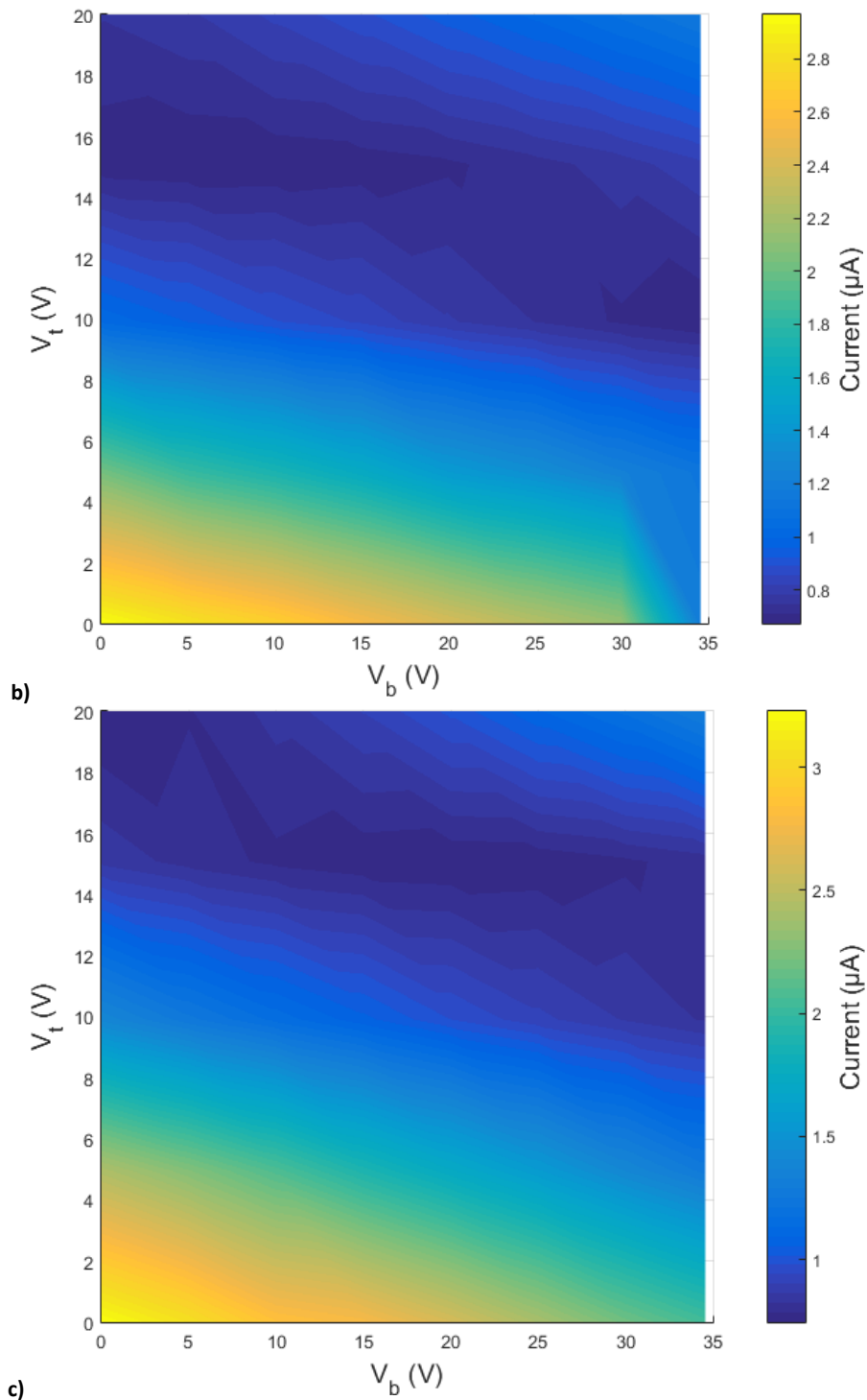


Figure 6.20, showing the gate of the device as a function of top and bottom gate voltage, with the current measured for a) 66K, b) 93K and c) 148K. There is no noticeable change in the environmental doping values, nor the resistance.

An optical fibre was then installed in the refrigerator by inserting it through a feedthrough into the chamber and then winding it around each temperature stage to give a good thermal gradient before aligning it with the detector, figure 6.21. The experiment in section 6.2.3 was repeated to highlight any detector sensitivity for red or blue photons, and to compare these to readings at room temperature.

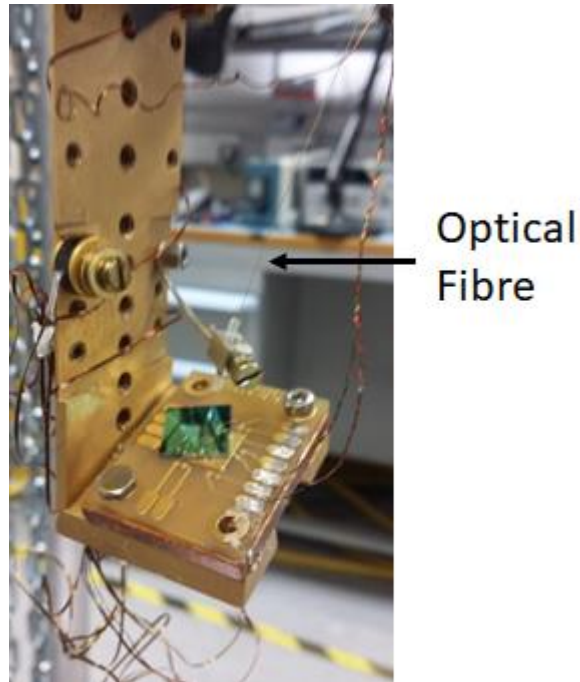


Figure 6.21, showing the alignment of the optical fibre with the detector on the “cold finger”.

At 166K, the device was gated for $V_b = 30\text{V}$ and $V_t = 0\text{-}20\text{V}$, which allowed the device to be tuned from hole carrier densities to electron carrier densities through the Dirac point, which was measured as $V_t \sim 10\text{V}$, figure 6.22a. The device was flashed for up to 10s with a blue cw laser for different V_t over a 10-minute period, figure 6.22b. These results suggest that photosensitivity is only observed for $V_G > V_{Dirac}$, with no demonstrable sensitivity, for instance, for $V_t = 10\text{V}$. However, for $V_t = 20\text{V}$, the current reacted to illumination by the blue laser in a similar fashion to that shown in section 6.2.3, figure 6.22c.

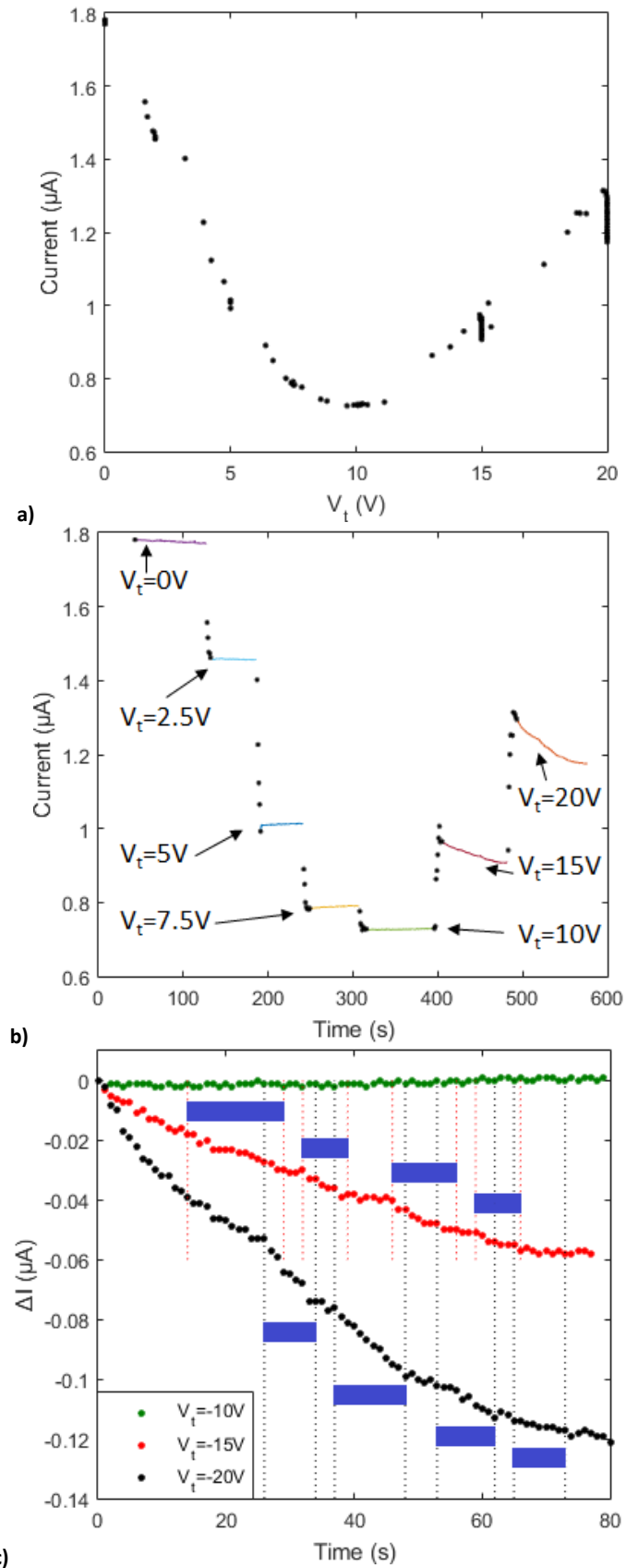


Figure 6.22 showing, at 166K, a) the gating of the device as a function of V_t for $V_b=30\text{V}$, and b) the illumination of the device for different gate voltages, where the dotted lines indicate the current as V_t transitions between one gate voltage and another. c) shows the response of the device to blue laser (indicated by the blue block) illumination for $V_t=10\text{V}$, 15V and 20V . This suggests that this effect is only observable at electron carrier densities.

The device was cooled to 134K, and the gate voltage was set to $V_b = 30V$ and $V_t = 20V$ to achieve electron carrier densities. The device was again illuminated, this time by both a red and a blue cw laser, to observe any modulation of the current because of the illumination. During the illumination by both the blue cw laser and the red cw laser, there was again an observed drift in the current due to the time dependent capacitance. There is a weak response to the blue cw laser, with a change in the rate of change of current during illumination by the blue cw laser as observed previously, which is indicated by the arrows in figure 6.23a. On the other hand, during illumination by the red cw laser, there is no comparable change in the current, figure 6.23b.

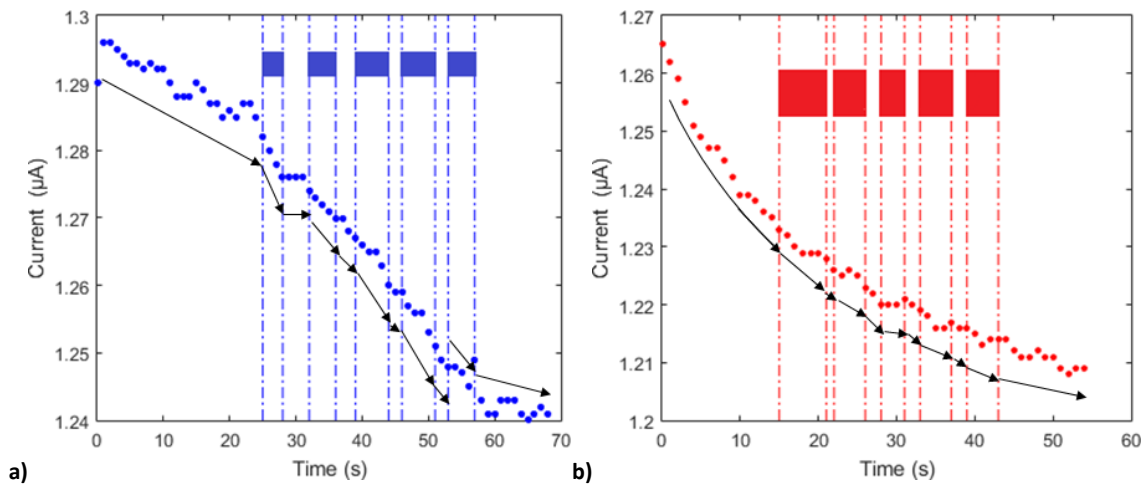


Figure 6.23 showing, at 134K, the change in the channel current due to illumination of the device by a) the blue laser and b) the red laser, indicated by the blue and red blocks respectively. One notes a weak photoresponse due to the illumination by the blue laser, with little to no effect by the red laser. The dotted lines indicate the periods of illumination by each laser.

The device was cooled further to 66K, and the devices was flashed again for both the red and blue cw lasers, at both hole carrier densities ($V_t = 20V$ and $V_b = 0V$) and electron carrier densities ($V_t = 20V$ and $V_b = 60V$). Little effect of the laser is observed for hole carrier densities for either the red or blue laser sources, figure 6.24a. For the electron carrier densities, however, one does note a slight change in current due to illumination by both the blue and the red lasers, as indicated by the arrows in figure 6.24b. This suggests that the mechanism leading to change in current because of the red cw laser illumination may have been affected by a thermal effect that was overcome by cooling to 66K, or perhaps by operating at a higher V_b , and therefore a higher Fermi level, than was used in figure 6.23.

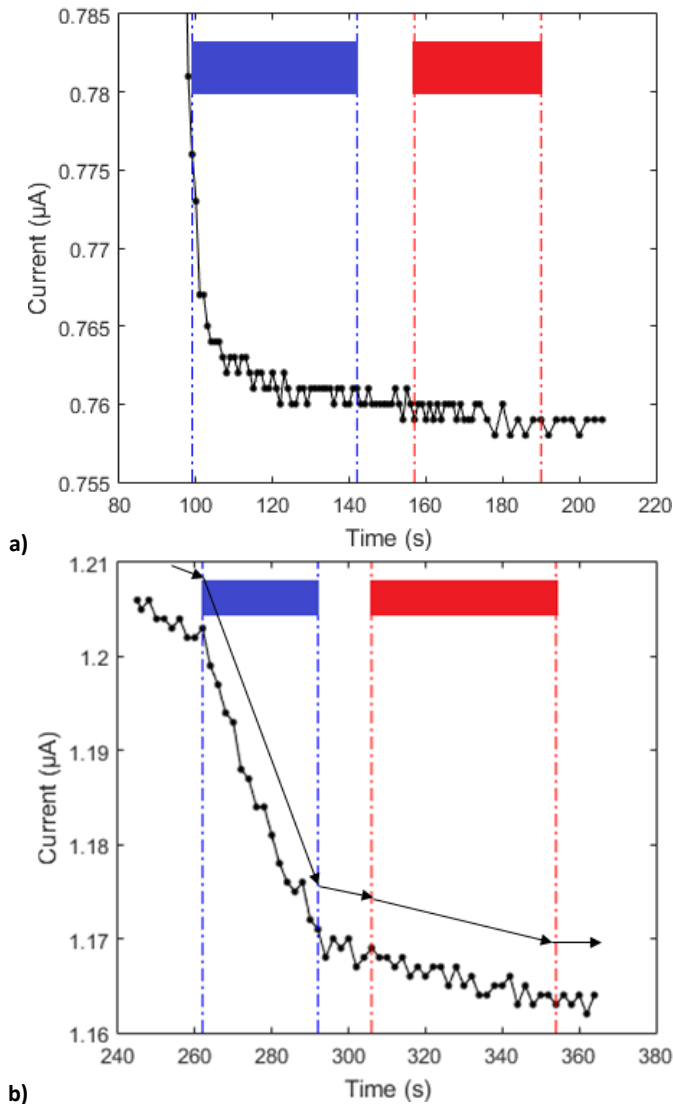


Figure 6.24 showing, at 66K, the change in current due to red and blue laser illumination for hole and electron carrier densities. In A), for hole carrier densities ($V_t=20V, V_b=0V$), there is again no notable effect of either laser source. In B), for electron carrier densities ($V_t=20V, V_b=60V$), there is a noticeable effect on the channel current resulting from illumination by the both the red cw laser and the blue cw laser.

6.4 What is the Mechanism?

Returning to considering the mechanism, it was shown previously that the detector had photosensitivity to a blue cw laser at room temperature, and a red cw laser for $T \sim 66K$. When the laser illuminated the detector, there was an apparent change in the current and in the rate of change of current. There was still photosensitivity even for a Fermi level in the valence band at energies in which the blue laser is not sufficiently energetic to cause the excitation of an electron into the conduction band. This suggests that the photosensitivity is not what would be expected given the concept in chapter 2, so the mechanism must be explained. If the mechanism in chapter 2 had

been observed, one would expect a current that would increase when illuminated by the laser, and then decrease when the illumination ceases. What has been observed in this chapter is an increase in current, with a change in the rate of change of the drift in the current, which very slowly returns to the initial value once the illumination ends.

But where are the photons being absorbed? A gate voltage is applied, so a depletion region is being opened in the silicon. However, as this is a cw source, many e-h pairs are excited in the depletion region and recombine very quickly. The absorption of the blue source could be explained by absorption close to the Si-SiO₂ interface, with a resulting change in the capacitance of the dielectric and p-doping due to recombining surface states. However, this does not explain the red laser response, which is only observed at cryogenic temperatures as it appears to be dominated by thermal effects at room temperatures.

It has been shown that the absorption is not due to direct photoexcitation from the valence band to the conduction band, as the strongest photoresponse at cryogenic temperatures is for electron carrier densities. On the weight of evidence, it is probably that the likely absorption mechanism at room temperature for the blue laser is absorption in the SiO₂ dielectric layer, which generates e-h pairs which recombine in trapped surface states. For the red laser, the sensitivity appears to be some thermal effect, such as heating of the charge carriers with a resulting change in the channel conductivity.

6.5 Summary

In this section, the intention was to demonstrate the ability of this detector to detect single photons, just through absorption by the bilayer graphene, with detection that would be gate tuneable, band gap and doping dependent, temperature sensitive and colour sensitive. This required isolation of the environmental doping values for the detector to allow for reliable gating.

The device, however, did not work as expected. In the process of identifying the environmental doping values, a time dependent change in the current was identified. Several options for a time dependent change in the current were available, including

gate leakage from the top and bottom gates, and doping by environmental dopants. Through different experiments the integrity of the dielectrics was demonstrated and, by using a charge sensitive preamplifier, the time dependent change in the bottom dielectric capacitance was identified. This effect, which prevented a constant magnitude band gap from being opened and appeared to be reduced when the device was cooled, suggested an effect related to the silicon dioxide substrate.

Some photosensitivity was demonstrated for the detector at both room temperature and cryogenic temperatures, with tests undertaken to identify whether the mechanism generating the current was due to the silicon, the silicon dioxide or the bilayer graphene. At room temperature, the observation of this photosensitivity was only observed in the absence of the current drift, with any sensitivity damped by the drift in the current. At cryogenic temperatures, the experimental results suggested that any photosensitivity occurs at electron carrier densities, and not for holes. The absorption mechanism for the blue cw laser was attributed to absorption in Si-SiO₂ states that generate e-h pairs which recombine in trapped states in the dielectric, although this may also be related to polarisation of these states. Photosensitivity to the red cw laser was demonstrated at 66K, which suggested that this mechanism may be damped out by thermal effects, and/or could be due to heating of charge carriers by the red laser that causes a change in the channel conductivity.

The measured photosensitivity did not, therefore, agree with the theoretical calculations from section 2, so further work is required to demonstrate the capacity for bilayer graphene to act as a cryogenic single photon counter with colour sensitivity. Initially, a further device needs to be manufactured that does not show the effects identified in this chapter, for instance by a successful demonstration of the opening of a small band gap. The detector capabilities can then be characterised; for instance, the temperature-resolution trade off needs to be identified and the rate of impact ionisation would need to be deduced in this regime. A figure of merit, such as the energy resolution, then needs to be identified.

7 Testing the Terahertz Detector with Terahertz Sources

7.1 Introduction

As discussed in earlier chapters, a terahertz detector was designed with a response optimised for photons with a frequency of 1.2THz. This used the Dyakonov-Shur effect to excite a plasmon wave between two contacts and generate a photovoltage that was measured using a lock-in amplifier. The detectors used beetle antennae, as designed in chapter 3, as the beetle antennae had an improved S11 response at 1.2THz compared to the bowtie antenna. The detectors were intended to be passive, with no V_{bias} applied to the detector; one antenna lobe is grounded, whilst the other is connected directly to the lock in amplifier, based on the technique proposed in the initial theoretical studies undertaken in ref. [123].

In this section, the detector was firstly used to attempt to detect terahertz photons by chopping the output from a passive terahertz source. Pulsed terahertz laser sources at the Aston University Institute of Photonic Technologies and the National Physical Laboratory were then used to characterise the detector by looking for modulation of the signal by the gate voltage, terahertz power and frequency of the illuminating photons. These results enabled the sensitivity of the detector to be characterised and several detector parameters, such as the signal to noise ratio (SNR) and noise equivalent power (NEP) to be deduced. Further routes to iterating the design, leading to improvements in the detector sensitivity for broadband and narrowband performance, were then considered.

7.2 Device Characterisation

The terahertz detectors were manufactured at the University of Cambridge, with the antennae arranged in a beetle arrangement to the design outlined in chapter 3. These were encapsulated with 90nm thick alumina to reduce gate hysteresis and promote more consistent electrical measurements. The device was mounted in a die cast aluminium box, with $V_{\text{bias}}=10\text{mV}$ across the graphene.

The device was gated to characterise the channel current as a function of gate voltage, figure 7.1, at both air pressure and when the environment was evacuated to a pressure of approximately 10^{-1} Torr (0.1mBar). The Dirac point is at $V_G \sim -5\text{V}$; this means that the graphene is n-doped, which can be achieved by using NH_3 in the CVD process [239]. At low pressure, the gate hysteresis is reduced, and there is a small shift in the Dirac point towards 0V due to the reduced number of n-dopants such as NH_3 .

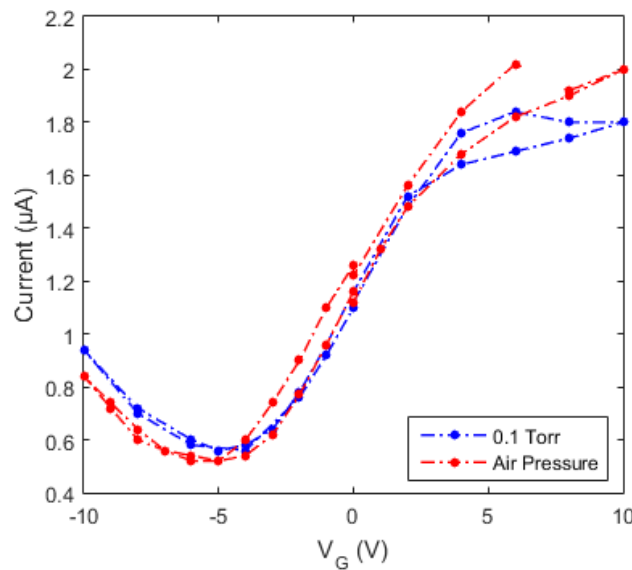


Figure 7.1. Current as a function of gate voltage at air pressure and low pressure. At low pressure, there is a small shift in the Dirac point towards 0V, and a reduction in gate hysteresis.

7.3 Basic Testing with a Passive Terahertz Source

Any hot object emits photons across the electromagnetic spectrum. This is described by Planck's law, where the spectral radiance, illustrated in figure 7.2, is given by

$$B_{\lambda}(\lambda, T) = 2hc^2\lambda^{-5} \left(e^{hc/\lambda k_B T} - 1 \right)^{-1}, \quad \text{Equation 7.1}$$

where λ is the wavelength, T is the temperature, c is the speed of light, h is Planck's constant, and k_B is Boltzmann's constant.

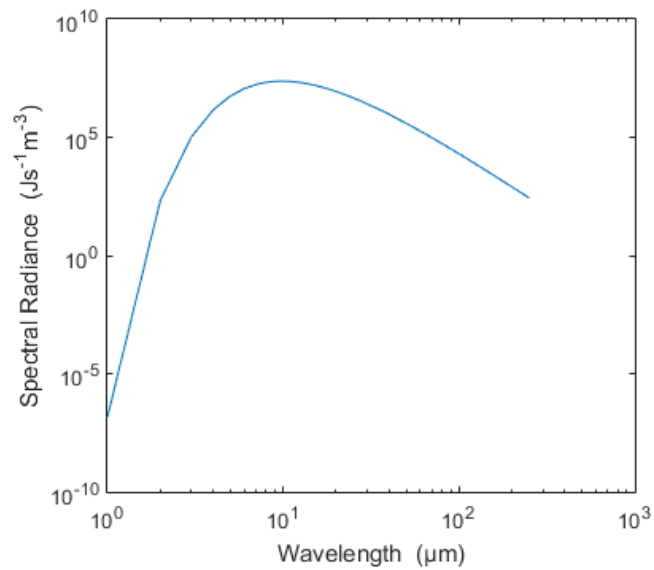


Figure 7.2, showing the spectral radiance for wavelengths between 0 μ m and 250 μ m for T=293K.

To identify any sensitivity to a passive terahertz source such as a hot object, the detector chip was connected to an ADA4817 current feedback op-amp and mounted inside a hermetically sealed, IP67 rated die cast aluminium box, figure 7.3a. A hole was drilled in the top, and a 2mm thick window of high density polyethylene (HDPE) was placed on top, figure 7.3b. HDPE was chosen as it is 85+% transparent for $\lambda > 200\mu$ m and opaque at visible frequencies [240].

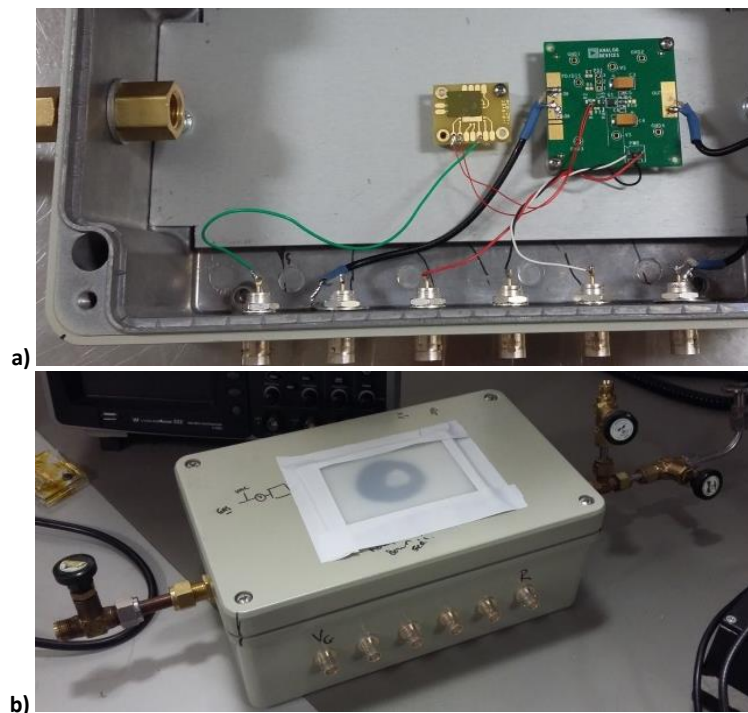


Figure 7.3 showing a) the layout for the THz electronics, located in a hermetically sealed box, and b) the box with the 2mm thick HDPE window, which is transparent at terahertz frequencies but opaque at UV frequencies.

To enable the air pressure in the box to be reduced, holes were drilled in the side of the box and Swagelok fittings connected. The GFET was mounted in the diecast box, with one contact grounded through the box, the other contact connected directly to an oscilloscope, and then a gate voltage was applied, figure 7.4a. A steel, optical chopper was placed in front of the HDPE aperture, and band pass filters for $\lambda=155\mu\text{m}$ and $215\mu\text{m}$ were mounted on the chopper to attempt to observe any chopping of the oscilloscope output. The box was pumped down with a roughing pump and demonstrated it could hold vacuum, figure 7.4b.

The HDPE window was tested with a Testo 875-1i thermal imaging camera [241], which has a sensitivity to temperatures between -20°C and 280°C . This corresponds to a peak spectral radiance for wavelengths between $5\mu\text{m}$ and $11\mu\text{m}$; at these wavelengths, the HDPE window is opaque. Terahertz frequencies emitted by the human body, which have a peak spectral radiance at a wavelength $\lambda\sim 9\mu\text{m}$ given a skin temperature $\sim 310\text{K}$ [242], are also reflected by the HDPE window, as shown in figure 7.4c for a hand.

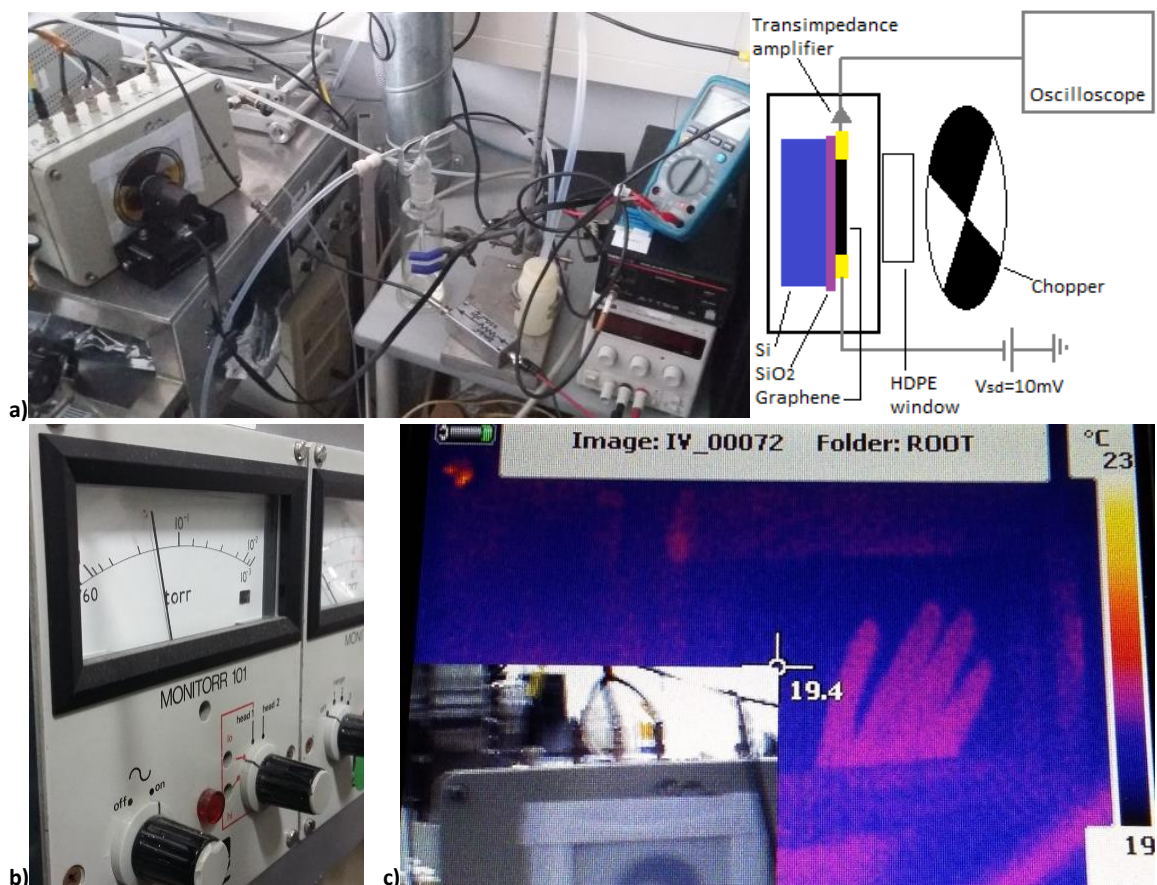
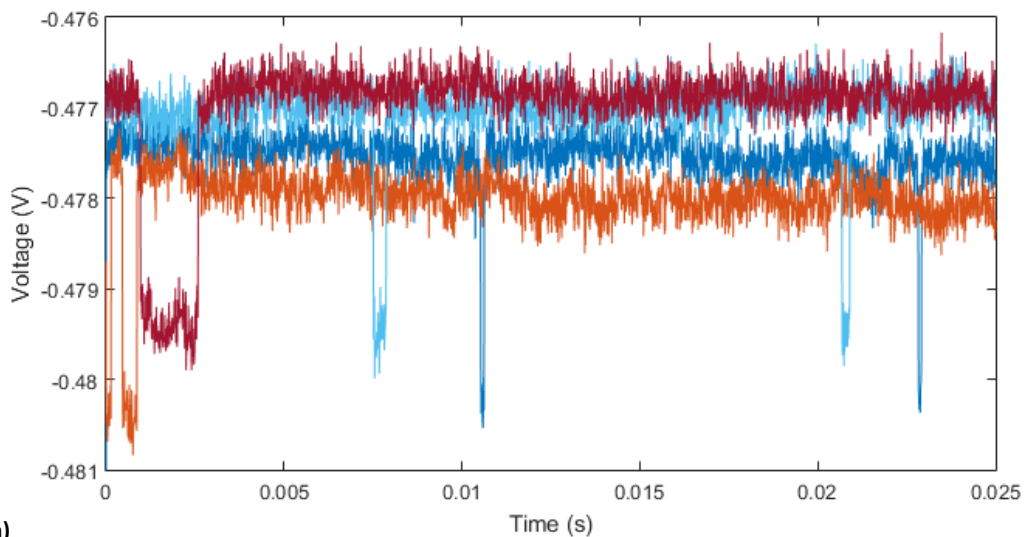
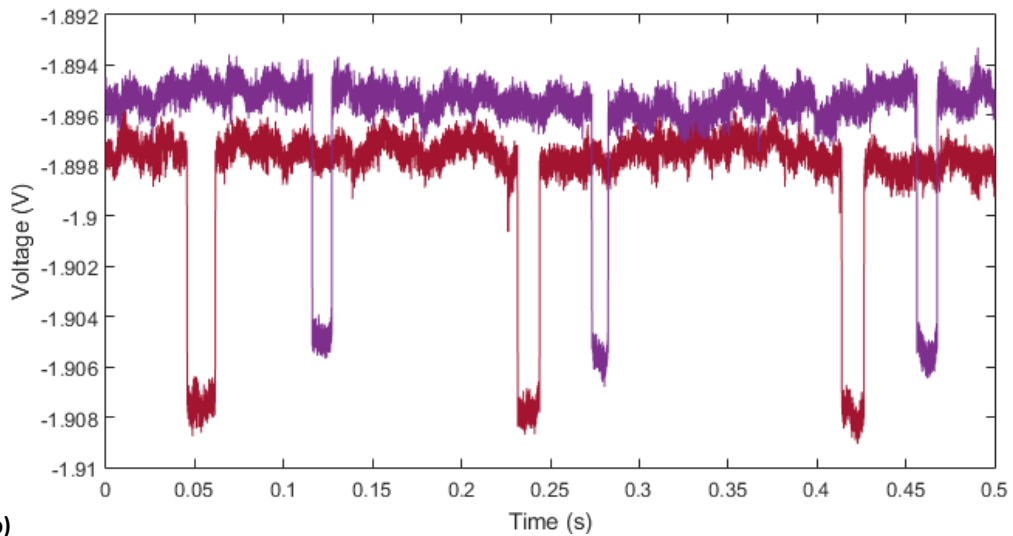


Figure 7.4 showing a) the experimental arrangement, with a chopper placed in front of the box, and b) the box holding a weak vacuum of $\sim 0.1\text{Torr}$, which it held for approximately one hour. C) shows the HDPE window is reflective of the blackbody radiation emitted from the human body.

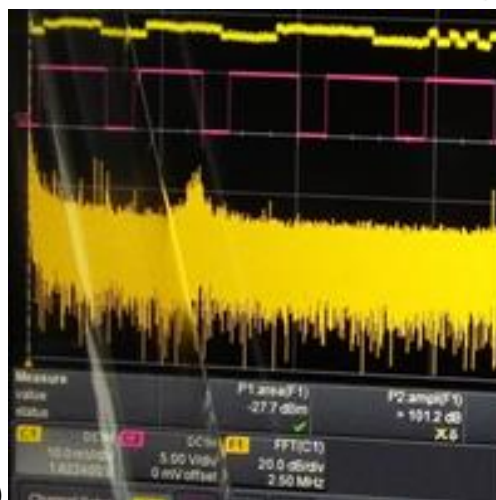
Basic tests were undertaken to attempt to observe any modulation of the signal by placing it next to blackbody source, including a body part, and hot mug, or a hot air gun. The oscilloscope was triggered off the chopper output, which revolved at 500Hz. In the presence of each of these sources, square waves were observed that had a variety of pulse widths and amplitudes; examples of these in the presence of a hot mug are shown in figure 7.5a-b. A square wave is what might have been expected from the oscilloscope readout – an offset in the voltage measured when the band pass filter blocked and unblocked the source from the detector.

However, these square waves were not synchronised with any trigger, as shown in figure 7.5c, and sometimes the same blackbody sources produced no response at all. This suggested that the square waves arose from a noise source. To test this, the coaxial cable was disconnected from the detector, terminated at one and connected to the oscilloscope at the other, and yet the square wave still appeared at times and were not synchronised with the trigger, figure 7.5d. Therefore, in this arrangement, the detector did not have any sensitivity to passive terahertz sources, with the and the square waves that were observed were attributed to other noise sources.





b)

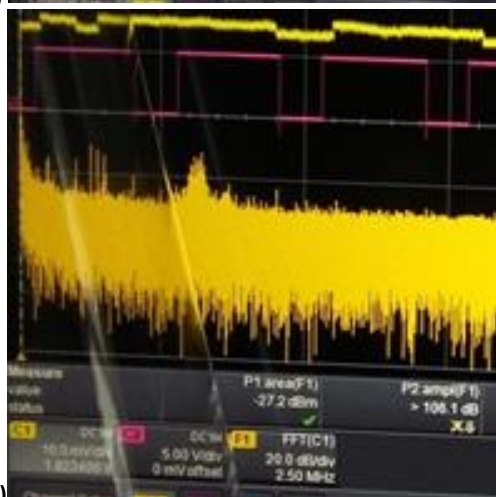


Detector Signal

500Hz trigger from chopper

Fourier transform of signal

c)



Detector Signal

500Hz trigger from chopper

Fourier transform of signal

d)

Figure 7.5 showing a) and b) example square waves of varying pulse width and magnitudes that were observed in the presence of a blackbody objects, in this case a mug of hot water, for gate voltages of $V_G = 1V$ and $V_G = 10V$ respectively. C) is a screenshot from the LeCroy oscilloscope, which show the square waves output from the detector. The square waves are observed in the output from the detector, although they are not synchronised with the chopper output that was being used as the trigger. D) shows a screenshot of the signal from the oscilloscope when the detector was removed and the coaxial cable had been shorted and essentially acting as an antenna, which indicated that the square waves originated from another source.

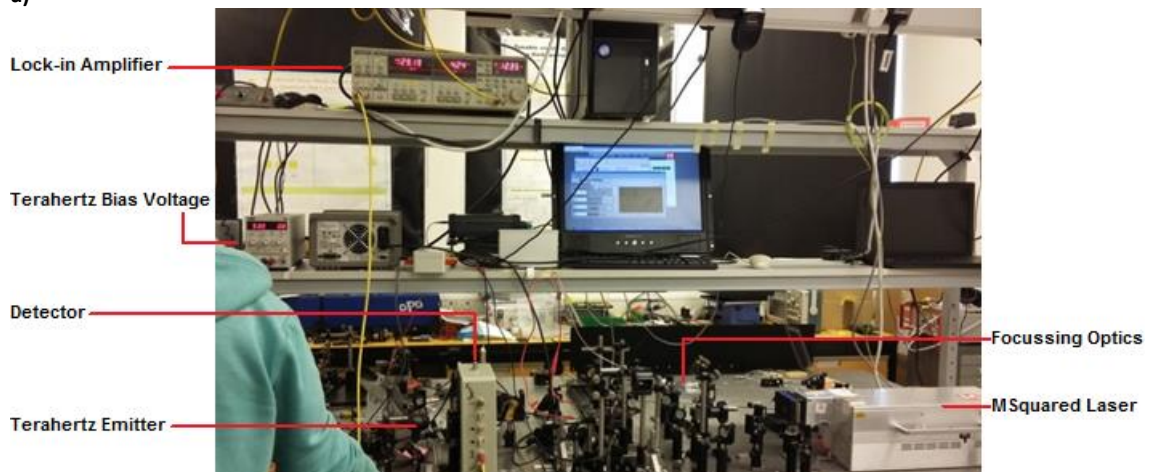
7.4 Testing with Terahertz Laser Sources to show Gate, Frequency and Power Modulation

The detector was taken to Aston University Institute of Photonic Technologies, Birmingham, and the National Physical Laboratory in London to test it on their terahertz laser sources. The measurements were synchronised to the $\sim\mu\text{W}$ terahertz source by either chopping the signal from a cw source or triggering from a pulsed source. Both sources were used to build evidence of terahertz sensitivity by investigating the signal behaviour with respect to the gate voltage, incident terahertz power, incident terahertz narrowband frequency and the measurement technique using the lock in amplifier.

7.4.1 Experimental Setup at Aston University Institute of Photonic Technologies

The wire bonded GFET was mounted in a diecast aluminium box and connected to BNC connectors. At Aston Institute of Photonic Technologies, it was connected to a Stanford SR830 lock-in amplifier, and illuminated by a Teravil LT-GaAs Terahertz Emitter [243] which was biased up to 55V and illuminated by an MSquared Sprite Laser. It was mounted in the arrangement shown in figure 7.6.

a)



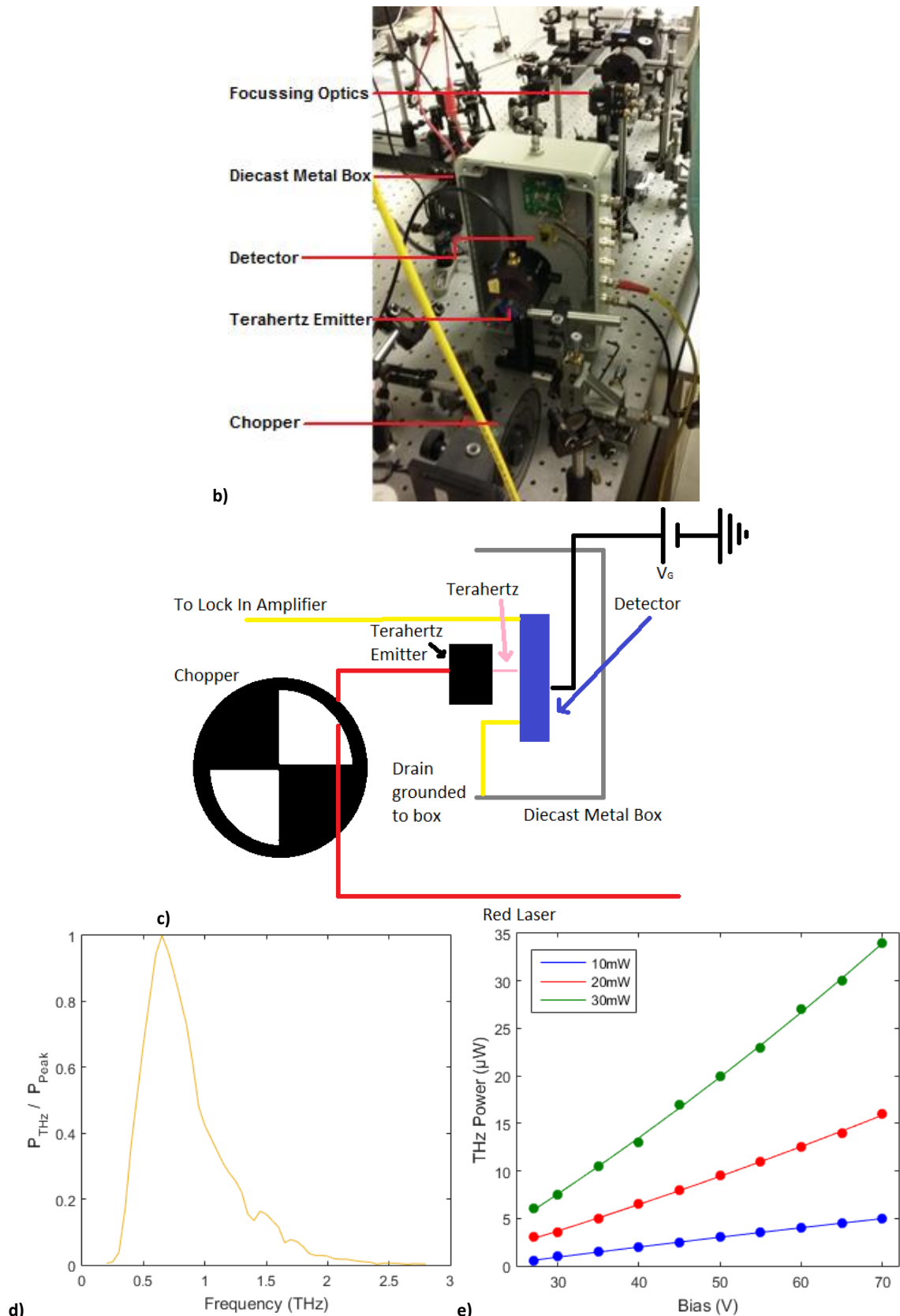


Figure 7.6, showing a) and b) the arrangement of the experimental setup and c) a schematic layout of the experimental set up. The terahertz emitter was a Teravil LT-GaAs emitter. The chopper rotated at 500Hz, and was used as the reference frequency for the lock in amplifier. D) shows the normalised power output of the laser source at terahertz frequencies, and e) shows the known power output of the Teravil emitter as a function of the terahertz bias voltage.

The Teravil LT-GaAs emitter is a photoconductive antenna. It works by illuminating the emitter with an ultrashort laser pulse (from the MSquared laser) which excites electron-hole pairs. The conductivity of the GaAs increases and results in a pulse of photoinduced charges accelerated by an external electric field – the radiated terahertz field can then be derived, and is related to the voltage bias applied to accelerate the electron-hole pairs apart [244] [245]. The broadband terahertz source, of a known power output as a function of frequency by a previous calibration using a Golay cell, has a peak power at approximately 600GHz, with a total power of order μW integrated over the frequency range, figure 7.6e. The terahertz source was modulated by an optical chopper at 500Hz which also provided the lock-in amplifier reference.

7.4.2 Experimental Setup at the National Physical Laboratory

The detector was also tested at the National Physical Laboratory (NPL), using two different systems – a Topica cw tuneable THz system and a pulsed system. For tests at NPL the detector was mounted in a small diecast box, figure 7.7a, with a hole drilled to allow for direct illumination of the graphene detector by the terahertz laser source. The detector was gated by applying $V_{bias} = 10\text{mV}$ across the graphene and varying the gate voltage, showing a Dirac point of between -5V and -10V, figure 7.7b.

As the terahertz photon can couple to both antenna nodes, and generate a photovoltage at each side of the detector, to measure a non-zero potential difference there needs to be some asymmetry in the experimental setup. To achieve this, one end of the detector was connected to the lock in amplifier with the other end grounded through the diecast box. Furthermore, to enable an AC coupled signal to be taken from the gate, an output was connected to the gate via a $2\text{M}\Omega$ resistor and a $1\mu\text{F}$ capacitor, figure 7.7a.

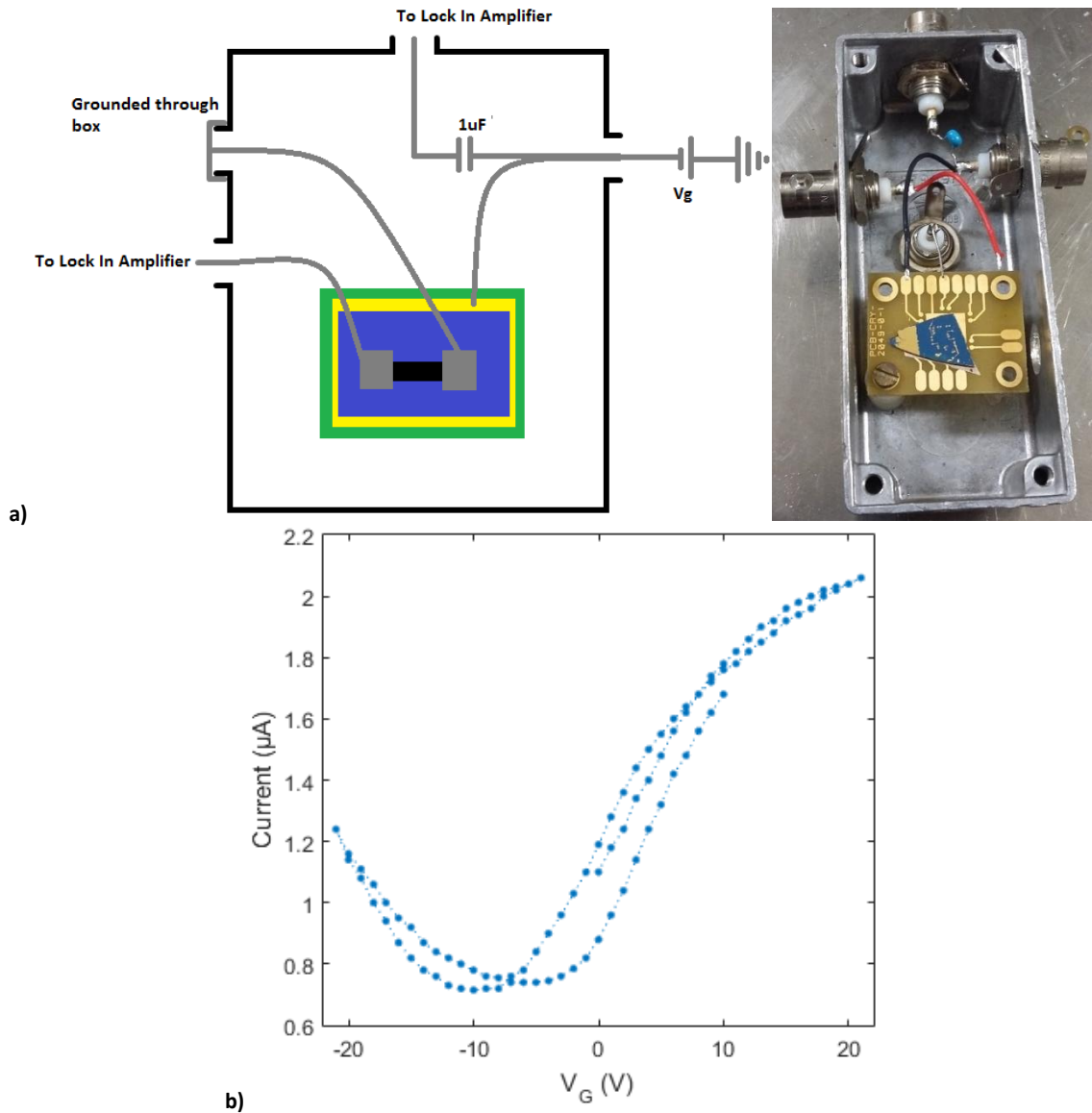


Figure 7.7, showing a) the GFET mounted in the diecast metal box and how it was connected, and b) the measurements from gating the device, which show a Dirac point at $V_G \sim -5$ to -10V .

The experimental setup of the tests is shown in figures 7.8a and 7.8b for the cw tuneable system and the pulsed system respectively. The cw tuneable system combines diode lasers and photomixers to generate a terahertz source that is tuneable up to 1.3THz, with a bandwidth of order $\sim 1\text{GHz}$. The signal was chopped at a given frequency which also provided the reference frequency for the lock-in amplifier.

For the pulsed system, a red laser pulsed at 80MHz was split – one of the beams was used to align the detector before it was shuttered off, and the other was used to excite a terahertz source subjected to a bias voltage, in a similar way to the technique used at Aston University. Due to issues with the equipment, only the in-phase component of the signal could be measured for some of the tests, but it still gave a good indication of

sensitivity to terahertz radiation. Furthermore, for the pulsed arrangement, the terahertz power was shuttered to allow measurement of the signal arising from the detector without terahertz illumination, which was indicative of the measured noise; shuttering was done by using a copper plate. The noise arose via coupling from the gate voltage power supply, the antenna bias power supply, and other unknown sources.

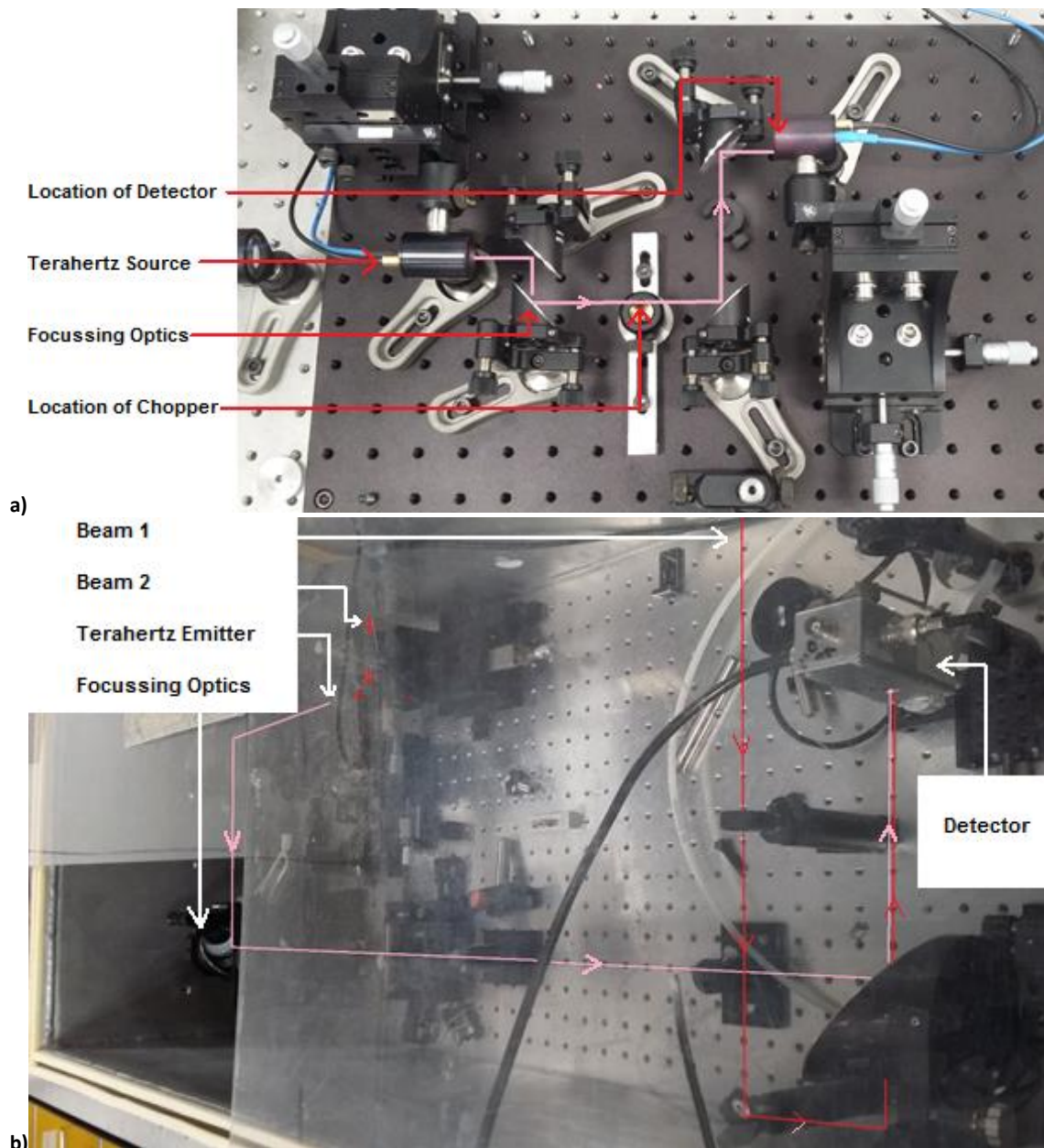


Figure 7.8 showing a) a Topica CW THz arrangement, with the path of the terahertz photons in pink, and the graphene detector in the location of the Golay cell at the top of the image. B) shows the pulsed terahertz arrangement, with a pulsed red optical photon (red line) split outside of the box, one beam allowing alignment of the detector, and the other half exciting a terahertz photon beam (pink) from an emitter held at a bias voltage.

Similar tests were conducted to those in the previous section to determine the sensitivity of the detector to variation in gate voltage, terahertz bias voltage (and hence terahertz power), and the use of band pass filters.

7.4.3 Using a Lock-In Amplifier

A lock in amplifier takes an input with a low signal to noise ratio and extracts a signal from this – few other techniques can do this. The signal measured from the detector is represented in frequency domain, and is amplified by the lock-in and multiplied by the lock-in reference, with the phase between the two locked. The signal is then passed through a low pass filter to retain the DC component. The time constant for the lock-in drives the time constant of the filter [246] [247].

The input signal, $V_s(t) = V_{s0}\sin(\omega_s t + \varphi)$, is modulated by a reference frequency $V_r(t) = V_{r0}\sin(\omega_r t)$, where ω_s is the signal frequency, ω_r is the reference frequency, t is the time, φ is the phase, and V_{s0} and V_{r0} are the signal and reference amplitudes respectively. The lock in amplifier multiplies the two signals together,

$$V_s V_r = V_{s0} V_{r0} \sin(\omega_s t + \varphi) \sin(\omega_r t), \quad \text{Equation 7.2}$$

and takes a time average of them over a set integration time, which leads to

$$\langle V_s V_r \rangle = \begin{cases} \frac{1}{2} V_{s0} V_{r0} \cos(\varphi) & \text{if } \omega_s = \omega_r \\ 0 & \text{otherwise} \end{cases} \quad \text{Equation 7.3}$$

Varying the phase between the input and reference signals allows the signal obtained by the lock in amplifier to be maximised. The signal can be made to be phase independent by adding a second phase sensitive detection that is proportional to $\sin\varphi$ [248]. The cosine and sine dependent terms are the in-phase and quadrature terms, given by

$$X = V_{s0} V_{r0} \cos(\varphi) \quad \text{Equation 7.4}$$

and

$$Y = V_{s0} V_{r0} \sin(\varphi) \quad \text{Equation 7.5}$$

respectively; when $\varphi=0$ there is only the in-phase component. The magnitude of the signal vector is given by

$$R = (X^2 + Y^2)^{1/2}, \quad \text{Equation 7.6}$$

whilst the phase is defined as

$$\varphi = \arctan(Y/X). \quad \text{Equation 7.7}$$

7.4.4 Modulating the Signal via the Gate Voltage

In chapter 3, the ability for the gate voltage to control the response of the detector via the Dyakonov-Shur effect was presented. In this section, results demonstrating modulation of the detector via the gate voltage are presented and discussed.

The detector was illuminated by the broadband terahertz emitter at Aston University, discussed previously in section 7.4.1. The gate voltage applied to the GFET, V_G , controlled the carrier density in the graphene channel, and the terahertz emitter bias, V_{THz} , controlled the power output from the broadband terahertz emitter. Both V_G and the terahertz emitter bias were varied and the resulting signal, V_{lockin} , was measured and plotted in the heatmap shown in figure 7.9a.

The modulation of the signal as a function of the gate voltage is illustrated for the greatest signal magnitude, figure 7.9b, which occurred for $V_{\text{THz}}=55\text{V}$. This indicates that the peak signal occurred close to the Dirac point, with a minimum signal close to $V_G=0\text{V}$. This can be compared favourably to the results discussed in ref. [124], where the peak output of their detector is closely related to the maximum change in conductivity as a function of gate voltage, and those in ref. [154], where the AC photocurrent, in this case arising from the generation of plasmons, between the two contacts as a function of gate voltage peaks close to the Dirac point.

The results also suggest gate voltage dependence, as expected from equations 3.1 and 3.2. In section 7.4.8, these results are compared to theoretically expected results by fitting the photocurrent.

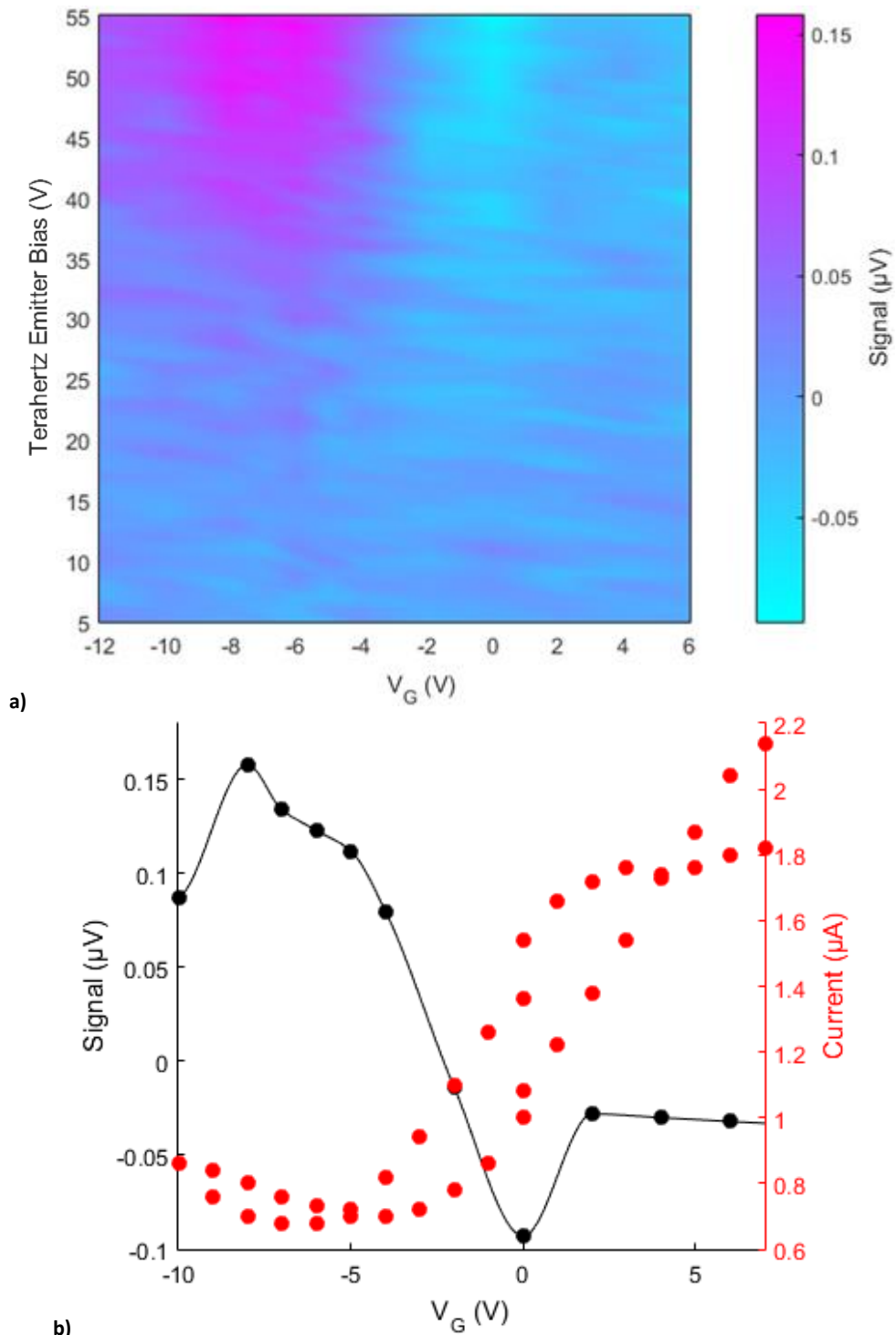


Figure 7.9, showing a) the signal obtained from the lock-in amplifier, V_{lockin} , represented on a heatmap as a function of the gate voltage, V_G , and the terahertz emitter bias, V_{THz} . B) shows the signal from the lock-in amplifier, for a terahertz emitter bias $V_{\text{THz}}=55\text{V}$, as a function of the gate voltage, V_G ; this is given by the black line. The drain-source current is also plot against gate voltage, given by the red dots. This shows that the peak V_{lockin} occurs close to the Dirac point, with the minimum magnitude signal for $V_G \sim 0\text{V}$.

This experiment was repeated with the cw source at NPL to again show modulation as a function of gate voltage, as well as illumination frequency. Figure 7.10 shows the same form as a function of gate voltage as was shown previously, with a peak at $\sim -5\text{V}$

and decreasing to a minimum at positive gate voltages. There is a large systematic error that affects each of the measurements, which is especially visible for the two measurements for 1.2THz in figure 7.9. The systematic errors arose from components such as the laser source and the gate voltage bias supply, and even from putting the Perspex shielding on the experimental setup, possibly causing pickup between different cables which gave rise to the greatest signal for illumination by 1.2THz photons. Reducing these systematic errors, for instance by improving the layout of the experimental setup and better electromagnetic shielding, would improve the chances of demonstrating narrowband sensitivity. On a positive note, the noise in the measurements as shown by the error bars is small in comparison to the measured signal, and less than 10% of the observed dynamic range.

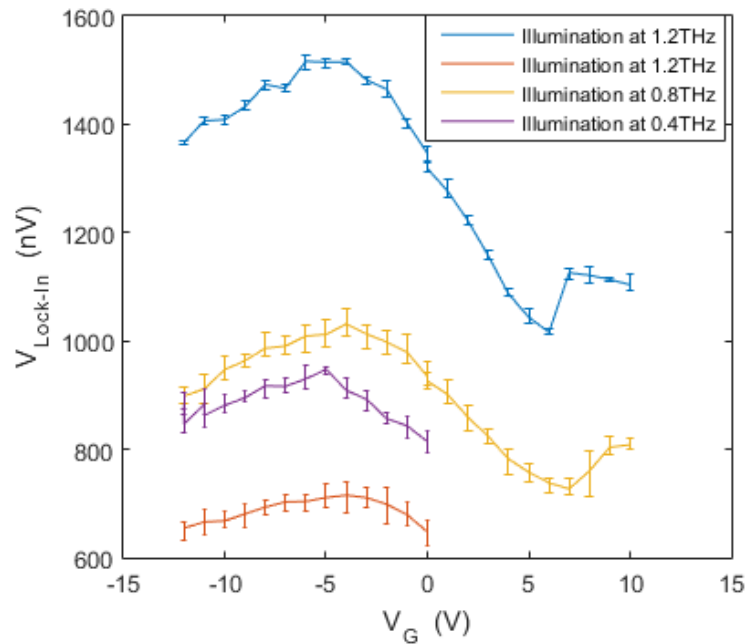


Figure 7.10, showing the measured lock in voltage as a function of gate voltage for different frequency illumination. The same behaviour as a function of gate voltage is observed, with a peak close to the Dirac point, and a minimum at positive voltages, this time at approximately 5V. These measurements include a series of systematic errors arising from the voltage and laser sources, which much be removed to improve the chances of narrowband detection.

At NPL, the experimental arrangement was then changed to use the more powerful pulsed broadband terahertz laser source, more closely resembling the emitter used at Aston University Institute of Photonic Technologies. These initial results show the same modulation due to the gate voltage, figure 7.11a, with a peak and a trough in the DC photovoltage related to the channel conductivity [124] and photovoltage [154] as a function of gate voltage when measuring the in-phase component only. While the

results in figure 7.11a were obtained by shuttering the terahertz signal to look for the change in V_{lockin} , the relative change in V_{lockin} was small in comparison to the absolute value of V_{lockin} , potentially leading to noisier results.

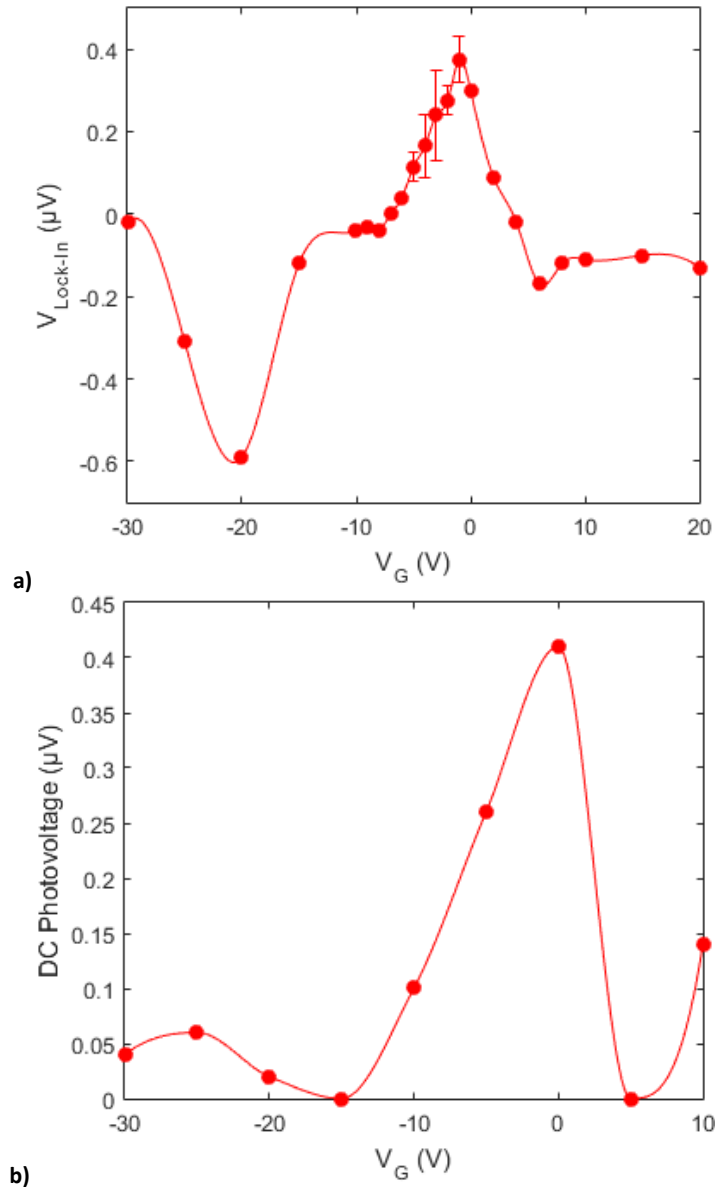


Figure 7.11, showing a) the measured signal as a function of gate voltage for the device in a single ended measurement, illuminated by the broadband pulsed terahertz source, and b) measurements of the same device, but using a differential mode on the lock in amplifier.

The detector was then changed into a different arrangement to utilise the differential mode of the lock in amplifier instead of the single ended mode. The measured signal magnitude from the repeated experiment, figure 7.11b, shows the same form as that measured in figure 7.11a. Both measurements show a peak for gate voltages $V_G \sim 0\text{V}$, and a local minimum for $V_G \sim -5\text{V}$. A further turning point occurs for $-20\text{V} > V_G > -25\text{V}$; at this point, for the single ended mode measurement $V_{\text{lockin}} < 0\text{V}$, and for the

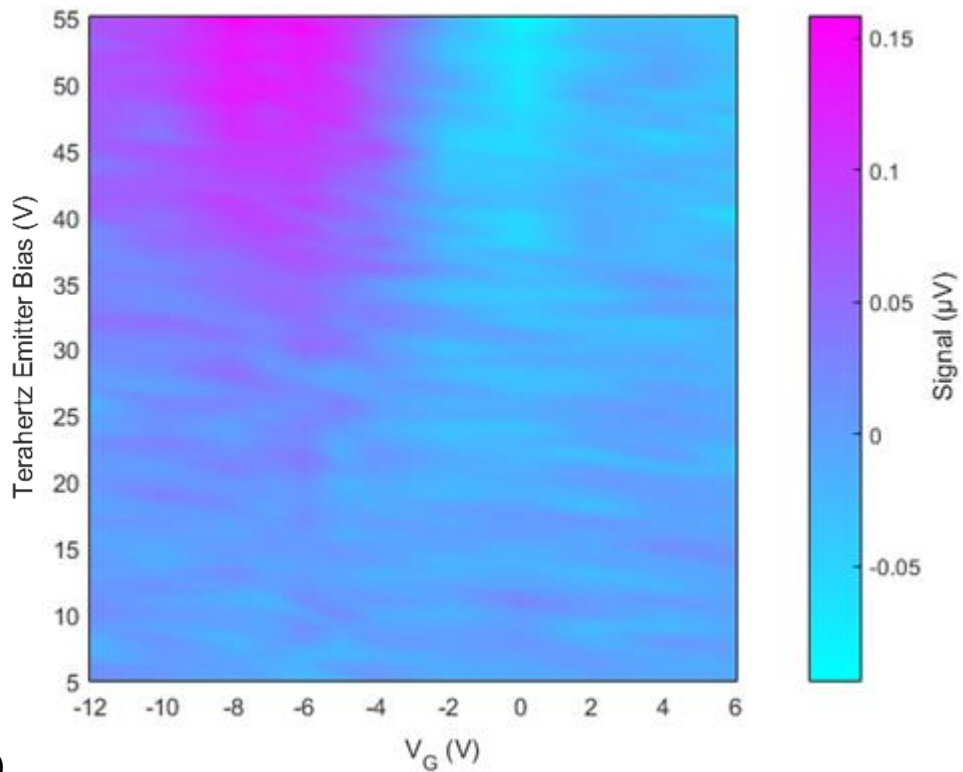
differential mode measurement $V_{\text{lockin}} > 0V$, as the latter measurement shows the signal magnitude.

The experimental results suggest that the detector demonstrates gate voltage modulation of the terahertz signal as measured by the lock in amplifier. This was shown in single ended mode at Aston University, and single and differential mode at NPL, for a passive detector with no voltage applied across the graphene channel. Theory suggests that the signal should be modulated by the channel conductivity and the AC photocurrent between the two contacts, both of which vary as a function of the gate voltage. In section 7.4.8 these results are compared to what one would expect theoretically, with an estimate made of the AC photocurrent in the channel.

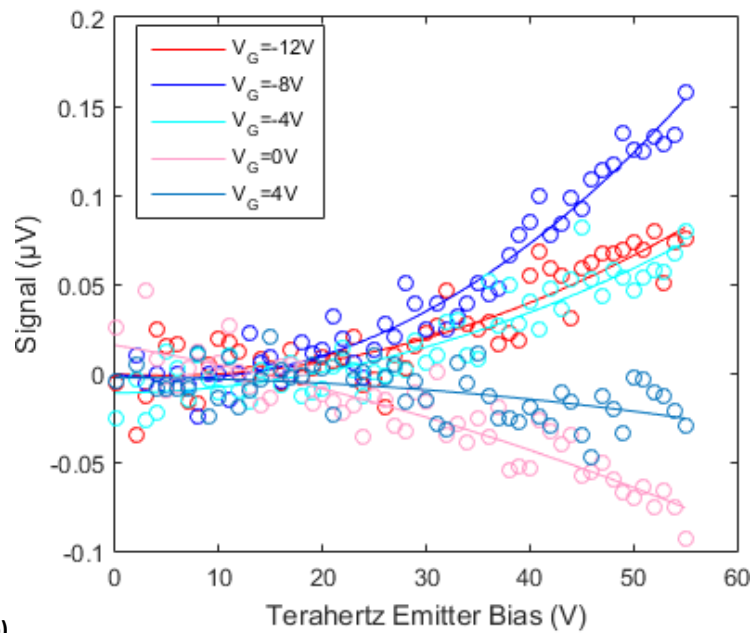
7.4.5 Modulating the Signal via Terahertz Power

The modulation of the signal from the detector as a function of terahertz power was also investigated. The emitted terahertz power from the emitter at Aston University scales quadratically with the bias voltage applied to it, figure 7.6e, with the power integrated across a broadband frequency range, figure 7.6d; therefore, modulation of the signal as a function of the terahertz power source was expected.

The voltage measured by the lock in amplifier was plotted as a function of the terahertz emitter bias for different gate voltages, figure 7.12a. In figure 7.12b the signal as a function of the terahertz emitter bias is shown, which shows an increase in signal with increasing emitter bias. The measured signal in figure 7.12b flips from positive to negative, likely due to the signal phase from the lock-in amplifier.



a)



b)

Figure 7.12, showing a) the signal as a function of applied bias and gate voltage on a heat map and b) the signal as a function of applied bias to the emitter, which scales quadratically as a function of antenna bias voltage.

Using the broadband source at Aston University, the signal was observed to scale with the square of the terahertz emitter bias voltage. The experiment was repeated using the broadband source at NPL, with both the single-ended and differential mode configurations investigated to see which was the most promising arrangement.

Both arrangements have a signal that scales like V_{bias}^2 , which was also shown in refs. [244] and [243]. This is because V_{bias} generates a field E_{bias} that accelerates charge carriers through the LT-GaAs wafer, which generates terahertz radiation with a power $P_{THz} = \langle E_{bias} \rangle^2$ [249]. The differential mode gives an improved signal to noise ratio because of the common mode noise rejection when compared to the single ended mode, although one also notes an increased V_{lockin} for differential mode too. This may be a systematic error, however, for differential mode measurements for $V_{bias} > 100V$.

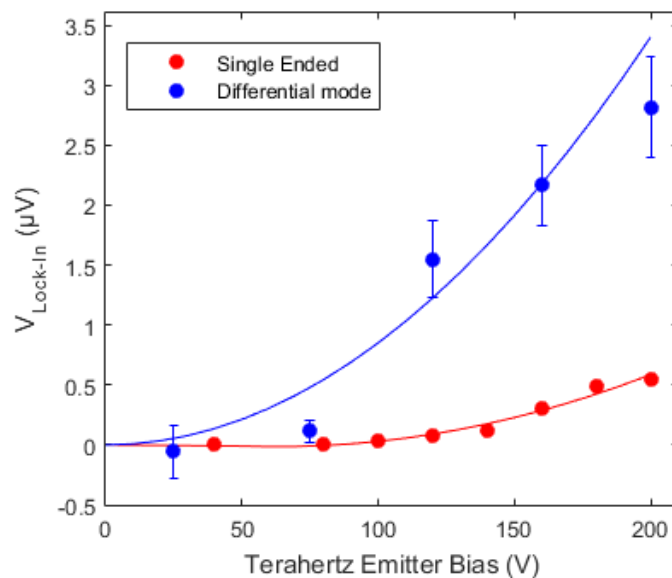


Figure 7.13, showing the measured signal in single ended and differential mode. The differential mode is approximately 6 times larger.

These results show the output from the detector modulated by the terahertz power. With a greater terahertz bias voltage, the power scales like V_{bias}^2 ; the increased power coupling to the antennae generates an increased number of plasmons along the channel, resulting in a greater measured V_{lockin} .

7.4.6 Signal Variation with Narrowband Illumination

Using the tuneable cw terahertz source at NPL with a bandwidth of $\sim 1GHz$, at a given power, the behaviour of the detector as a function of narrowband terahertz frequency illumination was also observed. The results, shown in figure 7.14, show a dynamic range up to 100nV across the tested frequency range for a gate voltage $V_G = -5V$.

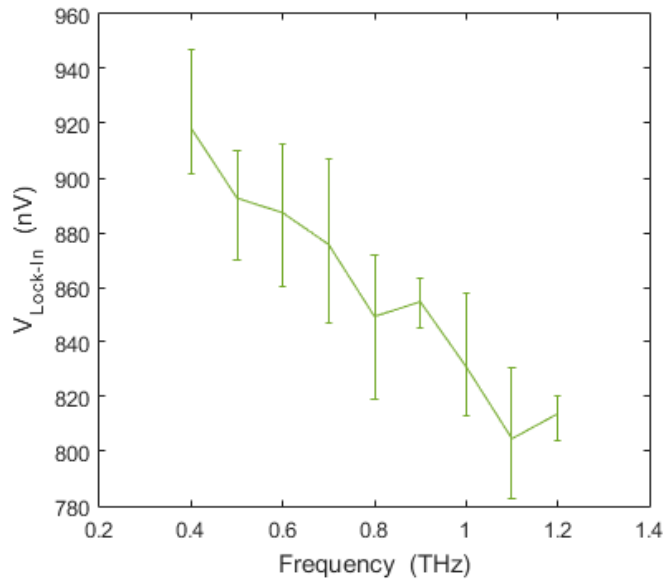


Figure 7.14, showing the signal variation for different terahertz frequency illumination, with a dynamic range up to 100nV.

Band pass filters for $\lambda=155\mu\text{m}$, $215\mu\text{m}$ and $850\mu\text{m}$ were used to obtain a narrowband laser source from the pulsed broadband source at NPL. The V_{lockin} generated by the narrowband laser source was then compared to the theoretical response of the detector modulated by the laser power output and the antenna. The signal, V_{lockin} , was obtained by reconstructing it from the in-phase component, X , and the phase angle θ , as described in section 7.4.3. For phase angles $\theta \neq 0^\circ$, this technique can become noisy.

To compare the theoretical and experimental signals, the measured signal and the theoretical detector response were both normalised for the reading at 1.4THz and plotted in figure 7.15. The error bars were calculated by finding the standard deviation of the measured V_{lockin} , with the noise in these readings likely to arise due to the experimental setup, potentially including ground loops and floating grounds arising from anodised experimental equipment. The results suggest some agreement between the theoretically expected and experimentally measured values, but many more readings are required for conclusive evidence of narrowband detection.

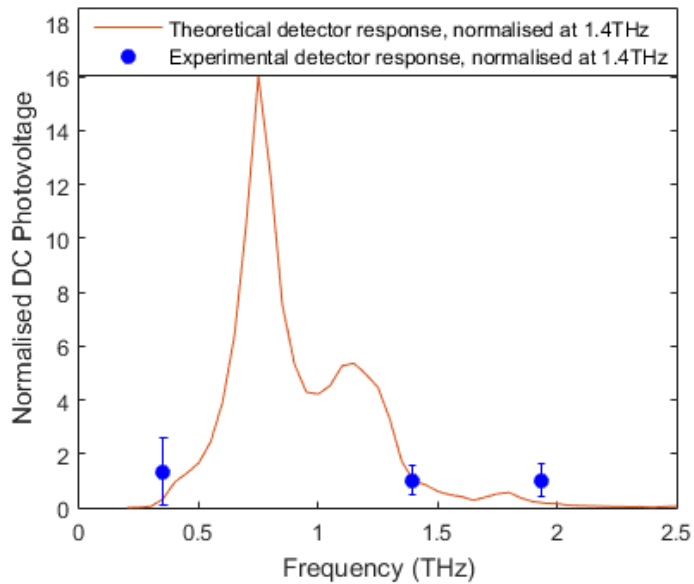


Figure 7.15, showing a comparison between the theoretical response of the detector due to the laser illumination power multiplied by the antenna response, and the measured results with the presence of the three band pass filters. Further experimental research should look to investigate the narrowband terahertz response as a function of frequency.

In summary, there is not yet any noticeable variation of the signal as a function of terahertz illumination frequency for conclusive demonstration of narrowband terahertz sensitivity. Figure 7.14 shows modulation by the signal modulation, but shows no agreement with the theoretically expected results; in figure 7.15, the comparison of the theoretical and experimental results shows some expected behaviour, but nothing conclusive. This is potentially due to issues such as systematic noise swamping any change due to the terahertz frequency; the power output of the laser at each required frequency as a proportion of the total terahertz power output being too low; the alignment of, and the attenuation due to, the band pass filters, and the agreement between the theoretically simulated antenna response and what is generated from the manufactured antenna. The next key area to developing this detector is to iterate the detector design to improve the power transfer from the antenna to conclusively demonstrate narrowband detection.

7.4.7 Rectification and the Asymmetry Argument

The terahertz photons couple to both antenna lobes, and develop an oscillating E-field across the graphene channel which, in the case of this detector, generates plasmons along the channel.

A rectification of the Fermi level is required to explain the mechanism that enables the detection of terahertz photons for the passive terahertz detector. A non-linear response arising from hydrodynamic theory establishes a DC photovoltage at each of the contacts. Some degree of asymmetry in the experiment setup is required to maximise the potential difference between the contacts, otherwise the measurements from either antenna arm subtracted from each other would give zero signal. The asymmetry argument is crucial in both single ended and differential mode operation of the lock-in amplifier, although the latter allows for common mode noise rejection and a resulting improvement in the signal to noise ratio. The orientation of the detector was also investigated to any dependence on the polarisation of the beam. Initial empirical evidence suggested that the greatest signal occurs when the E-field component of the terahertz source is polarised parallel to the antenna-channel-antenna axis, with no signal when the E-field is perpendicular to the antenna-channel-antenna axis.

A more stable arrangement was found by exploiting the asymmetry between the gate and the antenna, which essentially utilised the setup used in ref. [124]. For a generated E-field to modify the channel resistance and thus allow a DC photocurrent through rectification, the gate to antenna lobe coupling needs asymmetry so that the Fermi level also oscillates with the E-field. If the gate to antenna lobe coupling is symmetric then the Fermi level must be independent of the direction of the E-field, and hence there is no rectification or measured DC photovoltage. The E-field component must be orthogonal to the graphene channel; if the E-field is perpendicular to the antenna-channel-antenna axis, then no signal is measured as there is no Fermi level shift. This was achieved by AC coupling the lock-in amplifier to the gate through a capacitor with a $3\text{M}\Omega$ resistor to ground from the gate, as shown in figure 7.16. This option gives a high impedance route to ground for a stable measurement whilst enabling common mode noise rejection.

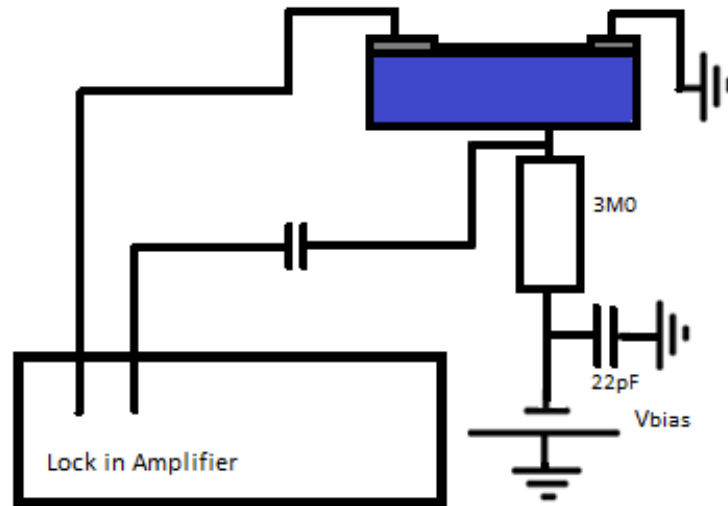


Figure 7.16 showing the optimised configuration for the most stable signal from the detector.

7.4.8 Comparing to Theory

To compare the theoretical behaviour of the detector to the results observed experimentally, the theoretical approach taken in chapter 3.3.1 was considered and developed further. The current as a function of the photon frequency was calculated by deducing the theoretical value for $\frac{I}{I_d}$ and then multiplying by the expected value for I_d , which is related to the AC photocurrent along the graphene channel with values of the order of those in ref. [154].

The theoretical response for a given gate voltage and photon frequency is given by multiplying together the theoretical current as a function of the photon frequency, the resistance of the graphene channel as a function of gate voltage, and the normalised power of the laser and the normalised response of the antenna response, both as a function of the photon frequency,

$$\textit{Theoretical Response}(V_G, \omega) = I(\omega)R(V_G)\tilde{P}_{THz}(\omega)\tilde{P}_{Antenna}(\omega), \quad \text{Equation 7.8}$$

where $I(\omega)$ is the current as a function of the incident frequency ω , $R(V_G)$ is the measured resistance as a function of gate voltage, $\tilde{P}_{THz}(\omega)$ is the normalised power transfer from the antenna related to the S11 response, and $\tilde{P}_{Antenna}(\omega)$ is the normalised output from the laser. This is illustrated as a heatmap in figure 7.17.

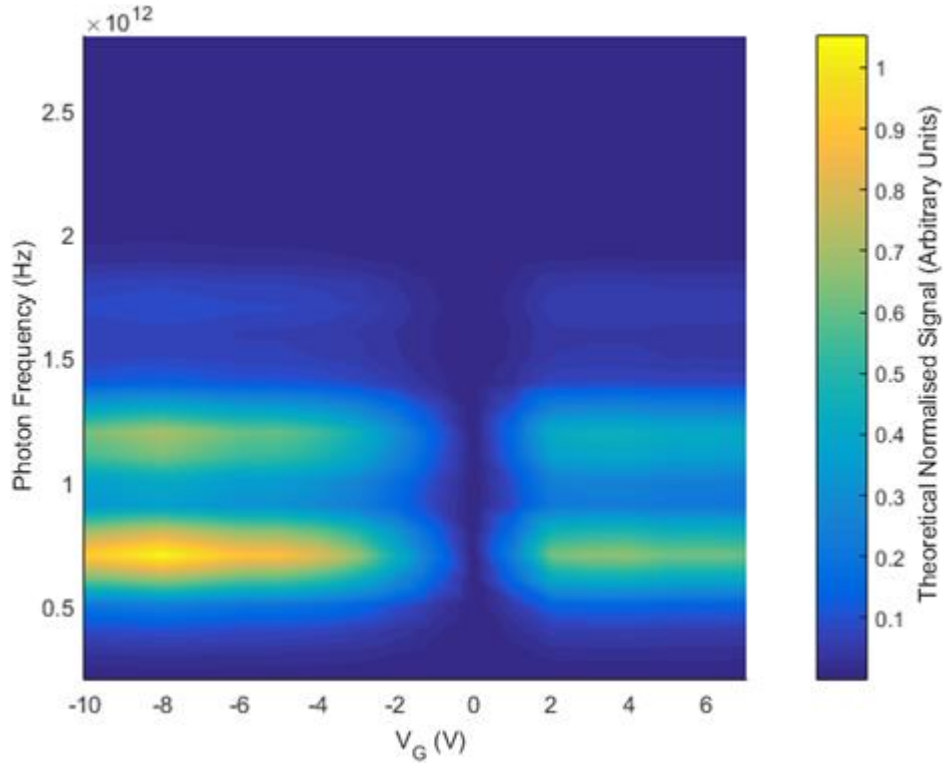


Figure 7.17, showing a heat map for the theoretical current as a function of photon frequency and gate voltage. Resonances occur as a function of frequency at approximately 0.7THz, 1.2THz and 1.7THz due to modulation by the laser power and the antenna response, with peak current close to the Dirac point of $V_G \sim -7V$, and a minimum at approximately 0V.

To obtain the theoretical broadband response as a function of gate voltage, equation 7.8 was integrated over the frequency range of the laser and antenna,

$$\text{Theoretical Response}(V_G) = \int_{0.2\text{THz}}^{2.8\text{THz}} I(\omega)R(V_G)\tilde{P}_{\text{THz}}(\omega)\tilde{P}_{\text{Antenna}}(\omega)d\omega.$$

Equation 7.9

As previously discussed, I_d is related to the AC photocurrent I_{PC} , which enabled I_{PC} to be estimated. An ansatz I_{PC} as a function of gate voltage was selected, figure 7.18a, based on the results given in ref. [154]. This has a positive peak current close to the Dirac point of $V_G \sim -7V$, which becomes negative further away from the Dirac point. The resulting theoretical signal, figure 7.18b, shows the previously observed behaviour with a peak close to the Dirac point, decreasing to a minimum, increasing and then remaining approximately constant for increasing gate voltage.

The theoretical results were fitted to normalised experimental data obtained at Aston University, as shown in figures 7.18c and 7.18d, to estimate I_{PC} . The estimated I_{PC} as a function of gate voltage is of order 100nA, with the peak I_{PC} close to the Dirac point

that becomes negative further away from the Dirac point, as shown in figure 7.18e. The results compare well to the results shown in ref. [154], with a theoretical current I of the expected order of magnitude given by $V_{DC}/R(V_G)$.

The same process was followed to estimate I_{PC} as a function of gate voltage from the results obtained at NPL in differential mode, previously shown in figure 7.11b. This demonstrates comparable results to those shown in figure 7.18a, as the peak I_{PC} occurs close to the Dirac point, illustrated in figure 7.18f. I_{PC} becomes negative at increasingly positive and negative gate voltages.

The results thus far in this section suggest that the mechanism that generated the signal arose from a plasma wave that propagated along the graphene channel and provided a measurable DC photovoltage. This is because the theoretically expected results obtained in this section, arising from the hydrodynamic approach discussed in ref. [123], lead to I_{PC} values that show good agreement with those in ref. [154] when fitted to the experimental data from both devices that were tested. Additionally, both theory and the experimental data demonstrate gate voltage sensitivity, especially to a broadband source, while acting passively.

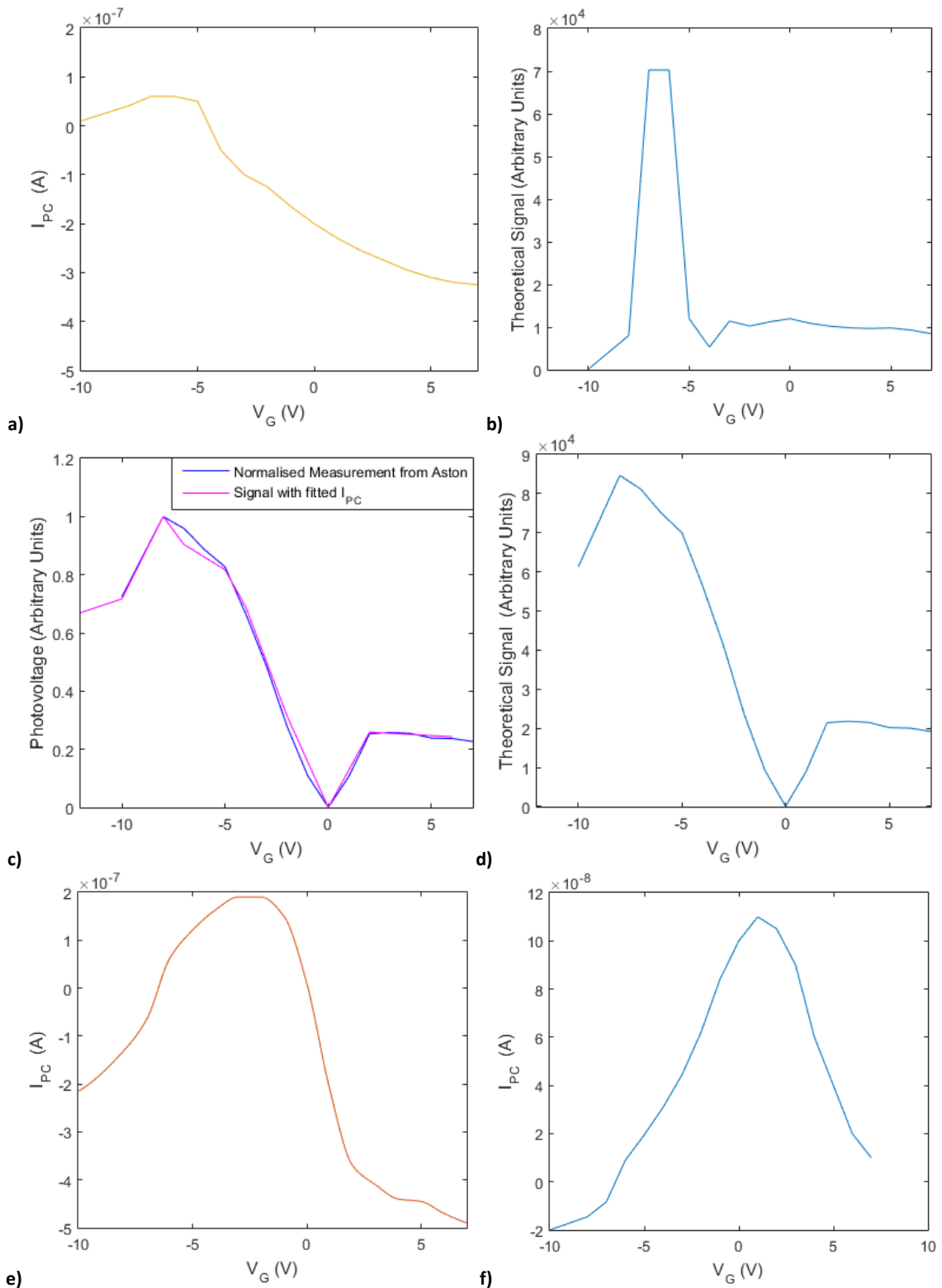


Figure 7.18, showing a) the ansatz I_{PC} selected for the simulation, based on the functionality shown in ref. [154]. B) shows the theoretical response of the detector for the initial photocurrent simulation shown in a). C) shows the normalised photovoltage response of the detector comparing the theoretical response and response from the experiment in Aston, enabling a better estimate of the photocurrent. D) shows the theoretical photovoltage of the detector in arbitrary units as a function of gate voltage. E) shows the I_{PC} resulting from fitting the theoretical values to the experimental data, which is also of the form shown in ref. [154] F) shows the same form of I_{PC} for the second device, using measurements taken at NPL in differential mode.

The behaviour of a narrowband detector was also simulated. The heatmap, figure 7.17, shows the generated photon frequency as a function of gate voltage and illumination frequency, with a maximum for gate voltages close to the Dirac point, and a minimum at 0V. As a function of the illumination frequency, resonances occur at approximately 700GHz, 1.2THz and a smaller peak at approximately 1.7THz which arise from the modulation by the laser power and the antenna response. Narrowband detection requires the detector response at a given frequency and gate voltage, in this case for a frequency of 1.2THz, to be maximised. By improving the response of the detector, for instance by improving the antenna response at 1.2THz, then one improves the ability of the detector to detect a narrowband source.

7.4.9 Detector Characteristics

The results from the illumination of the detector enable several figures of merit to be deduced, which allow comparisons between this passive terahertz detector and other similar detectors. By using figure 7.6b to convert between terahertz emitter voltage bias and the terahertz power emitted, the measured signal in figure 7.12b was recast in terms of the terahertz power to estimate the energy sensitivity as approximately $5\mu\text{W}$, as shown in figure 7.18. From figure 7.18, the peak responsivity was estimated as $7.7\pm 0.6\text{mVW}^{-1}$, given by the gradient of the data for $V_G=-8\text{V}$, assuming that all of the laser power couples to the antenna.

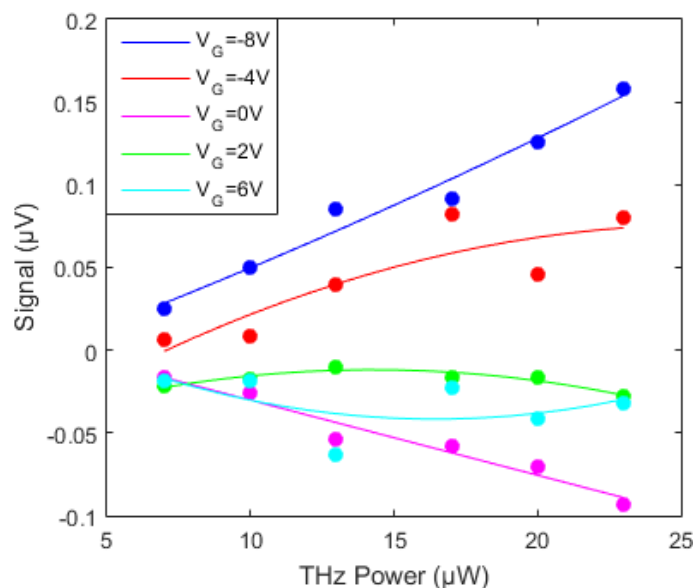


Figure 7.19 showing the measured signal as a function of terahertz power, indicating a sensitivity of at least $5\mu\text{W}$.

One deduces the NEP by calculating the signal to noise ratio, and then using

$$NEP = \frac{\text{Power Deposited}}{\text{Signal to Noise ratio}} \quad \text{Equation 7.10}$$

To give it in terms of $\text{WHz}^{-0.5}$ one needs to know the bandwidth, which is arrived at from Nyquist's theorem, given by

$$BW = 1/2\tau_{avg}, \quad \text{Equation 7.11}$$

where τ_{avg} is the time that the signal is averaged over. In this case, τ_{avg} is the 1s time constant on the lock in amplifier, hence the bandwidth is 0.5Hz.

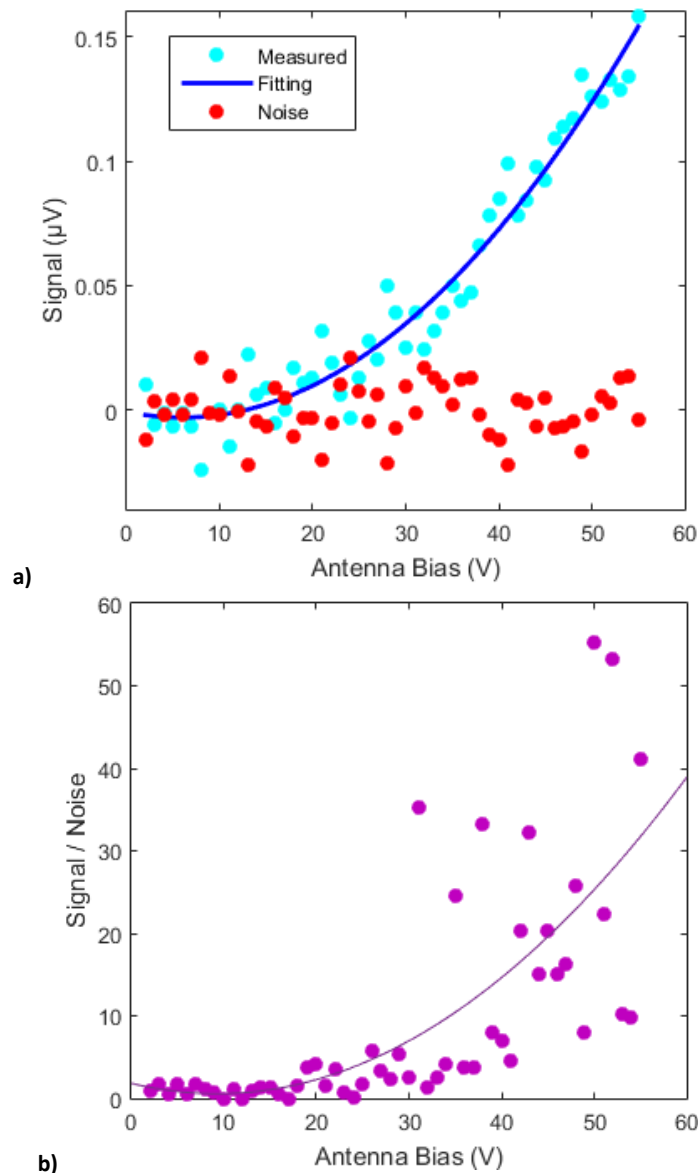


Figure 7.20, showing a) the measured signal as a function of antenna bias voltage with the calculated noise for -8V gate voltage. B) shows the signal divided by noise for every data point, indicating an SNR $\sim 35 \pm 5.6$ for an antenna bias of 55V

Using the data obtained at Aston University, a quadratic curve was fit to the data for $V_G = -8V$ so that the noise could be calculated, figure 7.20a. Plotting Signal/Noise against gate voltage suggests that, for an antenna bias of 55V, the $SNR \sim 35 \pm 5.6$, figure 7.20b. This results in $NEP \sim 0.6 \pm 0.11 \mu W$, or approximately $0.85 \pm 0.15 \mu W Hz^{-0.5}$ given a bandwidth of 0.5Hz that was obtained from the lock in amplifier.

Using the estimated NEP and responsivity, the product of these two values allowed for an estimate of the noise spectral power, equal to $6.55 \pm 1.2 nV Hz^{-0.5}$. To obtain an NEP value equivalent to other graphene-based terahertz photodetectors $\sim 1 nW Hz^{-0.5}$ the detector would, for example, need an improved responsivity to approximately $10 V W^{-1}$ and/or a reduced noise spectral power to $\sim 5 pV Hz^{-0.5}$. Anything below and right of the red line leads to an NEP of $1 nW Hz^{-0.5}$; the blue circle outlines where the detector currently sits in relation to this. There are several routes to potentially obtaining a greater NEP, for example by redesigning the antenna structure, changing the channel dimensions and obtaining a sample with greater mobility – these routes are discussed further in section 7.5.

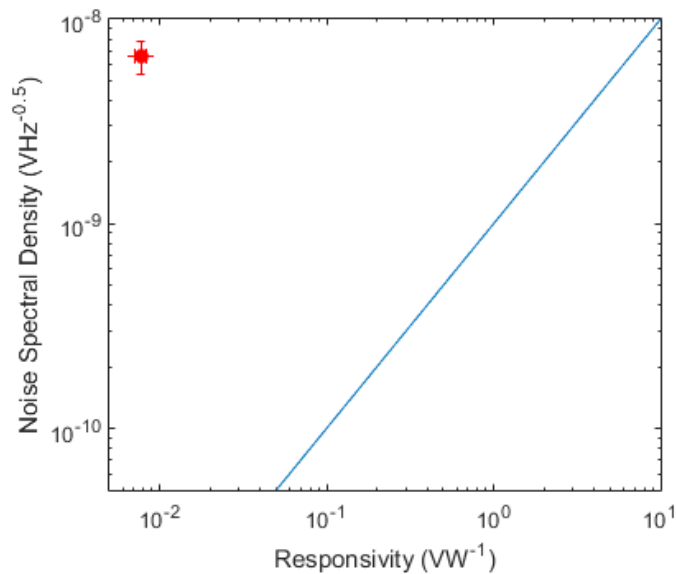


Figure 7.21, showing where the detector is now – indicated by the red circle - in comparison to the ambition of $NEP \sim 1 nW Hz^{-0.5}$, given by the blue line, in terms of the noise spectral density and the responsivity.

Using the resistance dependence for Johnson noise, one can estimate the peak room temperature Johnson noise component for this detector as a function of gate voltage as $10-15 nV Hz^{-0.5}$, and as $11-17 nV Hz^{-0.5}$ when including the $\sim 5 nV Hz^{-0.5}$ for the lock in

amplifier, figure 7.22. Flicker, or 1/f, noise provides a component of the total noise arising from a variety of sources.

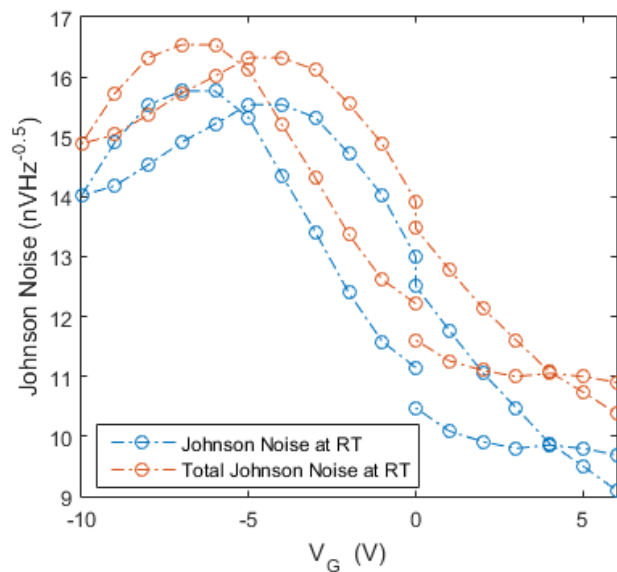


Figure 7.22 showing the Johnson noise at room temperature as a function of gate voltage, indicating a detector noise of 10-15nVHz^{-0.5}.

7.5 Further Device Iteration and Roadmap to Development

As outlined in the previous section, further iteration of the device would allow for an improved signal, resulting in an improved SNR and a reduced NEP, to obtain the target of $NEP \sim 1 \text{ nVHz}^{-0.5}$ and make this technology comparable to other graphene-based terahertz photodetectors. It would also improve the possibilities for narrowband detection. There are several options to redesigning the detector that could result in an improved detector response, such as by amending the antennae geometry, changing the channel width and using a sample with a greater carrier mobility.

Further iteration of the antennae geometry, for instance, could lead to an improved S11 parameter at 1.2THz, and therefore greater power transfer. An example antenna design, with a greater S11 magnitude response at 1.2THz, and reduced S11 magnitudes at other frequencies, is presented in figure 7.23. Additionally, greater impedance matching between the channel and the antenna would result in greater power transfer, as discussed previously in section 3.3.2. Redesigning the antenna structure is possible given the current state of the art of manufacturing processes.

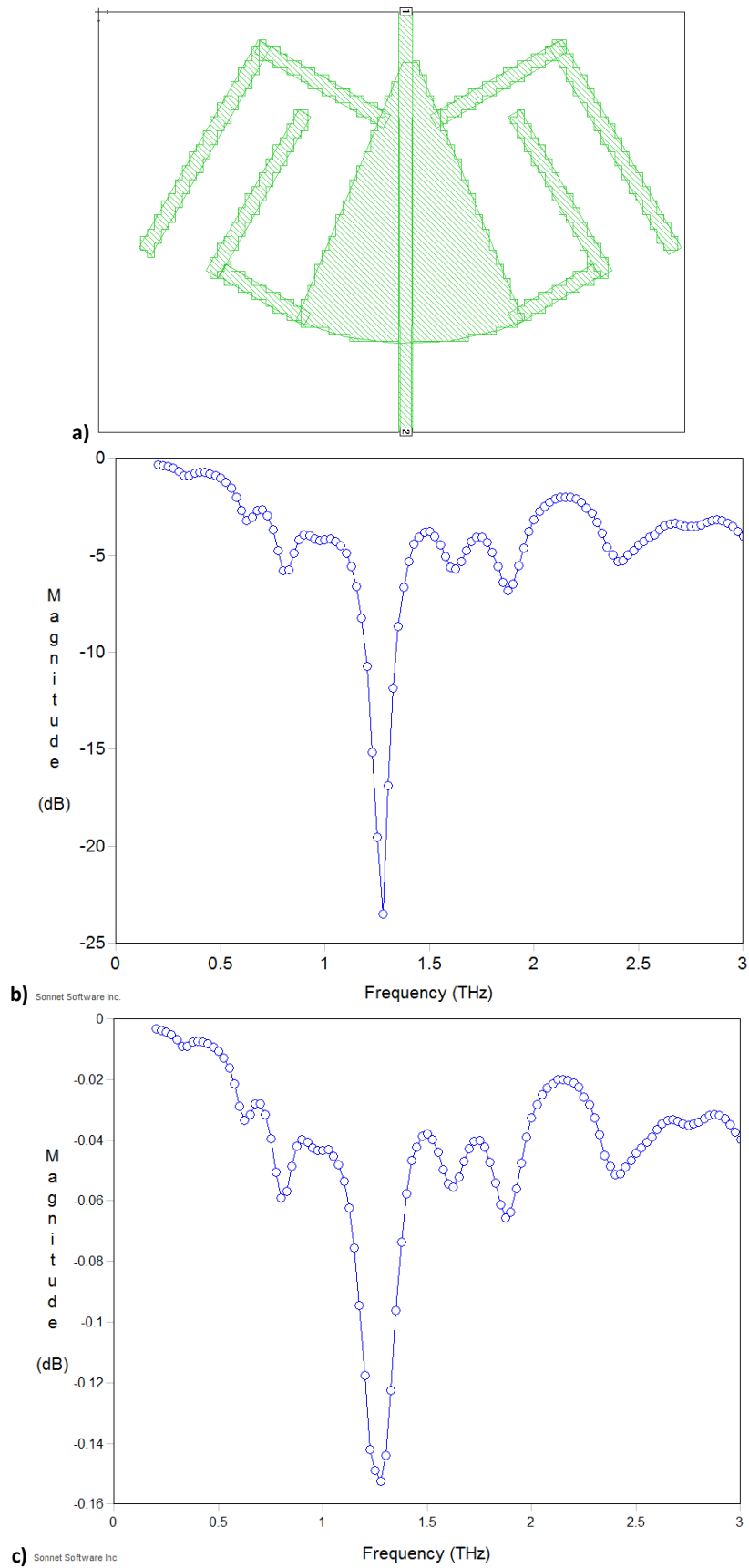


Figure 7.23 showing a) an iterated beetle antenna structure with b) one major resonance at 1.2THz (50 Ω termination on both ends) and c) with the simulated power transmission for a 5k Ω graphene channel.

The channel size is another detector parameter that could be iterated, and can be readily achieved given the current manufacturing state of the art. Whilst the detector was optimised for a response to photon frequencies around 1.2THz and has demonstrated passive broadband detection, currently the channel is well outside the maximum resonant behaviour that could be achieved by changing the channel dimensions. Changing the dimensions to ensure the plasma wave is resonant would result in a signal that is 5-20x greater than for the broadband, leading to an improved SNR and NEP. The resonant behaviour regime is discussed further in ref. [151].

A detector resonant detector has not yet been designed that operates in the resonant regime and exploits the D-S effect [123], as the simulated $\frac{I}{I_d}$ is limited by the momentum scattering time, τ , which is inherently related to the channel conductivity, σ , as shown in figure 3.3a. A greater channel conductivity and carrier mobility would improve the prospect for resonant plasma wave behaviour, and therefore a greater detector signal and a reduced NEP, as shown previously in figure 3.3b. The channel conductivity and carrier mobility is limited to $\sim 10000\text{cm}^2\text{V}^{-1}\text{s}^{-1}$ by the current state of the art of the manufacturing process, although improvements to this figure may be obtained in the future.

Another possible route to improve the response of the detector is to maximise the asymmetry in the detector, especially between the source and gate. One route to do this is to couple the gate to the source and antenna only, and not to the drain. This could involve using a deposited metal back gate such as ITO rather than a silicon wafer where it could couple more homogeneously. This could present a route to a flexible, passive, broadband and transparent terahertz detector with a plastic substrate and a patterned ITO back gate, as illustrated in figure 7.24.

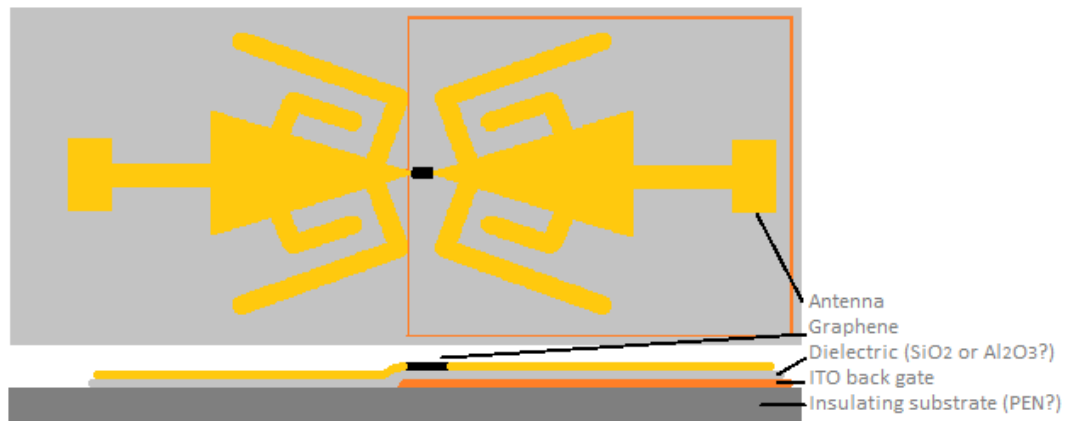


Figure 7.24 showing a potential detector design that maximises the asymmetry in the detector.

There are several areas of research that could be followed up to demonstrate the potential of this detector. For instance:

1. To demonstrate narrowband sensitivity of the detector, further illumination by a narrowband, tuneable terahertz source is required. This requires routes to reduce sources of the experimental noise in the setup.
2. Further research into the polarisation and position dependence of the signal.
3. Further routes for development and iteration include developing a future detector into a multi-pixel imaging array. This could be done by patterning the graphene using electron beam lithography in such a way that the channels are all aligned. The channels could be closely aligned, but simulations would have to be undertaken to confirm the effect of the antennae being further away from the graphene channels than they are at present.

7.6 Summary

The objectives for the terahertz photodetector were a passive detector which would be capable of narrowband detection around 1.2THz. In this chapter, experimental results using pulsed and continuous wave terahertz sources have been presented that enabled the characterisation of a passive, broadband terahertz detector.

Experimental testing has demonstrated modulation of the terahertz signal as a function of the gate voltage and the emitter bias voltage, with further work required to demonstrate modulation to the illuminating photon frequency. The detector was acting passively, with no bias voltage applied across the graphene channel, with an

estimated NEP of $0.85 \pm 0.15 \mu\text{WHz}^{-0.5}$ and a responsivity of $7.7 \pm 0.6 \text{mW}^{-1}$. This is some way off that of other terahertz photodetector technologies, but routes have been identified that could boost the signal, including redesigning the detector antennae and changing the graphene channel dimensions. There are several sources of noise that have been identified that need to be reduced to improve the observed signal, and iterated to find an electronic arrangement that provides the most stable signal.

Experimental testing has not yet categorically demonstrated narrowband detection through the trials with the continuous wave narrowband source and the use of bandpass filters. These initial results do, however, suggest some modulation which may be boosted through redesigning the antennae for an improved S11 value at 1.2THz.

8

Detector Characterisation of the Single X-ray Photon Counting GFET

8.1 Introduction

As discussed in chapter 4, the X-ray GFET was designed to achieve the greatest possible temporal and energy sensitivity with the aim of detecting low intensity X-Ray photons. Conceptually, the X-ray photon is absorbed in the Si absorber, generating e-h pairs that are funnelled by the gate voltage towards the silicon dioxide substrate. The modulation of the charge carrier density generates a field across the dielectric, which causes a change in the Fermi level and the channel conductivity due to the field effect.

In this section, the characterisation of the detector using an optical pulsed laser is presented to obtain the energy sensitivity, and different electronic arrangements are discussed to improve the signal to noise. The device was then illuminated by different X-ray sources to attempt to demonstrate X-ray sensitivity.

8.2 Characterising the Detector with an Optical Pulsed Laser

The GFET was illuminated by red and blue pulsed lasers to demonstrate photosensitivity and investigate the behaviour and sensitivity of the detector. Illumination by pulsed laser photons is the equivalent of depositing the energy from an X-ray photon directly in the absorber by creating all the secondary charge carriers immediately in the absorber detector without having the initial high energy photoelectron due to the X-ray which then thermalises. The same amount of energy is deposited in the absorber, but the pulsed laser photons do not have to go through a process of thermalizing.

The laser pulse provides deposited energy with an equivalent absorption coefficient in the silicon absorber to specific wavelengths of UV and soft X-ray single photons. The

wavelength dependence of the photon absorption depth in silicon, figure 8.1, shows the absorption of photons for wavelengths of 650nm and 405nm is analogous to soft X-rays $\sim 1\text{-}4\text{keV}$ and $\sim 500\text{eV}$ respectively, with the latter creating all its secondary charge carriers very close to the silicon dioxide interface.

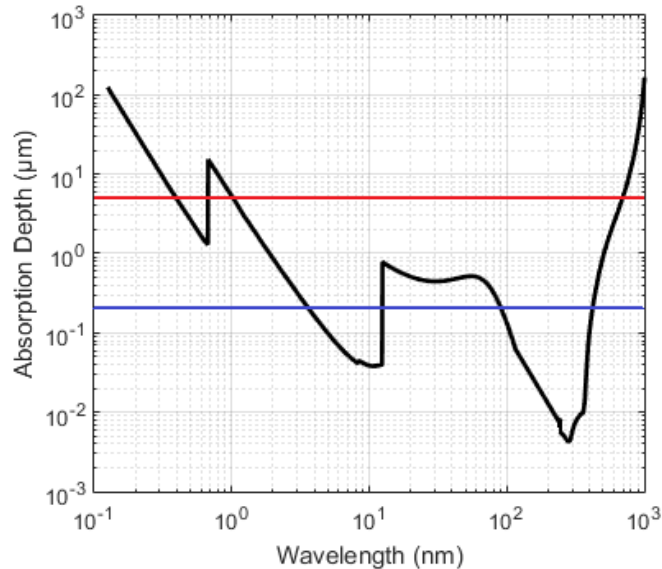


Figure 8.1, showing the wavelength dependence of photon absorption length for silicon. The red and blue lines show the absorption depth at 650nm and 405nm laser wavelengths respectively. Data was obtained from ref. [250] and ref. [251].

Whilst the eventual aim was to detect low intensity or single X-ray photon sources, using a pulsed optical laser source enabled initial experiments to characterise the behaviour of the detector and, in particular, its likely sensitivity. The pulsed laser offered many advantages for initial characterisation such as simple control of the deposited energy via variation of pulse width or by attenuation with ND filters, and providing a periodic strobe signal with which the detector output pulse, if present, will be synchronised c.f. the unknown random arrival time of X-ray events from an X-ray source. The latter capability is critical when trying to measure the sensitivity while looking for the smallest detectable pulse above the noise. The pulse width is much shorter than the carrier lifetime so that it resembles the immediate signal from an X-ray absorption.

8.2.1 Laser Characterisation with a SiPM

These pulsed lasers were calibrated using an Excelitas C30742-33 Series silicon photomultiplier (SiPM). Calibration of the number of photons per pulse was achieved by attenuating the laser pulser down to a few photons per pulse using calibrated ND

filters, and then measuring and histogramming the SiPM pulse amplitudes using a LeCroy HRO 64Zi 12-bit oscilloscope.

The calibration was performed with the lasers tightly focussed on the silicon; the same mode was used when illuminating the GFET device, with the silicon wafer on the GFET assumed to have the same quantum efficiency as the SiPM. Attenuation of the laser to the few photon level was required to prevent spatial saturation in the SiPM (i.e. multiple photons per SiPM cell) and so that the separate photon peaks would be visible in the pulse height distribution.

As the absorption coefficient, μ , for photon wavelengths $\lambda=405\text{nm}$ and $\lambda=650\text{nm}$ is $\mu = 7.5 \times 10^{-4} \text{cm}^{-1}$ and $\mu = 2.81 \times 10^{-3} \text{cm}^{-1}$ respectively [250], it was assumed that, for a sample thickness $x \geq 0.5\text{mm}$, all the photon energy would be absorbed in the absorber as the proportion of photons transmitted, related to $\exp(-\mu x)$, approximately equals 0. Any losses were assumed to be equivalent because the SiPM and GFET both have a silicon absorber. The red laser spot could be focussed more tightly than the blue, which may mean that less energy per unit area was deposited in the absorber, and the lasers were calibrated at their minimum pulse width of $\approx 50\text{ps}$.

The pulse height distributions were analysed by fitting Gaussians to each of the peaks in the histogram, figures 8.2a and 8.2b. The pulse height was plotted against the number of photoelectrons (PE) for each peak to estimate the voltage per PE, figures 8.2c and 8.2d. For the red laser, a value of -1.8mV per PE was obtained, with a mean of $\sim 10\text{PE}$ when the source is attenuated with an ND6 filter, which indicates an unattenuated pulse of approximately 10^7 photoelectrons. Equally, for the blue laser figure 8.2d shows -2.5mV per PE and $\sim 3 \times 10^6$ photoelectrons per pulse, respectively.

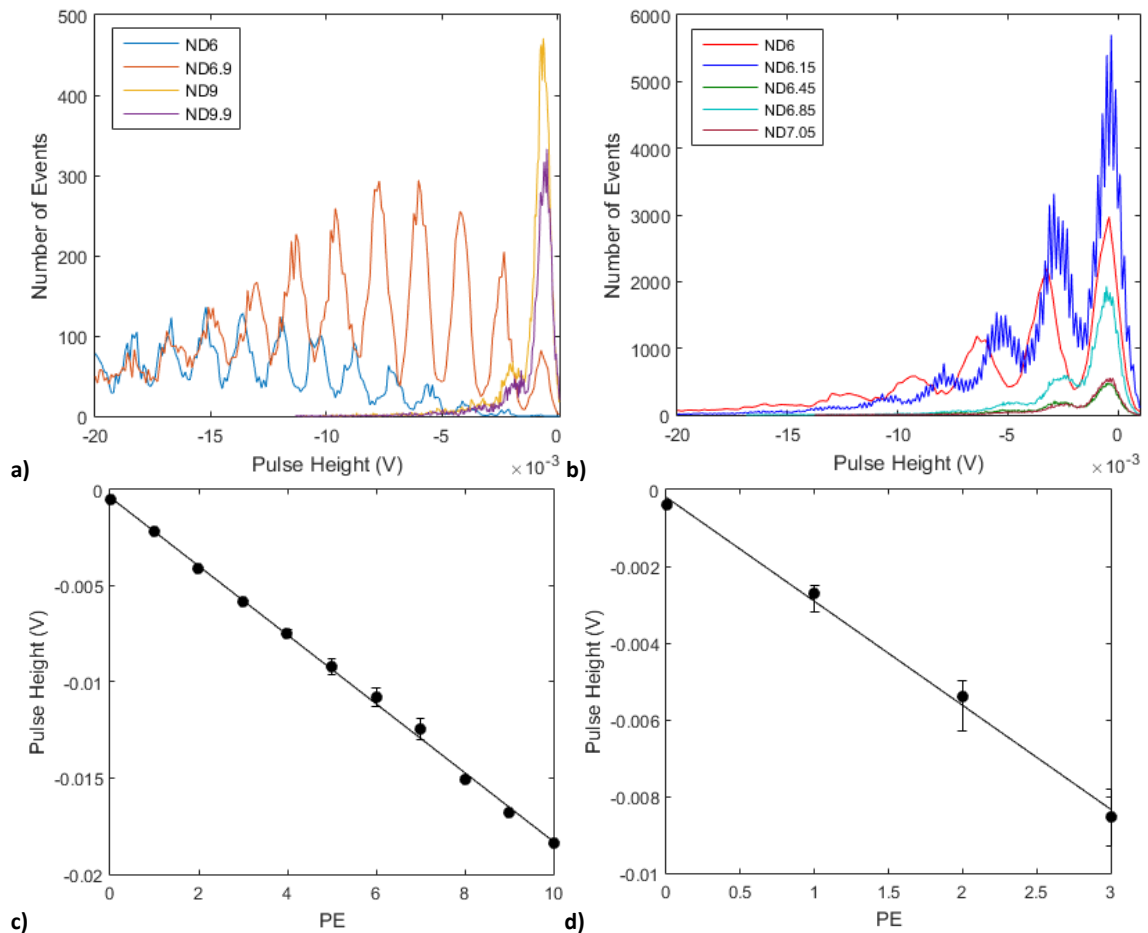


Figure 8.2, showing the SiPM pulse height distribution for the a) red and b) blue lasers. The OPE pedestal is shown for the smallest pulse height, with the intensity of each PE distributed in a Poisson envelope for different attenuation values. C) and d) show the relationship between the pulse height and PE for red and blue lasers, respectively, indicating the pulse height per PE.

8.2.2 Transimpedance Amplifier Arrangement

The GFET was connected to an Analog Devices ASA4817-1 amplifier in transimpedance mode. Both the GFET and transimpedance amplifier were then mounted in a diecast aluminium box for electromagnetic shielding, with a hole drilled in the lid to allow the photon source to be incident on the graphene.

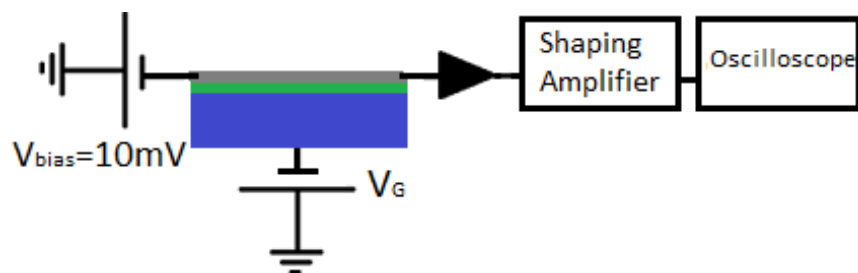


Figure 8.3, showing the transimpedance amplifier arrangement with the graphene (grey), SiO₂ (green) and Si (blue). A 10mV bias voltage was applied between the source and drain of the graphene, with the preamplifier output displayed on the oscilloscope.

The device was characterised by applying $V_{bias} = 10\text{mV}$ across the device, and the back gate voltage was varied while measuring the channel current. The $V_{bias} = 10\text{mV}$ was provided by a 1.5V battery in a voltage divider arrangement, which was a more stable, lower noise bias voltage source compared to the Keithley PSU. The resulting gate sweep, figure 8.4, shows that it is p-doped, with a Dirac point $V_{Dirac} \sim 10\text{V}$ gate voltage. These devices are generally p-type doped, which is attributed to adsorbed contaminants on the graphene from exposure to air and additionally, a significant number of trapped holes at the disordered SiO_2/Si interface [252] [253].

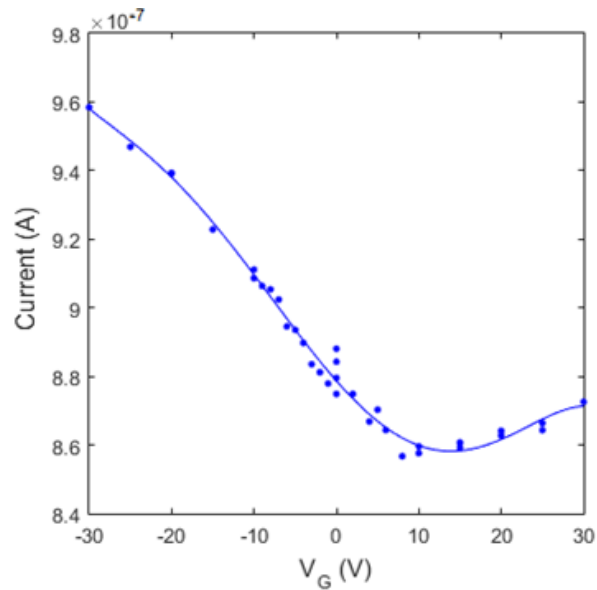


Figure 8.4 showing the current as a function of the gate voltage with the Dirac point at approximately 10V. As $V_{bias} = 10\text{mV}$, this indicates a channel resistance of $1.2\text{k}\Omega$.

8.2.2.1 Designing the Transimpedance Amplifier

A fast, current-sensitive preamplifier was fabricated using the ADA4817 amplifier in the circuit shown in figure 8.5. It was designed by Julian Thornhill, an electrical engineer at the University of Leicester, to filter any high frequency AC noise from the power supply and provide a low impedance ground for the fast current pulse developed by the changing graphene resistance through the capacitor, *point a*, onto the ground plane. The power supplies for the preamplifier, designed to run at $\pm 5\text{V}$, also had capacitors to reduce noise, *point b*. A further small capacitor was placed in parallel to the feedback resistor, *point c*, to give stability of the feedback loop. A larger feedback capacitor would have led to the preamplifier acting as an integrating charge sensitive preamplifier.

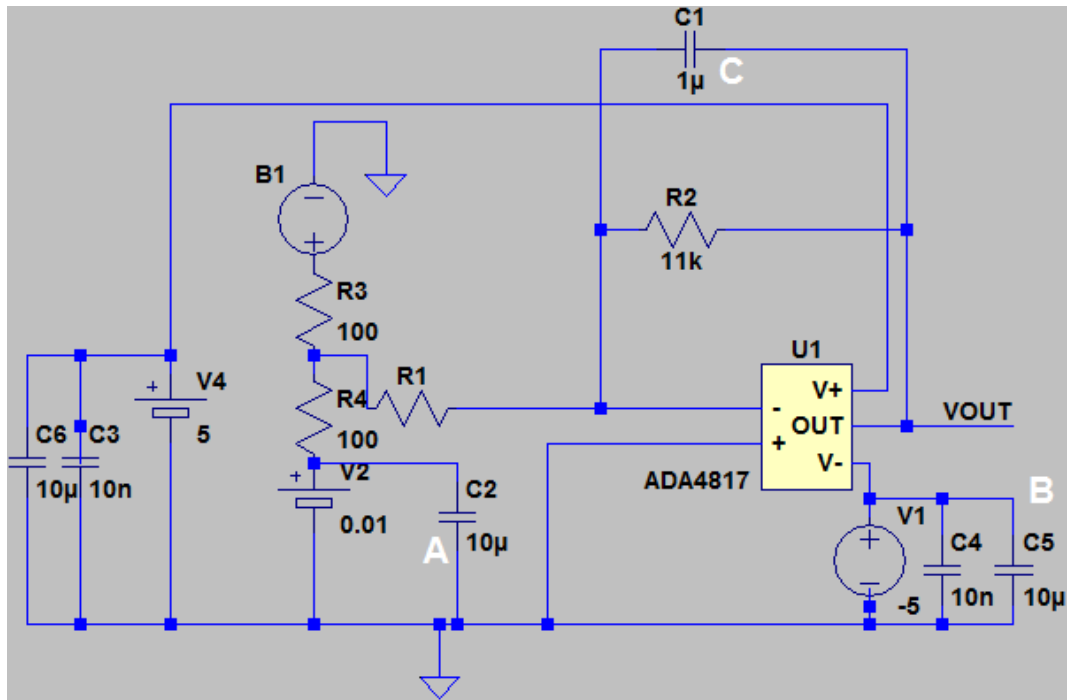


Figure 8.5. LT Spice Simulation setup for amplifier board. R1 represents the location of the graphene. Other components of the circuit were designed for high gain and to filter out high frequency AC noise.

The evaluation board was simulated using LTSpice software. A white noise source was added to the circuit, and the resistance was pulsed as a Gaussian over time to mimic the change in resistance due to the absorption of a photon. For different feedback capacitors, figures 8.6, there is a change in the pulse to become wider and smaller for increasing capacitances, with a reduction in the SNR; therefore, a good feedback capacitor is $\sim 1\text{pF}$.

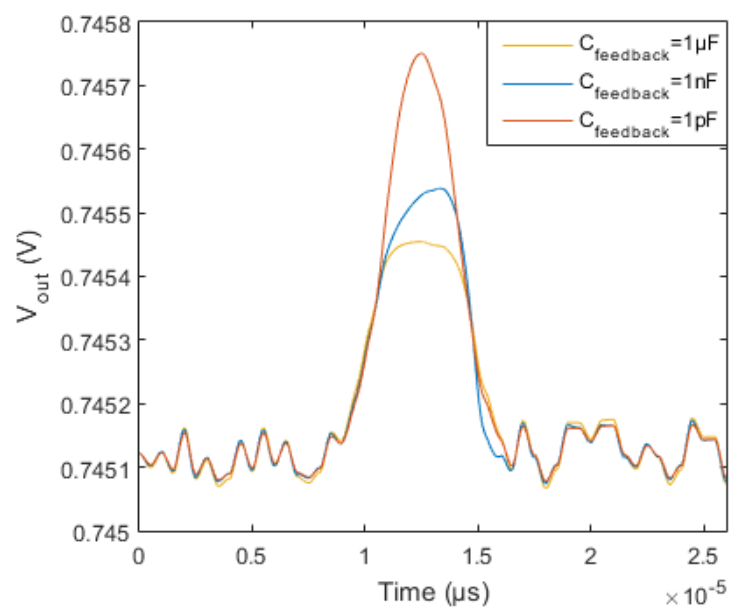


Figure 8.6, showing the LTSpice simulation for a pulse in the resistance of the graphene for feedback capacitors of 1pF , 1nF and 1μF .

8.2.2.2 Calibrating the Preamplifier

The preamplifier was calibrated by mounting a variable resistor in place of the graphene to identify the conversion between the resistance of the channel and the voltage output of the oscilloscope. The non-linear relationship between the load resistance and the amplitude, figure 8.7a, arises from the arrangement of the potential divider; for a low resistance, the voltage divider no longer provides 10mV across the graphene and therefore the measured amplitude decreases. The calibration takes the linear region above 4k Ω , giving a conversion factor of $\sim 3.6 \pm 0.28 \text{mV k}\Omega^{-1}$.

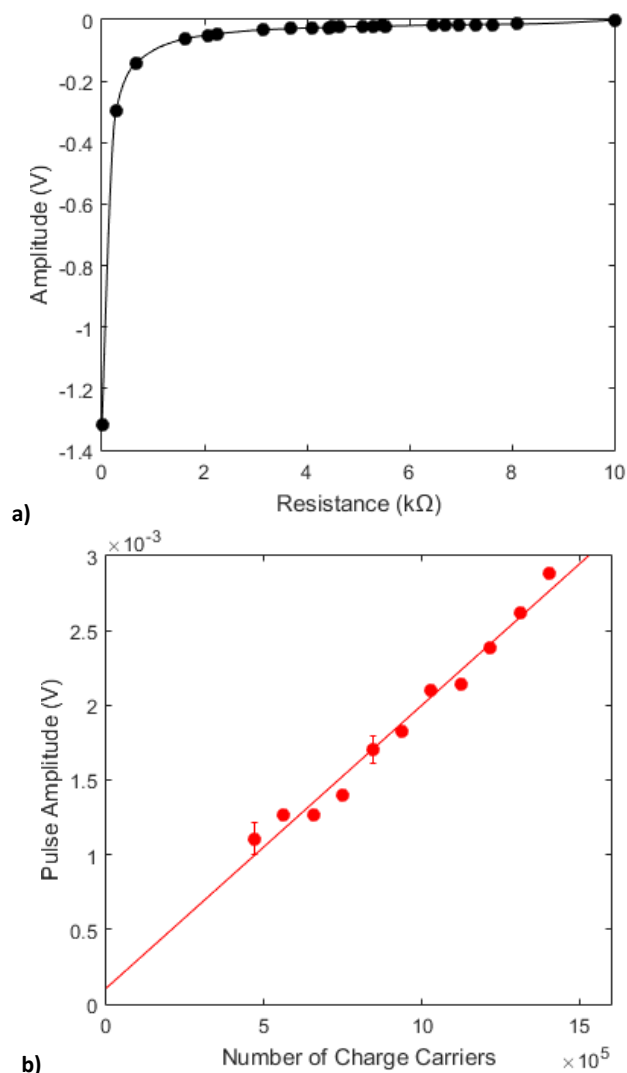


Figure 8.7, showing the calibration of the amplifier for a) the pulse amplitude as a function of channel resistance, and b) the pulse amplitude as a function of the number of charge carriers related to the presence of a capacitor.

A 1.5pF test capacitor was connected to the preamplifier, and a voltage pulse between 50mV and 150mV was applied to characterise the number of volts per charge carrier.

The number of charge carriers arising from the charge from the capacitor was plotted against the resulting pulse amplitude, figure 8.7b, resulting in a conversion factor of $1.89 \pm 0.09\text{nV}$ per charge carrier.

8.2.2.3 Initial Illumination

The device was illuminated by a pulsed optical laser with a wavelength of either 650nm or 405nm and pulse width down to approximately 50ps. Following the illumination of the detector, the current sensitive preamplifier detects the change in source-drain current and provides a voltage output, V_{pulse} , captured on an oscilloscope.

A photoresponse was detected immediately, with the output of the detector demonstrated to be dependent on the pulse frequency applied to the red pulse laser and back gate voltage applied to the detector, figures 8.8a and 8.8b respectively.

The signals generated in response to the red and blue lasers at different gate voltages, figure 8.8c, show a noticeable difference in the pulse width between the red and the blue signals, and with decays times of $\sim 4\mu\text{s}$ and $\sim 10\mu\text{s}$ respectively. This may be due to how well the laser is aligned with, and focussed onto, the detector – especially as the blue laser was not able to be focussed as well as the red. Alternatively it could be due to the red laser photons being absorbed deeper in the silicon, away from any interface states, which may have resulted in quicker recombination of the charge carriers. The detector signal has a very fast rise time and a fall time linked to the recombination time of the charge carriers in the silicon. The signal rise time, fall time and amplitude are therefore gate dependent and become faster with an increasing magnitude V_G .

There is a periodic noise at $\sim 200\text{kHz}$ in these readings, which arises from sources including pick up from the laser, which is synchronised with the triggering of the photon pulse, and ground loops which cause electromagnetic pick up. This was later improved by modifying the electronics grounding.

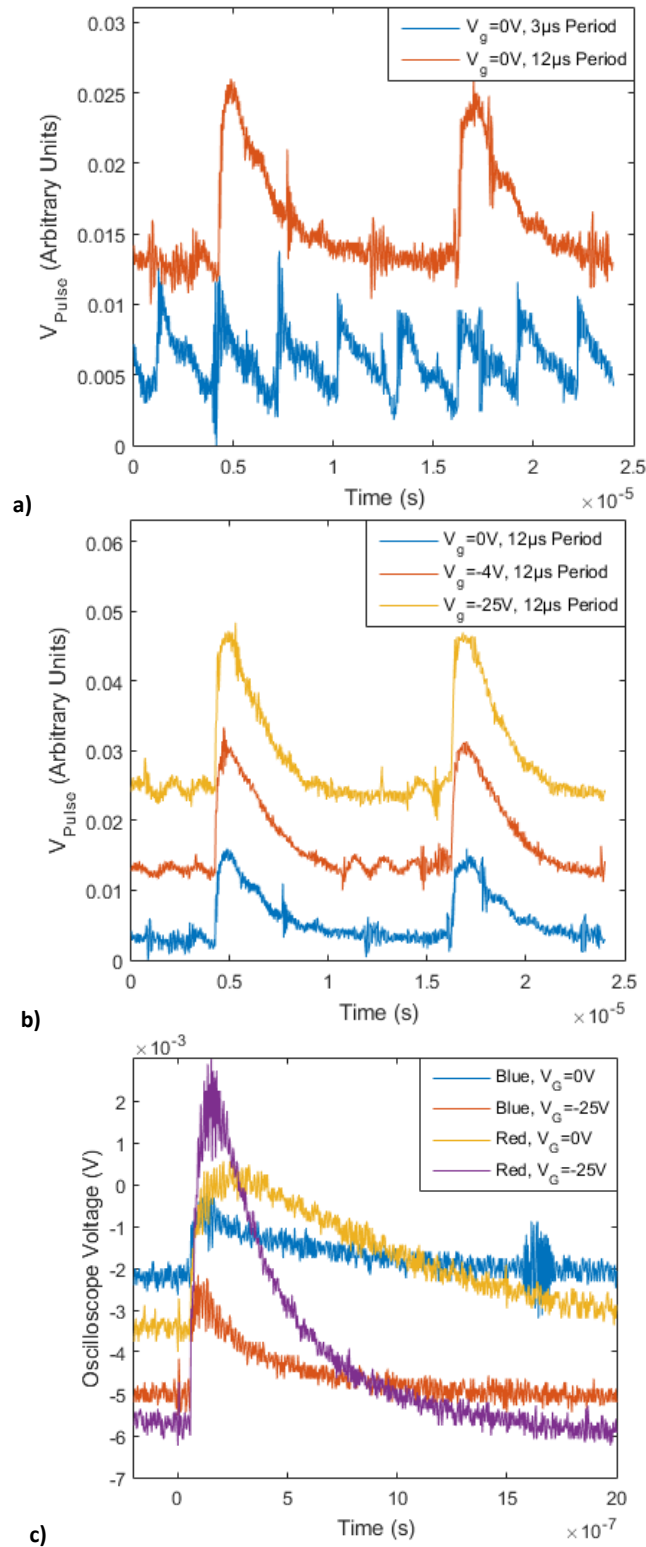


Figure 8.8, showing the initial response to illumination by different pulsed lasers. A) shows illumination of the detector by a pulsed red ($\lambda=650nm$) laser source with a $\sim 50ps$ (minimum) pulse width, which demonstrates that the photoresponse was related to the trigger frequency ($3\mu s$ or $12\mu s$, or $333kHz$ or $83kHz$ respectively). B) shows that the signal pulse height is related to the gate voltage V_G , smallest for $V_G = 0V$ and larger for $V_G = -25V$, when illuminated with a pulsed red laser source with a $50ps$ pulse width. There is an observed periodic noise at $\sim 200kHz$, likely due to noise from the laser. C) shows that the photoresponse differs between the red and blue pulsed laser sources at two different V_G , with an increased pulse height with the red pulse laser compared to the blue, and a rise time and a fall time that is faster for a more negative V_G .

8.2.2.4 Signal vs Gate Voltage: What is the Detection Mechanism?

The gate voltage V_G was varied over the range -30V to +10V, and the amplitudes and baseline of oscilloscope readout were measured for both the red and blue lasers. The pulse height was found to increase for increasingly negative gate voltages for red pulsed laser illumination, figure 8.9a and figure 8.9b, and saturated at $V_G \sim -15V$. The blue laser also saturated at approximately $V_G \sim -15V$, figure 8.9b, but with a much lower amplitude. For both the red and blue pulsed lasers, the voltage measured at the baseline became increasingly negative with a negative V_G , as the baseline represents the current through the channel which increases as V_G is further from the Dirac point.

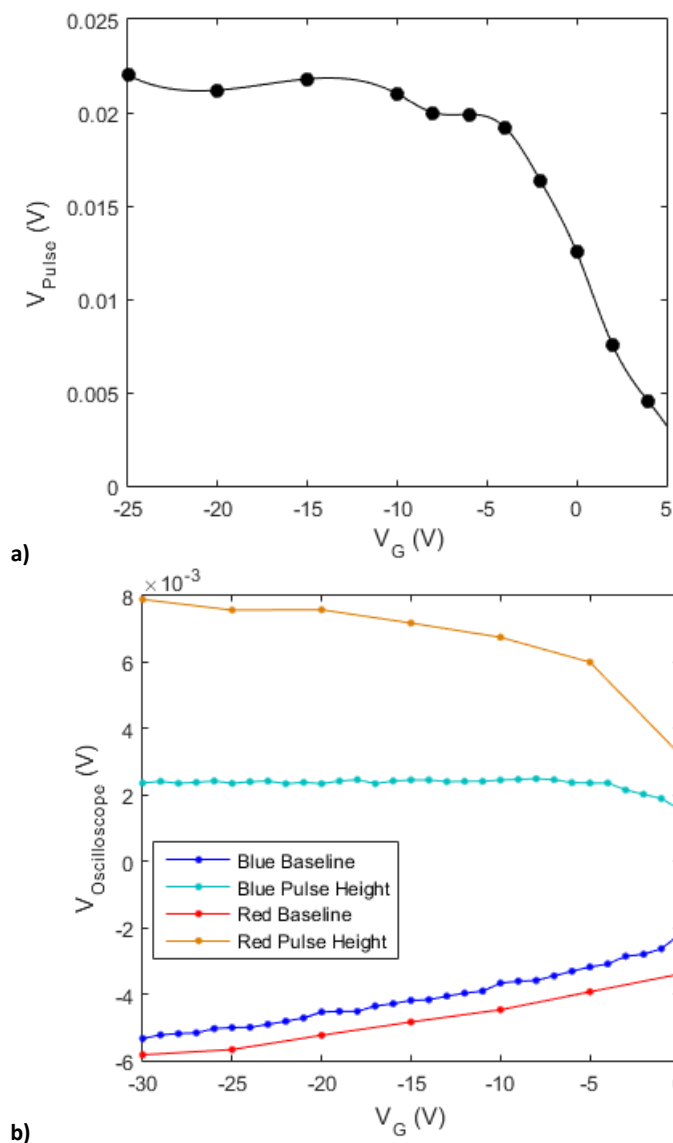


Figure 8.9, showing a) the signal pulse height increases for increasingly negative V_G . It saturates at $V_G \sim -15V$, likely due to the limits on carrier transport in the Si given by SRH recombination [2]. B) shows that the pulse height from the red and blue laser illumination both saturate at $V_G \sim -15V$, although at significantly different amplitudes. The baseline becomes negative with negative V_G as this represents the channel current which increases away from the V_{Dirac} .

One explanation for these observations is the generation of a depletion region within the silicon because of the gate voltage. A negative gate voltage attracts the majority carriers (holes) from the upper region of the absorber, adjacent to the insulator, producing a depletion region near the absorber-insulator interface [252] [253]. The width of the depletion region is given by [254]

$$x_d = \sqrt{\frac{2\epsilon_s(\varphi_l - V)}{qN_d}}, \quad \text{Equation 8.1}$$

where φ_l is the built-in potential given by

$$\varphi_l = \frac{k_B T}{q} \ln\left(\frac{N_d N_a}{n_i^2}\right), \quad \text{Equation 8.2}$$

V is the bias voltage, q is the charge of an electron, N_a is the acceptor density on one side of the depletion region, N_d is the donor density on the other side of the depletion region, ϵ_s is the substrate capacitance, T is the temperature, k_B is the Boltzmann constant, and n_i is the intrinsic carrier concentration. When the silicon wafer is forward biased, for $N_a = 1 \times 10^{14} \text{cm}^{-3}$ (equivalent to p-type silicon of $\rho \sim 100 \Omega \text{cm}$), $N_d = 1 \times 10^{14} \text{cm}^{-3}$, and $T = 300 \text{K}$, the values for the built-in potential and depletion width at different bias voltages are given in table 8-1.

| | | | | | | | | | |
|-------------------------|------|------|------|------|------|------|------|------|------|
| V_G (V) | -20 | -15 | -10 | -5 | -2.5 | -1 | -0.5 | 0 | 0.45 |
| φ_l (V) | 0.48 | 0.48 | 0.48 | 0.48 | 0.48 | 0.48 | 0.48 | 0.48 | 0.48 |
| x_d (μm) | 23.2 | 20.2 | 16.6 | 12 | 8.9 | 6.2 | 5.1 | 3.6 | 0.9 |

Table 8-1, showing the calculated built-in voltage and depletion region size in a forward-biased silicon wafer for $N_a = 1 \times 10^{14} \text{cm}^{-3}$ (equivalent to p-type silicon of $\rho \sim 100 \Omega \text{cm}$), $N_d = 1 \times 10^{14} \text{cm}^{-3}$, and $T = 300 \text{K}$. For a greater gate voltage, the width of the depletion region gets wider.

The red laser has a much larger absorption depth of $\sim 5 \mu\text{m}$ and is therefore absorbed much deeper in the absorber within the depletion region. Photons absorbed in the depletion region generate e-h pairs that scatter through the silicon in a region limited by the size of the depletion region to create a dipole aligned with the field across the silicon. For $V_G < 0 \text{V}$, the electrons migrate towards the Si/SiO₂ interface, and the holes drift towards the gate contact, the dipole strength and duration depending on their diffusion lengths and recombination times respectively. Blue photons have a mean absorption depth $\sim 200 \text{nm}$, close to or within the disordered region of the Si/SiO₂ interface layer and more likely to recombine rapidly due to higher defect density, resulting in lower dipole strength and duration and giving rise to a smaller

photoresponse as observed. At high incident flux, so many charge carriers are generated and then spread apart by the field across the substrate that the depletion region reduces because N_a and N_d increase.

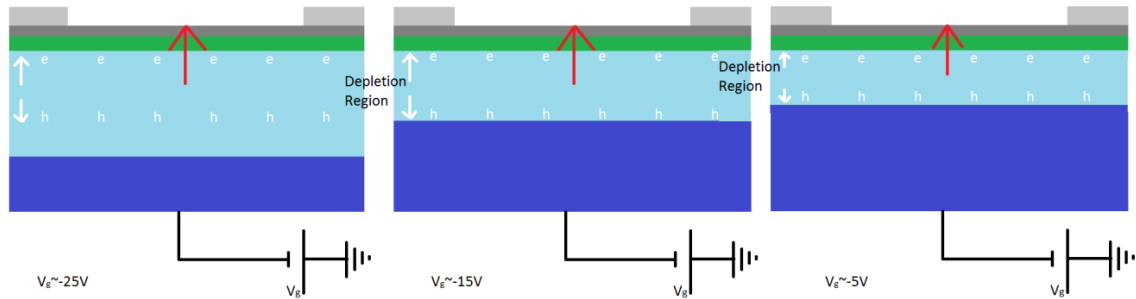


Figure 8.10 shows a schematic for the detection mechanism, with the dipole between the electron and hole pair larger for deeper depletion regions until it becomes limited by the SRH recombination time. The dipole created causes a field that changes the graphene conductivity.

The depletion region was assumed to open across an area in the silicon comparable to the size of the graphene sample, figure 8.10. The wafer was uniformly gated from the back, which establishes a field across the wafer to the source and drain contacts with equipotential lines like those simulated in figure 4.4b. This leads to a depletion region of the size of the graphene channel.

A more negative gate voltage opens a wider depletion region, and also results in a greater field to accelerate charge carriers apart, resulting in a greater dipole, a greater field applied to the graphene, and therefore a greater signal. The rise in the V_{pulse} peak occurs as the charge carriers are accelerated apart, and the fall occurs as the charge carriers recombine. For $V_G \ll 0V$, the pulse height saturates, which suggests that the charge carriers are not accelerated apart enough to take advantage of the widening depletion region before they recombine.

This suggests that the pulse height is limited by the Shockley-Read-Hall (SRH) recombination time [255]. Shockley-Read-Hall is a trap-assisted recombination process, where electrons and holes recombine by transitioning between the conduction band and the valence band via a trap state in the middle of the band gap. The recombination time of this process, the Shockley-Read-Hall recombination time, is dependent on many factors, including the majority and minority carrier concentrations, the trap energy and the temperature [255]. As the charge carriers recombine in the SRH time, if this is less than the time taken for the charge carrier to

reach the extent of the depletion region, then the magnitude of the dipole is limited, and therefore the pulse height saturates.

Alternatively, the signal could arise via bolometric- or photothermoelectric-like effects. The illumination of the sample could result in heating of the sample, and therefore a measurable change in sample resistance which decays as the sample cools [116] [256]. The decay time for a bolometer is typically of order $\tau = C/G$, where C is the heat capacity and G is the thermal conductance [116]. For this GFET $\tau \sim 30$ s, which is much longer than the decay time observed in figure 8.8. It is likely that this plays some effect, but this is likely to be small given by the magnitude of the signal decay time.

For a photothermoelectric-like effect, absorption of an incident photon excites an electron-hole pair, which relaxes via mechanisms such as impact ionisation. This could lead to heating of the sample, and to a measurable voltage via the Seebeck effect [257]. This mechanism is typically on the femtosecond scale, which is much faster than the observed nanosecond-scale recombination in figure 8.8, and suggests that this mechanism has little effect. This also requires photons to be absorbed directly in the graphene – 2.3% of the incident photons will be absorbed in the graphene, but the remaining 97.7% will be absorbed close to the surface of the silicon wafer.

While it is likely that the photothermoelectric-like effect and the bolometric like effect play some effect, it seems likely that the majority of the effect is due to excitation and recombination of electron-hole pairs in the silicon.

8.2.2.5 Attenuating the Laser Pulse – What is the Energy Sensitivity?

Initial illumination of the GFET suggested that there was a different photoresponse depending on whether the GFET was illuminated by the red or the blue pulsed laser. Previous results suggested that the red pulsed laser produced an observable photoresponse for the shortest laser pulse width ~ 50 ps, whereas the blue pulsed laser gave little or no response with the lowest pulse width, although a signal was observed for the highest (uncalibrated) pulse width.

In section 8.2.1, the laser was calibrated with a SiPM of similar quantum efficiency to the silicon wafer of the GFET. As the number of incident photons on the wafer should

therefore generate a similar number of photoelectrons, the energy deposited in the silicon per pulse used to excite photoelectrons, as a function of ND attenuation, was

$$E_{deposited} = \frac{(\#of\ PE\ per\ pulse)}{10^{ND}} \times (Ionisation\ Energy\ per\ PE) \quad \text{Equation 8.3}$$

where the number of PE per pulse from section 8.2.1, equal to 10^7 and 3×10^6 for the red and blue pulsed lasers respectively; ND is the value of the ND attenuation and the ionisation energy per PE for the silicon $W \sim 3.5\text{eV}$ [139]. This is the maximum energy deposited: less energy could be absorbed if the quantum efficiency of the silicon wafer is worse or if the laser is focussed in a way that less energy is absorbed (e.g. spatial saturation), which would mean that fewer charge carriers would be excited.

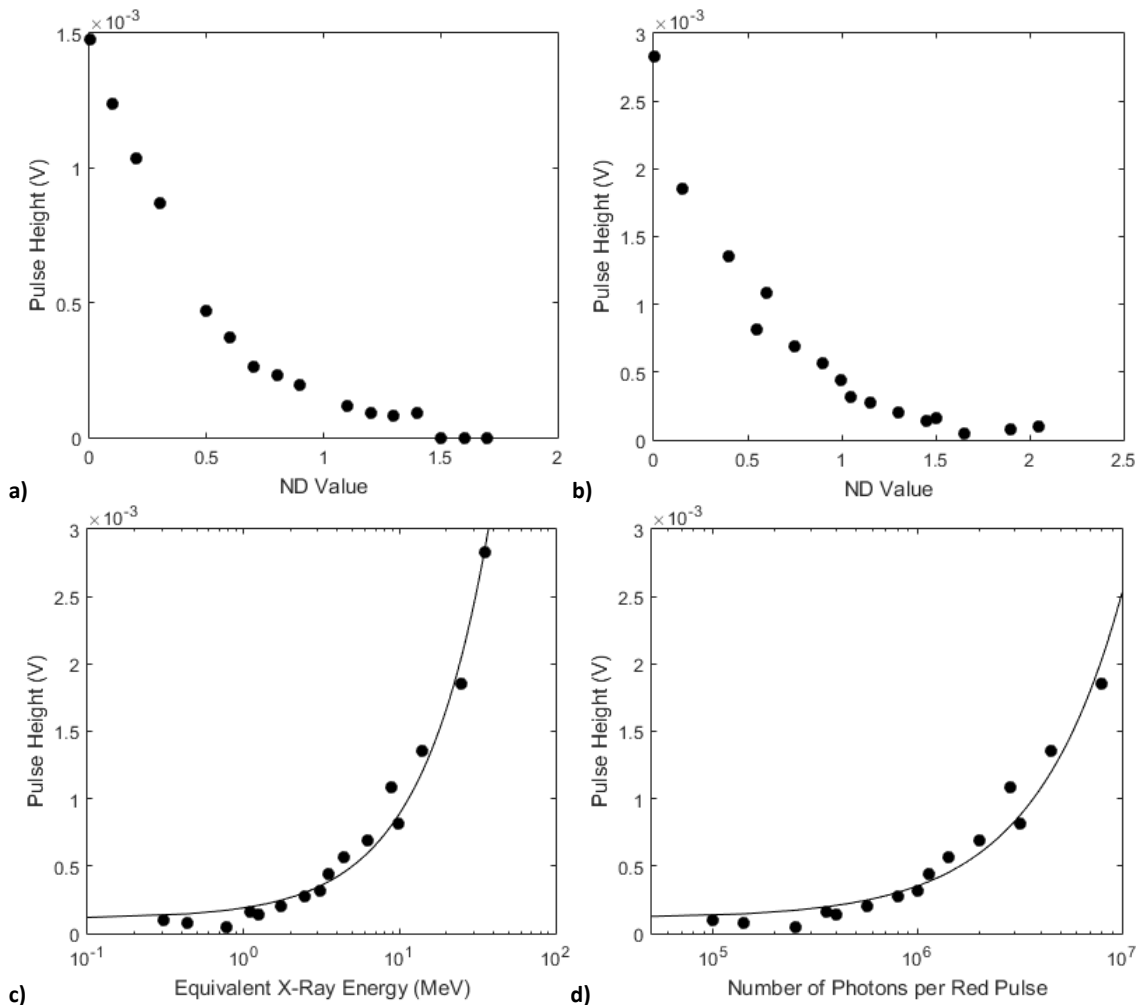


Figure 8.11 showing a) how the observed pulse height decreases with increasing ND attenuation of the blue pulsed laser with an 800ps pulse width. The noticeable dies off at about ND1.5. B) shows that the pulse height from the red pulsed laser decreases with ND attenuation. The observable peak dies off at about ND2.05. C) shows the relationship between the pulsed height and the estimated total energy deposited on the detector from a single laser pulse, equivalent to the energy deposited from a single X-ray photon. This suggests that the energy sensitivity is $\sim 300\text{keV}$. D) shows the pulse height in terms of the total number of photons incident on the absorber per pulse from the red pulsed laser.

For the blue laser, the noticeable signal disappears at approximately $ND = 1.5$, figure 8.11a, equivalent to an energy of 1MeV. The response arising from the red pulsed laser had a greater pulse height, and the signal disappeared at approximately $ND=2.05$, figure 8.11b. Using the calibrated SiPM response and the known ND attenuation, the energy sensitivity equivalent to the total energy of all photons incident on the detector per pulse was estimated as $\sim 300\text{keV}$, figure 8.11c. The absorption depth for these energies is not directly equivalent, however, due to the differing absorption depths for the red and blue laser wavelength compared to these x-ray energies.

Several options were available to improve the sensitivity, including iteration of the device geometry. The first attempt to improve the sensitivity was to use a low noise charge sensitive preamplifier, which is discussed in section 8.3.

8.2.2.6 Characterisation of Pulse Saturation

The photoresponse of the detector was investigated to explain the pulse saturation mechanism(s) as a function of the gate voltage. The detector was illuminated by a red pulsed laser photon source with a 50ps pulse width; attenuating filters of ND0, ND0.5 and ND1 were then used to attenuate the signal to provide 1×10^7 , 3.16×10^6 and 1×10^6 PE per pulse incident on the detector, respectively.

The output voltage from a transimpedance amplifier is related to the current input into the amplifier. In this transimpedance amplifier arrangement, the measured voltage output from the amplifier is indicative of the current through the graphene channel. The channel current is related to the gate voltage V_G , shown for example in figure 8.4. The channel current is represented by the baseline of the pulse, which in figure 8.12a is shown to be related to the gate voltage V_G but independent of the ND attenuation. The level of pulse saturation is dependent on the attenuation, figures 8.12b, as shown previously in figure 8.11a. The voltage at which the pulse saturates is independent of attenuation, which is shown in figure 8.12c by normalising $V_{oscilloscope}$ for each ND value. This behaviour also seen for blue pulsed lasers, figure 8.12d.

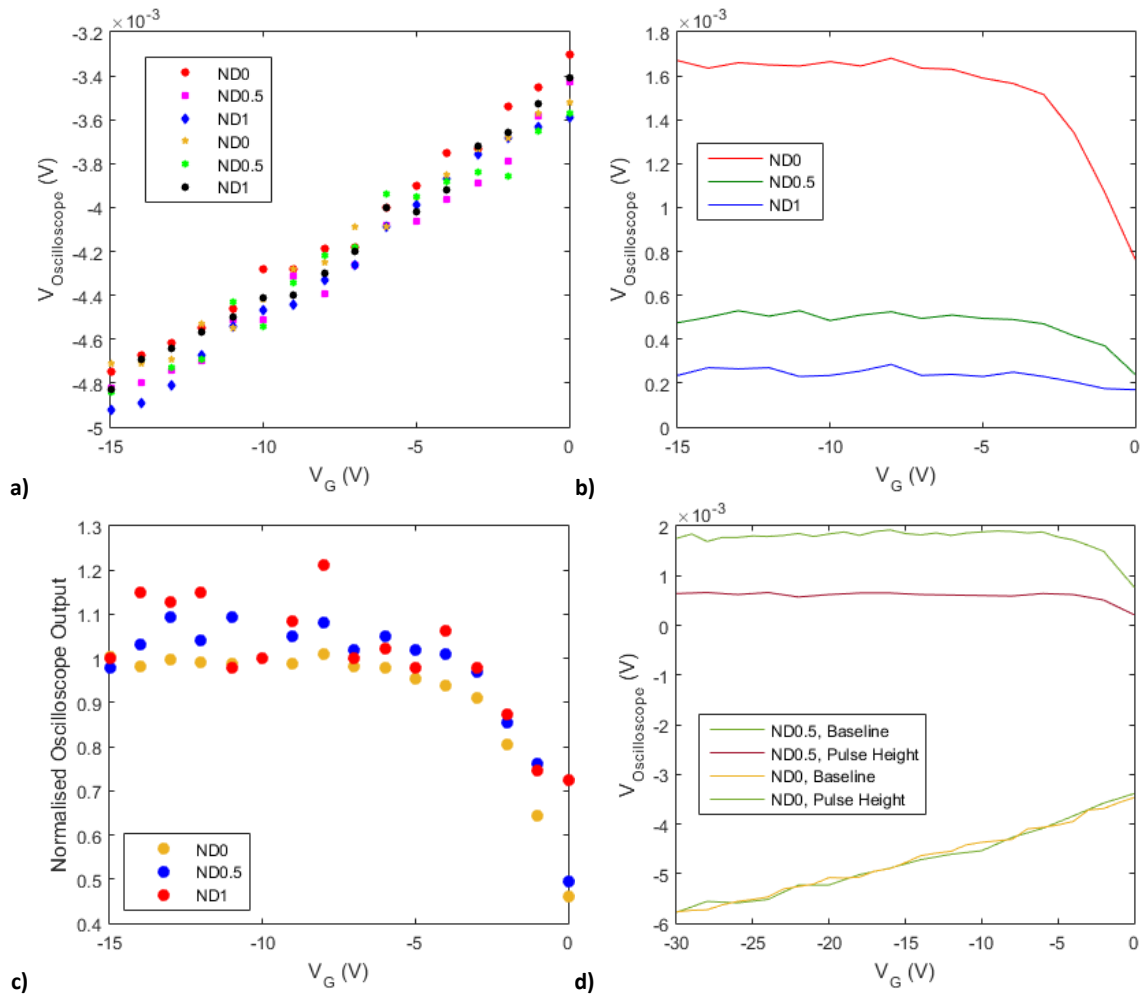


Figure 8.12, showing a) the baseline voltage versus gate voltage with the red laser for a range of ND values, showing no change with pulse amplitude, b) oscilloscope voltage against gate voltage at different attenuations, showing the difference in the signal amplitude with different attenuators (red laser, ~ 50 ps pulse width), c) the normalised oscilloscope voltage against gate voltage at different attenuations, showing no change with different attenuators (red laser, ~ 50 ps pulse width), and d) the oscilloscope voltage against gate voltage at different ND values, showing no change with different attenuators (blue laser, 800ps pulse width).

8.2.2.7 Extinguishing the Signal: Co-Located Pulsed and cw Illumination

Photons from a cw laser source co-located with the pulsed source on the GFET are absorbed in the silicon. The intensity of a cw source generates many electron-hole pairs, so it was postulated that this would affect the previously observed photoresponse. It was postulated that co-located cw and pulsed laser illumination would a) allow environmental p-doping due to the hole trapping in the oxide interface layer to be overcome, and b) result in the change of the amplitude of the pulse.

8.2.2.7.1 Continuous Red Laser

The device was illuminated with a Coherent SNF 635nm cw red laser [258] co-located with a red pulsed laser with a ~ 50 ps pulse width. The cw laser was attenuated with absorbing ND and diffusing filters for a gate voltage of -5V, figure 8.13a, to reduce the intensity of the CW laser. The signal amplitude was postulated to decrease due to saturation of the depletion region in the silicon absorber, which results from the generation of many electron-hole pairs and is related to the intensity of the cw source.

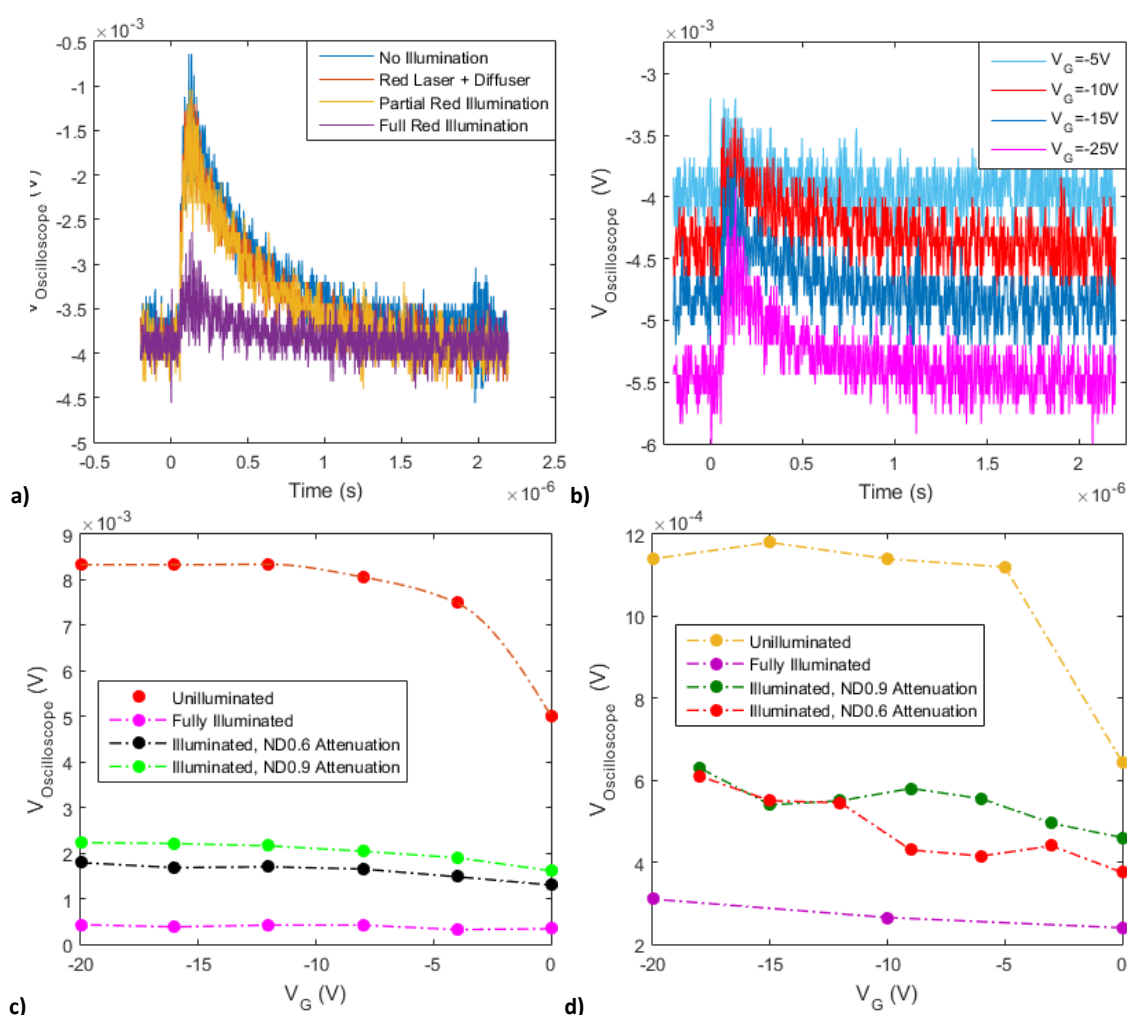


Figure 8.13, showing a) continuous illumination with different sources – no illumination, full laser illumination, partial red laser illumination and red laser illumination through a high grit ND diffuser [259]. B) shows the photoresponse for $V_g = -5$ V, -10 V, -15 V and -25 V which suggests that the signal can be retrieved, albeit smaller, by making V_g more negative. The amplitude of the signal for different V_g and illumination using c) the red pulsed laser (pulse width=800ps) and d) the blue pulsed laser (pulse width=800ps) shows how the signal still saturates at similar V_g , but the signal magnitude decreases with increasing illuminating intensity.

The signal amplitude recovered and gets larger for increasingly negative gate voltage, figure 8.13b, as the increased gate voltage overcame the initial saturation by opening

the depletion region again. As discussed in the previous section, the baseline is related to the current through the graphene channel and, in figure 8.13b, the baseline decreases for increasingly negative gate voltage, V_G , indicating an increased current away from the Dirac point.

The difference in the photoresponse for red and blue pulsed lasers, using an 800ps (maximum) pulse width, for the red continuous laser of varying source intensity is shown in figures 8.13c-d respectively. This shows that the red signal is larger than the blue, as was previously observed, with a peak height inversely proportional to the intensity of the source.

The flux of the red cw laser source incident on the GFET causes an exponential decrease in the pulse amplitude for increasing flux, figure 8.14, and the rate of change of the pulse amplitude with flux can be varied by varying the gate voltage to reopen the depletion region. This is attributed to two effects: firstly, with increasing flux the depletion region is increasingly diminished due to the creation of e-h pairs. These electron-hole pairs are then separated due to the electric field, and are constantly replenished due to the continuous laser source. With a very high flux there is a small depletion region, and therefore the absorption of the pulsed laser in the depletion region is increasingly unlikely, and will induce a dipole limited by the size of the depletion region.

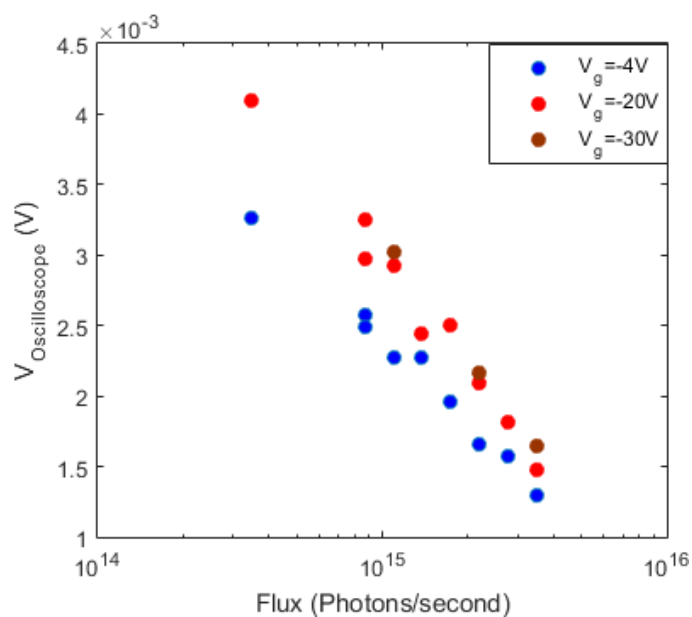


Figure 8.14 showing the oscilloscope voltage as a function of continuous laser flux. With a greater flux, the pulse height decreases. At more negative gate voltages, the pulse height is greater.

8.2.2.7.2 Continuous Blue Laser

The red cw laser was replaced with a blue cw laser, and it was predicted that these blue photons would be absorbed closer to the dielectric interface, which generates electron-hole pairs whose electrons would be trapped by the p-type environmental states close to the surface. As a result, holes would be liberated and removed by the negative gate voltage. This would shift the Dirac point to less positive gate voltages.

This is exactly what was observed, as shown in figure 8.15 by comparing the I-V curve before and after the illumination with the blue laser. Illumination caused a change in the graphene Fermi level by liberating p-type dopants, effectively pulling the Dirac point down towards 0V, with a corresponding increase in graphene resistivity. The effect was repeatable, and observed every time the cw blue laser illuminated the device. This technique was previously discussed in ref. [164] to liberate dopants resulting from gases adsorbed onto the surface, as an alternative to thermal annealing.

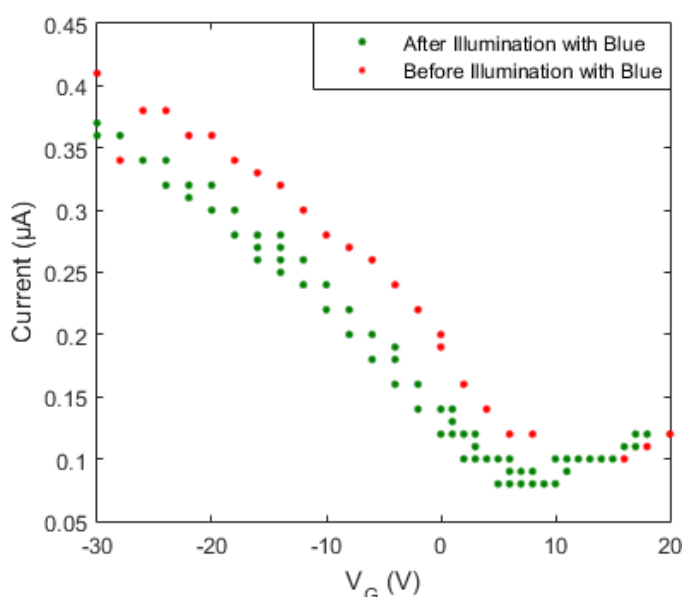


Figure 8.15. A comparison of the $I - V_G$ curve before and after blue cw laser illumination, showing the predicted shift in the current.

Once again, the signal was measured as a function of gate voltage for red and blue cw laser sources co-located with the blue pulsed laser source, with the cw laser sources attenuated by different ND filters. The results for red pulsed – blue cw, figure 8.16, and blue pulsed – blue cw, figure 8.17, again show the signal recovering for increasingly negative gate voltages and a greater pulse magnitude for a lower continuous laser source flux, with an exponential decrease in amplitude with increasing flux.

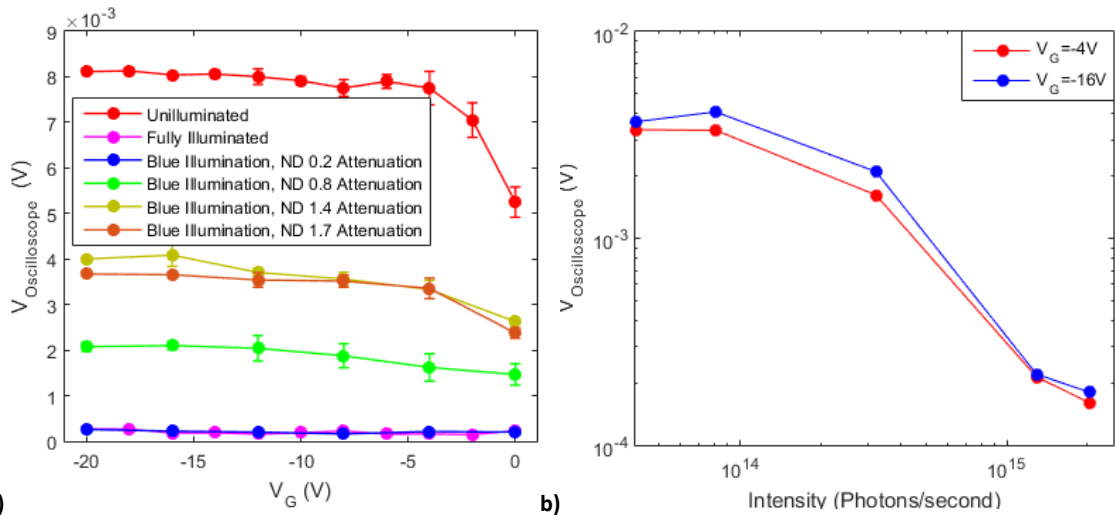


Figure 8.16. Red pulsed – Blue CW illumination showing a) the change in signal with V_G and b) the pulse amplitude as a function of flux. The pulse height from the detector is reduced with increasing cw laser flux, but it maintains the same saturation behaviour as previously observed.

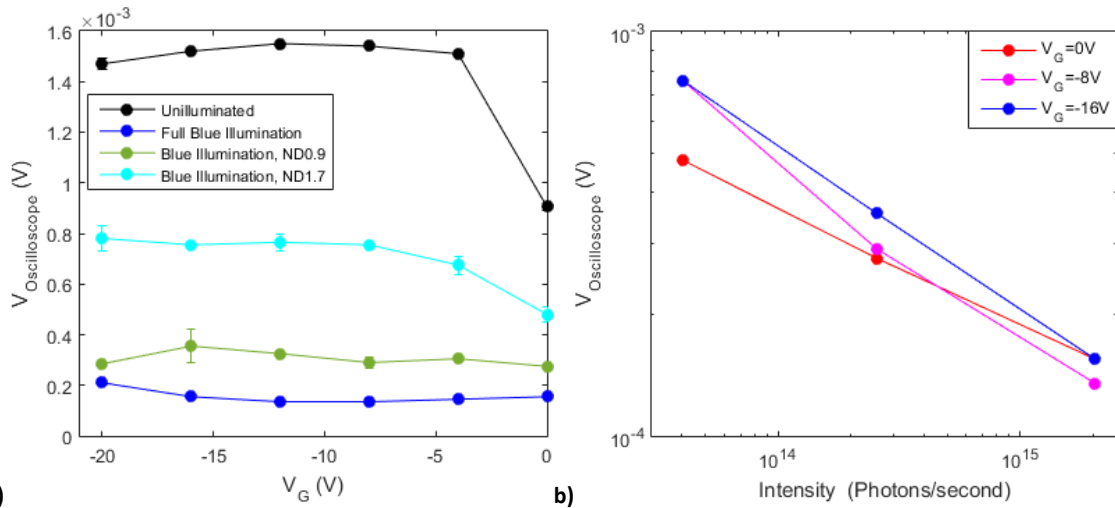


Figure 8.17. Blue pulsed – Blue CW illumination showing a) the change in signal with V_G and b) the pulse amplitude as a function of flux. The pulse height from the detector is reduced with increasing cw laser flux, but it maintains the same saturation behaviour as previously observed.

8.2.2.7.3 Improving the Signal Decay Time

As discussed in the literature, the X-ray GFETs fabricated and demonstrated by the Jovanovic group have a very long decay time, resulting in a very poor temporal bandwidth. This arises because of either the inability to clear charge carriers in a quick enough time and/or the bolometric cooling time linked to $\tau = C/G$, where C is the heat capacity and G is the thermal conductance [116]. The modulation of the signal by the Jovanovic group occurs when a large energy is deposited in the substrate, which could result in the generation of a large number of charge carriers that take a long time to recombine, and/or a lot of heating of the sample that takes a long to cool.

The results in this section suggest that a photosignal generated by charge carrier excitation and recombination can be quickly saturated and extinguished by illuminating with a red or blue cw laser. The laser pulse rate was approximately 80kHz, so it could be expected that the signal was saturated on a timescale of order 10s of μ s.

Using the blue cw laser also resulted in “annealing” of the device by liberating p-type dopants from environmental doping at the Si/SiO₂ interface, which are then swept out of the wafer by the gate voltage. V_{Dirac} was measurably reduced during illumination, figure 8.15, which allowed some effects of environmental doping to be overcome.

This technique was previously discussed in ref. [164] as an alternative to thermal annealing. This is likely to be a short-term effect that reduces V_{Dirac} while the device is being illuminated, but is reversed once the laser illumination ceases and dopants in the environment can adsorb onto the surface without hindrance. While this technique may be practical to implement manually on a single graphene channel, this technique is likely to be difficult to implement over many pixels on a larger detector because, for example, of the need to stop the cw illumination before the next unknown photon arrival. However, the effect of environmental doping can be mitigated by other means, such as channel encapsulation by alumina ALD.

8.2.2.8 Further Discussion of the Results

In previous sections the effects of varying the gate voltage and input pulse energy via attenuation and/or pulse width and photon energy has been observed. In this section, these observations are discussed further and related to physical effects.

In section 8.2.2.4, the saturation in the pulse height at increasingly negative gate voltages, for example in figures 8.9a-b, was considered in terms of electron-hole pair excitation/recombination and bolometric-like and photothermoelectric-like effects. Due to the gate voltage sensitivity and the decay time of the signal, the most likely mechanism for the signal was attributed to the opening of the depletion region and the drift of the charge carriers within this region. The drift of the charge carriers is limited by the recombination time, and the main contribution to this is Shockley-Read-Hall recombination. Other contributions to the recombination time come from

radiative recombination and Auger recombination, although these – in this case with a moderately doped silicon substrate – play little role. Assuming a purely Shockley-Read-Hall recombination, the recombination is time given by [260]

$$\tau = \frac{\tau_p [n + n_i \exp(\frac{E_t - E_i}{kT})] + \tau_n [p + n_i \exp(\frac{E_i - E_t}{kT})]}{pn - n_i^2}, \quad \text{Equation 8.4}$$

where $\tau_p = (\sigma_p N_t v_{th})^{-1}$, $\tau_n = (\sigma_n N_t v_{th})^{-1}$, $v_{th} \sim 2 \times 10^5 \text{ms}^{-1}$ is the thermal velocity for the electrons and holes [261], N_t is the trap density, $\sigma_p \sim 10^{-11} \text{cm}^{-2}$ and $\sigma_n \sim 10^{-15} \text{cm}^{-2}$ are the capture cross-sections [262], $E_t - E_i$ is the energy difference between the trap and the intrinsic Fermi level, n_i is the intrinsic electron concentration and n and p are the total charge carrier density for electrons and holes including the intrinsic, doping and excess charge carriers. A silicon wafer with $\rho \sim 1 \Omega \text{cm}$, corresponding to doping of $\sim 1.3 \times 10^{16} \text{cm}^{-3}$, has a recombination time of $\sim 2.5 \text{ns}$ and a diffusion length, given by $L_D = \sqrt{D\tau}$, where $D = 0.36 \text{cm}^2 \text{s}^{-1}$ is the diffusivity constant [261], equal to 250nm. A silicon wafer with $\rho \sim 100 \Omega \text{cm}$, corresponding to doping of $1.3 \times 10^{14} \text{cm}^{-3}$, has a recombination time of $\sim 250 \text{ns}$ and a diffusion length of $\sim 2.5 \mu \text{m}$. A silicon wafer with a higher resistivity has a longer scattering time and diffusion length, and the saturation point of the photoresponse theoretically moves to a more negative gate voltage.

Red and blue photons have dramatically different absorption depths in a silicon wafer, with absorption coefficients of $2 \times 10^{-6} \text{cm}$ at 405nm, and $5 \times 10^{-2} \text{cm}$ at 650nm. When the photon is incident on the silicon it excites an electron-hole pair which separates under the influence of the field within the postulated depletion region, with each carrier localised to a region roughly defined by the scattering length [263]. This generates a dipole moment due to an instantaneous asymmetry in electron and hole distributions, with other physics like the Stark effect also apparent [264]. With deeper absorption (i.e. for red photons and for X-Ray photons) there is a greater opportunity to open a significant dipole due to the drift of both the electrons and holes in opposite directions of order microns from the original point of excitation. At blue wavelengths, the shorter absorption depth is less than the diffusion length, so the dipole can only be opened by drift of the holes (electrons) towards the gate electrode for negative (positive) gate voltages. This effect may contribute to the smaller signal observed with the blue laser.

Additionally, the disordered Si/SiO₂ interface, with its higher trap density, may cause trapping and faster recombination of excited electron-hole pairs at the interface between the dielectric and the absorber, and can introduce positive oxide charges and the creation of fast surface states [252]. These trapping states, approximately 0.1µm deep, are independent of the doping of the silicon [265]. Significant hole trapping occurs at the interface [252] with this build up occurring for both penetrating and non-penetrating radiation [253]. The build-up of oxide charges on the interface is related to V_G , with $V_G < 0V$ having a smaller effect than $V_G > 0V$. Photon-generated electrons tend to recombine with positive traps while the holes are swept out of the oxide by the field. Thus, for blue pulsed laser photons, which are more likely to be absorbed in this layer, it is more likely that the charge carriers quickly recombine in the interface.

8.2.3 Improving the Sensitivity I: Charge Sensitive Amplifier

The electronics connected to the GFET were rearranged to reduce the noise and improve the energy sensitivity. The GFET was connected to Canberra 2001 charge sensitive preamplifiers [266] via capacitors that enabled them to mimic voltage sensitive preamplifiers. This was the most readily available and cost-effective solution to improving the bandwidth compared to a standard voltage sensitive preamplifier.

The Canberra 2001 charge sensitive preamplifiers were placed in different locations adjacent to the graphene – on the back gate, on the drain, on the source, and a combination of these, figure 8.18. In the case of coupling through the back gate, the gate voltage was applied through a HV port in the charge sensitive preamplifier over an internal 3GΩ resistor, while another BNC connector was used to couple to an oscilloscope to observe the change in charge through the gate.

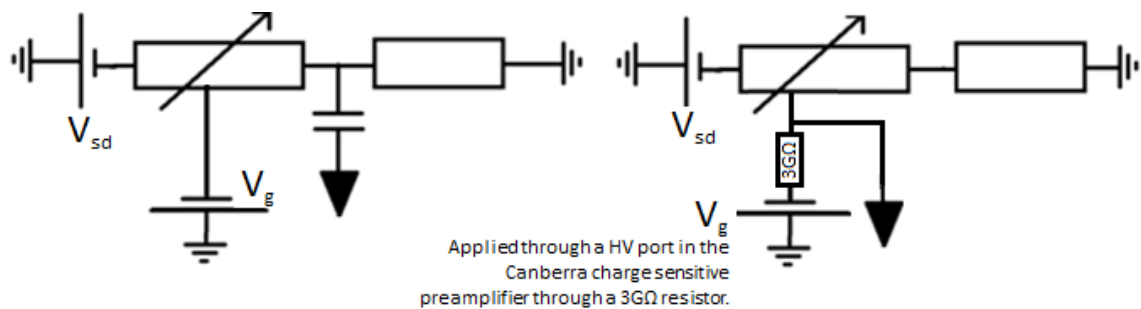


Figure 8.18, showing the position of the charge sensitive preamplifier after the graphene (left) and connected to the gate (right).

In the case where the charge sensitive preamplifier was located between the graphene and a load resistor, when the detector was illuminated there was a change in channel resistance resulting from the change in field applied to the graphene channel. This resulted in a change in the voltage dropped over the graphene relative to a load resistor placed in series with the graphene, and led to a voltage pulse that could be measured between the graphene and the load resistor. When this voltage pulse was applied through a capacitor, this produced a charge pulse that could be measured by the Canberra charge sensitive preamplifiers, which generated a voltage pulse, V_{pulse} .

In this section, the behaviour previously seen with the transimpedance amplifier were reproduced, with different arrangements studied to identify components of the signal and boost the energy sensitivity of the detector. The size of the capacitor and load resistors in each arrangement were iterated and the behaviour of the peak studied to improve the signal to noise ratio of the peak and ensure a measurable RC time. The optimal response was achieved for a large signal as possible, the lowest possible noise, and a fast RC time $\sim 100\text{ns}$.

8.2.3.1 Confirming the Initial Results

The photoresponse from the detector was measured by a charge sensitive preamplifier located between the graphene and the load resistor. The signal pulse height showed the same behaviour compared to those using the current sensitive preamplifier, with a pulse height that saturates for increasingly negatively gate voltages, figure 8.19a. As discussed previously, this saturation is attributed to charge carriers recombining within the SRH recombination time and not diffusing through the full extent of the depletion region, as previously discussed in sections 8.2.2.4 and 8.2.2.8.

The signal was attenuated to estimate the sensitivity of the detector, which suggested a sensitivity down to ND2.3 attenuation, figure 8.19. Using equation 2.3 this is equivalent to an energy of $E_{deposited} \sim 175\text{keV}$.

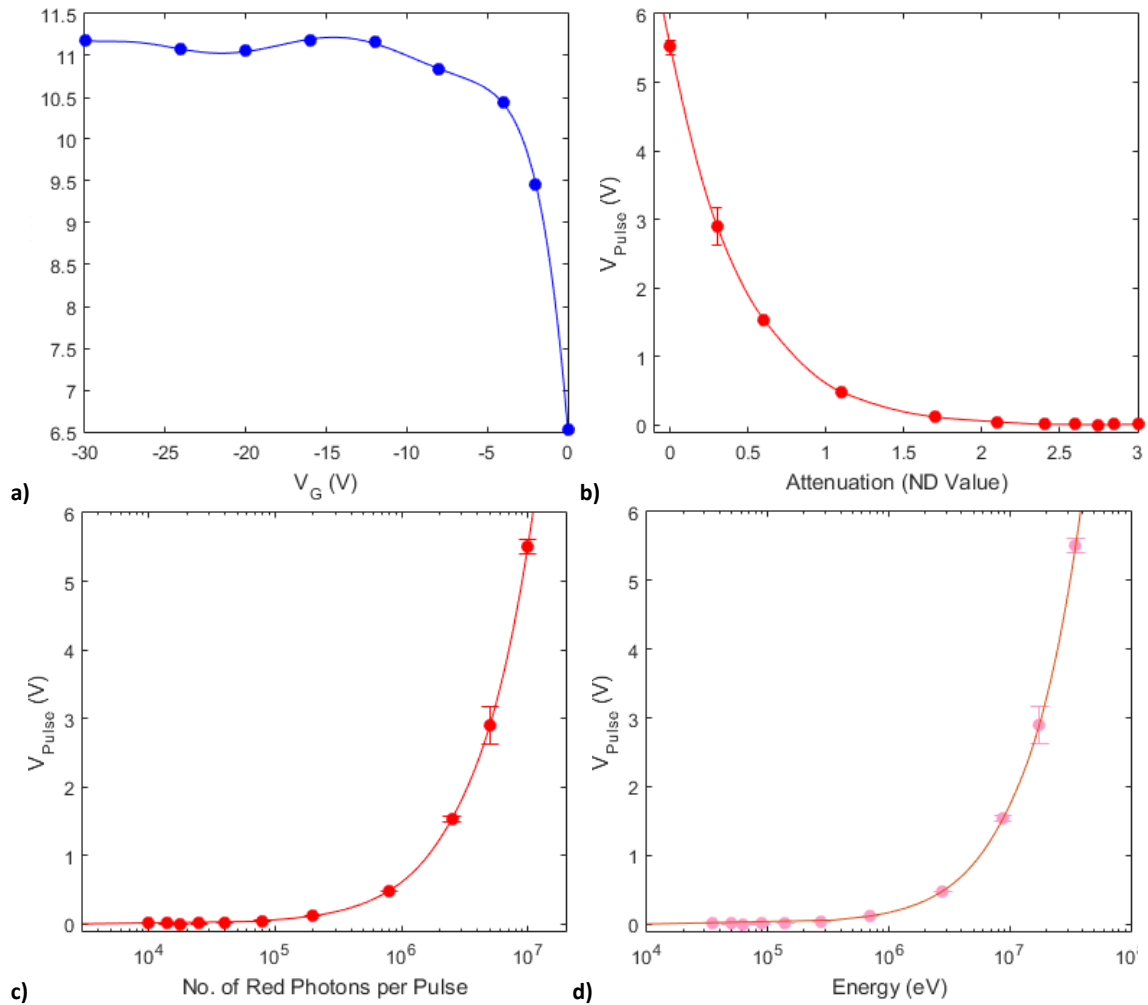


Figure 8.19 showing a) the dependence on the gate voltage in the charge sensitive preamplifier arrangement, with saturation in the pulse amplitude attributed to limits on carrier transport in the silicon due to SRH recombination. B) shows an exponential-like decay in the pulse height with increasing attenuation. C) shows an increase in the pulse height with increasing numbers of incident laser photons, while d) shows the energy deposited in the absorber, suggesting energy sensitivity to $\sim 175\text{keV}$.

8.2.3.2 Identifying the Graphene Contribution

To maximise the size of the signal a large load resistor was placed in series with the graphene, and a large V_{bias} applied across the graphene whilst maintaining the channel current less than $1\mu\text{A}$ to protect the integrity of the GFET. This was connected to a capacitor, of order 1nF , to give a large signal.

When V_{bias} was applied across the graphene and the device was illuminated by the laser, a change in V_{pulse} was observed that suggested there were two contributions to the signal, as shown in figure 8.20. To identify the signal pulse arising from the graphene, the pulses with and without V_{bias} were averaged over 10000 triggers, with

each V_{pulse} at each individual time stamp subtracted from each other with the same trigger values on the oscilloscope resulting in the small positive pulse in figure 8.20.

Therefore, it is unlikely that noise in the signal nor an offset in the V_{pulse} time stamp caused the appearance of the pulse attributed to the graphene. It is possible that other factors, such as changes in temperature, could have led to the appearance of the smaller pulse, although both datasets were taken immediately after each other so any change in temperature is likely to have been minimal. The same signal behaviour was observed again in further experiments, shown for example in figure 8.30c.

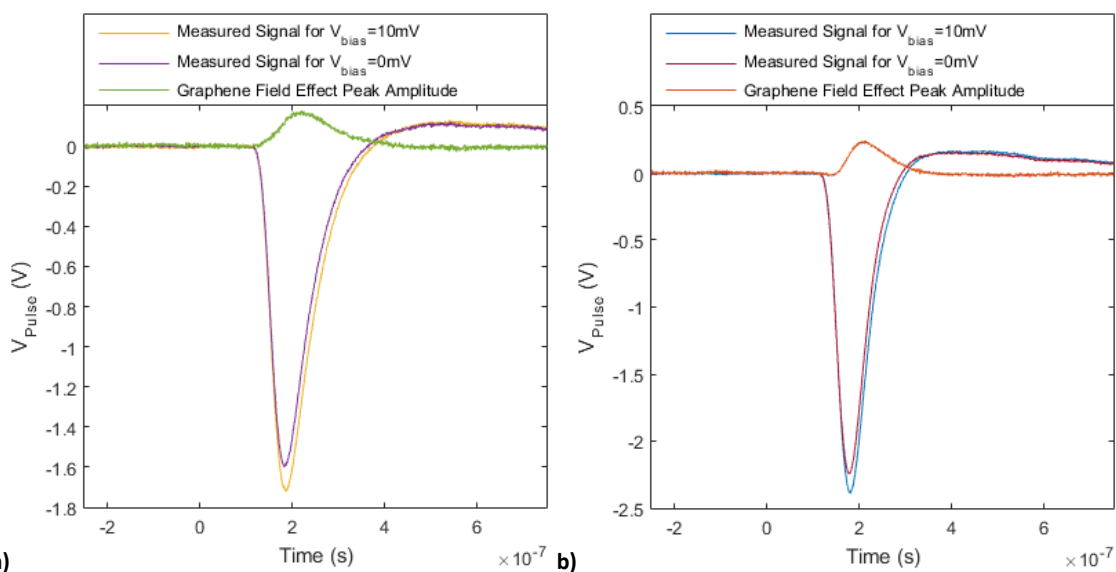


Figure 8.20, showing the difference in the pulse between $V_{bias}=10mV$ and $0mV$ to show a small pulse contribution attributed to the change in graphene resistance for a gate voltage of a) $0V$ and b) $-30V$. This contribution, by applying $V_{bias}>0V$, has a rise time and fall time of order $100ns$.

8.2.3.3 What is the Mechanism?

The presence of the larger invariant component of the signal, when $V_{bias} = 0mV$, suggests a signal mechanism that is independent of the DC path through the graphene, potentially through AC coupling.

One possible mechanism is capacitive coupling between the silicon wafer and the contacts across the $300nm$ SiO_2 dielectric. The charge carriers, generated in the depletion region, accumulate at the dielectric interface and generate an AC signal that is read out from the contact. This is illustrated in figure 8.21a, for $V_{bias} = 0mV$, and in figure 8.21b. The dielectric capacitance, C_D , that leads to the signal was measured by applying a $10mV$ amplitude square wave, V_S , across the dielectric. The resulting charge

pulse, Q_D , was measured via a Canberra 2001 charge sensitive preamplifier, and compared to the output charge pulse, Q_{test} , of a calibrated test capacitor, $C_{test} = 0.5\text{pF}$, with the same $V_S = 10\text{mV}$ voltage pulse. By saying that $\frac{Q_D}{C_D} = V_S = \frac{Q_{test}}{C_{test}}$, the dielectric capacitance was calculated as $C_D \sim 10\text{pF}$.

As discussed in section 8.2.2.4, for example, other potential mechanisms include bolometric and photothermoelectric-like effects. The bolometric effect seems unlikely given $V_{bias} = 0\text{mV}$, and that the observed pulse times are significantly slower than a signal with a bolometric decay constant $\tau = C/G$. A photothermoelectric-like effect would generate a photosignal by causing electronic heating in the graphene, before decaying. This is potentially unlikely, however, because only 2.3% of photons would be absorbed in the graphene layer, and the observed signal decay time is much quicker than is expected by the photothermoelectric effect.

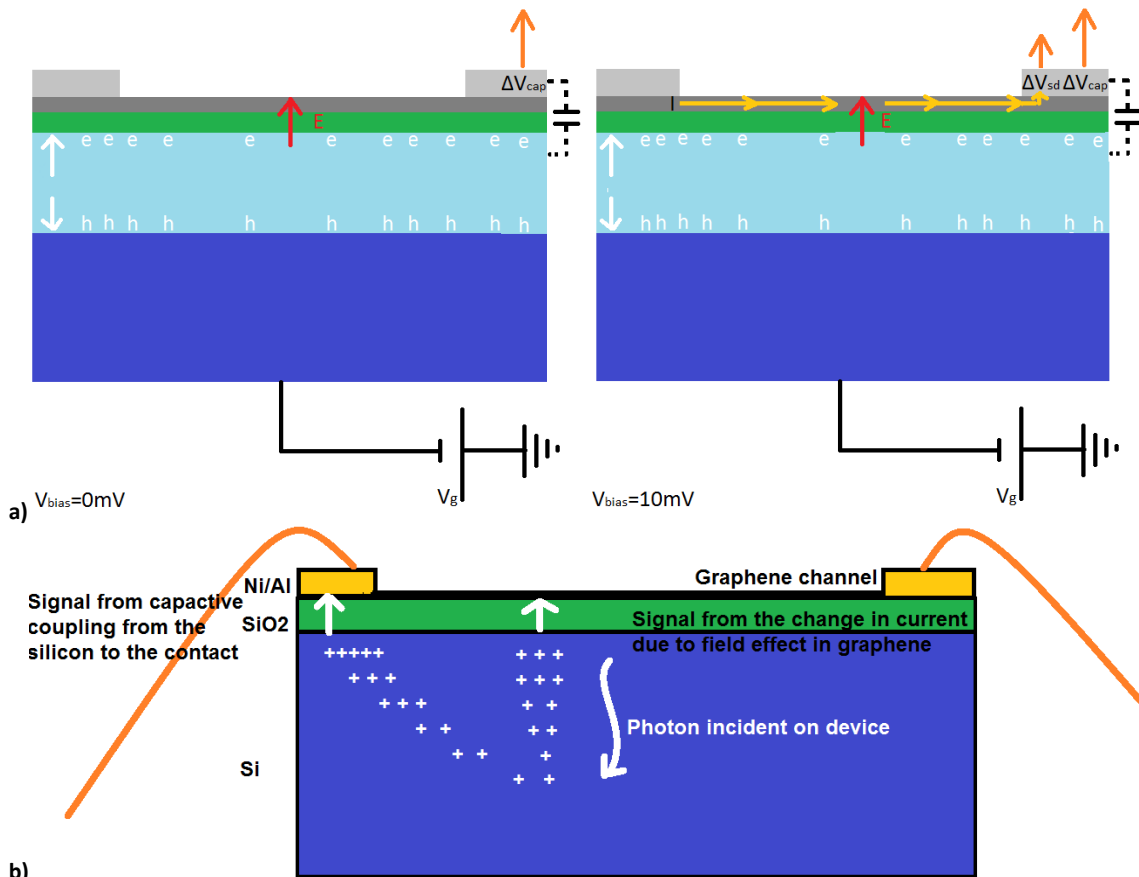


Figure 8.21, showing the origin of the two components of the photosignal. A) compares the arrangement for $V_{bias}=0\text{mV}$ and $V_{bias}=10\text{mV}$, indicating why a signal is seen even when $V_{bias} = 0\text{mV}$. The red arrow indicates the field across the dielectric layer, and the yellow arrow indicates the DC current through the graphene. B) shows the mechanism for the absorption of the photon in the silicon wafer, and illustrates how the silicon wafer and the contacts are capacitively coupled, while the DC current through the graphene is varied by changing the field when $V_{bias}=10\text{mV}$.

The second component of the signal was observed when $V_{bias} > 0\text{mV}$, which is much smaller in comparison to the peak attributed to capacitive coupling. When charge carriers are generated in the depletion after illumination, it is possible that they are funnelled and accumulate at the dielectric interface and result in a field across the dielectric. This would change the conductivity of the graphene channel when $V_{bias} > 0\text{mV}$ is applied between source and drain, as illustrated in figure 8.21b, and could potentially lead to an additional component of the photosignal. This component of the signal can be isolated by calculating the difference between the signal for $V_{bias} = 10\text{mV}$ and $V_{bias} = 0\text{mV}$, figure 8.20a.

8.2.3.4 Isolating the Signal Contributions

The experiment electronics were redesigned to directly identify the contributions to the signal arising from the graphene and from capacitive coupling between the silicon and the nickel-aluminium contacts that were observed when changing the voltage applied across the graphene. The GFET was placed between two load resistors, with two charge sensitive preamplifiers AC coupled to the source/drain as well, as illustrated in figure 8.22. This was to allow the signal at each side of the graphene to be analysed, which should be identical when the source voltage is removed, and from this to identify the contribution due to the graphene.

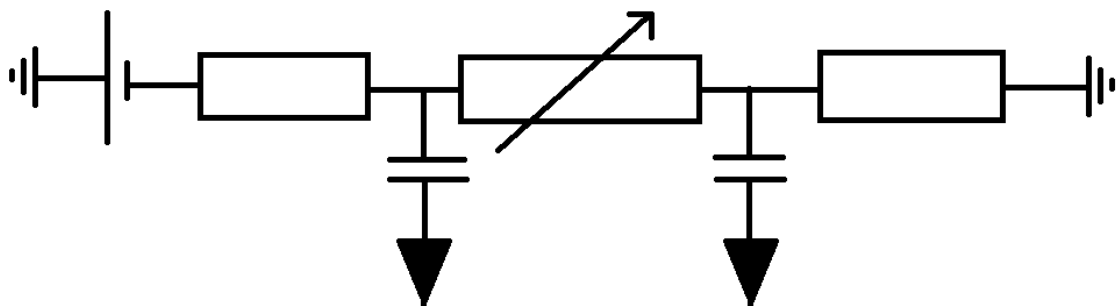


Figure 8.22, showing the wiring of the charge sensitive preamplifier arrangement with a resistor each side of the graphene to give a voltage change that gives a measurable change in charge due to the presence of the capacitor. The graphene is represented as a variable resistor, which is controlled by the gate voltage.

As a large RC time gives no signal from the graphene, the R and C values were reduced iteratively until a signal was identified that was dependent on V_{bias} . For small capacitances, a small signal but a faster RC time was observed, and for low resistances a small signal and a faster RC was observed with an increase in noise. By iterating the resistor and capacitor values, a signal was obtained where there was a noticeable

change in V_{Pulse} that was attributed to the mechanisms discussed in the previous section. In this case, 2.2pF capacitors and 1.1k Ω resistors were used.

Each side of the GFET was coupled to a charge sensitive preamplifier to identify the signal solely from the graphene. It was expected that the capacitive coupling signal would be symmetrical on either side and hence could be subtracted away. However, the signals were not of equal size, figure 8.23, as one side was approximately at least 3 times the magnitude as on the other. The two charge sensitive preamplifiers were switched over to ensure that this was not due to the sensitivity of the preamplifiers (i.e. if one detector was set to 2pCV⁻¹ and the other to 10pCV⁻¹). This indicated that regardless of which amplifier was coupled to the source or the drain, the relationship between the measured pulse heights was independent of the amplifier coupled to it, and the source side always had the greater signal.

This asymmetry was attributed to the difference in the capacitive coupling on each contact resulting from different sized contacts due to imperfect manufacturing techniques. Alternatively, this could be related to the location of the laser and how this affects where the charge carriers are generated, although this seems unlikely as the laser was focussed over an area that covered the entire channel.

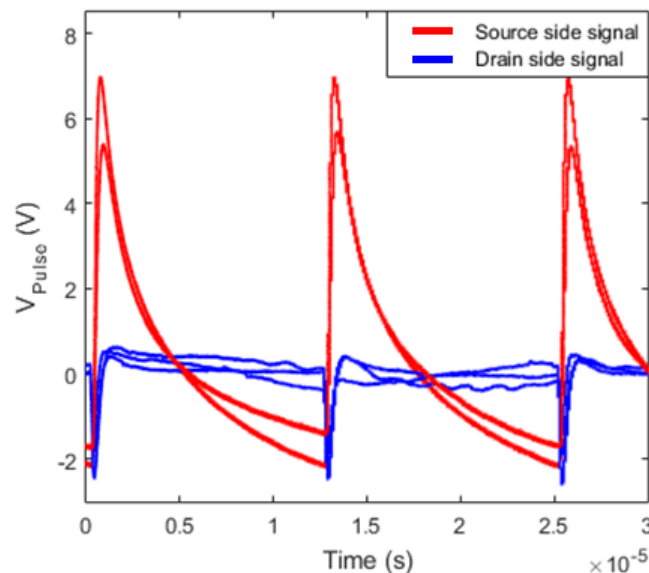


Figure 8.23. The different magnitude signal from the source side and drain side of the graphene (which remains the same when the charge sensitive preamplifiers are swapped over – i.e. the blue signal remains larger than the red signal)

As the signals were not identical it was not possible to use this route to measure the signal solely from the graphene directly. However, for a sensitive photodetector, it is

not ideal to lose a contribution to a signal (i.e. that from the silicon) but instead it is desirable to improve the contribution arising from the graphene.

8.2.3.5 Characteristics of the Signal Contributions

The contribution due to the graphene was identified by subtracting the pulse with $V_{bias} = 10\text{mV}$ applied from that with V_{bias} disconnected and the BNC connector terminated. The contribution to the signal, for $V_G = 0\text{V}$ and $V_G = -30\text{V}$, is approximately 10% of the total signal, as shown previously in figures 8.20a and 8.20b respectively.

From this, the contribution of the signal arising from the graphene was calculated as a function of V_G , figure 8.24. The pulse heights for the signals with $V_{bias} = 0\text{V}$ and $V_{bias} = 10\text{mV}$, and the pulse attributed to the contribution from the graphene, all saturate for increasingly negative gate voltages. Each signal was obtained by averaging over $N = 10000$ samples, with an error proportional to $N^{-0.5}$. Therefore, the contribution arising from the graphene is greater than the noise. The saturation occurs because the electron-hole pair, generated in the silicon by absorbing a photon, recombines within the SRH recombination time but does not take full advantage of the size of the depletion region. The resulting field applied to the graphene, and hence the measured signal, is therefore limited in magnitude.

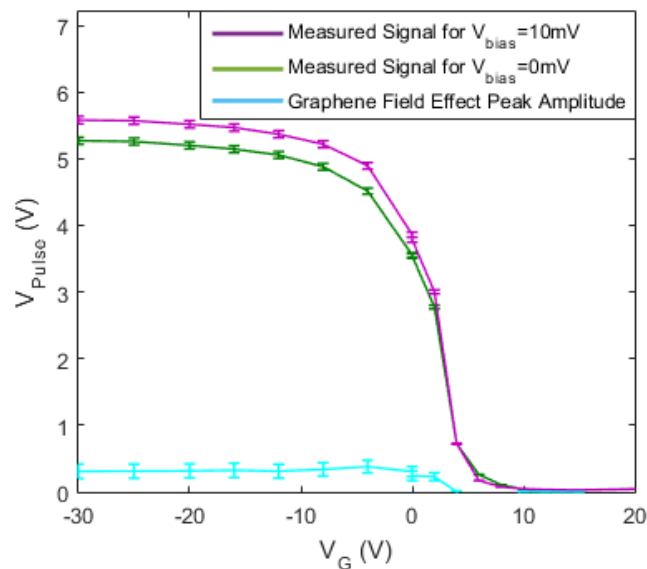


Figure 8.24, showing the change in the pulse amplitude with increasing V_G , and the proportion of the signal that arises from the change in graphene current and capacitive coupling between the silicon and the contacts. The magnitude of V_{Pulse} for the pulses with $V_{bias} = 10\text{mV}$ and $V_{bias} = 0\text{mV}$, and the signal attributed to the graphene, show saturation with increasingly negative V_G .

The calibrated pulsed laser was attenuated using a set of ND filters, and the corresponding energy deposited in the wafer was calculated using equation 8.3 to estimate the equivalent X-ray energy sensitivity of the detector. V_{Pulse} was measured for different attenuated signals, which indicated the sensitivity in terms of the equivalent X-ray photon energy as approximately 100keV, figure 8.25. The signal arising from the graphene also decreased with the pulse intensity as fewer electron-hole pairs are generated in the silicon and hence a smaller field is generated to change the conductivity of the graphene.

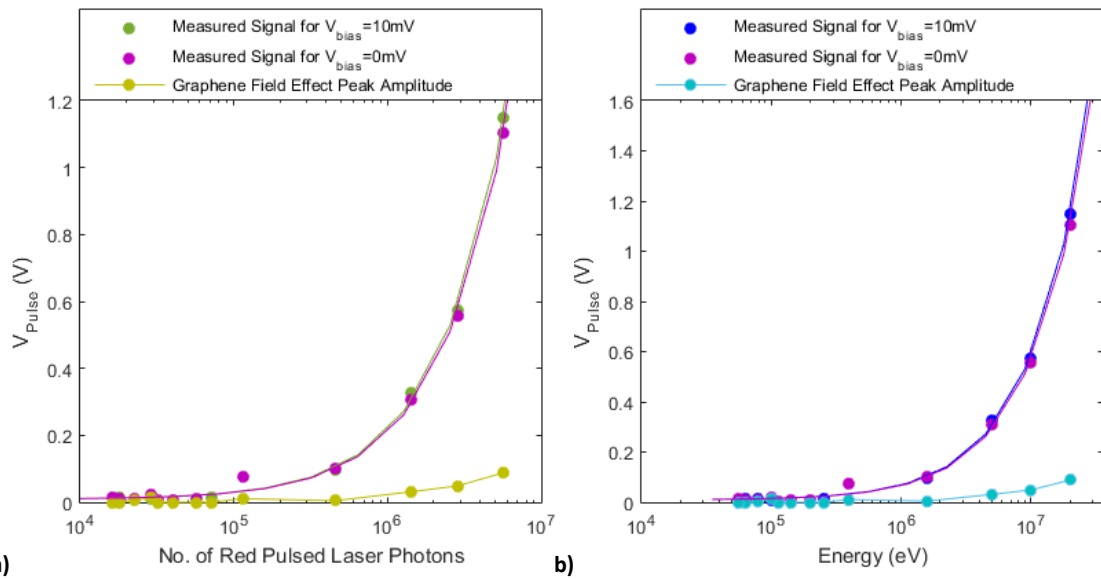


Figure 8.25, showing the magnitude of V_{Pulse} by attenuating the incident laser signal. A) shows the number of red pulsed laser photons incident on the graphene. B) shows the equivalent sensitivity of the detector for $V_{bias} = 10mV$ and $0mV$ and hence allowing the signal attributable to the graphene to be identified.

8.2.4 Improving the Sensitivity II: Lock In Amplifier

So far, the results for the GFET connected to current and charge sensitive preamplifiers and illuminated by attenuated pulsed lasers has resulted in an estimate of the energy sensitivity of the detector as $\sim 100keV$. To improve the SNR and the energy sensitivity further, a DSP7265 lock in amplifier was connected to the detector which measures the V_{RMS} of the photopeak that was previously observed. Four new devices were mounted, two on undoped silicon wafers and two that were on doped silicon wafers, which had measured current-gate voltage relationships as shown in figure 8.26a-d.

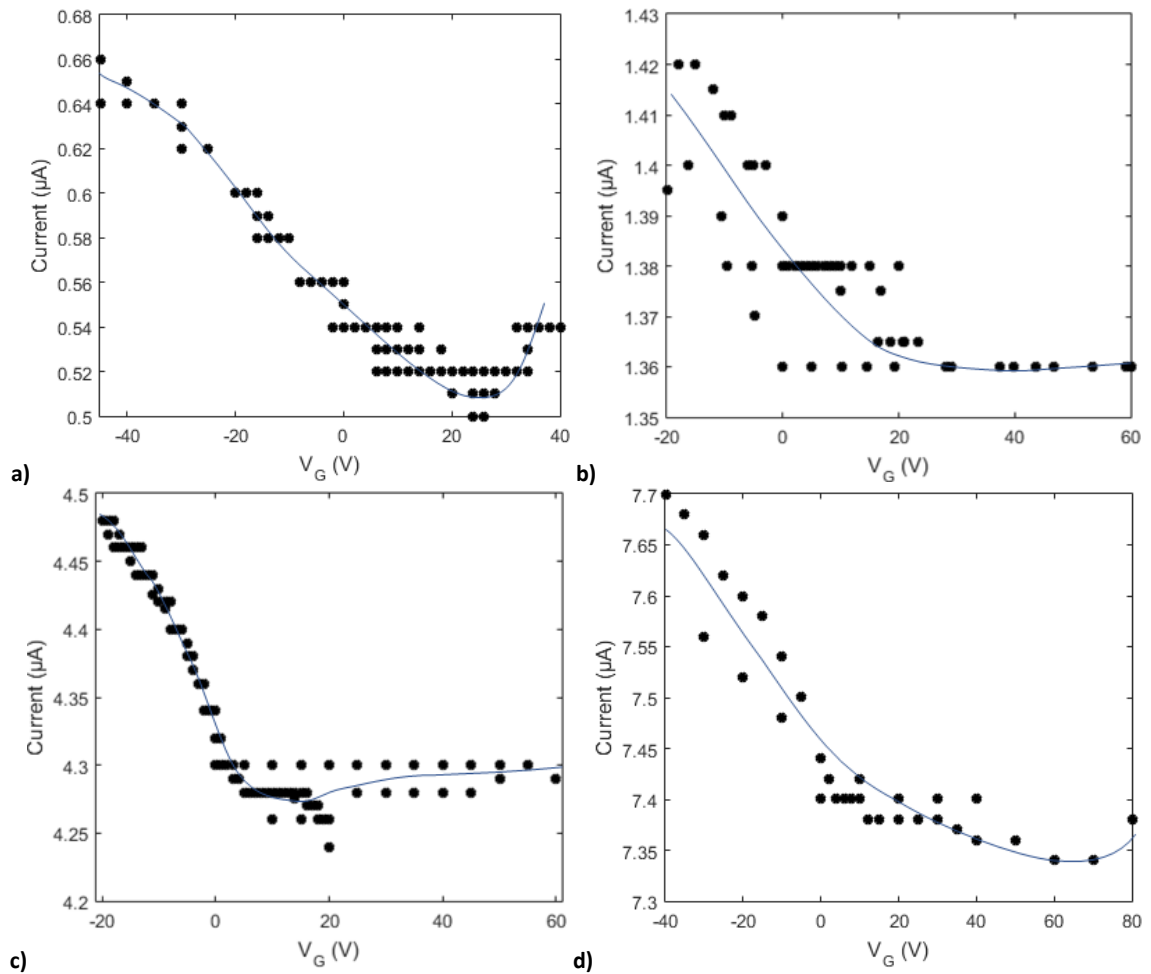


Figure 8.26 showing the channel current-gate voltage relationship for devices built on a) and b) undoped silicon samples, and c) and d) doped silicon samples. A clear Dirac point is seen in in a), which has good electron and hole mobility and $V_{Dirac} \sim 20$ V, whereas the other samples have good hole mobility and poor electron mobility so the Dirac point is less observable.

The previous tests were repeated to demonstrate the relationship between V_G and the V_{RMS} measured by the lock-in amplifier. For the highly doped silicon substrates, with $\rho \sim 1 \Omega\text{cm}$ equivalent to doping of 10^{16}cm^{-3} , there was no measured sensitivity when illuminated by the pulsed optical laser. On the other hand, the highly resistive silicon samples with $\rho \sim 10000 \Omega\text{cm}$, equivalent to doping of 10^{12}cm^{-3} , do show some photosensitivity, as the measured V_{RMS} increases and then saturates for increasing V_G , figures 8.27a and 8.27b, as shown in previous sections.

The difference in response between the low and high resistivity samples is likely to occur because of the recombination time. When an electron-hole pair is generated in the depletion region, the charge carriers will be spread apart by the field applied by the gate voltage. In highly p-doped samples, the electrons will recombine with the p-dopants in the sample, and therefore the signal will be lower. An undoped substrate

would reduce the recombination due to the doping in the sample, although it would also decrease the size of the depletion region. The choice of sample resistivity therefore needs to consider the size of the depletion region and the pulse height.

The results shown in figure 8.27a show a much larger V_{RMS} for readings between $V_G = 1V$ and $V_G = 16V$ than were observed in other datasets, which was attributed to misalignment of the ND filters resulting in a much larger signal. Nevertheless, the same behaviour as seen previously, i.e. increasing V_{RMS} and then saturation with increasing V_G , can be fit to the data points as shown in figure 8.27b.

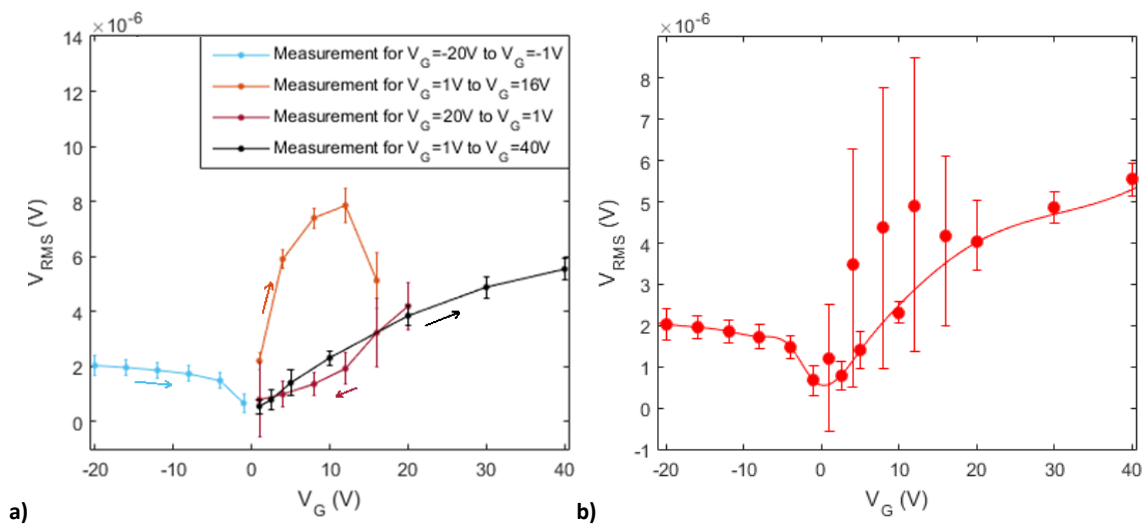


Figure 8.27, showing a) the measured V_{rms} from the lock in amplifier as a function of the gate voltage when the sample is illuminated by the red pulsed laser attenuated by ND1.7. The orange line, indicating measurements from $V_G=1V$ to $16V$, shows a greater V_{rms} than other readings at the same V_G . This is potentially due to misalignment of the laser or attenuator between these samples which would result in an increased photoresponse due to increased illumination, which was corrected for the datasets $V_G=20V \rightarrow 1V$ and $V_G=1V \rightarrow 40V$. Alternatively, this may be due to gate hysteresis affecting the electrical properties of the channel. However, in b) the fitted line to the average of all the measured V_{rms} values still shows the same saturating behaviour at greater V_G , albeit with greater error on the measurements between $V_G=1V$ and $V_G=16V$.

The potential sensitivity of the detector was tested in a similar arrangement to that used with the charge sensitive preamplifier, with the GFET connected to a charge sensitive preamplifier and then a lock in amplifier as shown in figure 8.28a. The charge sensitive preamplifier was left in the arrangement to see if any signal gain could be acquired from the preamplifier, but there was no added benefit.

The load resistor and capacitors were iterated to improve the sensitivity, figure 8.28b. The optimum V_{RMS} was found by matching the resistor on the drain side of the graphene to the resistance of the channel, and placing a larger capacitor before the

charge sensitive preamplifier. Although the larger capacitor also increased the noise of the measurements, this was overcome by using the lock in amplifier. In the end, a 22pF capacitor and a load resistor of $R_{load} = R_{graphene} = 12k\Omega$ were used, where $R_{graphene}$ is the resistance of the graphene.

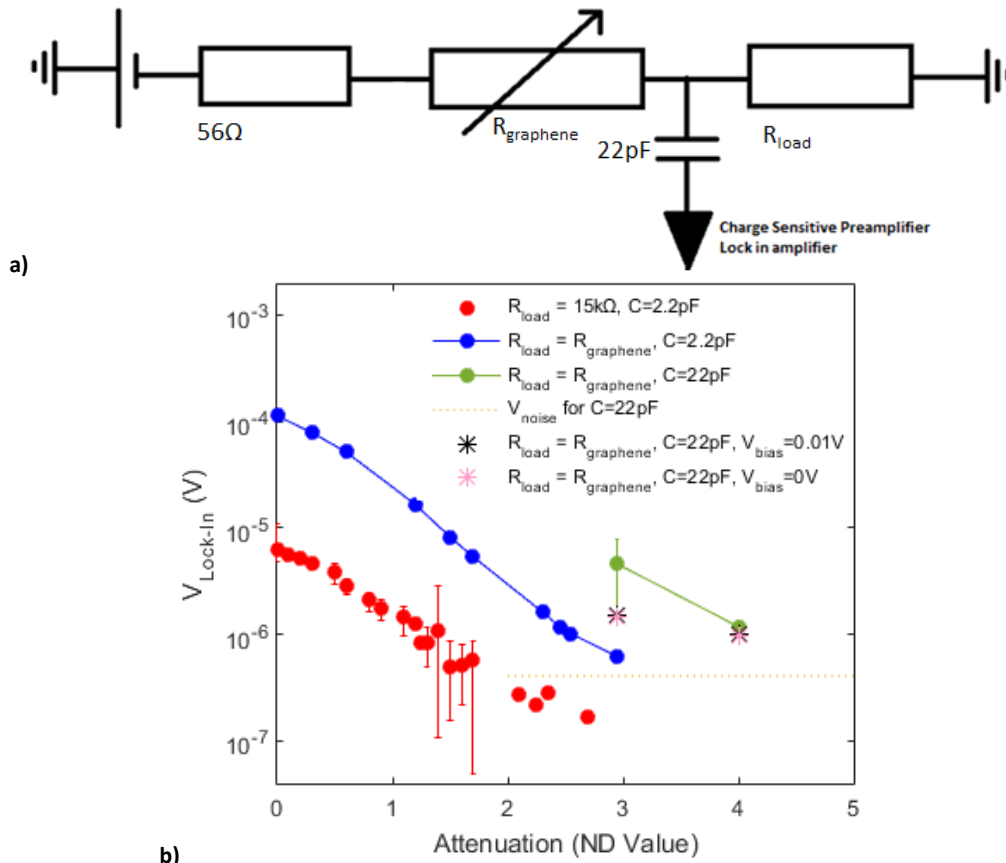


Figure 8.28, showing a) the setup used for optimised detection. B) shows the photoresponse, $V_{lock-in}$, when the device is illuminated by a red pulsed laser as a function of the ND attenuation for different R_{load} and capacitor values. Impedance matching the load resistor to the graphene resistance, $R_{load}=R_{graphene}$, increased $V_{lock-in}$ by a factor ~ 10 . When the capacitor was changed from 2.2pF to 22pF, the measured $V_{lock-in}$ again increased by a factor ~ 10 . The noise in the measurements, V_{noise} , was measured by calculating by attenuating the signal by ND7, such that the incident $PE \ll 1$ and therefore very little illumination of the detector. A photoresponse $V_{lock-in} > V_{noise}$ suggested sensitivity at this attenuation. For ND4, this is the equivalent of 10^3 photons, or $\sim 3-5keV$. The black and pink asterisks indicate the signal for $V_{bias}=10mV$ and $V_{bias}=0mV$, replicating the measurements from the previous section, with a small increase with V_{bias} applied.

In this configuration, the detector was illuminated by the red pulsed laser attenuated by ND attenuators, and the signal from the detector was measured on a lock-in amplifier, $V_{lock-in}$. The noise in the measurements, V_{noise} , was estimated by attenuating the laser by ND7 so there was very little illumination of the detector and the generated $PE \ll 1$. When the detector was illuminated with a red pulsed laser attenuated by ND4 (equivalent to $\sim 10^3 PE$ or $\sim 5keV$) with an integration time of 1s, the

measured signal $V_{lock-in} > V_{noise}$. This suggests energy sensitivity to equal to low energy X-ray photons $\sim 5\text{keV}$ using pulsed optical lasers.

The signal to noise ratio in the transimpedance amplifier and charge sensitive preamplifier arrangements prevented demonstration of sensitivity at these energies. On the other hand, as discussed in section 7.4.3, the lock-in amplifier can extract a small signal (as low as nV) from a large noise component, so the factor ~ 100 improvement in detector sensitivity using a lock-in amplifier, equivalent to $\sim 5\text{keV}$ photon energies, is realistic. The use of a lock-in amplifier with X-ray sources is discussed in section 8.3.1.

However, using a lock-in amplifier does mean sacrificing the ability to resolve single photons because the signal is integrated over $\sim 1\text{s}$. Further iteration of the detector is therefore required to improve the SNR and to overcome the requirement for a specialised lock in amplifier, as the latter limits potential applications of the detector in space and medical sciences. The lock in amplifier uses a basic mathematical frequency analysis technique, so it may be possible to develop a more compact lock in amplifier, as discussed in Appendix 5 using a LeCroy oscilloscope.

8.2.5 Improving the Sensitivity III: Voltage Preamplifier

Lock-in amplifiers are expensive, complex equipment that would be difficult to incorporate into a detector system for everyday uses. Instead of the lock-in amplifier used in the previous section, the GFET was connected to a Stanford SR850 low noise voltage preamplifier to attempt to demonstrate radiation sensitivity, figure 8.29. The voltage amplifier had a lower bandwidth, of order 100MHz c.f. $\sim 1\text{GHz}$ for the charge preamplifier, but had lower noise and built in high pass and low pass filters. The signal obtained from the graphene via the voltage preamplifier was then displayed on the LeCroy oscilloscope.

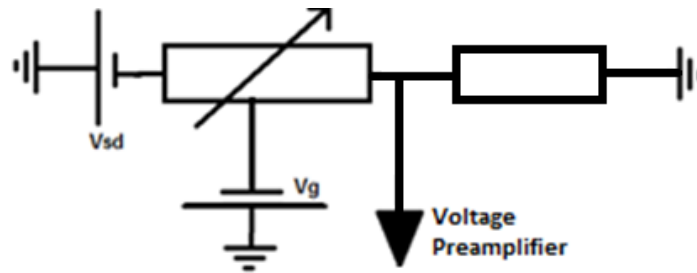
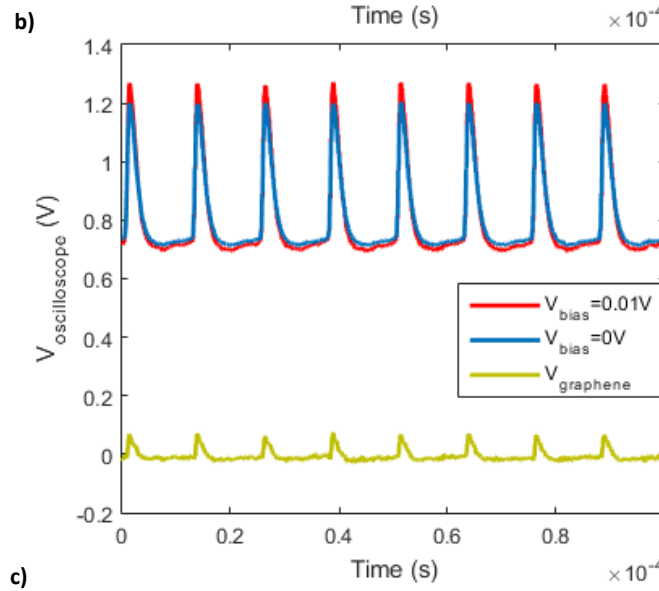
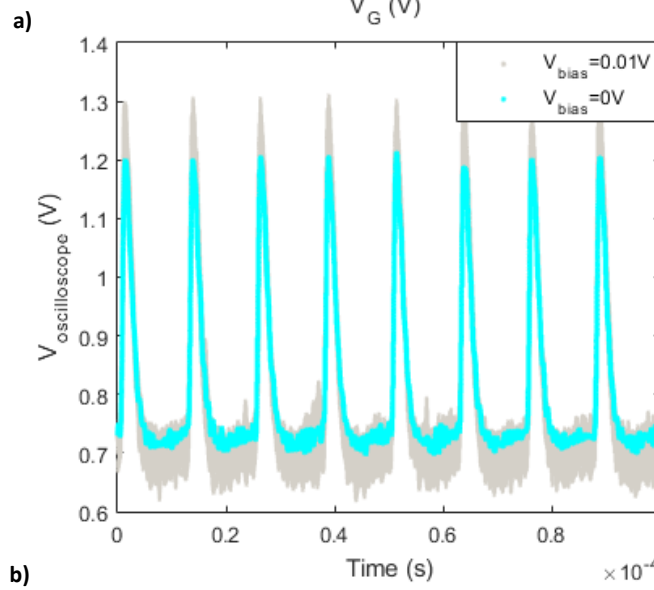
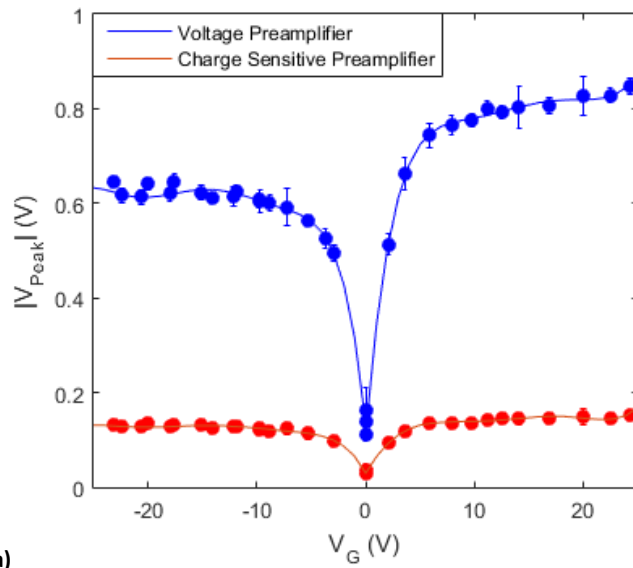


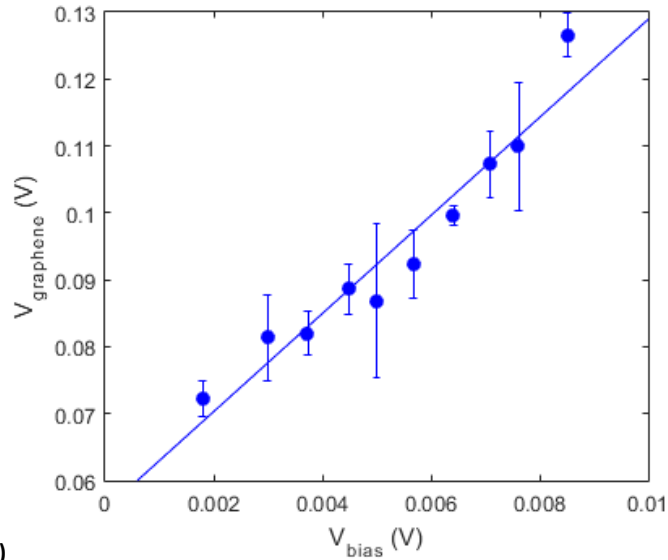
Figure 8.29 showing the detector electronics used with the voltage preamplifier.

Firstly, the previously observed behaviour of the detector was replicated. The gate voltage, V_G , was measured between $V_G = -20V$ and $V_G = 20V$ to identify the previously observed saturation in the magnitude of the photopulse. When the red pulsed laser was unattenuated, this pulse height saturated at $\pm 5-10V$, figure 8.30a. The asymmetry observed in this arrangement may have occurred because of the difference in the electron and hole mobility in silicon, which would affect the magnitude of field generated in the substrate before charge carrier recombination. A photopulse was observed for positive and negative gate voltages as the silicon wafer is highly resistive and therefore both hole and electrons relax more slowly. Whereas, for lightly p-doped silicon used in section 8.2.2, electrons recombined quicker so only produced a peak at negative gate voltages, while there was no sensitivity at all for heavily doped samples.

In this arrangement, i.e. using the voltage preamplifier, the signal was again shown to consist of a component arising from the graphene – approximately 10% - and another component arising from AC coupling between the absorber and the contact, figures 8.30b and 8.30c. The former was shown to arise from a DC source by varying V_{bias} across the graphene, with a resulting linear change in $V_{graphene}$, figure 8.30d. Therefore, a greater V_{bias} provides a greater signal because the current through the channel, and therefore the change in current following the illumination, is greater so long as the current remains within safe limits. Equally so, with an improved graphene channel mobility, there is a greater change in the channel current for a given change in the gate voltage V_G , and therefore the component of total signal would increase.



c)



d)

Figure 8.30, showing a) the previously observed gate dependent photopeak magnitude, which saturates at ± 5 -10V. In b), the signal changes when $V_{\text{bias}}=10\text{mV}$ is applied across the graphene and the device is illuminated by an unattenuated laser pulse for $V_G=20\text{V}$ and in c) the difference of the average of those readings suggests that the signal is formed of a component from AC coupling between the absorber contacts, and a component from the graphene V_{graphene} . In D), the magnitude of V_{graphene} increases for increasing V_{bias} across the graphene.

8.2.6 Detector Parameters

The illumination of the detector from pulsed optical photons allows for an estimate of the several detector parameters, such as the on-off ratio $\frac{I_{\text{on}}}{I_{\text{off}}}$, the count rate, energy resolution and SNR.

The on-off ratio is defined as the ratio of the current between the on state and the off state [267], $\frac{I_{\text{on}}}{I_{\text{off}}}$. Using a lock in amplifier and illuminating by a pulsed red laser attenuated by ND4, equivalent to approximately 1000 photons, lead to the results shown in figure 8.28b. From this, with an off state given by the noise and the on state resulting from illumination by the laser, $\frac{I_{\text{on}}}{I_{\text{off}}} \sim 2$.

The pulse heights obtained from the voltage preamplifier, figure 8.30b, were histogrammed to allow the signal to noise ratio (SNR), energy resolution $\frac{E}{\Delta E}$ and noise equivalent power (NEP) to be estimated for this setup. The histogrammed pulse heights in figure 8.31a show a mean pulse height of $V_{\text{pulse}} \sim 0.5\text{V}$, and a full width half maximum (FWHM) of $FWHM_{\text{pulse}} \sim 0.02\text{V}$ such that $\sigma_{\text{pulse}} \sim 0.085\text{V}$. The SNR can be approximated as the signal V_{pulse} divided by the standard deviation,

$SNR \sim \frac{V_{pulse}}{\sigma_{pulse}} \sim 58.5$. This is less than the $SNR \sim 200$ that was obtained for an antenna-coupled graphene photodetector, when it was illuminated by photons with $\lambda=532\text{nm}$ with a 1s bandwidth [268]. The $SNR \sim 3$ discussed in ref. [269] is for an illumination of 1.8-5.9nW, which is significantly less than the $\frac{\text{Laser Pulse Energy}}{\text{Pulse Time}} = \frac{100\text{pJ}}{50\text{ps}} = 2\text{W}$ deposition from the pulsed laser [270] used in this project.

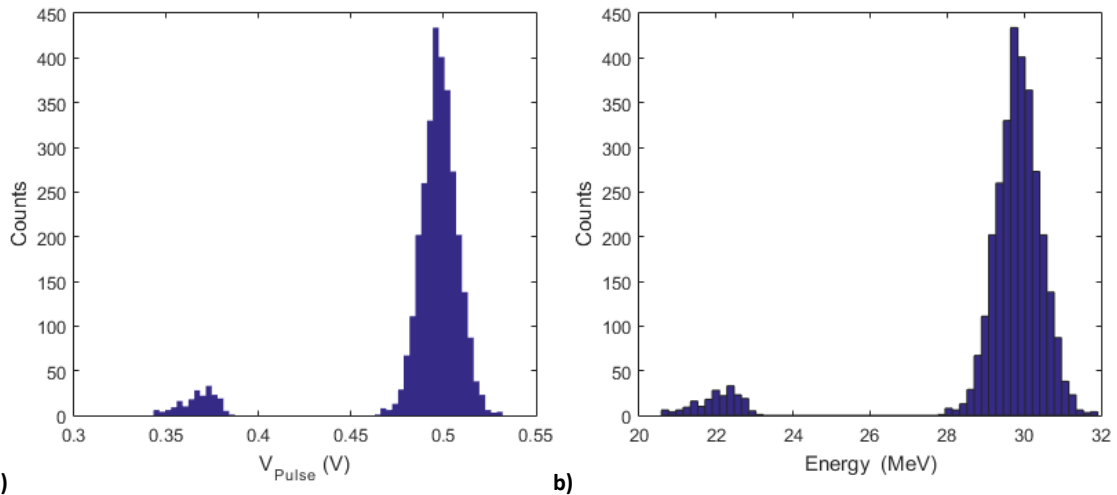


Figure 8.31, showing a histogram of the energy detected by the GFET, extrapolated from figure 8.30b. Fitting to this gives $FWHM=1130\text{keV}$. There is also a small satellite peak at $E \sim 22.5\text{MeV}$.

The corresponding energy for each V_{pulse} was found by scaling by the relationship between the incident energy deposited and the pulse height, for instance in figure 8.19d. For unattenuated illumination by the red laser, this is equivalent to 30MeV being absorbed in the silicon. This gives a $FWHM$ of 1130keV, and hence $\sigma = 480\text{keV}$. This is much greater than sigma due to assuming Poisson limited photon statistics of the laser pulse, which can be approximated by $(10^7)^{-0.5}$.

Assuming the entire laser signal $E \sim 30\text{MeV}$ is absorbed by the silicon, this suggests that the energy resolution $\frac{\Delta E}{E} = 0.016$ for this detector arrangement. This occurs for an attenuation of $\sim ND1.8$. A lock-in amplifier, or another very sensitive technique, is therefore required to have energy sensitivity sufficient for single X-ray detection. Also, for an energy deposition of 30MeV, using equation 7.10 leads to $NEP = 450\text{kW}$.

8.3 Demonstrating X-ray Sensitivity

As discussed in section 8.2.4, the X-ray detector had a suggested energy sensitivity of $\sim 5\text{keV}$ when a lock-in amplifier was used to integrate over multiple measurements.

This is an energy equivalent to a train of single X-ray photons from an Fe-55 source incident on the detector.

The absorption coefficient for the silicon absorber, figure 8.32a, can be used to characterise the theoretical transparency for different photon energies, given that transmission from the wafer goes like $\exp(-\mu x)$, where μ is the absorption coefficient in units of length^{-1} , and x is the distance into the wafer.

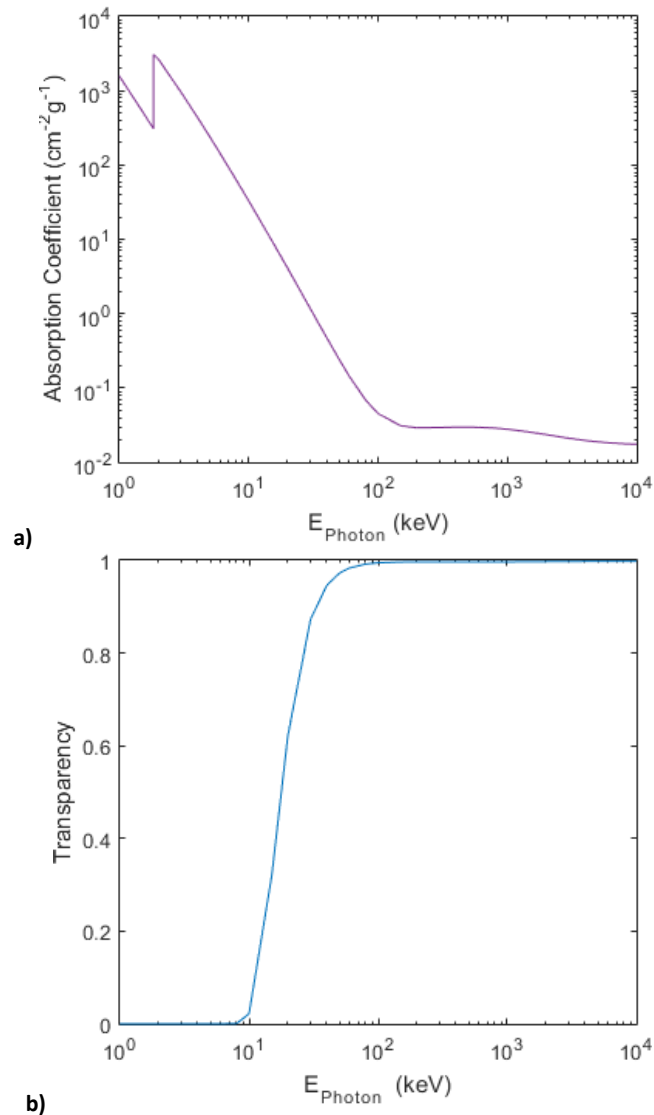


Figure 8.32 showing a) the absorption coefficient for silicon at different energies, and b) the calculated transparency of a 0.5mm thick Si wafer.

The absorber has a good stopping power for photon energies below 10keV, such as X-ray photons from Fe-55. To generate electron-hole pairs, these X-ray photons would have to be absorbed in the depletion region to be detected. As discussed in table 8-1 in section 8.2.2.4, for $N_a = N_d = 1 \times 10^{14} \text{cm}^{-3}$, where N_a and N_d are the acceptor and

donor concentrations respectively, the theoretical depletion width is $23.2\mu\text{m}$ at $V_G = -20V$, and $3.6\mu\text{m}$ at $V_G = 0V$.

The absorber appears transparent to higher energy photons, figure 8.32b. For Cd-109 it appears $\sim 80\%$ transparent, and for Am-241 and Co-60 source it appears $>99\%$ transparent. The poor stopping power of the device for high energy photons indicates the need to modify the device geometry for thicker and/or denser absorber materials with improved stopping power.

8.3.1 X-ray Sensitivity: Using a Lock-In Amplifier

The energy sensitivity equivalent to $\sim 5\text{keV}$ was obtained with a lock in amplifier by integrating over many samples, so this was the first route to demonstrating X-ray sensitivity. It was not possible to chop or modulate the signal from the radioactive sources, such as by using a chopping wheel, as it was either too slow or induced radiative noise in any measurements. Therefore, the source location and attenuation was varied to observe modulation of $V_{lock-in}$ and hence identify X-ray sensitivity to a 3GBq Fe-55 source.

Even though there was no reference with which to trigger the lock in amplifier, as the activity of the sample was so high one experiment attempted to detect incident X-rays by choosing an arbitrary reference set to the frequency used to trigger the laser, which is akin to this being an internal reference frequency, and an integration time of 1s .

The measurement of $V_{lock-in}$ did not show any noticeable modulation of the signal, with values of $V_{lock-in}$ that were within the noise measurements taken when the source was not illuminating the sample, figure 8.33. There was an r^{-2} -like feature, figure 8.33, that could be attributed to moving the source further from the detector. However, the measured signal is well within the noise, so this suggests that the detector did not have sensitivity to the X-ray source. Further research is required to reduce the noise, improve the signal to noise ratio and fully understand the signal properties to determine whether the r^{-2} feature was real, and whether this is due to the irradiation by the X-ray source.

In previous sections, the detector indicated energy sensitivity equivalent to the energy of a single Fe-55 X-ray photon when it was probed by a pulsed laser photon while using a lock-in amplifier integrating over 1s. These photons are absorbed close to the surface of the detector, and generate multiple charge carriers from each of the incident photons in the laser pulse that generate a field and cause a change in the channel conductivity.

If the X-ray energy detector sensitivity estimate is incorrect, then this would explain why no modulation due the X-ray source is observed. On the other hand, if the X-ray detector sensitivity using this technique is accurate, then a response to irradiation by trains of Fe-55 X-ray photons should be expected. Each X-ray photon excites a single electron-hole pair in the detector, which causes secondary charge carriers to be excited as the primary relaxes. If the secondary excitation/primary relaxation process is not efficient or effective, perhaps due to charge trapping in the substrate, then an insufficient number of charge carriers (much less than the number generated by the incident laser pulse) will be generated close to the surface, and therefore no signal will be observed.

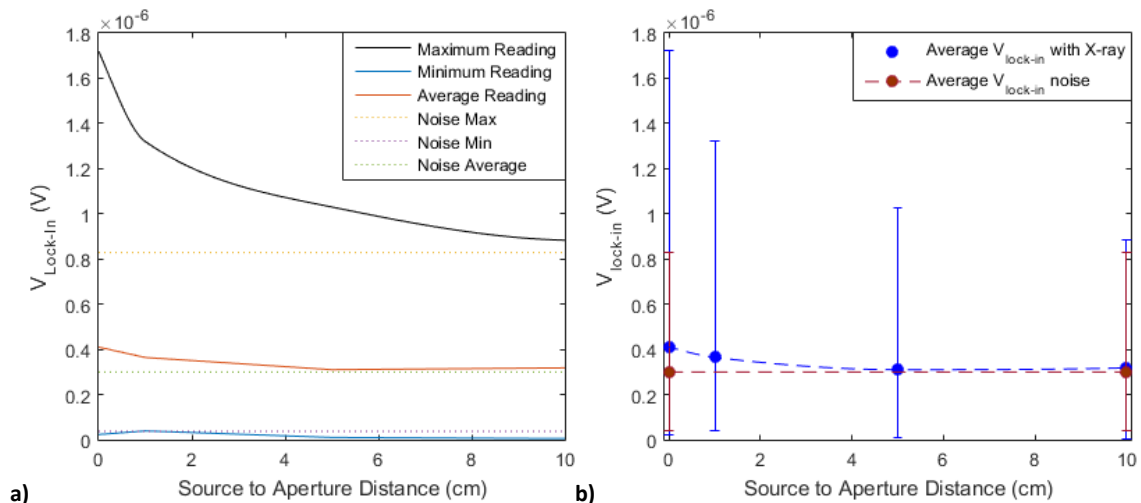


Figure 8.33 showing an r^{-2} -like decrease in the signal as the radioactive source is being moved away from the detector, although this signal is well within the noise. These results suggest that there is little to no detector sensitivity to this source. Further work is required to improve the SNR in this arrangement.

To attempt to omit the primary charge carrier relaxation process, a brief experiment considered a route to observing sensitivity via a scintillator. A gadolinium oxysulphide (GOS) scintillator was placed over the detector aperture, approximately 20mm from the detector, and then illuminated with an Fe-55 source, as well as higher energy

sources including Am-241 and Cd-109. The intention was to generate visible photons that would, potentially, present the same behaviour as a function of gate voltage as was observed in section 8.2.3. However, there was no sensitivity observed in this arrangement, as shown in figure 8.34. This is likely because the photon yield was too low, even for Am-241, and poorly collimated with a photon intensity that decreases like r^{-2} .

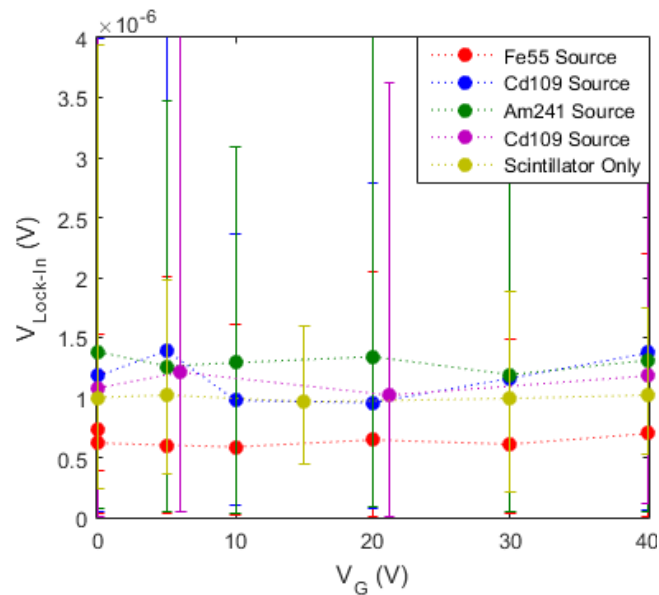


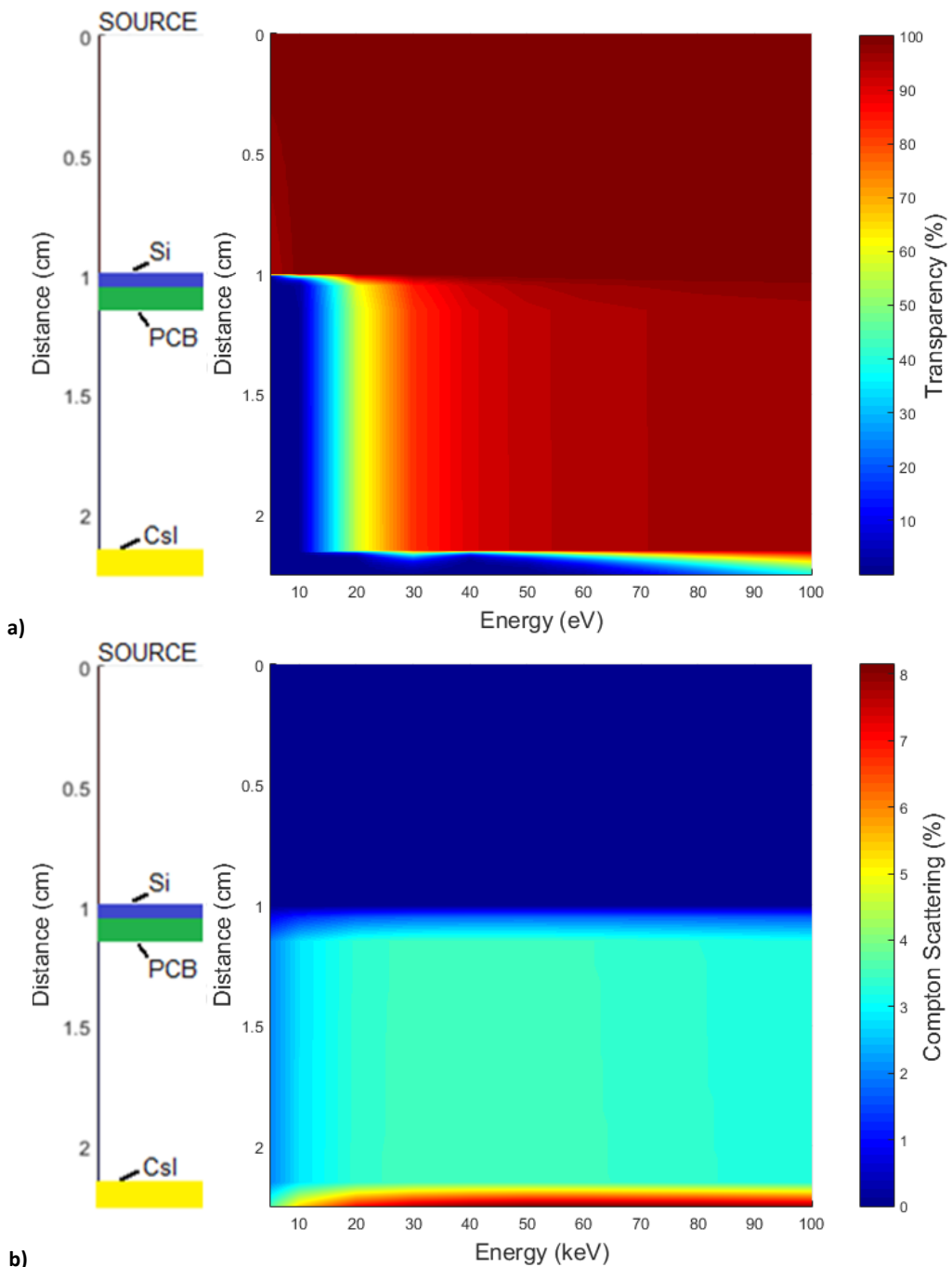
Figure 8.34 showing the response for different V_G and X-ray sources using a GOS scintillator 20mm above the graphene sample.

8.3.2 X-ray Sensitivity: Voltage Preamplifiers, Compton Scattering and SiPMs

Further tests were undertaken by replacing the lock in amplifier with a voltage preamplifier, which again showed no sensitivity to X-ray photons from Fe-55 or Cd-109. Therefore, a different approach was needed to provide a trigger synchronous with the X-ray detection by the GFET, from which the signal could be obtained.

One route to obtaining a trigger was to consider the Compton scattering of an X-ray photon in the absorber which could then be detected by a second detector. In this case, a CsI scintillator was placed on top of an Excelitas SiPM biased to $V_{bias} = V_{breakdown} + 5V = 100V$. A Cd-109 source was placed 1cm above the 0.5mm thick Si wafer and the 1mm thick PCB, followed by a second 1cm air gap and a 1mm thick CsI scintillator as illustrated in figure 8.35a.

Figure 8.35a also shows the theoretical transparency as a function of distance beneath the radioactive source and X-ray energy, which indicates that the silicon wafer is opaque at low energy X-ray photons but is transparent at higher energies. Similarly, in figure 8.35b, the percentage of Compton scattering events is shown as a function of distance and X-ray energy, which demonstrates that the percentage of Compton scattering events is greatest for the most energetic photons. This arrangement is a very inefficient route to demonstrate detection, with less than 1% of the incident photons causing Compton scattering in the silicon wafer.



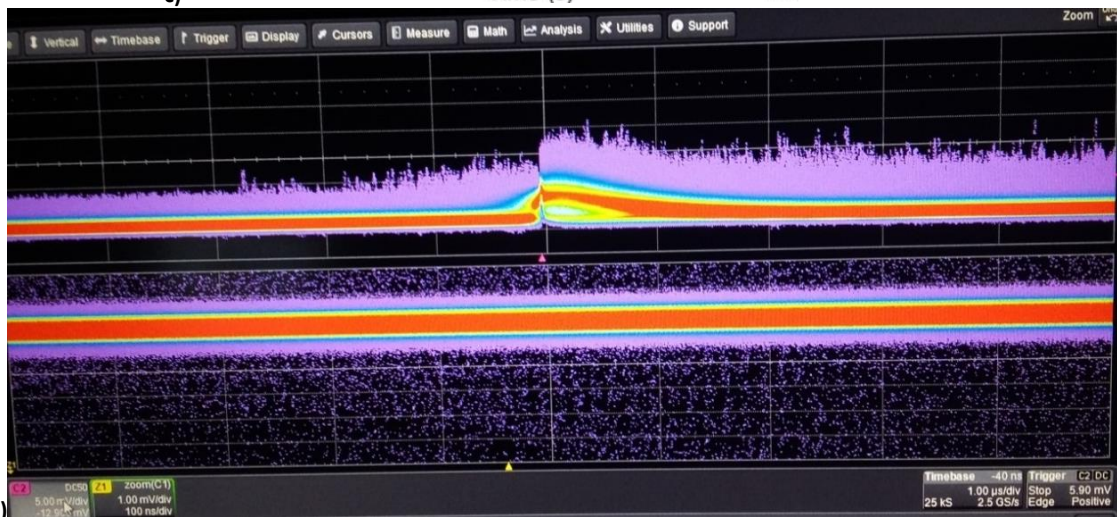
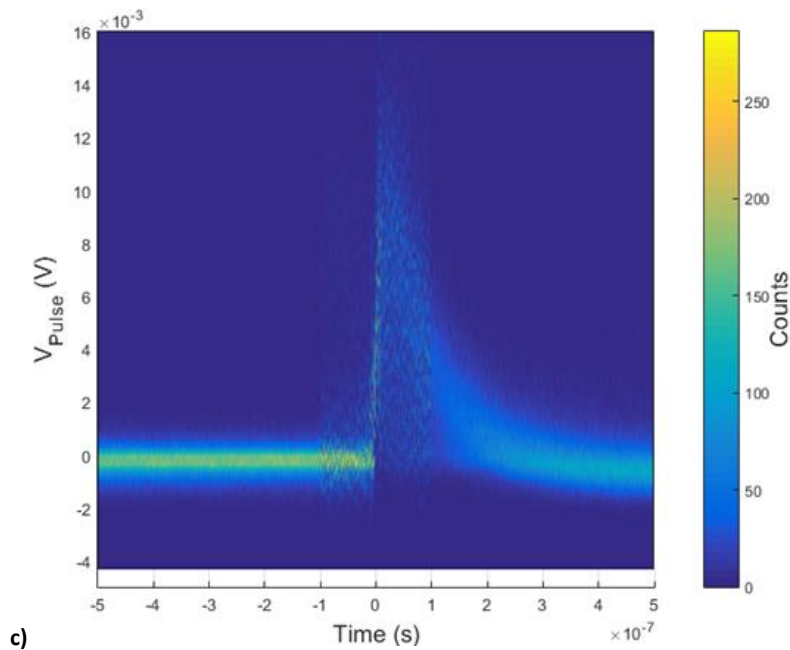


Figure 8.35, showing a) the theoretical transparency of the experimental setup as a function of distance and photon energies – the silicon is opaque at low photon energies and transparent at higher photon energies. B) shows that the theoretical proportion of Compton scattering events is greatest for the most energetic photon energies, although with only 1% of the incident photons generating Compton scattering events in the silicon wafer. C) shows the signal from the SiPM with a CsI scintillator for a Cd-109 source, with d) comparing the response from the SiPM (top) and graphene (bottom). There is no observable peak that suggests X-ray sensitivity.

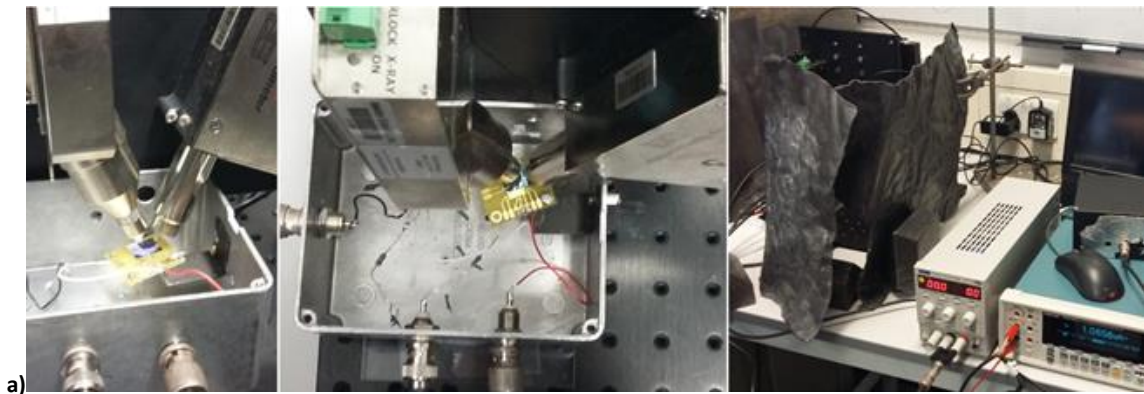
The rising edge of the signal from the SiPM, figure 8.35c, was used to trigger the oscilloscope reading from the GFET. When the detector was illuminated with an X-ray source, there was no peak synchronised with the rising edge of the SiPM signal, as shown in the persistence graphs in figure 8.35d, where the top output is that from the SiPM and the bottom is that from the graphene. A peak would have indicated X-ray detection by the GFET, so this suggests that there is no sensitivity to an X-ray source.

8.3.3 X-ray Sensitivity: Is there any at all?

When probing the detector with a red pulsed laser while using a lock-in amplifier, the detector demonstrated behaviour that suggested energy sensitivity equivalent to a single 3-5keV X-ray photon. However, when the detector was illuminated by several different energy X-ray sources, and using different experimental setups including a lock-in amplifier, a voltage preamplifier, and by using a SiPM to provide a trigger to identify Compton scattering, there was no observable sensitivity to X-ray photons. This raised two important questions: “how accurate were the energy sensitivity calculations with the red pulsed laser”, and “is there any sensitivity to X-ray energies at all?”.

To further investigate whether there was any X-ray sensitivity, the GFET was illuminated by an Amptek X-ray generator [271], as shown in figure 8.36a. The X-ray generator can be operated at different voltages and currents, with an output energy distribution that peaks at ~10kV, ~22kV and ~25kV, figure 8.36b [271]. A bias voltage $V_{bias} = 10\text{mV}$ was applied between the source and the drain of the GFET as previously, and the device was gated to $V_g = V_{Dirac} \sim 95\text{V}$, as shown in figure 8.36c. The change in the current through the graphene channel resulting from the irradiation by the X-ray generator, $\Delta I(P_{XR}) = \frac{V_{bias}}{\Delta R(P_{XR})}$, was then used to indicate sensitivity of the detector, where $\Delta R(P_{XR})$ is the change in the channel resistance because of the total X-ray power incident on the detector, and $\Delta I(P_{XR})$ is the corresponding change in current.

Illuminating the detector with the X-ray generator did demonstrate some modulation of the current. This was shown to be dependent on the bias voltage, V_{XR} , applied to the generator, the beam current, I_F , and the gate voltage, V_G , applied to the detector.



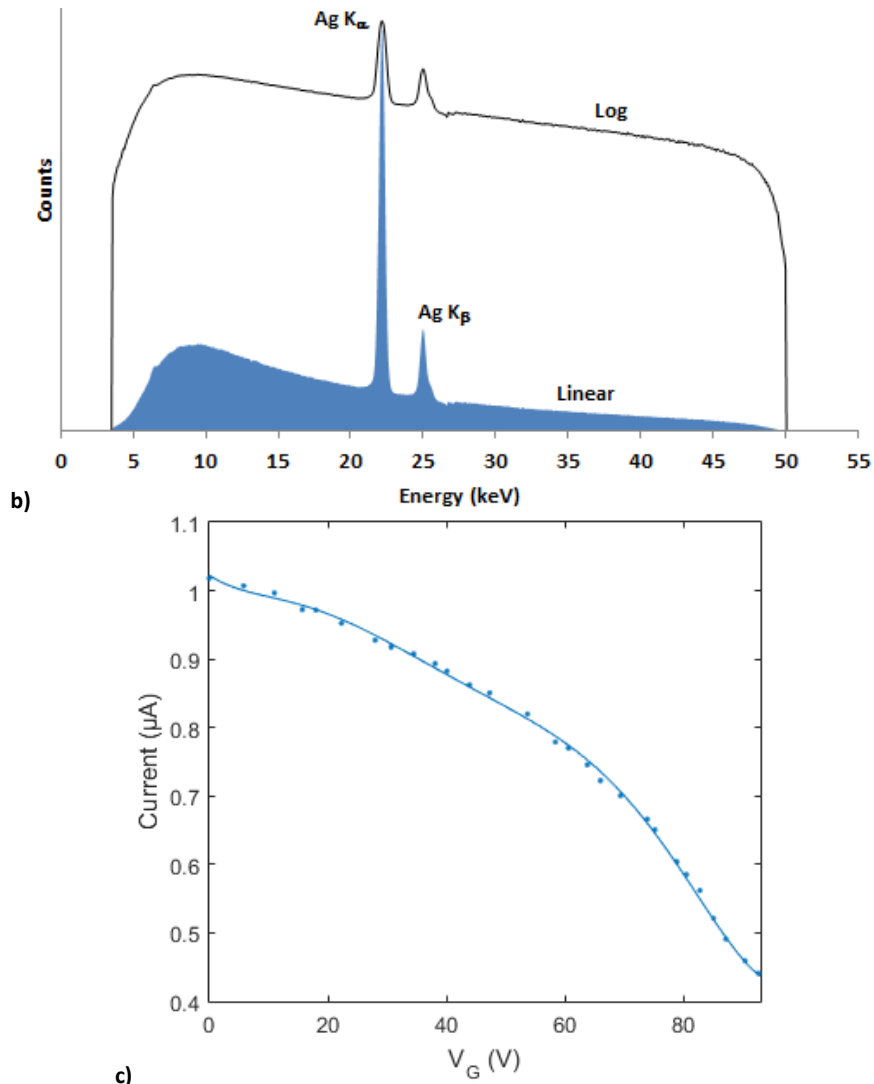


Figure 8.36, showing a) the experimental setup, with the GFET directly illuminated by the Amptek X-ray generator. B) shows the output X-ray energy spectrum of the Amptek generator, previously shown in ref. [271]. C) shows the measured current through the graphene as a function of V_G .

The response of the detector was firstly investigated for $V_{XR}=25\text{kV}$ and $I_F = 25\mu\text{A}$ for a range of gate voltages. The change in the channel current during illumination, ΔI , was observed to be dependent on the value of V_G and whether it resulted in electron or hole carrier densities in the graphene channel, figure 8.37a. For $V_G = 0\text{V}$, the current increased slowly, and continued to increase after the X-ray is turned off, potentially due to the lack of a field across the absorber to funnel charge carriers to the surface.

At higher voltages, the change in current starts to slowly stabilise and decrease after the X-ray illumination is turned off, although at some instances the change in current stops before the X-ray illumination is turned off. For $V_G = 90\text{V}$, the current increased quickly until it reaches a peak and then decreases before the X-ray source was turned off. This suggests a change in the field applied to the graphene at this point. It is

unlikely to be because of the intensity of the source resulting in the saturation of the silicon and extinguishing the signal, as shown in section 8.2.2.7, because the intensity was the same for all the results. Similarly, for $V_G = 100\text{V}$ equal to electron carrier densities, the application of a field causes the change in current ΔI to switch polarity as the current reduces towards and through the Dirac point, and then increased again. It then returned to its original position after the X-ray source was switched off, although it did not go back through the Dirac point to return to the original channel current.

If the signal mechanism is related to the absorption of an X-ray photon, which then thermalises and generates secondary charge carriers then, for $V_G \neq 0\text{V}$, the charge carriers are accelerated to the gate or to the dielectric. For $V_G = 0\text{V}$, the current may not be decreasing because the charge carriers are not being funnelled away from the dielectric quickly. The peak seen for $V_G = 90\text{V}$ and the failure to return through the Dirac point for $V_G = 100\text{V}$ is perhaps due to a change in the field arising from charge trapping in the silicon, or perhaps saturation of the signal at high V_G as measured in section 8.2.2 and 8.2.3. Both effects would change the magnitude of the field and thus the change in current, and may explain why the current hits a peak before the X-ray source is turned off. Further experimental work, especially with a GFET with a much lower V_{Dirac} , may identify the cause of this.

If the mechanism is due to heating, the signal would be expected to decrease when the X-ray illumination is turned off as the detector starts to cool. This is not observed for $V_G = 0\text{V}$ as the current continues to increase after illumination ceases, and for $V_G = 90\text{V}$ and 100V as the current changes before the illumination ends. This suggests that another factor affects the current, perhaps because of the carrier density determined by the gate voltage, although this is unclear and requires further investigation.

After the X-ray source has been switched off, a current $I = \frac{V_{bias}}{R}$ still flows through the circuit but it returns towards its original value. This is because, as the charge carriers recombine in the silicon the field \vec{E} that was generated diminishes or, if the signal is due to bolometry, the sample cools to an equilibrium temperature. Both effects cause the Fermi level to return to its original position, and therefore the channel current/resistance returns to its original value too.

The rate of change of current through the sample, $\frac{\Delta I}{\Delta t}$, was plotted against $\frac{\Delta I}{\Delta V_G}$, which is related to the mobility and is sample dependent, as shown in figure 8.37b. This suggests that a sample with a greater hole or electron mobility will result in a greater rate of change of current, and therefore a greater sensitivity, as a smaller field would be required to generate a change in current.

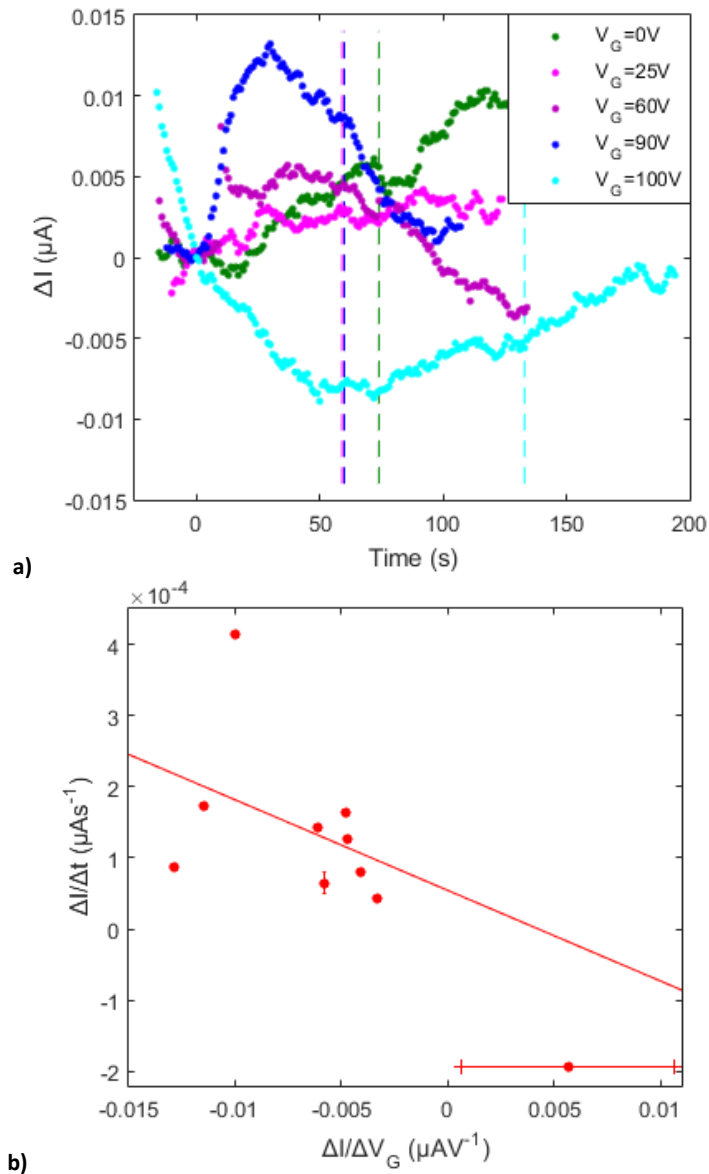


Figure 8.37, showing a) the effect of changing the V_G , with a rate of increase of the current from illumination to peak reflecting the $\frac{\Delta I}{\Delta V_G}$ of the device, given by figure 8.36c, at that V_G , with the current decreasing for electron carrier densities as the modulated gate voltage approaches V_{Dirac} . The X-ray source was turned on at 0 seconds, and the dashed lines indicate when the X-ray signal was turned off. B) shows the rate of change of current against $\frac{\Delta I}{\Delta V_G}$ obtained from figure 8.36c, which shows that a graphene sample with a greater mobility will result in a greater change in the current. Note that the $\frac{\Delta I}{\Delta V_G}$ value for $\frac{\Delta I}{\Delta t} = -200 \mu\text{As}^{-1}$, obtained for $V_G = 100\text{V}$ for electron carrier densities, was unavailable so is represented by the horizontal line given for $\frac{\Delta I}{\Delta V_G} > 0$.

The sensitivity of the detector was then investigated for different combinations of V_{XR} and I_F , which are both related to the energy deposited in the silicon wafer. Assuming absorption within the absorber and subsequent thermalisation of the initial charge carrier and excitation of secondary charge carriers, a greater energy deposition should generate more charge carriers, resulting in a larger field across the dielectric and therefore a greater change in current. Increasing V_{XR} also relates to the maximum photon energy output from the X-ray generator, figure 8.36b, and therefore the absorption depth.

The measured change of current, ΔI , for different V_{XR} with $I_F = 5\mu\text{A}$, $10\mu\text{A}$ and $100\mu\text{A}$ are shown in figure 8.38a-c, respectively. With increasing V_{XR} and I_F the power output from the X-ray generator increases, and the rate of change of current increases. Depending on the mechanism, this suggests that the increasing X-ray dosage generates a larger field that changes the current quicker; or increases the temperature of the detector, and hence the channel current, quicker.

There is a sinusoidal like behaviour in figure 8.38b which can be seen for $V_{XR} = 10\text{kV}$ and $V_{XR} = 50\text{kV}$. In the former, the current decreases once the X-ray source is switched off at $t = 90\text{s}$, but then increases approximately 3nA at $t \sim 120\text{s}$, and decays very slowly overall. In the latter case, the current appears to hit a maximum current at $\Delta I = 6\text{nA}$ with some sinusoidal-like change in current with a peak-to-peak of 1.5nA after that. The reason behind this is unclear, but this could perhaps be due to heating of the detector by the X-ray source resulting in a sustained increase in the channel current. Further experimental work is required to isolate and identify the cause of this sinusoidal behaviour.

In figure 8.38c, the detector response appears to saturate for very high x-ray generator beam currents. A very high beam current and bias voltage, $V_{XR} = 25\text{kV}$ and $I_F = 100\mu\text{A}$, causes a greater energy deposition in the absorber, generating many charge carriers. As discussed in section 8.2.2.7, when many charge carriers are absorbed in the depletion region, the depletion region is saturated and the signal extinguished. In section 8.2.2.7 this was accomplished with a cw laser – in this case, the same effect appears to happen because of the incident X-ray photons. This means the maximum current is measured

before the X-ray source is switched off. For $V_{XR} = 10\text{kV}$ and $I_F = 100\mu\text{A}$, less energy is deposited in the detector, so fewer charge carriers are generated and therefore the detector does not saturate as it reaches the maximum current when the X-ray generator is switched off. However, the channel current does decrease to a higher measurement than initially, settling at $\Delta I \sim 2\text{nA}$, which may be due to heating of the graphene because of the X-ray illumination, or damage to the detector. If this technique was to be used in a commercial or industrial application, the current would have to return to the original current, so further experimental work is required.

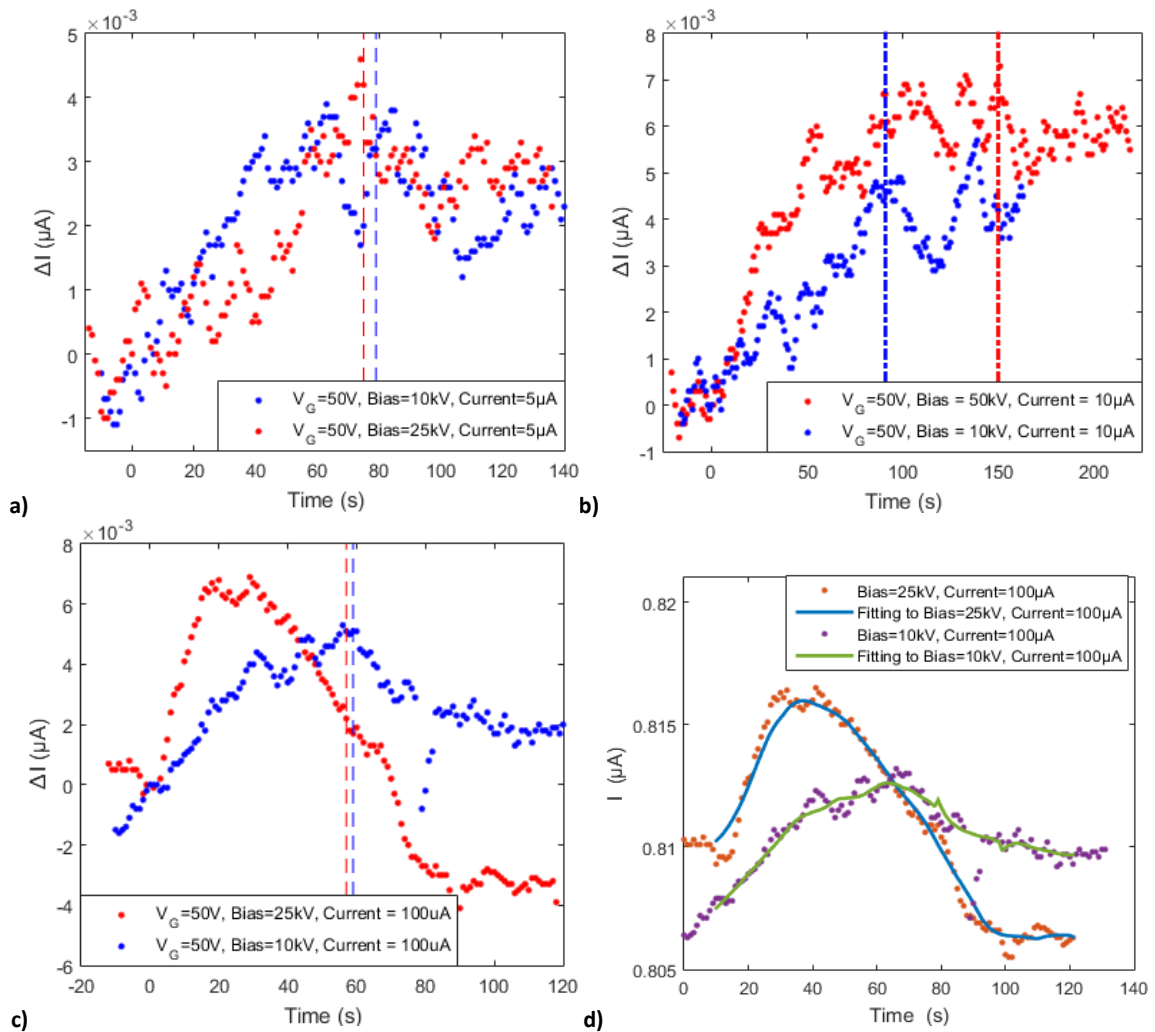


Figure 8.38, showing the signal for different for V_{XR} for a) $I_F = 5\mu\text{A}$, b) $I_F = 10\mu\text{A}$ and c) $I_F = 100\mu\text{A}$. D) shows the results for c) with a moving window function 10s wide applied to the results. These results show that an increasing V_{XR} , and hence increasing maximum power, causes the peak ΔI to increase, with the change occurring at a faster rate. The X-ray source was turned on at $t = 0$ seconds, and the dashed lines indicate when the X-ray signal was turned off. In figure 8.38c, the signal is decreased event when the X-ray source was still irradiating the detector – this was attributed to the extinguishing of the signal via the saturation of the depletion region.

The same tests were made to investigate the dependence on I_F . Increasing I_F for a given generator voltage does not increase the maximum possible X-ray photon energy, but does increase the total power emitted. A greater power emitted by the X-ray generator, with more energy absorbed by the detector, corresponds to the generation of more charge carriers in the absorber, or more heating of the absorber. Once again, an increase in the rate of change of current is observed that is related to the increase in I_F , for $V_{XR} = 10\text{kV}$ and 25kV , figures 8.39a and 8.39b respectively.

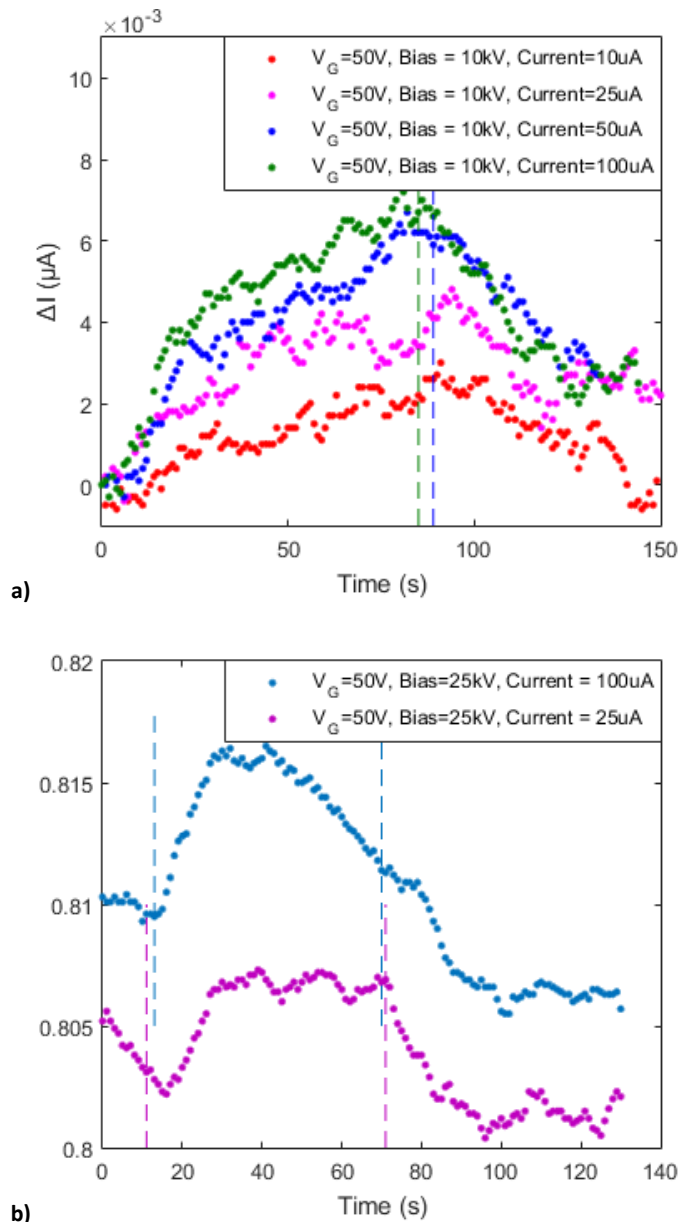


Figure 8.39, showing the signal for a) $V_{XR} = 10\text{kV}$ and $I_F = 10\text{--}100\ \mu\text{A}$, and b) $V_{XR} = 25\text{kV}$ and $I_F = 25$ and $100\ \mu\text{A}$. These show that, with an increasing beam current, and hence total illumination power, the peak signal current increases with the change occurring at a faster rate. In a) the X-ray source was turned on at 0 seconds and in b) it was turned on at the first dashed line, and for both datasets the final dashed line indicates when the X-ray signal was turned off. This clearly shows that the signal turns on and off with the X-ray source.

8.3.3.1 Detector Parameters

Once some X-ray sensitivity had been identified, it was possible to determine some of the X-ray detector parameters as was done for the pulsed optical laser study in section 8.2.6, and try to compare this to other X-ray detectors including those developed by the Jovanovic group.

Assuming that all of the energy from the X-ray photons is absorbed, modulation of the signal was observed to as low as $V_{XR} = 10\text{kV}$ and $I_F = 5\mu\text{A}$, and therefore there the detector has a sensitivity to less than 50mW. A rough estimate for the SNR and NEP was made for an integration time of 60s, and hence a bandwidth of 8.3mHz. A 20s wide moving average window was applied to figure 8.38c, and the SNR was estimated around the peak signal output for different values of V_{XR} for $I_F = 100\mu\text{A}$, as summarised in table 8-2.

An NEP of 0.061W, or 4.7J given a 60s integration time, is significantly worse than the NEP of state of the art X-ray detectors imaging detectors, with an NEP of 2.5eV achieved in ref. [272], for example, for a calorimeter at soft X-ray energies.

| V_{XR} (kV) | I_F (μA) | SNR | NEP(W) | NEP(WHz ^{-0.5}) |
|---------------|-------------------------|-----|--------|---------------------------|
| 10 | 100 | 16 | 0.061 | 0.68 |
| 25 | 100 | 5.5 | 0.454 | 5 |

Table 8-2, summarising the detector SNR and NEP for different values of V_{XR} for $I_F = 100\mu\text{A}$, calculated around the signal peak in figure 8.38c.

Detectors with sensitivity to soft X-ray energies are a focus of research for medical applications, for instance Angiography [273] to study blood vessels, and dual-energy X-ray absorptiometry (DEXA) [274], used to study bone density. The X-ray generator emits approximately 1Sv/h at a distance of 30cm for $V_{XR} = 50\text{kV}$, $I_F = 80\mu\text{A}$. At a distance of 1cm from the X-ray generator, for $V_{XR} = 10\text{kV}$, $I_F = 10\mu\text{A}$, there is a noticeable modulation of the measured current through the graphene channel while it is being irradiated, figure 8.38a. In this arrangement, the detector receives a radiation dosage of approximately 5mSvs^{-1} , which this is much greater than the total dosage applied during an Angiogram, 7-15mSv, and significantly greater than the estimated dosage during a DEXA procedure of approximately $1\mu\text{Sv}$ [275]. Therefore, further iteration is required to improve the device sensitivity for any future medical application.

8.3.4 Detection Mechanism and Experimental Verification

The observed change in current occurs following the absorption of X-ray photons in the silicon wafer. As discussed previously, papers in the literature [74] [75] [80] [81] [82] [83] [125] suggested that current modulation occurs because of the excitation of electron-hole pairs in the depletion region in the silicon wafer. As this primary electron-hole pair thermalises, further electron hole-pairs are excited. These are accelerated apart by the application of the gate voltage, and the resulting dipole causes a field to be applied across the substrate. This changes the Fermi level of the graphene, and therefore the channel conductivity.

While illumination by the visible laser resulted in a change in the channel current, which could be explained through this mechanism, detection of X-ray photons was inconsistent. There was no sensitivity observed for the X-ray sources such as Fe-55, while the channel current through the graphene changed during irradiation by the X-ray generator. This anomaly suggests that something in the silicon is preventing a single X-ray photon from generating a signal via this mechanism. Alternatively, it suggests that another mechanism, such as the photothermoelectric effect or heating of the wafer, results in the signal.

8.3.4.1 Poor Thermalisation

A measurable signal was observed in previous sections when as few as ~ 50000 photoelectrons were generated in the silicon wafer, without using a lock-in amplifier. These photoelectrons are generated within a timescale of the laser pulse width and close to the Si/SiO₂ interface when a red laser pulse is incident on the wafer.

On the other hand, for X-ray absorption, the absorption is much deeper for 10keV photons than 1eV photons, with 54.6% absorption of the signal within the top 0.1mm of the wafer compared to 100% of the signal for 1eV photons. The generated photoelectrons are further from the surface, so the modulation of the carrier density beneath the graphene, and hence the field applied to the graphene, will be reduced. The primary electron-hole pair excited by the single X-ray photon would need to thermalise and generate nearly 50000 more electron-hole pairs to produce a

comparable signal. If the number of generated secondary electrons is less than $N = E/W$, where E is the energy of the photon and W is the average electron-hole pair creation energy, then the primary charge carrier may not be thermalising and producing enough charge carriers for a measurable signal.

Thermalisation often occurs due to phonon emission and absorption, so poor thermalisation could be due to slow hot carrier thermalisation which, for the case of hafnium nitride [276], has previously been attributed to a large phononic band gap. The greater carrier density in the presence of the Amptek X-ray generator could result in the long current decay time, given the increase in recombination time observed for increased carrier densities in fig. 4.9a.

If slow thermalisation was the issue, then the only way to achieve a signal would be to use a more intense source or for more photons to be absorbed in the wafer. The reason for the discrepancy between the lack of a signal for the Fe-55 source and the observed signal from the Amptek X-ray generator may, therefore, be that the Fe-55 source failed to generate enough electron-hole pairs simultaneously, whereas the Amptek X-ray generator produced enough for a measurable signal. The Fe-55 source had activity of $\sim 3\text{GBq}$, so on average one 5keV X-ray photon would be absorbed by the 0.5mm Si wafer every 300ps. The Amptek X-Ray generator has a flux of $10^6\text{s}^{-1}\text{mm}^{-2}$ at 30cm across a beam area of 12.5mm^2 , which indicates a flux of $1.13 \times 10^{10}\text{s}^{-1}$, or once every $\sim 80\text{ps}$. As the flux from the X-ray generator is more than three times greater, three times more photoelectrons are generated if thermalisation is assumed to be poor in the silicon wafer. This means a greater field would be applied to the graphene, leading to a more measurable change in the graphene channel conductivity.

The results in section 8.3.3 show some gate voltage sensitivity, which suggests that the acceleration of charge carriers in the wafer, and/or the opening of the depletion region, play a role in the mechanism. This could suggest that the electron-hole pairs excited by the X-ray sources, with more excited by the X-ray generator compared to the 3GBq Fe-55 source due to the greater flux, are accelerated apart due to the gate voltage, with a field established due to the dipole. If this was a bolometric-like effect, then there would be less dependence on the gate voltage.

8.3.4.2 Photothermoelectric Effect

Another option that could have resulted in the signal is the photothermoelectric (PTE), or Seebeck, effect. As discussed in chapter 1, this effect is where regions with different doping generate a measurable potential related to the Seebeck coefficient and the temperature gradient between the two regions [257]. Potentially, the X-ray illumination could lead to heating of the silicon wafer or the graphene channel, and generate a signal in the form of a measurable current. The X-ray GFET had Ni/Al contacts and a uniform Si/SiO₂ back gate, so the regions with different Seebeck coefficients could have occurred by local doping in the silicon wafer or non-uniformity of the contacts. The photothermoelectric effect for graphene due to illumination by visible photons occurs on the femtosecond scale, and charge carriers recombine on the nanosecond scale [116]. Little work in the literature has considered the photothermoelectric effect in graphene due to X-ray illumination.

The photothermoelectric effect is also observed in silicon [277], but given that the graphene and silicon are not in electrical contact the only way this could have resulted in a photosignal is via AC coupling between the silicon wafer and the Ni/Al contacts. This could possibly be the source of the signal observed for $V_{bias} = 0V$ in section 8.2.3, but the DC current measurement in section 8.3.3 is unlikely to come from this source.

8.3.4.3 Bolometry and Calorimetry

Bolometers and calorimeters are also used to convert deposited photon energy into a change in temperature in an absorber, which leads to a change in resistance of the channel [116]. This has previously been utilised for graphene, especially for terahertz detectors, where the graphene lattice itself is heated [256]. Given the silicon and graphene are in thermal contact, it is possible that the X-ray photons caused the heating of the silicon wafer, which in turn caused heating of the graphene so that the channel current changed.

Silicon-based bolometers and calorimeters have previously been developed across a wide energy range [278] [279]. This often occurs at low temperature [279], but X-ray calorimetry has been demonstrated at room temperature [280]. An x-ray calorimeter

has a signal that decays exponentially with a decay time $\tau = C/G$, where C is the heat capacity and G is the thermal conductance [281]. At room temperature, $C \sim 700 \text{Jkg}^{-1}\text{K}^{-1}$ and the thermal conductivity $k = GL \sim 130 \text{Wm}^{-1}\text{K}^{-1}$ [282], where L is the thickness of the sample. Given that $L \sim 500 \mu\text{m}$, the density of silicon is 2328kgm^{-3} and the cross-sectional area of the wafer is $1 \times 10^{-4} \text{m}^2$, $C \sim 0.08 \text{JK}^{-1}$ and $G \sim 26 \text{WK}^{-1}$, and therefore $\tau = C/G \sim 3 \text{ms}$. If the cross-sectional area was instead assumed to be the focal spot size of the Amptek X-ray generator $\sim 1 \times 10^{-6} \text{m}^2$ [163], then $\tau = C/G \sim 0.3 \text{s}$. If the cross-sectional area was the size of the graphene channel $\sim 10^{-8} \text{m}^2$, then $\tau = C/G \sim 30 \text{s}$ which is closer to the decay time of the current.

It is therefore possible that a bolometric effect could be what is observed following illumination by the Amptek X-ray generator, with the long decay time τ due to the heat capacity of the silicon wafer and thermal conductance between the silicon wafer and the graphene. The gate voltage dependence that was observed in section 8.3.3 may have occurred because the gate voltage varies the heat capacity of the graphene [283]; it also controls the graphene carrier density, which affects the change in conductance when carrier heating occurs in the graphene occurs.

8.3.4.4 The SiO₂ Dielectric

Another possible source of the signal observed in section 8.3.3 is the generation of charges in the silicon dioxide layer [284], potentially due to charging of defects in the SiO₂ layer during X-ray irradiation [285]. In ref. [286], a 12keV X-ray photon generated charge carriers in the insulating layer, which recombine and/or are funnelled to the edges of the dielectric, with some trapped in the interface states. For $V_G > 0 \text{V}$, holes generated in the dielectric will be funnelled towards the top of the dielectric, which may explain the p-doping that was observed in figure 8.37a. The long signal decay time observed following the X-ray irradiation may suggest that the dipole generated by the electron and hole in the silicon dioxide, which diminishes and ultimately leads to electron-hole pair recombination, occurs over a very long timescale.

However, for a 500nm thick SiO₂ layer, only 0.02% of incident 10keV photons are absorbed in this layer. Therefore, it seems unlikely that this mechanism plays a significant role in generating the signal.

8.3.4.5 Experimental Verification

It is not entirely clear what the mechanism is that causes the sensitivity to the X-ray generator. However, it seems likely that it is related either to modulation of the carrier density beneath the graphene and thus a field applied to the graphene, especially given the gate voltage sensitivity that was observed, or because of calorimeter-like heating of the silicon, especially given the very long signal decay time.

There are several routes to potential experimental verification. Each of these would give an indication as to whether the signal was due to photogating, bolometry, or a combination of both, or something else.

For instance, by changing the theoretical decay constant $\tau = C/G$, if there was a corresponding changing in the measured decay constant of the current, then this would suggest that the signal mechanism was related to bolometry. This could be achieved by varying the temperature during illumination by the X-ray source, which would change the thermal conductance of the silicon wafer [287], or by changing the dimensions of the wafer and graphene channel.

Alternatively, a source with a greater activity would generate more photoelectrons in the silicon wafer. If the flux of the X-ray source was increased three-fold to that used by the X-ray generator and a signal was observed, then this would suggest that photogating is responsible for the mechanism.

It is possible that some of the signal could arise via gate leakage through the back gate substrate, although this is unlikely because the device was still able to be gated, as shown in figure 8.26. To ensure that this is not the case, a picoammeter could be used to measure the gate leakage and analyse the integrity of the dielectric. Additionally, characterisation of the dielectric behaviour could be achieved by following the steps used to probe the bottom and top gates for the bilayer graphene detector in section 6.2.4, for instance by using a voltage step and a charge sensitive preamplifier.

It may be possible to measure the phononic band gap in the silicon wafer. If this was very large, then this may suggest that the lack of signal was due to poor thermalisation of charge carriers. In ref. [276], the phononic band gap was probed by ultrafast transient absorption spectroscopy to show long carrier lifetimes, which they attribute to the mass difference between constituent atoms causing a wide phonon band gap. The phonon band gap could be calculated using high-resolution electron energy spectroscopy (HREEL), as was achieved in ref. [288].

8.4 Further Routes to Improved Device Sensitivity

From this research, there are several options that could result in improved detector sensitivity, including iterating the device design and using improved electronics. However, the former is limited by the current state of the art of graphene device fabrication and the technologies and techniques used, so further developments in this area may be required before further developments can be made for the detector.

This research has shown that only the samples on the highly resistive silicon wafers showed any sensitivity to the pulsed optical photons. This is most likely due to the carrier lifetime and the low collection field available with the gate voltage optimised for graphene sensitivity. Therefore, silicon wafers with $\rho \sim 10000 \Omega \text{cm}$, or materials such as cadmium zinc telluride (CZT) that have equivalent or better X-ray detection properties, should be considered for future detectors. CZT provides for a better stopping power, a large band gap $E_G \sim 1.5 \text{eV}$ [289] and a long carrier lifetime [290]. Fabrication of graphene-based devices onto other semiconductor substrates, such as germanium, is only just beginning but with promising prospects for the future.

The devices were fabricated using electron beam lithography or photolithography. The electron beam lithography hardware that was used is a widely available piece of equipment, and puts an upper limit on the thickness of the substrate that can be used for the manufacture of these devices, with 0.5mm thick wafers typically used. To improve the absorption of the X-ray photons by the absorber, a denser and/or thicker absorber is required as 0.5mm thick silicon wafers are typically 99.9% transparent to energies above 50keV.

Another way to improve the SNR of the detector is to improve the performance of the electronics connected to the GFET, for instance by using a higher bandwidth, lower noise voltage preamplifier more suited to the IV measurement technique that has been employed. Another opportunity is to investigate adaptive shaping techniques; to improve the SNR, in the ideal solution the shaping amplifier integration time would be long enough to reduce any white noise, but not too long otherwise the signal could be missed. A long integration time also prevents fast detection of X-ray photons. A code employing software-implemented pulse shaping was written and is outlined further in Appendix 4, which showed that the noise associated with a measurement could be reduced by an order of magnitude with resulting improvements to the SNR.

The ambition for the X-ray detector would be to fabricate a multi-pixel array for imaging. This could be fabricated using standard techniques such as masking via photolithography, with the array designed to be as closely packed together as possible. The ideal solution for a low-resolution imaging array would be a custom front end multichannel ASIC, utilising a channel per pixel to maximise throughput, with preamplifiers designed to optimise measurement of the dynamic graphene IV characteristic. If the ASIC was implemented as a 2D array with the same format as the pixels, this could be vertically integrated into a compact 2D imaging device.

8.5 Summary

In summary, a pulsed optical laser was used to demonstrate the behaviour and equivalent X-ray energy sensitivity of a GFET detector.

The energy sensitivity was improved by changing the electronics connected to the GFET from a current sensitive amplifier to a charge sensitive amplifier. Using a lock in amplifier and impedance matching the graphene and load resistor along with a large capacitor, the energy sensitivity was improved to achieve an equivalent energy sensitivity of $\sim 5\text{keV}$ for a 1s integration time. The sensitivity of the detector was shown to be driven by the gate voltage, with a pulse height which saturated at gate voltages. It was proposed that this was because the charge carriers generated in depletion region recombined quicker than they could reach the edges of the depletion

region, so the dipole generated in wafer was reduced. As a result, the field applied to the graphene was smaller, and there the change in conductivity was smaller.

The signal following the absorption of a laser pulse is likely to comprise of two components, one attributed to capacitive coupling between the absorber and the contacts, and the other due to modulation of the graphene channel current. The component through the graphene provided $\sim 10\%$ of the signal which could be varied by tuning V_{bias} across the graphene sample and by improving the carrier mobility. The signal was fast, with a rise time up to 100ns and decay time on the timescale of the SRH recombination time. When illuminated by a unattenuated red pulsed laser generating $\sim 10^7$ PE per pulse, the detector had an $SNR \sim 58.5$, with an energy resolution $\Delta E \sim 480$ keV and $\Delta E/E = 0.016$.

After showing energy sensitivity to ~ 5 keV using a lock-in amplifier, the GFET was illuminated by different X-ray sources, such as Fe-55 and Cd-109. No conclusive X-ray sensitivity was observed for these sources, although an interesting r^{-2} -like dependence was observed with the lock in amplifier when the source was moved away from the aperture. Further attempts to obtain a trigger for the signal, for instance via Compton scattered events using a SiPM and a scintillator, also proved unsuccessful.

To ensure that there was X-ray sensitivity, the GFET was illuminated by an Amptek X-ray generator, which modulated the signal due to the gate voltage, generator voltage and beam current. Assuming that the GFET absorbed all the X-ray photons generated by the X-ray generator, the detector was sensitive to illumination by a source less than 50mW whilst receiving a source dose ~ 5 msVs $^{-1}$. Further improvement to the detector are required for future applications, e.g. in medical sciences. The detector also indicated an NEP of order 0.1W, which is significantly worse than current state of the art X-ray detectors used in space science, so a lot more iteration of the devices is required for any applications in this sector.

The discrepancy between the lack of signal for the X-ray source and the measured modulation of the channel current due to the X-ray generator suggested that the signal mechanism is a result of more than just photogating. While the current from the X-ray generator showed gate voltage sensitivity, which could suggest photogating, it also

had a very long decay time ~ 100 s. The long decay time, which was not observed for the red and blue pulsed laser illumination, was of order $\tau = C/G$ which suggested that the X-ray illumination heated the silicon wafer, and generated a signal through a bolometric-like mechanism. It is unclear which mechanism provides the signal, so further experimental work to investigate changing $\tau = C/G$, for instance through changing the temperature and/or more intense X-ray sources, is required.

Further optimisation of the device geometry may provide better energy sensitivity to single soft X-ray photons. This could be achieved by considering optimised electronics and iterating the device geometry and material, including identifying an absorber with a greater stopping power and a longer recombination time. The contribution from the graphene could be improved by using a sample with greater carrier mobility, or by using a top and bottom gated structure to control the Fermi level and open the depletion region in the silicon independently to maximise the measured V_{Pulse} .

9 Conclusion

9.1 Summary of the Project

This project has considered several different graphene-based single and low intensity photon counting photodetectors, by utilising essentially the same graphene field effect transistor structure to exploit different wavelength photons coupling to different components of the detector for terahertz, visible and X-ray sensitivity. Each of these detectors was considered from the concept and theoretical simulations to fabrication and then onto experimental analysis; some have been more successful than others. Some of the pitfalls and issues with current photodetector technologies have been considered, such as the cost and complexity, temporal and energy resolution of detectors, the potential requirement for complicated cryogenic cooling and the lack of tuneability. By considering some of the fundamental properties of graphene, the potential for new graphene-based photodetectors from the terahertz to X-ray was highlighted as an interesting solution for future photodetection applications.

The project started by conceptualising, simulating and designing a bilayer graphene single photon counting photodetector, which utilised the tuneable band gap of Bernal-stacked bilayer graphene to enable a tuneable single photon counting photodetector with colour sensitivity. Theoretical studies demonstrated the potential for colour sensitivity, in addition to a temperature-resolution trade off that could enable the detector to operate at higher temperatures than similar detectors, such as STJs and MKIDs, are capable of, enabling the use of cheaper and less complex cryogenic cooling. The detector was fabricated and then investigated at room temperature and cryogenic temperatures by illuminating with red and blue cw lasers. The proposed mechanism to detect visible photons by exciting charge carriers into the conduction band across a

tuneable band gap with subsequent thermalisation, as discussed in chapter 2, has not yet been observed. However, some photosensitivity to blue and red cw lasers was observed, which is likely to arise from photoabsorption by Si-SiO₂ interface states, especially for blue photons.

Two photodetectors were developed as part of the EXPRO+ contract with the European Space Agency. The passive terahertz detector was designed for sensitivity to frequencies around 1.2THz, and utilised the Dyakonov-Shur principle to generate a plasmon wave between the source and drain, with a DC photovoltage measured without any bias voltage being applied across the channel itself. Each element of the detector was simulated, including the channel dimensions, the dielectric, the channel conductivity and the response from the antennae. A novel “beetle” antenna, with a strong S11 resonance at 1.2THz was fabricated for improved narrowband performance. Illumination of the detector at Aston University and NPL showed modulation due to the gate voltage and the terahertz power over a broadband source, with further work required to demonstrate modulation due to the narrowband terahertz frequencies; these results were backed up by theoretical analysis. The detector showed an NEP of $0.85 \pm 0.15 \mu\text{WHz}^{-0.5}$ and a responsivity of $7.7 \pm 0.6 \text{mVW}^{-1}$, which is lower than other existing graphene-based detectors, although this detector is passive. ESA has recognised this work as having raised the TRL level from level 1 to 2-3.

The X-ray detector attempted to build on existing work in the literature by utilising a simple change in channel conductivity arising from the field effect to demonstrate photosensitivity. Each component of the detector was simulated, including the carrier behaviour in the absorber and carrier transport properties in the graphene to improve the detector’s ability to detect single X-ray photons. The GFET was initially illuminated by a pulsed laser that, coupled with improving the associated electronics, demonstrated energy sensitivity down to $\sim 100\text{keV}$ with a voltage preamplifier, or as low as $\sim 5\text{keV}$ using a lock in amplifier. The energy resolution for 30MeV was approximately $\Delta E \sim 480\text{keV}$, with an SNR of approximately 58.5. Probing with pulsed visible laser photons suggested there were two contributions to the total signal, one which was attributed to capacitive coupling between the absorber and contacts, with the smaller signal attributed to a change in resistance of the graphene, which could be

changed by varying V_{bias} across the channel. When the detector was illuminated by closed Fe-55 and Cd-109 samples there was no definitive X-ray energy sensitivity, although there was a response when the device was illuminated by an X-ray generator emitting a power of at least 50mW. This discrepancy suggested that the signal from the detector, also seen in other papers in the literature, was potentially due to a mechanism such as bolometry as well as, or instead of, photogating. The mechanism is still unclear, and further work has been suggested that may enable the mechanism to be identified. Further iteration of the device design and electronics may then enable detection of a single X-ray photon from a closed source. ESA has recognised this work as having raised the TRL level from 1 to 1 / 2.

9.2 Proposed Next Stages of Development

As discussed in chapters 6, 7 and 8, there are several modification routes for the devices that could boost the detector performance and behaviour. According to ESA, the work in this project has boosted the TRL level from 1→1 or 2 for the X-ray detector, and from 1→ 2 or 3 for the terahertz detector. To boost the TRL level further, further demonstration of X-ray detection - working towards single X-ray photons - and terahertz detection - for narrowband sources - is required.

The concept for the bilayer graphene is very new, so it requires a lot more research to develop this proposal. To develop this concept, further devices are required that do not exhibit the dynamic capacitance that was observed in chapter 6. There is still scope to cool the detector further to attempt to observe the postulates made in chapter 2, including temperature-resolution trade off and colour sensitivity.

For the terahertz detector, this research has demonstrated proof of concept for a novel passive broadband terahertz detector using a simple GFET structure, but narrowband detection has not yet been conclusively demonstrated. To improve the likelihood of passive narrowband detection around 1.2THz, further iteration of the antenna design is required to improve the S11 response and hence the power transfer at this frequency. An improved NEP could also be obtained by changing the device structure, for instance by changing the homogeneous coupling between the absorber and the contacts – perhaps by using a sputtered contact instead as discussed in section

7.5. To date the terahertz signal has required the use of a lock in amplifier, so for any future application of this technology one would likely require a more compact lock in amplifier or another means of measuring the signal.

Work is still required to identify the mechanism that generates the response to X-ray generator observed in section 8.3.3 and the inability to observe X-ray photons from X-ray sources such as Fe-55, which could be explained by the signal being due to photogating or bolometry. As outlined in section 8.3.4, there are several routes that may achieve this, including cooling the detector, using detectors of different dimensions, or sources with higher activity. There are also routes to iterating the device design and electronics that may also improve the energy sensitivity, including an absorber with a better stopping power and a longer recombination time. Better optimised electronics are also required, including a faster voltage preamplifier or a specialised lock in amplifier. If the ability to detect a single X-ray photon is achieved, then work to improve the energy resolution could eventually lead to fabricating the device into a multi-pixel array.

Other concepts for photodetector technologies that utilise similar physics were also briefly considered in this project. A flexible UV GFET (FUVGFET), fabricated on a PEN with an ITO gate, was developed to investigate a flexible, UV sensitive detector; this is discussed further in Appendix 5. Other areas that could be developed include a selective protein sensor for biomedical applications that, conceptually, uses functionalised graphene to bind with a specific protein, resulting in a change in the channel conductivity; this is discussed further in Appendix 6.

9.3 Final Remarks

This thesis has considered the various challenges facing graphene-based single and low intensity photon counting photodetectors and their prospects at a technological level. Future applications of single photon counting photodetectors require high detection efficiency with wavelength specificity, good temporal resolution and low dark counts. Graphene's high mobility, tuneable band gap (in bilayer graphene), strong dependence of conductivity on electric field, ultralow noise, as well as other properties make it particularly suitable for this application.

In many ways, graphene offers an exciting route forward for future photodetectors; for instance, at visible wavelengths, current detector technologies such as MKIDs and STJs can count single photons but are limited by a temporal resolution of $\sim 1\mu\text{s}$. By contrast, graphene photodetectors have shown detection on a femtosecond timescale, while the concept that has been developed in this project is aimed at demonstrating colour sensitivity and temperature/resolution trade off to allow for a reduction in the cost and size of an operating system including expensive cryogenic techniques, two factors crucial to implementation in space science. Successful future development of this detector could enable more sensitive detectors, owing to the avoidance of wavelength dispersive elements, with potential applications in single photon fluorescence spectroscopy and the ability to sense multiple fluorophores simultaneously.

Future graphene-based terahertz detectors could have applications in areas such as security, astronomy and medical sciences. This research has demonstrated a new passive broadband terahertz detector which does not have to be powered, with a sensitivity that can be controlled by V_G and a signal that is related to the incident energy. Work to demonstrate narrowband sensitivity is ongoing, with some initial results that require following up. Narrowband detection at 1.2THz is in a regime where significant research could be undertaken and has not yet been fully exploited.

Many options are available for detection of single X-ray photons, such as STJs and MCP-PMTs. STJs have good energy resolution, but must be operated at cryogenic temperatures, whilst MCP-PMTs have a timing resolution on the order of picoseconds, but provide very poor to no energy resolution. For the graphene-based X-ray detector, experimental research with pulsed optical lasers, which simulated the absorption of energy equivalent to an X-ray photon, suggested energy sensitivity to 100keV X-ray photons or potentially as low as $\sim 5\text{keV}$ X-ray photons when using a lock-in amplifier. No X-ray photon sensitivity was observed with a close X-ray source, although some sensitivity was demonstrated using an Amptek X-ray generator emitting a power of 50mW, which has motivated further work to identify the mechanism that causes this inconsistency. There is ample scope for further iteration of the detector design and electronics operation which could improve the energy sensitivity, with a view to potential long-term applications in space and medical sciences.

Development of graphene-based detectors for future applications requires improved fabrication techniques and the development of integrated manufacturing pathways, with improved homogeneity and control of layer number, defect density and doping during growth, with a view to longer term industrial scale synthesis. CVD graphene arguably is one of the most scalable routes for future graphene synthesis, but other techniques are being developed that could also be applicable.

This work has shown that one simple detector structure could be fabricated into three different detectors, with potential for graphene-based photodetectors to cover an energy range from THz to X-rays. With several benefits over existing photodetector technologies, the future for graphene as a photodetector is promising.

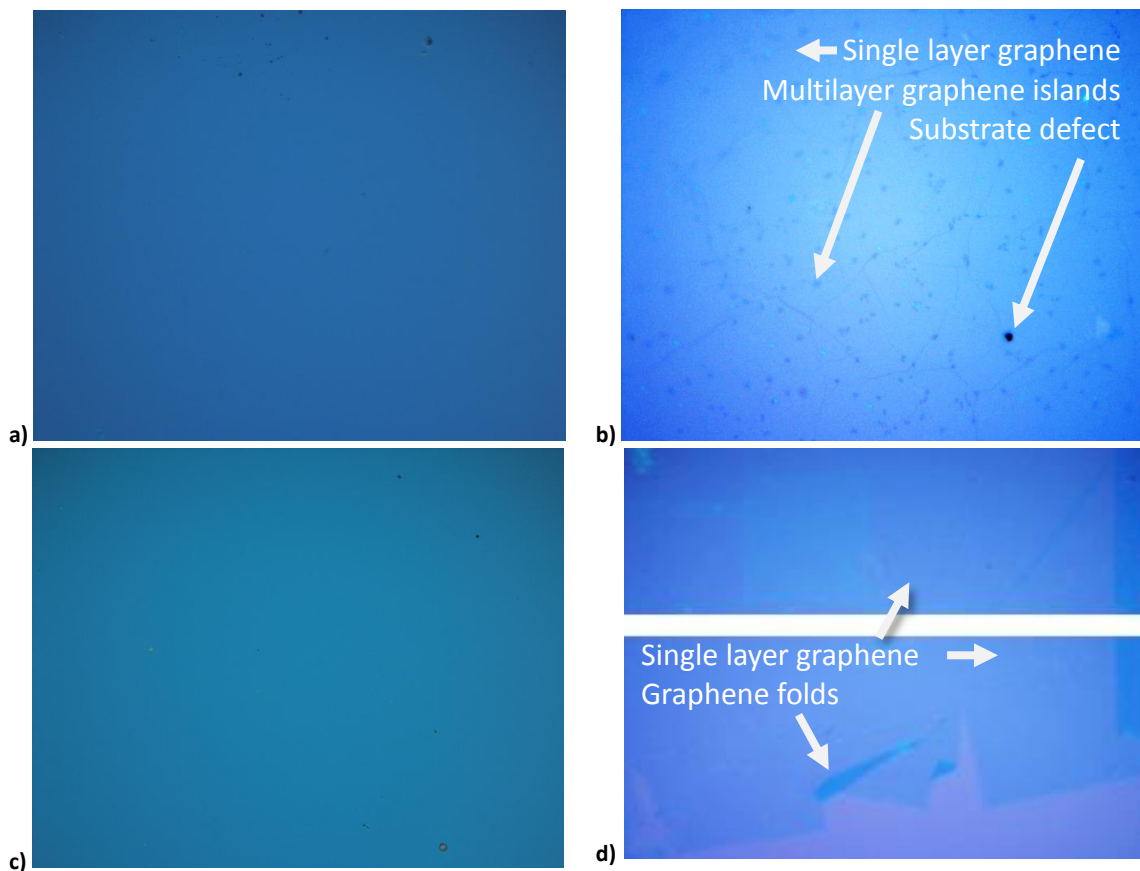
Appendix I – Sample Analysis for European Space Agency

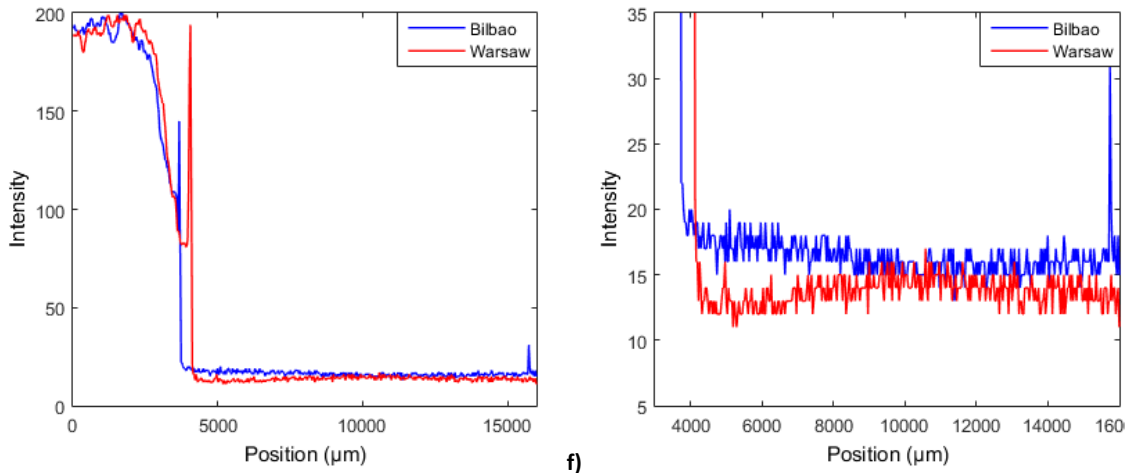
As part of work undertaken for the European Space Agency, samples obtained from institutions in Manchester, Cambridge, Prague, Warsaw and Bilbao were analysed. In Appendix I, analysis using optical microscopy, scanning electron microscopy and Raman spectroscopy is presented, which was submitted to ESA in spring 2015.

Appendix I-a – Optical Microscopy

Optical microscopy was used to characterise the quality of graphene synthesis and transfer, and the layer number through changes in the optical absorption.

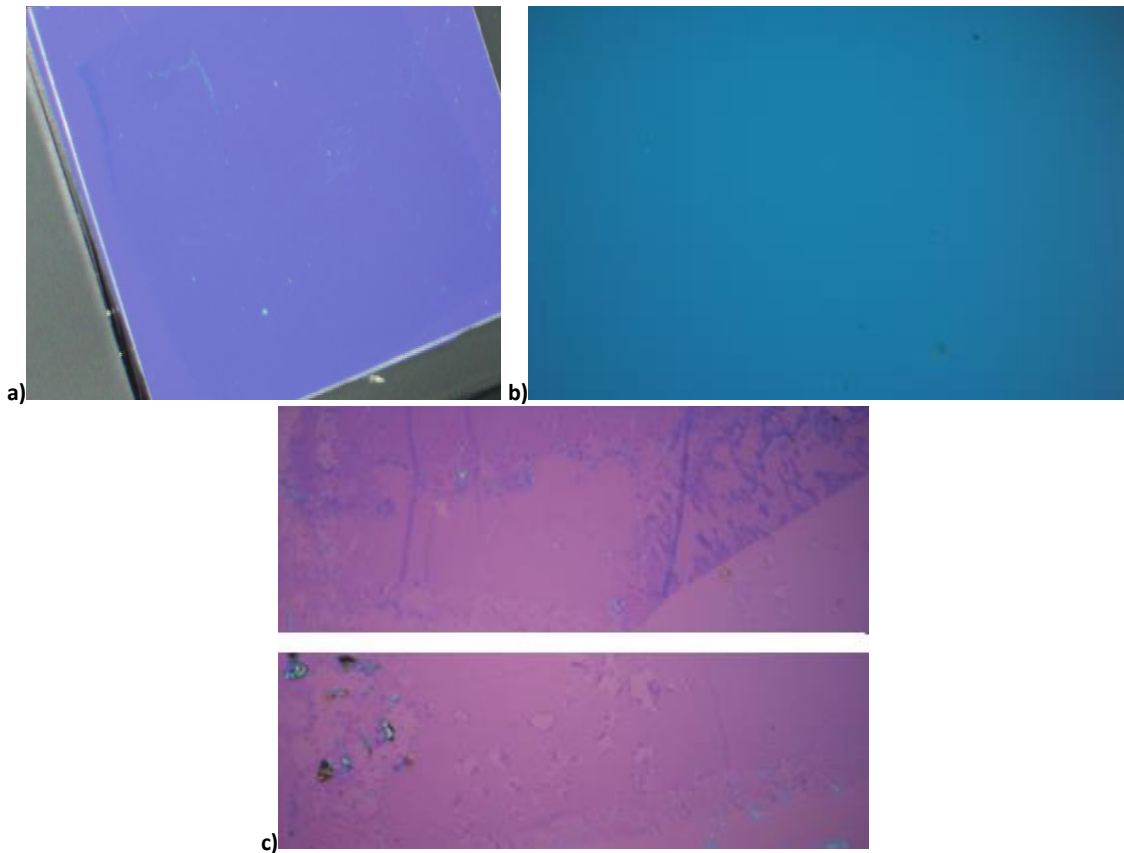
Samples synthesised in Bilbao and Warsaw show few defects for 10x and 50x magnification, figures I-a1.a-d. Optical transmission measurements show a relatively constant absorption, indicating wide scale single layer graphene coverage, figure I-a1.e-f.





e) f)
Figure I-a1 showing samples from Bilbao and Warsaw. A) and b) show the sample from Bilbao under 10x and 50x magnification respectively, indicating some small multilayer graphene areas on a largely single layer graphene region. C) and d) show the sample from Warsaw under 10x and 50x magnification respectively, indicating regions where the graphene has folded during the transfer process. E) and f) show a comparison between the transmission intensity of these samples.

Samples fabricated in Prague, figures I-a2.a-c, had a fold in the graphene arising from the transfer. There are also tears and impurities on the surface of the graphene, which are likely to arise during the growth and transfer phases.



a) b) c)
Figure I-a2 showing three samples from Prague under a) 5x, b) 10x and c) 50x magnification, which shows the tears and folds of the sample.

The graphene sample obtained from Manchester had been fabricated into a device, with the graphene etched into a circle, figure I-a3.a. At 20x magnification, figure I-a3.b, contaminants such as PMMA residue along with damage to the graphene were observed. The optical absorption of the sample was characterised along the centre of the device, figures I-a3.c and I-a3.d, which showed an optical transmission that decreases by $\sim 2.3\%$ in the presence of the graphene, with spikes in the transmission due to the gold contacts.

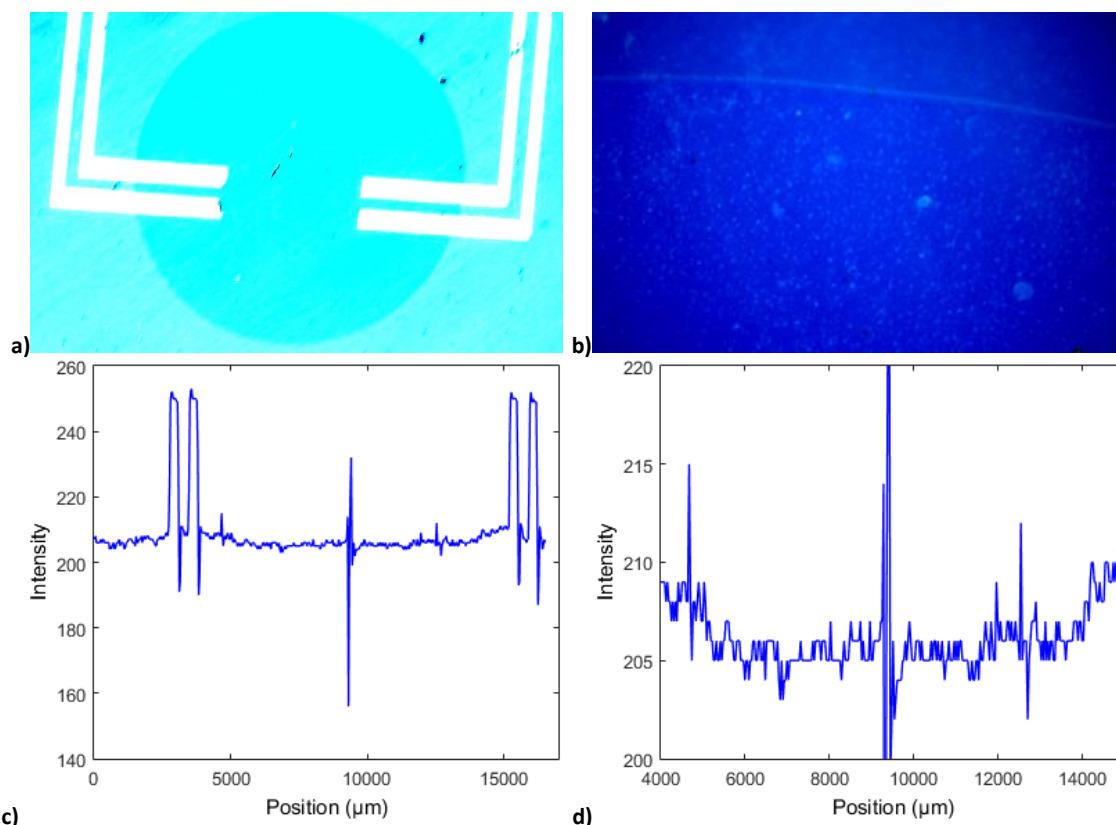


Figure I-a3, showing samples from Manchester at a) 5x magnification and b) 20x magnification. c) and d) shows the optical transmission from the sample as a function of position, with an approximately 2.3% drop in transmission intensity in the presence of the graphene channel.

Samples grown at the University of Cambridge, figure I-a4.a-b, show the difference between a uniform single layer graphene sheet and multilayer islands on the sample respectively. There is observable damage to the sample, including scratches visible in figure I-a4.b, which may have arisen during the growth or transfer process.

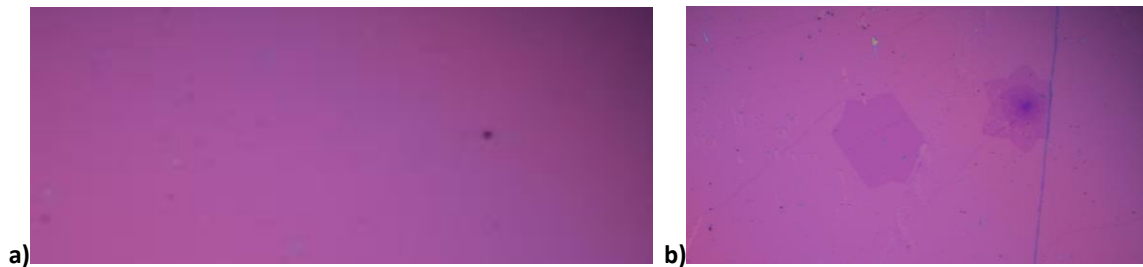


Figure I-a4, showing samples from Cambridge of a) single layer graphene, and b) bilayer and multilayer graphene islands.

Appendix I-b – Scanning Electron Microscopy (SEM)

Samples from Warsaw, Bilbao and Prague were also analysed using SEM to characterise the layer number and identify any folds, creases or tears or remnants from the growth and transfer of the graphene. Layer analysis was accomplished by comparing the SEM contrast as a function of acceleration voltage qualitatively against the results in ref. [225].

In the sample grown in Warsaw, figure I-b1.a, there is a large black spot on the sample that could be because of a hole in the graphene or contamination in the transfer process, and a tear in the graphene just below this. Lines are also visible that are due to the CVD growth on copper. The sample from Bilbao, figure I-b1.b, has a few defects and non-uniformities in the sample and the Si/SiO₂ wafer, although, in comparison to figure I-b1.a, this appears better quality.

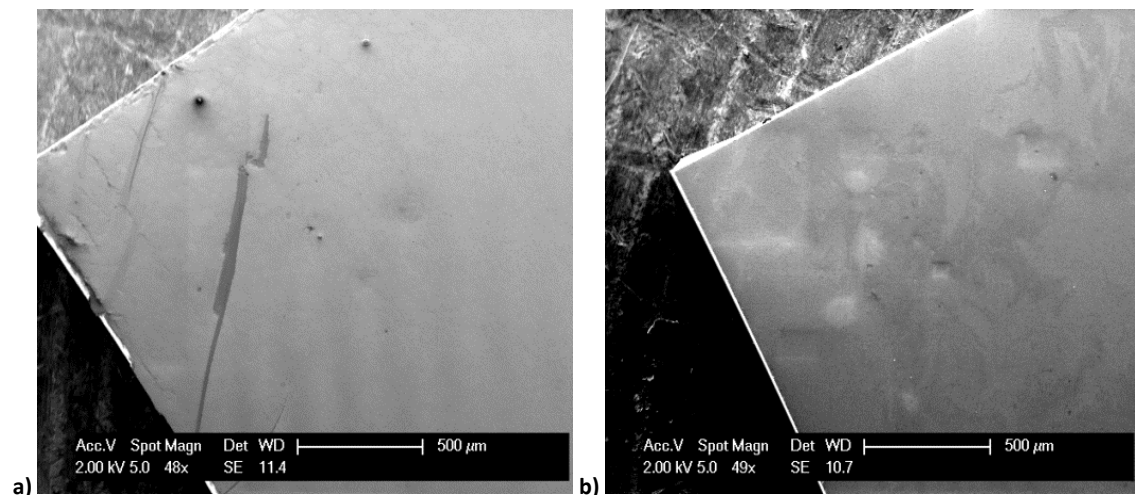


Figure I-b1 showing SEM results for samples from a) Warsaw and b) Bilbao. This shows areas of damage to the sample, including tears and other defects.

The SEM analysis of the sample from Prague shows up a number of defects such as a fold in the graphene (figure I-b2.a), a tear in the graphene (figure I-b2.c), a bilayer

region (figure I-b2.d), PMMA remnants from the transfer process (figure I-b2.e) and lines from the CVD growth on copper (figure I-b2.f). These issues occur during the fabrication processes, with ongoing research looking at improving these industrial processes.

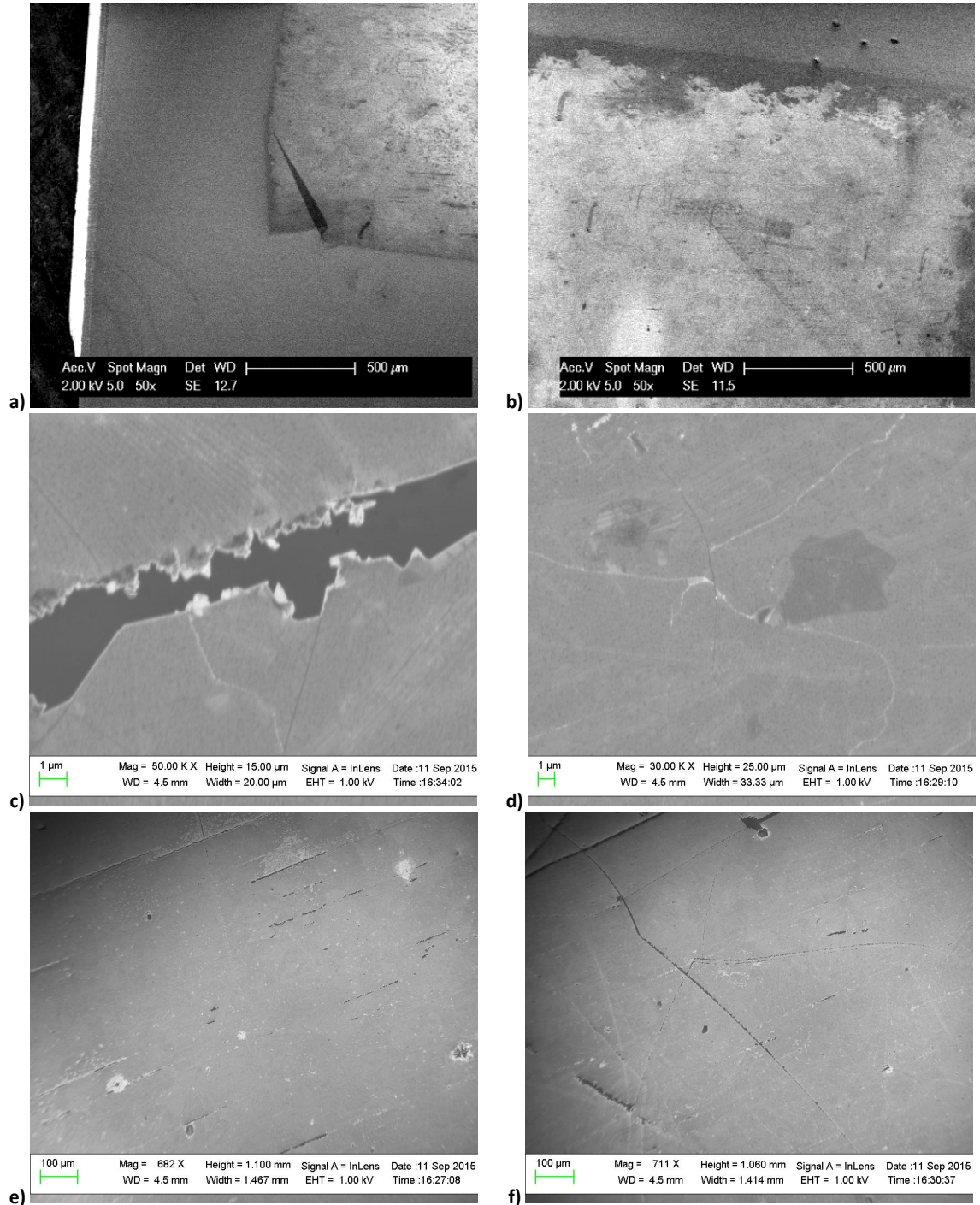


Figure I-b2.a show SEM images of the samples from Prague. In these samples there are observable tears, scratches, bilayer sections, folds, growth lines and PMMA remnants from the transfer process that indicate the quality of the graphene.

The SEM contrast is defined as $Contrast = \frac{I}{I_0}$, where I is the intensity from areas of graphene coverage and I_0 is the intensity from areas covered only by the substrate [225]. Using the results in figure I-b2 for several different SEM voltages, the SEM contrast can be used to estimate the number of layers in the sample, and shows a drop in the SEM contrast at approximately 5kV, figure I-b3, as indicated in ref. [225].

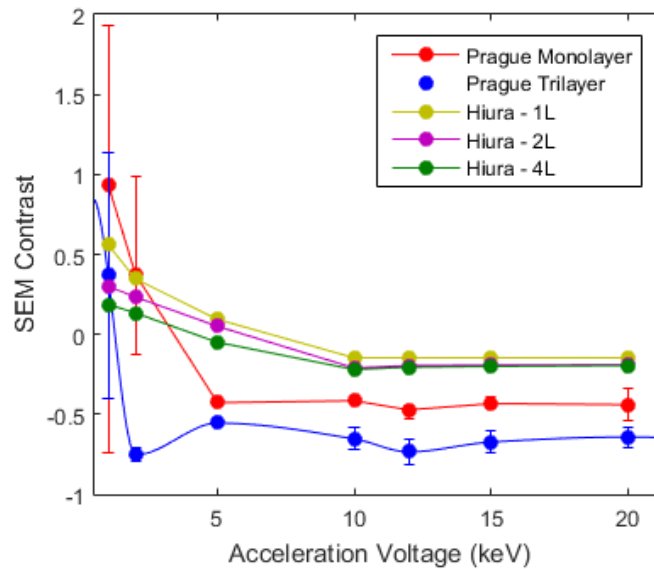


Figure I-b3, showing SEM images and contrasts for monolayer and trilayer samples from Prague, compared to the results from ref. [225]. This shows a significant drop in the SEM contrast between 0 and 5keV.

Appendix I-c – Raman Spectroscopy

Each sample was analysed using Raman spectroscopy to determine the number of layers and the defect and dopant densities, as described in chapter 1.3.5.1. The spectra for the samples are shown in Figure I-c1, and summarised in table I-c1.

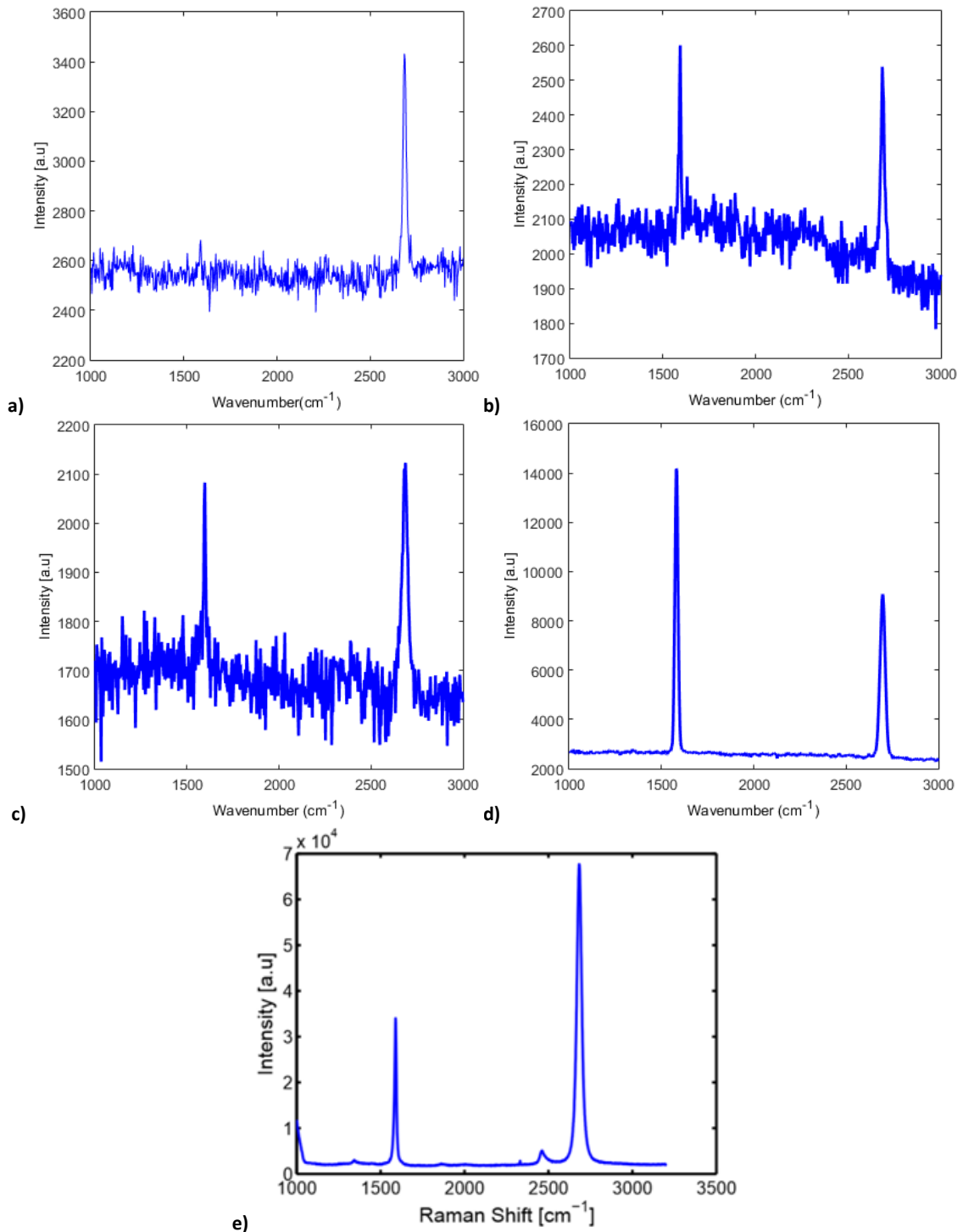


Figure I-c.1 showing the Raman spectra for samples from a) Manchester, b) Bilbao, c) Warsaw, d) Prague and e) Cambridge. The spectrum of the sample from Manchester shows no identifiable G peak, potentially due to a low intensity peak, a poor sample or problems with the Raman spectrometer. The spectrum of the sample in e) was taken at the University of Cambridge.

Each sample has a small D peak, with the resulting defect density calculated as outlined in ref. [113]. The samples from Prague and Cambridge have the lowest defect density, while the samples from Manchester have the highest defect density; unlike the sample from Cambridge, however, the sample from Manchester had already been manufactured into a device. Therefore, the process of depositing gold electrodes onto the graphene may have affected the quality of the graphene.

| Sample Manufacturer | Spectra No. | I_D/I_G | I_{2D}/I_G | I_{2D}/I_D | Defect Density | Nature of 2D Peak | No. of Layers |
|---------------------|-------------|-----------|--------------|--------------|-----------------------------------|-------------------|---------------|
| Warsaw | 1 | 0.706 | 1.352 | 1.915 | $3.95 \times 10^5 \text{cm}^{-2}$ | Sharp | 1 |
| Bilbao | 1 | 0.489 | 0.375 | 0.767 | $3.28 \times 10^5 \text{cm}^{-2}$ | Sharp | 1 |
| Cambridge | 1 | 0.091 | 2 | 22 | $1.42 \times 10^5 \text{cm}^{-2}$ | Sharp | 1 |
| Manchester | 1 | 1.000 | 1.296 | 1.296 | $4.7 \times 10^5 \text{cm}^{-2}$ | Sharp | 1 |
| Prague | 1 | 0.17857 | 0.6429 | 3.6 | $1.98 \times 10^5 \text{cm}^{-2}$ | Sharp | 1 |

Table I-c1. The data for each of the samples.

Appendix II – Cryostat Pump Down, Cool Down and Warm up Procedure

To pump the cart down:

- Drop the fridge in and bolt together. Turn on pumping cart.
- Open PV0 and PV1 and wait for CH2 to drop to 10^{-2} mbar or lower.
- Start the Turbo pump, activate CH3, close PV1 and open PV2. Wait for CH1 to drop to $<5 \times 10^{-2}$ mbar. Alternate PV1 and PV2 to ensure CH3 is not too large.
- Connect the pumping line to the refrigerator, and open PV2, PV4 and PV5.
- Allow to CH1 reach less than 5×10^{-2} mbar again, close PV2, open PV1 and slowly PV3 (gate valve).
- Allow CH3 to reach less than 5×10^{-6} mbar. Turn on compressor and water → cooling starts.

To cool the fridge down to 3-4K:

- Close V1 (in the helium-3 line) when $T < 240$ K. The idea is to use the He-3 as an exchange gas and accelerate the cooling.
- Set the Sorb to 35-40 K.
- Cryogenic pumping is observed when Penning gauge pressure drops when the fridge is isolated (i.e. PV5 closed). This is of order 1×10^{-8} mbar. Close PV5. Pumping down to 4K commences, taking approximately 24 hours.

To cool down from 3-4K to 0.3K:

- Open V1, and set the Heat Switch to 18K. Leave until the Sorb cools down below 10 K (usually $\sim 6-7$ K).
- Close V1. Set the Sorb to 35-40K. Wait until it stabilises, typically 30 minutes.
- Open V1 briefly, turn the Sorb heater off and set the heat switch to 18K.

To warm up:

- Turn off the compressor and transformer. One minute later, turn off the water coolant valves.
- Open V1 on the He-3 line. Turn off the heat switch and Sorb.
- Turn off PV3, PV4 and PV5.
- Leave the fridge to return to room temperature and pressure. This typically takes 24 hours from 4K.
- Disengage the fridge and the pumping cart. Open PV5. Lift the fridge.

Appendix III- Improved Sensitivity using an Oscilloscope-based Lock In Amplifier

As discussed in chapter 7, the lock in amplifier works by multiplying together the detector signal and a reference signal and taking a time average – basic mathematical processes. A brief experiment investigated whether it was possible for a LeCroy oscilloscope to replicate the basic process taken by a lock in amplifier to attempt to increase the detectors sensitivity to pulsed optical photons, such as in the arrangement shown in figures III-1.a and III-1.b. The laser pulses for the pulsed optical laser were triggered on the front edge of a square wave at 80kHz, with a sinusoidal wave generated at the same frequency. Using the math functions built into the oscilloscope, the response from the detector was multiplied by the sinusoidal wave over 1s of data, and a time average taken.

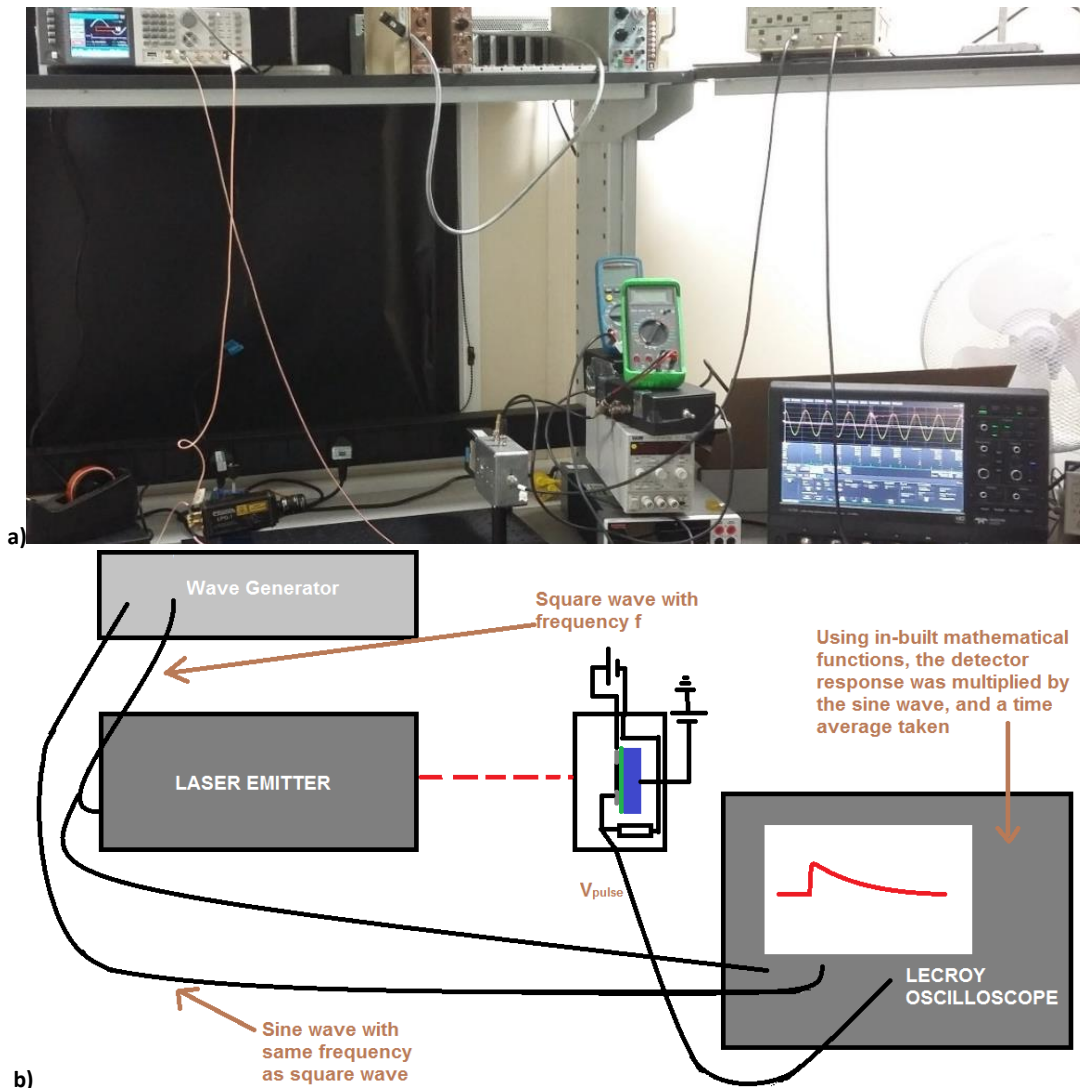


Figure III-1, showing a) and b) the experimental setup for the detector, showing how the lock in amplifier approach was arrived at.

Without the lock in amplifier the detector sensitivity was limited to attenuation up to ND2.9; with the homemade lock in amplifier, figure II-2 shows several readings suggesting sensitivity as low as ND3.5-ND4, equivalent to $\sim 3\text{-}5\text{keV}$, or the energy of one X-ray photon from an Fe-55 source.

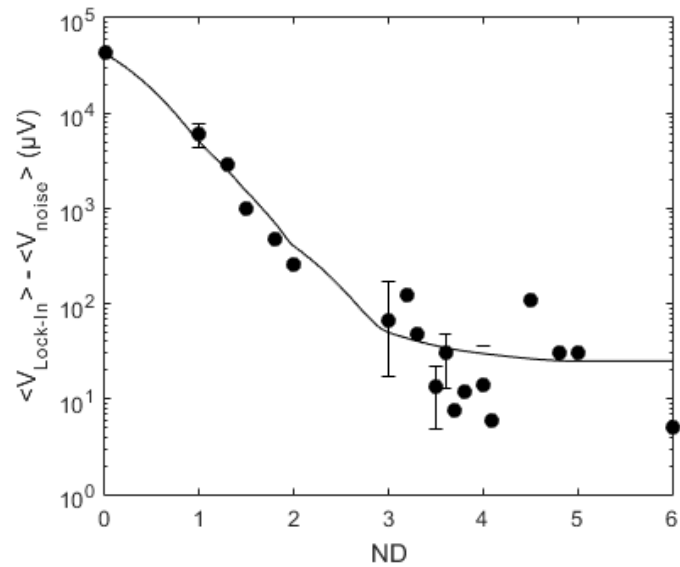


Figure III-2, showing several separate readings with a mean greater than the noise at $\sim \text{ND}3.5$, equivalent to $\sim 3\text{-}5\text{keV}$. The noise was obtained by measuring the background signal with a 100% attenuator blocking the signal.

Appendix IV - Adaptive Electronics to Optimise the X-ray Detector Sensitivity

A small piece of work was done to investigate how the shaping time could be optimised prior to detection of the next X-ray photon. The idea was to enable the best compromise between fast detection and reduced noise.

Firstly, a moving window deconvolution was applied to a signal for a given window size, equivalent to the integration time. A moving average filter was then applied, and this whole process is repeated 60 times for different window sizes. From the simulated maximum peak value after the moving average filter is applied the noise for each window is calculated. Using a measured pulse with a white noise of 10% of the measured signal voltage, in figure IV-1 an optimum window of $\sim 3\mu\text{s}$ resulted in the minimum noise. This clearly shows the contributions from the $1/f$ noise, parallel (shot) noise and series (Johnson) noise [291].

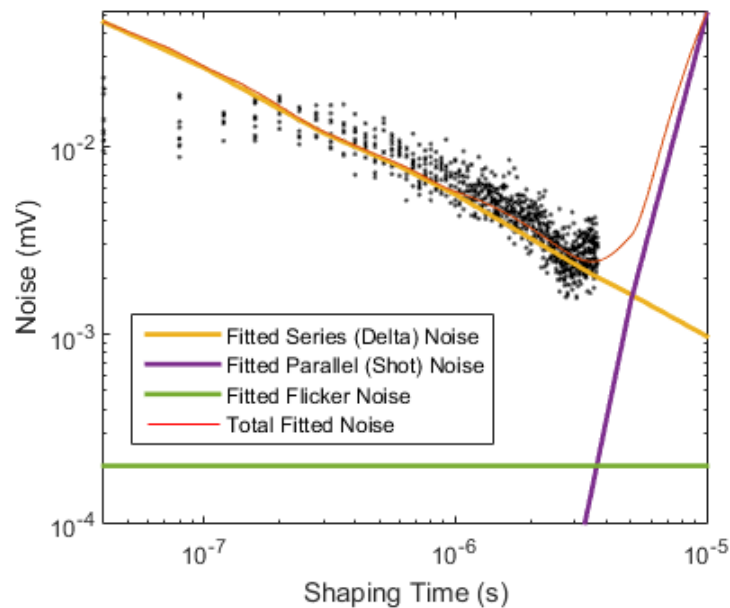


Figure IV-1, showing the contributions to the noise of one of the measurements on the oscilloscope, with a minimum noise time for a window of approximately $3\mu\text{s}$.

The computation time was measured for each window size. This gave an indication of the relationship between computation time and window time, figure IV-2.a, and maximum X-ray detection rate (given by the inverse computation time), figure IV-2.b. However, with more efficient coding the maximum X-ray rate could be vastly improved. The relationship between noise and maximum X-ray photon rate, with the former minimised and the latter maximised, is shown in figure IV-2.c

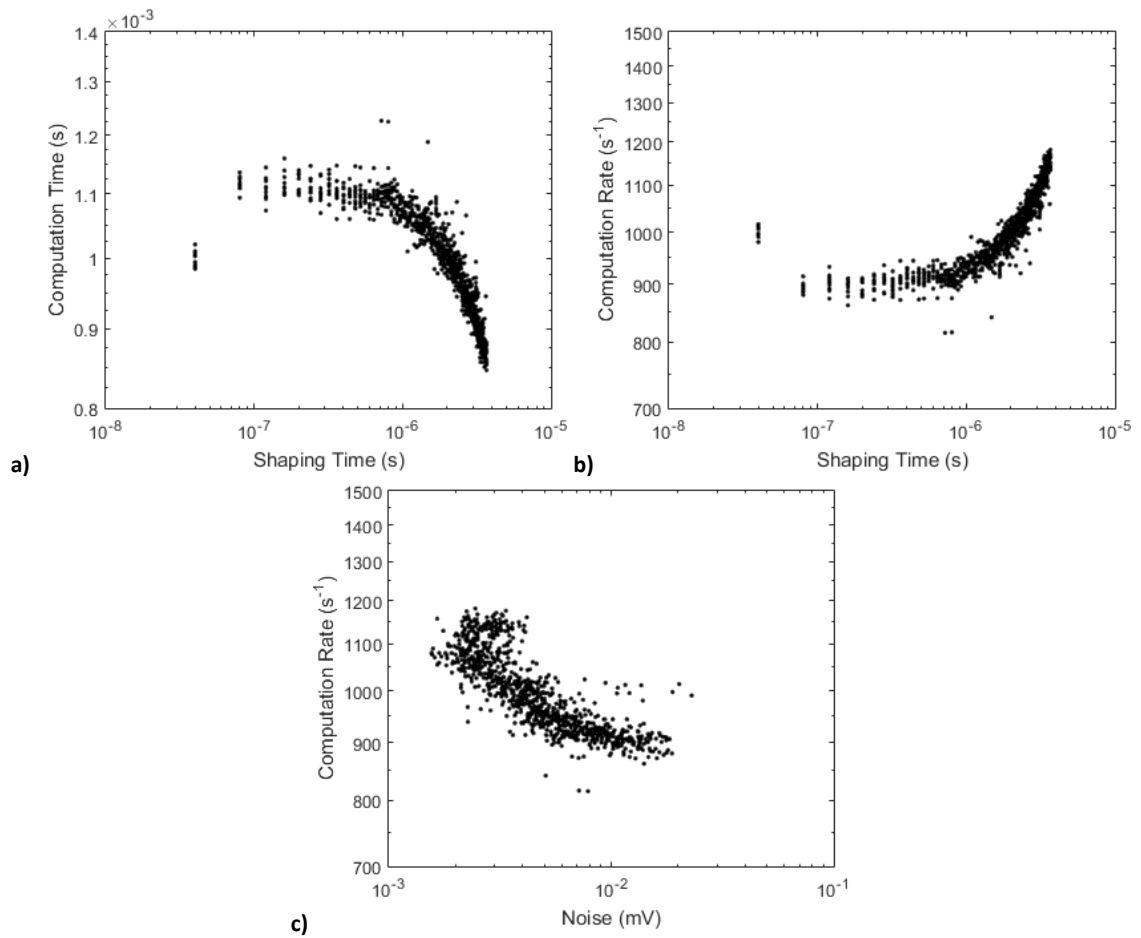


Figure IV-2, showing a) the relationship between integration time and computation time, and b) shows the corresponding rate. C) shows the trade-off between noise and computation rate. These simulations could be improved by more efficient coding.

Appendix V - Developing a Flexible UV GFET (FUVGFET)

The X-ray GFET, discussed in chapters 4 and 8, utilised the coupling of X-ray photons to the substrate to generate charge carriers that changed the conductivity of the graphene channel via the field effect. A similar detector for UV wavelengths could be developed by using an indium tin oxide (ITO) absorber, as ITO is transparent at visible wavelengths but opaque at UV wavelengths. Conceptually, incident UV photons would be absorbed by the ITO absorber in the FUVGFET, resulting in a possible change of the graphene channel conductivity.

One FUVGFET was fabricated on a PEN substrate with 40nm Al₂O₃ dielectric and sputtered ITO gates and contacts deposited on the device, figures 9.1a-b. The graphene was transferred using the process outlined in chapter 5. Electrodes were deposited by masking the contacts via photolithography, figure V.1, and then sputtering ~30nm ITO. To be able to make electrical contact to the back gate, the alumina layer was etched away using a 10+30ml water+phosphoric acid solution heated to 80 degrees, with one end placed in the solution for 20s.

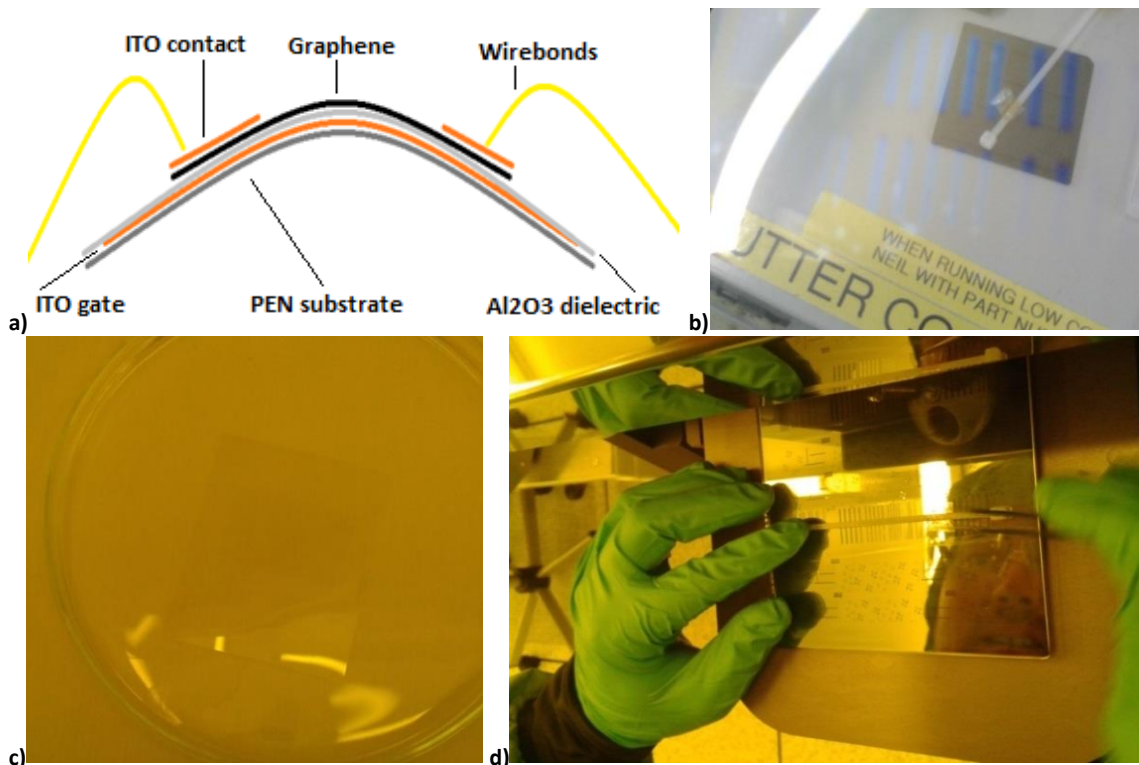


Figure V-1 showing a) the device schematic with a PEN substrate, ITO back gate and contacts and an alumina dielectric, and b) shows the final fabricate device. c) shows the device after the graphene transfer step, and d) the application of the tie wrap mask during photolithography.

The device was successfully wired together by using conductive carbon wire glue which enabled it to be gated, figure V.2. This showed a slight p-doping with $V_{\text{Dirac}} \sim 2\text{V}$, which is low considering this is an unencapsulated device, perhaps due to the lack of p-doping adsorbates in the Si/SiO₂ interface. The carrier mobility was estimated as $\sim 2300\text{cm}^2\text{V}^{-1}\text{s}^{-1}$ and $\sim 600\text{cm}^2\text{V}^{-1}\text{s}^{-1}$ for the holes and electrons respectively.

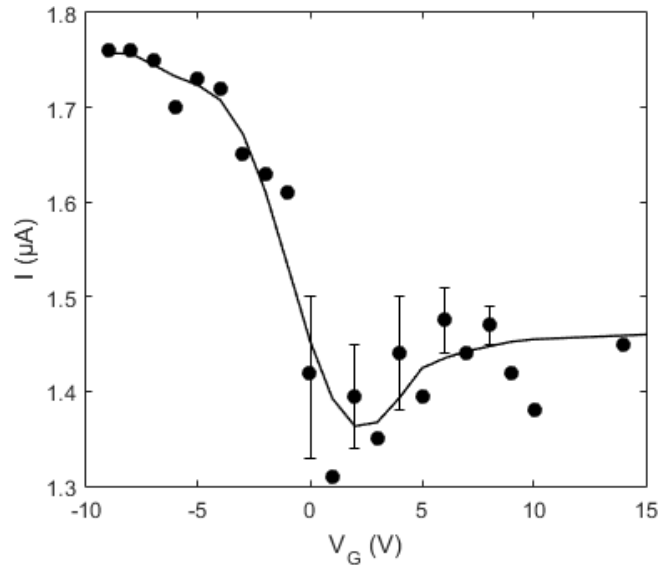


Figure V-2 showing the gating of the device, with $V_{\text{Dirac}} \sim 2\text{V}$, a hole mobility of $\sim 2300\text{cm}^2\text{V}^{-1}\text{s}^{-1}$ and an electron mobility of $\sim 600\text{cm}^2\text{V}^{-1}\text{s}^{-1}$.

Some basic tests were done to understand the application of strain to the detector to use it as a transparent strain sensor. The device was partially mounted on a solid quartz surface and the wires for the gate, source and drain were attached with carbon glue. One end of the device was then held at different angles to induce strain on the graphene channel, V.3a. This changed the current quite significantly, figure V.3b-c, due to the introduction of a pseudo-vector potential from the strain; the current as a function of strain angle was then plot, figure V.2d, which shows with more strain a greater change in current is measured.

The sensitivity of I_{ds} to a UV source was investigated by illuminating with a UV emitting pen. As shown in figure V.3d, this show a change in the graphene channel conductivity attributable to the absorption of the UV by the ITO film.

An FUVGFET could enable fast detection by a flexible, transparent detector at UV wavelengths, with potential applications in areas such as secure space-to-space

communications, pollution monitoring, flame sensing and early missile plume detection, along with possible applications related to strain sensing [292].

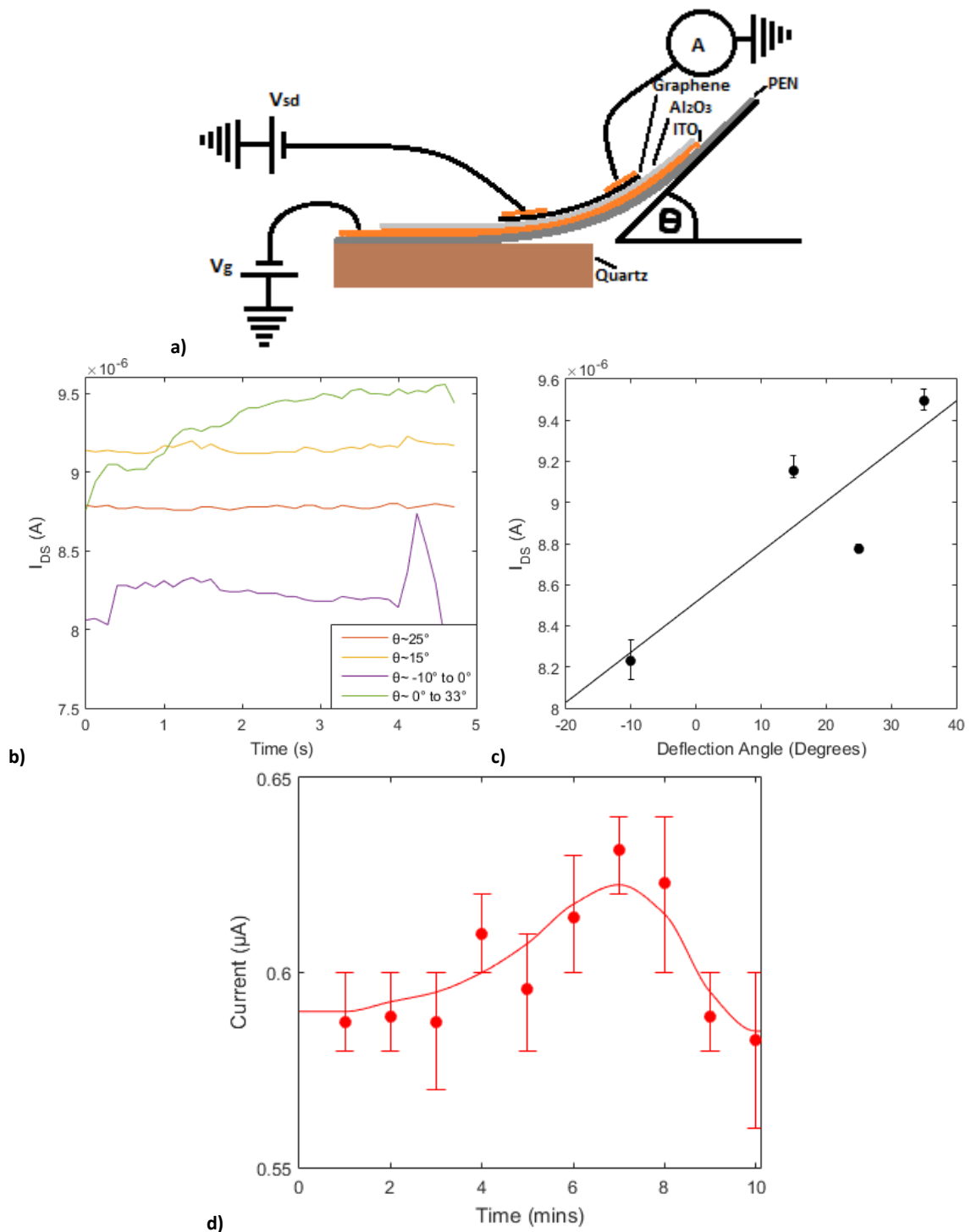


Figure V-3 showing a) the setup of the strain sensing experiment, b) the change in current over time at different straining angles, and c) the channel current as a function of deflection angle. D) shows some change in the channel current in the presence of a UV source over several minutes.

Appendix VI – Graphene for Selective Protein Sensing

GFETs have been developed with very good sensitivity, enough to detect single gas molecules [164]. This could also lead to other sensitive detectors, such as a GFET-like selective protein sensor for biomedical applications.

Research by the Jamieson Group at the University of Glasgow (formerly at the University of Leicester) has demonstrated many instances of alpha-helix mediated peptide-protein binding, with the peptide binding to only one protein. Functionalising the graphene with the peptide would provide a vehicle to exploiting the peptide-protein binding as a sensor. The stapled peptide scaffold essentially acts as the “glue” to adhere the protein to the graphene, and the presence of a protein coupled to the peptide+graphene would, conceptually, change the doping of the graphene resulting in a measurable change in the graphene channel current in the presence of the protein present in a bodily fluid, the back gate could then be used to optimise the sensitivity of the detector. Many alpha-helix mediated protein-peptide binding candidates have been identified, but none of these have medical applications. The hippDB database enabled possible candidates to be identified that do medical applications and are unlikely to be membrane proteins, such as the ERRalpha protein (3D24) [293].

Initial devices, without the peptide functionalisation, were fabricated using the same techniques described in chapter 5, to the design shown in figure VI.1, to enable basic experiments on the concept. None of these devices were successfully gated, but the wafers were still able to be used for Fourier transform infrared (FTIR) spectroscopy. New devices could now be developed that would overcome these fabrication problems.

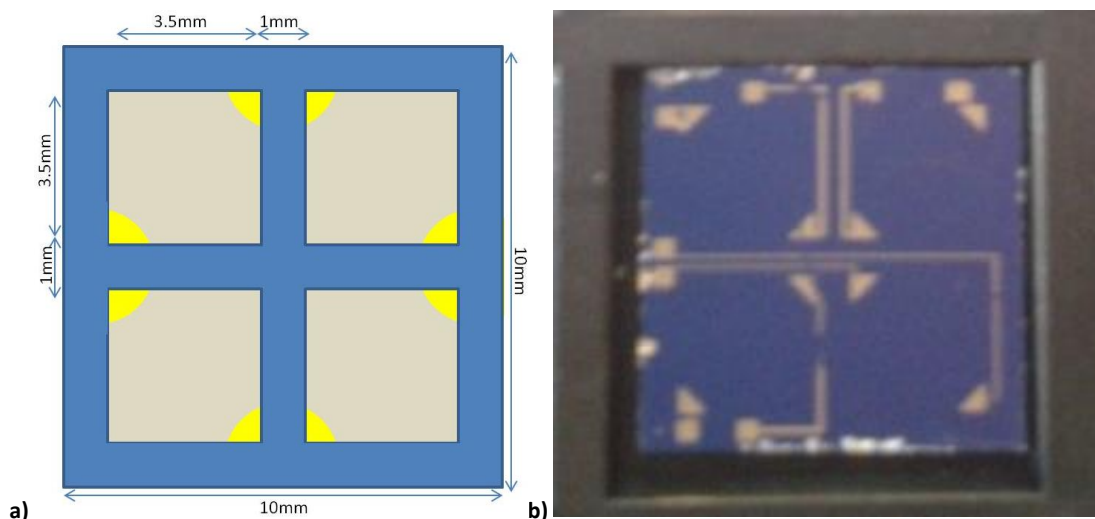


Figure VI-1 showing a) the initial concept for the device, b) a fabricated device with a mask.

FTIR spectroscopy was briefly investigated to observe how the peptide binds to the graphene when it is on a Si/SiO₂ substrate. Initial tests used an alkene-based peptide in a sodium phosphate/water buffer that was deposited onto the device and allowed to dry in air. Further peptide+buffer depositions were made with the intention of seeing the change in the FTIR spectrum with increasing washing, which may indicate a specific binding site for a protein.

The buffer was made of 0.5ml of 0.5M sodium phosphate solution which was diluted in deionised (DI) water to 50ml to form a buffer, and then 0.3mg of this peptide was dissolved in 1ml of buffer. Several different spectra were taken to identify any spectroscopic changes due to binding, as shown in figure VI.2, when

- the buffer solution had just been dropped onto the test plate
- the buffer solution had dried on the plate, and
- the buffer+peptide was wet and then dried in air for approximately 1 hour.

The buffer + peptide solution was then dropped onto the graphene to form a bubble approximately 5mm in diameter. This was left to dry in air for 1 hour, and a spectrum was then taken. The sample was then washed with the buffer/peptide solution to wash off anything that did not bind, and to aid additional functionalisation. This was left to dry in air for 12 hours and a further spectrum was taken. The graphene was then washed with DI to remove any loose peptide, and allowed to dry in air for 6 hours. A spectrum was then taken of this to observe any further binding.

The results in figure VI.2, plotted in arbitrary units of transmission due to the necessity to change/redo background samples after cleaning, allows for several observations. The peak at 1100cm^{-1} is due to the SiO_2/Si wafer, and the well-defined peak at approximately 2500cm^{-1} is from CO_2 in the air. Peaks from water in the buffer solution are observed at 3200cm^{-1} and 1800cm^{-1} . The peptide used for these initial tests had peaks at 3300cm^{-1} , 2950cm^{-1} , 1650cm^{-1} , 1550cm^{-1} and 1150cm^{-1} . After washing, it is possible to note a small increase in the magnitude of the peaks at $\sim 1650\text{cm}^{-1}$ and $\sim 1550\text{cm}^{-1}$ that may be due to the binding of the peptide to the graphene.

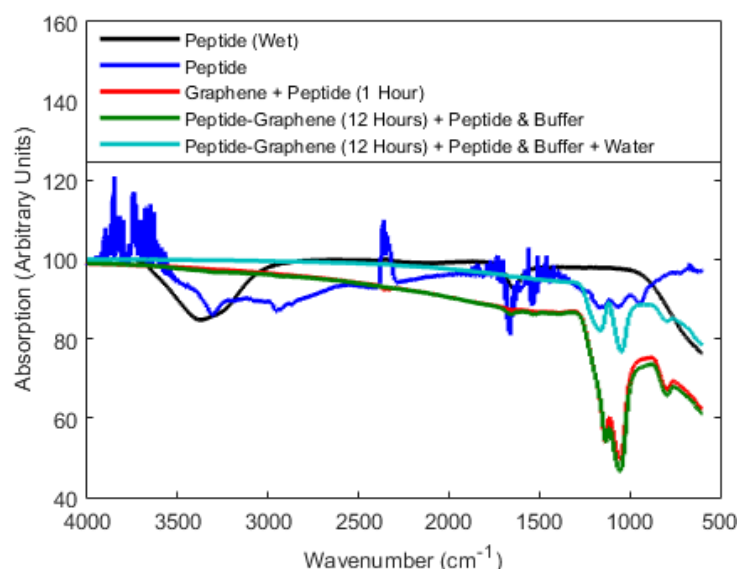
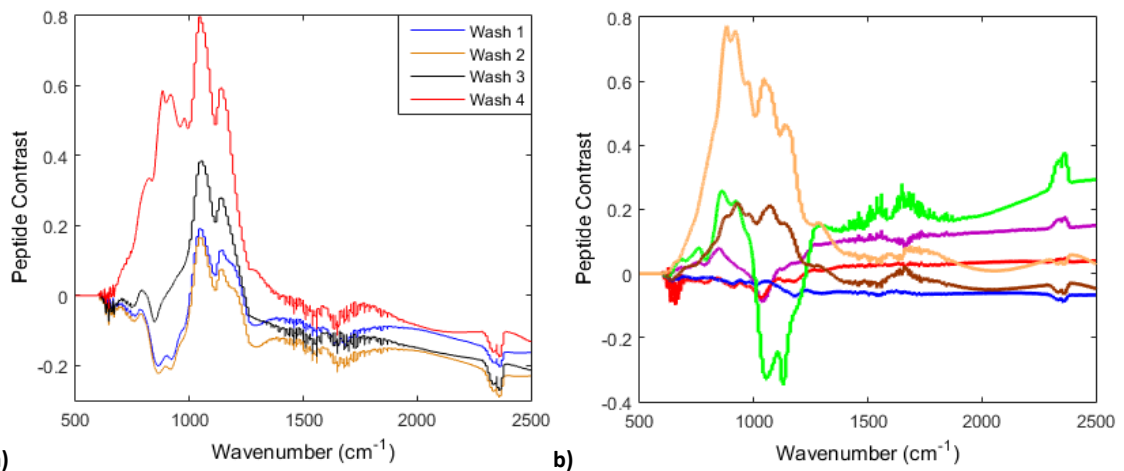


Figure VI-2. FTIR Spectra Readings for alkene samples deposited onto the GFET. The alkene peptide has many characteristic peaks at 3300cm^{-1} , 2950cm^{-1} , 1650cm^{-1} , 1550cm^{-1} and 1150cm^{-1} .

The tests were redone using a new peptide, SMRT1. For these tests, 1mg of a peptide was dissolved in 1ml of the DI water-sodium phosphate buffer. It was then pipetted onto a graphene/silicon wafer, allowed to dry in air and FTIR samples taken. This was washed with deionised water and buffer, before more of the peptide was pipetted on.

To characterise the change in the spectra, a peptide contrast was defined as the change in the absorption spectra relative to 600cm^{-1} . The difference between the different “events” – i.e. the wash number ($2 \rightarrow 1$, $3 \rightarrow 1$, $4 \rightarrow 1$ etc), figure VI-3, for two different reference points for one sample appears to show an increase in the “peptide contrast” at approximately 1000cm^{-1} for both samples with increasing dosage of the peptide scaffold onto the graphene. This suggests a specific bond between the graphene and the peptide scaffold, potentially a C-O bond, which could result in the functionalisation of the graphene and therefore any incident protein binding to the

peptide could change the conductivity of the graphene. However, many further tests are required.



a) **b)**
Figure VI-3 showing the “peptide contrast” against wavenumber for two different reference points on a sample. This appears to show an increase in the peptide contrast as a function of number of washes at 1050cm⁻¹, although this requires much more experimental research to confirm these initial observations.

Bibliography

- [1] J. O. D. Williams, J. S. Lapington, M. Roy and I. B. Hutchinson, "Graphene as a Novel Single Photon Counting Optical and IR Photodetector," *IET*, 2015.
- [2] J. O. D. Williams, J. A. Alexander-Webber, J. S. Lapington, M. Roy, I. B. Hutchinson, A. A. Sagade, M.-B. Martin, P. Braeuninger-Weimer, A. Cabrero-Vilatela, R. Wang, S. Hofmann, A. De Luca and F. Udrea, "Towards a Graphene-Based Low Intensity Photon Counting Photodetector," *Sensors*, vol. 16, no. 9, p. 1351, 2016.
- [3] J. O. D. Williams, J. A. Alexander-Webber, J. S. Lapington, M. Roy, I. B. Hutchinson, A. A. Sagade, M.-B. Martin, P. Braeuninger-Weimer, A. Cabrero-Vilatela, R. Wang, A. De Luca, F. Udrea and S. Hofmann, "Towards a Graphene-Based Low Intensity Photon Counting Photodetector," in *Conference Proceedings of IEEE*, 2016.
- [4] H. N. Rydon, N. H. P. Smith and D. Williams, "The Beckmann Rearrangement of the Dioximes of Anthraquinone and 1:5-Dichloroanthraquinone," *Journal of the Chemical Society*, vol. 356, pp. 1900-1905, 1957.
- [5] J. D. Holdsworth, G. Scott and D. Williams, "Mechanisms of antioxidant action: sulphur-containing antioxidants," *Journal of the Chemical Society*, vol. 906, pp. 4692-4699, 1964.
- [6] M. I. Katsnelson, *Graphene: Carbon in Two Dimensions*, Cambridge University Press, 2012.
- [7] C. Lee, X. Wei, J. W. Kysar and J. Hone, "Measurement of the elastic properties and intrinsic strength of monolayer graphene," *Science*, vol. 321, no. 5887, pp. 385-388, 2008.
- [8] K. I. Bolotin, K. J. Sikes, Z. Jiang, M. Klima, G. Fudenberg, J. Hone, P. Kim and H. L. Stormer, "Ultrahigh electron mobility in suspended graphene," *Solid State Communications*, vol. 146, no. 9-10, pp. 351-355, 2008.
- [9] E. H. Hwang, S. Adam and S. Das Sarma, "Carrier Transport in Two-Dimensional Graphene Layers," *Physics Review Letters*, vol. 98, no. 186806, 2007.
- [10] R. R. Nair, P. Blake, A. N. Grigorenko, K. S. Novoselov, T. J. Booth, T. Stauber, N. M. R. Peres and A. K. Geim, "Fine Structure Constant Defines Visual Transparency of Graphene," *Science*, vol. 320, p. 1308, 2008.
- [11] A. K. Geim, "Graphene: Status and Prospects," *Science*, vol. 324, no. 1530, 2009.
- [12] E. McCann and M. Koshino, "The Electronic Properties of Bilayer Graphene," *IOP*, vol. 76, pp. 1-28, 2013.
- [13] K. S. Novoselov, A. K. Geim, S. V. Morozov, D. Jiang, M. I. Katsnelson, I. V. Grigorieva, S. V. Dubonos and A. A. Firsov, "Two Dimensional Gas of Massless Dirac Fermions in Graphene," *Nature*, vol. 438, pp. 197-200, 2005.
- [14] D. F. Santavicca, F. W. Carter and D. E. Prober, "Proposal for a GHz Count Rate Near-IR Single-Photon Detector Based on a Nanoscale Superconducting Transition Edge Sensor," *Arxiv*, p. <http://arxiv.org/ftp/arxiv/papers/1202/1202.4722.pdf>, 2012.
- [15] M. Rajteri, E. Taralli, C. Portesi and E. Monticone, "Single Photon Light Detection with Transition Edge Sensors," *Nuovo Cimento - Societa Italiana di Fisica Sezione C*, vol. 31, no. 4, pp. 549-555, 2009.
- [16] B. Dierickx, Q. Yao, N. Witrouwen, D. Uwaerts, S. Vandewiele and P. Gao, "X-ray Photon Counting and Two-Colour X-ray Imaging Using Indirect Detection," *Photon-Counting Image Sensors*, vol. 16, no. 6, 2016.
- [17] G. W. Fraser, J. S. Heslop-Harrison, T. Schwarzacher, A. D. Holland, P. Verhoeve and A. Peacock, "Detection of multiple fluorescent labels using superconducting tunnel

- junctions," *Review of Scientific Instruments*, vol. 74, no. 9, 2003.
- [18] L. C. Comandar, B. Frohlich, M. Lucamarini, K. A. Patel, A. W. Sharpe, J. F. Dynes, Z. L. Yuan, R. V. Penty and A. J. Shields, "Room temperature single-photon detectors for high bit rate quantum key distribution," *Applied Physics Letters*, vol. 104, no. 021101, 2014.
- [19] M. D. Eisaman, J. Fan, A. Migdall and S. V. Polyakov, "Single-photon sources and detectors," *Rev. Sci. Instrum*, vol. 82, no. 071101, 2011.
- [20] A. Korneev, Y. Vachtomin, O. D. Minaeva, K. Smirnov, O. Okunev, G. Gol'tsman, C. Zinoni, N. Chauvin, L. Balet, F. Marsili, D. Bitauld, B. Alloing, L. H. Li, A. Fiore, L. Lunghi, A. Gerardino, M. Halder, C. Jorel and H. Zbinden, "Single-photon detection system for quantum optics applications," *IEEE Journal of Selected Topics in Quantum Electronics*, vol. 13, no. 4, pp. 944-951, 2007.
- [21] R. H. Hadfield, "Single-photon detectors for optical quantum information applications," *Nature Photonics*, vol. 3, pp. 696-705, 2009.
- [22] M. Varnava, D. E. Browne and T. Rudolph, "How Good Must Single Photon Sources and Detectors Be for Efficient Linear Optical Quantum Computation?," *Physical Review Letters*, vol. 100, no. 060502, 2008.
- [23] K. S. Novoselov, A. K. Geim, S. V. Morozov, D. Jiang, Y. Zhang, S. V. Dubonos, I. V. Grigorieva and A. A. Firsov, "Electric Field in Atomically Thin Carbon Films," *Science*, vol. 306, no. 5696, pp. 666-669, 2004.
- [24] A. H. Castro Neto, F. Guinea, N. M. Peres, K. S. Novoselov and A. K. Geim, "The electronic properties of graphene," *Reviews of Modern Physics*, vol. 81, p. 109, 2009.
- [25] M. Wahl, "Time Correlated Single Photon Counting," [Online]. Available: https://www.picoquant.com/images/uploads/page/files/7253/technote_tcspc.pdf. [Accessed June 2016].
- [26] D. D. Martin and P. Verhoeve, "Superconducting Tunnel Junctions," *ISSI SR*, vol. 9, pp. 441-457, 2010.
- [27] [Online]. Available: <http://starcryo.com/stj-x-ray-spectrometers/>. [Accessed June 2016].
- [28] Princeton, "Josephson Junctions," [Online]. Available: <http://www.princeton.edu/~romalis/PHYS210/stj.htm>.
- [29] N. G. Czakon, A. Vaykonakis, J. Schlaerth, M. I. Hollister, S. Golwala, P. K. Day, J. S. Gao, J. Glenn, H. LeDuc, P. R. Maloney, B. Mazin, O. Noroozian, H. T. Nguyen, J. Sayers, J. E. Vaillancourt and J. Zmuidzinas, "Microwave Kinetic Inductance Detector (MKID) Camera Testing for Submillimeter Astronomy," [Online]. Available: http://web.physics.ucsb.edu/~bmazin/Papers/preprint/czakon_LTD13.pdf. [Accessed June 2016].
- [30] B. A. Mazin, "Microwave Kinetic Inductance Detectors: The First Decade," in *AIP The Thirteenth International Workshop on Low Temperature Detectors*, Stanford, California, 2009.
- [31] S. Doyle, "Lumped Element Kinetic Inductance Detectors," [Online]. Available: http://www.astro.cardiff.ac.uk/~spxsmd/Lumped_Element_Kinetic_Inductance_Detectors.pdf. [Accessed April 2008].
- [32] S. White, M. Chiu, M. Diwan, G. Atoyan and V. Issakov, "Design of a 10 picosecond Time of Flight Detector using Avalanche Photodiodes," *Arxiv*, vol. <http://arxiv.org/abs/0901.2530>.
- [33] C. H. Tan, R. B. Gomes, J. P. David, A. M. Barnett, D. J. Bassford, J. E. Lees and J. Shien, "Avalanche Gain and Energy Resolution of Semiconductor X-Ray Detectors," *IEEE Transactions on Electron Devices*, vol. 58, no. 6, 2011.
- [34] Excelitas, "Avalanche photodiode - A user guide," [Online]. Available:

- http://www.excelitas.com/downloads/app_apd_a_user_guide.pdf. [Accessed June 2016].
- [35] T. Oshima, Y. Yamakawa, H. Kurabayashi, A. Hoshnino, Y. Ishisaki, T. Ohashi, K. Mitsuda and K. Tanaka, "A High Energy Resolution Gamma-Ray TES Microcalorimeter with Fast Response Time," *Journal of Low Temperature Physics*, vol. 151, pp. 430-435, 2008.
- [36] Figueroa Group, MIT, [Online]. Available: http://web.mit.edu/figueroagroup/ucal/ucal_tes/. [Accessed April 2015].
- [37] S.-F. Lee, J. M. Gildemeister, W. Holmes, A. T. Lee and P. L. Richards, "Voltage-biased superconducting transition-edge bolometer with strong electrothermal feedback operated at 370mK," *Applied Optics*, vol. 37, no. 16, pp. 3391-3397, 1998.
- [38] A. Bulter, "Single-Photon Counting Detectors for the Visible Range Between 300 and 1000nm," in *Springer Series on Fluorescence*, Springer, 2014, pp. 23-42.
- [39] K. Oba, H. Kume, K. Wakamori and K. Nakatsugawa, "MCP-PMTs as Ultra-fast Wide-band and Infrared-sensitive Detectors," *Advances in Electronics and Electron Physics*, vol. 74, pp. 87-96, 1988.
- [40] European Space Agency, [Online]. Available: <http://sci.esa.int/sci-fmi/36783-optical-droids/?secured=-1>. [Accessed March 2017].
- [41] A. Monfardini, A. Benoit, A. Bideaud, L. Swenson, A. Cruciani, P. Camus, C. Hoffmann, F. X. Deser, S. Doyle, P. Ade, P. Mauskopf, C. Tucker, M. Roesch, S. Leclercq, K. F. Schuster, A. Endo, A. Baryshev, J. J. A. Baselmans, L. Ferrari, S. J. C. Yates, O. Bourrion, J. Macias-Perez, C. Vescovi, M. Calvo and C. Giordano, "A Dual-Band Millimeter-Wave Kinetic Inductance Camera for the IRAM 30m Telescope," *The Astrophysical Journal Supplementary Series*, vol. 194, no. 24, 2011.
- [42] J. van Rantwijk, M. Grim, D. van Loon, S. Yates, A. Baryshev and J. Baselmans, "Multiplexed Readout for 1000-pixel Arrays of Microwave Kinetic Inductance Detectors," *IEEE Transactions on Microwave Theory and Techniques*, vol. 64, no. 6, pp. 1876-1883, 2016.
- [43] P. K. Day, H. G. LeDuc, B. A. Mazin, A. Vayonakis and J. Zmuidzinas, "A broadband superconducting detector suitable for use in large arrays," *Nature*, vol. 425, pp. 817-821, 2003.
- [44] F. Xia, "Electrons en masse," *Nature Nanotechnology*, vol. 9, pp. 575-576, 2014.
- [45] H. Yoon, C. Forsythe, L. Wang, N. Tombros, K. Watanabe, T. Taniguchi, J. Hone, P. Kim and D. Ham, "Measurement of Collective Dynamical Mass of Dirac Fermions in Graphene," *Nature Nanotechnology*, vol. 9, pp. 594-599, 2014.
- [46] A. E. Lita, A. J. Miller and S. W. Nam, "Counting near-infrared single-photons with 95% efficiency," *International Online Journal of Optics*, vol. 16, no. 5, pp. 3032-3040, 2008.
- [47] [Online]. Available: <https://micro.magnet.fsu.edu/primer/digitalimaging/concepts/photomultipliers.html>. [Accessed 2016 April 8].
- [48] Hamamatsu, "X-Ray Detector Handbook," [Online]. Available: https://www.hamamatsu.com/resources/pdf/ssd/e09_handbook_xray_detectors.pdf. [Accessed 8 April 2016].
- [49] G. Llosa, N. Belcari, M. G. Bisogni, G. Collazuol, S. Marcatili, S. Moehrs, F. Morsani, C. Piemonte and A. Del Guerra, "Energy and Timing Resolution Studies with Silicon Photomultipliers (SiPM) and 4-Pixel SiPM Matrices for PET," *IEEE Transactions on Nuclear Science*, vol. 56, no. 3, pp. 543-548, 2009.
- [50] H. Matsuo, "Photon Statistics for Space Terahertz Astronomy," 2014. [Online]. Available: <http://www.nrao.edu/meetings/isstt/papers/2014/2014067000.pdf>. [Accessed January

- 2016].
- [51] H. Matsuo, 2014. [Online]. Available: http://fisica.iaps.inaf.it/2014-02-15-Fisica-Presentations/pres_FISICA-Matsuo.pdf. [Accessed January 2016].
 - [52] H. Matsuo, "Requirements on Photon Counting Detectors for Terahertz Interferometry," *Journal of Low Temperature Physics*, vol. 167, no. 5, pp. 840-845, 2012.
 - [53] E. Hajime, F. Go, M. Hiroshi, S. Shigetomo and U. Masahiro, "SIS Detectors for Terahertz Photon Counting System," in *16th International Workshop on Low Temperature Detectors*, Grenoble, 2015.
 - [54] C. B. McKittrick, D. E. Prober and B. S. Karasik, "Performance of Graphene Thermal Photon Detectors," *Journal of Applied Physics*, vol. 113, 2013.
 - [55] K. J. Tielrooij, L. Piatkowski, M. Massicotte, A. Woessner, Q. Ma, Y. Lee, K. S. Myrho, C. N. Lau, P. Jarillo-Herrero, N. F. van Hulst and F. H. L. Koppens, "Generation of photovoltage in graphene on a femtosecond timescale through efficient carrier heating," *Nature Nanotechnology*, vol. doi:10.1038/nnano.2015.54, 2015.
 - [56] D. W. Boukhvalov, M. I. Katsnelson and A. I. Lichtenstein, "Hydrogen on graphene: Electronic structure, total energy, structure distortions and magnetism from first-principles calculations," *Physical Review B*, vol. 77, no. 035427, 2008.
 - [57] M. Dresselhaus, "From Graphene to Graphite to Nanotubes to Graphene," 2008. [Online]. Available: http://www.graphene.gatech.edu/publications/APS_08_Graphene_Tutorial_Dresselhaus.pdf. [Accessed April 2015].
 - [58] M. Hoppner, S. Seiro, A. Chikina, A. Fedorov, M. Guttler, S. Danzenbacher, A. Generalov, K. Kummer, S. Patil, S. L. Molodtsov, Y. Kucherenko, C. Geibel, V. N. Strocov, M. Shi, M. Radovic, T. Schmitt, C. Laubschat and D. V. Vyalikh, "Interplay of Dirac fermions and heavy quasiparticles in solids," *arXiv:1301.0729v*, 2013.
 - [59] M. I. Katsnelson, "Minimal Conductivity in Bilayer Graphene," *European Physical Journal*, vol. 52, pp. 151-153, 2006.
 - [60] N. Walet, "Advanced Quantum Mechanics 2 - Graphene," University of Manchester, [Online]. Available: <http://oer.physics.manchester.ac.uk/AQM2/Notes/Notes-6.4.html#toc-Section-6.4>. [Accessed May 2014].
 - [61] J. D. Bjorken and S. D. Drell, *Relativistic Quantum Mechanics*, New York: McGraw-Hill, 1964.
 - [62] R. S. Deacon, K. C. Chuang, R. J. Nicholas, K. S. Novoselov and A. K. Geim, "Cyclotron resonance study of the electron and hole velocity in graphene monolayers," *Physical Review B*, vol. 76, no. 081406, 2007.
 - [63] D. C. Elias, R. V. Gorbachev, A. S. Mayorov, S. V. Morozov, A. A. Zhukov, P. Blake, L. A. Ponomarenko, I. V. Grigorieva, K. S. Novoselov, F. Guinea and A. K. Geim, "Dirac cones reshaped by interaction effects in suspended graphene," *Nature Physics*, vol. DOI:10.1038, p. 701, 2011.
 - [64] S. Das Sarma, S. Adam, E. H. Hwang and E. Rossi, "Electronic transport in two dimensional graphene," *Review of Modern Physics*, vol. 83, no. 407, 2011.
 - [65] Y. Zhang, T.-T. Tang, C. Girit, Z. Hao, M. C. Martin, A. Zettl, M. F. Crommie, Y. R. Shen and F. Wang, "Direct Observation of a Widely Tunable Bandgap in Bilayer Graphene," *Nature*, vol. 459, pp. 820-823, 2009.
 - [66] C. J. Nicol and E. J. Tabert, "Dynamical conductivity of AA-stacked bilayer graphene," *Phys Rev B*, vol. 86, no. 075439, 2012.
 - [67] K. M. Borysenko, J. T. Mullen, X. Li, Y. G. Semenov, J. M. Zavada, M. Burongirano Nardelli and K. W. Kim, "Electron-phonon interactions in bilayer graphene," *Physical Review B*,

vol. 83, no. 161402, 2011.

- [68] F. Yavari, C. Kritzinger, C. Gaire, L. Song, H. Gullapalli, T. Borca-Tasciuc, P. M. Ajayan and N. Koratkar, "Tunable Bandgap in Graphene by the Controlled Adsorption of Water Molecules," *Small*, vol. 6, no. 22, pp. 2535-2538, 2010.
- [69] R. Balog, B. Jorgensen, L. Nilsson, M. Andersen, E. Rienks, M. Bianchi, M. Fanetti, E. Laegsgaard, A. Baraldi, S. Lizzit, Z. Sljivancanin, F. Besenbacher, B. Hammer, T. G. Pedersen, P. Hofmann and L. Hornekaer, "Bandgap Opening in Graphene Induced by Patterned Hydrogen Adsorption," *Nature Materials*, vol. 9, pp. 315-319, 2010.
- [70] J.-K. Lee, S. Yamazaki, H. Yun, J. Park, G. P. Kennedy, G.-T. Kim, O. Pietzsch, R. Wiesendanger, S. Lee, S. Hong, U. Detlaff-Weglikowska and S. Roth, "Modification of Electrical Properties of Graphene by Substrate-Induced Nanomodulation," *Nano*, no. 13, pp. 3494-3500, 2013.
- [71] W. Zhang, C.-T. Lin, K.-K. Liu, T. Tite, C.-Y. Su, C.-H. Chang, Y.-H. Lee, C.-W. Chu, K.-H. Wei, J.-L. Kuo and L.-J. Li, "Opening an Electrical Band Gap of Bilayer Graphene with Molecular Doping," *Nano*, vol. 5, no. 9, pp. 7517-7524, 2011.
- [72] J. B. Oostinga, H. B. Heersche, X. Liu, A. F. Morpurgo and L. M. Vandersypen, "Gate-induced insulating state in bilayer graphene devices," *Nature*, vol. 7, 2008.
- [73] A. A. Sagade, D. Neumaier, D. Schall, M. Otto, A. Pesquera, A. Centeno, A. Zurutuza Elorza and H. Kurz, "Highly air stable passivation of graphene based field effect devices," *Nanoscale*, vol. 7, pp. 3558-3564, 2015.
- [74] O. Koybasi, I. Childres, I. Jovanovic and Y. Chen, "Design and Simulation of a Graphene DEPFET Detector," *IEEE Nuclear Science Symposium and Medical Imaging Conference Record*, p. 4249, 2012.
- [75] A. Patil, O. Koybasi, G. Lopez, M. Foxe, I. Childres, C. Roecker, J. Boguski, J. Gu, M. L. Bolen, M. A. Capano, P. Ye, I. Jovanovic and Y. P. Chen, "Graphene Field Effect Transistor as Radiation Sensor," *IEEE*, p. 455, 2011.
- [76] B. Zhan, C. Li, J. Yang, G. Jenkins, W. Huang and X. Dong, "Graphene Field-Effect Transistor and Its Application for Electronic Sensing," *Small*, vol. 10, no. 20, pp. 4042-4065, 2014.
- [77] M. Foxe, E. Cazalas, H. Lamm, A. Majcher, C. Piotrowski, I. Childres, A. Patil, Y. P. Chen and I. Jovanovic, "Graphene-Based Neutron Detectors," *IEEE*, p. 352, 2011.
- [78] M. Foxe, G. Lopez, I. Childres, R. Jalilian, C. Roecker, J. Boguski, I. Jovanovic and Y. P. Chen, "Detection of Ionizing Radiation Using Graphene Field Effect Transistors," *IEEE*, p. 90, 2009.
- [79] Z. A. Van Veldhoven, J. A. Alexander-Webber, A. A. Sagade, P. Braeuninger-Weimer and S. Hofmann, "Electronic properties of CVD graphene: The role of grain boundaries, atmospheric doping and encapsulation by ALD," *Phys. Stat. Sol. B*, vol. 253, no. 12, 2016.
- [80] M. Foxe, G. Lopez, I. Childres, A. Patil, C. Roecker, J. Boguski, I. Jovanovic and Y. P. Chen, "Graphene Field-Effect Transistors on Undoped Semiconductor Substrates for Radiation Detectors," *IEEE Transactions on Nanotechnology*, vol. 11, no. 3, pp. 581-587, 2012.
- [81] I. Jovanovic, E. Cazalas, I. Childres, A. Patil, O. Koybasi and Y. P. Chen, "Graphene field effect transistor-based detectors for detection of ionising radiation," in *2013 3rd International Conference on Advancements in Nuclear Instrumentation, Measurement Methods and Their Applications, ANIMMA 2013*, 2013.
- [82] O. Koybasi, E. Cazalas, I. Childres, I. Jovanovic and Y. P. Chen, "Detection of light, X-rays and gamma rays using graphene field effect transistors fabricated on SiC, CdTe and AlGaAs/GaAs substrates," *IEEE Nuclear Science Symposium Conference Record*, 2013.
- [83] O. Koybasi, I. Childres, I. Jovanovic and Y. P. Chen, "Graphene field effect transistor as a

- radiation and photo detector," *Proceedings of SPIE - The International Society for Optical Engineering*, 2012.
- [84] V. Vyurkov and V. Ryzhii, "Effect of Coulomb scattering on graphene conductivity," *arXiv:0807.3880*, 2008.
- [85] N. F. Mott, *Metal-Insulator Transitions*, London: Taylor & Francis, 1974.
- [86] N. F. Mott and E. A. Davis, *Electron-Processes in Non-Crystalline Materials*, Oxford: Clarendon, 1979.
- [87] M. I. Katsnelson, "Zitterbewegung, chirality, and minimal conductivity in graphene," *European Physical Journal B*, vol. 51, pp. 157-160, 2006.
- [88] Y. M. Blanter and M. Buttiker, "Shot Noise in Mesoscopic Conductors," *Physics Reports*, vol. 336, no. 1, 2000.
- [89] K. Zou, X. Hong and J. Zhu, "Effective mass of electrons and holes in bilayer graphene: Electron-hole asymmetry and electron-electron interaction," *Physical Review B*, vol. 84, no. 085408, 2011.
- [90] K. I. Bolotin, K. J. Sikes, J. Hone, H. L. Stormer and P. Kim, "Temperature-Dependent Transport in Suspended Graphene," *Physical Review Letters*, vol. 101, no. 096802, 2008.
- [91] J. M. Ziman, *Electrons and Phonons. The Theory of Transport Phenomena*, Oxford: Oxford University Press, 2001.
- [92] S. V. Morozov, K. S. Novoselov, M. I. Katsnelson, F. Schedin, D. C. Elias, J. A. Jaszczak and A. K. Geim, "Giant Intrinsic Carrier Mobilities in Graphene and Its Bilayer," *Physical Review Letters*, vol. 100, no. 016602, 2008.
- [93] M. Koshino and T. Ando, "Transport in bilayer graphene: Calculations within a self-consistent Born approximation," *Physical Review B*, vol. 73, no. 245403, 2006.
- [94] M. I. Katsnelson, F. Guinea and A. K. Geim, "Scattering of electrons in graphene by clusters of impurities," *Physical Review B*, vol. 79, no. 195426, 2009.
- [95] M. Hofmann, Y.-P. Hsieh, K.-W. Chang, H.-G. Tsai and T.-T. Chen, "Dopant morphology as the factor limiting graphene conductivity," *Scientific Reports*, vol. 5, no. 17393, 2015.
- [96] F. Kadi, T. Winzer, A. Knorr and E. Malic, "Impact of doping on the carrier dynamics in graphene," *Scientific Reports*, vol. 5, no. 16841, 2015.
- [97] C. R. Dean, A. F. Young, I. Meric, C. Lee, L. Wang, S. Sorgenfrei, K. Watanabe, T. Taniguchi, P. Kim, K. L. Shepard and J. Hone, "Boron nitride substrates for high-quality graphene electronics," *Nature Nanotechnology*, vol. 5, pp. 722-726, 2010.
- [98] E. Mariani and F. von Oppen, "Flexural phonons in free-standing graphene," *Physical Review Letters*, vol. 100, no. 076801, 2008.
- [99] E. Mariani and F. von Oppen, "Temperature-dependent resistivity of suspended graphene," *Physical Review B*, vol. 82, no. 195403, 2010.
- [100] F. Amet, J. R. Williams, K. Watanabe, T. Taniguchi and D. Goldhaber-Gordon, "Insulating Behavior at the Neutrality Point in Single-Layer Graphene," *Physical Review Letters*, vol. 110, no. 216601, 2013.
- [101] L. Dong, J. Hansen, P. Xu, M. L. Ackerman, S. D. Barber, J. K. Schoelz, D. Qi and P. M. Thibado, "Electromechanical properties of freestanding graphene functionalised with tin oxide (SnO₂) nanoparticles," *Applied Physics Letters*, vol. 101, no. 061601, 2012.
- [102] S. Yuan, H. De Raedt and M. I. Katsnelson, "Modelling electronic structure and transport properties of graphene with resonant scattering centres," *Physics Review B*, vol. 82, no. 115448, 2010.
- [103] B. DeMarco, S. B. Papp and D. S. Jin, "Pauli Blocking of Collisions in a Quantum Degenerate Atomic Fermi Gas," *Physical Review Letters*, vol. 86, no. 24, pp. 5409-5412,

2001.

- [104] A. N. Grigorenko, M. Polini and K. S. Novoselov, "Graphene plasmonics," *Nature Photonics*, vol. 6, p. 749, 2012.
- [105] L. A. Falkovsky, "Optical Properties of Graphene," *Journal of Physics: conference Series*, vol. 129, no. 012004, 2008.
- [106] F. Wang, Y. Zhang, C. Tian, C. Girit, A. Zettl, M. Crommie and Y. Ron Shen, "Gate-Variable Optical Transitions in Graphene," *Science*, vol. 320, pp. 206-208, 2008.
- [107] P. Blake, E. W. Hill, A. H. Castro Neto, K. S. Novoselov, D. Jiang, R. Yang, T. J. Booth and A. K. Geim, "Making graphene visible," *Applied Physics Letters*, vol. 91, no. 063124, 2007.
- [108] Y. Liu, R. Cheng, L. Liao, H. Zhou, J. Bai, G. Liu, L. Liu, Y. Huang and X. Duan, "Plasmon resonance enhance multicolour photodetection by graphene," *Nature Communications*, vol. 2, no. 579, 2011.
- [109] F. Xia, T. Mueller, R. Golizadeh-Mojarad, M. Freitag, Y.-m. Lin, J. Tsang, V. Perebeinos and P. Avouris, "Photocurrent Imaging and Efficient Photon Detection in a Graphene Transistor," *Nano Letters*, vol. 9, no. 3, pp. 1039-1044, 2009.
- [110] T. Mueller, F. Xia and P. Avouris, "Graphene photodetectors for high-speed optical communications," *Nature Photonics*, vol. 4, pp. 297-301, 2010.
- [111] F. Rana, "Graphene Terahertz Plasmon Oscillators," *IEEE Transactions on Nanotechnology*, vol. 7, no. 1, pp. 91-99, 2008.
- [112] E. Pop, V. Varshney and A. K. Roy, "Thermal Properties of Graphene: Fundamentals and Applications," *MRS Bulletin*, vol. 37, pp. 1273-1280, 2012.
- [113] A. C. Ferrari and D. M. Basko, "Raman Spectroscopy as a versatile tool for studying the properties of graphene," *Nature Nanotechnology*, vol. 8, pp. 235-246, 2013.
- [114] P. H. Tan, W. P. Han, W. J. Zhao, Z. H. Wu, K. Chang, H. Wang, N. Bonini, N. Marzari, N. Pugno, G. Savini, A. Lombardo and A. C. Ferrari, "The shear mode of multilayer graphene," *Nature Materials*, vol. 11, no. 4, pp. 294-300, 2012.
- [115] S. Milana, "Determination of shear modulus and out of plane Young's modulus of layered materials by raman spectroscopy," Lausanne, 2015.
- [116] F. H. L. Koppens, T. Mueller, P. Avouris, A. C. Ferrari, M. S. Vitiello and M. Polini, "Photodetectors based on graphene, other two-dimensional materials and hybrid systems," *Nature Nanotechnology*, vol. 9, no. DOI: 10.1038, pp. 780-793, 2014.
- [117] S. A. Jensen, K.-J. Tielrooij, F. Koppens and M. Bonn, "Hot Carrier Multiplication in Graphene".
- [118] T. Winzer and E. Malic, "Impact of Auger Processes on Carrier Dynamics in Graphene," *Physical Review B*, vol. 85, 2012.
- [119] T. Winzer, A. Knorr and E. Malic, "Carrier Multiplication in Graphene," 2010.
- [120] D. De Fazio, I. Goykhman, M. Bruna, A. Eiden, S. Milana, D. Yoon, U. Sassi, M. Barbone, D. Dumcenco, K. Marinov, A. Kis and A. C. Ferrari, "High Responsivity, Large-Area Graphene/MoS2 Flexible Photodetectors," *Arxiv*, p. <http://arxiv.org/pdf/1512.08312v1.pdf>, 2015.
- [121] J. C. W. Song, M. S. Rudner, C. M. Marcus and L. S. Levitov, "Hot Carrier Transport and Photocurrent Response in Graphene," *Nano Letters*, vol. 11, pp. 4688-4692, 2011.
- [122] J. Yan, M. H. Kim, J. A. Elle, A. B. Sushkov, G. S. Jenkins, H. M. Milchberg, M. S. Fuhrer and H. D. Drew, "Dual-gated bilayer graphene hot-electron bolometer," *Nature Nanotechnology*, vol. 7, pp. 472-478, 2012.
- [123] A. Tomadin, A. Tredicucci, V. Pellegrini, M. S. Vitiello and M. Polini, "Photocurrent-based

- detection of Terahertz radiation in graphene," *Applied Physics Letters*, vol. 103, no. 211120, 2013.
- [124] L. Vicarelli, M. S. Vitiello, D. Coquillat, A. Lombardo, A. C. Ferrari, W. Knap, M. Polini, V. Pellegrini and A. Tredicucci, "Graphene field effect transistors as room-temperature Terahertz detectors," *Nature Materials*, vol. 11, no. 865, 2012.
- [125] E. Cazalas, B. K. Sarker, M. E. Moore, I. Childres, Y. P. Chen and I. Jovanovic, "Position sensitivity of graphene field effect transistors to X-rays," *Applied Physics Letters*, vol. 106, no. 223503, 2015.
- [126] F. Xia, T. Mueller, Y.-M. Lin, A. Valdes-Garcia and P. Avouris, "Ultrafast Graphene Photodetector," *Nature*, vol. 4, pp. 839-843, 2009.
- [127] F. Hetsch, N. Zhao, S. V. Kershaw and A. L. Rogach, "Quantum Dot Field Effect Transistors," *Materials Today*, vol. 16, no. 9, pp. 312-325, 2013.
- [128] P. J. Jeon, Y. T. Lee, J. Y. Lim, J. S. Kim, D. K. Hwang and S. Im, "Black Phosphorus-Zinc Oxide Nanomaterial Heterojunction for p-n Diode and Junction Field Effect Transistor," *Nano Letters*, vol. 16, pp. 1293-1298, 2016.
- [129] M. Bucsema, D. J. Groenendijk, S. L. Blanter, G. A. Steele, H. S. van den Zant and A. Castellanos-Gomez, "Fast and Broadband Photoresponse of Few-Layer Black Phosphorus Field Effect Transistors," *Nano Letters*, vol. 14, no. 3347-3352, 2014.
- [130] Y. Zhang, T. Liu, B. Meng, X. Li, G. Liang, X. Hu and Q. J. Wang, "Broadband High Photoresponse from Pure Monolayer Graphene Photodetector," *Nature Communications*, vol. 4, no. 1811, 2013.
- [131] Excelitas, [Online]. Available: <http://www.excelitas.com/Pages/Product/Avalanche-Photodiodes-for-Near-Infrared-NIR-950-nm-1-4-um.aspx>. [Accessed April 2018].
- [132] X. Chen, C. Ding, H. Pan, K. Huang, J. Laurat, G. Wu and E. Wu, "Temporal and spatial multiplexed infrared single-photon counter based on high-speed avalanche photodiode," *Scientific Reports*, vol. 7, p. 4600, 2017.
- [133] X. Cai, A. B. Sushkov, R. J. Suess, M. M. Jadidi, G. S. Jenkins, L. O. Nyakiti, R. L. Myers-Ward, S. Li, J. Yan, D. K. Gaskill, T. E. Murphy, H. D. Drew and M. S. Fuhrer, "Sensitive Room-Temperature Terahertz Detection via Photothermoelectric Effect in Graphene," *Nature Nanotechnology*, 2014.
- [134] D. S. Jessop, S. J. Kindness, L. Xiao, P. Braeuninger-Weimer, H. Lin, Y. Ren, C. X. Ren, S. Hofmann, J. A. Zeitler, H. E. Beere, D. A. Ritchie and R. Degl'Innocenti, "Graphene based plasmonic terahertz amplitude modulator operating above 100MHz," *Applied Physics Letters*, vol. 108, no. 171101, 2016.
- [135] B. S. Karasik, A. V. Sergeev and D. E. Prober, "Nanobolometers for THz Photon Detection," *Arxiv*, 2011.
- [136] D. T. Gillespie, "Exact Stochastic Simulation of Coupled Chemical Reactions," *The Journal of Physical Chemistry*, vol. 81, no. 25, 1977.
- [137] K. M. Borysenko and J. T. Mullen, "First Principles Analysis of Electron-Phonon Interactions in Graphene," 2009.
- [138] M. Saeidmanesh, M. H. Ghadiry, M. Khaledian, M. J. Kiani and R. Ismail, "Carrier scattering and impact ionisation in bilayer graphene," *Journal of Computational Electronics*, vol. 13, pp. 180-185, 2014.
- [139] G. W. Fraser, A. F. Abbey, A. Holland, K. McCarthy, A. Owens and A. Wells, "The X-Ray Energy Response of Silicon Part A. Theory," *Nuclear Instruments and Methods in Physics Research*, vol. 350, pp. 368-378, 1994.
- [140] E. J. Nicol and J. P. Carbotte, "Optical conductivity of bilayer graphene with and without an asymmetry gap," *Arxiv*, p. 0801.1836v2, 2013.

- [141] F. J. Garcia de Abajo, "Multiple Excitation of Confined Graphene Plasmons by Single Free Electrons," vol. arXiv:1311.4690v, 2013.
- [142] K. J. Tielrooij, J. C. W. Song, S. A. Jensen, A. Centeno, A. Pesquera, A. Zurutuza, M. Bonn, L. S. Levitov and F. H. L. Koppens, "Photoexcitation cascade and multiple hot-carrier generation in graphene," *Nature Physics*, vol. DOI:10.1038/NPHYS2564, 2013.
- [143] European Space Agency, "Future Missions Preparations Office," [Online]. Available: <http://sci.esa.int/science-e/www/object/index.cfm?fobjectid=41034>.
- [144] University of Heidelberg, [Online]. Available: http://www.kip.uni-heidelberg.de/~coulon/Lectures/Detectors/Free_PDFs/Lecture10.pdf. [Accessed May 2014].
- [145] M. R. Connolly, E. D. Herbschleb, R. K. Puddy, M. Roy, D. Anderson, G. A. C. Jones, P. Makysym and C. G. Smith, "Reading and Writing Charge on Graphene Devices," no. <http://arxiv.org/abs/1111.0560>, 2011.
- [146] NIST, [Online]. Available: <https://www.nist.gov/pml/engineering-physics-division/hall-effect>. [Accessed December 2017].
- [147] OSA Publishing, [Online]. Available: <https://www.osapublishing.org/oe/fulltext.cfm?uri=oe=19=17=16244&id=221720>. [Accessed September 2015].
- [148] D. Ginley, H. Hosono and D. C. Paine, *Handbook of Transparent Conductors*, Springer Science and Business, 2010.
- [149] S. Boubanga-Tombet, F. Teppe, D. Coquillat, S. Nadar, N. Dyakonova, H. Videlier, W. Knap, A. Shchepetov, C. Gardes, Y. Roelens, S. Bollaet, D. Seliuta, R. Vadoklis and G. Valusis, "Current driven resonant plasma wave detection of terahertz radiation: Toward the Dyakonov-Shur instability," *Applied Physics Letters*, vol. 92, no. 212101, 2008.
- [150] A. Tomadin and M. Polini, "Theory of the Plasma-wave Photoresponse of a Gated Graphene Sheet," *Arxiv*, no. <https://arxiv.org/pdf/1307.0734.pdf>, 2013.
- [151] W. Knap, M. I. Dyakonov, D. Coquillat, F. Teppe, N. Dyakanova, J. Lusakowski, K. Karpierz, M. Sakowicz, G. Valusis, D. Seliuta, I. Kasalynas, A. El Fatimy, Y. M. Meziani and T. Otsuji, "Field Effect Transistors for Terahertz Detection: Physics and First Imaging Applications," *Journal of Infrared, Millimeter and Terahertz Waves*, vol. 30, no. 12, 2009.
- [152] W. Knap, S. Romyantsev, M. S. Vitiello, D. Coquillat, S. Blin, N. Dyakanova, M. Shur, F. Teppe, A. Tredicucci and T. Nagatsuma, "Nanometer size field effect transistors for terahertz detectors," *Nanotechnology*, vol. 24, no. 214002, 2013.
- [153] University of Colorado, [Online]. Available: https://www.colorado.edu/physics/phys4340/phys4340_sp09/notes/Drude%20notes.pdf. [Accessed December 2017].
- [154] M. Freitag, T. Low, F. Xia and P. Avouris, "Photoconductivity of biased graphene," *Nature Photonics*, vol. 7, pp. 53-59, 2013.
- [155] Y. Mushiaki. [Online]. Available: <http://www.sm.rim.or.jp/~ymushiak/sub.musrelation.html>. [Accessed December 2017].
- [156] "Antenna Theory," [Online]. Available: <http://www.antenna-theory.com/antennas/wideband/log-periodic.php>. [Accessed 7 April 2016].
- [157] [Online]. Available: http://www.ece.ucsb.edu/~long/ece145a/Notes4_Sparams.pdf. [Accessed December 2017].
- [158] Sonnet Software Inc, [Online]. Available: <https://www.sonnetsoftware.com/products/lite/>. [Accessed December 2017].
- [159] T. S. Bird, N. Rypkema and K. W. Smart, "Antenna Impedance Matching for Maximum

- Power Transfer in Wireless Sensor Networks,” in *IEEE Sensors*, 2009.
- [160] [Online]. Available: <http://www.antenna-theory.com/basics/impedance.php>. [Accessed December 2017].
- [161] J. W. Adkisson, T. J. Dunbar, J. P. Gambino, M. J. Leitch and E. J. Nowak, “Graphene Field Effect Transistor”. United States Patent US 8,673,683 B2, 18 March 2014.
- [162] Ketek GmbH, [Online]. Available: <https://www.ketek.net/sdd/technology/working-principle/>. [Accessed December 2017].
- [163] Amptek, [Online]. Available: <http://amptek.com/silicon-drift-detector-application-note/>. [Accessed December 2017].
- [164] F. Schedin, A. K. Geim, S. V. Morozov, E. W. Hill, P. Blake, M. I. Katsnelson and K. S. Novoselov, “Detection of individual gas molecules absorbed on graphene,” *Nature Materials*, vol. 6, pp. 652-655, 2007.
- [165] [Online]. Available: <http://fismed.ciemat.es/GAMOS/>. [Accessed December 2017].
- [166] [Online]. Available: <http://www.gel.usherbrooke.ca/casino/What.html>. [Accessed December 2017].
- [167] [Online]. Available: <https://www.comsol.com/>. [Accessed December 2017].
- [168] I. Meric, M. Y. Han, A. F. Young, B. Ozyilmaz, P. Kim and K. L. Shepard, “Current saturation in zero-bandgap, top-gated graphene field effect transistors,” *Nature Nanotechnology*, 2008.
- [169] V. Ryzhii, M. Ryzhii and T. Otsuji, “Thermionic and tunneling transport mechanisms in graphene field-effect transistors,” *Physica Status Solidi*, vol. 205, no. 7, pp. 1527-1533, 2008.
- [170] C.-C. Lu, Y.-C. Lin, C.-H. Yeh, J.-C. Huang and P.-W. Chiu, “High Mobility Flexible Graphene Field-Effect Transistors with Self-Healing Gate Dielectrics,” *ACS Nano*, vol. 6, no. 5, pp. 4469-4474, 2012.
- [171] X. Hong, A. Posadas, K. Zou, C. H. Ahn and J. Zhu, “High-Mobility Few-Layer Graphene Field Effect Transistors Fabricated on Epitaxial Ferroelectric Gate Oxides,” *Physical Review Letters*, vol. 102, no. 136808, 2009.
- [172] B. J. Kim, H. Jang, S.-K. Lee, B. H. Hong, J.-H. Ahn and J. H. Cho, “High-Performance Flexible Graphene Field Effect Transistors with Ion Gel Gate Dielectrics,” *Nanoletters*, vol. 10, pp. 3464-3466, 2010.
- [173] P. Ramnani, M. R. Neupane, S. Ge, A. A. Balandin, R. K. Lake and A. Mulchandani, “Raman spectra of twisted CVD bilayer graphene,” *Carbon*, vol. 123, pp. 302-306, 2017.
- [174] J. Song, T. Y. Ko and S. Ryu, “Raman Spectroscopy Study of Annealing-Induced Effects on Graphene Prepared by Micromechanical Exfoliation,” *Bulletin on Korean Chemical Society*, vol. 31, no. 2679, 2010.
- [175] X. F. Fan, W. T. Zheng, V. Chihai, Z. X. Shen and J.-L. Kuo, “Interaction between graphene and the surface of SiO₂,” *Journal of Physics: Condensed Matter*, vol. 305004, 2012.
- [176] S. Hofmann, P. Braeuninger-Weimer and R. S. Weatherup, “CVD-Enabled Graphene Manufacture and Technology,” *Journal of Physical Chemistry Letter*, vol. 6, pp. 2714-2721, 2015.
- [177] K. E. Whitener and P. E. Sheehan, “Graphene Synthesis,” *Diamond and Related Materials*, vol. 46, pp. 25-34, 2004.
- [178] W. A. de Heer, C. Berger, X. Wu, P. N. First, E. H. Conrad, X. Li, T. Li, M. Sprinkle, J. Hass, M. L. Sadowski, M. Potemski and G. Martinez, “Epitaxial Graphene,” *Solid State Communications*, vol. 143, no. 92, 2007.

- [179] N. Camara, G. Rius, J. R. Huntringer, A. Tiberj, N. Mestres, P. Godignon and J. Camassel, "Selective epitaxial growth of graphene on SiC," *Applied Physics Letters*, vol. 93, 2008.
- [180] P. W. Sutter, J.-I. Flege and E. A. Sutter, "Epitaxial graphene on ruthenium," *Nature Materials*, vol. 7, pp. 406-411, 2008.
- [181] M. Suemitsu and H. Fukidome, "Epitaxial graphene on silicon substrates," *Journal of Physics D: Applied Physics*, vol. 43, no. 374012, 2010.
- [182] M. Ruan, Y. Hu, Z. Guo, R. Dong, J. Palmer, J. Hankinson, C. Berger and W. A. de Heer, "Epitaxial graphene on silicon carbide: Introduction to structured graphene," *MRS Bulletin*, vol. 37, no. 12, pp. 1138-1147, 2012.
- [183] S. P. Cooil, F. Song, G. T. Williams, O. R. Roberts, D. P. Langstaff, B. Jorgensen, K. Hoydalsvik, D. W. Breiby, E. Wahlstrom, D. A. Evans and J. W. Wells, "Iron-mediated growth of epitaxial graphene on SiC and diamond," *Carbon*, vol. 50, no. 14, pp. 5099-5105, 2012.
- [184] S. P. Cooil, J. W. Wells, D. Hu, Y. R. Niu, A. A. Zakharov, M. Bianchi and D. A. Evans, "Controlling the growth of epitaxial graphene on metalized diamond (111) surface," *Applied Physics Letters*, vol. 107, no. 18, p. 181603, 2015.
- [185] J. Huang, J. A. Alexander-Webber, T. J. B. M. Janssen, A. Tzakenchuk, T. Yager, S. Lara-Avila, S. Kubatkin, R. L. Myers-Ward, V. D. Wheeler and D. K. Gaskill, "Hot carrier relaxation of Dirac fermions in bilayer epitaxial graphene," *Journal of Physics: Condensed Matter*, vol. 27, no. 16, 2015.
- [186] C. Melios, V. Panchal, C. E. Giusca, W. Strupinski, S. R. P. Silva and O. Kazakova, "Carrier type inversion in quasi-free standing graphene: studies of local electronic and structural properties," *Scientific Reports*, vol. 5, 2015.
- [187] Y.-P. Lin, Y. Ksari and J.-M. Themlin, "Hydrogenation of the buffer-layer graphene on 6H-SiC(0001): A possible route for the engineering of graphene-based devices," *Nano Research*, vol. 8, no. 3, pp. 839-850, 2015.
- [188] Nature Nanotechnology, "Ten years in two dimensions," *Nature Nanotechnology*, vol. 9, p. 725, 2014.
- [189] J.-H. Lee, E. K. Lee, W.-J. Joo, Y. Jang, B.-S. Kim, J. Y. Lim, S.-H. Choi, S. J. Ahn, J. R. Ahn, M.-H. Park, C.-W. Yang, B. L. Choi, S.-W. Hwang and D. Whang, "Wafer-Scale Growth of Single-Crystal Monolayer Graphene on Reusable Hydrogen-Terminated Germanium," *Science*, vol. 344, no. 6181, pp. 286-289, 2014.
- [190] S. Caneva, R. S. Weatherup, B. C. Bayer, R. Blume, A. Cabrero-Vilatela, P. Braeuninger-Weimer, M.-B. Martin, R. Wang, C. Baehtz, R. Schloegl, J. C. Meyer and S. Hofmann, "Controlling Catalyst Bulk Reservoir Effects for Monolayer Hexagonal Boron Nitride CVD," *Nano Letters*, vol. 16, pp. 1250-1261, 2016.
- [191] M. Piquemal-Banci, R. Galceran, S. Caneva, M.-B. Martin, R. S. Weatherup, P. R. Kidambi, K. Bouzouane, S. Xavier, A. Anane, F. Petroff, A. Fert, J. Robertson, S. Hofmann, B. Dlubak and P. Seneor, "Magnetic tunnel junctions with monolayer hexagonal boron nitride tunnel barriers," *Applied Physics Letters*, vol. 108, p. 102404, 2016.
- [192] K. Kang, S. Xie, L. Huang, Y. Han, P. Y. Huang, K. F. Mak, C.-J. Kim, D. Muller and J. Park, "High-mobility three-atom-thick semiconducting films with wafer-scale homogeneity," *Nature*, vol. 520, pp. 656-660, 2015.
- [193] G. R. Bhimanapati, Z. Lin, V. Meunier, Y. Jung, J. Cha, S. Das, D. Xiao, Y. Son, M. S. Strano, V. R. Cooper, L. Liang, S. G. Louie, E. Ringe, W. Zhou, S. S. Kim, R. R. Naik, B. G. Sumpter, H. Terrones, F. Xia, Y. Wang, J. Zhu, D. Akinwande, N. Alem, J. A. Schuller, R. E. Schaak, M. Terrones and J. A. Robinson, "Recent Advances in Two-Dimensional Materials Beyond Graphene," *ACS Nano*, vol. 9, no. 12, pp. 11509-11539, 2015.

- [194] P. R. Kidambi, R. Blume, J. Kling, J. B. Wagner, C. Baehtz, R. S. Weatherup, R. Schloegl, B. C. Bayer and S. Hofmann, "In Situ Observations during Chemical Vapour Deposition of Hexagonal Boron Nitride on Polycrystalline Copper," *Chemistry of Materials*, vol. 26, no. 22, pp. 6380-6392, 2014.
- [195] S. Caneva, R. S. Weatherup, B. C. Bayer, B. Brennan, S. J. Spencer, K. Mingard, A. Cabrero-Vilatela, C. Baehtz, A. J. Pollard and S. Hofmann, "Nucleation Control for Large, Single Crystalline Domains of Monolayer Hexagonal Boron Nitride via Si-Doped Fe Catalysts," *Nanoletters*, vol. 15, pp. 1867-1875, 2015.
- [196] L. Fu, Y. Sun, N. Wu, R. G. Mendes, L. Chen, Z. Xu, T. Zhang, M. H. Rummeli, B. Rellinghaus, D. Pohl, L. Zhuang and L. Fu, "Direct Growth of MoS₂/h-BN Heterostructures via a Sulfide-Resistance Alloy," *ACS Nano*, vol. 10, no. 2, pp. 2063-2070, 2016.
- [197] J. Robinson, "Growing Vertical in the Flatland," *ACS Nano*, vol. 10, no. 1, pp. 42-45, 2016.
- [198] X. Liu, I. Balla, H. Bergeron, G. P. Campbell, M. J. Bedzyk and M. C. Hersam, "Rotationally Commensurate Growth of MOS₂ on Epitaxial Graphene," *ACS Nano*, vol. 10, no. 1, pp. 1067-1075, 2016.
- [199] G. Nandamuri, S. Roumimov and R. Solanki, "Chemical vapour deposition of graphene films," *Nanotechnology*, vol. 21, no. 145604, 2010.
- [200] A. Cabrero-Vilatela, R. S. Weatherup, P. Braeuninger-Weimer, S. Caneva and S. Hofmann, "Towards a general growth model for graphene CVD on transition metal catalysts," *Nanoscale*, vol. 8, pp. 2149-2158, 2016.
- [201] V. Babenko, A. T. Murdock, A. A. Koos, J. Britton, A. Crossley, P. Holdway, J. Moffat, J. Huang, J. A. Alexander-Webber, R. J. Nicholas and N. Grobert, "Rapid epitaxy-free graphene synthesis on silicidated polycrystalline platinum," *Nature Communications*, vol. 6, 2015.
- [202] T. Wu, X. Zhang, Q. Yuan, J. Xue, G. Lu, Z. Liu, H. Wang, H. Wang, F. Ding, Q. Yu, X. Xie and M. Jiang, "Fast growth of inch-sized single crystalline graphene from a controlled single nucleus on Cu-Ni alloys," *Nature Materials*, vol. 15, pp. 43-47, 2015.
- [203] R. Degl'Innocenti, D. S. Jessop, C. W. Sol, L. Xiao, S. J. Kindness, H. Lin, J. A. Zeitler, P. Braeuninger-Weimer, S. Hofmann, Y. Ren, V. S. Kamboj, J. P. Griffiths, H. E. Beere and D. A. Ritchie, "Fast Modulation of Terahertz Quantum Cascade Lasers Using Graphene Loaded Plasmonic Antennas," *ACS Photonics*, vol. 3, pp. 464-470, 2016.
- [204] M. Batzill, "The surface science of graphene: Metal interfaces, CVD synthesis, nanoribbons, chemical modifications and defects," *Surface Science Reports*, vol. 67, pp. 83-115, 2012.
- [205] Y. Hao, L. Wang, Y. Liu, H. Chen, X. Wang, C. Tan, S. Nie, J. W. Suk, T. Jiang, T. Liang, J. Xiao, W. Ye, C. R. Dean, B. I. Yakobson, K. F. McCarty, P. Kim, J. Hone, L. Colombo and R. S. Ruoff, "Oxygen-activated growth and bandgap tunability of large single-crystal bilayer graphene," *Nature Nanotechnology*, vol. 11, pp. 426-431, 2016.
- [206] Y. Hao, M. S. Bharathi, L. Wang, Y. Liu, H. Chen, S. Nie, X. Wang, H. Chou, C. Tan, B. Fallahzad, H. Ramanarayan, C. W. Magnuson, E. Tutuc, B. I. Yakobson, K. F. McCarty, Y. W. Zhang, P. Kim, J. Hone, L. Colombo and R. S. Ruoff, "The role of surface oxygen in the growth of large single-crystal graphene on copper," *Science*, vol. 342, no. 6159, pp. 720-723, 2013.
- [207] L. Brown, R. Hovden, P. Huang, M. Wojcik, D. A. Muller and J. Park, "Twinning and Twisting of Tri- and Bilayer Graphene," *Nano Letters*, vol. 12, no. 3, pp. 1609-1615, 2012.

- [208] J.-B. Liu, P.-J. Li, Y.-F. Chen, Z.-G. Wang, F. Qi, J.-R. He, B.-J. Zheng, J.-H. Zhou, W.-L. Zhang, L. Gu and Y.-R. Li, "Observation of tunable electrical bandgap in large-area twistered bilayer graphene synthesised by chemical vapour deposition," *Scientific Reports*, vol. 5, 2015.
- [209] S. Nie, W. Wu, S. Xing, Q. Yu, J. Bao, S.-s. Pei and K. F. McCarty, "Growth from below: bilayer graphene on copper by chemical vapor deposition," *IOP New Journal of Physics*, vol. 14, 2012.
- [210] S. Graphenea, "Method of manufacturing a graphene monolayer on insulating surfaces". United States of America Patent US20140001152, 2 January 2014.
- [211] J. Song, F.-Y. Kam, R.-Q. Png, W.-L. Seah, J.-M. Zhuo, G.-K. Lim, P. H. K. Ho and L.-L. Chua, "A general method for transferring graphene onto soft surfaces," *Nature Nanotechnology*, vol. 8, pp. 356-362, 2013.
- [212] G. J. M. Fechine, I. Martin-Fernandez, G. Yiapanis, R. Bentini, E. S. Kulkarni, R. V. B. de Oliveria, X. Hu, I. Yarovsky, A. H. Castro Neto and B. Ozyuilmaz, "Direct Dry Transfer of Chemical Vapour Deposition Graphene to Polymeric Substrates," *Carbon*, vol. 83, pp. 224-231, 2015.
- [213] Microchemicals, "Lift-off Processes with Photoresists," November 2013. [Online]. Available: http://www.microchemicals.com/technical_information/lift_off_photoresist.pdf. [Accessed June 2016].
- [214] [Online]. Available: <https://www.microsi.com/the-difference-between-positive-and-negative-photoresist/>. [Accessed December 2017].
- [215] [Online]. Available: <http://precisionatomics.com/Products/products.html>. [Accessed December 2017].
- [216] A. V. Kretinin, Y. Cao, J. S. Tu, G. L. Yu, R. Jalil, K. S. Novoselov, S. J. Haigh, A. Gholinia, A. Mishchenko, M. Lozada, T. Georgiou, C. R. Woods, F. Withers, P. Blake, G. Eda, A. Wirsig, C. Hucho, K. Watanabe, T. Taniguchi, A. K. Geim and R. V. Gorbachev, "Electronic Properties of Graphene Encapsulated with Different Two-Dimensional Atomic Crystals," *Nano Letters*, vol. 14, no. 6, pp. 3270-3276, 2014.
- [217] Y. Jie, J. Kunpeng, S. Yajuan, C. Yang and Z. Chao, "Hysteresis analysis of graphene transistor under repeated test and gate voltage stress," *Journal of Semiconductors*, vol. 35, no. 9, 2014.
- [218] S. Sanders, A. Cabrero-Vilatela, P. R. Kidambi, J. A. Alexander-Webber, C. Weijtens, P. Braeuninger-Weimer, A. I. Aria, M. M. Qasim, T. D. Wilkinson, J. Robertson, S. Hofmann and J. Meyer, "Engineering high charge transfer n-doping of graphene electrodes and its application to organic electronics," *Nanoscale*, vol. 7, pp. 13135-13142, 2015.
- [219] J. Meyer, P. R. Kidambi, B. C. Bayer, C. Weijtens, A. Kuhn, A. Centeno, A. Pesquera, A. Zurutuza, J. Robertson and S. Hofmann, "Charge Transfer Doping and Band Alignment of Graphene Electrodes for Efficient Organic Light Emitting Diodes," *Scientific Reports*, vol. 4, 2014.
- [220] J. Dauber, B. Terres, S. Trelenkamp and C. Stampfer, "Encapsulating graphene by ultra-thin alumina for reducing process contaminations," *Physica Status Solidi B*, vol. 249, no. 12, pp. 2526-2529, 2012.
- [221] [Online]. Available: <http://bondingsource.com/techdata/4445.pdf>. [Accessed December 2017].
- [222] Z. H. Ni, H. M. Wang, Z. Q. Luo, Y. Y. Wang, Y. Ting, Y. H. Wu and Z. X. Shen, "The effect of vacuum annealing on graphene," *Journal of Raman Spectroscopy*, vol. 41, pp. 479-483, 2009.

- [223] "Scanning Electron Microscopy," Materials Evaluation and Engineering, Inc, [Online]. Available: <http://www.mee-inc.com/hamm/scanning-electron-microscopy-sem/>. [Accessed March 2015].
- [224] D. McMullan, "Scanning Electron Microscopy 1928-1965," in *Microscopy Society of America*, Cincinnati, 1993.
- [225] H. Hiura, H. Miyazaki and K. Tsukagoshi, "Determination of the Number of Graphene Layers: Discrete Distribution of the Secondary Electron Intensity Derived from Individual Graphene Layers," *Applied Physics Express*, vol. 3, no. 9, 2010.
- [226] S. Bertolazzi, J. Brivio, A. Radenovic, A. Kis, H. Wilson, L. Prsbrey, E. Minot, A. Tselev, M. Philips, M. Viani, D. Walters and R. Proksch, "Exploring flatland: AFM of mechanical and electrical properties of graphene, MoS₂ and other low-dimensional materials," *Microscopy and Analysis*, 2013.
- [227] T. Burnett, R. Yakomova and O. Kazakova, "Mapping of Local Electrical Properties in Epitaxial Graphene Using Electrostatic Force Microscopy," *Nanoletters*, vol. 11, no. 6, pp. 2324-2328, 2011.
- [228] J. Heath, July 2013. [Online]. Available: <http://www.microscopy-analysis.com/blog/blog-articles/exploring-graphene-atomic-force-microscopy>.
- [229] NPL, [Online]. Available: <http://www.npl.co.uk/topics/graphene/structural-characterisation-of-graphene-with-afm>. [Accessed April 2015].
- [230] P. Zhou, S. Yang, Q. Sun, L. Chen, P. Wang, S. Ding and D. W. Zhang, "Direct Deposition of Uniform High-k Dielectrics on Graphene," *Scientific Reports*, no. doi:10.1038/srep06448, 2014.
- [231] Y. Jie, J. Kunpeng, S. Yajuan, C. Yang and Z. Chao, "Hysteresis analysis of graphene transistor under repeated test and gate voltage stress," *Journal of Semiconductors*, vol. 35, no. 9, 2014.
- [232] H. Wang, Y. Wu, C. Cong, J. Shang and T. Yu, "Hysteresis of Electronic Transport in Graphene Transistors," *ACS Nano*, vol. 4, no. 12, pp. 7221-7228, 2010.
- [233] M. Niedermayer, K. Lakhmankiy, M. Kumph, S. Partel, J. Edlinger, M. Brownutt and R. Blatt, "Cryogenic surface ion trap based on intrinsic silicon," *New Journal of Physics*, vol. 2016, p. 113068, 2014.
- [234] Oxford Instruments, [Online]. Available: http://www.oxford-instruments.cn/OxfordInstruments/media/nanoscience/Principles-of-dilution-refrigeration_v14.pdf. [Accessed March 2018].
- [235] [Online]. Available: http://imu.web.psi.ch/docu/manuals/bulk_manuals/OxfordInstruments/Dolly_Mark_II/Heliox_Principle_of_Operation_and_Control.pdf. [Accessed February 2018].
- [236] Farnell, [Online]. Available: http://www.farnell.com/datasheets/1884498.pdf?_ga=2.226750741.90370598.1515876324-1060051753.1515876324. [Accessed January 2018].
- [237] Epotek, [Online]. Available: [http://www.epotek.com/site/files/brochures/pdfs/SAS-Cryogenic_Temperature_and_Epoxy\(1\).pdf](http://www.epotek.com/site/files/brochures/pdfs/SAS-Cryogenic_Temperature_and_Epoxy(1).pdf). [Accessed January 2018].
- [238] V. Savinov, Novel Toroidal and Superconducting Metamaterials, University of Southampton, 2014.
- [239] Z. Luo, S. Lim, Z. Tian, J. Shang, L. Lai, B. Macdonald, C. Fu, Z. Shen, T. Yu and J. Lin, "Pyridinic N doped graphene: synthesis, electronic structure and electrocatalytic property," *Journal of Materials Chemistry*, vol. 8038, 2011.
- [240] Janis, [Online]. Available: <https://www.janis.com/products/AccessoriesandAncillaryEquipment/WindowTransmiss>

- ionCurves.aspx. [Accessed January 2018].
- [241] Testo, [Online]. Available: https://www.testo.co.uk/testo-875-1i-thermal-imaging-camera?gclid=EAlaIqobChMIpe-VzbaF2AIVEuEbCh2NJwLIEAAYBCAAEgJsw_D_BwE. [Accessed December 2017].
- [242] [Online]. Available: http://www.spectralcalc.com/blackbody_calculator/blackbody.php. [Accessed February 2018].
- [243] Teravil, [Online]. Available: <http://www.teravil.it/emitter.php>. [Accessed February 2018].
- [244] S. I. Lepeshov, A. Gorodetsky, A. E. Krasnok, E. U. Rafailov and P. A. Belov, "Enhancement of Terahertz Photoconductive Antennas and Photomixers Operation by Optical Nanoantennas," *Arxiv*, vol. arXiv:1607.07233v, 2016.
- [245] D. H. Auston, K. P. Cheung and P. R. Smith, "Picosecond Photoconducting Hertzian Dipoles," *Journal of Applied Physics*, vol. 45, pp. 284-286, 1984.
- [246] Stanford Research Systems, [Online]. Available: www.thinksrs.com/downloads/PDFs/ApplicationNotes/AboutLIAs.pdf. [Accessed 22 September 2016].
- [247] J. M. Maxson. [Online]. Available: <http://www.lehigh.edu/~jph7/website/Physics262/aMaxsonLockIn.pdf>. [Accessed 22 September 2016].
- [248] Stanford Research Systems, [Online]. Available: <http://www.thinksrs.com/downloads/PDFs/ApplicationNotes/AboutLIAs.pdf>. [Accessed 24 December 2016].
- [249] M. R. Stone, M. Naftaly, R. E. Miles, J. R. Fletcher and D. P. Steenson, "Electrical and Radiation Characteristics of Semilarge Photoconductive Terahertz Emitters," *IEEE Transactions on Microwave Theory and Techniques*, vol. 52, no. 10, pp. 2420-2429, 2004.
- [250] "PV Education," [Online]. Available: <http://www.pveducation.org/pvcdrom/materials/optical-properties-of-silicon>. [Accessed December 2017].
- [251] NIST, [Online]. Available: <https://physics.nist.gov/cgi-bin/ffast/ffast.pl?Z=14&Formula=>ype=5&range=S&lower=0.001&upper=433&density=>. [Accessed December 2017].
- [252] D. R. Lamb, "Some Electrical Properties of the Silicon-Silicon Dioxide System," *Thin Solid Films*, vol. 5, pp. 247-276, 1970.
- [253] M. Schulz, "Interface States at the SiO₂-Si Interface," *Surface Science*, vol. 132, pp. 422-455, 1983.
- [254] [Online]. Available: https://ecee.colorado.edu/~bart/book/book/chapter4/ch4_3.htm. [Accessed March 2018].
- [255] D. K. Schroder, "Carrier Lifetimes in Silicon," *IEEE Transactions on Electron Devices*, 1997.
- [256] U. Sassi, R. Parret, S. Nanot, M. Bruna, S. Borini, D. De Fazio, Z. Zhao, E. Lidorikis, F. H. L. Koppens, A. C. Ferrari and A. Colli, "Graphene-based mid-infrared room-temperature pyroelectric bolometers with ultrahigh temperature coefficient of resistance," *Nature Communications*, vol. 8, p. 14311, 2017.
- [257] Z. Tian, S. Lee and G. Chen, "A Comprehensive Review of Heat Transfer in Thermoelectric Materials and Devices," *Arxiv*, 2014.
- [258] Coherent, [Online]. Available: <https://www.coherent.com/assets/pdf/2011-Diode-Laser->

- Modules-and-Pattern-Generators-Catalog.pdf#page=45. [Accessed January 2018].
- [259] Thorlabs, [Online]. Available: https://www.thorlabs.com/newgrouppage9.cfm?objectgroup_id=6905. [Accessed February 2018].
- [260] [Online]. Available: <http://dunham.ee.washington.edu/ee531/notes/SemiRev.pdf>. [Accessed January 2018].
- [261] [Online]. Available: <http://www.ioffe.ru/SVA/NSM/Semicond/Si/electric.html>. [Accessed December 2017].
- [262] O. Madelung, U. Rossler and M. Schulz, "Silicon, capture coefficients and capture cross-sections for impurities and defects," in *Impurities and Defects in Group IV Elements, IV-IV and III-V Compounds Part a: Group IV Elements*, Berlin, Heidelberg, Springer, 2002, pp. 1-11.
- [263] M. Tuan Trinh, M. Y. Sfeir, J. J. Choi, J. S. Owen and X. Zhu, "A Hot Electron-Hole Pair Breaks the Symmetry of a Semiconductor Quantum Dot," *Nanoletters*, vol. 13, pp. 6091-6097, 2013.
- [264] M. Tuan Trinh, X. Wu, D. Niesner and X.-Y. Zhu, "Many-body interaction in photoexcited lead iodide perovskite," *Journal of Materials Chemistry A*, vol. 3, pp. 9285-9290, 2015.
- [265] C. N. Berglund, "Surface States at Steam-Grown Silicon-Silicon Dioxide Interfaces," *IEEE Transactions on Electron Devices*, vol. 13, no. 101, pp. 701-705, 1966.
- [266] Mirion Technologies, [Online]. Available: http://www.canberra.com/products/radiochemistry_lab/nim-preamplifiers.asp. [Accessed January 2018].
- [267] University of Potsdam, [Online]. Available: <http://www.uni-potsdam.de/u/physik/fprakti/anleiW5.pdf>. [Accessed January 2018].
- [268] C. Chakraborty, R. Beams, K. M. Goodfellow, G. W. Wicks, L. Novotny and A. N. Vamivakas, "Optical Antenna Enhanced Graphene Photodetector," *Applied Physics Letters*, vol. 105, p. 241114, 2014.
- [269] S. W. Howell, I. Ruiz, P. S. Davids, R. K. Harrison, S. W. Smith, M. D. Goldflam, J. B. Martin, N. J. Martinez and T. E. Beechem, "Graphene-Insulator-Semiconductor Junction for Hybrid Photodetection Modalities," *Scientific Reports*, vol. 7, p. 14651, 2017.
- [270] Photek, [Online]. Available: <http://www.photek.com/pdf/datasheets/electronics/LPG-650.pdf>. [Accessed March 2018].
- [271] Amptek, [Online]. Available: <http://amptek.com/products/mini-x-ray-tube/>. [Accessed January 2018].
- [272] H. Akamatsu, L. Gottardi, J. van der Kuur, C. P. de Vries, K. Ravensburg, J. S. Adams, S. R. Bandler, M. P. Bruijn, J. A. Chervenak, C. A. Kilbourne, M. Kiviranta, A. J. van der Linden, B. D. Jackson and S. J. Smith, "Development of frequency domain multiplexing for the X-ray Integral Field Unit (X-IFU) on the Athena," in *Proceedings Volume 9905, Space Telescopes and Instrumentation 2016: Ultraviolet to Gamma Ray*, Edinburgh, 2016.
- [273] [Online]. Available: <http://www.nhs.uk/conditions/angiography/Pages/Introduction.aspx>. [Accessed March 2017].
- [274] [Online]. Available: <http://www.nhs.uk/conditions/DEXA-scan/Pages/Introduction.aspx>. [Accessed March 2017].
- [275] [Online]. Available: <http://www.xrayrisk.com/calculator/calculator-normal-studies.php?id=45>. [Accessed March 2017].

- [276] S. Chung, S. Shrestha, X. Wen, Y. Feng, N. Gupta, H. Xia, P. Yu, J. Tang and G. Conlbeer, "Evidence for a large phononic band gap leading to slow hot carrier thermalisation," *2014 IOP Conf. Ser Mater. Sci. Eng*, vol. 68, no. 012002, 2014.
- [277] J. G. Harper, H. E. Matthews and R. H. Bube, "Photothermoelectric Effects in Semiconductors: n- and p-Type Silicon," *Journal of Applied Physics*, vol. 41, no. 765, 1970.
- [278] L. Dobrzanski, E. Nossarzewska-Orlowska, Z. Nowak and J. Piotrowski, "Micromachine silicon bolometers as detectors of soft X-ray, ultraviolet, visible and infrared radiation," *Sensors and Actuators A: Physical*, vol. 60, no. 1-3, pp. 154-159, 1997.
- [279] F. S. Porter. [Online]. Available: <http://www.issibern.ch/forads/sr-009-28.pdf>. [Accessed March 2018].
- [280] T. Tanaka, M. Kato, N. Saito, K. Tono, M. Yabashi and T. Ishikawa, "Room-temperature calorimeter for x-ray free-electron lasers," *Rev. Sci. Instrum.*, vol. 86, no. 9, p. 093104, 2015.
- [281] NASA, [Online]. Available: https://phonon.gsfc.nasa.gov/qcal/qcal_basics.html. [Accessed March 2018].
- [282] Ioffe Physico-Technical Institute, [Online]. Available: <http://www.ioffe.ru/SVA/NSM/Semicond/Si/thermal.html>. [Accessed March 2018].
- [283] X. Du, D. E. Prober, H. Vora and C. McKitterick, "Graphene-based bolometers," *Arxiv*, vol. <https://arxiv.org/ftp/arxiv/papers/1308/1308.4065.pdf>, 2013.
- [284] A. A. Ausman Jr. and F. B. McLean, "Electron-hole pair creation energy in SiO₂," *Applied Physics Letters*, vol. 26, no. 173, 1975.
- [285] P. Prochazka, D. Marecek, Z. Liskova, J. Cechal and T. Sikola, "X-ray induced electrostatic graphene doping via defect charging in gate dielectric," *Scientific Reports*, vol. 7, no. 563, 2017.
- [286] J. Zhang, E. Fretwurst, R. Klanner, H. Perrey, I. Pintilie, T. Poehlsen and J. Schwandt, "Study of X-ray radiation damage in silicon sensors," *Journal of Instrumentation*, vol. 6, 2011.
- [287] C. Prakash, "Thermal conductivity variation of silicon with temperature," *Microelectronics Reliability*, vol. 18, no. 4, p. 333, 1978.
- [288] T. Aizawa, S. Suehara and S. Otani, "Silicene on Zirconium Carbide," *Journal of Physical Chemistry*, vol. 118, pp. 23049-23057, 2014.
- [289] [Online]. Available: <http://cds.cern.ch/record/510171/files/0107398.pdf>. [Accessed March 2017].
- [290] E. Kamieniecki, "Effect of charge trapping on effective carrier lifetime in compound semiconductors: High Resistivity CdZnTe," *Journal of Applied Physics*, vol. 116, no. 193702, 2014.
- [291] R. H. Redus, "Monte Carlo Time Domain Noise Simulation in Nuclear Electronics," in *2008 IEEE Nuclear Science Symposium Conference Record*, Dresden, 2008.
- [292] Laser Focus World, [Online]. Available: <http://www.laserfocusworld.com/articles/print/volume-45/issue-9/features/ultraviolet-detectors-nitrides-push-performance-of-uv-photodiodes.html>. [Accessed November 2017].
- [293] [Online]. Available: <http://www.rcsb.org/pdb/explore/explore.do?sessionId=8EC214AE54A80DDF3B5BD0584638E388?structureId=3D24>. [Accessed March 2017].